Active tectonics of the Ordos Plateau, China

Timothy A. Middleton

Thesis submitted to the University of Oxford

for the degree of Doctor of Philosophy

in

Geology and Mineralogy



Department of Earth Sciences and Worcester College,

University of Oxford

Trinity Term, 2016

Supervised by Professor Richard Walker and Professor Barry Parsons

Declaration

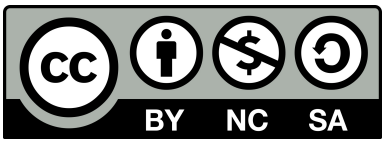
The contents of this thesis are all my own work, except where otherwise stated. The views and opinions expressed herein are mine and not necessarily those of any other person or body unless so attributed.

Citation: Middleton, T. A. (2016), Active tectonics of the Ordos Plateau, China, D.Phil. thesis, University of Oxford, Department of Earth Sciences, Oxford, UK.

Keywords: Continental Earthquakes, Faulting, Active Tectonics, Ordos Plateau, China.

This thesis has been typeset using LaTeX 2$_\varepsilon$, released under the LaTeX Project Public License (LPPL), and references were compiled using BibTeX. Most of the figures were produced using the open source Generic Mapping Tools (GMT) software, released under the GNU General Public License.

This work is licensed under the Creative Commons Attribution-NonCommercial-ShareAlike 4.0 International License. To view a copy of this license, visit the Creative Commons website.



Printed in the United Kingdom.

Abstract

Active tectonics of the Ordos Plateau, China

Timothy A. Middleton
Worcester College, Oxford

Trinity Term, 2016

This thesis is concerned with the active tectonics of the Ordos Plateau in northern China, an apparently non-deforming portion of continental lithosphere that sits at the northeastern edge of the India-Eurasia collision zone. Numerous, large-magnitude, historical earthquakes have occurred at the margins of the plateau, including some of the deadliest earthquakes in recorded human history. Furthermore, the adjacent North China Plain is one of the most densely populated regions on the planet, meaning that reliable seismic hazard assessments are of paramount importance.

We investigate the 1739 Yinchuan earthquake, on the western side of the Ordos Plateau, using ^{14}C dating and a new high-resolution Pleiades DEM of the entire rupture. We find that the event took place on the East Helanshan Fault and had a magnitude in the range M_w 7.1 to M_w 7.6, smaller than previously suggested. We then use IRSL and ^{10}Be dating, along with high-resolution Pleiades DEMs, to determine a right-lateral slip rate on the Luoshan Fault of 4.3±0.4 mm/a and a throw rate on the East Helanshan Fault of < 0.8±0.1 mm/a, indicating that north-south right-lateral shearing is the predominant tectonic motion on the western side of the Ordos Plateau. In the northern Shanxi Grabens, at the northeastern corner of the plateau, we observe good agreement between Quaternary, seismic and geodetic rates of strain, and we find that the region is extending at around 1 to 2 mm/a at an azimuth of approximately 151 °. However, there is a notable seismic strain rate deficit since 1750, which could indicate that we are quite late in the earthquake cycle with the potential for large earthquakes in the relatively near future. Finally, we combine our results with information from the literature to propose a kinematic model for the whole Ordos Plateau. We suggest that the plateau behaves as a pinned block, rotating anticlockwise within a large-scale WNW-ESE left-lateral shear zone. The previously enigmatic normal faulting at the margins of the Ordos block can then be explained as wedge-shaped grabens that develop during widening of the overall zone, or en echelon features that accommodate principally right-lateral motion.

Extended Abstract

Active tectonics of the Ordos Plateau, China

Timothy A. Middleton

Worcester College, Oxford

Trinity Term, 2016

This thesis focuses on the active faulting at the margins of the Ordos Plateau, which lies immediately northeast of the Tibetan Plateau in northern China. In Chapter 1 we start by describing general theories of continental deformation and some of the large-scale features of the India-Eurasia collision zone. The Ordos Plateau is of particular interest because it appears to behave as a non-deforming crustal block (with major earthquakes only occurring at the margins of the plateau), within a continental collision zone that is otherwise well modelled as a continuously deforming medium. We then describe the nature of seismic hazard on the continents, and in China specifically. Large death tolls in recent Chinese earthquakes, including the 1920 Haiyuan, the 1976 Tangshan and the 2008 Wenchuan events, are one of the main motivations for the type of research conducted in the rest of this thesis. Subsequent chapters examine different aspects of the active tectonics of the Ordos Plateau at a range of temporal and spatial scales.

In Chapter 2 we investigate a large continental normal-faulting earthquake which occurred in the Yinchuan Graben on the western side of the Ordos Plateau on 3rd January 1739. This event is of significance for two reasons. Firstly, it has been suggested on the basis of historical records of shaking that this was a magnitude 8.0 event. If this is true, the 1739 earthquake would be one of the largest continental normal-faulting earthquakes ever recorded and this should prompt us to consider the factors contributing to its unusual

size. Secondly, there has been some debate in the literature about the causative structure, with at least three different faults posited as the seismogenic source. We use five ^{14}C ages to date a series of scarps on the East Helanshan Fault, which lies to the west of the graben. We bracket the time of scarp formation to the last 350 years and hence conclude that the East Helanshan Fault was responsible for the 1739 earthquake. We then use high-resolution, stereo imagery from the Pleiades satellites to build a 1 to 2 m resolution digital elevation model (DEM) of the fault and combine this with field observations to map the rupture in detail. We then construct a throw distribution, determine the slip vector azimuth and re-assess the earthquake magnitude using simple scaling relationships. We conclude that the 1739 earthquake had a rupture length of approximately 87 km, a maximum throw of 5.1 m and an average throw of 3.0 m, yielding a best estimate magnitude in the range of M_w 7.1 to M_w 7.6. We suggest that the previous magnitude estimates are biased by enhanced shaking of the sediments within the Yinchuan Graben.

Analysis of the locus, style and rates of faulting is fundamental to understanding the kinematics of continental deformation. Previous studies have suggested that the Ordos Plateau behaves rigidly and rotates anticlockwise within a large-scale zone of WNW-ESE left-lateral shearing. For this rotation to be accommodated the eastern and western margins of the plateau should be undergoing right-lateral shearing, and yet the dominant faulting style appears to be extensional. In Chapters 3 and 4 we focus specifically on the kinematics of the faults bounding the western margin of the Ordos Plateau and make new slip rate estimates for two of the major faults in the region: the right-lateral strike-slip Luoshan Fault and the normal-slip East Helanshan Fault. We use IRSL dating of offset landforms with high-resolution imagery and image-derived topography from the Pleiades satellites to determine an average right-lateral slip rate of 4.3±0.4 mm/a (1σ uncertainties) on the Luoshan Fault. Similarly, we use ^{10}Be exposure dating to determine a vertical throw rate on the East Helanshan Fault of $< 0.8\pm0.1$ mm/a, corresponding to an extension rate of $< 1.0\pm0.1$ mm/a (1σ uncertainties). We therefore conclude that right-lateral shearing is the dominant motion occurring in the western Ordos region.

Discrepancies between geological, seismic and geodetic rates of strain can indicate that rates of crustal deformation, and hence seismic hazard, are varying through time. In

Chapter 5 we focus on the northern Shanxi Grabens, at the northeastern corner of the Ordos Plateau, where previous studies have found extension rates of anywhere between 0 and 6 mm/a at an azimuth of between 95 and 180 °. We determine extension rates across the northern Shanxi Grabens from: offset geomorphological features and a variety of Quaternary dating techniques (including new IRSL and Ar-Ar ages); a Kostrov summation using a 700 year catalogue of historical earthquakes; and recent campaign GPS measurements. We observe good agreement between Quaternary, seismic and geodetic rates of strain, and we find that the northern Shanxi Grabens are extending at around 1 to 2 mm/a at an azimuth of ≈ 151 °. The azimuth of extension is particularly well constrained and can be reliably inferred from catalogues of small earthquakes. We do not find evidence for any substantial variations in extension rate through time, though there is a notable seismic strain rate deficit since 1750. This deficit could indicate aseismic accommodation of deformation, or that we are quite late in the earthquake cycle with the potential for larger earthquakes in the relatively near future. The lack of recent earthquakes in the northern Shanxi Grabens may also be explained by models of continental deformation that involve complex fault interactions across large regions; earthquakes may be switching from one set of faults to another on timescales of hundreds to thousands of years.

Finally, in Chapter 6, we summarise the active tectonics of the whole Ordos Plateau, incorporating our results from the previous chapters. We include Quaternary fault slip rates, a new set of Kostrov summations, and the latest campaign GPS measurements. We describe previous kinematic models for the Ordos region and then develop our own anticlockwise rotation model, which also accounts for the widespread normal faulting that is apparent at many of the margins of the Ordos block. Simple calculations are used to predict how we would expect our model to behave. We conclude that the majority of observations are consistent with our proposed kinematic model in which the Ordos Plateau rotates anticlockwise within a large-scale zone of WNW-ESE left-lateral shearing. Left-lateral shear of ≈ 8 mm/a exists to the west of the plateau, of which ≈ 4.5 mm/a is taken up on the Haiyuan Fault. Around 3 mm/a is absorbed as shortening in the Liupanshan, leaving ≈ 5 mm/a of shear to be taken up by anticlockwise rotation of the whole Ordos

Plateau. This is achieved via right-lateral motion on the eastern and western sides of the block at Quaternary rates of ≈ 4 mm/a. However, we also note that the recent GPS is not able to detect any right-lateral motion in the central Shanxi Grabens on the eastern side of the plateau. Again, this discrepancy could be explained by a complex earthquake switching model in which regional strains are accommodated on different sets of faults at different times.

Acknowledgements

First and foremost I would like to thank my supervisors, Richard Walker and Barry Parsons, for their continual guidance throughout the last four years. Yu's birthday celebrations in China (and the subsequent karaoke) will live long in the memory. I am also indebted to Philip England for many stimulating and helpful discussions about continental tectonics, and to my examiners Conall Mac Niocaill and Alex Densmore for their constructive feedback.

I have been fortunate to have received financial support for this work from the Natural Environment Research Council (NERC) and a University of Cambridge Harkness Scholarship. Funding for fieldwork, satellite imagery and Quaternary dating has also been provided by the Centre for Observation and Modelling of Earthquakes, Volcanoes and Tectonics (COMET), the Looking inside the Continents from Space (LiCS) large grant, and the NERC/ESRC Earthquakes without Frontiers (EwF) consortium.

50.03 (or S4 for the oldies) has been a fruitful place to work. John Elliott, in particular, has always been incredibly generous with his time and expertise. His meticulous approach and GMT wizardry have greatly improved this thesis. David Mackenzie's technical know-how and superior patience with computers have also proved invaluable on many occasions. Discussions with Al Sloan and Austin Elliott regularly yielded thoughtful new avenues to pursue. Meanwhile, the wider COMET entourage—especially Grace Campbell, Richard Walters, Eleanor Ainscoe, Will Hutchison, Christoph Gruetzner, Ekbal Hussain and Ruth Amey—have provided cheery smiles and warm encouragement. Lastly, I owe a huge debt of gratitude to Yu Zhou. Translator, tour guide, field assistant, navigator, tutor, proof-reader, co-red-wine-drinker, panda-joker-extraordinaire and friend: much of this would not have been possible without you.

Two very enjoyable field trips in China were made possible by Peizhen Zhang and his colleagues at the China Earthquake Administration. Weitao Wang, Qiyun Lei, Zhikun Ren, Jingxing Yu, Xiaogang Song and Ji Ma all gave willingly of their time in the field and searched diligently for "eggs and tomatoes" on the menu of every restaurant we visited. Our drivers, Wuxiong Cheng, Zhigang Ma and Cheng Fu (Mr Fu), remained ever jovial and patient as I pored over grubby Google Earth printouts swearing that, "there's a road here somewhere". Mr Fu should also be thanked for introducing us to báijiǔ (Chinese wine). In large quantities. Every night. Without exception. Fanghui Deng and Yiming Chen have tirelessly searched the Chinese literature on my behalf. And a short, bonus field trip to Dixie Valley in the Basin and Range was made possible by the kind hospitality of Steve Angster.

The nature of research in tectonic geomorphology is such that one becomes heavily reliant on collaborators who are experts in various Quaternary dating techniques. Stephen Harris readily identified my radiocarbon samples, whilst Richard Staff and Hayley Sula took care of them in the lab. Ed Rhodes masterfully guided me through the intricate world of luminescence dating and Rob Ashurst assisted with many of my samples in the dark room. Dylan Rood's enthusiasm and efficiency helped to brighten the otherwise grey weeks spent working on cosmogenic samples in East Kilbride. Owen Green, Steve Wyatt, Victoria Forbes, Maria Miguens-Rodriguez and Kathy Keefe all assisted at various stages of sample preparation. Finally, Sarah Sherlock and James Malley helped adeptly with my Ar-Ar samples. Back in Oxford, the Postgrads12 team have provided camaraderie and distraction, whilst Steve Usher and May Chung have been on hand to help troubleshoot my computer woes.

Outside of the office, I would like to thank my housemates at 22: Tom, Anna and Matt. It has been most enjoyable sharing culinary experiments, micro table tennis and, most of all, the famous "book of quotations" with you over the last two years. Long may it ruin our burgeoning political careers. Asger and Phil: many thanks for your friendship and all of the burritos. I am also hugely thankful for the communities I have been a part of at the University Church and the Woodroffe Society; you have all provided valuable

ongoing support. There are also many others who have contributed in various ways. Alas, I don't have space to name you all here.

Finally, I owe an awful lot to my family. My parents have nurtured me (emotionally, nutritionally and financially) throughout my decades in education. I am exceptionally grateful and I promise to get a "real job" one day (just not quite yet). Ian, the detailed statistics on your near-daily athletic endeavours have reminded me that I have no excuse for feeling as tired as I do. Thank you. And lastly, Claire, your love and companionship have made the past few years inestimably more fun. If Graham Norton had not been there to distract you, then this thesis would have taken considerably longer to finish.

Contents

Declaration . . . iii

Abstract . . . vii

Extended Abstract . . . ix

Acknowledgements . . . xiii

Contents . . . xxi

List of Figures . . . xxvii

List of Tables . . . xxviii

1 Introduction **1**

1.1 Continental tectonics . . . 1

1.2 The India-Eurasia collision . . . 3

1.3 Regional tectonic setting of the Ordos Plateau . . . 6

1.3.1 The rigidity of the Ordos Plateau . . . 6

1.3.2 Extension around the Ordos Plateau . . . 8

1.4 Earthquake hazard . . . 9

1.4.1 Earthquake hazard on the continents . . . 9

1.4.2 Earthquake hazard in China . . . 12

1.5 Overview of this thesis . . . 19

1.6 Publications arising from this thesis . . . 22

2 The 1739 Yinchuan earthquake **25**

2.1 Introduction . . . 25

2.2 Tectonic setting . . . 29

2.2.1 Active faulting . . . 29

2.2.2 The deep structure of the Yinchuan Graben . . . 30
2.3 Background to the 1739 earthquake . . . 32
2.4 Methods . . . 35
2.4.1 ^{14}C dating . . . 35
2.4.2 DEM construction and DEM resolution . . . 36
2.4.3 Measurement of topographic profiles . . . 38
2.4.4 Scarp mapping and type locality calibration . . . 42
2.5 Results . . . 43
2.5.1 Palaeoseismological work on the East Helanshan Fault . . . 43
2.5.2 Geomorphology of the 1739 rupture . . . 50
2.6 Discussion . . . 59
2.6.1 The causative fault for the 1739 earthquake . . . 59
2.6.2 Characterising the 1739 earthquake . . . 62
2.7 Conclusions . . . 70

3 Slip rate on the Luoshan Fault 73
3.1 Introduction . . . 73
3.2 Tectonic setting . . . 75
3.3 Methods . . . 78
3.3.1 Pleiades data and DEM construction . . . 78
3.3.2 Offset measurements . . . 79
3.3.3 IRSL dating of offset features . . . 81
3.4 The Luoshan Fault . . . 84
3.4.1 Xiaoluoshan section . . . 87
3.4.2 Tanzhuangzicun section . . . 92
3.4.3 Shiyaodong site . . . 94
3.4.4 Machanggou site . . . 97
3.5 Discussion . . . 98

4 Throw rate on the East Helanshan Fault 99
4.1 Introduction . . . 99

4.2 Tectonic setting . . . 100
4.3 Methods . . . 102
4.3.1 Pleiades data and DEM construction . . . 102
4.3.2 Offset measurements . . . 104
4.3.3 ^{10}Be dating of offset features . . . 104
4.3.4 IRSL dating of offset features . . . 108
4.4 The East Helanshan Fault . . . 108
4.4.1 T5 at the northern end of the Suyukou scarps . . . 108
4.4.2 Central Suyukou scarps . . . 111
4.4.3 Helanshan range front . . . 115
4.4.4 Northern end of the East Helanshan Fault . . . 118
4.5 Discussion . . . 121
4.5.1 Rates of faulting along the western Ordos Plateau . . . 121
4.5.2 A geometric model for the western Ordos Plateau . . . 125
4.6 Conclusions . . . 126

5 Extension in the northern Shanxi Grabens 129

5.1 Introduction . . . 129
5.2 Previous work in the northern Shanxi Grabens . . . 130
5.3 Tectonic setting . . . 132
5.4 Methods . . . 135
5.4.1 DEMs and offset measurements . . . 135
5.4.2 Quaternary dating of offset features . . . 136
5.4.3 Ar-Ar dating . . . 137
5.4.4 Kostrov summations . . . 140
5.4.5 Strain rate field from GPS . . . 143
5.5 Fault slip rates from Quaternary geology . . . 144
5.5.1 Yuguang Graben Fault . . . 145
5.5.2 Liulengshan Fault . . . 149
5.5.3 Kouquan-Emokou Fault . . . 155

5.5.4 Summary of fault slip rates from Quaternary geology 157
5.6 Strain rates from seismicity 160
5.6.1 Rate of moment release in the northern Shanxi Grabens 160
5.6.2 Kostrov summations 160
5.7 Strain rate field from GPS 165
5.8 Discussion 170
5.8.1 Earthquake recurrence times from geodetic strain rates 170
5.8.2 Comparing magnitudes of strain 171
5.8.3 Comparing patterns of strain 173
5.9 Conclusions 177

6 Kinematics of the Ordos Plateau 179

6.1 Introduction: geological history and setting 179
6.2 Quaternary fault slip rates at the margins of the Ordos Plateau 182
6.2.1 The Haiyuan Fault 187
6.2.2 The Zhangjiakou-Bohai-Penglai Fault zone 189
6.2.3 The northern Ordos: the Linhe and Hetao Grabens 189
6.2.4 The southern Ordos: the Weihe Graben 195
6.2.5 The western Ordos: the Yinchuan Graben, the Luoshan and the Liupanshan 199
6.2.6 The eastern Ordos: the Shanxi Grabens 202
6.3 Kostrov summations at the margins of the Ordos Plateau 206
6.4 Present-day motions from GPS observations 214
6.4.1 A GPS-derived continuously varying strain rate field 214
6.4.2 Slip rate on the Zhangjiakou-Bohai-Penglai Fault zone 222
6.4.3 Slip rates on the Xizhoushan and Huoshan Faults 224
6.4.4 Slip rate on the Luonan and Danfeng Faults 224
6.4.5 Slip rates in the North China Plain 228
6.5 Existing kinematic models for the Ordos Plateau 230
6.5.1 Grabens as conjugate shear fractures 230

6.5.2 Anticlockwise rotation . . . 231
6.5.3 Left-lateral slip and rotation . . . 234
6.5.4 Crustal strength contrasts . . . 237
6.5.5 Existing Euler poles for the rotation of the Ordos Plateau . . . 237
6.6 The kinematic model proposed in this study . . . 240
6.6.1 Details of the kinematic model . . . 243
6.6.2 Tests of the kinematic model . . . 245
6.7 Discussion . . . 250
6.8 Conclusions from the whole thesis . . . 253
6.9 Suggestions for future work . . . 255

Bibliography **259**

Appendices **287**

A Walker steelyard beam balance **287**
A.1 Density determinations for ^{10}Be samples . . . 287

B Mathematical details **289**
B.1 Kostrov summations and principal strain rates . . . 289
B.2 Strain rate field from GPS . . . 291
B.2.1 Solving for the best-fitting rigid body rotation . . . 291
B.2.2 Calculating the strain rate field from GPS . . . 293
B.2.3 The effect of selecting different α values . . . 297
B.3 Calculating earthquake recurrence times . . . 299

C Interpreting strain rates **301**
C.1 Expected pattern of faulting from strain rates . . . 301

D Cardboard model of Ordos Plateau kinematics **305**
D.1 Video of the cardboard model . . . 305

List of Figures

1.1 From plate tectonics to continuum models of continental deformation . . . 2
1.2 Analogue plasticine models of the India-Eurasia collision . . . 4
1.3 Rigid inclusions in the India-Eurasia collision zone . . . 5
1.4 Instrumental earthquakes around the Ordos Plateau . . . 7
1.5 Maps of earthquake-related deaths 1900-2014 . . . 10
1.6 Earthquake deaths on the continents and at plate boundaries . . . 11
1.7 Historical earthquakes around the Ordos Plateau . . . 12
1.8 Chinese province boundaries . . . 14
1.9 Population density, seismic hazard and strain rate in northeastern Asia . . . 16
1.10 Population density map for the Ordos Plateau . . . 17
1.11 Seismic hazard map for the Ordos Plateau . . . 18
1.12 GPS-derived strain rate for the Ordos Plateau . . . 19
1.13 Regions covered by subsequent chapters in the thesis . . . 20
1.14 Methods for determining fault slip rates on different timescales . . . 21

2.1 Regional setting of the 1739 earthquake . . . 26
2.2 Fault map and cross-section for the Yinchuan Graben . . . 28
2.3 Pleiades DEM and rupture map for the 1739 earthquake . . . 34
2.4 Point density statistics for the Pleiades DEM . . . 37
2.5 Comparison of profiles from Pleiades DEM and theodolite . . . 41
2.6 Road-cut exposure through the Suyukou scarps . . . 45
2.7 Sampling sites on the Suyukou scarps . . . 47
2.8 ^{14}C dates from the Suyukou scarps . . . 49

2.9 Fault scarps in the Xiashigou segment 1 . . . 52
2.10 Fault scarps in the Xiashigou segment 2 . . . 53
2.11 Lack of scarps behind Shizuishan city . . . 54
2.12 Fault scarps in the Jianquan segment . . . 54
2.13 Fault scarps in the Hongguozigou segment . . . 58
2.14 Summary of results in the Yinchuan Graben . . . 60
2.15 Offset T0 surface near the Great Wall . . . 61
2.16 Throw distribution for the 1739 earthquake . . . 63
2.17 Determination of slip vector azimuth . . . 66

3.1 Regional setting of the western Ordos Plateau . . . 74
3.2 Tectonic map of the western Ordos Plateau, Ningxia Province . . . 77
3.3 Luoshan Fault: location map and Pleiades DEM . . . 85
3.4 Geomorphological maps along the Luoshan Fault . . . 86
3.5 Lateral offsets on the Xiaoluoshan section . . . 90
3.6 Field photographs on the Xiaoluoshan section . . . 91
3.7 Lateral offsets on the Tanzhuangzicun section . . . 93
3.8 Lateral offsets at Shiyaodong and Machanggou . . . 95

4.1 Suyukou scarps: Pleiades DEM, geomorphology and surface roughness map 103
4.2 Pleiades imagery and topographic profiles for T5 alluvial surface . . . 109
4.3 ^{10}Be age results . . . 110
4.4 T1, T2, and T3 alluvial surfaces at the Suyukou scarps . . . 113
4.5 ^{10}Be samples from the Helanshan range front . . . 116
4.6 Lateral offsets at the northern end of the East Helanshan Fault . . . 119
4.7 Campaign GPS measurements in the western Ordos . . . 122
4.8 Geometric model of the faulting in the western Ordos . . . 126

5.1 Regional setting of the northern Shanxi Grabens . . . 132
5.2 Fault map for the northern Shanxi Grabens . . . 134
5.3 Ar-Ar plateau age diagram . . . 139
5.4 Fault scarps and topographic profiles at Guangling, Yuguang Graben Fault 146

5.5 Field photographs on the Yuguang Graben Fault 147
5.6 Field sites at the Jiugongkou overlap zone, Yuguang Graben Fault 148
5.7 Field sites at Qifengpocun, Liulengshan Fault 151
5.8 Field photographs of fault exposures on the Liulengshan Fault 154
5.9 Fault scarp and basaltic flow north of Datong 156
5.10 Summary of Quaternary extension rates in the northern Shanxi Grabens . 159
5.11 Historical earthquakes and moment release in the northern Shanxi Grabens 162
5.12 Kostrov summations for the northern Shanxi Grabens 163
5.13 Determining a continuous strain rate field from GPS 167
5.14 Second invariant of strain rate field and rotation rates 168
5.15 Extension from GPS profiles across the northern Shanxi Grabens 169
5.16 Fault striations, T axes and principal extension directions 175
5.17 Comparison of extension rates and extension azimuths 177

6.1 Major tectonic divisions in northeastern Asia 180
6.2 Lithospheric thickness map for the Ordos Plateau 181
6.3 Old fault maps for the Ordos Plateau 183
6.4 New fault map for the Ordos Plateau 186
6.5 Haiyuan Fault 188
6.6 Zhangjiakou-Bohai-Penglai Fault zone 190
6.7 Westward continuation of the Zhangjiakou-Bohai-Penglai Fault zone 191
6.8 Fault map for the Linhe and Hetao Grabens 192
6.9 Sketch of the Linhe and Hetao Grabens 194
6.10 Fault map for the Weihe Graben 196
6.11 Field photographs from the Weihe Graben 197
6.12 Fault map for the western Ordos Plateau 201
6.13 Fault map for the Shanxi Grabens 203
6.14 Kostrov summations at the margins of the Ordos Plateau 211
6.15 A GPS-derived strain rate field for the whole Ordos Plateau 216
6.16 Effect on the strain rate field of varying α and r_{max} 217

6.17 Final strain rate field for $\alpha = 80$ km and $r_{max} = 200$ km 218
6.18 Second invariant of strain rate field for $\alpha = 80$ km and $r_{max} = 200$ km . . . 219
6.19 Comparison between Kostrov summations and GPS-derived strain rates . . 220
6.20 Inferred mechanisms for historical earthquakes around the Ordos Plateau . 221
6.21 Slip rate on the Zhangjiakou-Bohai-Penglai Fault zone from GPS 223
6.22 GPS motion in the Shanxi Grabens 225
6.23 Offset gullies on the Xizhoushan and Huoshan Faults 226
6.24 GPS motion on the Luonan and Danfeng Faults 227
6.25 GPS motion in the North China Plain 229
6.26 Previous conjugate shear fracture models 230
6.27 Conjugate shear fracture model for Ordos Plateau kinematics 231
6.28 Previous anticlockwise rotation models 232
6.29 Previous left-lateral slip and rotation models 235
6.30 Left-lateral slip and rotation model for Ordos Plateau kinematics 235
6.31 Previous Euler poles 238
6.32 Kinematic model proposed in this study 242
6.33 Block rotation cartoon 1 243
6.34 Block rotation cartoon 2 244
6.35 Locations of previous palaeomagnetic samples 246
6.36 Left-lateral shearing across the Ordos block from GPS 248
6.37 Widening of overall zone from GPS 250
6.38 Reid-type and Wallace-type earthquake recurrence behaviour 252

A.1 Walker steelyard beam balance 288

B.1 Rigid body rotation 292
B.2 Strains from GPS 293
B.3 Azimuth histograms for different values of α 298

C.1 Interpretation of strain rate crosses 302
C.2 $tan\,(\phi)$ curve for faulting patterns 303
C.3 Phasor diagram for faulting patterns 303

List of Tables

1.1 The ten deadliest earthquakes globally since 1900 13

1.2 Translations of a few common Chinese characters 22

2.1 Vertical offset measurements from the Pleiades DEM 39

2.2 ^{14}C dating results 44

2.3 Fault parameters and magnitude estimates 68

3.1 Horizontal offset measurements on the Luoshan Fault 80

3.2 IRSL dating results for the Luoshan Fault 81

3.3 Calculated slip rates on the Luoshan Fault 88

4.1 ^{10}Be dating results 105

4.2 IRSL dating results for the East Helanshan Fault 108

4.3 Calculated throw rates and slip rates on the East Helanshan Fault 112

5.1 IRSL and Ar-Ar dating results from the northern Shanxi Grabens 137

5.2 Focal parameters (FP) for historical earthquakes in the northern Shanxi Grabens 142

5.3 Summary of Quaternary rates for major faults in the northern Shanxi Grabens 158

5.4 Summary of principal strain rate results from Kostrov summations in the northern Shanxi Grabens 161

5.5 Azimuths of maximum extension estimated from fault striations in the northern Shanxi Grabens 176

6.1 Summary of Quaternary rates for major faults around the Ordos Plateau . 184
6.2 Focal parameters for historical earthquakes around the Ordos Plateau . . . 207
6.3 Summary of results from Kostrov summations and GPS around the Ordos Plateau 213
6.4 Euler poles and rotation rates for previous kinematic models 239

Chapter 1

Introduction

1.1 Continental tectonics

This thesis is concerned with continental kinematics: descriptions of the tectonic deformation occurring at the surface of the Earth. The theory of plate tectonics states that the Earth's surface can be broken up into a number of rigid shell-like plates, whose relative motion can be described as rotations about Euler poles (*McKenzie and Parker*, 1967). All of the deformation is taken up in narrow zones tens to hundreds of kilometres wide at the edges of the plates, with no intraplate deformation.

It is widely recognised that plate tectonic theory is a good description of plate boundary kinematics for the oceanic plates, but on the continents the situation is not so simple. Here, shallow seismicity extends thousands of kilometres away from the plate "boundaries", indicating that tectonic deformation is distributed across large networks of faults (*Thatcher*, 2009). For instance, in the India-Eurasia collision zone, 40 mm/a of relative motion is accommodated in a region that extends from Afghanistan in the west to the North China Plain in the east, and from the Himalayan front in the south to the Baikal rift in the north (*DeMets et al.*, 1990, 1994; *England and Molnar*, 1997; *Wang et al.*, 2001). Furthermore, the style of faulting in continental interiors is not always predictable from the nearby plate motions; for example, conjugate strike-slip faulting or reverse faulting can both accommodate shortening (*McKenzie and Jackson*, 1983; *Jackson and McKenzie*, 1988).

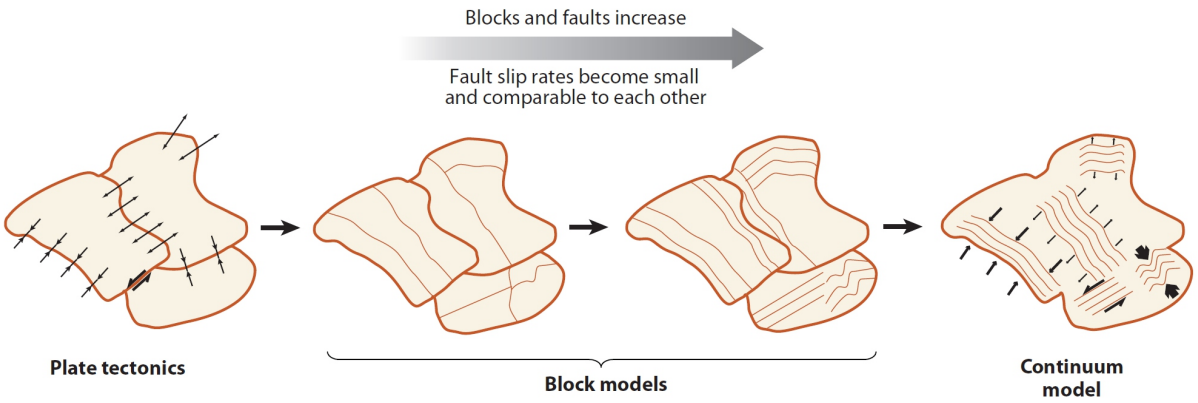


Figure 1.1: Cartoon from *Thatcher* (2009) showing the continuous spectrum of kinematic descriptions, from plate tectonics, through block models, to continuum models. Fault slip rates become comparable to each other over the course of the transition. Bold lines denote major block boundary faults, and thin lines are faults delimiting smaller blocks.

Since the advent of plate tectonics, two end-member models have therefore been formulated to try to describe continental tectonics (see Figure 1.1). One possible solution to the problem is to split the continents into smaller rigid blocks (or microplates) on the 100 to 1000 km length scale (*Molnar and Tapponnier*, 1975; *Peltzer and Saucier*, 1996; *Tapponnier et al.*, 2001). These rigid blocks are separated by major lithospheric faults and driven by forces at their edges, much like in plate tectonics. In theory, the motion of each block can be determined from measurements of surface motion and the slip rates on the bounding faults can be predicted (*Meade and Hager*, 2005; *Hammond et al.*, 2011). Such block models have been widely applied to explain the active tectonics of northeast Asia (*Deng et al.*, 2003; *Fan and Ma*, 2003; *Li et al.*, 2003), and in China it is suggested that 80 to 90% of earthquakes with $M > 7$ have occurred at the boundaries of proposed rigid blocks (*Zhang et al.*, 2003a). Yet it is unclear how useful these descriptions really are: many supposedly rigid blocks also appear to deform internally (*Zhang and Gan*, 2008).

The second solution is to treat the continental lithosphere as a continuously deforming viscous fluid, driven by both boundary forces and buoyancy forces within the fluid (*Bird and Piper*, 1980; *England and McKenzie*, 1982; *Houseman and England*, 1986; *Flesch et al.*, 2001; *England and Molnar*, 2005). These continuum models are typically concerned with length scales larger than the thickness of the lithosphere ($\approx$ 100 km) and do not

attempt to characterise the upper crustal deformation occurring on smaller length scales. Block models approach continuum models as the number of blocks is increased and the dimension of each block is decreased (see Figure 1.1).

Block models of continental deformation tend to concentrate strain at block boundaries and hence underestimate the strain in the interior of blocks. Furthermore, without a complete fault map, there is a serious risk of underestimating the seismic hazard away from the known faults. On the other hand, continuum models tend to smear out regions of high strain rate and neglect the manifestly discontinuous behaviour of the seismogenic upper crust. In addition, block modelling often assumes that surface motion is controlled by the strength of the upper crust, whereas continuum modelling assumes that deformation is principally driven by flow in the lower lithosphere (*Bourne et al.*, 1998).

1.2 The India-Eurasia collision

India collided with Eurasia ≈ 50 Ma ago resulting in the formation of the Tibetan Plateau (*Green et al.*, 2008; *Molnar and Stock*, 2009). *Molnar et al.* (1993) estimated that the rate of convergence between India and Eurasia halved from 100 to 50 mm/a between 50 and 40 Ma ago, whilst *Molnar and Stock* (2009) indicated a further slowing of India's convergence between 20 and 10 Ma ago of more than 40%. In total, an estimated 2500 km of convergence has been accommodated (*Zhang et al.*, 1995).

Today, it is thought that the India-Eurasia collision continues via a combination of lateral extrusion and vertical thickening. In the case of lateral extrusion, essentially rigid blocks are separated by major strike-slip faults such that lithospheric deformation is concentrated into narrow zones (*Tapponnier and Molnar*, 1976; *Tapponnier et al.*, 1982; *Peltzer and Tapponnier*, 1988; *Peltzer et al.*, 1989; *Avouac and Tapponnier*, 1993; *Replumaz and Tapponnier*, 2003). The lateral extrusion model therefore suggests high slip rates on the major strike-slip faults to the north and east of the Tibetan Plateau: for example, *Peltzer and Tapponnier* (1988) estimated a total geological offset on the Karakoram Fault of 1000 km and *Peltzer et al.* (1989) estimated a total offset on the Altyn Tagh Fault of 500 km with a slip rate of 20 to 30 mm/a. The central idea is that the overall

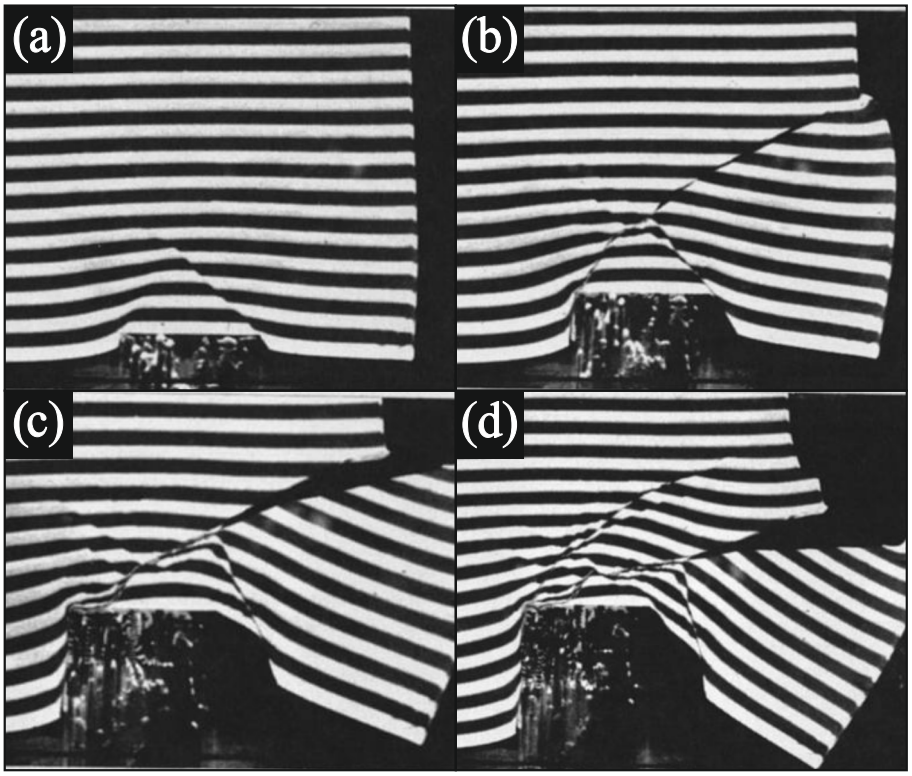


Figure 1.2: Analogue plasticine models of the India-Eurasia collision and lateral extrusion from *Peltzer and Tapponnier* (1988). (a), (b), (c) and (d) show four successive stages of deformation as the rigid indenter is moved north into the plasticine strips. Plane strain (no vertical thickening) was maintained by keeping the plasticine between two horizontal perspex plates. The plasticine was unconstrained on the right hand side of the box.

pattern of faulting in Asia appears qualitatively analogous to the result of indenting a plastic medium with a rigid body in plane strain, a concept that has been illustrated using plasticine models (see Figure 1.2) (*Tapponnier et al.*, 1982; *Peltzer and Tapponnier*, 1988). The resulting slip lines, predicted by slip-line field theory, correspond to the major strike-slip faults in Tibet (*Tapponnier and Molnar*, 1976). Furthermore, the theory predicts secondary tension (and hence extension) at large distances from the initial indenter—corresponding to observed extension in the Baikal rift and northern China.

In the other end-member, representation of the continental lithosphere as a thin, viscous shell tends to favour crustal thickening and lower slip rates on the major strike-slip faults (*England and McKenzie*, 1982; *England and Houseman*, 1985; *England et al.*, 1985; *England and Houseman*, 1986). Though the debate continues, these models are generally preferred because: slip-line field theory is strictly only applicable at the onset of deformation and breaks down as deformation progresses; viscous shell models allow for the full

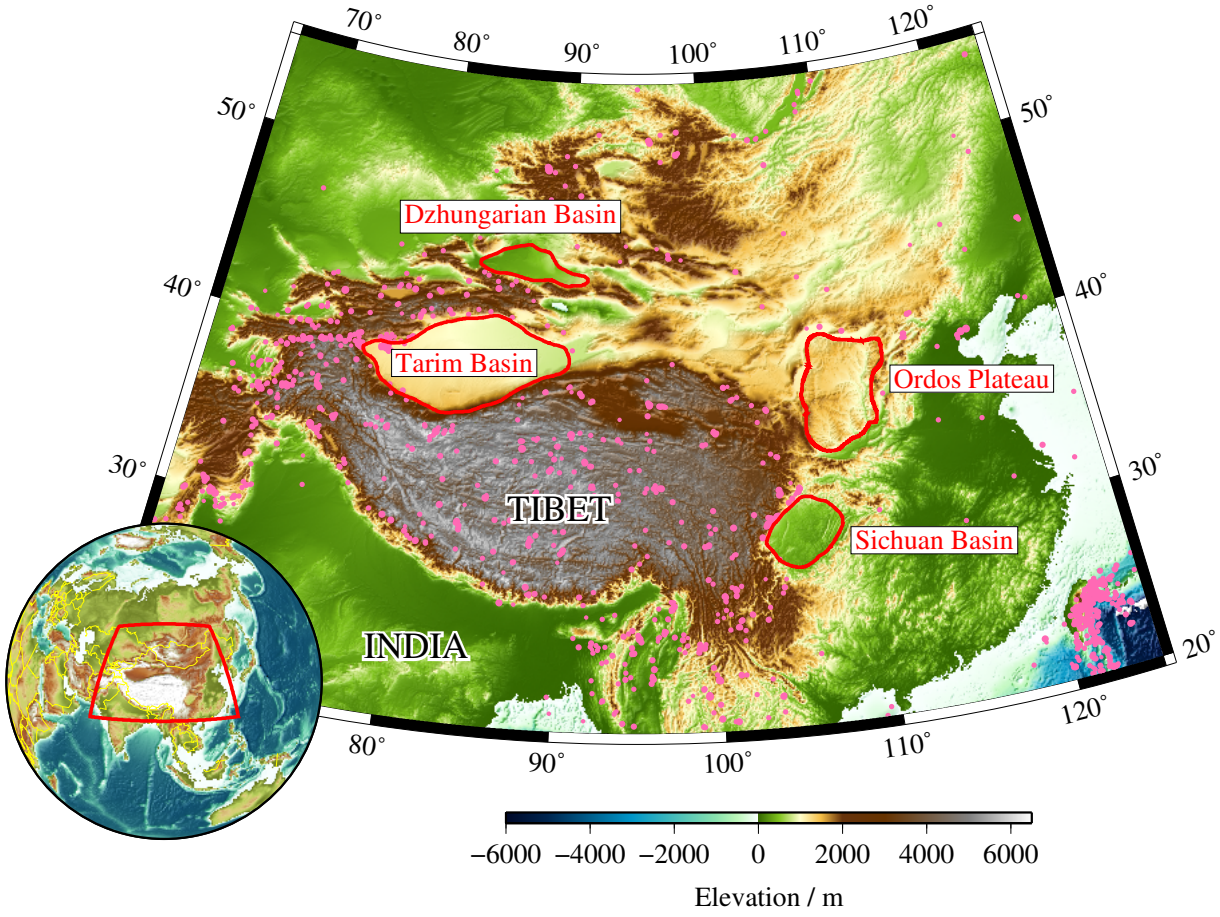


Figure 1.3: Albers equal-area projection of the SRTM topography in the India-Eurasia collision zone (*Farr et al.*, 2007). Pink dots indicate locations of earthquakes from the Global CMT catalogue between 1976 and 2013 (*Ekström et al.*, 2012). Red polygons outline suggested rigid blocks within the collision zone.

three-dimensional nature of the India-Eurasia collision (the assumption of plane strain is clearly not appropriate for the thickened Tibetan crust); and they consider the importance of gravitational potential energy differences in driving deformation. Furthermore, a number of studies have questioned the large offsets and high slip rates on the major strike-slip faults: *Searle* (1996) found a total offset on the Karakoram Fault of less than 120 km, whilst recent geological and geodetic work suggest a lower slip rate on the Altyn Tagh Fault of 9 mm/a (*Shen et al.*, 2001; *Cowgill*, 2007; *He et al.*, 2013a).

Within the India-Eurasia collision zone, there are also regions that appear not to deform, namely the Tarim Basin, the Dzhungarian Basin, the Ordos Plateau and the Sichuan Basin (see Figure 1.3) (*Tapponnier and Molnar*, 1977; *England and Houseman*, 1985; *Zhang and Gan*, 2008). It is thought that these regions are rheologically different

to the rest of the orogenic belt because they comprise remnants of Precambrian cratonic lithosphere (*Avouac and Tapponnier*, 1993). It is important to understand the active tectonics of such regions because non-deforming blocks tend to localise strain, and hence seismic hazard, at their margins (*Molnar and Dayem*, 2010), yet the style of faulting and rates of motion of these blocks are not always predictable from nearby plate velocities (*McKenzie and Jackson*, 1983; *Jackson and McKenzie*, 1988). As such, models of the collision zone that consist of a continuously deforming fluid, but that also incorporate inclusions of much higher viscosity, are probably most appropriate for providing a complete description of the deformation (*England and Houseman*, 1985; *Wang et al.*, 2005; *Zhang and Gan*, 2008; *Zhang*, 2013).

1.3 Regional tectonic setting of the Ordos Plateau

In this thesis we examine the active tectonics of one of the apparently non-deforming regions within the India-Eurasia collision zone: the Ordos Plateau, which lies immediately northeast of the Tibetan Plateau in northern central China (see Figure 1.3).

1.3.1 The rigidity of the Ordos Plateau

The crystalline basement underlying the Ordos Plateau is thought to comprise Mesoarchaean granulite (from 3200 to 2800 Ma ago) and is part of the oldest continental craton in China, which had assembled by the Neoproterozoic (800 Ma ago) (*Ye et al.*, 1987; *Gilder et al.*, 1991; *Zhang et al.*, 1998; *Liu and Yang*, 2000). This basement is covered by largely undeformed Triassic rocks and hundreds of metres of Quaternary aeolian loess (*Zhang and Gan*, 2008).

A number of lines of evidence attest to the apparent rigidity of the Ordos Plateau. Firstly, *Zhang and Gan* (2008) showed from recent GPS measurements that the strain at the margins of the plateau is an order of magnitude larger than in the interior. Secondly, no major active faults have been mapped in the interior of the plateau (*Tapponnier and Molnar*, 1977; *Deng et al.*, 2007), though it is conceivable that any that do exist have been covered by loess. Thirdly, Figure 1.4 shows that recent seismicity is concentrated

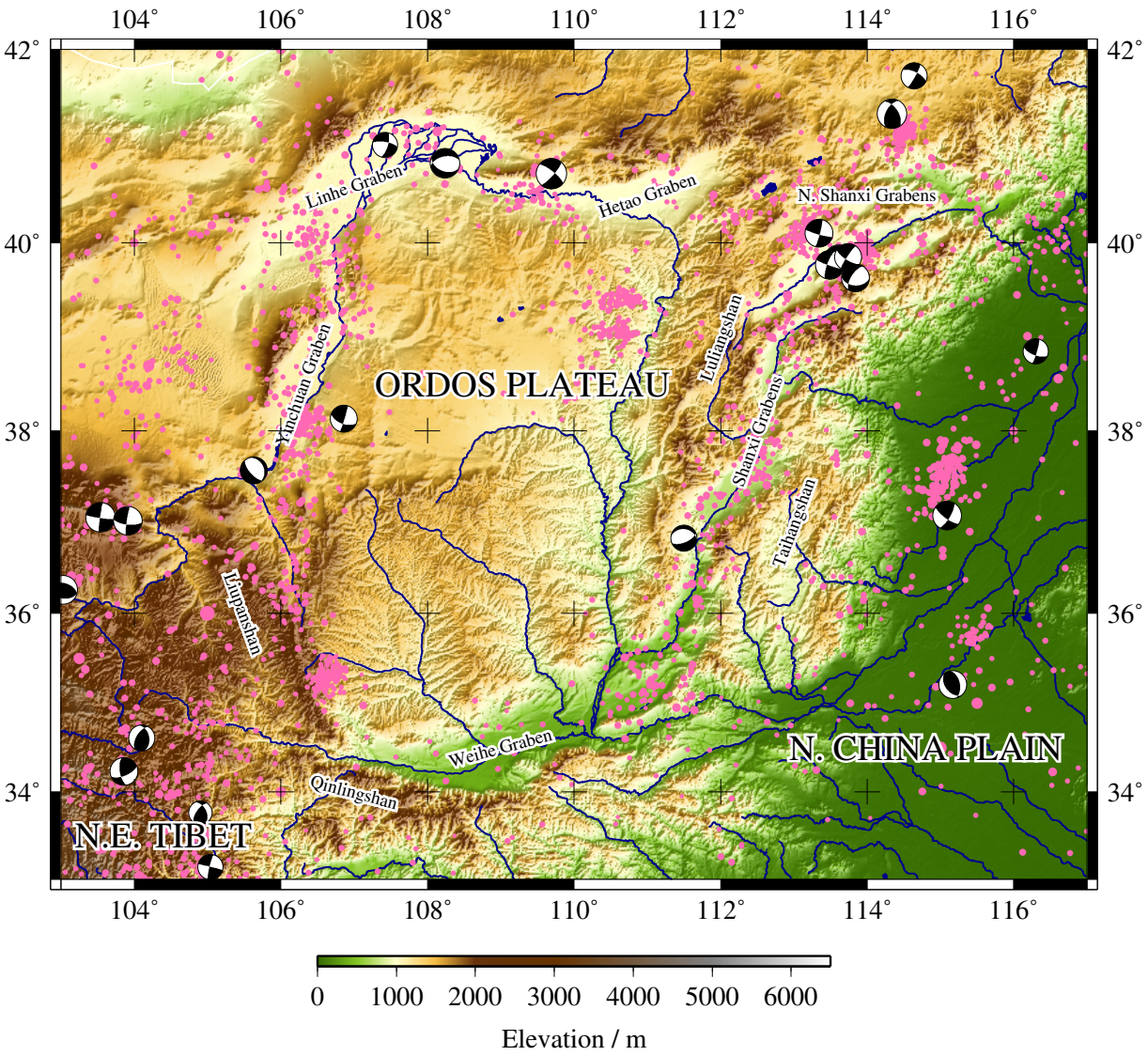


Figure 1.4: SRTM topography (*Farr et al.*, 2007) of the Ordos Plateau in northeastern China. Rivers are indicated in dark blue. Focal mechanisms from the Global CMT catalogue (*Ekström et al.*, 2012) are shown for earthquakes since 1976 with magnitudes greater than M_w 5.0. Pink dots indicate earthquakes of M_w 2.0-5.0 between 1920 and 2011 from the ISC catalogue (*International Seismological Centre*, 2013).

at the margins of the plateau, indicating that the interior is not deforming. (The small number of low magnitude events in the northeastern Ordos are potentially related to mining activity and do not correspond to any known active faults.) Finally, high seismic velocities and low heat flow measurements further suggest that the lithosphere beneath the Ordos Plateau is cold, hard, and therefore potentially rigid (*Hu et al.*, 2000; *Zhang et al.*, 2003a; *Zhang and Gan*, 2008).

1.3.2 Extension around the Ordos Plateau

An enigmatic feature of the Ordos Plateau is that although it sits within the India-Eurasia collision zone—and hence in a region of overall north-south shortening—it is surrounded by large normal faults and extensional grabens on almost all of its boundaries, suggesting that the region is extending in all directions. The plateau is bordered by the Linhe and Hetao Grabens in the north, the Weihe Graben in the south, the Yinchuan Graben in the west, and the Shanxi Grabens in the east—reverse faulting is only found in the Liupanshan (Liupan mountains) to the southwest of the plateau (see Figure 1.4). The Linhe, Hetao, Yinchuan and Weihe Grabens are all thought to have initiated in the Early Tertiary, possibly as early as the Late Eocene (*Ye et al.*, 1987; *Zhang et al.*, 1998, 2003b), and thin Oligocene and Miocene deposits are found in all of these basins (*Ye et al.*, 1987; *Ma and Wu*, 1987). The Early Tertiary phase of graben formation was also accompanied by widespread extension and subsequent thermal subsidence throughout much of the North China Plain (*Zhang et al.*, 1998). However, the main period of graben development around the Ordos Plateau—and the initial opening of the Shanxi Grabens in the east and northeast—is thought to have occurred during the Pliocene and Quaternary (*Xu and Ma*, 1992; *Xu et al.*, 1993; *Zhang et al.*, 1998, 2003b). Early to Middle Pleistocene tholeiitic and alkaline flood basalts and volcanic cinder cones are also found in the northern Shanxi Grabens, though it is thought that they may be related to the Inner Mongolia Plateau basaltic volcanism to the north (*Ye et al.*, 1987; *Xu et al.*, 1993; *Zhang et al.*, 1998).

Three factors are considered to be potentially important causes of the regional extension in northeastern China: the India-Eurasia collision, gravitational spreading of the Tibetan Plateau, and the subduction of the Pacific and Philippine Sea plates along the eastern margin of Eurasia (*Northrup et al.*, 1995; *Zhang et al.*, 2003b; *Liu et al.*, 2007). Some evidence suggests that extension along the eastern margin of Eurasia began in the Late Cretaceous (*Ma and Wu*, 1987), some 10 to 20 Ma prior to the initiation of the India-Eurasia collision in the Eocene (*Searle et al.*, 1987). Therefore, one explanation for the extension is that it is the result of a deceleration in the rate of subduction of the Pacific plate beneath the eastern Eurasian margin (*Northrup et al.*, 1995). The onset of

Early Tertiary rifting in northern China appears to correlate with a decrease in the rate of subduction from 120 to 140 mm/a in the Late Cretaceous to 30 to 40 mm/a in the Eocene (*Northrup et al.*, 1995; *Zhang et al.*, 2003b). The far-field cause of this change in subduction rate is unclear, but it could relate to a change in the coupling between the convecting mantle and the overlying plates or a reconfiguration of plate boundaries elsewhere on the globe (*Northrup et al.*, 1995). However, *Liu et al.* (2007) concluded from a dynamic model that, although subduction in the Pacific was important for the tectonics of northeastern China early in the Cenozoic, the deformation which occurs today can be largely explained by the gravitational spreading of the Tibetan Plateau. This agrees with *Zhang et al.* (1985), *Ye et al.* (1987), *Zhang et al.* (1998) and *Zhang et al.* (2003b), who concluded that Early Tertiary extension was related to Pacific subduction, whilst Pliocene and Quaternary extension was linked to the India-Eurasia collision. In this thesis we consider how the extension at the margins of the Ordos Plateau contributes to the present-day regional kinematics.

1.4 Earthquake hazard

1.4.1 Earthquake hazard on the continents

Since 1900 more than 2 million people have died in earthquakes globally (*USGS*, 2016) and approximately 60% of these deaths have occurred in the Alpine-Himalayan belt (see Figure 1.5), especially in Italy, Turkey, Iran, Pakistan, India and China. The number of earthquake fatalities has increased over the centuries due to increased human exposure to seismic hazard (*Tucker*, 2004; *Bilham*, 2004; *Jackson*, 2008; *Bilham*, 2009; *Tucker*, 2013). This reflects both population rise and inflating population densities in vulnerable urban areas. Furthermore, the growth of many cities is constrained by water supply or topography, often resulting in population concentrations immediately adjacent to major active faults (*Jackson*, 2008).

However, most earthquake deaths in recent years have resulted not from $M > 8$ earthquakes at plate boundaries, but from $M < 8$ earthquakes in the continental interiors (see

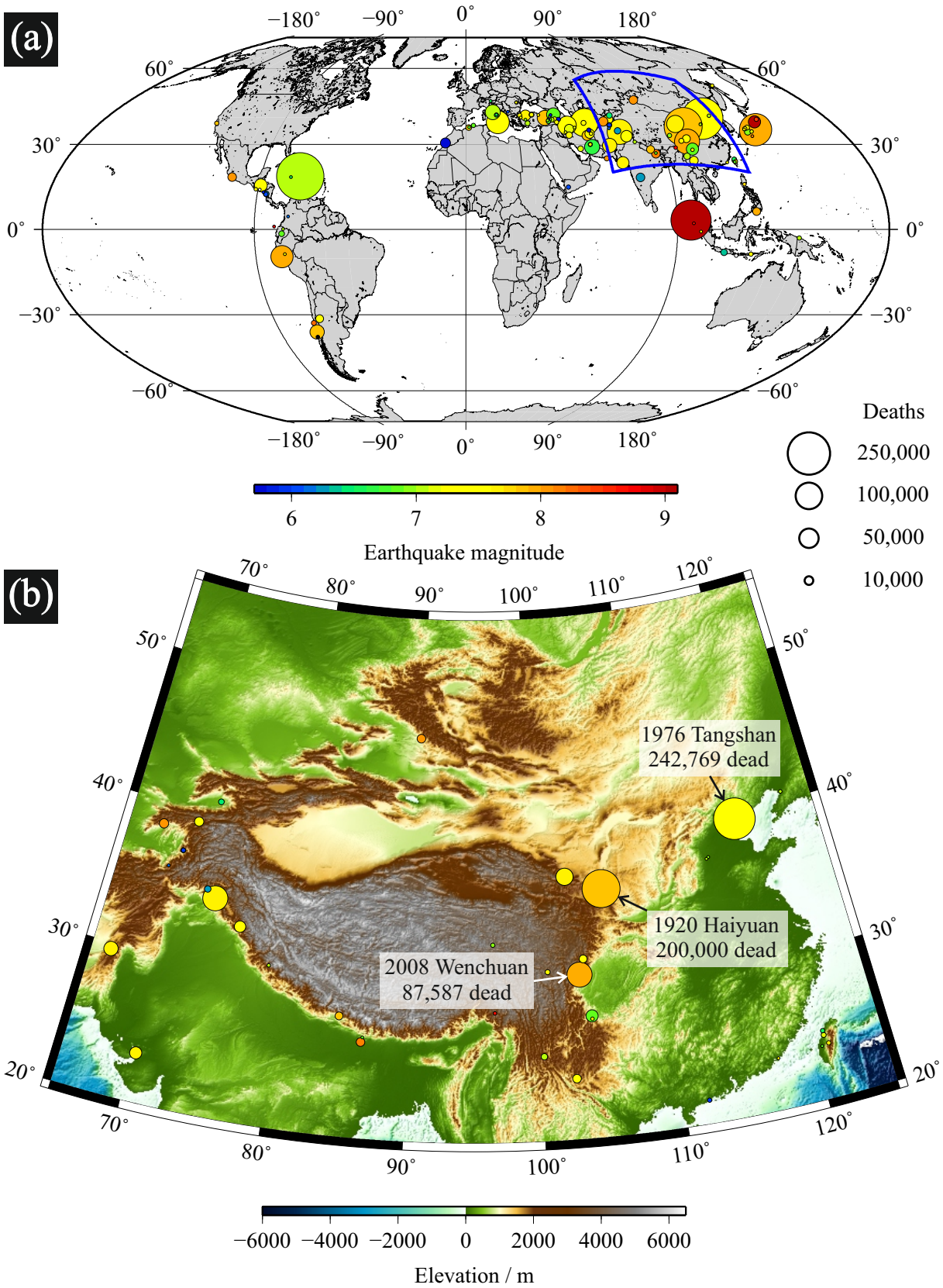


Figure 1.5: (a) Global map of earthquake related deaths for 1900-2014 with fatalities > 1000, updated from *Elliott* (2009). Data from *USGS* (2016). Blue polygon marks location of (b). The area of each circle is proportional to the number of deaths and the colour corresponds to the earthquake magnitude. See also Table 1.1. (b) Albers equal-area projection of the SRTM topography in the India-Eurasia collision zone (*Farr et al.*, 2007). Earthquakes displayed the same as in (a).

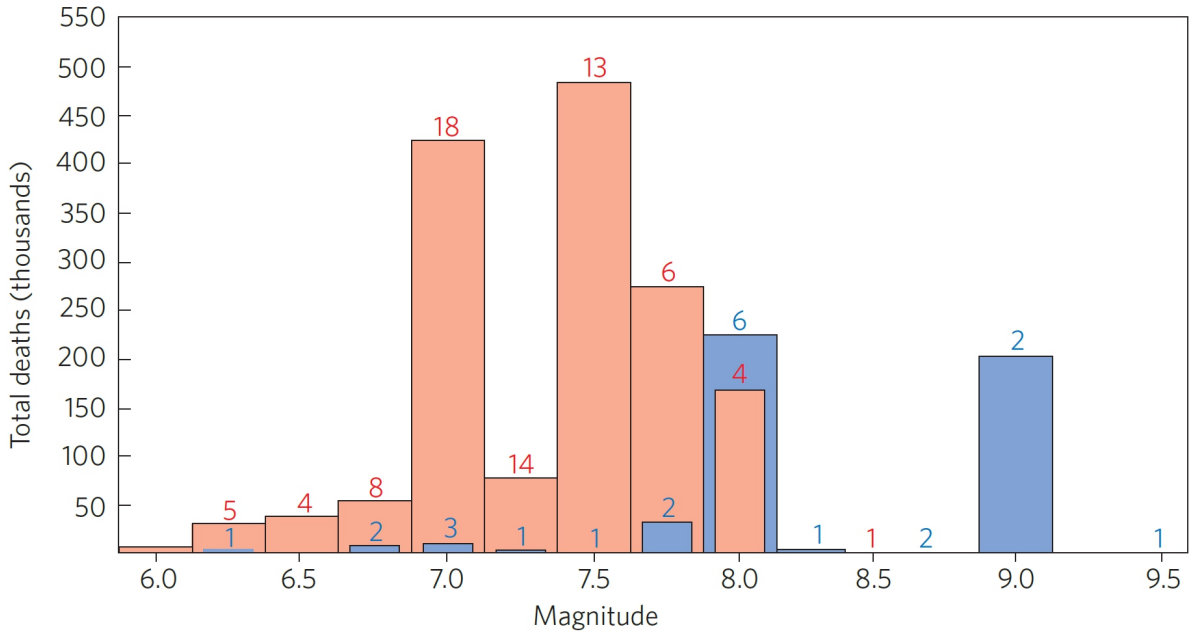


Figure 1.6: Histogram from *England and Jackson* (2011) showing earthquake deaths over the last century for continental interiors (in red) and plate boundaries (in blue). The earthquakes are grouped into magnitude bins 0.25 units wide and the number of earthquakes in each bin is shown above each bar.

Figure 1.6) (*England and Jackson*, 2011). The 2004 Sumatra earthquake is an exception (see Table 1.1), but in this case many fatalities were as a result of the following tsunami. At plate boundaries, slip rates tend to be fast and well known, recurrence intervals tend to be short, and communities tend to be relatively well-prepared (e.g. in terms of building codes and evacuation plans) for future disasters. By contrast, on the continents, not all faults have been mapped, slip rates are often slow and poorly constrained, recurrence intervals are longer (often much longer than generational memory), and many communities are not ready for future earthquakes. Indeed, given the long recurrence intervals on the continents, many of the most damaging continental earthquakes in recent years have occurred on faults that had not previously been mapped or whose hazard had not been properly recognised: for example, the 2003 Bam earthquake in Iran, the 2005 Kashmir earthquake in Pakistan and the 2008 Wenchuan earthquake in China (*England and Jackson*, 2011; *Zhang*, 2013).

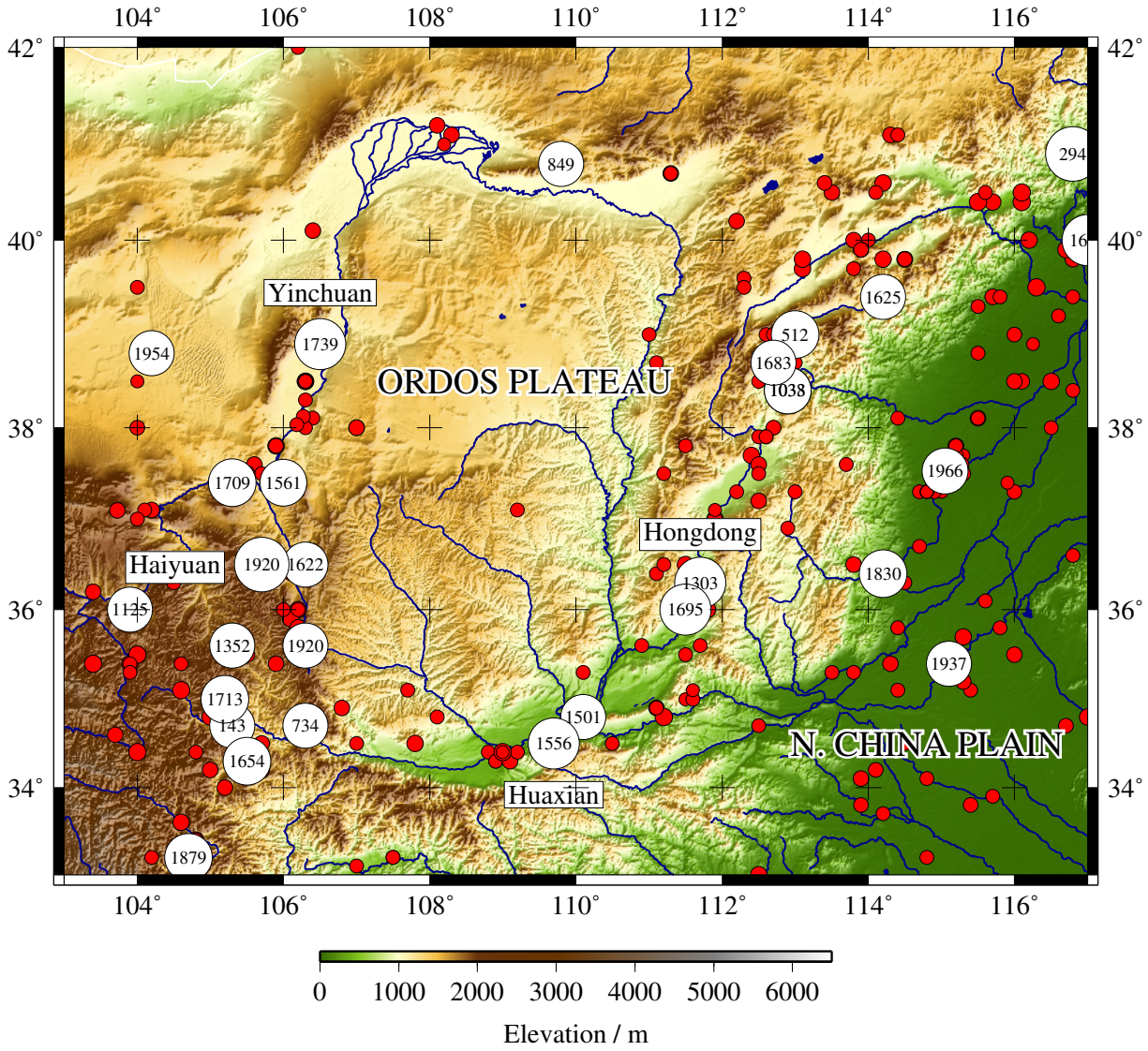


Figure 1.7: SRTM topography (*Farr et al.*, 2007) of the Ordos Plateau in northeastern China. Rivers are indicated in dark blue. Historical earthquakes with $M_w \geq 7$ are shown by white circles, including the year in which they occurred. The 1303 Hongdong, 1556 Huaxian, 1739 Yinchuan and 1920 Haiyuan events are labelled individually. Historical earthquakes with $5 \leq M_w < 7$ are shown as red dots. Data comes from *Lee et al.* (1976), *Lee et al.* (1978) and *Liu et al.* (2011).

1.4.2 Earthquake hazard in China

China has arguably the longest and most complete historical earthquake records of anywhere in the world, extending back well over 2000 years (*Lee et al.*, 1976, 1978; *Wang*, 2004; *Liu et al.*, 2011). Dynasty records are present from around 200 BC onwards, though much of the early parts of these catalogues are incomplete until the arrival of widespread printing in around 1000 AD. In addition, it is likely that many earthquakes were misrepresented by court historians since they were often viewed as punishments to the emperor

Table 1.1: The ten deadliest earthquakes globally since 1900

Year	Month	Day	Location	Latitude	Longitude	Magnitude	Deaths[a]
2010	1	12	Haiti	18.4 °N	72.6 °W	7.0	316,000
1976	7	27	Tangshan, China	39.6 °N	118 °E	7.5	242,769[b]
2004	12	26	Sumatra, Indonesia	3.3 °N	95.9 °E	9.1	227,898
1920	12	16	Haiyuan, China	36.5 °N	105.7 °E	7.8	200,000
1923	9	1	Kanto, Japan	35.3 °N	139.5 °E	7.9	142,800
1948	10	5	Ashgabat, Turkmenistan	38.0 °N	58.3 °E	7.3	110,000
2008	5	12	Wenchuan, China	31.0 °N	103.3 °E	7.9	87,587
2005	10	8	Kashmir, Pakistan	34.5 °N	73.6 °E	7.6	86,000
1908	12	28	Messina, Italy	38.2 °N	15.7 °E	7.2	72,000
1970	5	31	Chimbote, Peru	9.4 °S	78.9 °W	7.9	70,000

[a] Data from *USGS* (2016).
[b] Official figure, though some estimates are as high as 655,000 fatalities.

of the time. Nonetheless, it is thought that the earthquake catalogues in northern China are complete for $M_s \geq 6$ events since 1291 and for $M_s \geq 4.75$ events since 1484 (*Huang et al.*, 1994).

Many of the most damaging historical earthquakes in China have occurred at the margins of the Ordos Plateau (see Figure 1.7), including around 19 earthquakes with $M_w \geq 7$ (*Zhang et al.*, 2003a). The apparently M 8.2 1556 Huaxian earthquake, which occurred in the Weihe Graben to the south of the Ordos Plateau, is thought to be the deadliest earthquake in history, resulting in the deaths of an estimated 830,000 people (*Hou et al.*, 1998; *Yuan and Feng*, 2010; *Feng et al.*, 2016; *Zhou*, 2016). Other major historical events include the M 8 1303 Hongdong earthquake on the Huoshan Fault, which killed ≈ 200,000 people, and the supposedly M 8 1739 Yinchuan earthquake, which killed ≈ 50,000 people (see Chapter 2).

More recently, in the twentieth century, earthquake deaths in China have accounted for more than 50% of the global total (*Jordan et al.*, 2011). Three of the ten deadliest earthquakes globally since 1900 occurred in China (see Table 1.1), and all three had epicentres near the Ordos Plateau (see Figure 1.5). The 16th December 1920 Haiyuan earthquake ruptured ≈ 200 km of the eastern Haiyuan Fault at the junction between the Tibetan and Ordos Plateaus (*Zhang et al.*, 1987; *Ren et al.*, 2015). Magnitude estimates for the earthquake range between 7.8 (*USGS*, 2016) and 8.7 (*Zhang et al.*, 1987). Approximately 200,000 people are believed to have been killed and many thousands of towns

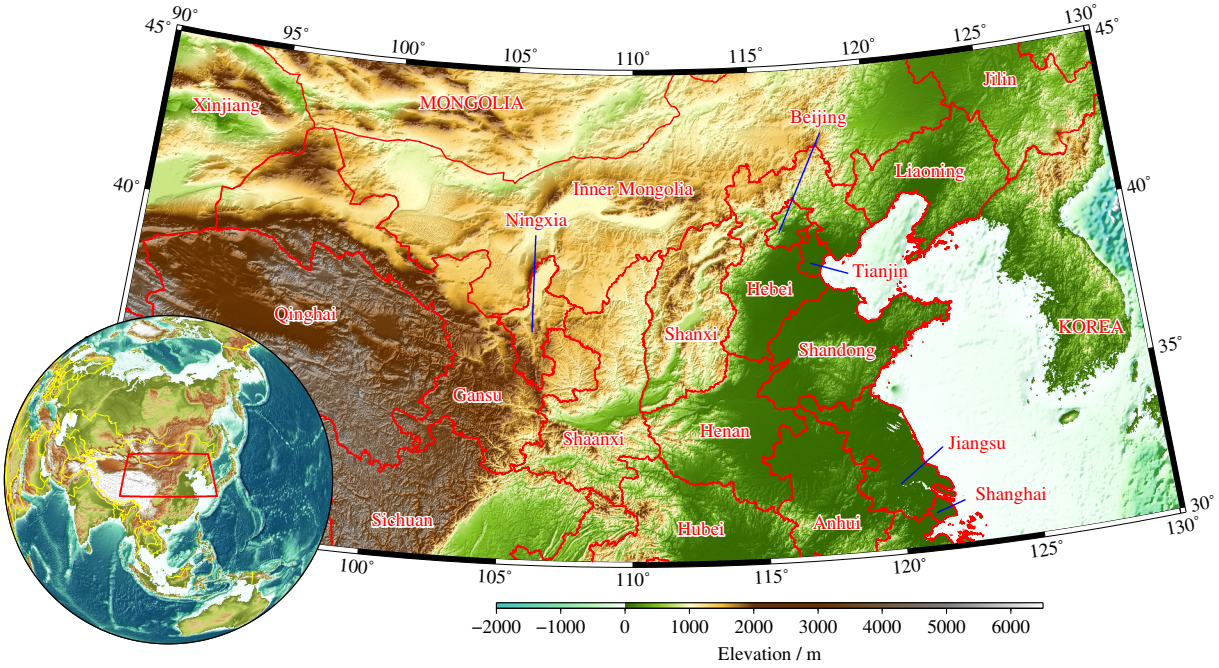
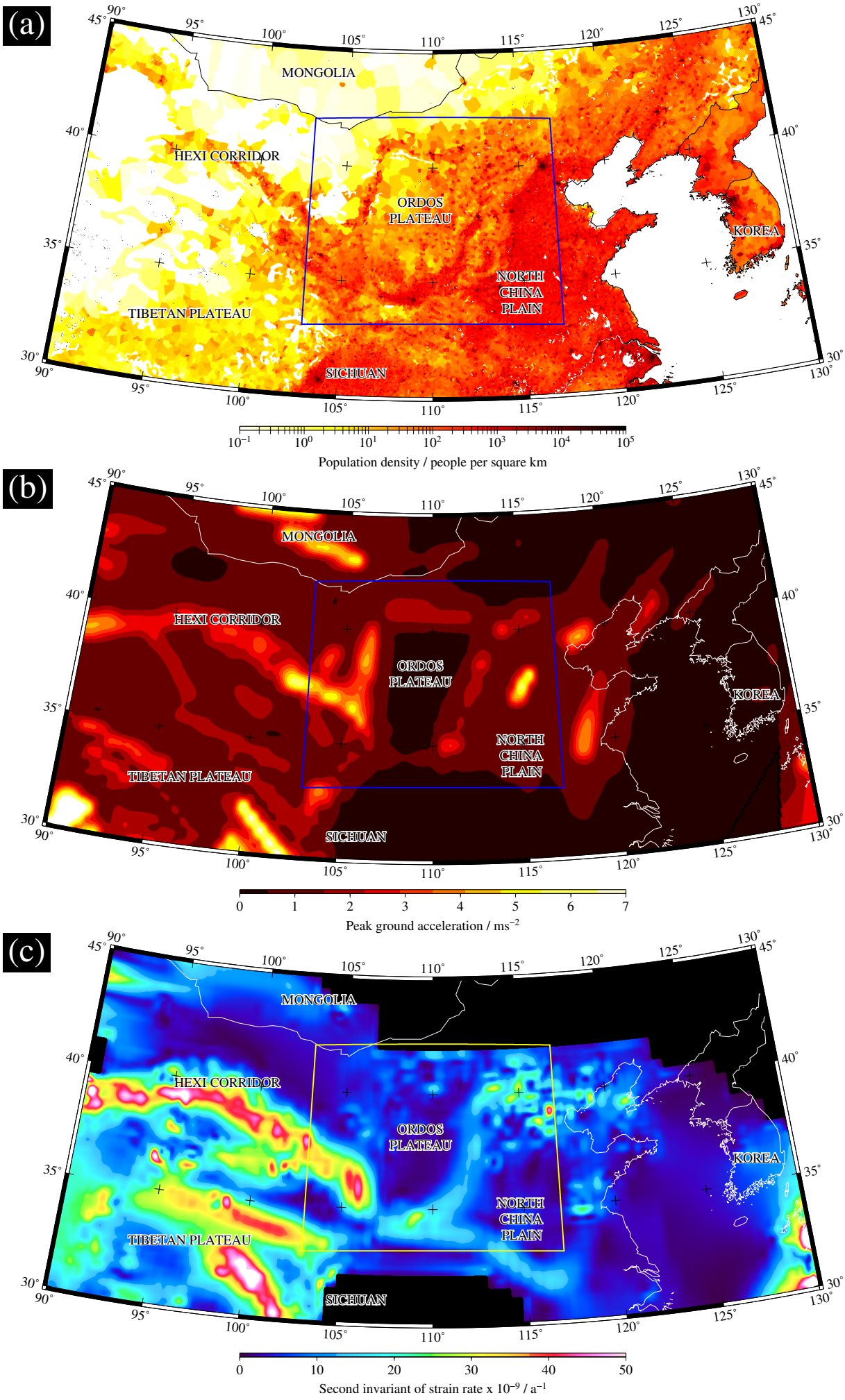


Figure 1.8: Albers equal-area projection of the SRTM topography in northern China (*Farr et al.*, 2007). Inset globe shows the location of Figure 1.8 within Asia. Province boundaries from *Hijmans* (2009).

and villages were destroyed (*Zhang et al.*, 1987). The M_w 7.8 27th July 1976 Tangshan earthquake occurred in the North China Plain, 150 km east of Beijing. The official death toll is listed as 242,769, but some estimates are as high as 655,000 (*Bilham*, 2009; *USGS*, 2016). The earthquake occurred at 3:43 am local time and many people are thought to have choked to death on the dust generated by building collapse (*Wang*, 2006). The mortality rate for the city of Tangshan was between 20 and 35% (*Bilham*, 2004), and the total economic loss is estimated at $2 billion (*Zhang et al.*, 2003a). The M_w 7.9 12th May 2008 Wenchuan earthquake ruptured ≈ 300 km of the Longmenshan range front in two separate sub-events (*Toda et al.*, 2008). 87,587 people are estimated to have been killed and hundreds of thousands of people were injured (*Wang et al.*, 2010).

The Ordos Plateau spans parts of the provinces of Inner Mongolia, Ningxia, Gansu, Hebei, Beijing, Shanxi and Shaanxi (see Figure 1.8). Together, these provinces have a combined population of over 220 million people; the adjacent North China Plain is one of the most densely populated regions on the planet (see Figures 1.9 (a) and 1.10—and note the logarithmic colour scales). In China as a whole approximately half of the population live in large crowded cities, whilst the remainder of the population live in rural


(a)
MONGOLIA
HEXI CORRIDOR
ORDOS PLATEAU
KOREA
NORTH CHINA PLAIN
TIBETAN PLATEAU
SICHUAN
10^{-1} 10^{0} 10^{1} 10^{2} 10^{3} 10^{4} 10^{5}
Population density / people per square km
(b)
MONGOLIA
HEXI CORRIDOR
ORDOS PLATEAU
KOREA
NORTH CHINA PLAIN
TIBETAN PLATEAU
SICHUAN
0 1 2 3 4 5 6 7
Peak ground acceleration / ms^{-2}
(c)
MONGOLIA
HEXI CORRIDOR
ORDOS PLATEAU
KOREA
NORTH CHINA PLAIN
TIBETAN PLATEAU
SICHUAN
0 10 20 30 40 50
Second invariant of strain rate x 10^{-9} / a^{-1}

areas, typically in highly vulnerable buildings. Secondary hazards are also important: for example, large fractions of the deaths in the 1556 Huaxian earthquake and the 1920 Haiyuan earthquake are attributable to landslides—and the thick loess covering much of the Ordos Plateau is especially susceptible to landsliding.

Figure 1.10 shows that population densities are particularly high at the margins of the Ordos Plateau, immediately adjacent to the main active faults; it is likely that attractive locations for settlements (in terms of topography and water supply) have been directly controlled by the tectonics. But as settlements have grown into major cities, the seismic hazard has been exacerbated. Furthermore, if this hazard is not mitigated, the situation is likely to get worse: a number of parts of the Ordos Plateau are covered by the new "Silk Road Economic Belt", a Eurasian investment plan worth hundreds of billions of dollars that aims to improve communications, transport and trade (*Zhu and Zou*, 2006; *Bai and Wang*, 2014). The belt roughly follows the old Silk Road and includes Beijing, the Shanxi Grabens, the Weihe Graben, Xi'an, and the Hexi Corridor.

The first Chinese seismic hazard maps were produced in the 1950s on the principle that earthquakes of the same magnitude were likely to recur in locations where they had occurred previously (*Zhang et al.*, 1999a; *Jordan et al.*, 2011). A second version was published in 1977 and was used to inform national building codes (*Zhang et al.*, 1999a; *Jordan et al.*, 2011). The seismic hazard map shown in Figures 1.9 (b) and 1.11 was constructed as part of the *Global Seismic Hazard Assessment Program* (GSHAP) and is based on historical earthquake catalogues and previously defined "seismic zones" (*Zhang et al.*, 1999a). The map clearly highlights regions of hazard at the margins of the Ordos Plateau, but many of the regions of highest hazard simply correspond to the locations of

Figure 1.9 *(preceding page)*: Albers equal-area projections covering the same region of northeast Asia as Figure 1.8. (a) Population density map based on 2015 census data and adjusted to match the 2015 revision of the *United Nations World Population Prospects* country totals (*Columbia University*, 2015; *Doxsey-Whitfield et al.*, 2015). Colour indicates the number of people per square kilometre on a logarithmic scale. Blue box shows location of Figure 1.10. (b) Map of seismic hazard from the *Global Seismic Hazard Assessment Program* (GSHAP) (*Zhang et al.*, 1999a). Colours indicate the peak ground acceleration (in ms^{-2}) with a 10% exceedance probability in the next 50 years. Blue box shows location of Figure 1.11. (c) Second invariant of the GPS-derived strain rate tensor from the UNAVCO *Global Strain Rate Map* (*Kreemer et al.*, 2003). Yellow box shows location of Figure 1.12.

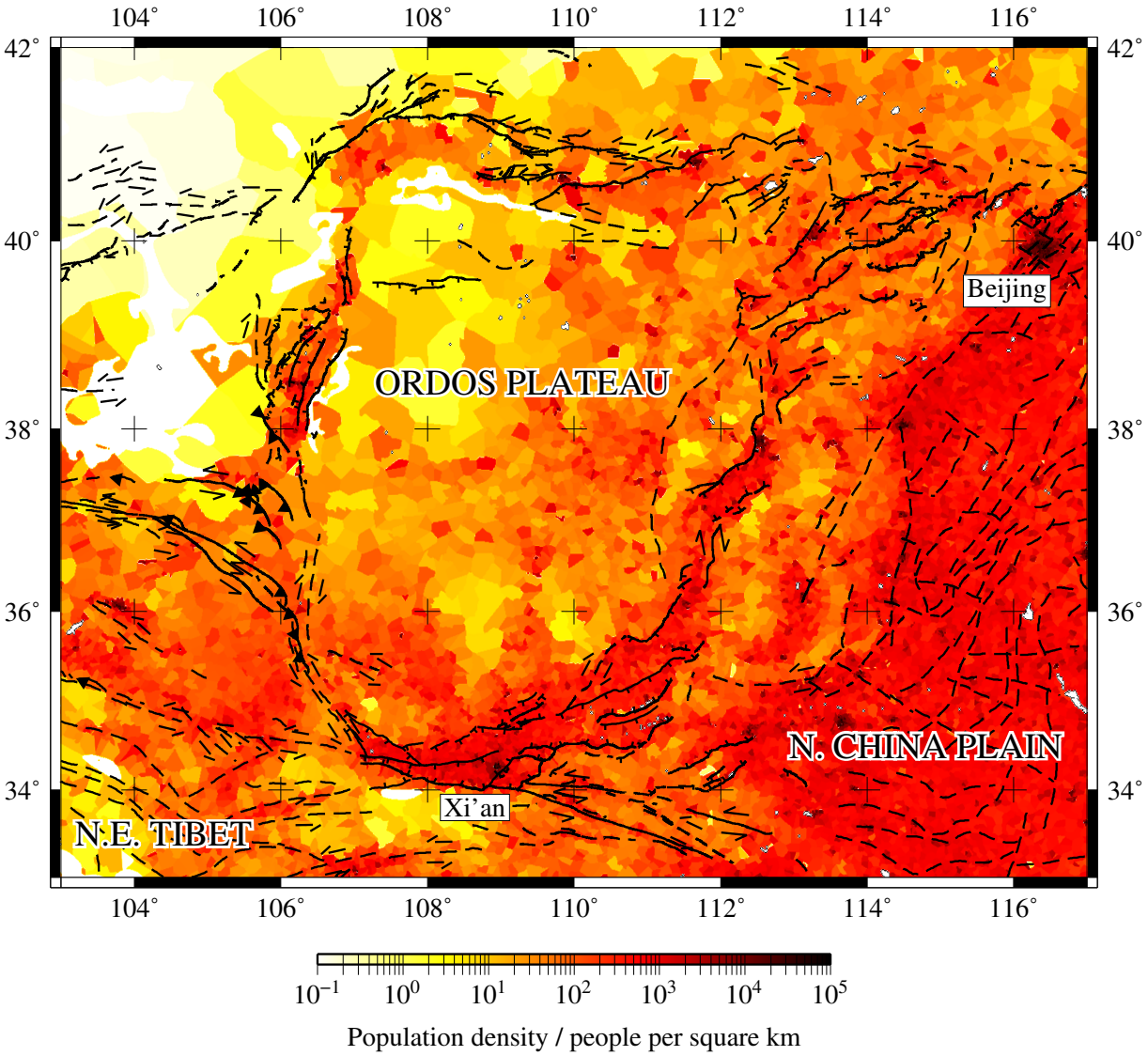


Figure 1.10: Population density map for the Ordos Plateau based on 2015 census data and adjusted to match the 2015 revision of the *United Nations World Population Prospects* country totals (*Columbia University*, 2015; *Doxsey-Whitfield et al.*, 2015). Colour indicates the number of people per square kilometre on a logarithmic scale. Faults from Figure 6.4 are also shown.

recent earthquakes, such as the 1920 Haiyuan event and the 1966 Xingtai earthquakes to the east of the plateau. The usefulness of this sort of hazard map, especially in continental regions that are known to have faults with low slip rates and long recurrence intervals, has therefore been questioned (*Stein et al.*, 2012; *Stein and Friedrich*, 2014). For example, Figure 1.9 (b) does not highlight the Longmenshan as a region of notable hazard, and yet this was the location of the subsequent 2008 Wenchuan earthquake.

An alternative approach to seismic hazard has therefore been to use geodetic measurements to map the current rate of strain accumulation (see Figures 1.9 (c) and 1.12).

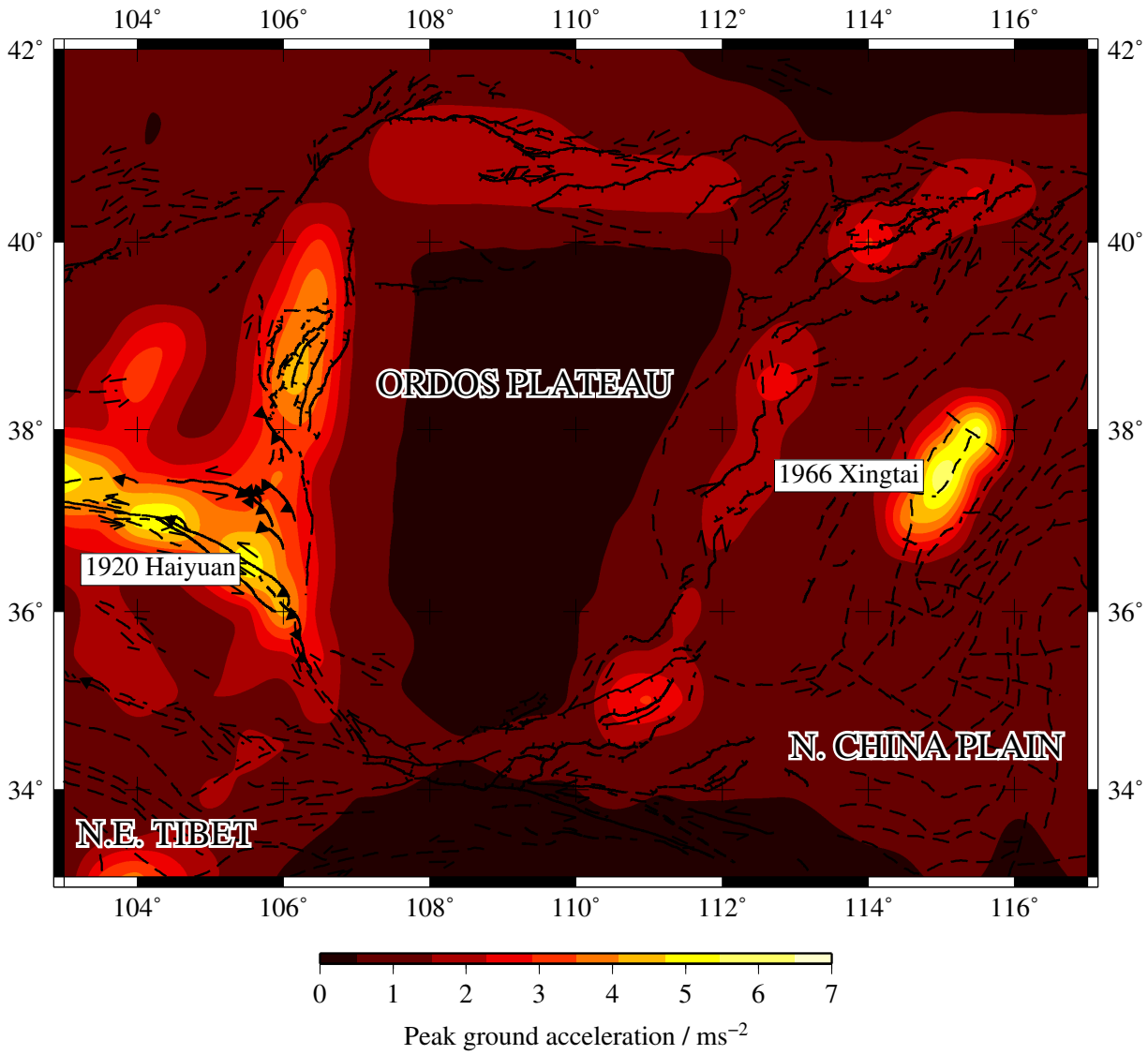


Figure 1.11: Map of seismic hazard for the Ordos Plateau from the *Global Seismic Hazard Assessment Program* (GSHAP) (*Zhang et al.*, 1999a). Colours indicate the peak ground acceleration (in ms^{-2}) with a 10% exceedance probability in the next 50 years. Faults from Figure 6.4 are also shown.

Figure 1.12 again indicates the highest seismic hazard in the vicinity of the 1920 Haiyuan earthquake, but it also highlights potential hazards in the northern Shanxi Grabens and the Weihe Graben that are not evident in the GSHAP map. That said, the strain rate map does not indicate any significant deformation in the Yinchuan Graben to the west of the plateau, and yet, given that this was the location of the 1739 earthquake, the GSHAP map suggests that this is a region of future seismic hazard.

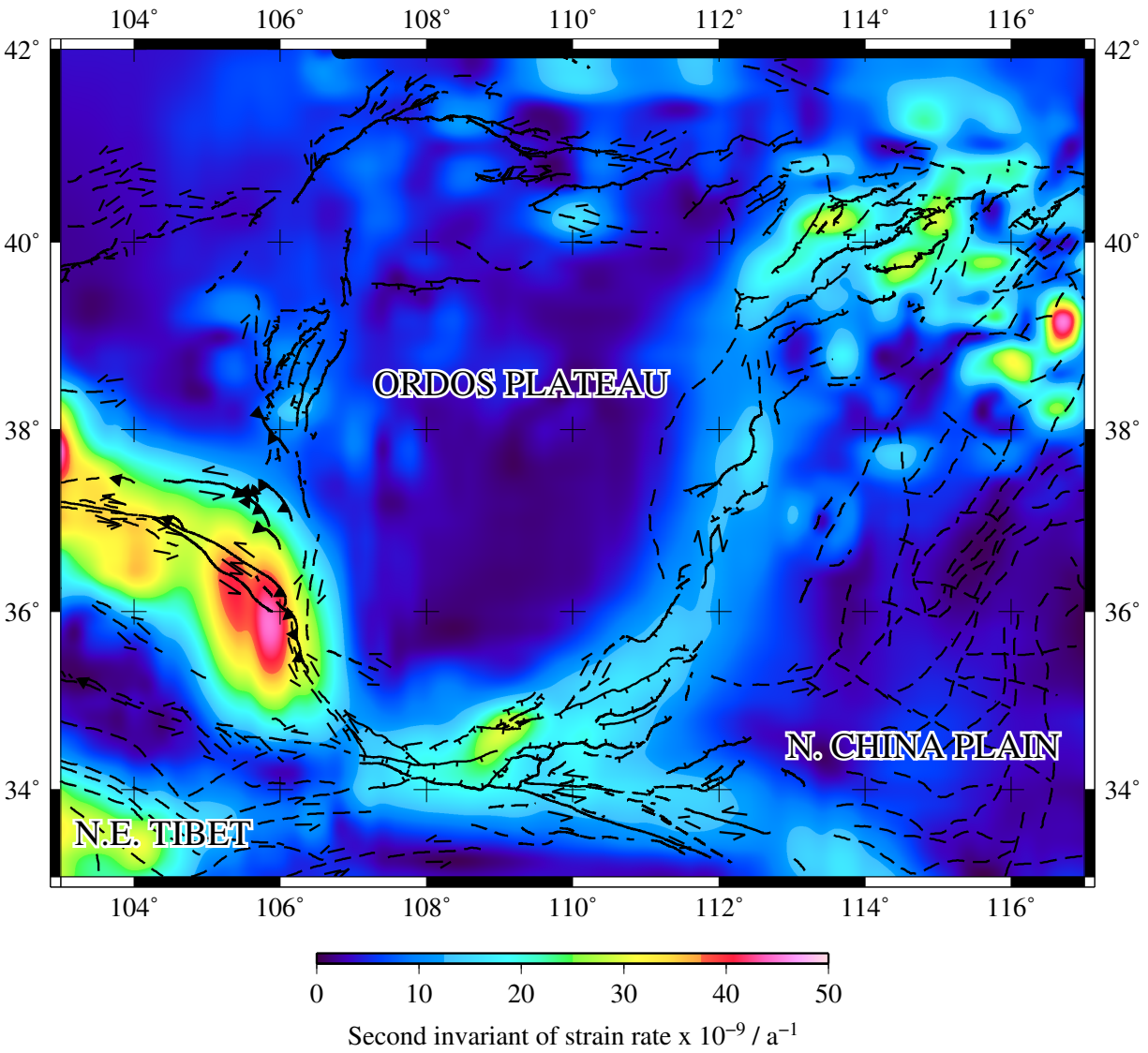


Figure 1.12: Second invariant of the GPS-derived strain rate tensor from the UNAVCO *Global Strain Rate Map* (*Kreemer et al.*, 2003). Faults from Figure 6.4 are also shown.

1.5 Overview of this thesis

The motivation for this thesis is twofold. Firstly, the Ordos Plateau appears to be a rigid crustal block that is included within a broad zone of continental deformation. Our approach is to describe the kinematics of the Ordos Plateau, for which we need to map the distribution of active faults at the margins of the block, determine their sense of slip, and measure their slip rates. By studying the faulting in this way, we aim to examine how the plateau interacts with neighbouring deforming regions, and assess the role that it plays in the overall India-Eurasia collision. Secondly, and more importantly from a societal perspective, the earthquake hazard in this part of the world is significant. The

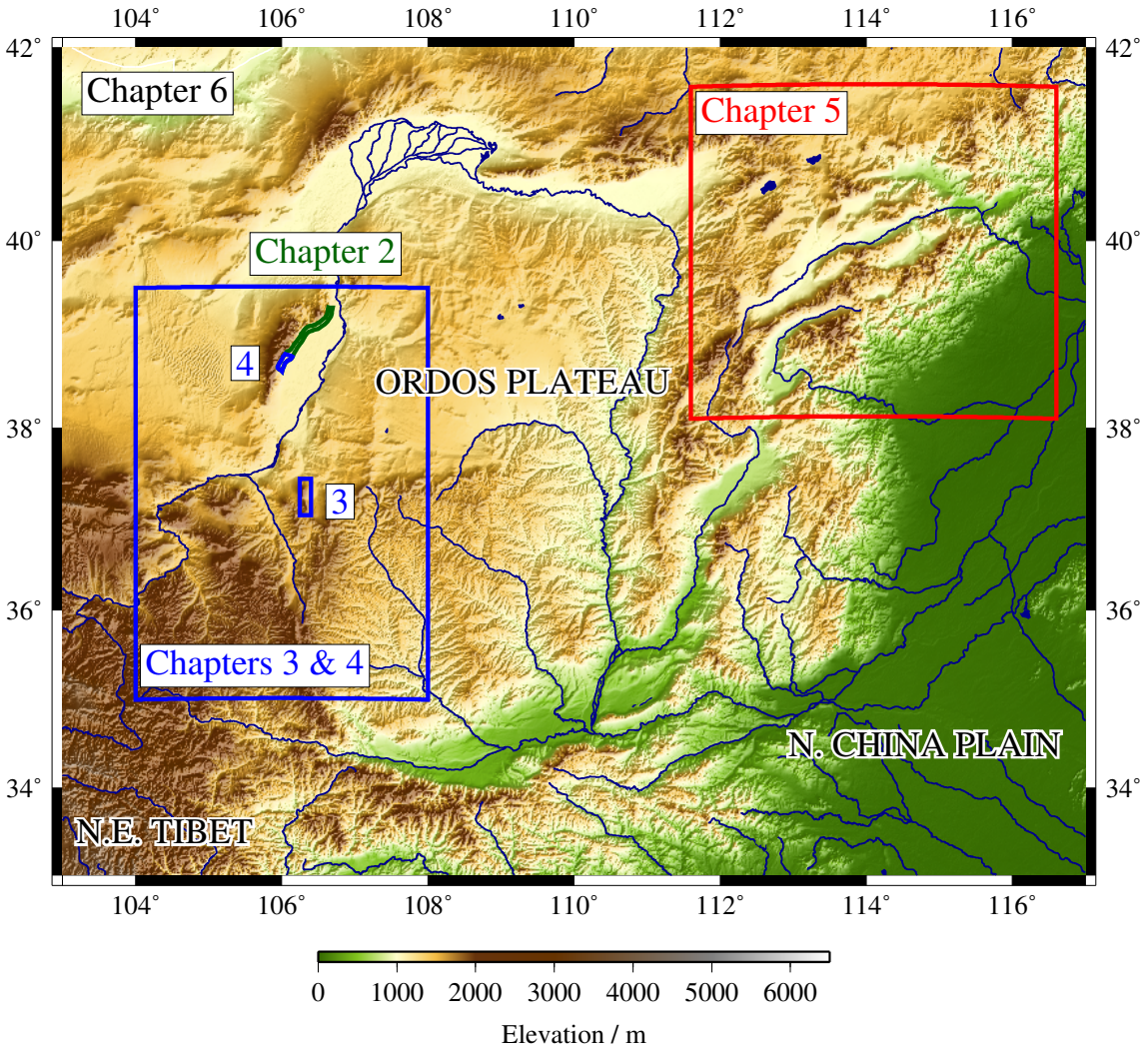


Figure 1.13: SRTM topography (*Farr et al.*, 2007) of the Ordos Plateau in northeastern China. Rivers are indicated in dark blue. Coloured polygons indicate the geographical regions covered in subsequent chapters of this thesis.

detailed study of individual historical earthquakes and the relative activities of different faults form vital parts of future seismic hazard assessments. We aim to contribute to this endeavour.

In this thesis we use data that spans a range of spatial and temporal scales. In Chapter 2 we undertake a detailed forensic study of a single historical earthquake rupture; in Chapters 3 and 4 we determine slip rates for two principal faults and consider the importance of these faults within their regional context; in Chapter 5 we expand our spatial view to look at the behaviour of a population of active faults; finally, in Chapter 6, we summarise the active tectonics of the whole Ordos Plateau (see Figure 1.13).

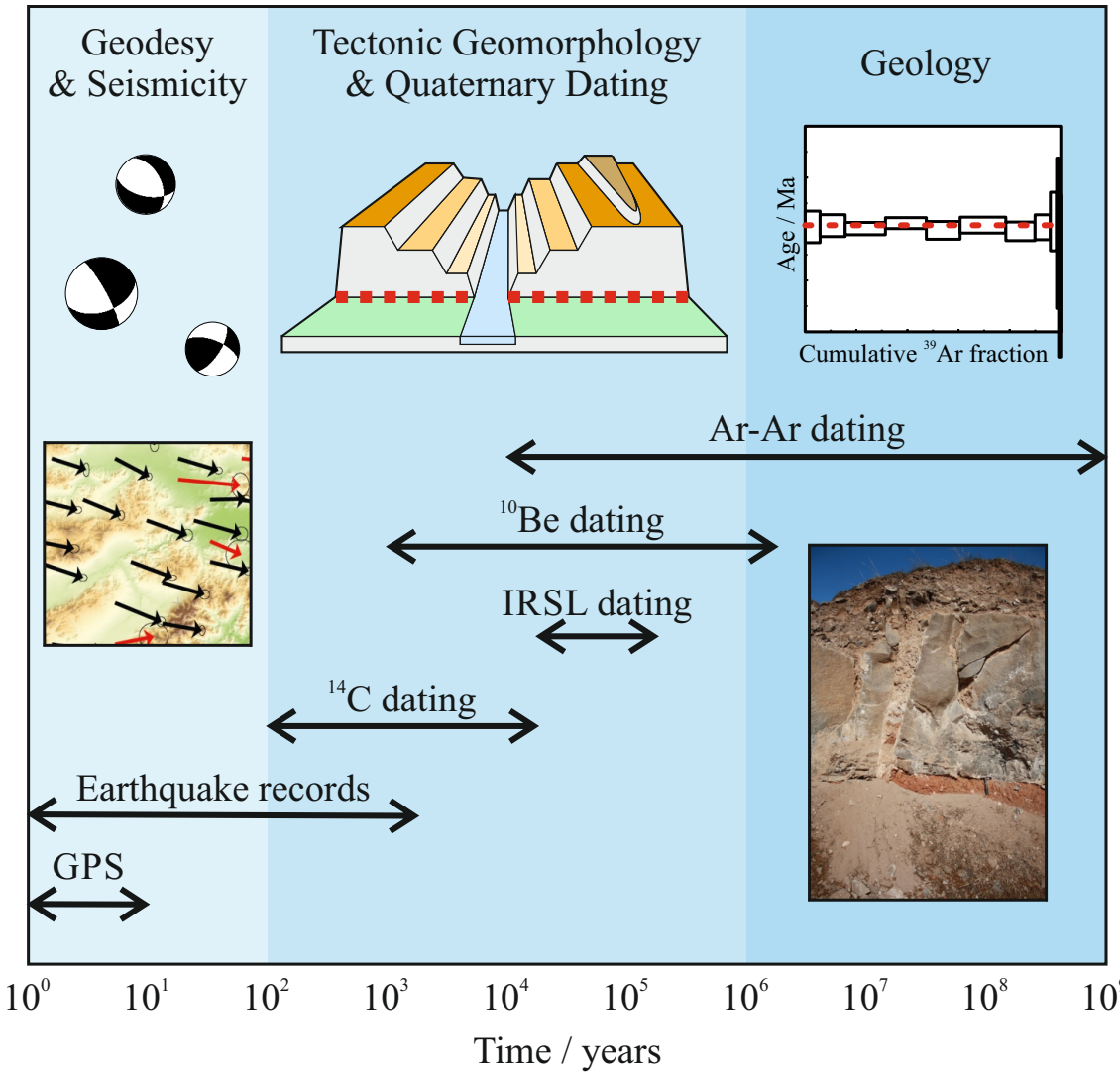


Figure 1.14: Methods used in this thesis for measuring slip rates or strain rates on active faults over different time periods. Diagram modified from *Benedetti and van der Woerd* (2014) and dating ranges are from *Burbank and Anderson* (2012). Geodetic measurements can generate decadal slip-rate determinations; records of seismicity can be used for decadal or centennial strain rates; Quaternary dating of offset geomorphological features yields slip rates over millennia to hundreds of thousands of years; and geology reveals slip rates over millions of years.

We make use of geodetic methods, which typically measure interseismic strain accumulation; seismic methods, which may only cover one or two earthquake cycles; and Quaternary and geological dating, which typically cover multiple seismic cycles. The full range of techniques used in this thesis is shown in Figure 1.14. Detailed methods are included in the chapter where each technique is first used.

Finally, table 1.2 lists English translations of a number of Chinese characters that commonly form part of place names used in this thesis.

Table 1.2: Translations of a few common Chinese characters

Chinese character	Pīnyīn (transliteration)	English translation
山	shān	mountains
村	cūn	village
河	hé	river
谷	gǔ	valley
北	běi	north
东	dōng	east
南	nán	south
西	xī	west
大	dà	big
小	xiǎo	little

1.6 Publications arising from this thesis

The work in Chapter 2 has been published as:

> Middleton, T. A., Walker, R. T., Parsons, B., Lei, Q., Zhou, Y., & Ren, Z. (2016). A major, intraplate, normal-faulting earthquake: the 1739 Yinchuan event in northern China. Journal of Geophysical Research, 121, 293-320.

Chapters 3 and 4 and part of Chapter 6 have been published as:

> Middleton, T. A., Walker, R. T., Rood, D. H., Rhodes. E. J., Parsons, B., Lei, Q., Elliott, J. R., Ren, Z., & Zhou, Y. (2016). The tectonics of the western Ordos Plateau, Ningxia, China: slip rates on the Luoshan and East Helanshan Faults. Tectonics, 35, 2754-2777.

Chapter 5 is currently in press as:

> Middleton, T. A., Elliott, J. R., Rhodes, E. J., Sherlock, S., Walker, R. T., Wang, W., Yu, J., & Zhou, Y. Extension rates across the northern Shanxi Grabens, China, from Quaternary geology, seismicity and geodesy. Geophysical Journal International.

Sections 6.3 and 6.4 from Chapter 6 have been submitted for publication as:

> Middleton, T. A., Parsons, B. & Walker, R. T. Comparison of seismic and geodetic strain rates at the margins of the Ordos Plateau, northern China. Geophysical Journal International.

Sections 6.1 and 6.2 and other parts of Chapter 6 have been submitted for publication as:

Middleton, T. A., Walker, R. T. & Parsons, B. The kinematics of the Ordos Plateau, northern China. Geosphere.

I have also been involved in fieldwork in Kazakhstan, which has been published as:

Campbell, G., Walker, R. T., Abdrakhmatov, K., Jackson, J., Elliott, J., Mackenzie, D., Middleton, T. A., Schwenninger, J.-L. (2015). Great earthquakes in low-strain-rate continental interiors: an example from SE Kazakhstan. Journal of Geophysical Research, 120, 5507-5534.

Chapter 2

The 1739 Yinchuan earthquake

2.1 Introduction

Continental normal-faulting earthquakes greater than magnitude 7.0 are uncommon. The few recent examples include: the M_w 7.2 1915 Pleasant Valley (Nevada) event (*Jackson and Leeder*, 1994), the M_w 7.4 1957 Muya (Siberia) event (*Molnar et al.*, 1984), the M_w 7.3 1959 Hebgen Lake (Montana) event (*Jackson and White*, 1989), and the M_w 7.0 2006 Mozambique event (*Copley et al.*, 2012). Studying large normal-faulting earthquakes is challenging: they typically occur in slowly deforming regions with long repeat times and very few of them have occurred during the instrumental period. Nonetheless, though these events are comparatively infrequent, their large sizes mean that they still pose a significant seismic hazard, particularly in densely populated areas. In order to expand the catalogue of such events, we need to look further back into history. However, historical records alone are not sufficient to allow us to estimate reliable fault parameters and earthquake magnitudes. It is therefore important that the interpretation of historical records is combined with geological observations made in the field.

In this chapter we focus on the 1739 Yinchuan earthquake, located on the western side of the Ordos Plateau in northern China (see Figure 2.1), in which 50,000 people are thought to have been killed (*Zhang et al.*, 1986). The recorded intensities of shaking (see Figures 2.1 and 2.2) have previously been combined with empirical relationships to suggest that this was a magnitude 8.0 event (*Zhang et al.*, 1986; *State Seismological Bureau and*

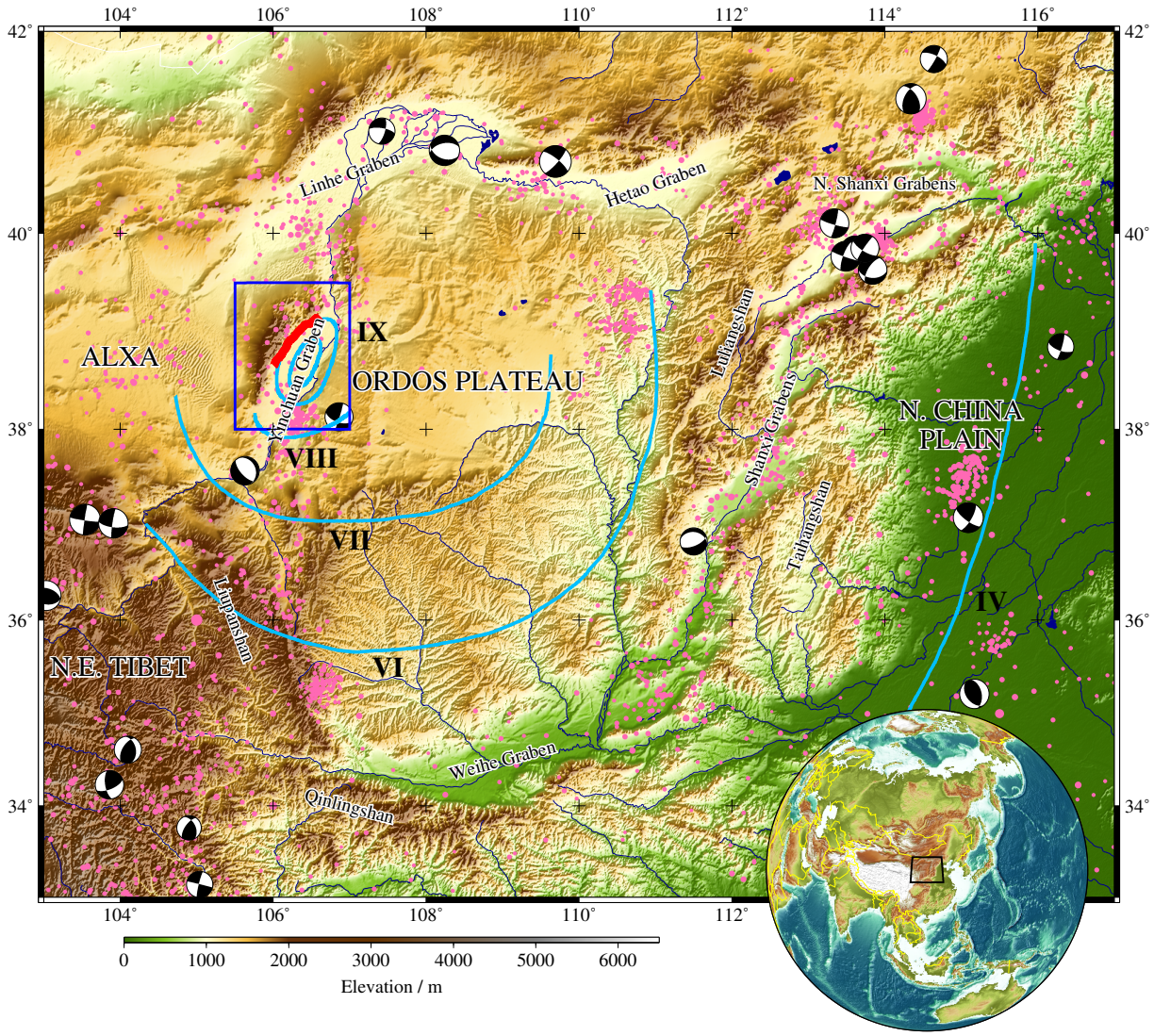
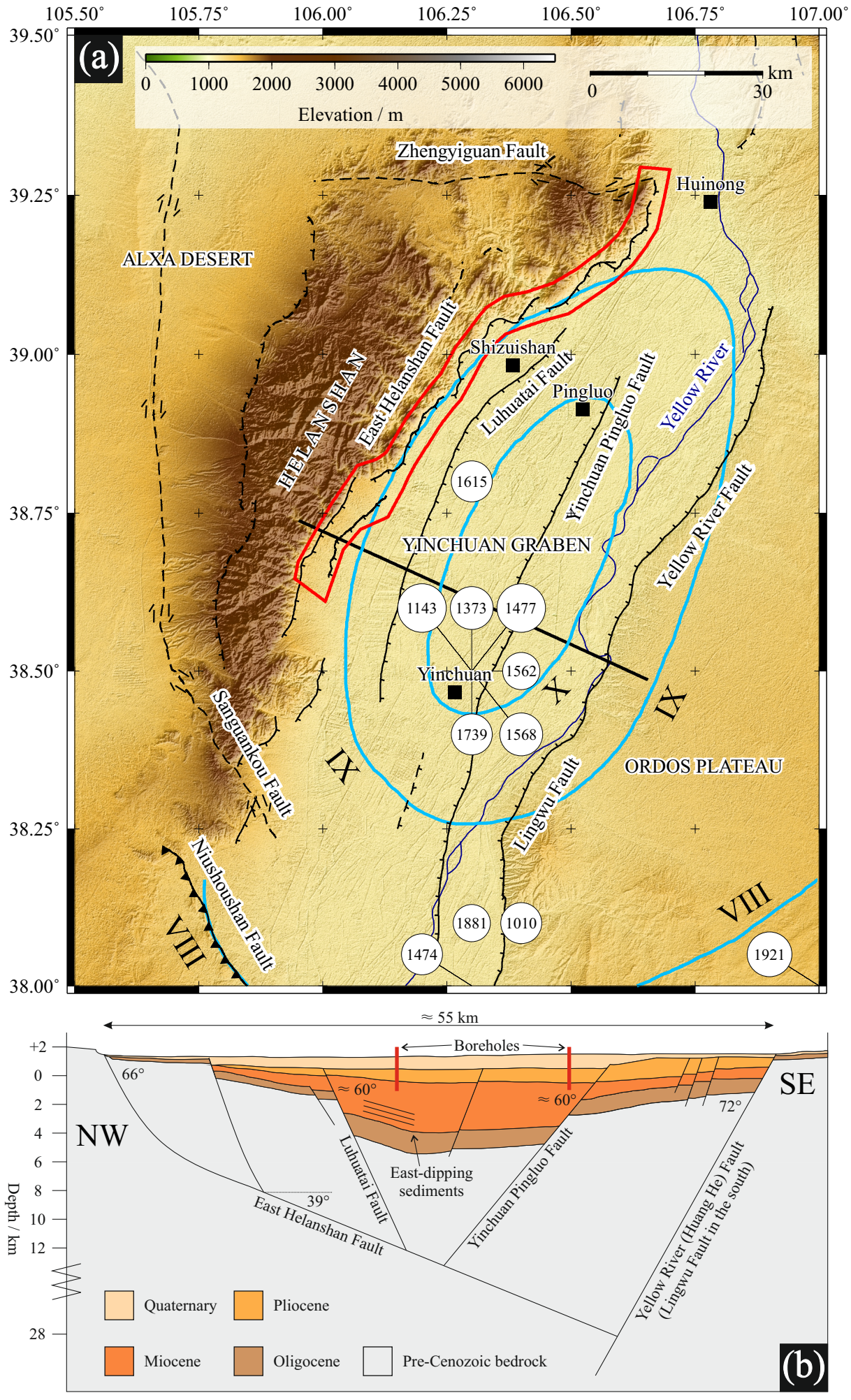


Figure 2.1: SRTM topography (*Farr et al.*, 2007) of the Ordos Plateau in northeastern China. Focal mechanisms from the Global CMT catalogue (*Ekström et al.*, 2012) are shown for earthquakes since 1976 with magnitudes greater than M_w 5.0. Pink dots indicate earthquakes of M_w 2.0-5.0 between 1920 and 2011 from the ISC catalogue (*International Seismological Centre*, 2013). Rivers are indicated in dark blue and inset globe shows the location of Figure 2.1 within Asia. The East Helanshan Fault is highlighted in red and isoseismals for the 1739 earthquake according to the *New Chinese Intensity Scale* are shown in light blue (*State Seismological Bureau and Fudan University*, 1990). The dark blue box indicates the region shown in Figure 2.2.

Fudan University, 1990) and many subsequent authors have since assumed that this is the correct magnitude (*Deng and Liao*, 1996; *Bai and Jiao*, 2005; *Lin et al.*, 2013; *Lei et al.*, 2015; *Lin et al.*, 2015a). If the magnitude of the Yinchuan earthquake has been correctly estimated it would be amongst the largest continental normal-faulting earthquakes ever recorded. The city of Yinchuan now has a population of nearly 2 million people and a similarly large event in future is likely to be even more destructive.


105.50°
105.75°
106.00°
106.25°
106.50°
106.75°
107.00°
39.50°
39.25°
39.00°
38.75°
38.50°
38.25°
38.00°
(a)
0 1000 2000 3000 4000 5000 6000
Elevation / m
0 30 km
Zhengyiguan Fault
Huinong
ALXA DESERT
HELANSHAN
East Helanshan Fault
Shizuishan
Luhuatai Fault
Pingluo
Yinchuan Pingluo Fault
Yellow River
Yellow River Fault
1615
YINCHUAN GRABEN
1143
1373
1477
Yinchuan
1562
1739
1568
IX
X
IX
ORDOS PLATEAU
Sanguankou Fault
Lingwu Fault
Niushoushan Fault
VIII
VIII
1881
1010
1474
1921
≈ 55 km
Boreholes
+2
0
2
4
6
8
10
12
28
Depth / km
66°
≈ 60°
≈ 60°
72°
NW
SE
Luhuatai Fault
East-dipping sediments
39°
East Helanshan Fault
Yinchuan Pingluo Fault
Yellow River (Huang He) Fault (Lingwu Fault in the south)
Quaternary
Pliocene
Miocene
Oligocene
Pre-Cenozoic bedrock
(b)

M_w 8.0 equates to a seismic moment of 1.11×10^{21} Nm. Previous studies have indicated a rupture length of around 88 km (*Deng and Liao*, 1996) and, using the relationship $M_0 = \mu A\bar{u}$ (where μ is the modulus of rigidity, A is the fault plane area and $\bar{u}$ is the average slip (*Hanks and Kanamori*, 1979)), this would suggest fault slip of 10 to 13 m and a slip-to-length ratio of between 1.1 and 1.5×10^{-4} (using a fault dip of 39° (*Fang et al.*, 2009) and different seismogenic thicknesses of 20 and 28 km and respectively). These values are somewhat larger than typical slip-to-length ratios which are of the order of 10^{-5} to 10^{-4} (*Scholz*, 1982, 2002). Unusually large slip-to-length ratios have been seen elsewhere—2.2×10^{-4} for the Assam earthquake (*Bilham and England*, 2001), and around 3×10^{-4} for the Bhuj earthquake (*Copley et al.*, 2011)—but such examples are rare. If the Yinchuan earthquake is really as large as cited and does have such a large slip-to-length ratio, then the factors that contributed to such an unusual event deserve detailed consideration. Additionally, there has been some disagreement in the literature about the causative fault for the 1739 earthquake; the East Helanshan, Yinchuan-Pingluo and Yellow River Faults have all been suggested (see Section 2.3) (*Zhang et al.*, 1986; *Deng and Liao*, 1996; *Bai and Jiao*, 2005; *Chai et al.*, 2006; *Lin et al.*, 2013; *Lei et al.*, 2015; *Lin et al.*, 2015a).

Here, prompted by recent debate on the causative fault, we examine the source parameters of the 1739 earthquake and use ^{14}C dating of Holocene material to provide further support for the East Helanshan Fault being the causative fault (see Figure 2.2). We use high-resolution (0.5 m) stereo imagery from the Pleiades satellites to produce a 1 to 2 m

Figure 2.2 *(preceding page)*: (a) ASTER GDEM topography of the Yinchuan Graben. Faults, marked as thin black lines, have been mapped from satellite imagery (source: http://earth.google.com) based upon earlier fault maps from *Tapponnier and Molnar* (1977), *Zhang et al.* (1986) and *Deng and Liao* (1996). Faults that are inferred or show no evidence of Quaternary activity are marked by dashed lines. Cities are marked by black squares. Historical earthquakes from *Lee et al.* (1976) and *Lee et al.* (1978) are shown by white circles, including the year in which they occurred. The Yellow River, which flows to the north, is marked in dark blue. Red outline indicates coverage of Pleiades data. Thick black line shows approximate location of profile in (b). Isoseismals for the 1739 earthquake according to the *New Chinese Intensity Scale* are shown in light blue (*State Seismological Bureau and Fudan University*, 1990). (b) Sketch (interpretive) cross-section across the Yinchuan Graben based on seismic reflection data and previous figures in *Liu et al.* (2008), *Fang et al.* (2009), *Lei et al.* (2014) and *Lei et al.* (2015). Note that the depth scale is not linear and that the faults are only schematic due to the variable vertical exaggeration.

resolution digital elevation model (DEM) of the entire length of the East Helanshan Fault (see Section 2.4.2 for a discussion of the resolution of the DEM) and combine this with new field observations to map the scarps along the range front in detail. The high-resolution topography enables us to identify and make measurements of the scarps along this fault in many more locations than was previously possible from isolated field observations alone. Finally, we use our observations and measurements to construct a throw distribution, estimate the slip vector azimuth and re-assess the magnitude of the event.

2.2 Tectonic setting

2.2.1 Active faulting

The Yinchuan Graben is approximately 50 km wide and 160 km long and lies at the northern end of Ningxia Province on the western side of the Ordos Plateau in northern China (see Figure 2.1). The graben is bounded by north-south trending normal faults (see Figure 2.2). On the western side of the graben lies the East Helanshan Fault, whilst the eastern side of the graben is bordered by the Yellow River (Huang He) Fault (*Zhang et al.*, 1986). Few surface outcrops of the Yellow River Fault have been conclusively identified, though linear features are visible in satellite imagery and the structure has been confirmed on seismic reflection profiles (*Liu et al.*, 2008; *Fang et al.*, 2009; *Lin et al.*, 2015a). Further, parallel, normal faults exist within the graben itself, the most prominent of which are the Luhuatai and Yinchuan-Pingluo Faults (*Zhang et al.*, 1986). These structures are buried beneath Quaternary sediments but are inferred from the seismic reflection profiles across the graben (*Liu et al.*, 2008; *Fang et al.*, 2009).

The graben is bounded at its southern end by a series of strike-slip and reverse faults, including the Sanguankou and Niushoushan Faults, which strike northwest-southeast (see Figure 2.2 (a)). These faults straddle the complex transition from shortening in the north-eastern corner of the Tibetan Plateau to apparently east-west extension in the Yinchuan Graben itself, as implied by the north-south normal faulting (*Zhang et al.*, 1990). Meanwhile, to the north of the graben, the east-west Zhengyiguan right-lateral strike-slip fault

cuts basement rocks in the Helanshan (Helan mountains) and potentially provides a structural termination at this end of the graben (*Zhang et al.*, 1986).

The Yinchuan Graben is thought to have extended at 2.9±1.0 mm/a since the Pliocene, based on a cross-sectional area balance (*Zhang et al.*, 1998). The centre of the graben contains 1 to 1.6 km of Quaternary sediments and approximately 6 km of pre-Quaternary deposits that have accumulated since the late Eocene (*Zhang et al.*, 1990). *Zhao et al.* (2007b) calculate sedimentation rates based on sediment thicknesses and ages of approximately 0.1 mm/a from the Eocene to the Miocene, about 0.5 mm/a in the Pliocene, and around 0.6 mm/a in the Quaternary. However, comparing the extension rate measured by *Zhang et al.* (1998) to the sedimentation rate since the Pliocene suggests that either the basin is under-filled, or that the extension rate is an overestimate.

As well as the 1739 event, various other historical earthquakes have been documented in the Yinchuan Graben (see Figure 2.2) (*Lee et al.*, 1976, 1978; *Liu et al.*, 2011). In particular, two events, with inferred magnitudes of approximately 6.5, occurred in 1143 and 1477. Many of these earthquakes plot on top of the city of Yinchuan, though this is presumably because they were only reported in the major population centre at the time (see Figure 2.2 (a)).

2.2.2 The deep structure of the Yinchuan Graben

Although work on the structure of the Yinchuan Graben extends back as far as the 1950s (*Fang et al.*, 2009), most of it was conducted by the petroleum industry and little has been reported in the academic literature. However, the deep structure of the Yinchuan Graben is of significant importance for this study because the dip and depth extent of the major faults place important constraints on the maximum magnitude of the earthquakes they can generate.

Liu et al. (2008) published a seismic reflection profile that extends to 5 seconds two way travel time (TWTT), which roughly corresponds to a depth of 10 km. They showed the East Helanshan, Luhuatai, Yinchuan-Pingluo and Yellow River Faults, and a few other minor faults. The faults appear to have steep dips (of approximately 60 °) and do

not extend below 5 seconds TWTT. The sediments on this profile appear to dip to the east and they are thickest in the centre of the basin, between the Luhuatai and Yinchuan-Pingluo Faults (see Figure 2.2 (b)). On the basis of this, and other unpublished profiles, a number of authors have drawn similar interpretive cross-sections (*Zhang et al.*, 1986; *He et al.*, 2005; *Zhao et al.*, 2007a; *Lei et al.*, 2014, 2015).

The only deeper information comes from a second seismic reflection profile, which extends down to 15 seconds TWTT (approximately 50 km), published by *Fang et al.* (2009). According to their interpretation, the East Helanshan Fault dips at around 39 ° to the southeast (steepening near the surface) and extends to a depth of 28 km, where it meets the Yellow River Fault, which dips at around 72 ° to the northwest (see Figure 2.2 (b)). The Luhuatai and Yinchuan-Pingluo Faults both retain relatively steep dips (approximately 60 °) and intersect the East Helanshan Fault at depths of 12 and 18 km respectively. *Fang et al.* (2009) concluded that the Yellow River Fault is the major, graben-controlling structure, which would be consistent with the apparently east-dipping sediments shown by *Liu et al.* (2008) and the fact that the Yellow River is on the eastern side of the Yinchuan Graben (see Figure 2.2 (a)). Nonetheless, given the relative lack of published seismic reflection data, our interpretive cross-section in Figure 2.2 (b) remains provisional and we do not have tight constraints on the internal graben structure.

The Helanshan reach a maximum elevation of 3557 m (*Zhang et al.*, 1990), but different suggestions have been made about the origin of this topography. *Liu et al.* (2010) used apatite fission track dating to determine that rapid uplift of the Helanshan began 10 to 12 Ma ago. This uplift was quickest in the north and immediately adjacent to the East Helanshan Fault, resulting in a tilting of the range towards the southwest. Some authors have therefore concluded that the entire topography of the Helanshan is due to footwall uplift on the East Helanshan Fault (e.g. *He et al.*, 2005). However, the rocks exposed in the Helanshan are a remnant of the Western Ordos fold-and-thrust belt, which formed between the Early-Middle and Late Jurassic (*Liu*, 2000; *Darby and Ritts*, 2002). It is therefore likely that at least some of the Helanshan topography pre-dates extension in the Yinchuan Graben. The thin basin fill in the hanging wall of the East Helanshan Fault

and its apparently shallow dip (as proposed by *Fang et al.* (2009)—see also Figure 2.2 (b)) may be related to it reactivating one of a series of older reverse faults.

2.3 Background to the 1739 earthquake

The Yinchuan earthquake took place on 3rd January 1739 at around 18:00 UTC (*Zhang et al.*, 1986). Ground shaking in the centre of the Yinchuan Graben, particularly around the cities of Yinchuan and Pingluo, reached intensity X on the *New Chinese Intensity Scale* (see Figures 2.1 and 2.2) and lasted for up to two hours after the earthquake—presumably because of aftershocks (*Zhang et al.*, 1986; *State Seismological Bureau and Fudan University*, 1990). Further aftershocks were recorded for a number of years after the earthquake, including a magnitude 5.5 event on 13th February 1739 (*Zhang et al.*, 1986). In Yinchuan city the west and north pagodas were severely damaged, whilst in Pingluo the high temple was completely destroyed. In the zone of greatest shaking, which stretches between Yinchuan and Pingluo, historical documents also record: temples, pagodas, offices, houses and city walls that all collapsed; surface cracks up to 100 m long; and some buildings which subsided by up to 7 m due to the shaking (*Zhang et al.*, 1986).

Given the number of faults in the Yinchuan Graben, the causative fault for the 1739 earthquake has been the subject of some debate in the literature. Some authors have attributed it to the Yinchuan-Pingluo Fault (*Liao and Pan*, 1982; *Chai et al.*, 2006; *Lin et al.*, 2013). Their principal reason for doing so is that the surface projection of this buried fault runs NNE-SSW directly under the city of Yinchuan and appears to coincide with the zone of maximum shaking on the isoseismal map. However, the Yinchuan Graben is filled with over 7 km of sediments (*Zhang et al.*, 1990). These sediments may have amplified the seismic waves during the earthquake, leading to greatest ground motion in the centre of the graben regardless of the location of the causative fault. The isoseismals are also elongated in a direction that is parallel to all four faults in the graben, so their shape does not help to determine the fault responsible.

Others, meanwhile, believe that the Yellow River Fault was the causative fault (*Li and Wan*, 1984; *Lin et al.*, 2015a). *Lin et al.* (2015a), for example, identified an 8 km

stretch of the fault between 39.010 °N, 106.884 °E and 39.073 °N, 106.906 °E. They did not observe any fresh scarps, but they found an offset sand layer with a ^{14}C age of 2650±30 years before present.

In 1965, though, a series of apparently fresh earthquake scarps were discovered along the East Helanshan Fault, on the western side of the Yinchuan Graben, by the Northwest Seismic Expedition of the Chinese Academy of Sciences (*Liao and Pan*, 1982). *Deng and Liao* (1996) subsequently identified four locations along the range front, at Suyukou, Xiashigou, Jianquan and Hongguozigou, where scarps could be seen (see Figure 2.3). Numerous authors have therefore attributed the 1739 event to the East Helanshan Fault (*Zhang et al.*, 1982; *Deng et al.*, 1984b; *Zhang et al.*, 1986; *Deng and Liao*, 1996; *Bai and Jiao*, 2005; *Lei et al.*, 2015). Although it seems most likely that these fresh-looking scarps are the ones that relate to the 1739 event, this has not yet been corroborated by dating offset Holocene surfaces.

A number of morphological observations of the scarps along the East Helanshan Fault have previously been made, largely on the Suyukou and Hongguozigou segments. *Deng and Liao* (1996) noted that the Xiashigou and Jianquan scarps offset the latest alluvial fans by 1 to 2 m, but little else is currently known about the scarps in these two locations.

The Suyukou scarps total around 16.5 km in length and lie 3 to 4 km southeast of the Helanshan range front, 30 km northwest of the city of Yinchuan (*Deng and Liao*, 1996). The scarps vary in height up to a maximum of approximately 11 m, and the different levels have been interpreted to represent a series of normal-faulting earthquake ruptures within the Quaternary (*Deng and Liao*, 1996). In this chapter, however, we are only concerned with the lowest of these scarps, which is the one that may relate to the 1739 event. *Zhang et al.* (1986) and *Deng and Liao* (1996) obtained maximum single-event scarp heights at Suyukou of 4.6 m and 4.4 m respectively. *Deng and Liao* (1996) also opened a number of trenches across the Suyukou scarps. They reported results from one of these trenches (at 38.706 °N, 106.028 °E) in which they identified several colluvial wedges, the most recent of which they interpreted to be from the 1739 event (see Figure 2.3 for location). They did not have age control on this most recent faulting event, but they had a ^{14}C age for the previous colluvial wedge of 2720±60 years before present. In addition, *Deng and*

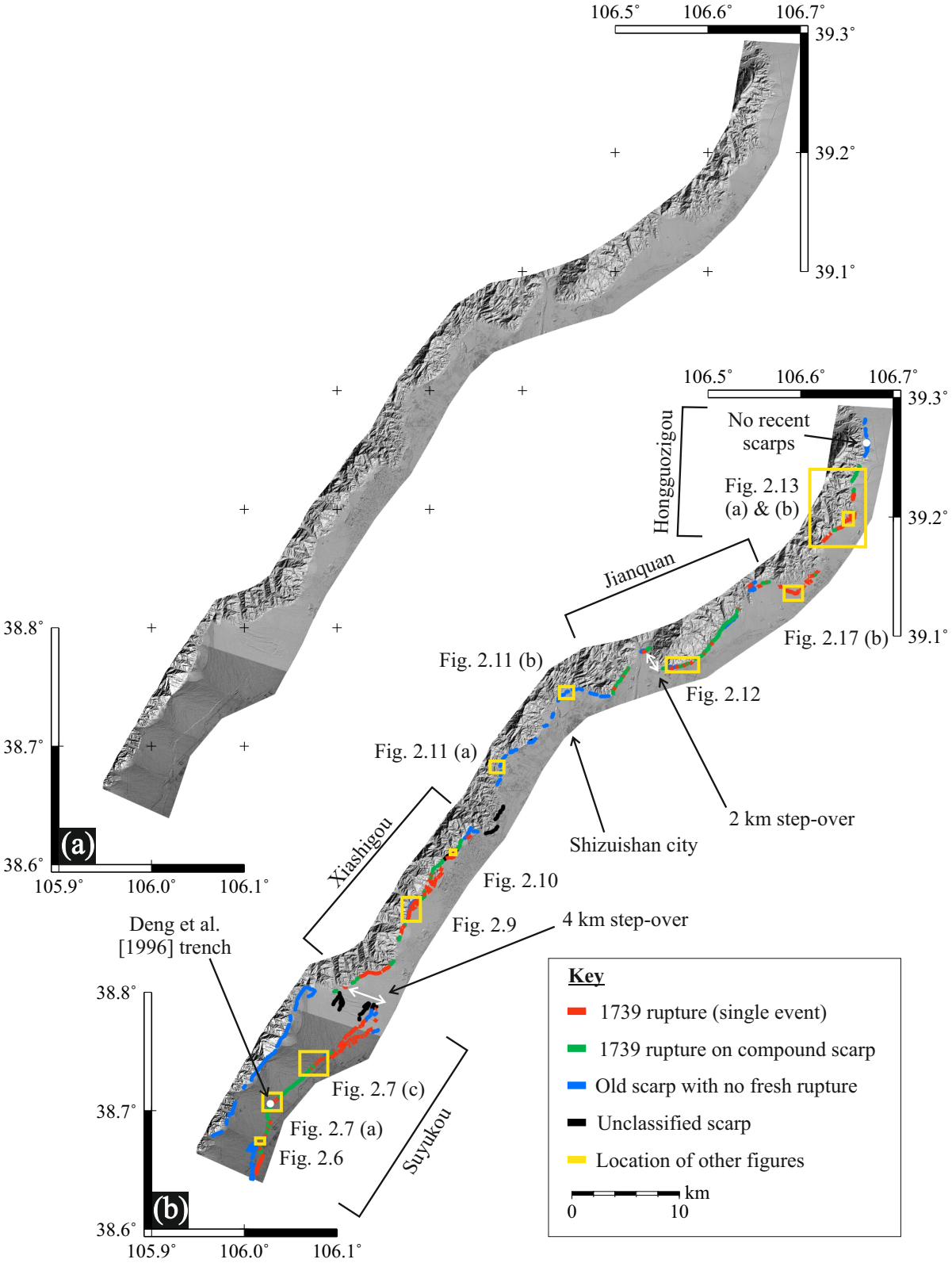


Figure 2.3: (a) High-resolution (1 to 2 m), shaded digital elevation model (DEM) of the East Helanshan Fault derived from Pleiades stereo imagery (location shown in Figure 2.2). (b) Annotated version of (a) including mapped scarps and the locations of other figures.

Liao (1996) measured surface fault dips in their trenches of between 65 and 85 °, with an average of 75 °.

The Hongguozigou scarps are 3.5 to 4 km long and lie some 65 km north of Suyukou along the Helanshan range front, about 12 km southwest of Huinong city (*Zhang et al.*, 1986; *Deng and Liao*, 1996). *Zhang et al.* (1986) recorded a maximum single-event scarp height on this section of 5.3 m, with a typical average of 2 to 3 m. At the northern end of these scarps, three parallel fault strands intersect part of the Great Wall of China that dates from 1531, during the Ming Dynasty (*Ding*, 1981). This site has been the cause of much controversy. Some authors argue that the Great Wall at this location was offset during the 1739 earthquake (e.g. *Zhang et al.*, 1986; *Deng and Liao*, 1996; *Lei et al.*, 2015), whilst other studies propose that it was built on top of pre-existing scarps that were not reactivated in 1739 (e.g. *Lin et al.*, 2013, 2015a). The situation has been further confused by re-building of the wall and human landscape modification that has obscured much of the original field data.

2.4 Methods

2.4.1 ^{14}C dating

We collected five ^{14}C samples from the lowest of the Suyukou scarps in order to try to bracket the timing of the most recent earthquake. Three samples were from deposits in the immediate footwall of the fault that were uplifted during the most recent earthquake, and hence should pre-date the last faulting event; the other two samples were from a post-earthquake deposit that overlay a colluvial wedge, and hence should post-date the last faulting event (see Section 2.5.1 for sample locations). Unfortunately, we were not able to find any ^{14}C samples at other sites further north along the East Helanshan Fault. The samples were dated at the Oxford Radiocarbon Accelerator Unit (ORAU) at the Research Laboratory for Archaeology and the History of Art (RLAHA). Details of the methods used during sample preparation can be found in *Bronk Ramsey et al.* (2004) and

Brock et al. (2010). Ages were then calibrated using version 4.2.4 of the OxCal program (*Bronk Ramsey and Lee*, 2013) applying the atmospheric curve of *Reimer et al.* (2013).

2.4.2 DEM construction and DEM resolution

We constructed a high-resolution DEM of the East Helanshan Fault from five stereo pairs of Pleiades images that were acquired on 23rd April, 17th July, 24th July and 25th July 2014. The images were processed using the Leica Photogrammetry Suite (LPS) module of the ERDAS Imagine software (*Parsons et al.*, 2014; *Zhou et al.*, 2015). Tie points were used to compensate for the orientation errors in the original rational polynomial function (RPF) sensor model that approximates the relationship between image and ground coordinate systems. Having refined the RPF model, a pixel-by-pixel matching procedure was implemented with a window size of 9×9 pixels and a correlation coefficient of 0.3 to 0.7. Other parameters were tried, but this combination was found to give a good balance between point density and topographic smoothing. The apparent offset of a given point on the ground between the two images was then triangulated in order to determine the three-dimensional position of that point. The resulting point cloud from pairwise matching was filtered by averaging within a block of 1 m and then gridded with a pixel spacing of 1 m (using the WGS84 ellipsoid and the UTM 48 N coordinate system) using continuous curvature splines in tension and a tension factor of 0.75 (*Smith and Wessel*, 1990). The imagery was then orthorectified using the Pleiades DEM. The final hill-shaded DEM is shown in Figure 2.3 (a).

Figures 2.4 (a) and 2.4 (b) display statistics for the whole of the Pleiades DEM. When gridded on 1 m by 1 m grid cells, 48% of cells contain at least one point; with 2 m by 2 m cells, 68% of cells contain at least one point. Figures 2.4 (c) and 2.4 (d) show similar statistics for a 200 m wide polygon that follows the trace of the scarp. Within this polygon, 60% of 1 m by 1 m grid cells and 79% of 2 m by 2 m grid cells contain at least one point. However, for the Suyukou section of the DEM, 17% of 1 m by 1 m grid cells and 34% of 2 m by 2 m grid cells contain at least one point (see Figures 2.4 (e) and 2.4 (f)). Figure 2.4 (g) shows an example of part of the point cloud on the Suyukou

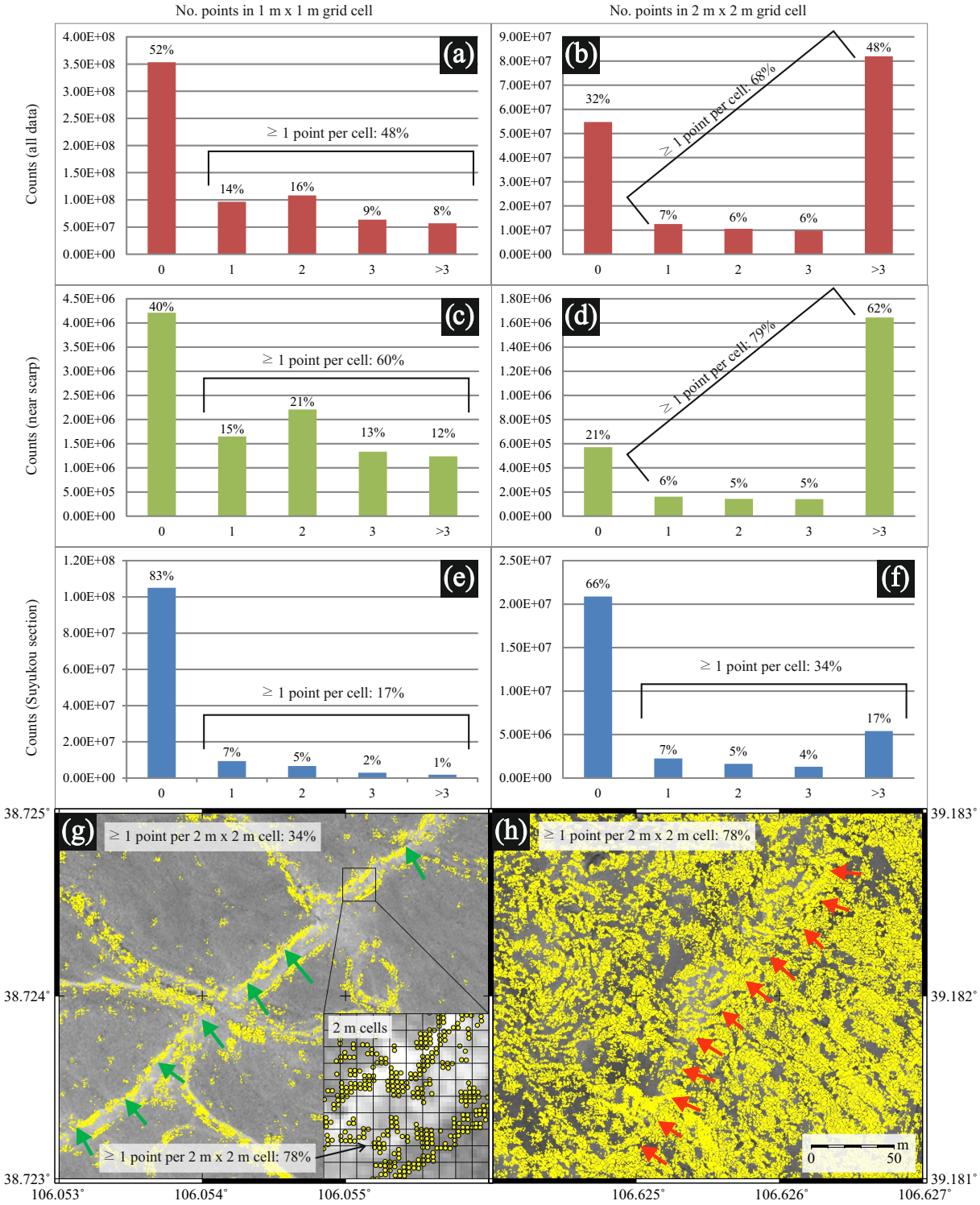


Figure 2.4: (a) Statistics for the whole DEM when gridded on 1 m by 1 m cells. (b) Statistics for the whole DEM when gridded on 2 m by 2 m cells. (c) Statistics for an approximately 200 m wide swath around the scarp when gridded on 1 m by 1 m cells. (d) Statistics for an approximately 200 m wide swath around the scarp when gridded on 2 m by 2 m cells. (e) Statistics for the Suyukou section of the DEM when gridded on 1 m by 1 m cells. (f) Statistics for the Suyukou section of the DEM when gridded on 2 m by 2 m cells. (g) Pleiades imagery and raw point cloud for part of the Suyukou section of the DEM. Compound scarps are marked by green arrows. Zoomed view shows that in the region around the scarp 78% of 2 m by 2 m grid cells contain at least one point. (h) Pleiades imagery and raw point cloud for part of the Hongguozigou section of the DEM, at the same scale as (g). Single-event scarps are marked by red arrows.

scarps; Figure 2.4 (h) shows part of the point cloud on the Hongguozigou scarps at the same scale. It is thought that the significantly less dense point cloud on the Suyukou section is due to the large proportion of this region (more than 50%) that is covered by flat, featureless alluvial fans. However, the zoom in Figure 2.4 (g) indicates that adjacent to the scarp 78% of 2 m by 2 m grid cells contain at least one point, which is similar to the resolution achieved in other sections of the DEM. The horizontal resolution of the Pleiades DEM varies spatially, but, for the regions we are interested in, it is typically between 1 and 2 m.

2.4.3 Measurement of topographic profiles

A number of topographic profiles and vertical offset measurements across the scarp are presented in Sections 2.5.2 and 2.6.2. These measurements were made on the high-resolution Pleiades DEM at locations where we identified a single-event scarp (see Section 2.4.4). The offset measurements were made on the raw Pleiades point cloud by taking swath profiles, perpendicular to the local fault trace, that were 10 to 20 m wide and at least 100 m long and then projecting all points within this swath onto a line. Separate straight lines were fitted to the heights above the scarp and those below the scarp with a simple least squares regression. Using the optical imagery to help identify unmodified fan surfaces, the data to fit was selected by hand, being careful to avoid vegetation and eroded channels. If the slopes of the two lines differed by 1° or more, the profile was discarded since it was deemed not possible to adequately match the upper and lower surfaces in such cases. For the remaining profiles, parallel straight lines were then fitted to the data above and below the scarp in order to measure the vertical offset. The root mean square (RMS) residual in fitting these lines was then taken as the error on the offset measurement. Also, on the basis of our scarp mapping (see Section 2.4.4), we estimated the local fault strike at each location where a vertical offset measurement had been made. We assumed a typical error of $\pm 5^\circ$ on each of these estimates of fault strike. In total, measurements were made at 41 sites and then combined with field data from Suyukou and Hongguozigou by *Deng and*

Table 2.1: Vertical offset measurements from the Pleiades DEM

Profile number	Distance along strike / km	Local fault strike / °	Swath width / m	Slope difference[a] / °	Vertical offset / m	RMS residual / m
1	0.65	23	20.7	1.0	2.0	0.5
2	0.95	40	20.4	0.3	0.4	0.6
3	1.25	18	19.8	-0.1	2.8	0.5
SD16[b]	2.12	-10	N/A	N/A	2.7	N/A
SD15[b]	2.22	1	N/A	N/A	3.2	N/A
4	2.43	33	20.8	-0.6	4.3	0.6
5	2.91	41	20.1	0.9	2.1	0.7
8	6.27	46	14.9	0.9	2.9	0.5
SD27[b]	6.37	44	N/A	N/A	3.1	N/A
SD28[b]	6.47	38	N/A	N/A	3.3	N/A
9	6.48	45	10.3	-0.2	2.7	0.6
11	10.79	47	20.3	-0.3	2.7	0.8
SD50[b]	10.85	44	N/A	N/A	4.4	N/A
13	11.31	42	20.4	-0.4	3.2	0.5
SD54[b]	11.46	47	N/A	N/A	3.9	N/A
14	11.49	49	20.1	-1.0	5.1	0.8
SD55[b]	11.70	36	N/A	N/A	3.0	N/A
15	11.71	41	17.8	-0.2	1.8	0.5
16	11.83	51	20.2	-0.2	2.4	0.6
SD56[b]	12.00	51	N/A	N/A	3.4	N/A
18	12.12	61	20.9	0.8	2.9	1.3
SD58[b]	12.18	54	N/A	N/A	2.0	N/A
19	12.32	103	20.1	-0.4	1.2	0.6
SD61[b]	12.70	34	N/A	N/A	1.2	N/A
20	12.79	38	20.6	-0.6	1.4	0.7
21	13.92	48	20.1	0.2	1.8	0.7
23	14.28	12	20.2	-0.1	1.0	0.6
24+25[c]	14.53	49	N/A	N/A	3.3	1.2
26	16.73	33	20.3	-1.0	2.5	0.9
27	17.21	63	20.8	-0.8	1.4	0.6
28	18.03	42	20.1	0.1	2.0	0.5
29	18.62	53	20.9	0.4	1.0	0.5
30	18.87	27	20.5	-0.4	3.3	0.6
31	21.18	70	20.0	-0.2	4.3	0.5
33	22.13	54	20.6	-0.4	2.3	0.8
36	28.39	36	10.6	-0.3	3.0	0.5
38	32.27	41	20.3	0.9	4.9	0.7
43	58.27	50	20.4	0.8	3.9	0.8
46	60.85	92	10.3	-0.3	1.2	0.5
47	61.31	49	10.4	-0.5	1.5	0.5

[a] Difference in slope between regression lines fitted to the point cloud data above and below the scarp.
[b] Identification code used by *Deng and Liao* (1996); SD refers to Suyukou and HD to Hongguozigou.
[c] Profiles from two parallel fault strands added together.

Table 2.1: (continued) Vertical offset measurements from the Pleiades DEM

Profile number	Distance along strike / km	Local fault strike / °	Swath width / m	Slope difference[a] / °	Vertical offset / m	RMS residual / m
51	73.39	91	10.6	0.0	2.4	0.4
53	73.52	101	10.2	-0.5	2.7	0.3
55	73.92	35	10.5	-0.3	4.7	0.5
56	74.23	31	10.5	0.1	4.1	0.6
58	74.71	60	10.2	-0.2	3.6	0.5
59+60[c]	75.14	52	N/A	N/A	4.7	0.7
61	75.99	73	10.3	0.4	3.2	0.6
HD717-2[b]	80.86	62	N/A	N/A	1.1	N/A
HD717-3[b]	81.12	82	N/A	N/A	1.2	N/A
64	81.36	44	10.5	-0.4	3.7	0.5
65	81.64	26	10.4	-0.6	2.2	0.4
66	81.91	66	10.2	-0.7	3.7	0.5
71	82.87	38	10.0	0.4	1.4	0.6

[a] Difference in slope between regression lines fitted to the point cloud data above and below the scarp.
[b] Identification code used by *Deng and Liao* (1996); SD refers to Suyukou and HD to Hongguozigou.
[c] Profiles from two parallel fault strands added together.

Liao (1996) to give a complete suite of 53 measurements. All of these data are given in Table 2.1.

In order to assess the reliability of topographic profiles measured on the Pleiades DEM we compared one of our measurements to a theodolite profile from the same location measured in the field by *Deng and Liao* (1996) (see Figure 2.5 (a)). In Figure 2.5 (b) the grey circles show all of the points from within the swath that were used to make the offset measurement, whilst the black line shows a simple profile from the centre of the swath. Note that in profiles on subsequent figures we have not shown the grey points, even though this data was used to make all of the offset measurements that we quote. Figure 2.5 (c) indicates that the steepness of the free face is not entirely captured by the Pleiades DEM, but that the vertical offset measured according to our method agrees with the field measurement to within their stated errors.

Additionally, we tested the effect of using different swath widths. At the location of profile 53 (marked B-B′ in Figure 2.17 (b)), we tried swath widths of between 5 m and 40 m (in increments of 5 m) and the measured offset varied by less than 0.2 m between all

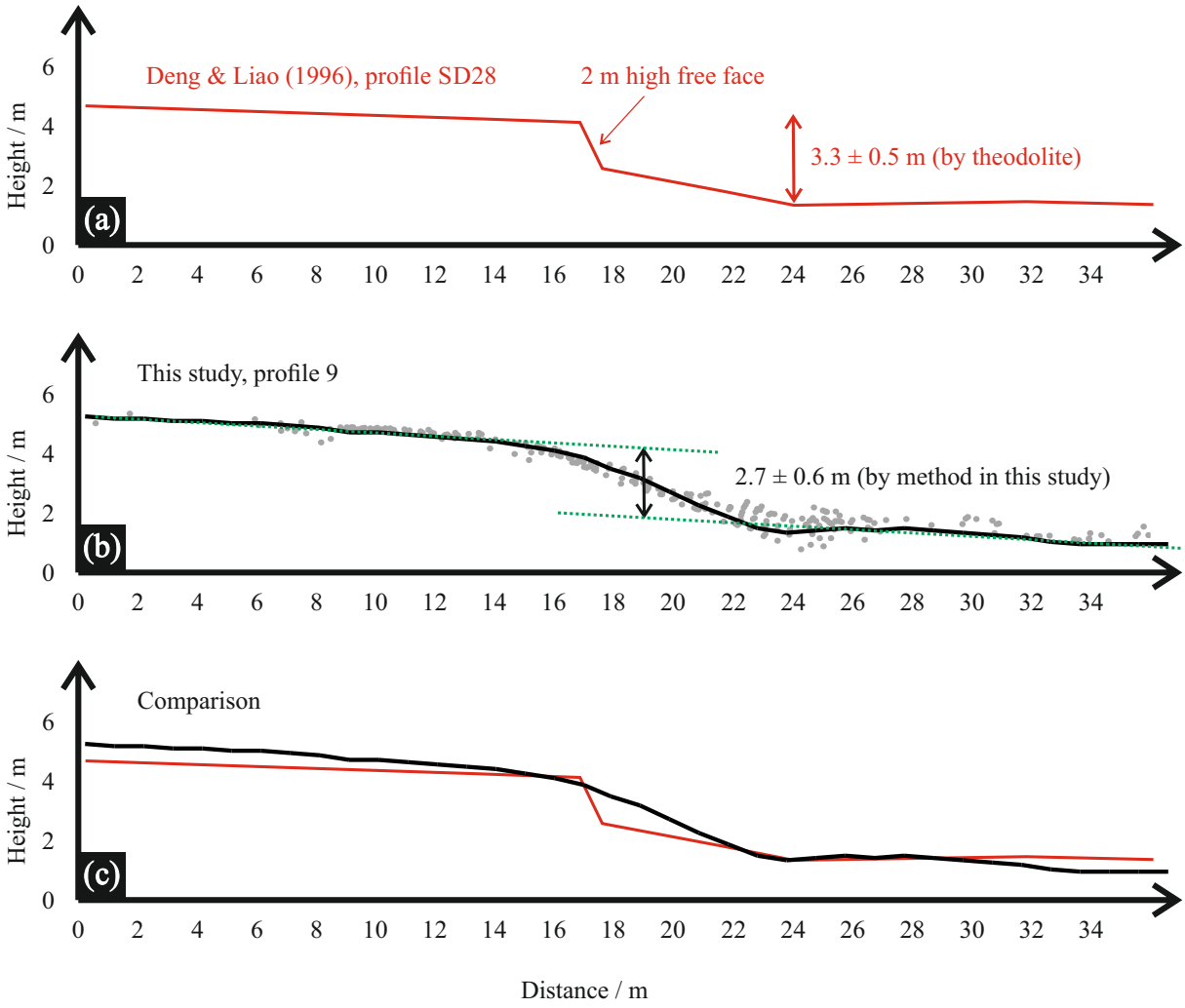


Figure 2.5: (a) Profile SD28 from *Deng and Liao* (1996) measured by theodolite. This profile is measured at the location marked p9 in Figure 2.7 (b). *Deng and Liao* (1996) record a vertical offset of 3.3 m and a 2 m high free face. We estimate an error of ±0.5 m on their offset measurement. Note that there is no vertical exaggeration on this plot. (b) Profile 9 from this study measured from the Pleiades DEM at the same location and displayed at the same scale. Black line shows single profile and grey points show data from within the swath that was used to obtain our vertical offset measurement of 2.7±0.6 m using the method described in Section 2.4.3. Note that we used a 250 m long profile for this measurement and only the central section is shown here. (c) Comparison of the two profiles.

eight measurements. Meanwhile, the estimated error increased from ±0.3 m for the 5 m swath to ±0.6 m for the 40 m wide swath. This indicates that our approach of taking a single 10 to 20 m wide swath at each measurement site is appropriate for obtaining a set of offset measurements that allow us to investigate larger-scale changes in throw along strike.

2.4.4 Scarp mapping and type locality calibration

Previous authors have strongly suggested that the Suyukou scarps were produced in the 1739 earthquake (*Zhang et al.*, 1982; *Deng et al.*, 1984b; *Zhang et al.*, 1986; *Deng and Liao*, 1996; *Bai and Jiao*, 2005). Here, we describe the morphology of the Suyukou scarps in detail, and how they show up on the Pleiades DEM. We then use these observations to inform our mapping of the other scarps along the East Helanshan Fault.

The Suyukou scarps vary in strike between about 10 ° and 50 °, cutting through a series of four, large, coalesced, alluvial fans (*Deng and Liao*, 1996). The fan material is unconsolidated and very coarse, comprising sub-angular gravel, cobbles and boulders (see Figure 2.6 (c) and inset in Figure 2.7 (a)). A 2 to 3 m high free face, with a dip of between 70 ° and 90 °, exists along approximately 70% of the Suyukou scarps (*Zhang et al.*, 1986). We used the existence of this free face as an indication of recent rupture. *Zhang et al.* (1986) also considered how the free face has been degraded and found that it has largely disappeared on scarps less than 2 m high (though the rate of erosion is also likely to depend on the properties of the footwall material). In many sections the free face rides on a cumulative scarp, but in some locations, adjacent to active river channels, a fresh, single-event scarp is visible. On the compound scarps, a distinct bevel separates the free face from the top of the scarp, and a debris slope, with a 30 ° angle of repose, is common below the free face. In some places, the scarp has been eroded by episodic gully incision, depositing secondary splay fans on the hanging wall side. The predominant wind direction is from the west, resulting in significant accumulations of aeolian loess in the lee of the scarp.

On the Pleiades DEM, the Suyukou scarps appear as sharp topographic discontinuities. We were not able to resolve the free face (see Section 2.4.3), but having observed it during our field reconnaissance in a number of locations, we were then able to trace it along strike in the DEM. A slope map derived from the Pleiades DEM was also used to help distinguish between freshly-ruptured and older scarps. Scarps that had shown a free face in the field had typical slopes of 30 to 45 ° on the DEM, whereas scarps with no free face had typical slopes of 20 to 25 °.

In the Pleiades DEM and imagery, compound scarps could be distinguished from single-event scarps by the relative width of the scarp (see Figure 2.7 (c)). We were also able to identify terrace risers (using both the DEM and the slope map), which allowed us to differentiate single-event scarps bordering the youngest surface from compound scarps bordering the older surfaces. Also, knowing that the maximum single-event, vertical offset from the places visited by *Zhang et al.* (1986) and *Deng and Liao* (1996) was around 4 to 5 m, we were able to classify any scarps more than 10 m high as compound scarps. Scarps that were 5 to 10 m in height were only classified as single-event scarps if we were able to verify in the field that they showed a single free face and no bevel at the top of the scarp. This said, differentiating between the different generations of scarps was not always straightforward and to some degree the results are subjective—there were also some scarps that we were not able to classify. The resulting map is shown in Figure 2.3 (b). We discuss the main features of this map in Section 2.5.2.

2.5 Results

2.5.1 Palaeoseismological work on the East Helanshan Fault

Road-cut exposure

Our first sample site is at the southernmost end of the Suyukou scarps (38.674 °N, 106.016 °E), 360 m southwest of the road leading from Yinchuan to the range front (see Figure 2.3 for location). Major, industrial landscape modification is taking place at this site and when we visited in March 2014 a new road excavation had just been cut through the scarp (see Figure 2.6). At this location the fault forms a braided pattern with at least two subsidiary scarps (see Figure 2.6 (b)). We measure a total throw across all three scarps on the Pleiades DEM of 4.3±0.6 m. The road cutting exposes a cross-section of the main scarp with its preserved free face (see Figure 2.6 (c)). The scarp footwall is composed of sub-horizontal deposits of unconsolidated, sub-angular fan gravels. Clasts range in size from sand grade to 20 cm in diameter. The same gravels are just visible in the exposed parts of the hanging wall, enabling us to measure a fault slip on the central

Table 2.2: ^{14}C dating results

Sample number	Location	Latitude °	Longitude °	Elevation m	Description	Age / ^{14}C years BP	Calibrated date range / years
1	Road-cut site	106.01570	38.67350	1180	Faecal pellet	1.170±0.004	Modern
2	Road-cut site	106.01570	38.67350	1180	Faecal pellet	1.158±0.004	Modern
3	First river site	106.03300	38.71070	1227	Gymnosperm wood	279±28	1514-1795 AD (95.4%)
4	First river site	106.03290	38.71080	1225	Charcoal	1130±31	777-989 AD (95.4%)
5	Second river site	106.07449	38.74066	1187	Bivalve shell	2099±31	199-45 BC (95.4%)

All ^{14}C samples were dated at the Oxford Radiocarbon Accelerator Unit (ORAU) at the Research Laboratory for Archaeology and the History of Art (RLAHA). Details of the methods used during sample preparation can be found in *Bronk Ramsey et al.* (2004) and *Brock et al.* (2010).

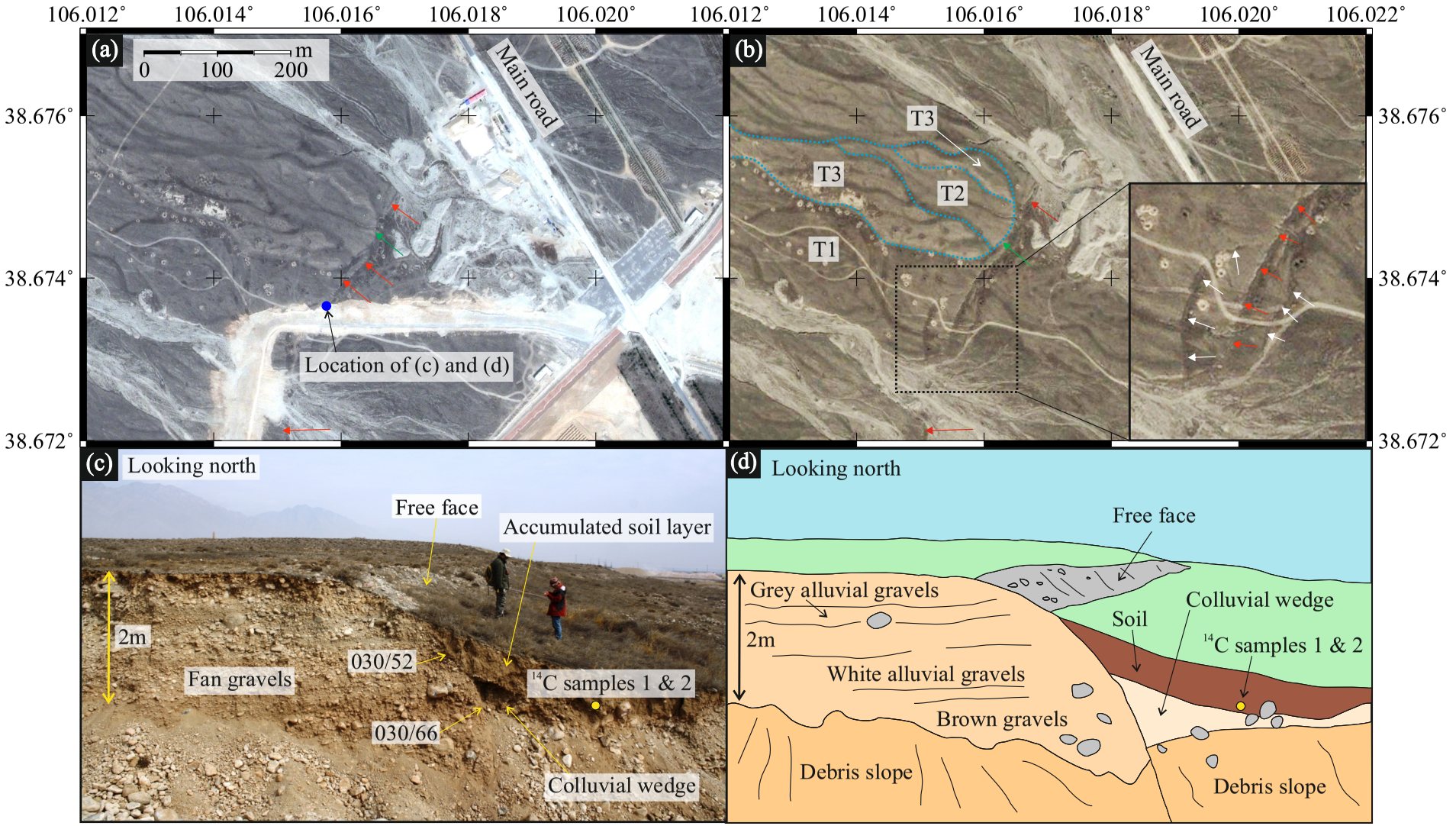


Figure 2.6: (a) Pleiades imagery of a road-cut exposure through the Suyukou scarps. Single-event scarps are marked by red arrows; compound scarps are marked by green arrows. (b) Google Earth imagery from September 2012 (source: http://earth.google.com) of the same location at the same scale prior to the building of the road. Three terrace levels, outlined in blue, are identifiable in the footwall of the fault. Zoomed image shows three separate fault strands. Main strand marked by red arrows and subsidiary strands marked by white arrows. The total throw across all three strands is 4.3 m. (c) Annotated field photograph (taken at 38.674 °N, 106.016 °E) showing a cross-section through the main fault strand at the road-cut exposure. Yellow circle indicates the location of ^{14}C samples 1 and 2 for dating the accumulated post-earthquake soil. (d) Sketch of the same view as in (c) indicating the principal units exposed in this section.

strand of 3.95 m. We also record a surface fault dip of 66°, shallowing to 52° near the eroded top of the scarp. (This is in agreement with the surface fault dip measurements made in nearby trenches by *Deng and Liao* (1996), which varied between 65° and 85°, but is substantially different to the 39° fault dip at depth suggested by the seismic profile in *Fang et al.* (2009)—see also Figure 2.2 (b).) Together, the 3.95 m slip and 66° dip suggest a vertical offset on the central strand of 3.6 m, which is consistent with the total throw of 4.3 m across all three strands. (We do not have estimates of slip on the other two strands.) The hanging wall gravels are covered by a colluvial wedge, also composed of fan gravels though with noticeably less consistent clast orientations and even poorer consolidation. The colluvial wedge is overlain by a 70 cm thick layer of brown soil, sand and loess that has accumulated since the most recent faulting event. ^{14}C samples 1 and 2 (both faecal pellets) are from within this post-earthquake soil between 60 and 70 cm below the ground surface (see Figures 2.6 (c) and 2.6 (d)). Both samples from the road-cut exposure give modern ages (see Table 2.2).

First river exposure

The second sample site is at 38.710°N, 106.033°E, where a major braided river channel from the Helanshan crosses the Suyukou scarps. On the footwall side, a stepped series of river terraces is preserved adjacent to the channel, potentially corresponding to a sequence of earthquakes at this location (*Deng and Liao*, 1996). The lowest terrace (T1), which is interpreted to represent the most recent earthquake, is typically around 3 m above the hanging wall level. Remnant islands of this surface that have not yet been completely removed by fluvial erosion are also visible within the main channel itself, further supporting the idea that they represent a relatively young, single-event scarp (see Figures 2.7 (a) and 2.7 (b)). The footwall material here is similar to that seen at the road-cut site, though with a slightly larger proportion of finer clasts; in places the gravel layers are interbedded with fluvial sands and silts. ^{14}C samples 3 and 4 are from the exposed side of one of the T1 islands within the river and hence from the immediate footwall of the fault (see Figure 2.7 (b)). Sample 3 is a piece of gymnosperm wood from a fluvial sand layer approximately 70 cm below the ground surface. This sand layer is overlain by a 60 cm thick

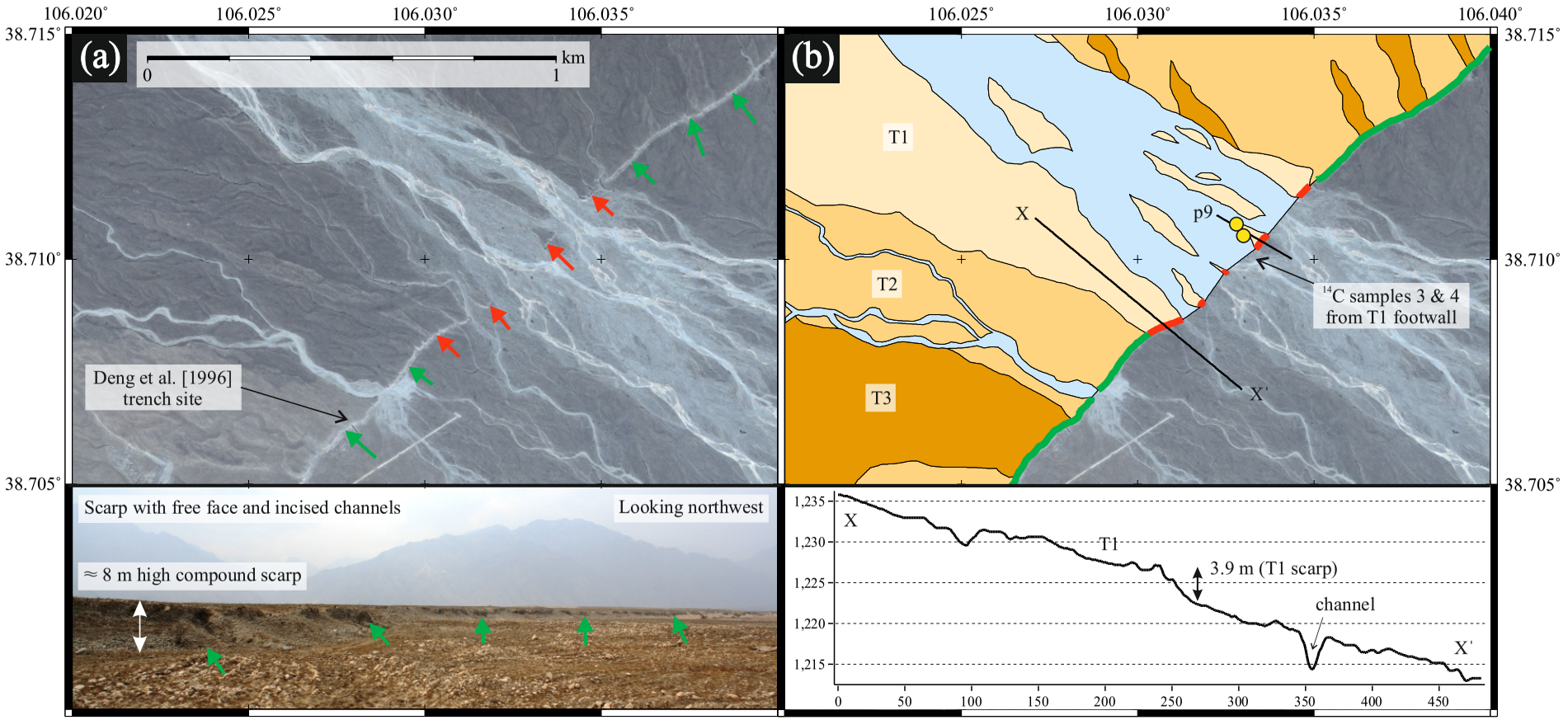


Figure 2.7: (a) Pleiades imagery of a major river crossing the Suyukou scarps at 38.710 °N, 106.033 °E. Single-event scarps are marked by red arrows; compound scarps are marked by green arrows. Inset photograph shows free face preserved on many of the scarps. (b) Annotated geomorphological map of the same site, showing different generations of alluvial fan surfaces. The inset profile indicates a typical scarp height for the youngest terrace (T1). Fault scarps are mapped in red, green and blue according to the key. Yellow circles indicate ^{14}C samples 3 and 4 taken from the uplifted terrace material in the immediate footwall. p9 indicates another profile, shown in Figure 2.5.

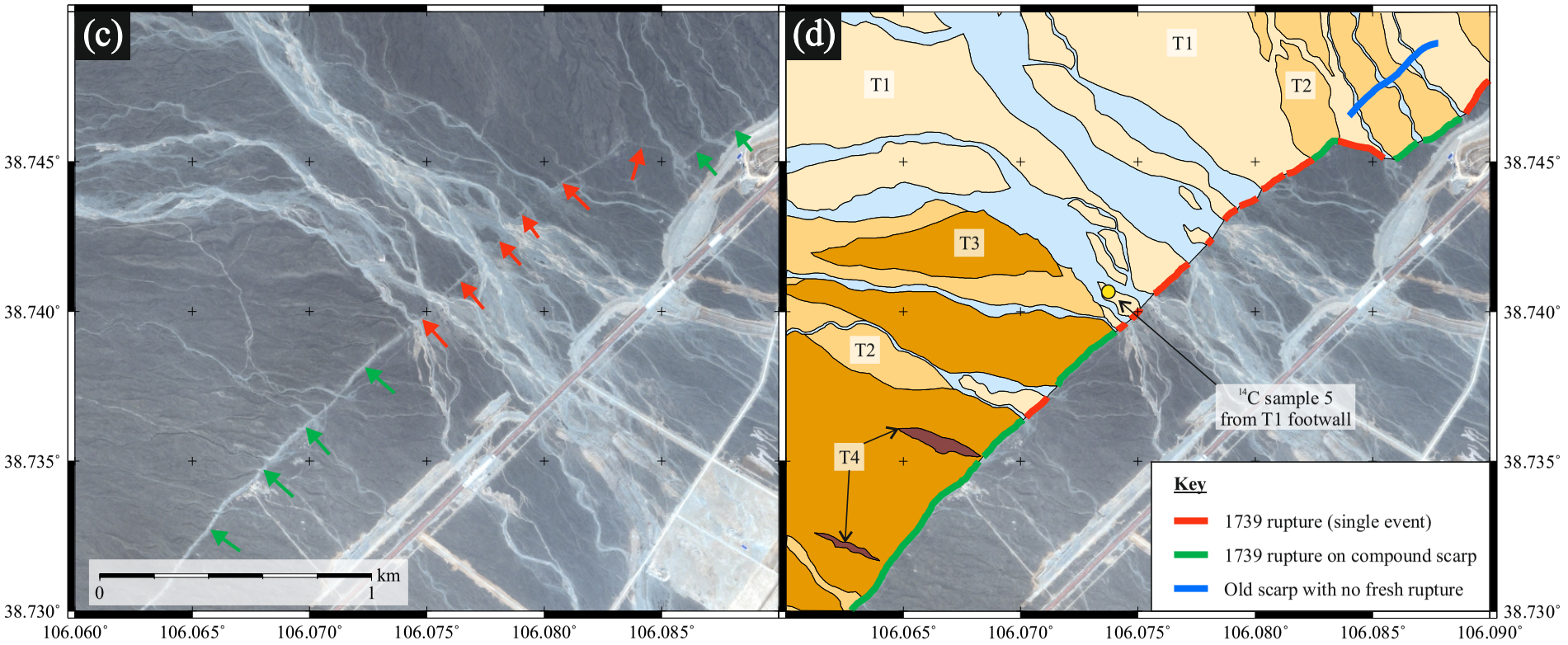


Figure 2.7: (continued) (c) and (d) show another river crossing site on the Suyukou scarps at 38.741 °N, 106.075 °E with similar annotations to (a) and (b). ^{14}C sample 5 was taken here.

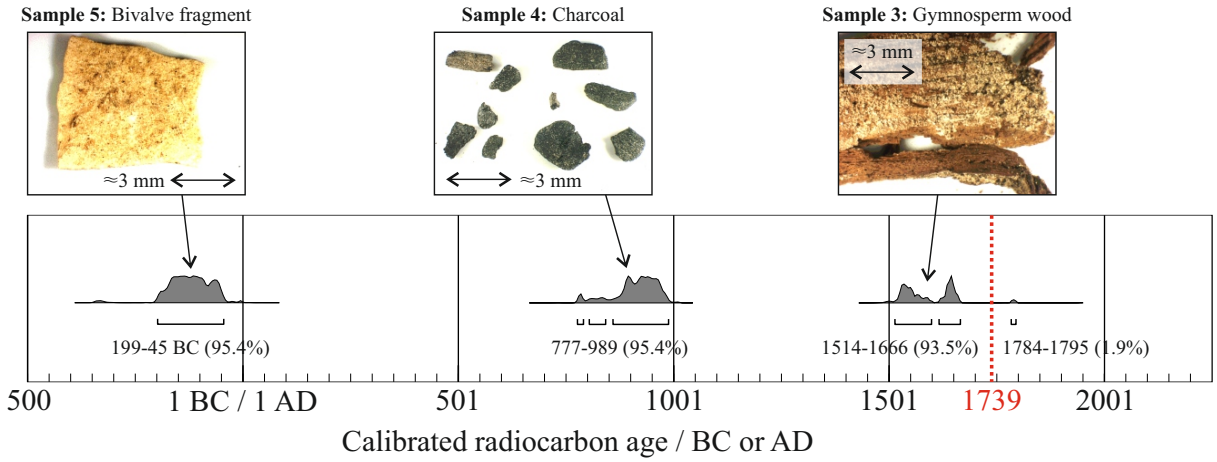


Figure 2.8: Time line showing the calibrated radiocarbon ages of ^{14}C samples 3, 4 and 5 from the T1 terrace (locations shown in Figures 2.7 (b) and (d)). Grey histograms show normalised probability density functions, indicating the range of possible ages for each sample within certain percentage confidence limits. All three samples pre-date 1739.

unit of poorly sorted, sub-angular alluvial gravels and around 10 cm of soil development. Sample 4 is a fleck of charcoal from a sand lens 80 cm below the ground surface. It is also overlain by a single unit of poorly sorted, sub-angular alluvial gravels. Sample 3 provides a calibrated radiocarbon date of 1514 to 1795 AD (95.4% probability, i.e. within two standard deviations of the mean) and sample 4 provides a calibrated radiocarbon date of 777 to 989 AD (95.4% probability). These ages are shown in Figure 2.8 and Table 2.2.

Second river exposure

The final sample site is at 38.741 °N, 106.075 °E, where another major river from the Helanshan crosses and dissects the Suyukou scarps (see Figures 2.7 (c) and 2.7 (d)). The geomorphology is very similar to that at the first river exposure. ^{14}C sample 5, a single fragment of bivalve shell, is from the side of the T1 surface on the footwall side at a depth of 40 cm (see Figure 2.7 (d)). The sample is from within a 50 cm thick layer of yellow-brown sand and silt, overlain by 10 cm of rounded gravels. Sample 5 provides a calibrated radiocarbon date of 199 to 45 BC (95.4% probability). The age result is also shown in Figure 2.8 and Table 2.2.

Interpretation of dating results

All three footwall samples pre-date 1739. The only possible exception is that, within the two standard deviation range, there is a very small probability (1.9%) that sample 3 is younger than 1739 (see Figure 2.8). Nonetheless, taken together, the samples indicate that the material preserved in the T1 terrace was almost certainly deposited prior to 1666 (the limiting age of sample 3 for a probability of 93.5%). Combined with the modern ages for the post-earthquake soil at the road-cut site, we therefore have strong evidence that the uplift of T1 has occurred between 1666 and the present day. The only recorded earthquake of any significant magnitude ($M_w > 5$) in this time-frame and at this location is the 1739 event. We therefore conclude that the 1739 Yinchuan earthquake occurred on the East Helanshan Fault.

2.5.2 Geomorphology of the 1739 rupture

We map an end-to-end rupture length of 87 km (see Figure 2.3 (b)), verifying the ends of the rupture in the field. Although the fault continues to both the north and the south, there are no signs of recent surface displacement in the form of a free face or similar at, for example, 39.262 °N, 106.671 °E in the north and 38.540 °N, 105.986 °E in the south. Although the ends of the named segments (Suyukou, Xiashigou, Jianquan and Hongguozigou) correspond to geometrical discontinuities along the fault, we do not presuppose any knowledge of kinematic segmentation; the names are merely convenient short-hand for referring to different portions of the fault. We also identify two step-over zones: one left step of about 4 km between the end of the Suyukou segment and the start of the Xiashigou segment, and a right step of around 2 km in the middle of the Jianquan segment (see Figure 2.3). We note that the first of these step-overs is accompanied by a number of sub-parallel scarps on the intervening relay ramp, at least some of which ruptured in 1739. The second step-over occurs at a sharp bend in the range front and it is unclear as to whether or not these segments are linked at depth. Additionally, we observe that the rupture trace is not simple: it is corrugated, with changes in local fault strike of up to 70 °. In a number of locations there also appear to be multiple active strands.

The fault geometry will be discussed further in Section 2.6.2, but we note here that such a complex rupture pattern is not unexpected; the M_s 6.8 1954 Dixie Valley earthquake in western Nevada, for example, displayed a similar pattern (*Caskey et al.*, 1996).

Xiashigou

Figure 2.9 shows part of the Xiashigou segment at the location first identified by *Deng and Liao* (1996) (see Figure 2.3 for location). Here, a series of scarps are apparent adjacent to the range front. The Pleiades DEM and Google Earth imagery also show evidence for two fresher rupture strands that diverge from the range front. Figures 2.9 (c) and 2.9 (d) show field photographs from two locations on the Xiashigou segment. We observe a free face at both of these locations, indicating that the scarp seen in the DEM is likely from 1739 (according to the criteria set out in Section 2.4.4). The topographic profiles in Figures 2.9 (e) and 2.9 (f) both show a vertical offset of 1.5±0.5 m, which is consistent with the previous measurements of 1 to 2 m made by *Deng and Liao* (1996). However, the photographs in Figures 2.9 (c) and 2.9 (d) show scarp heights (measured in the field) of 3 m and 0.6 m respectively. These heights are measured vertically from the proximal hanging wall, so it is to be expected that they differ from the nearby topographic profiles where alluvial surfaces are fitted over a horizontal distance of 100 m or more. It is also likely that there is some variability in the geomorphological expression of the fault along strike over relatively short distances.

Figure 2.10 also shows part of the Xiashigou segment (see Figure 2.3 for location). Again, a free face is seen in the field and the scarp can be followed across an alluvial fan in the Pleiades imagery. At this site we measure a vertical offset of 3.4±0.8 m from the Pleiades DEM. The fresh scarps can be followed almost continuously from the location of Figure 2.9 to the location of Figure 2.10 except for a few short sections where the scarps have been eroded or obscured by human activity.

Shizuishan city

We could not identify any fresh scarps in the Pleiades DEM for a length of approximately 15 km between the Xiashigou and Jianquan segments, a region where the range front is

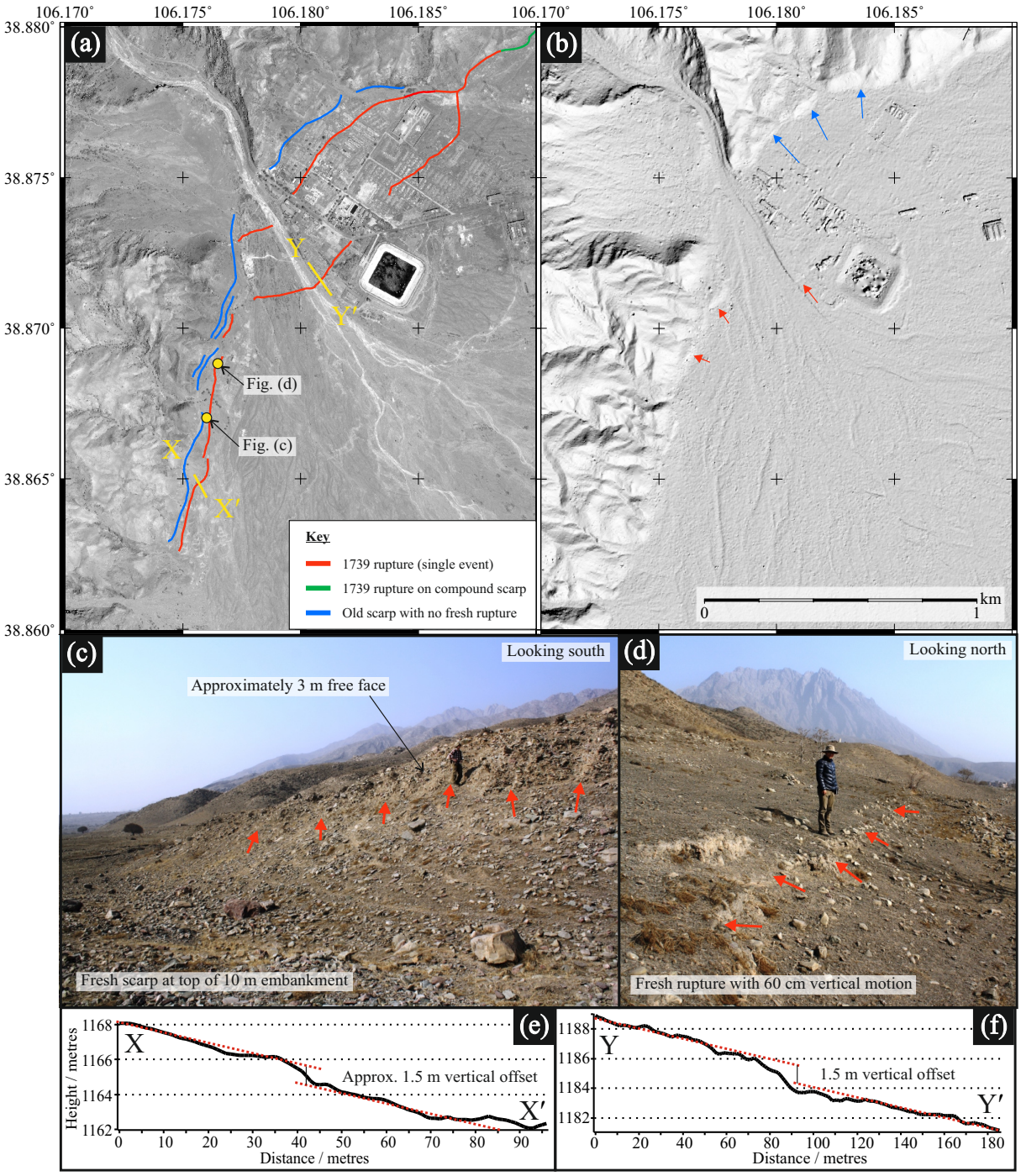


Figure 2.9: (a) Pleiades imagery of the Xiashigou portion of the East Helanshan Fault. Fault scarps are mapped in red, green and blue according to the key. Yellow dots indicate sites visited in the field and shown in (c) and (d). (b) Pleiades DEM of the same region as (a). Red arrows indicate places where the 1739 rupture is particularly clear on the DEM; blue arrows point to an older, smoother, compound scarp. (c) and (d) Field photographs from 38.867 °N, 106.176 °E and 38.869 °N, 106.176 °E showing evidence for a fresh rupture and its associated free face in alluvial gravels on the Xiashigou segment. (e) and (f) Topographic profiles from the Pleiades DEM at the locations marked in (a) showing the vertical offset at two other locations on the Xiashigou segment.

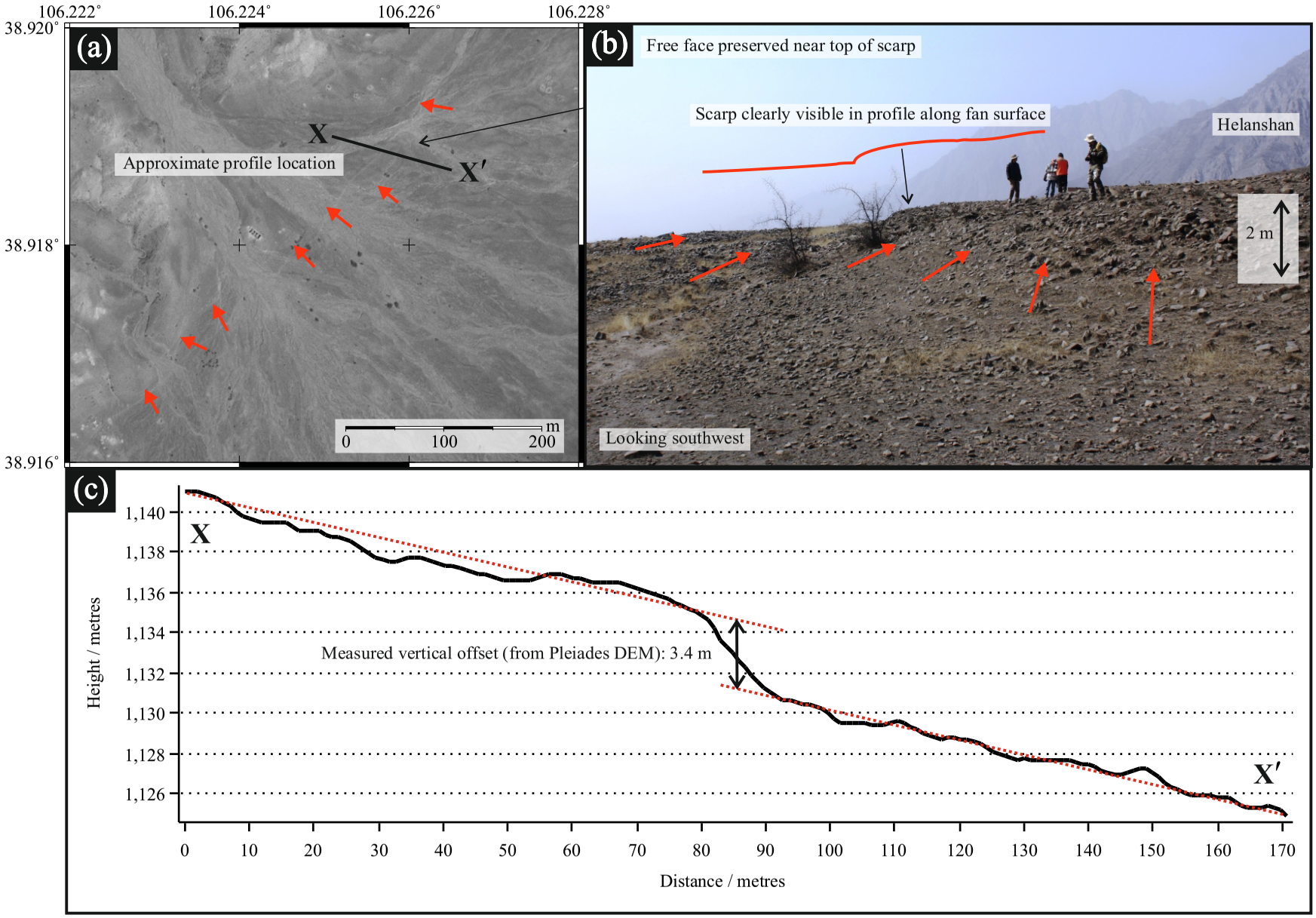


Figure 2.10: (a) Pleiades imagery of part of the Xiashigou segment of the East Helanshan Fault. The location of the 1739 rupture trace is indicated by red arrows. (b) Field photograph taken at 38.919 °N, 106.226 °E showing the 1739 rupture and the characteristic free face. (c) Topographic profile from the Pleiades DEM at the location marked in (a) showing a vertical offset at this location of 3.4 m.

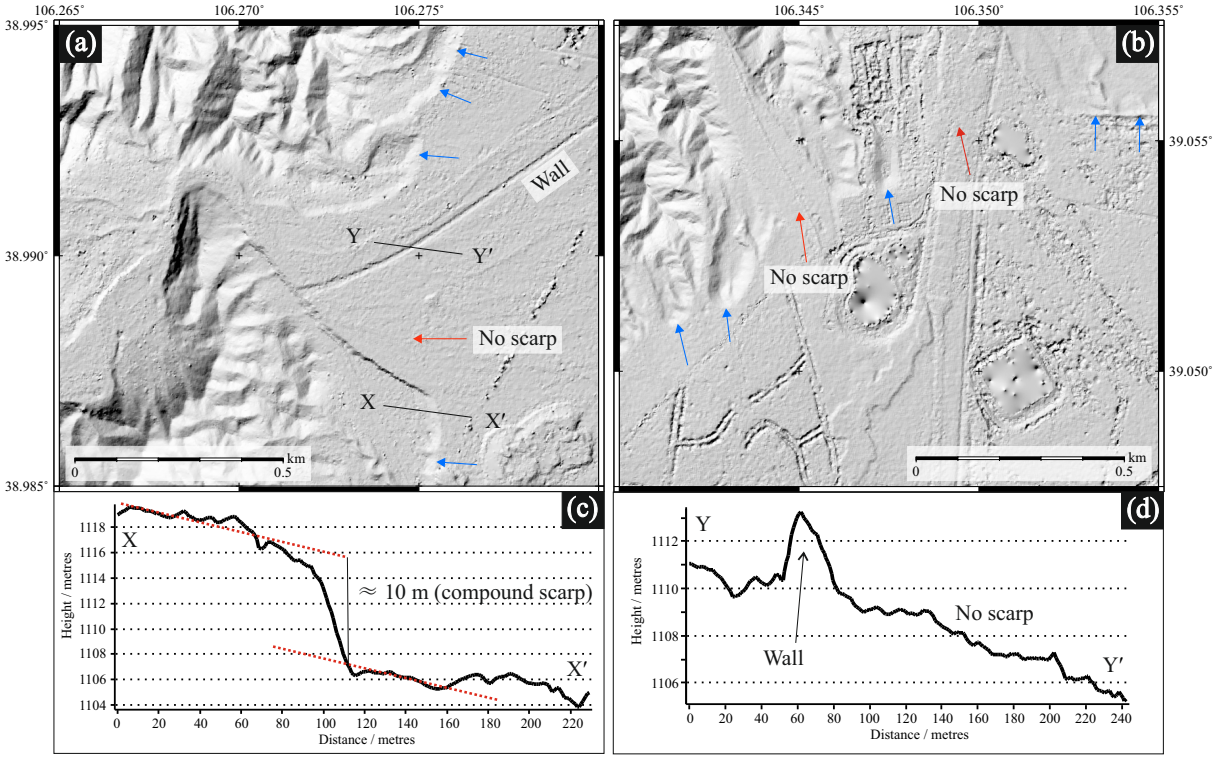


Figure 2.11: (a) Zoomed in view of the Pleiades DEM at the range front northwest of Shizuishan city. Blue arrows highlight an old (compound) fault scarp. The undisturbed alluvial material highlighted by the red arrow suggests that the 1739 earthquake did not rupture this portion of the range front. (b) Similar DEM view from a location just to the north, also indicating a lack of fresh rupture on this portion of the range front. (c) Topographic profile X-X′ across the compound scarp. (d) Topographic profile Y-Y′ across the undisturbed alluvial material.

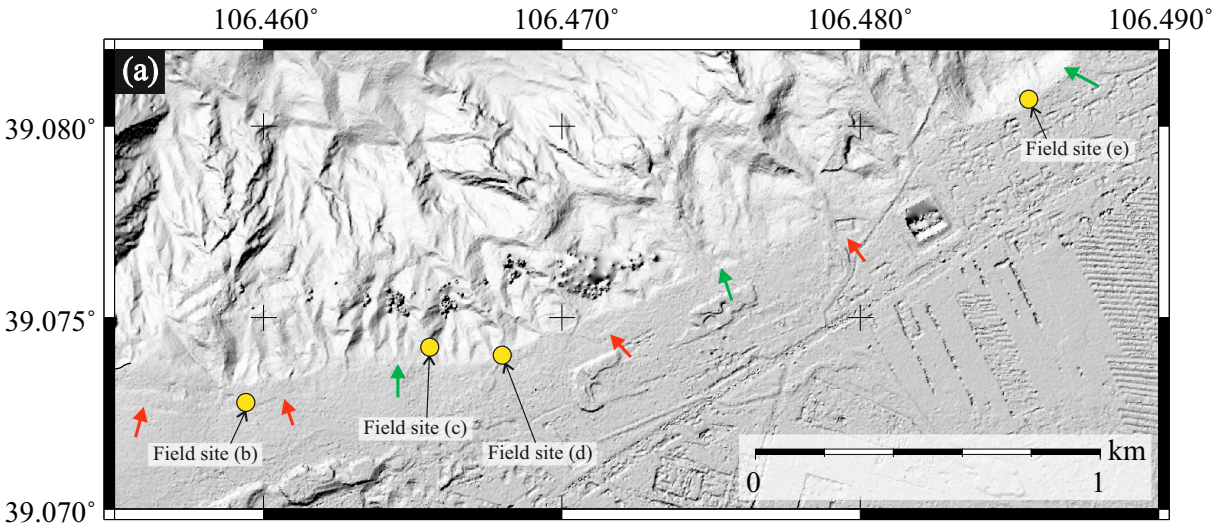


Figure 2.12: (a) Zoomed in view of the Pleiades DEM at the range front near Jianquan. Single-event scarps are marked by red arrows; compound scarps are marked by green arrows. In some places the rupture steps away from the range front and an older scarp is visible behind the most recent one. Yellow dots indicate field locations.

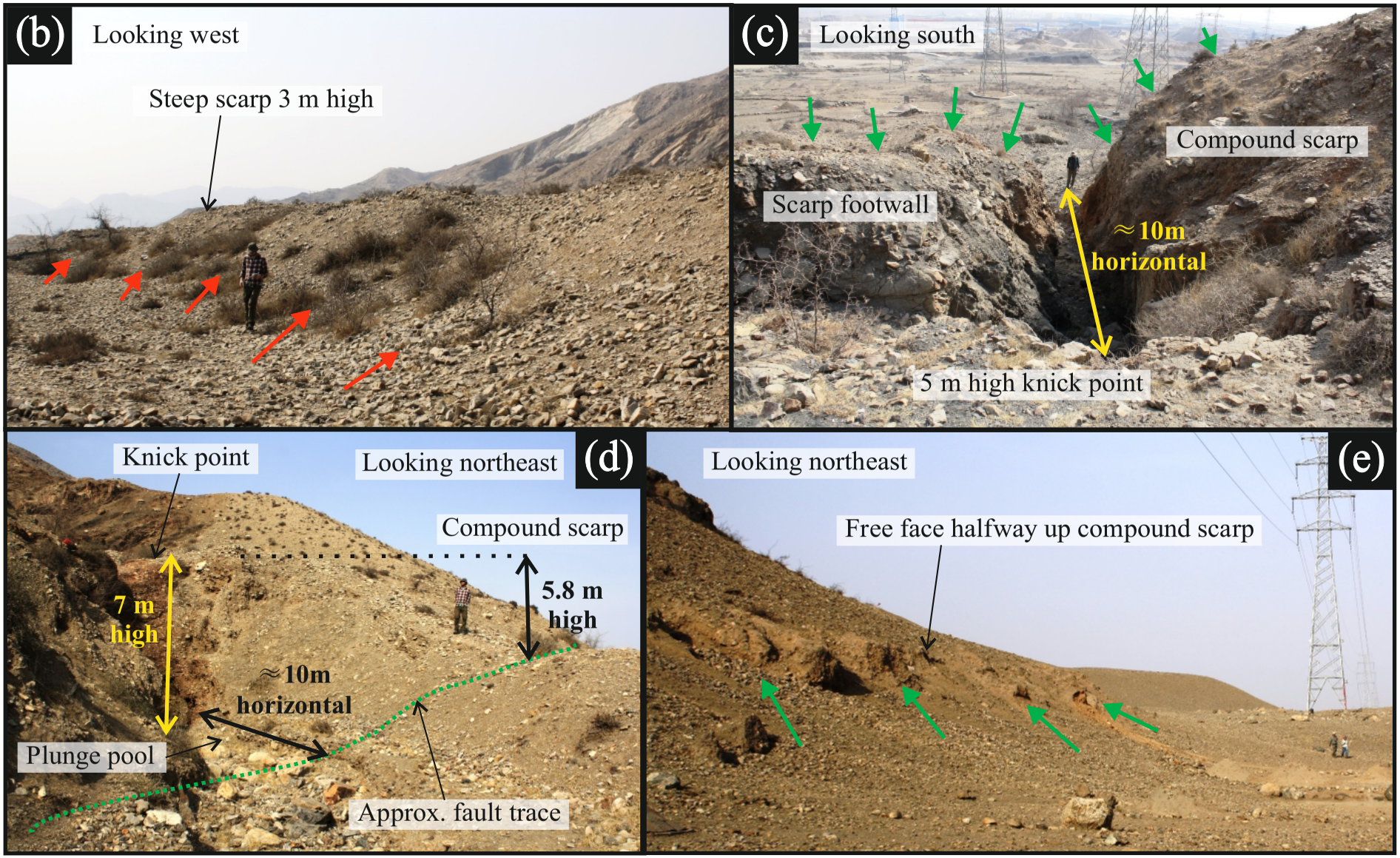


Figure 2.12: (continued) (b) & (e) Field photographs (taken at 39.073 °N, 106.459 °E and 39.081 °N, 106.486 °E) of the 1739 scarp in alluvial material near Jianquan. (c) & (d) Field photographs (taken at 39.074 °N, 106.466 °E and 39.074 °N, 106.468 °E) of knick points approximately 10 m behind the 1739 scarp at Jianquan.

embayed and the intervening land is largely covered by Shizuishan city (see Figure 2.3). This includes both the Helanshan range front and the alluvial fans to the southeast of the mountains. Figure 2.11 shows zoomed views of two portions of the Pleiades DEM at the range front behind Shizuishan city (see Figure 2.3 for locations). In both cases, old compound scarps can be seen with vertical offsets of around 10 m. However, no scarps are visible in the more recent fan sediments immediately abutting channels draining the Helanshan.

Jianquan

Figure 2.12 shows part of the Jianquan segment, northeast of the step-over (see Figure 2.3 for location). As for the Xiashigou segment, the key piece of evidence for these scarps being from the 1739 event is the observation of a fresh, free face in the field (see Figures 2.12 (b) and 2.12 (e)). Along this section, we observe a number of knick points, typically 5 to 7 m high, about 10 m north of the scarp in gullies crossing the fault (see Figures 2.12 (c) and 2.12 (d)). If the knick points are from 1739 this would imply a retreat rate of approximately 35 mm/a, but this seems too fast given that these gullies have quite small upstream catchments (*Whittaker and Boulton*, 2012). Nonetheless, though the knick points are unlikely to be from 1739, they do attest to recent changes in base level across the Jianquan segment of the East Helanshan Fault.

Hongguozigou

The Hongguozigou segment comprises both the 4 km of scarps near the Great Wall site (*Zhang et al.*, 1986; *Deng and Liao*, 1996) and a series of fresh-looking scarps, including a near right-angle change in fault strike, which we identify from the Pleiades DEM (see Figures 2.13 and 2.17 (b) and Figure 2.3 for locations). At the Great Wall site, the fault splits into three stands: the two strands to the northwest dip southeast, whilst the third is antithetic and dips to the northwest. The Great Wall runs from the southeast to the northwest, crossing all three fault strands before culminating in a beacon stand and a dog-leg to the west in the Helanshan (see Figure 2.13 (b)). The surrounding area is part of a cemetery and the geomorphology has been extensively modified by human

constructions. A major, recent building project has also covered much of the site (see Google Earth imagery from February 2015 onwards).

Original observations of displacement at the Great Wall site were made by *Liao and Pan* (1982) and *Zhang et al.* (1986). *Zhang et al.* (1986) measured a cumulative offset across all three fault strands of 2.7 m vertically and 3 m right-laterally. They also noted that the northwesternmost strand must be a compound scarp, since the scarp height is 3 to 4 m whereas the vertical offset of the wall at this location is only 0.95 m. However, *Lin et al.* (2013) offered a contrasting view and presented a detailed argument for why the Great Wall was not offset in the 1739 earthquake.

On the northwesternmost fault strand, we believe that it is not possible to reach any conclusion about the displacement because the wall here was rebuilt in the 1980s to include an offset in the new stonework (see Figure 2.13 (b)). The only evidence for an offset on this strand is from an unpublished photograph that apparently dates to 1973 (*Zhang et al.*, 1986). Similarly, we are not able to observe any offsets on the southeasternmost fault strand due to collapse and erosion of the wall (see Figure 2.13 (b)). On the central strand, *Lin et al.* (2013) made the case that if you allow for erosion of the wall and follow the lines of adobe bricks within the wall then the bricks are always parallel to the topography, indicating that the wall was built on a pre-existing scarp and that there was no dislocation in 1739 (see Figure 2.13 (e)). However, any reconstructions based on projections and extrapolations of these curved lines of bricks remain equivocal.

Since both the Great Wall and the surrounding fan surface have been so extensively modified we can no longer tell very much from the Great Wall site itself. Nonetheless, there are two key pieces of evidence that lead us to conclude that the rupture did pass through the Great Wall site. Firstly, the wall has collapsed at precisely the location of the scarp on the central fault strand (see Figure 2.13 (e)). Secondly, and more importantly, we observed scarps in the field with preserved free faces, both to the northeast and to the southwest of the Great Wall site. In Figures 2.13 (c) and 2.13 (d), 4 km to the north of the Great Wall site, we see a pale grey band of over-steepening at the base of the Helanshan with preserved portions of free face in alluvial material. A single gully and two boulder ridges also appear to show evidence of right-lateral motion (see Section 4.4.4). Similarly,

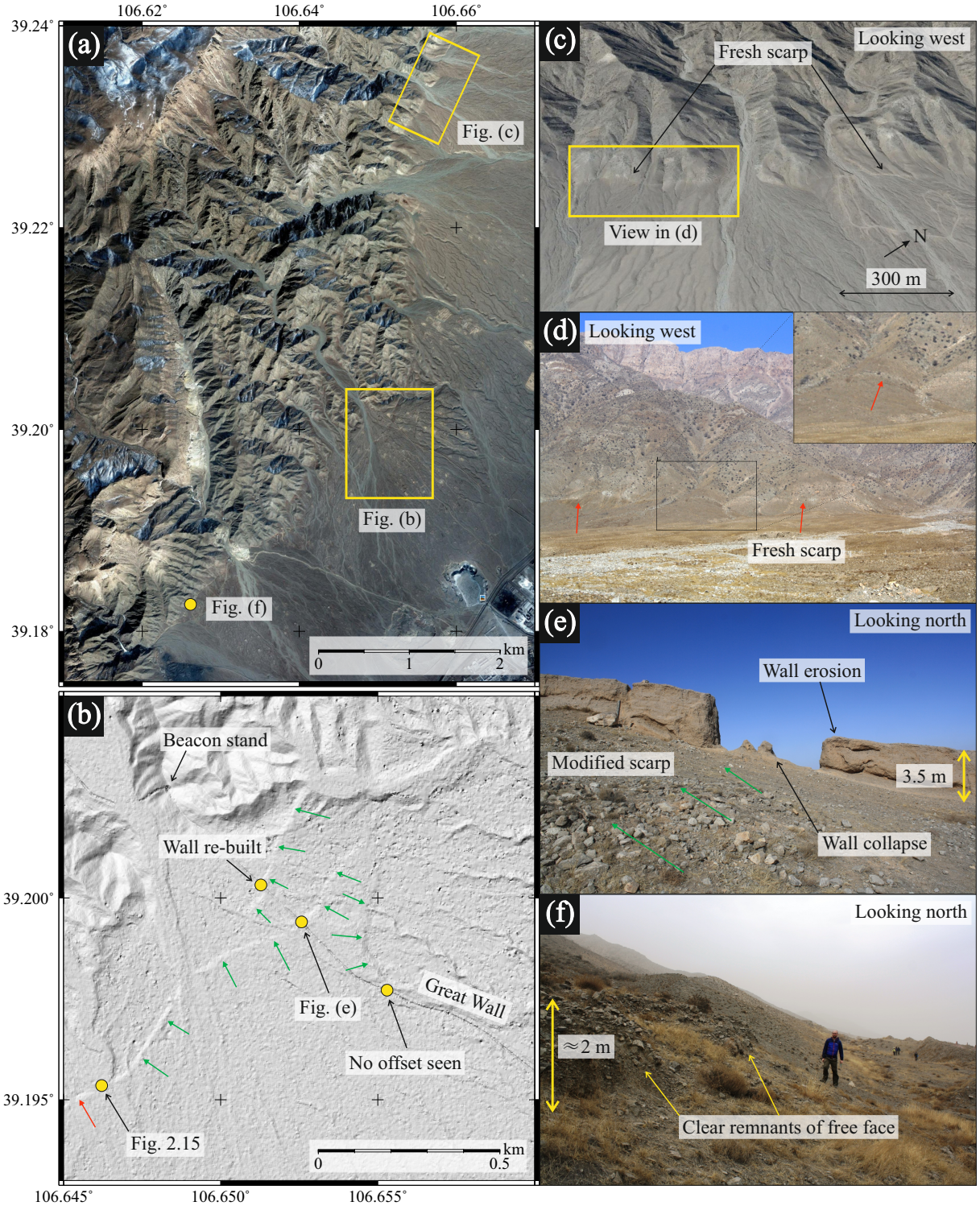


Figure 2.13: (a) Google Earth imagery from February 2010 (source: http://earth.google.com) of the Hongguozigou portion of the East Helanshan Fault towards the northern end of the 1739 rupture. (b) Zoomed in view of the Pleiades DEM at the Great Wall site. Red arrows indicate single-event fault scarps; green arrows indicate compound scarps. The southeasternmost fault strand is antithetic. (c) Perspective Google Earth view of the range front north of the Great Wall site at the location marked in (a). (d) Field photograph (taken at 39.236 °N, 106.657 °E) showing part of the same view as (c), with clear evidence for a fresh rupture. Zoom shows fresh scarp in more detail. (e) Field photograph (taken at 39.199 °N, 106.653 °E) of the Great Wall crossing the central strand of the three fault strands shown in (b). (f) Field photograph (taken at 39.182 °N, 106.626 °E) of the fault 3 km southwest of the Great Wall site. Remnants of a free face are still visible.

in Figure 2.13 (f), 3 km to the southwest of the Great Wall site, we see 2 m high remnants of a free face in angular alluvial gravels. We therefore conclude that the 1739 rupture did go through the Great Wall site.

2.6 Discussion

2.6.1 The causative fault for the 1739 earthquake

In Section 2.5.1 we showed by way of ^{14}C dating that the formation of the Suyukou scarps can be bracketed to the last 350 years. We also noted that these scarps show a characteristically fresh free face. In Section 2.5.2 we were then able to identify the same scarp morphology at a number of other locations along the East Helanshan Fault (see Figures 2.9, 2.10, 2.12 and 2.13). This leads us to conclude that the East Helanshan Fault was the causative structure for the 1739 Yinchuan earthquake.

This result is consistent with almost all of the previous palaeoseismological studies in the Yinchuan Graben (see Figure 2.14). *Lei et al.* (2015) and *Lei et al.* (2008) found from trenching and boreholes on the Yinchuan-Pingluo Fault that the last surface-rupturing earthquake was more than 3400 years ago (as constrained by a single ^{14}C date). Given the large magnitude of the 1739 earthquake it is highly likely that it produced surface ruptures and, therefore, that it did not occur on the Yinchuan-Pingluo Fault. However, we cannot completely rule out the possibility of some sub-surface slip on this fault. Similarly, the Luhuatai Fault is believed to show no evidence for recent surface ruptures: *Wang et al.* (2007) indicated that the fault is buried to a depth of at least 25 m under sediments that date from $\approx$ 124 ka ago.

Lin et al. (2015a) suggested that the 1739 event occurred on the Yellow River Fault (see Section 2.3). However, they were only able to find surface expression of this fault for a length of 8 km. Scaling relationships suggest that the expected surface rupture length of a M_w 7.6 earthquake, for example, would be of the order of 100 km (*Wells and Coppersmith*, 1994). Although some scarps may have been eroded or covered by migrating dunes from the Ordos Plateau, it seems surprising that no other scarps have been found

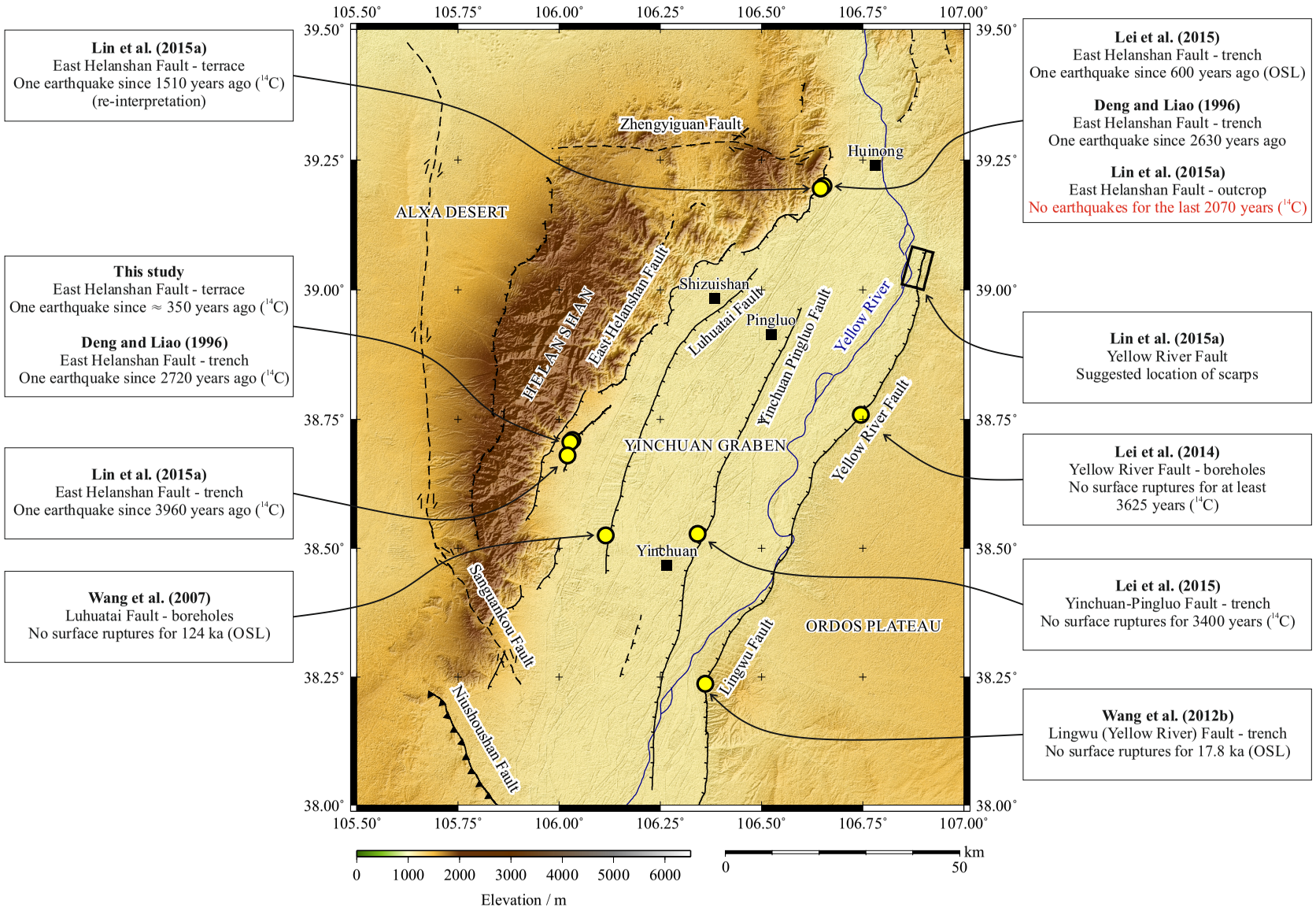


Figure 2.14: ASTER GDEM topography of the Yinchuan Graben. Faults as in Figure 2.2. Cities are marked by black squares. The Yellow River, which flows to the north, is marked in dark blue. Yellow circles mark sites where observations have been made about the recent activity of the four principal faults in the graben (*Deng and Liao*, 1996; *Wang et al.*, 2007, 2012b; *Lei et al.*, 2014, 2015; *Lin et al.*, 2015a). With the exception of one observation (in red) by *Lin et al.* (2015a), all of the data are consistent with the East Helanshan Fault being the causative fault for the 1739 event.

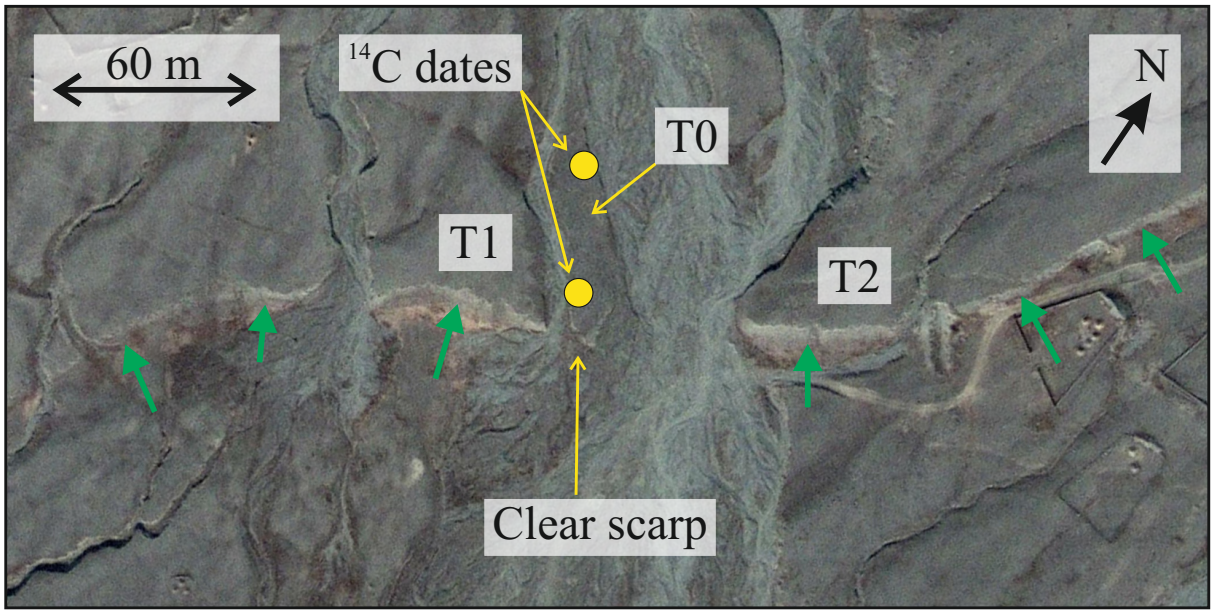


Figure 2.15: Google Earth imagery from February 2010 (source: http://earth.google.com) of part of the Hongguozigou scarps (at 39.195 °N, 106.646 °E) on the East Helanshan Fault (see Figure 2.13 (b) for location). Green arrows indicate compound scarps. Terrace labels according to *Lin et al.* (2015a). Yellow circles show approximate locations of ^{14}C samples obtained by *Lin et al.* (2015a). A clear scarp is seen cutting the T0 surface.

along the Yellow River Fault if this was the causative structure. Furthermore, *Lei et al.* (2014) found from a composite drilling profile on the northern section of the Yellow River Fault, approximately 25 km southeast of Pingluo, that no earthquakes have occurred here for at least 3625±35 years (single ^{14}C date). *Wang et al.* (2012b) excavated a trench on the Lingwu Fault, the southern extension of the Yellow River Fault, at a location 30 km SSE of Yinchuan and found that that no earthquakes have occurred on this segment for at least 17.8±0.8 ka (optically stimulated luminescence (OSL) date).

The trenching work by *Deng and Liao* (1996), *Lin et al.* (2015a) and *Lei et al.* (2015) at Suyukou and Hongguozigou is also consistent with the 1739 earthquake taking place on the East Helanshan Fault (see Figure 2.14 for details). The only data that disagree with this conclusion are four dates obtained near the Great Wall site by *Lin et al.* (2015a). They found ^{14}C ages for scarp-mantling talus of 2070±30 and 2060±30 years before present. However, on the basis of their outcrop photographs and sketches we were not able to verify the exact context of these samples. They also have ^{14}C ages of 1660±30 and 1510±30 years before present from a surface they label as T0, which they say is not offset. However,

Google Earth imagery appears to show a fresh scarp in their T0 surface (at 39.195 °N, 106.646 °E), suggesting that the surface pre-dates, rather than post-dates, the most recent earthquake (see Figure 2.15).

The combined evidence agrees with our conclusion and strongly suggests that the East Helanshan Fault was the primary causative structure, although we cannot completely rule out some additional sub-surface slip on the Luhuatai, Yinchuan-Pingluo and Yellow River Faults. As discussed in Section 2.3, the fact that the greatest shaking was felt in the centre of the graben is likely to be because the thick sediments (*Zhang et al.*, 1990) amplified the seismic waves. Furthermore, if the seismic reflection data from *Fang et al.* (2009) are correct in saying that the Yellow River Fault was the major graben-forming structure (see Figure 2.2 (b)), then this implies that the Yellow River Fault is no longer as active as it must have been in the past.

2.6.2 Characterising the 1739 earthquake

Throw distribution

During our mapping of the East Helanshan scarps (see Section 2.5.2) we were unable to resolve any lateral offsets either in the field or from the Pleiades DEM (except for the one site north of the Great Wall, see Section 4.4.4). We also made very few observations of fault dip. Nonetheless, at the road-cut site on the Suyukou scarps (see Figure 2.6 (c)) we measured a fault dip of 66 °. The nearest throw measurement is 4.3±0.6 m, giving a slip of 4.7±0.7 m assuming pure dip-slip motion. Meanwhile, adjacent to the Great Wall on the central fault strand, *Liao and Pan* (1982) recorded a fault dip in their trench of 70 °. Our nearest throw measurement from a location where there is only a single rupture strand is 3.9±0.7 m, giving a fault slip of 4.2±0.7 m. However, we do not have enough fault dip observations to be able to convert all of our vertical offset measurements into slip on the fault. We therefore plot the variation of throw along strike (see Section 2.4.3 for a description of how these throw measurements were made). The position of each throw measurement was projected onto a straight line joining the two ends of the rupture in order to determine its distance along strike. The results are recorded in Table 2.1, and

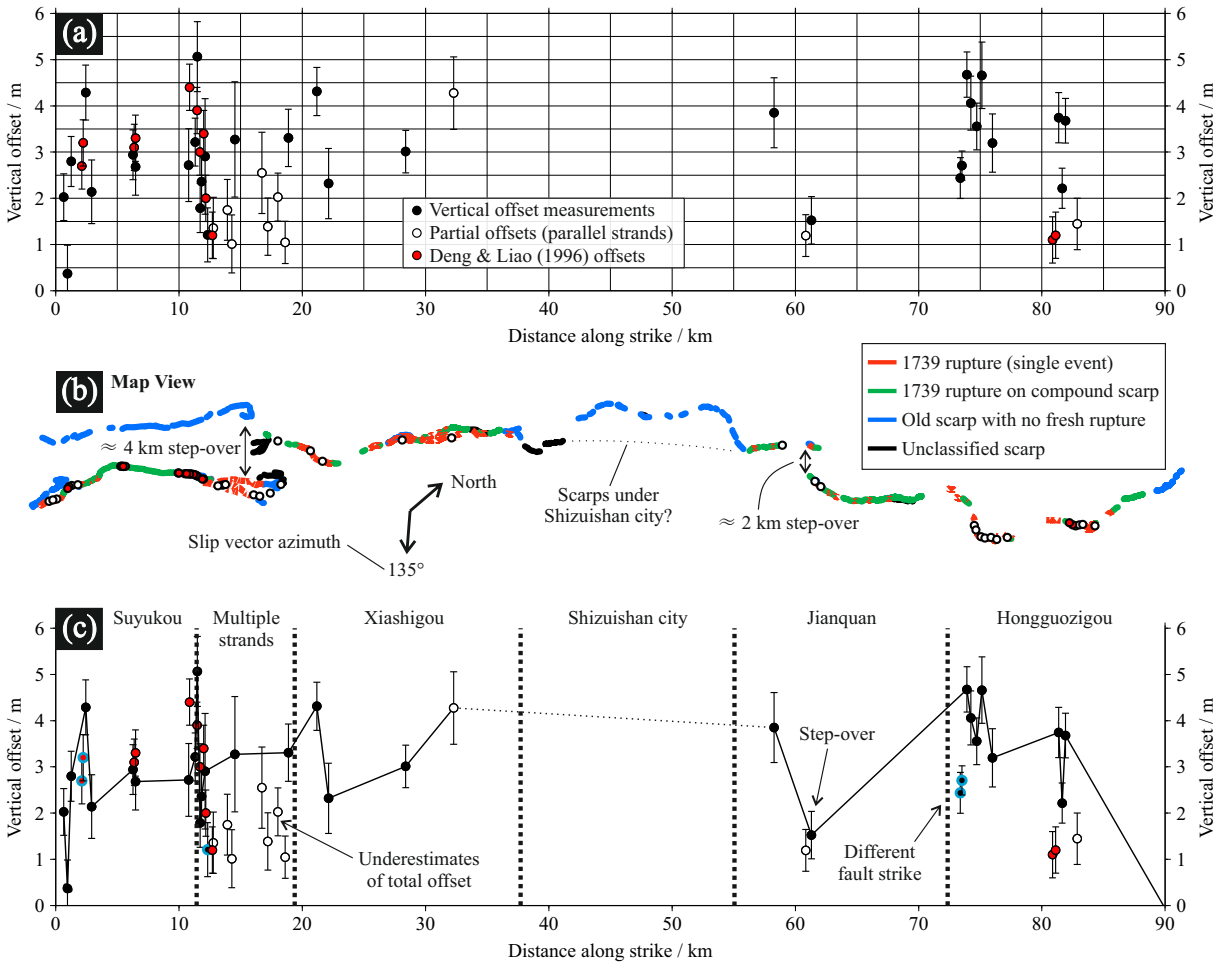


Figure 2.16: (a) Throw distribution (vertical offset versus distance along strike) for the 1739 Yinchuan earthquake. Points marked in white indicate locations where the measurement is unlikely to represent the total vertical offset because of the existence of parallel rupture strands that have not been summed together. Red points are data from *Deng and Liao* (1996). Error bars show RMS residuals from offset measurement process (see Section 2.4.3). (b) Map view of fault scarps from the 1739 earthquake. Measurement points for data in this study are shown by white circles and measurement points for data from *Deng and Liao* (1996) are shown by red circles. (c) Interpreted throw distribution containing the same data as in (a). Points ringed in blue indicate measurements made on sections with a significantly different local fault strike. The black line joins consecutive offset measurements along strike (from this study), excluding partial offsets and measurements with different local fault strike.

displayed in Figure 2.16 (a). *Deng and Liao* (1996) did not quote any errors on their results, so for this plot we have assumed errors of ±0.5 m on their offset measurements.

The field data from *Deng and Liao* (1996) at the Suyukou scarps—for example from 2 km, 6 km and 11 km along strike—agree well with our measurements, confirming that our DEM is of sufficiently high resolution to make such measurements. The two offsets from *Deng and Liao* (1996) on the Hongguozigou scarps of 1.1 and 1.2 m are, however, noticeably smaller than our results. During the measurement of our offsets we discarded

the profiles from the locations immediately adjacent to the sites measured by *Deng and Liao* (1996) because the difference in slope above and below the scarp was more than 1 °. Nonetheless, we obtained offsets of 2.1 and 3.0 m at nearby sites. It is possible that *Deng and Liao* (1996) did not adequately take account of the difference in slope angle when making their measurements.

Figure 2.16 (c) is an attempt to estimate a throw distribution based on the point data shown in Figure 2.16 (a). Points ringed in blue indicate measurements where the local fault strike is significantly different to the overall average and therefore highlight places where we might expect to see a smaller vertical offset. The black line joins consecutive offset measurements along strike (from this study), excluding partial offsets and measurements with a different local fault strike. The line returns to zero at a distance of nearly 90 km, corresponding to our field site at 39.262 °N, 106.671 °E where no sign of recent rupture was observed. As expected, most of the partial offset measurements fall below this line, for example along the section between 12 and 19 km along strike. At a distance of approximately 12 km, towards the northern end of the Suyukou scarps, there is a throw minimum as the fault splits into multiple strands and approaches the step-over. Similarly, at a distance of about 61 km, at the step-over within the Jianquan segment, there is a second throw minimum. These throw minima at fault step-overs may imply that the segments either side do not yet form a continuous, through-going structure at depth (*Kim and Sanderson*, 2005).

In Section 2.5.2 we noted that no surface fault scarps were seen along the central section of the rupture, behind Shizuishan city. The range front is embayed at this location (see Figure 2.16 (b)), so one possible explanation for the lack of scarps is that the 1739 rupture cut off this corner in the range front and went through what is now the centre of the city. Rapid urban sprawl could have since removed all traces of this portion of the rupture. Another possibility is that there were no original surface ruptures on this section of the fault. This would further imply that the 1739 earthquake occurred as two separate sub-events, an idea that would be consistent with the historical records that mention ground shaking continuing for two whole hours (*Zhang et al.*, 1986). We do not have sufficient data to definitively adjudicate between these two hypotheses. However, we note that

the measured throws at sites either side of Shizuishan city (see Figure 2.16 (c)) do not appear to be tailing off in the way that we might expect for the ends of fault segments (according to an elliptical growth model), indicating that two sub-events is perhaps less likely (*Peacock*, 2002; *Kim and Sanderson*, 2005).

Slip vector azimuth

We were not able to observe any fault plane exposures and so could not measure the orientations of any striations. However, there are two other ways in which we can estimate the slip vector azimuth. Firstly, although we have no way of verifying the previous measurements from the Great Wall site, we can try using them to see what they suggest about the slip direction (see Section 2.5.2). *Zhang et al.* (1986) recorded a cumulative vertical offset across the three fault strands at this site of 2.7 m. Combined with an average fault dip of 72 ° from the three trenches opened adjacent to the Great Wall by *Liao and Pan* (1982), we obtain fault-normal motion of 0.9 m. *Zhang et al.* (1986) also recorded cumulative right-lateral motion of 3 m, enabling us to estimate that the slip vector is 164 ° from the strike direction. The average local fault strike measured by *Liao and Pan* (1982) is 30 °, giving us a slip vector azimuth of 194 °.

The second method makes use of the observation, noted in Section 2.5.2, that there are a few locations where the rupture changes strike by 70 ° over a length scale of less than 100 m (see Figure 2.17 (b)). At rupture bends such as this one we observe a marked change in the throw on moving round the bend and we can use this change to estimate the slip vector azimuth. Predicting how throw is expected to vary with local fault strike would require detailed knowledge of the fault dip and assumptions about how the orientation of the slip vector might change along strike. However, we note that for uniform horizontal extension along the whole fault length, the fault-perpendicular motion (and hence the vertical offset due to this component of the slip) will be greatest for portions of the fault that are perpendicular to the slip vector azimuth.

Figure 2.17 (a) shows our vertical offset measurements plotted against local fault strike. The black curve approximately envelops that data and is intended only to illustrate that there is a broad peak in the data at around 40 to 50 °, suggesting a slip vector azimuth

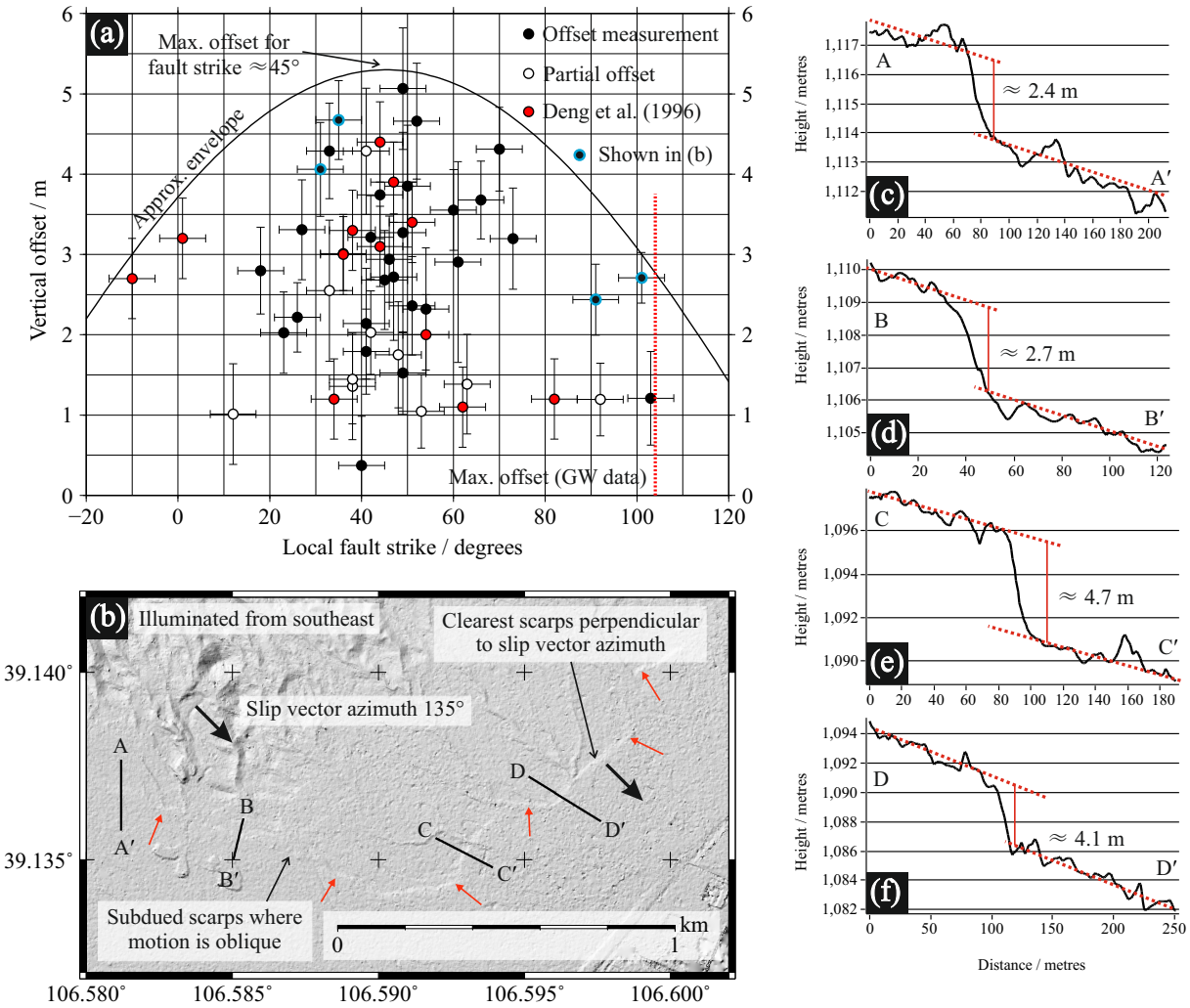


Figure 2.17: (a) Plot of vertical offset measured on the Pleiades DEM against local fault strike. Points marked in white indicate locations where the measurement is unlikely to represent the total vertical offset because of the existence of parallel rupture strands. Red points are data from *Deng and Liao* (1996). Points ringed in blue are measurements from the sites shown in (b). The black curve is an approximate data envelope. The dotted red line indicates the local fault strike (104 °) for which we would expect the maximum vertical offset based on the slip vector azimuth calculated from the data at the Great Wall site. (b) Zoomed in view of the DEM at a location on the Hongguozigou segment where the fault (marked by red arrows) changes strike abruptly by about 70 °. The largest scarps (illuminated in white) occur along segments striking at approximately 45 °, perpendicular to the suggested slip vector azimuth of 135 °. (c), (d), (e) & (f) Topographic profiles at the locations marked in (b) to show the difference in scarp height when the local fault strike is different. Note the varying scales on these plots.

perpendicular to this orientation (i.e. 130 to 140 °). This result is consistent with the example shown in Figure 2.17 (b). Here, the clearest scarps are those striking at around 40 to 50 °. This is also borne out by the topographic profiles in Figures 2.17 (c), 2.17 (d), 2.17 (e) and 2.17 (f). Profiles A-A′ and B-B′ are from segments with strikes of 91 ° and 101 °, and show vertical offsets of 2.4 and 2.7 m respectively. Meanwhile, profiles C-C′

and D-D′ are from segments with strikes of 35 ° and 31 °, and show vertical offsets of 4.7 and 4.1 m.

However, there remains a large discrepancy between the slip vector azimuth of 194 ° from the Great Wall measurements and the slip vector azimuth of 130 to 140 ° from our data. The dotted red line on Figure 2.17 (a) indicates the fault strike at which we would expect the largest vertical offset (104 °) if the Great Wall measurements are correct, and it is noticeably displaced from the observed peak. If this discrepancy is real it could indicate either a significant change in slip vector azimuth at the northernmost end of the rupture, or a spatial partitioning of dip-slip and strike-slip motion. For example, almost pure normal motion on the East Helanshan Fault could be accompanied by right-lateral motion on a fault or faults within the graben for the majority of its length south of the Great Wall. Our single field site north of the Great Wall (see Figures 2.13 (c) and 2.13 (d)) did appear to show evidence of right-lateral offsets (see Section 2.5.2), but rotation of the slip vector, the presence of partitioned faulting, and whether or not the 1739 earthquake involved additional slip on parallel structures, all remain speculative.

Estimating the magnitude

In this section we estimate a range of possible magnitudes for the 1739 earthquake based on observations and measurements made in this study. However, we also consider the likely upper bounds on all the relevant parameters in order to work out the maximum conceivable magnitude for the event (see Table 2.3).

According to our mapping, the end-to-end length of the 1739 rupture is 87 km (see Section 2.5.2 and Figure 2.3). However, it is not clear to what extent the surface salients and embayments reflect the deeper fault structure. If we assume that some of the surface sinuosity does reflect real changes at depth and use a rupture trace made of ten points, with one point approximately every 10 km, we obtain a rupture length of 94 km. We therefore take 94 km as our upper bound on fault length.

The maximum throw measured in this study is 5.1 m (see Table 2.1). Assuming the surface fault dip of 66 ° measured at the road-cut exposure is representative (see Figure 2.6) and that motion is pure dip-slip, the maximum slip on the fault plane at the

Table 2.3: Fault parameters and magnitude estimates

Parameter	Best Estimate	Upper Bound
Fault parameters		
Fault length / km	87	94
Seismogenic thickness / km	20	28[a]
Fault dip / °	39	39[a]
Surface fault dip / °	66	66
Down-dip width / km	32	44
Fault area / km^2	2765	4182
Maximum throw / m	5.1	8.0
Maximum slip / m	5.6	8.8
Average throw / m	3.0	4.5
Average slip / m	3.3	4.9
Slip-to-length ratio (β)	3.8×10^{-5}	5.2×10^{-5}
Magnitude estimates		
M_w from fault length[b]	7.4	7.5
M_w from fault plane area[b]	7.4	7.6
M_w from maximum slip[b]	7.2	7.3
M_w from average slip[b]	7.1	7.2
M_w from $M_0 = \mu A \bar{u}$	7.6	7.8

[a] 28 km seismogenic thickness and 39 ° fault dip from *Fang et al.* (2009).
[b] Scaling relationships from *Wells and Coppersmith* (1994).

surface is 5.6 m. Similarly, the average throw measured in this study is 3.0 m and, again assuming a fault dip of 66 °, we obtain an average slip of 3.3 m.

However, we are missing data for the central portion of the rupture, between 32 and 58 km along strike (see Figure 2.16), and, assuming that there were not two separate sub-events, it is in the central portion that we might expect the maximum throw (e.g. *Peacock*, 2002; *Kim and Sanderson*, 2005; *Faure Walker et al.*, 2009). We therefore propose taking upper bounds on the maximum and average throw of 8 m and 4.5 m respectively, giving upper bounds on the maximum and average slip (using a dip of 66 °) of 8.8 m and 4.9 m respectively.

We estimate down-dip width from seismogenic thickness and fault dip at depth. *Cheng et al.* (2014) noted that most earthquakes in the vicinity of the Yinchuan Graben occur above 20 km. This is in agreement with previous estimates of seismogenic thickness by *Wesnousky et al.* (1984) and *Molnar et al.* (1984). Estimates of the sub-surface fault dip based on seismic reflection data vary from 39 ° (*Fang et al.*, 2009) to approximately 60 °

(*He et al.*, 2005; *Liu et al.*, 2008). Here, though, we use the dip of 39 ° from *Fang et al.* (2009) since it is the only available seismic reflection profile that goes deep enough to include the whole seismogenic layer. (We also note that the maximum down-dip width is obtained for the shallowest fault dip at depth.) In combination with the seismogenic thickness of 20 km, we obtain a down-dip width of 32 km and a fault plane area of 2765 km^2. However, *Fang et al.* (2009) also suggested from their seismic reflection data that the base of the East Helanshan Fault can be traced to a depth of 28 km. If this is correct and the whole fault is seismogenic, we find upper bounds of 44 km for down-dip width and 4182 km^2 for fault plane area.

Applying scaling relationships between moment magnitude and each of fault length, fault plane area, maximum slip and average slip we obtain M_w 7.4, M_w 7.4, M_w 7.2 and M_w 7.1 respectively (*Wells and Coppersmith*, 1994). Using the same relationships with our upper bounds gives M_w 7.5, M_w 7.6, M_w 7.3 and M_w 7.2 respectively. We also calculate seismic moment (M_0) using the relationship $M_0 = \mu A \bar{u}$. Using a modulus of rigidity of 3×10^{10} Pa and the parameters listed above we obtain a best estimate seismic moment of 2.72×10^{20} Nm and an upper bound of 6.18×10^{20} Nm, which correspond to moment magnitudes of 7.6 and 7.8. Finally, we also calculate slip-to-length ratios of 3.8×10^{-5} and 5.2×10^{-5} for our best estimate and upper bound parameters respectively. Table 2.3 lists all of these results and the parameters required to make the estimates.

Our data suggest that the previously proposed magnitude of 8.0 (*Zhang et al.*, 1986; *State Seismological Bureau and Fudan University*, 1990) may be an overestimate of the size of the 1739 earthquake due to amplification effects within the graben sediments. On the basis of the various fault parameters obtained in this study we suggest a preferred magnitude in the range M_w 7.1 to M_w 7.6. A M_w 7.8 event is only found by taking the upper bound for every single parameter. Even if motion also occurred at depth on faults within the graben interior, a M_w 8.0 event would require an additional moment release of 5.5×10^{20} Nm, equivalent to slip of approximately 10 m on one of these other faults (using $M_0 = \mu A \bar{u}$ and our upper bound of M_w 7.8 for the motion on the East Helanshan Fault).

Our results therefore put the Yinchuan earthquake in line with other normal-faulting earthquakes that have been observed in the instrumental period such as the M_w 7.2

Pleasant Valley and M_w 7.3 Hebgen Lake events, though these earthquakes had shorter rupture lengths (of 60 and 30 km respectively) (*Jackson and White*, 1989). Similarly, our best estimate slip-to-length ratio of 3.8×10^{-5} is in accord with generally accepted values of between 10^{-5} to 10^{-4} (*Scholz*, 1982, 2002). In other words, the 1739 Yinchuan earthquake, though still a major normal-faulting event, is not extraordinarily large and unique circumstances do not need to be invoked in order to understand its occurrence.

In terms of future seismic hazard, the reduced magnitude estimate indicates that a smaller earthquake than previously thought caused the intensity of shaking and amount of damage that was observed in 1739. In addition, the reduced magnitude estimate implies an increased frequency of such earthquakes; a recurrence interval that is 57% shorter (assuming a slip-to-length ratio of 5×10^{-5}) is needed to accommodate a given strain rate across the East Helanshan Fault with M_w 7.6 events rather than M_w 8.0 events.

2.7 Conclusions

^{14}C dating very strongly suggests that the Suyukou scarps, at the southern end of the East Helanshan rupture, are from 1739. The similar morphology of other scarps along the same range front, with a characteristic free face, also strongly suggests that the East Helanshan Fault was the causative fault for the 1739 event. Our Pleiades DEM (with a horizontal resolution of 1 to 2 m) was shown to be of sufficiently high quality to enable much of the 1739 rupture to be mapped, thereby significantly extending what is known from field observations alone. Recent landscape modification at the controversial Great Wall site has made previous studies hard to assess, but observations of the scarps either side confirm that the wall must have been offset in 1739. Measurements of vertical displacement and local fault strike indicate a slip vector azimuth of 130 to 140 ° in the 1739 earthquake. We also measure a total rupture length of 87 km, a maximum throw of 5.1 m and an average throw of 3.0 m. Based on our best estimate fault parameters we calculate a moment magnitude for the earthquake in the range M_w 7.1 to M_w 7.6.

This study of the 1739 earthquake in the Yinchuan Graben has demonstrated the importance of using geological data preserved in the landscape and up-to-date surveying

techniques to re-examine historical earthquakes. We have also shown how high-resolution satellite-derived DEMs can be employed in tectonic studies to make detailed measurements of individual earthquake ruptures. Furthermore, given the rapid urban expansion and extensive human modification of the landscape in our study region, our data provides an important archive of the geomorphological evidence associated with this earthquake. Together, the geological data and new techniques have enabled us to provide further, tight constraints on the principal causative fault for the 1739 event and to discover that the earthquake was not as large, or as extraordinary, as previously thought.

Chapter 3

Slip rate on the Luoshan Fault

3.1 Introduction

In Chapter 1 we outlined the evidence for treating the Ordos Plateau as a rigid crustal block. Geological and GPS measurements both indicate that the Ordos block is situated within a large, left-lateral shear zone and should be rotating anticlockwise about a vertical axis (*Xu and Ma*, 1992; *Xu et al.*, 1993; *Avouac and Tapponnier*, 1993; *Xu et al.*, 1994; *Zhang et al.*, 1995; *Peltzer and Saucier*, 1996; *Zhang et al.*, 1998; *Zhao et al.*, 2015). If this anticlockwise rotation is indeed important for the kinematics of the Ordos Plateau (see Chapter 6 for further discussion of this), we would expect to see dominantly right-lateral motion on both the eastern and western sides of the plateau as it rotates with respect to the Alxa Desert in the west and the North China Plain in the east. It is therefore unclear why the plateau is surrounded by large normal faults and extensional grabens on almost all sides (see Figure 3.1). Could large-scale transtensional shearing be accommodated purely by en echelon normal faulting and vertical axis rotations of smaller, intervening crustal blocks—as seen, for example, in the Walker Lane of the western United States (*Wesnousky et al.*, 2012)?

On the eastern side of the Ordos Plateau it is thought that right-lateral shearing does occur through normal faulting on the en echelon Shanxi Grabens and right-lateral slip on the Xizhoushan Fault (at 5.7 mm/a) and the Huoshan Fault (at 5.0 mm/a) (*Xu et al.*, 1986; *Xu and Deng*, 1990; *Xu et al.*, 1993) (see Chapter 6 for further details and maps

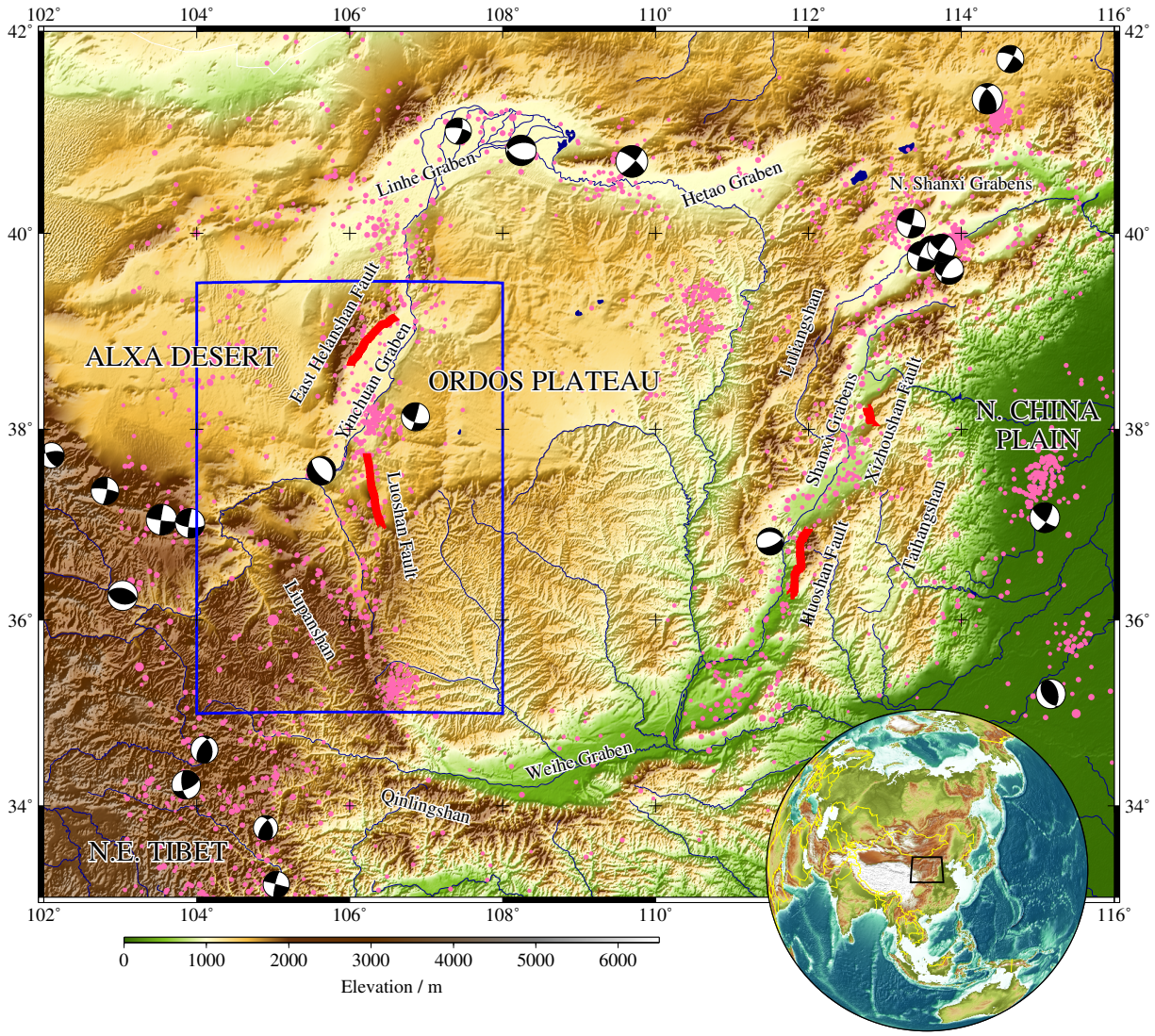


Figure 3.1: SRTM topography (*Farr et al.*, 2007) of the Ordos Plateau in northeastern China. Focal mechanisms from the Global CMT catalogue (*Ekström et al.*, 2012) are shown for earthquakes since 1976 with magnitudes greater than M_w 5.0. Pink dots indicate earthquakes of M_w 2.0-5.0 between 1920 and 2011 from the ISC catalogue (*International Seismological Centre*, 2013). Rivers are indicated in dark blue and inset globe shows the location of Figure 3.1 within Asia. The East Helanshan, Luoshan, Xizhoushan and Huoshan Faults are highlighted in red. The blue box indicates the region shown in Figure 3.2.

of these faults). On the western side of the Ordos Plateau, right-lateral faults have also been identified, but their rates of motion and relative importance are debated (*Deng et al.*, 1984a; *Min et al.*, 1992, 1993; *Zhang et al.*, 1998; *Min et al.*, 2003).

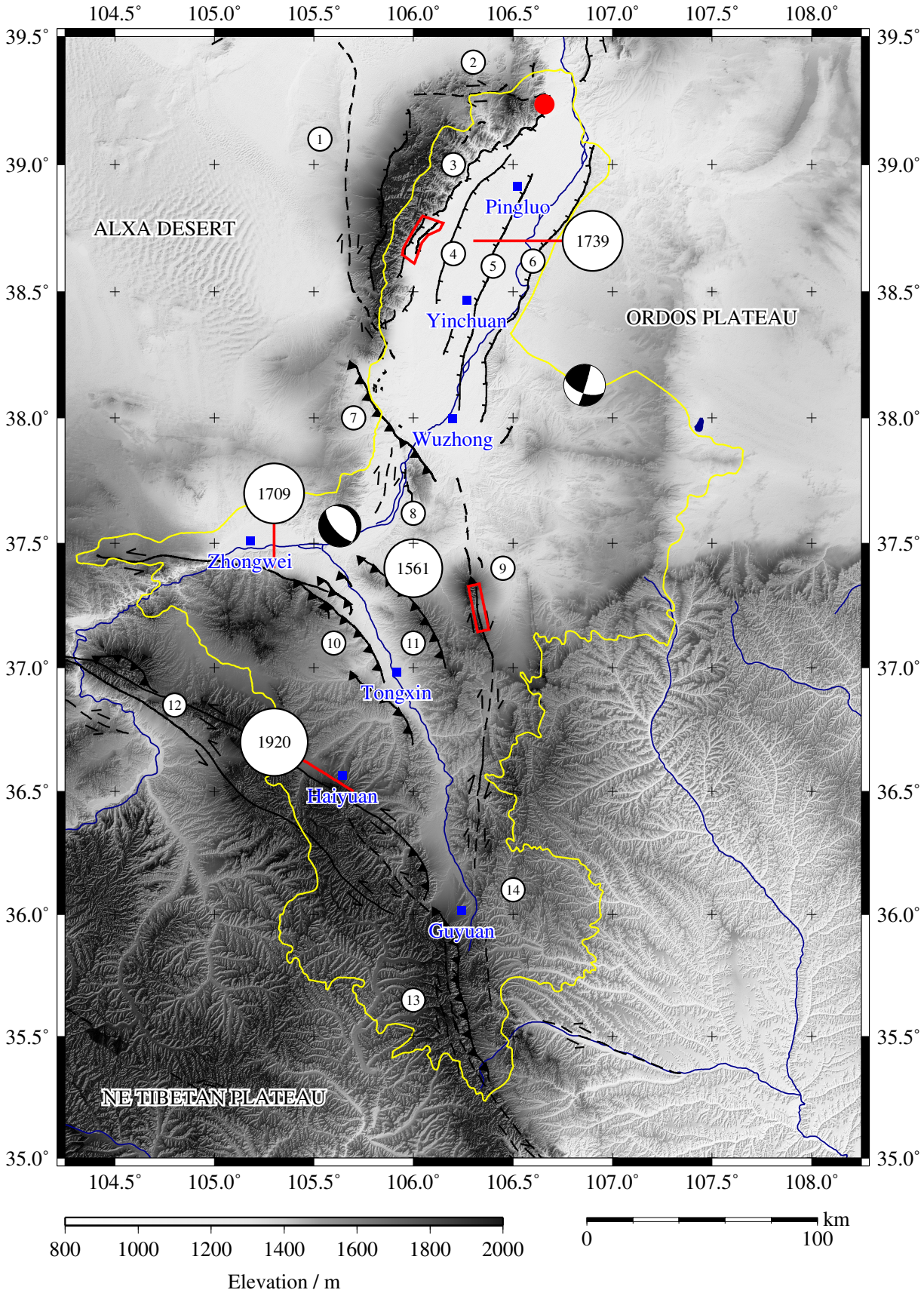
Here, we therefore focus on the faulting in the western Ordos and examine the relative importance of right-lateral and extensional slip by determining Holocene rates for two of the major faults within the region. In this Chapter we obtain a slip rate for the right-lateral Luoshan Fault; in Chapter 4 we obtain a throw rate on the normal East

Helanshan Fault and use this to calculate an extension rate across the Yinchuan Graben (see Figure 3.1). In both cases we compare our results to the latest campaign GPS measurements (the continuous data in this region is not dense enough to allow a meaningful comparison). We specifically chose to study these two faults because of their clear geomorphological expression in the satellite imagery and the apparent availability of offset surfaces for Quaternary dating; many of the other faults in the western Ordos are poorly exposed or buried under basin sediments. We then use our results in Chapter 6 to inform our proposed kinematic model—a model that incorporates both anticlockwise rotation and the widespread normal faulting.

3.2 Tectonic setting

The western Ordos region straddles the transition from the shortening occurring in the northeastern corner of the Tibetan Plateau to the apparent extension occurring across the Yinchuan Graben. Many recent studies have indicated that deformation in northeastern Tibet has accelerated since about 15 Ma ago and that the orientation of the regional stress field has changed since about 20 Ma ago (e.g. *Molnar and Stock*, 2009; *Yuan et al.*, 2013 and references therein). Within the western Ordos region, apatite fission track dating reveals initiation of rapid uplift and exhumation of the Helanshan 10-12 Ma ago (*Liu et al.*, 2010) and the Liupanshan around 8 Ma ago (*Zheng et al.*, 2006) (see Figure 3.1 for locations). It seems likely that motions at the margins of the Ordos Plateau are sensitive to changes in the stress field in northeastern Tibet and were initiated at a similar time (e.g. *Wang et al.*, 2013; *Chen et al.*, 2015).

Four large, historical earthquakes have occurred in the vicinity (see Figure 3.2): the M 7.3 1561 earthquake near the Luoshan Fault (*Min et al.*, 2003); the M 7.5 1709 oblique left-lateral strike-slip-faulting Zhongwei earthquake (*Nie and Lin*, 1993; *Min et al.*, 2001); the M_w 7.1-7.6 1739 normal-faulting Yinchuan earthquake (see Chapter 2); and the M_w 7.8 1920 left-lateral strike-slip-faulting Haiyuan earthquake (*Zhang et al.*, 1987, 1988; *Burchfiel et al.*, 1991; *Lasserre et al.*, 2002; *Liu-Zeng et al.*, 2007; *Ren et al.*, 2015).


104.5°
105.0°
105.5°
106.0°
106.5°
107.0°
107.5°
108.0°
39.5°
39.0°
38.5°
38.0°
37.5°
37.0°
36.5°
36.0°
35.5°
35.0°
ALXA DESERT
ORDOS PLATEAU
NE TIBETAN PLATEAU
Pingluo
Yinchuan
Wuzhong
Zhongwei
Tongxin
Haiyuan
Guyuan
1739
1709
1561
1920
1
2
3
4
5
6
7
8
9
10
11
12
13
14
800
1000
1200
1400
1600
1800
2000
Elevation / m
0
100
km

The left-lateral Haiyuan Fault, with a Late Quaternary slip rate of 4.5±1.0 mm/a at its eastern end (*Li et al.*, 2009a), runs along the northeastern edge of the Tibetan Plateau and enters the southern part of Ningxia Province, on the western side of the Ordos Plateau, striking northwest-southeast and terminating in a series of reverse faults (see Figure 3.2). These reverse faults form a south trending fold-and-thrust zone that extends as far as the Liupanshan at the southernmost extent of the province (*Deng et al.*, 1984a; *Li et al.*, 2013). The M 7.8 1920 earthquake occurred on the easternmost part of the Haiyuan Fault (*Zhang et al.*, 1987; *Ren et al.*, 2015).

To the north of the Haiyuan Fault are two more oblique reverse faults: the Tianjinshan-Miboshan Fault (also called the Zhongwei-Tongxin Fault) and the Yantongshan Fault (see Figure 3.2). The M 7.5 1709 Zhongwei earthquake is thought to have occurred on the Tianjinshan-Miboshan Fault. The existence and orientation of these ranges implies northeast-southwest crustal shortening, which is in agreement with modern GPS studies (*Gan et al.*, 2007; *Li et al.*, 2013). Meanwhile, the Luoshan Fault lies to the east of the Yantongshan Fault and the Niushoushan Fault to the north (see Figure 3.2). Recent work on the Niushoushan Fault suggests a Late Quaternary right-lateral slip rate of ≈ 0.4 mm/a (*Lei et al.*, 2016).

The Luoshan Fault is approximately 60 km long and runs along the eastern side of the Luoshan (Luo Mountains) (*Min et al.*, 2003). The Luoshan comprise two ranges: the

Figure 3.2 *(preceding page)*: SRTM topography (30 m resolution) of the study area in the western Ordos region, Ningxia Province, northern China (*Farr et al.*, 2007). The province is outlined in yellow and cities are marked by blue squares. Focal mechanisms for earthquakes since 1976 with magnitudes greater than M_w 5.0 are from the Global CMT catalogue (*Ekström et al.*, 2012). Major historical earthquakes are shown by white circles, including the year in which they occurred (*Liu et al.*, 2011). Red outlines indicate coverage of Pleiades data for the Luoshan Fault (this chapter) and the East Helanshan Fault (Chapter 4). Red circle indicates field site at the northern end of the East Helanshan Fault (see Figure 4.6). Faults, marked as thin black lines, have been mapped from satellite imagery (source: http://earth.google.com) based upon earlier fault maps from *Tapponnier and Molnar* (1977), *Deng et al.* (1984a), *Zhang et al.* (1990), *Darby and Ritts* (2002) and *Darby et al.* (2005). Faults that are inferred or show no clear evidence of Quaternary activity are marked by dashed lines. Faults are numbered as follows: 1 Alxa Desert Fault; 2 Zhengyiguan Fault; 3 East Helanshan Fault; 4 Luhuatai Fault; 5 Yinchuan-Pingluo Fault; 6 Yellow River (Huang He) Fault; 7 Niushoushan Fault; 8 Baima Fault; 9 Luoshan Fault; 10 Tianjinshan-Miboshan (Zhongwei-Tongxin) Fault; 11 Yantongshan Fault; 12 Haiyuan Fault; 13 Liupanshan Fault; 14 Yunwushan Fault.

Daluoshan (Big Luo Mountains) to the north and the Xiaoluoshan (Small Luo Mountains) to the south, both of which are composed of Ordovician basement (see Figure 3.3). The Luoshan Fault was originally thought to be a left-lateral strike-slip fault (*The Research Group on Active Fault System around Ordos Massif*, 1988; *Zhang et al.*, 1990; *Zhou et al.*, 2000), but a detailed re-assessment found numerous examples of right-lateral offsets in Quaternary and Holocene material (*Min et al.*, 1992, 1993, 2003). Evidence for recent, right-lateral motion is also seen further south on the Yunwushan Fault in the form of displaced river channels (for example at 36.635 °N, 106.349 °E and 36.531 °N, 106.333 °E—see Figure 3.2). *Min et al.* (2003) used two thermoluminescence (TL) ages to estimate a minimum, right-lateral slip rate on the Luoshan Fault since the Late Pleistocene of 2.15±0.20 mm/a. The fault was also assigned a right-lateral rate of 3 mm/a on the *Map of Active Tectonics in China* (*Deng et al.*, 2007). *Min et al.* (2003) also suggested that the M 7.3 1561 earthquake occurred on the Luoshan Fault (see Figure 3.2) on the basis that comparatively young-looking gullies (1 m deep) recorded offsets of 1.5 to 5.4 m and that a free face was visible on some scarps, particularly near the village of Zhangjiashanpo (see Figure 3.3 (a) for location). Given the uncertainty about the kinematics of the Luoshan Fault and the paucity of slip rate constraints, we re-visit the fault in this study using up-to-date luminescence methods and modern satellite imagery.

3.3 Methods

3.3.1 Pleiades data and DEM construction

We acquired Pleiades stereo imagery of the central portion of the Luoshan Fault on 18th July 2014 (see Figure 3.2 for data coverage). We then constructed a high-resolution digital elevation model (DEM) according to the methodology outlined in Chapter 2, Section 2.4.2. The final hill-shaded DEM is shown in Figure 3.3 (b).

The resulting DEM for the Luoshan Fault has a horizontal resolution of 1 to 2 m (48% of 1 m by 1 m grid cells contain at least one point, whilst 74% of 2 m by 2 m grid cells contain at least one point). A surface roughness map was calculated from the DEM

by finding the standard deviation of the slope in a 9×9 m moving window (*Frankel and Dolan*, 2007; *Grohmann et al.*, 2011). We used the DEM in combination with the surface roughness data and the original imagery to map the fault scarps and geomorphology in detail, tying our remote sensing observations to our field investigations. Surface roughness data and geomorphological maps are shown in later figures in the results section.

3.3.2 Offset measurements

We measured vertical offsets across fault traces by drawing swath profiles across the raw point cloud data and fitting lines above and below the scarp. See Chapter 2, Section 2.4.3 for the full methodology. The quoted errors on our vertical offset measurements refer to the root mean square (RMS) residuals from this line fitting process. The reliability of this method was previously tested by comparing the results to theodolite profiles measured in the field and by varying the swath width (see Section 2.4.3).

We determined horizontal offset measurements from the original Pleiades imagery and then checked our results on the DEMs and roughness maps where necessary. At each location, we fitted straight lines by eye to either a channel thalweg or the top or bottom of a terrace riser on both sides of the fault. The chosen feature to fit depended on its state of preservation and its clarity in the imagery. Where possible, we used terrace risers instead of channel thalwegs for highly sinuous channels. We preferred up-slope risers where possible as they are less prone to post-offset channel erosion (*Cowgill*, 2007). We also made use of our field observations of the geomorphology at specific sites to guide our line fitting. We then measured the apparent horizontal offset between the two piercing points, where these lines intersected our mapped fault trace. However, the aleatoric uncertainty associated with the individual measurement is much smaller than the epistemic uncertainty associated with the geomorphological reconstruction (*Scharer et al.*, 2014; *Elliott et al.*, 2015). In our case, the aleatoric uncertainty was typically 0.5 m, as constrained by the pixel sizes in the Pleiades images, whereas the epistemic uncertainty was likely to be as much as tens of metres in some instances. Therefore, in order to estimate realistic errors on our offset measurements, we combined measurements

Table 3.1: Horizontal offset measurements on the Luoshan Fault

Feature	Latitude[a] / °	Longitude[a] / °	Lateral offset / m
	Xiaoluoshan		
Thalweg	37.1840	106.3353	30.2
Thalweg	37.1826	106.3358	41.2
Riser top	37.1816	106.3361	29.2
Riser top	37.1811	106.3364	33.1
Riser top	37.1790	106.3374	40.2
Riser bottom	37.1789	106.3374	44.4
Riser top	37.1775	106.3379	35.2
Riser top	37.1766	106.3381	39.7
Riser top	37.1760	106.3384	42.0
			37.2±5.5[b]
	Tanzhuangzicun		
Riser top	37.4266	106.2793	57.0
Riser bottom	37.4263	106.2793	54.5
Riser top	37.4261	106.2793	61.4
Riser top	37.4232	106.2799	47.5
Riser top	37.4228	106.2799	48.0
Riser top	37.4173	106.2806	50.9
Riser top	37.4168	106.2806	45.8
Thalweg	37.4146	106.2810	50.1
Riser top	37.4120	106.2814	37.2
Riser top	37.4117	106.2814	54.0
			50.6±6.7[c]
	Shiyaodong		
Thalweg	37.2521	106.3201	33.8
Thalweg	37.2508	106.3203	48.5
Thalweg	37.2493	106.3205	44.5
Thalweg	37.2483	106.3204	41.9
Thalweg	37.2466	106.3201	36.9
			41.1±5.9[d]

[a] Latitudes and longitudes are for the intersection of the western piercing line with the mapped fault trace.
[b] Mean offset and standard deviation for the Xiaoluoshan section.
[c] Mean offset and standard deviation for the Tanzhuangzicun section.
[d] Mean offset and standard deviation for the Shiyaodong section, re-measured after *Min et al.* (2003).

from sets of geomorphological features that appeared to have been displaced by the same amount. We did this on the basis of field observations and by cutting the imagery along the fault trace and restoring one side of it to look for sets of features that all recorded the same offset. We then found the mean and standard deviation for each suite of offset measurements. Our horizontal offset measurements are recorded in Table 3.1.

3.3.3 IRSL dating of offset features

The fluvial sediments exposed along the Luoshan Fault contained abundant silt and fine sand horizons, so we used infrared stimulated luminescence (IRSL) dating to constrain the ages of offset alluvial fan surfaces at two separate sites along the fault; unfortunately, radiocarbon dating was not possible due to the absence of datable material. The IRSL dating technique and methodology are described in detail below and the final results are shown in Table 3.2.

Table 3.2: IRSL dating results for the Luoshan Fault

Location	Name	Lat °	Long °	Elevation m	Depth m	Equivalent Dose[a] Gy	Dose Rate[a] mGy a^{-1}	Age[a] ka
Xiaoluoshan Fault	1	106.3350	37.1850	1761	2.13	536±39	3.80±0.16	141±12
Xiaoluoshan Fault	2	106.3397	37.1780	1766	0.55	33.0±1.4	3.61±0.16	9.16±0.57
Daluoshan Fault	3	106.2800	37.4250	1422	1.69	39.6±2.8	3.74±0.16	10.6±0.9

[a] Including 1σ analytical uncertainties.

Background to IRSL dating

The decay of radioisotopes, typically ^{40}K, ^{238}U, ^{235}U, and ^{232}Th, within a sedimentary deposit along with bombardment by cosmic rays cause electrons in individual mineral grains to be promoted from the valence band to the conduction band. Some of these energised electrons become trapped at metastable defects in the crystal lattice, including those produced by chemical substitutions. A small amount of additional energy from heat (thermoluminescence, TL), visible light (optically stimulated luminescence, OSL) or infrared radiation (infrared stimulated luminescence, IRSL) can evict electrons from these traps. The electrons then recombine at luminescence centres, emitting photons in the process (*Burbank and Anderson*, 2012). Some electron traps are reset by brief heating at around 200 to 400 °C or by exposure to daylight (bleaching). Where conditions are suitable, the burial age of a sediment can be determined by measuring the luminescence signal of a quartz or feldspar grain. The intensity of the luminescence signal is a function of the total dose of radiation that the sample has received over time (equivalent dose or D_e). The age of the deposit is then equal to D_e divided by the rate at which the sample was irradiated by the surrounding radioisotopes.

The technique that is usually employed to date sediments is quartz OSL, as originally suggested by *Huntley et al.* (1985), and the most commonly-used method is the single aliquot regenerative dose (SAR) protocol of *Murray and Wintle* (2000). This method measures the natural luminescence signals of sample aliquots, each typically comprising a few hundred grains. Each aliquot is then subsequently exposed to known doses of radiation in the laboratory and re-measured a number of times to construct a luminescence growth curve. This allows the natural luminescence signal to be converted into an estimate of D_e (*Burbank and Anderson*, 2012). In cases where not all grains were fully reset by daylight exposure, for example rapidly deposited high energy fluvial sediments, different approaches have been adopted to isolate a representative D_e value.

Quartz OSL has been used successfully in numerous locations. However, some samples, particularly those from mountainous or tectonically-active regions that contain grains recently eroded from bedrock, display low OSL signal sensitivities and ages can be hard to determine (*Rhodes*, 2015). In other words, the luminescence signal generated per unit of radiation exposure is very low (*Lawson et al.*, 2012). Potassium feldspars (K-feldspars), however, typically have much higher luminescence sensitivities than quartz (*Rhodes*, 2011) and can therefore be used in more challenging sedimentary contexts. K-feldspars have several potential disadvantages, though. They can exhibit anomalous fading due to quantum mechanical tunnelling, resulting in age underestimations, and have signals that are less rapidly reduced by light exposure.

Feldspar IRSL signals were first proposed for dating by *Hütt et al.* (1988). *Lamothe et al.* (1994) demonstrated successful K-feldspar IRSL dating incorporating fading correction, while *Buylaert et al.* (2009) used a "post-IR IRSL" SAR protocol to isolate a more stable IRSL signal component. Single grain post-IR IRSL approaches that have the potential to overcome both of the major limitations have been developed by several authors (*Reimann et al.*, 2012; *Neudorf et al.*, 2012; *Trauerstein et al.*, 2012, 2014; *Smedley et al.*, 2012, 2015). *Rhodes* (2015) used a post-IR IRSL approach, with both conventional and improved K-feldspar mineral separates, to date high energy fluvial samples from slip rate and palaeoseismic contexts that spanned 400 to 80,000 years, and found good agreement with independent age control. This latter approach was used for the samples dated in the

present study. The improved "Super-K" mineral separation provides samples with many sensitive grains; single-grain measurements yield D_e estimates for as many as 70 to 95% of grains (*Rhodes*, 2015).

Methodology for IRSL dating

Samples for feldspar IRSL dating were collected in 5 cm diameter steel tubes, hammered horizontally into clean vertical sediment sections. The samples were prepared and analysed in the Department of Geography at the University of Sheffield under low-intensity laboratory lighting. The samples were treated with dilute HCl to remove carbonates and then dry-sieved to 180-212 μm. K-feldspars were extracted by flotation in a centrifuge using sodium polytungstate solution with a density of 2.565 g/cm^3. The grains were rinsed thoroughly and etched in 10% HF for 10 minutes to remove their outer surfaces, then rinsed and dried. Finally, samples were sieved again to remove grains < 180 μm.

Grains were mounted in specialist holders, each comprising one hundred 300 μm diameter holes, for measurement on a Ris TL-DA-XX DASH automated luminescence reader fitted with blue filters (BG3 and BG39) with an XY single grain (SG) attachment incorporating a 150 mW IR laser emitting at 830 nm. SAR cycles were used to construct a growth curve, as described in *Rhodes* (2015). Each SAR cycle comprised: (1) regenerative dose (or none for the natural measurement), (2) preheat for 60 s at 250 °C, (3) SG IRSL 2.5 s measurement at 90% laser power at 50 °C, (4) SG IRSL (2.5 s at 90% power, 225 °C), (5) beta test dose of $\approx$ 10 Gy, (6) preheat 2 (60 s at 250 °C), (7) SG IRSL (2.5 s at 90% power, 50 °C), (8) SG IRSL (2.5 s at 90% power, 225 °C), (9) Hot bleach at 290 °C (40 s at 90% power using 870 nm IR diodes). Samples were given regenerative doses in five steps up to around 650 Gy, a zero dose, and a repeat of the first dose step to assess recycling (*Rhodes*, 2011).

Analysis procedures followed those described by *Rhodes* (2015), using exponential plus linear fits to derive each single grain equivalent dose. Age estimates were based on combined equivalent dose values, selecting the minimum consistent values (incorporating an additional 15% overdispersion to allow for microdosimetry variations, caused by inhomogeneity in the location of K, U and Th within the sediment, and other effects),

and rejecting higher values that were interpreted as incompletely reset grains (*Rhodes*, 2015). Finite equivalent dose values were evaluated for between 8 and 40% of the measured grains (200 per sample), and minimum values were based on between 18 and 88% of these. Maximum single grain initial IRSL sensitivities were around 1.5×10^5 counts s^{-1} Gy^{-1}.

3.4 The Luoshan Fault

At its northern end, the Luoshan Fault strikes at 353 ° and runs along the eastern side of the Luoshan mountains just west of Tanzhuangzicun (see Figure 3.3). Gullies draining these mountains dissect an alluvial apron, draining first to the east and then curving to the north to follow the local slope, and preserve evidence of right-lateral offsets. Moving south, the fault strike changes to 330 ° around the northern end of the Daluoshan. Surface offsets are harder to identify, but *Min et al.* (2003) found evidence of thrusting in this section. The fault then tracks south, with a strike of 358 °, cutting across at least four different generations of alluvial fans (F1-4, where F1 is the youngest and F4 is the oldest) emanating from the Daluoshan (see Figures 3.4 (a) and 3.4 (b)). The older fans are more heavily incised and the channels on these surfaces are more sinuous. Multiple, parallel scarps are seen in this section, most of which include a component of uplift on their western side; the youngest fans preserve a vertical offset of 1.1±0.3 m (see Figure 3.4 (b)). At the southern end of the Daluoshan section, the fault makes a small dog-leg to the southeast and forms a 5 to 10 m high, 500 m long pressure ridge at 37.240 °N, 106.322 °E.

Moving south again, the fault lies along the eastern side of the Xiaoluoshan with a strike of 342 °. It cuts across the heads of a number of alluvial fans, most of which appear to be of the same age on the basis of their colour and texture (for example, see Figures 3.4 (c) and 3.4 (d)). The streams draining the Xiaoluoshan preserve a number of examples of right-lateral offsets and the fans here are uniformly uplifted on the eastern side of the fault trace by 5.0±1.4 m (see Figure 3.4 (d)). The fault continues at this orientation to the southern end of the Xiaoluoshan, 9 km south of Zhangjiashanpo. In addition, a series of 12 to 23 m high east-facing scarps are present east of the main strike-slip

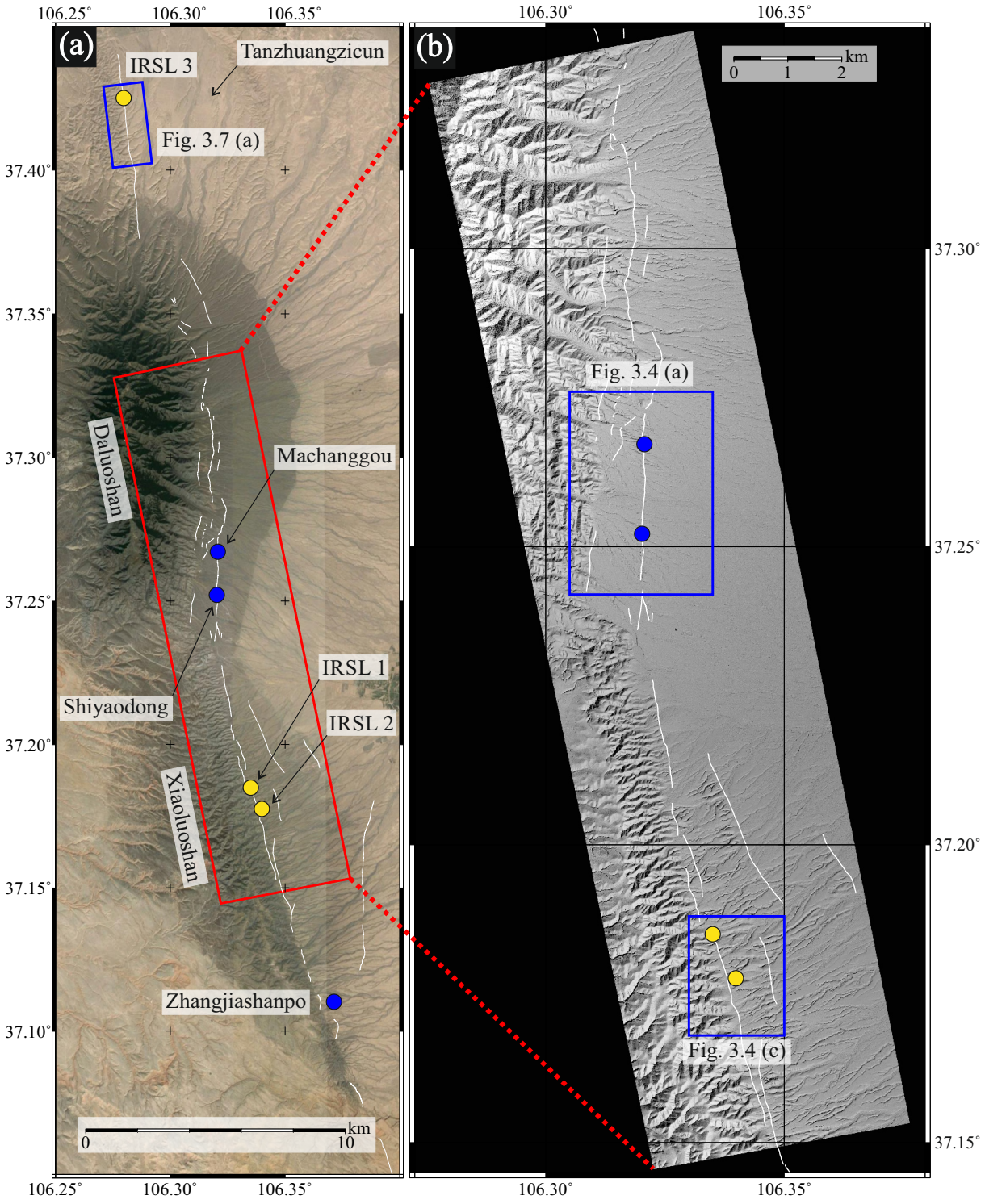


Figure 3.3: (a) Google Earth imagery from April and December 2013 (source: http://earth.google.com) of the Luoshan Fault with fault scarps mapped in white. Slip rate sites in this study are marked by yellow dots; sites from *Min et al.* (2003) are marked by blue dots. Red polygon shows coverage of Pleiades data. (b) Pleiades DEM of the central portion of the Luoshan Fault. Blue polygons show locations of other figures.

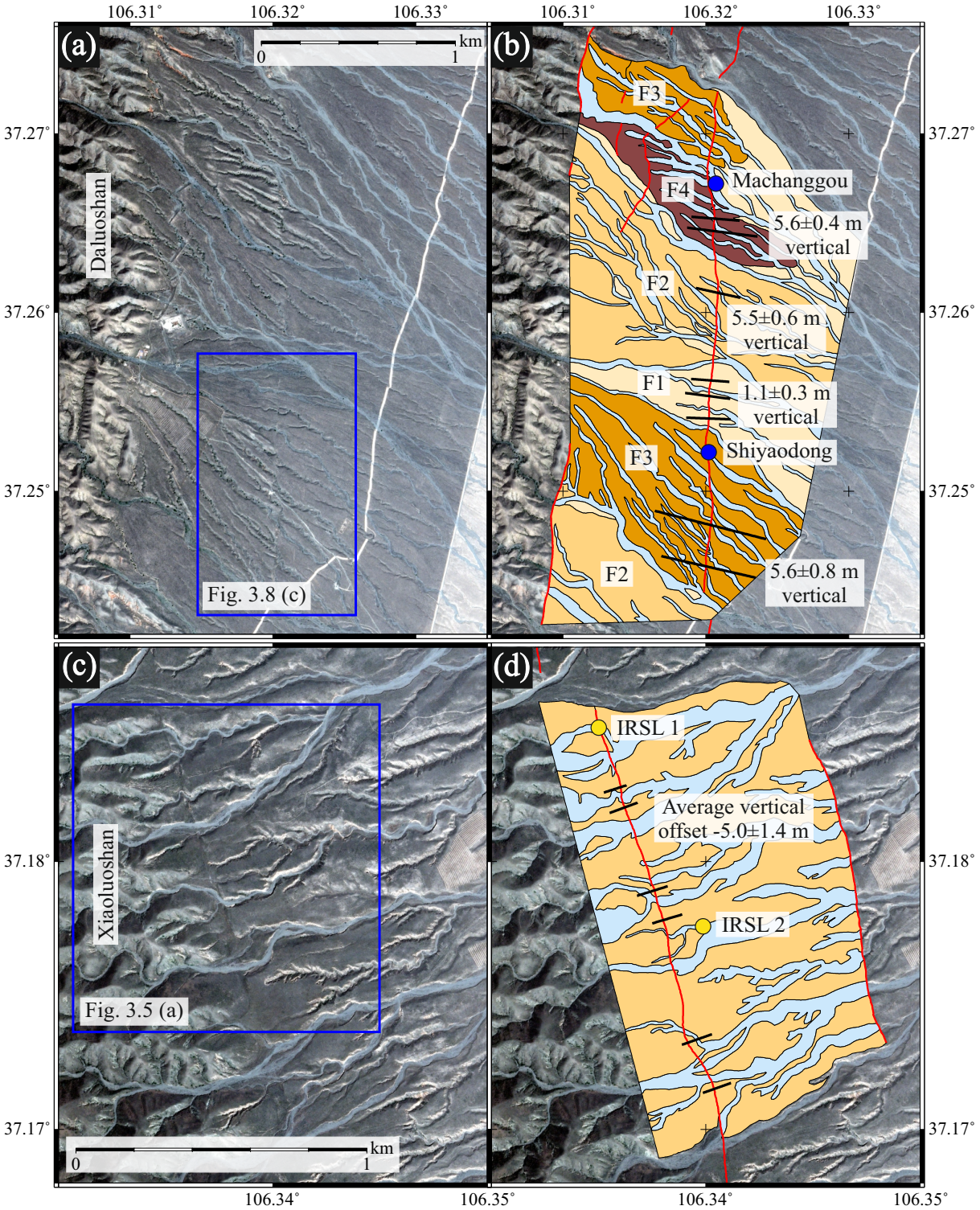


Figure 3.4: (a) Zoom of the Pleiades imagery adjacent to the Daluoshan in the vicinity of the slip rate sites used by *Min et al.* (2003). Blue polygon shows location of Figure 3.8 (c). (b) Annotated version of (a) with alluvial surfaces of different ages shown in different shades of brown (F1-4) and fault scarps mapped in red. Black lines indicate locations of topographic profiles used to estimate vertical offset preserved by each fan surface. (c) Zoom of the Pleiades imagery adjacent to the Xiaoluoshan in the vicinity of the slip rate sites used in this study. Blue polygon shows location of Figure 3.5 (a). (d) Annotated version of (c). Black lines indicate locations of topographic profiles used to estimate average vertical offset preserved by this alluvial apron.

fault, between 106.34 °E and 106.39 °E (see Figure 3.3 (a)). We interpret these scarps to represent superficial spatial separation of strike-slip and reverse components of motion onto two parallel fault strands.

The smallest vertical offset (1.1±0.3 m, at 37.255 °N, 106.320 °E) was measured where the local fault strike is 003 ° (see Figure 3.4 (b)). Other sections of the fault, with more northwesterly strikes, showed larger vertical offsets indicating a greater amount of shortening. We therefore deduce that pure strike-slip motion occurs at an azimuth slightly east of 003 °.

Slip rate sites at Xiaoluoshan, Tanzhuangzicun, Shiyaodong and Machanggou are described separately below. The quoted errors refer to 1σ analytical uncertainties unless otherwise stated. In order to calculate errors on our slip rate estimates we propagated fractional uncertainties from our offset measurements and age results in quadrature.

3.4.1 Xiaoluoshan section

Overview and offset measurement

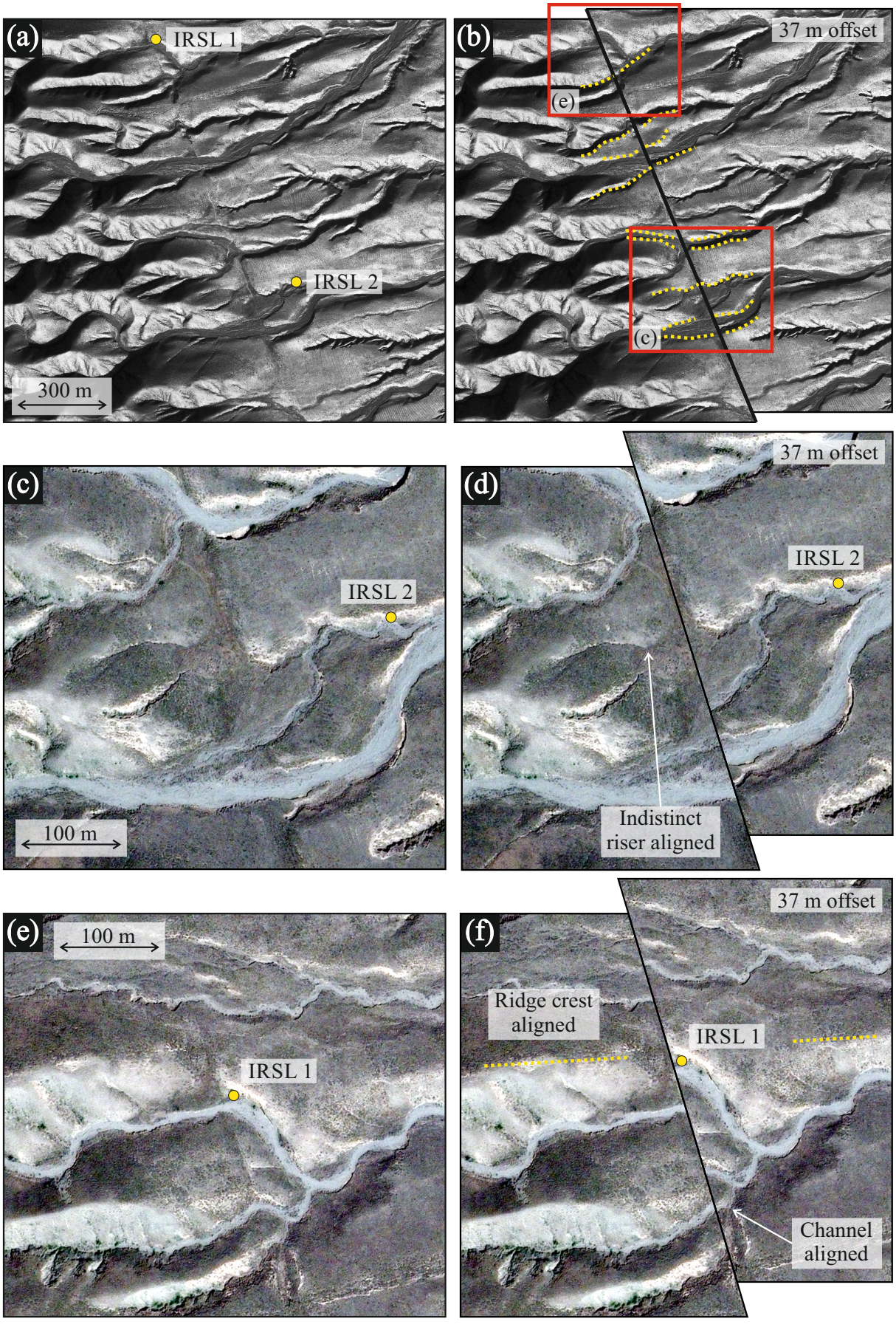
Our first slip rate sites on the Luoshan Fault are adjacent to the Xiaoluoshan (see Figure 3.3 (c)). Here, the fault cuts through an alluvial apron on the eastern side of the mountains and a large number of channels (with approximately 300 m spacing) flow eastwards across the fault trace, draining the Xiaoluoshan. Almost all of these channels show evidence of tens of metres of right-lateral offset. There is also a small amount of uplift (approximately 5 m) on the eastern side of the fault trace (see Figure 3.4 (d)).

Given the uniform colour and texture of the fan surfaces in Figure 3.4 (c), and the fact that they all preserve similar vertical offsets, we suggest that the area is covered by a single alluvial apron, composed of coalesced fans of similar ages. This being the case, we also expect all geomorphological markers to preserve similar horizontal offsets. We measure the horizontal offsets of nine different markers (six channel riser tops, one channel riser bottom and two channel thalwegs—see yellow lines in Figure 3.5 (b)) according to the methodology described in Section 3.3.2, and obtain a mean offset of 37.2±5.5 m and a range of 29.2 to 44.4 m (see Table 3.1). Figures 3.5 (c) and 3.5 (d) show that a 37 m

Table 3.3: Calculated slip rates on the Luoshan Fault

Location	Sample No.	Latitude °	Longitude °	Age ka	Error ka	Horizontal Offset m	Error m	Slip rate mm/a	Error mm/a
			Luoshan Fault						
Xiaoluoshan	IRSL 1	37.1850	106.3350	141	12	37.2	5.5	> 0.26	0.05
Xiaoluoshan	IRSL 2	37.1780	106.3397	9.16	0.57	37.2	5.5	4.1	0.7
Tanzhuangzicun	IRSL 3	37.4250	106.2800	10.6	0.9	50.6	6.7	4.8	0.8
Shiyaodong[a]	TL	37.2519	106.3204	9.80	0.75	41.1	5.9	4.2	0.7
Machanggou[b]	TL	37.2672	106.3207	69.0	5.4	171	10	> 2.5	0.2
Average								**4.3**[c]	**0.4**[d]

[a] Re-assessment of the data from Shiyaodong (*Min et al.*, 2003).
[b] Data from *Min et al.* (2003).
[c] Error-weighted average of samples IRSL 2, IRSL 3 and TL from Shiyaodong. IRSL 1 and Machanggou excluded for the reasons explained in the text—see Sections 3.4.1 and 3.4.4.
[d] Error is the weighted standard deviation of the three slip rate estimates.


(a)
IRSL 1
IRSL 2
300 m
(b)
37 m offset
(e)
(c)
(c)
IRSL 2
100 m
(d)
37 m offset
IRSL 2
Indistinct
riser aligned
(e)
100 m
IRSL 1
(f)
37 m offset
Ridge crest
aligned
IRSL 1
Channel
aligned

restoration aligns an indistinct riser on the western side of the fault trace with a more pronounced channel margin (the site of IRSL sample 2) on the uplifted eastern side. At the site of IRSL sample 1, the right-lateral fault motion is superposed on a pre-existing channel meander so the horizontal offset is harder to determine. However, Figures 3.5 (e) and 3.5 (f) show that the 37 m restoration aligns both a channel thalweg to the south of the sampling site and a ridge crest adjacent to the site.

Age constraints and slip rate

IRSL sample 2 is taken from a channel riser on the eastern side of the fault at 37.178 °N, 106.340 °E. The sample is from a patch of slightly coarser sand interbedded with fine-grained, brown loess at a depth of 55 cm. An angular gravel layer with 10 cm clasts is visible approximately 30 cm above the sample (see Figure 3.6 (b)), ensuring that we are dating material that was deposited prior to or during a fluvial regime, rather than aeolian deposits that have accumulated after fan abandonment. The IRSL sample provides an age of 9.2±0.6 ka (see Table 3.2).

IRSL sample 1 is taken from the same alluvial surface, 930 m to the northwest of IRSL sample 2, at 37.185 °N, 106.335 °E. The sample is from a fine-grained, brown loess 1.5 m below the ground surface. However, due to local erosion at the site, we estimate from adjacent outcrops that this corresponds to 2.1 m below the top of the alluvial fan. The sample is overlain by a coarser sand layer and two distinct gravel layers with 5 cm, sub-angular clasts of dark, Palaeozoic bedrock (see Figure 3.5 (d)). The sample provides an age of 141±12 ka (see Table 3.2).

Figure 3.5 ***(preceding page)*:** (a) 0.5 m resolution Worldview imagery showing a section of the Luoshan Fault adjacent to the Xiaoluoshan (see Figure 3.4 for precise location). The fault cuts across the image from NNW to SSE. The locations of IRSL samples 1 and 2 are indicated by yellow circles. (b) 37 m restoration, aligning various channel thalwegs and terrace risers (highlighted in yellow). Red boxes indicate locations of figures below. (c) 0.5 m resolution Pleiades imagery of the region marked in (b) and showing the location of IRSL sample 2. (d) Same as (c) with a 37 m restoration, aligning the sampled terrace riser. (e) 0.5 m resolution Pleiades imagery of the region marked in (b) and showing the location of IRSL sample 1. (f) Same as (e) with a 37 m restoration, aligning the channel thalweg to the south of the image and the ridge crest adjacent to the sampling site.

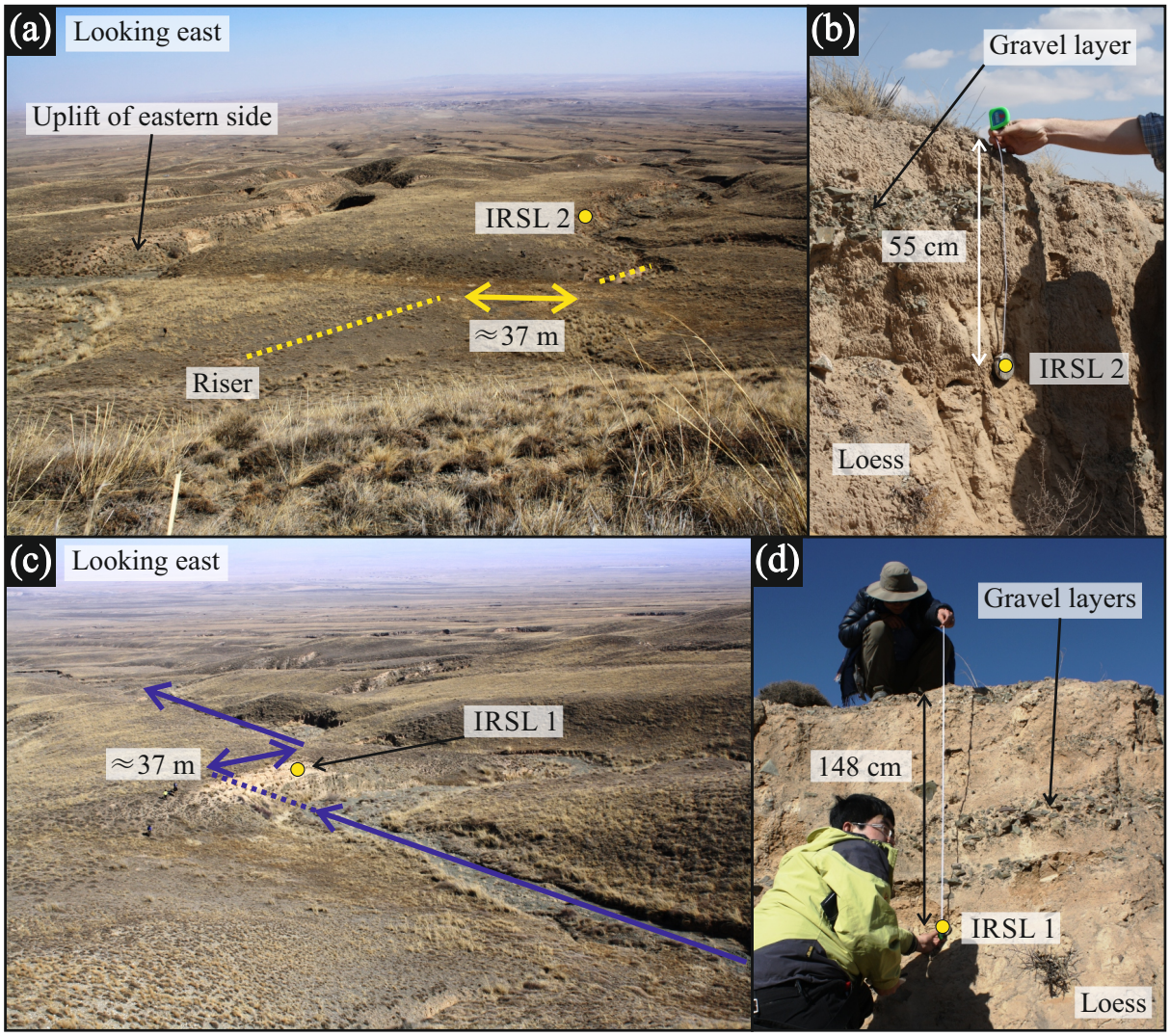


Figure 3.6: (a) Field photograph (taken at 37.178 °N, 106.340 °E) showing an overview of IRSL sample site 2. A riser on the western side of the fault trace, highlighted in yellow, can be identified by a change in the grass cover. (b) Close-up field photograph showing the sedimentary context of IRSL sample 2. (c) Field photograph (taken at 37.185 °N, 106.335 °E) showing an overview of IRSL sample site 1. There is a large meander in the stream at the location of the fault trace, but the far-field offset is of the order of 37 m. (d) Close-up field photograph showing the sedimentary context of IRSL sample 1.

The mean offset (37 m) and the age of IRSL sample 2 allow us to calculate a minimum slip rate of 4.1±0.7 mm/a (see Table 3.3). Meanwhile, IRSL sample 1 indicates a minimum slip rate of 0.26±0.05 mm/a (see Table 3.3). IRSL sample 1 is from deeper in the stratigraphy than IRSL sample 2, and may therefore represent sediments from a period of fan aggradation older than the most recent fan-forming episode. It is therefore unlikely to represent the age of the observed offset and can only be taken as a minimum

age constraint. We therefore exclude IRSL sample 1 from our determination of a mean fault slip rate in Table 3.3. The slip rate results are also discussed further in Section 3.5.

3.4.2 Tanzhuangzicun section

Overview and offset measurement

Our next slip rate site on the Luoshan Fault is at its northern end, beyond the end of the Daluoshan and around 1.75 km west of the village of Tanzhuangzicun (see Figure 3.3 (a)). This section of the fault strikes at 355 ° and cuts across an alluvial apron into which a number of channels have been incised (see Figure 3.7 (a)). The colour, texture and degree of incision on this apron suggest that it is composed of deposits of a similar age. The alluvial surface itself has been modified and terraced for agriculture (see Figures 3.7 (b) and (c)) and some very young streams have developed on top of this modified surface. However, evidence for right-lateral fault motion has been preserved by the channel margins of a set of more heavily incised streams. The whole fan surface slopes gently to the north and so the channels are offset in the opposite direction to the regional gradient. We also see evidence of eroded corners of channel risers on the down-slope edges of the channels (see Figures 3.7 (d) and (e)) (*Cowgill*, 2007).

We record a mean offset of this single alluvial surface of 50.6±6.7 m and a range of 37.2 to 61.4 m based on ten different geomorphological markers (eight channel riser tops, one channel riser bottom and one channel thalweg) (see Table 3.1). Figures 3.7 (d) and (e) show how a 51 m restoration aligns all of these markers (to within our error of ≈ 7 m), including those immediately adjacent to the site of IRSL sample 3.

Age constraints and slip rate

IRSL sample 3 is from 37.425 °N, 106.280 °E, just to the east of the fault trace. The sample is from fairly homogeneous, fine, yellow-brown loess, 169 cm below the ground surface and approximately 15 cm below a 10 cm thick gravel layer with 5 cm clasts of angular material (see Figure 3.7 (g)). The sample provides an age of 10.6±0.9 ka (see

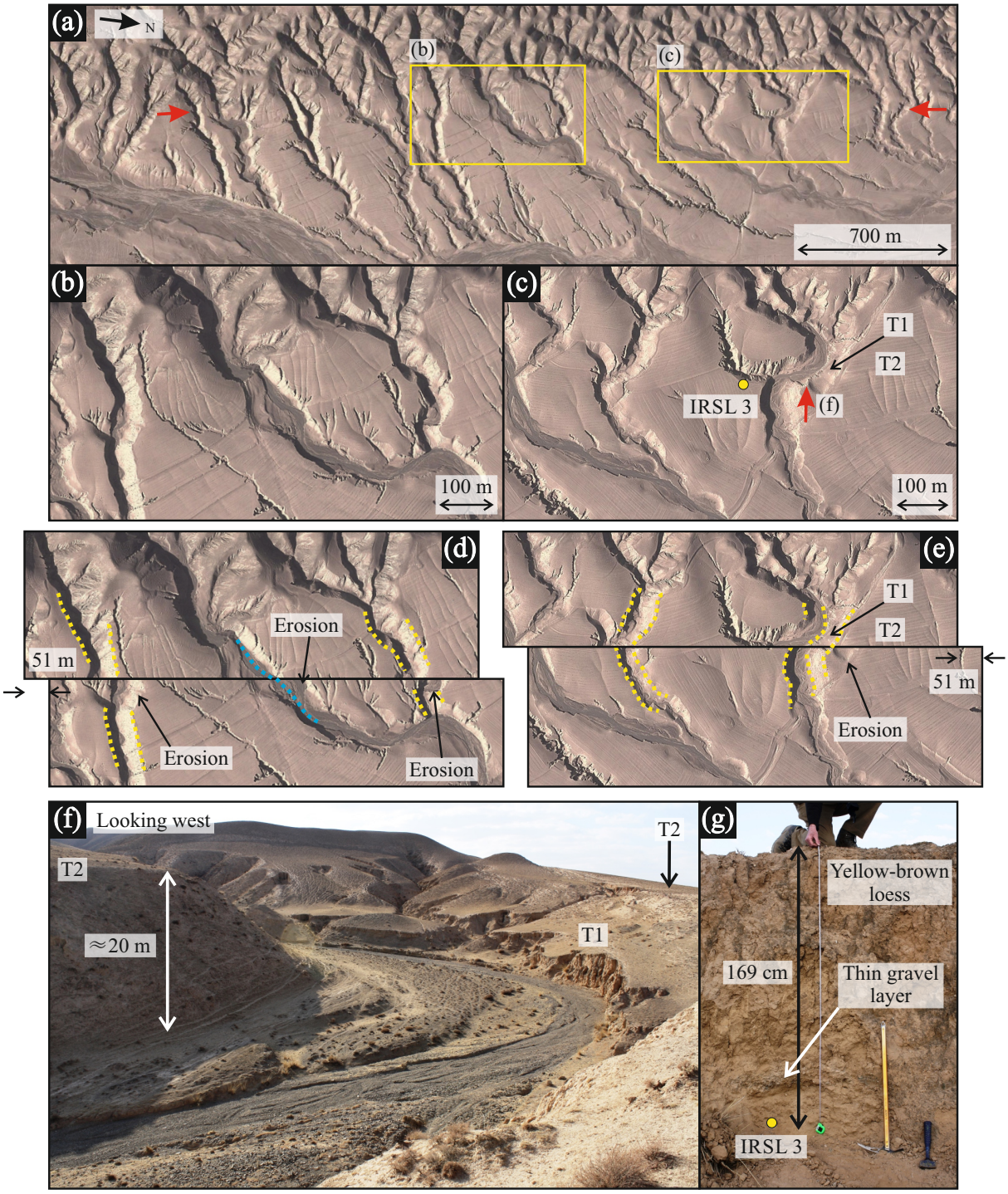


Figure 3.7: (a) Google Earth imagery from December 2013 (source: http://earth.google.com) of the Luoshan Fault north of the Daluoshan and around 1.75 km west of the village of Tanzhuangzicun (see Figure 3.3 (a) for precise location). Fault location is marked by red arrows. (b) Zoomed in view of the Google Earth imagery at the location marked in (a). (c) Zoomed in view of the Google Earth imagery at the location marked in (a). The location of IRSL sample 3 (at 37.425 °N, 106.280 °E) is indicated by the yellow circle. (d) Restoration of (b) indicating 51 m of right-lateral offset. Aligned channel risers are highlighted in yellow and an aligned channel thalweg is shown in blue. Eroded corners of channel margins on down-slope (i.e. northern) side are also indicated. (e) Restoration of (c) indicating 51 m of right-lateral offset. Yellow lines highlight alignment of channel risers. (f) Field photograph (taken at the location indicated in (c) showing the two terrace levels adjacent to this channel. (g) Field photograph showing the sedimentary context of IRSL sample 3.

Table 3.2). The mean offset (51 m) and the age of IRSL sample 3 allow us to calculate a minimum slip rate at this site of 4.8±0.8 mm/a (see Table 3.3).

3.4.3 Shiyaodong site

Overview and offset measurement

Min et al. (2003) used TL dates from two sites (Shiyaodong and Machanggou) at the southern end of the Daluoshan section to obtain their slip rate estimate of 2.15±0.20 mm/a (see Figure 3.4 (b)). Here, we use the high-resolution Pleiades DEM and our geomorphological mapping to re-estimate the offsets at their sites.

At the southern end of the Daluoshan section, four different generations of alluvial fans (F1-4, where F1 is the youngest and F4 is the oldest) can be identified on the basis of: their colour and surface texture in the optical imagery; the degree of incision in the fan surfaces (older surfaces have wider and deeper channels); and the sinuosity of the incising channels (older surfaces tend to have more sinuous channels). The different alluvial fans are also evident on slope and roughness maps: surfaces initially become smoother with age, before becoming rougher again due to the channel incision (see Figures 3.8 (a) and 3.8 (b), which are of the same area as Figure 3.4 (b)) (*Frankel and Dolan*, 2007). The Shiyaodong site is on the F3 surface and *Min et al.* (2003) measured an offset of 18±1 m on the basis of a topographic map that they constructed from a total station survey. However, although an 18 m restoration at this site re-aligns nearby gullies on a younger terrace surface, it does not appear to re-align the gully that *Min et al.* (2003) sampled (see Figure 3.8 (d)). The restoration is also complicated by the fact that the channels on the F3 surface are highly sinuous, leading to a large degree of ambiguity in the amount of slip. However, we re-measure the horizontal offsets of five piercing lines for channel thalwegs incised into the F3 surface and obtain a mean offset of 41.1±5.9 m and range of 33.8 to 48.5 m (see Table 3.1 and Figures 3.8 (e) and 3.8 (f)).

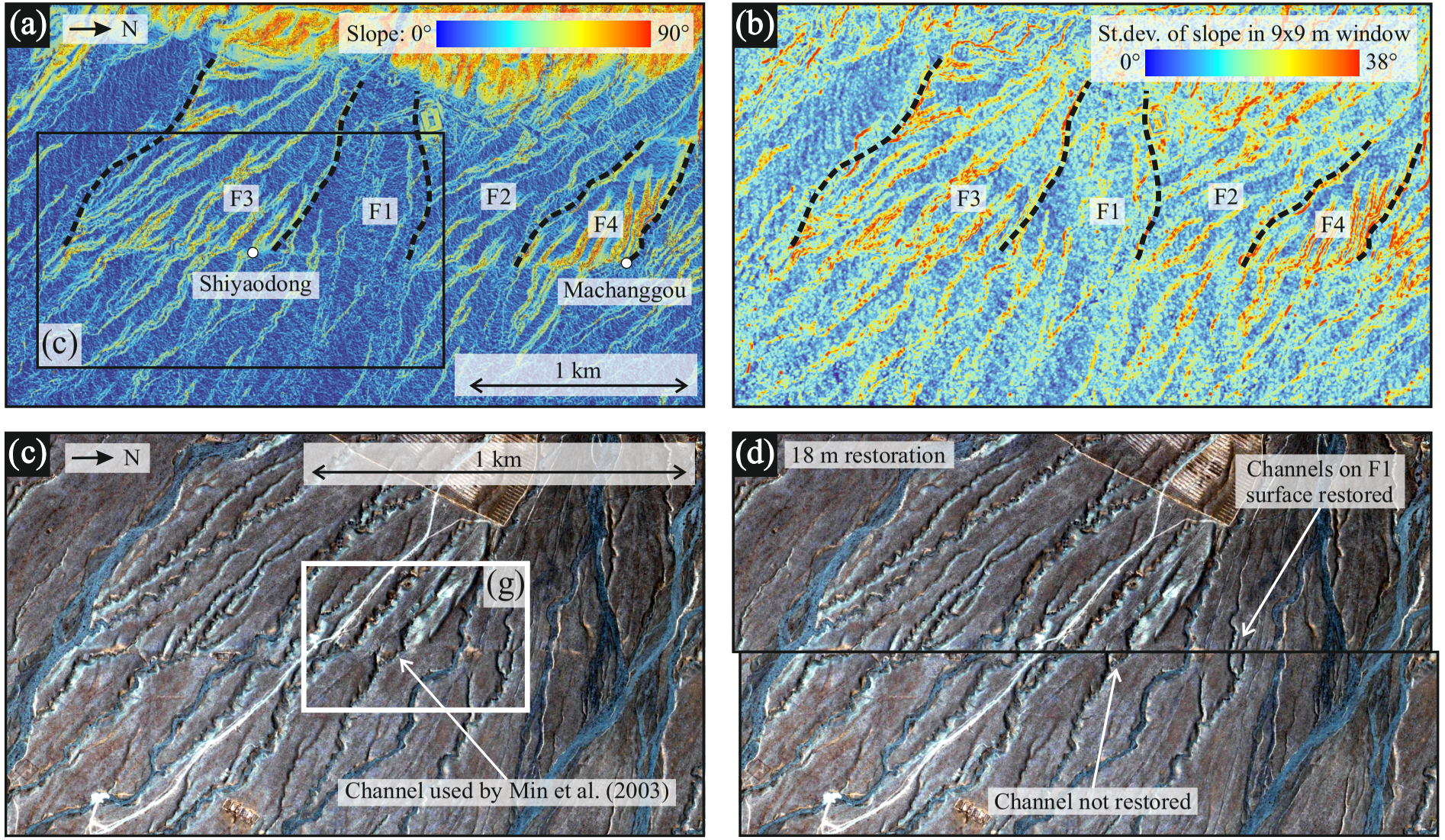


Figure 3.8: (a) Slope map derived from the Pleiades DEM. Region covered is the same as in Figure 3.4 (a). White dots show location of slip rate sites used by *Min et al.* (2003). (b) Surface roughness map of the same area derived from the Pleiades DEM by taking the standard deviation of the slope of the DEM in a 9×9 m moving window (*Frankel and Dolan*, 2007). (c) Contrast enhanced Pleiades imagery of the Shiyaodong site from *Min et al.* (2003) indicating the gully used for their slip rate estimate. (d) 18 m reconstruction, showing that gullies on the F1 surface are restored, but not those on the F3 surface.

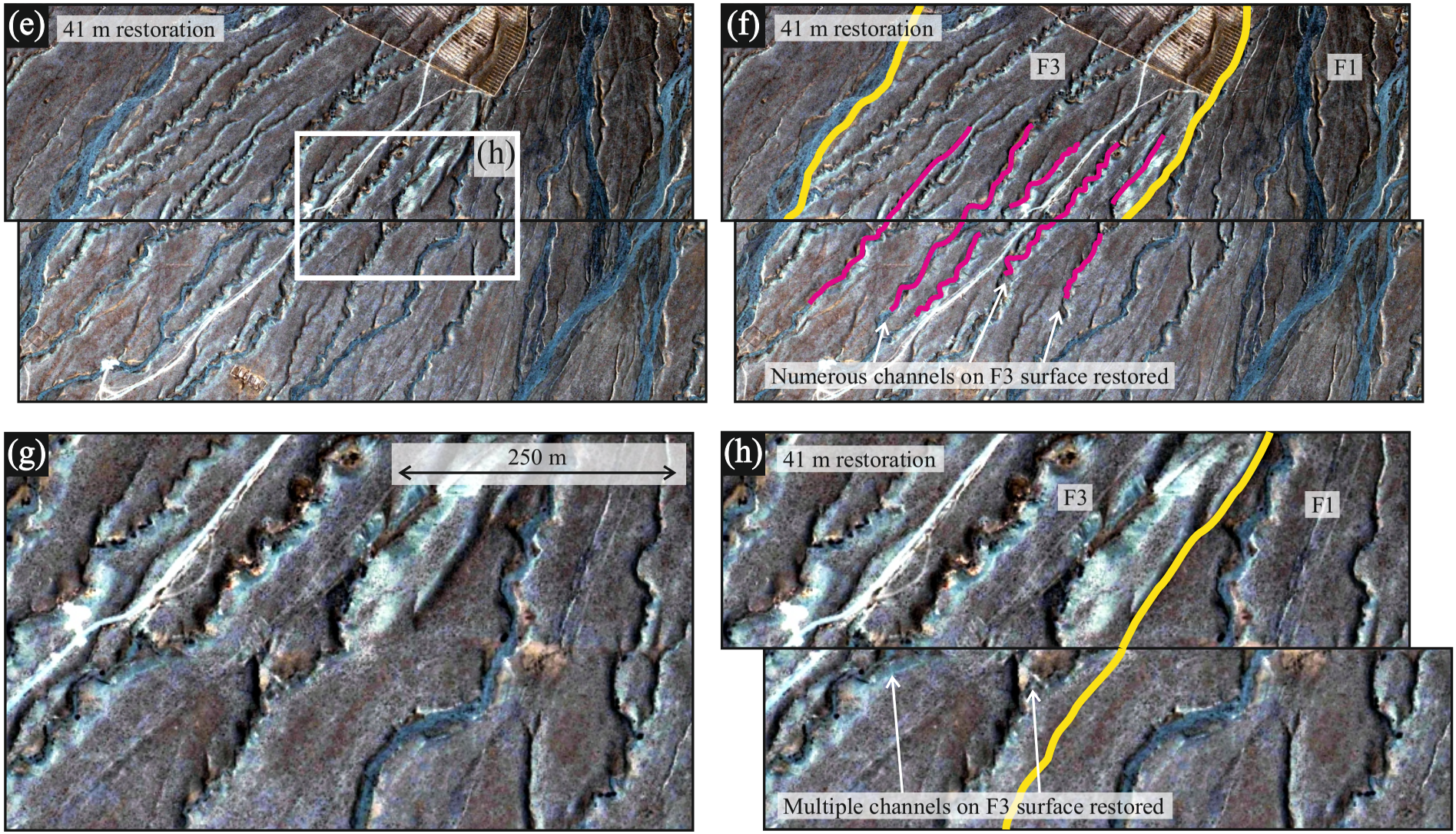


Figure 3.8: (continued) (e) 41 m reconstruction, which properly aligns gullies on the F3 surface. (f) Annotated version of (e) showing that multiple channels on the F3 surface can be restored with 41 m of right-lateral slip. Yellow lines indicate the edge of the F3 surface; pink lines show aligned channels. (g) Zoomed in view of the gullies on the F3 and F1 surfaces at the location marked in (c). (h) Zoomed in view of the 41 m restoration, showing that gullies on the F3 surface are restored, but not those on the F1 surface. Yellow lines indicate the edge of the F3 surface.

Age constraints and slip rate

At Shiyaodong (37.252 °N, 106.320 °E) *Min et al.* (2003) obtained a TL age of 9.80±0.75 ka for the F3 surface. Using our new offset measurement we therefore estimate a new slip rate of 4.2±0.7 mm/a (see Table 3.3).

3.4.4 Machanggou site

Overview and offset measurement

At the Machanggou site, 1.7 km north of Shiyaodong (see Figure 3.4 (b)), *Min et al.* (2003) measured an offset of 171±10 m. However, according to our geomorphological mapping (see Figures 3.4 (b), 3.8 (a) and 3.8 (b)), the channel *Min et al.* (2003) investigated runs along the side of the F4 surface rather than being incised into it. Their measured offset may therefore not be representative of the displacement recorded by F4.

Age constraints and slip rate

At Machanggou (37.267 °N, 106.321 °E), *Min et al.* (2003) obtained a TL age of 69.0±5.4 ka. However, their sample was from 3 m below the surface of F4 and so may well be significantly older than the last episode of deposition on the F4 surface (as we interpreted for our IRSL sample 1).

Due to the uncertainty in the offset measurement and the age constraint at this site, we are only able to estimate a minimum slip rate of 2.5±0.2 mm/a at Machanggou (see Table 3.3). Furthermore, we measured similar vertical offsets for F2, F3 and F4 (see Figure 3.4 (b)), suggesting that all three of these surfaces preserve the same fault activity. The abandonment of these fan surfaces is likely to have been climatically controlled and hence the best constraint on the slip rate at this site would be provided by dating the youngest of these fans (F2). The F4 surface is probably notably older than the initiation of scarp formation at this site, and the slip rate from *Min et al.* (2003), based on the age from F4, is therefore likely to be a significant underestimate. Hence, we opt not to include this result in our mean slip rate for the whole fault (see Table 3.3).

3.5 Discussion

The agreement between our slip rate results from IRSL samples 2 and 3 (to within their 1σ analytical errors) and our re-assessment of the Shiyaodong site indicate that the right-lateral Holocene slip rate on the Luoshan Fault is ≈ 4 mm/a and we calculate a mean rate along the whole fault length of 4.3±0.4 mm/a (where the error now refers to the weighted standard deviation of the three slip rate estimates, see Table 4.3). We exclude IRSL sample 1 and the TL date from Machanggou for the reasons described in Sections 3.4.1 and 3.4.4. Furthermore, at all three of these sites the fans were dated to approximately 10 ka ago (and the measured horizontal offsets are similar). This common age suggests that the deposition of these fans (the alluvial aprons at Xiashigou and Tanzhuangzicun and the F3 surface at Shiyaodong) was principally controlled by climate. It is possible that the ending of the Younger Dryas period around 11.7 ka ago, which brought generally warmer and wetter conditions, was the impetus for extensive erosion in the Luoshan and subsequent deposition of large quantities of alluvium on its eastern side. This sort of climatic control on fan deposition has previously been suggested in a number of other locations (e.g. *Nissen et al.*, 2009; *Ganev et al.*, 2012; *Hetzel*, 2013).

Whilst it is notable that the three slip rate estimates, from three different locations along the fault, are in agreement, our average rate obscures potential variations in slip rate along strike. For example, our largest slip rate estimate of 4.8±0.8 mm/a was at our northernmost site, Tanzhuangzicun, close to the northern termination of fault-related topography. This is at odds with the usual expectation that fault slip rates should become smaller towards the fault tips (e.g. *Faure Walker et al.*, 2009). This could indicate that the Luoshan Fault continues further north into the Yinchuan Graben, but is perhaps mantled by sediments or does not slip obliquely and so does not produce any fault-related topography. Nonetheless, our key result from the Luoshan Fault is that the slip rate is comparatively large (i.e. > 4 mm/a), which shows that this fault is one of the principal active structures in the western Ordos region. In Section 4.5.1 we will compare our result to a geodetic slip rate estimate and consider the wider implications for faulting in the whole western Ordos region.

Chapter 4

Throw rate on the East Helanshan Fault

4.1 Introduction

The Yinchuan Graben is a major structural feature on the western side of the Ordos Plateau: sediments reach a total thickness of around 6 or 7 km (see Chapter 2 and Figure 2.2) and the adjacent Helanshan reach a maximum elevation of 3557 m (*Zhang et al.*, 1990). The East Helanshan Fault, which was the seismogenic source for the devastating 1739 Yinchuan earthquake (see Chapter 2), appears from the topographic contrast across the range front and the fresh tectonic geomorphology to be one of the most active faults in the western Ordos region.

In this chapter we combine cosmogenic ^{10}Be dating, IRSL dating and our Pleiades DEM of the southern end of the East Helanshan Fault (see Chapter 2) to determine a throw rate (and hence an extension rate) for the East Helanshan Fault. We then compare this extension rate to our result from the Luoshan Fault in Chapter 3 and propose a geometric model for the pattern of faulting in the western Ordos. This then has implications for the overall kinematics of the whole Ordos Plateau (see Sections 3.1 and 6.6.2).

4.2 Tectonic setting

The Yinchuan Graben is sited at the northern end of Ningxia Province, where the deformation appears to be markedly different from that described for the Luoshan Fault (see Chapter 3). Four major, northeast-southwest trending normal faults cut Cenozoic and Quaternary strata, accommodating apparently northwest-southeast extension. From west to east these faults are: the East Helanshan Fault, the Luhuatai Fault, the Yinchuan-Pingluo Fault, and the Yellow River Fault (see Figure 3.2).

The East Helanshan Fault is approximately 120 km long and runs along the eastern side of the Helanshan (Helan mountains). *Zhang et al.* (1990) estimated a Quaternary throw rate for the East Helanshan Fault of 0.5 to 0.8 mm/a on the basis of the thickness of Quaternary sediments in the basin. The throw rate on the Yellow River Fault is estimated from TL ages of offset river terraces to be around 0.23 to 0.25 mm/a (*Liao et al.*, 2000). Throw rates on the Yinchuan-Pingluo and Luhuatai Faults are estimated from composite drilling profiles to be 0.14 mm/a (^{14}C date) and 0.18 mm/a (luminescence date) respectively (*Lei et al.*, 2008, 2011, 2015). According to a cross-sectional area balance, the whole Yinchuan Graben is thought to have extended at 2.9±1.0 mm/a since the Pliocene, although this result relies on the interpretation of seismic reflection profiles (*Zhang et al.*, 1998). The graben contains 1 to 1.6 km of Quaternary sediments and approximately 6 km of pre-Quaternary deposits that have accumulated since the Late Eocene (*Zhang et al.*, 1990).

A series of fresh scarps are present along the East Helanshan Fault (*Liao and Pan*, 1982). The southernmost of these scarps are called the Suyukou scarps, which vary in strike between 10 and 50 ° and cut through four, large, coalesced, alluvial fans some 3 km from the range front. From south to north, these fans are called the Baisikou, Suyukou, Helankou and Chaqikou Fans (see Figure 4.1 (b)) (*Deng and Liao*, 1996). *Deng and Liao* (1996) also identified four separate terrace levels in the scarp footwalls, from T1 (the youngest, typically 3 m above the adjacent hanging wall and thought to be from the 1739 Yinchuan earthquake—see Chapter 2) to T4 (the oldest, up to 11 m above the hanging wall). It is possible that the abandonment of these terrace surfaces was driven by

climatic changes, specifically changes in precipitation which would have altered both the rate of erosion in the Helanshan and the rate of transport of material to the range front. However, the terraces are typically poorly developed or non-existent on the hanging wall side of the fault trace (*Deng and Liao*, 1996). Furthermore, the terraces form staircase-like patterns either side of active channels at the fault trace, with an increase in scarp height of ≈ 3 m for each "step" of the staircase. It is therefore likely, though not certain, that terrace creation along the Suyukou scarps was tectonically induced. Each ≈ 3 m would then correspond to an earthquake, though perhaps not every earthquake would have been large enough to trigger terrace abandonment and hence the terraces may not preserve records of intervening events.

The Baisikou, Suyukou and Helankou Fans are mainly mantled by the T2 surface, with only scattered remnants of T3 and T4; the T1 surface is found adjacent to currently active channels. The Chaqikou Fan comprises primarily the T1 and T2 surfaces. The different terraces can be correlated across the different fans primarily on the basis of their similar scarp heights at the fault trace: ≈ 3 m for T1, ≈ 6 m for T2 and so on. Furthermore, all four fans comprise very similar material—poorly consolidated, sub-angular gravels to boulders—and have similar upstream catchments. Landforms older than T4 are only preserved in a few small areas. Firstly, at the range front, some higher, presumably older terraces are preserved adjacent to minor catchments. Secondly, at the northern end of the Chaqikou Fan, there is a remnant of a heavily incised terrace (coloured dark brown in Figure 4.1 (b)), which is cut by multiple fault scarps and pre-dates T4. We call this terrace T5.

On the basis of palaeoseismic trenching and radiocarbon dating at the Suyukou scarps (and further north on the East Helanshan Fault), *Deng and Liao* (1996) concluded that at least three earthquakes occurred on this fault prior to 1739: 2600 years ago, 4600-6300 years ago, and 8400 years ago. If each of these earthquakes triggered the abandonment of a terrace in the alluvial fans, then the offsets measured on the terraces can be used to calculate a throw rate. *Deng and Liao* (1996) measured a total terrace offset for the last three events of 8.4 m. Combined with a maximum age for the antepenultimate event of 6300 years, this would yield a minimum throw rate of 1.3 mm/a. However,

this one-to-one correlation between trench ages and preserved terraces may well not be justified. In this study, we therefore seek to provide the first direct measurement of the Late Quaternary throw rate on the East Helanshan Fault by conducting ^{10}Be dating of the terrace surfaces themselves and by making new vertical offset measurements from high-resolution topography. We also use IRSL dates to assess the lateral slip rate on the East Helanshan Fault at its northern end.

4.3 Methods

4.3.1 Pleiades data and DEM construction

We acquired Pleiades stereo imagery of the southern portion of the East Helanshan Fault on 23rd April and 17th July 2014 (see Figure 3.2 for data coverage). We then constructed a high-resolution digital elevation model (DEM) according to the methodology outlined in Chapter 2, Section 2.4.2. The final hill-shaded DEM is shown in Figure 4.1 (a).

The resulting DEM for the southern end of the East Helanshan Fault has a horizontal resolution, at least around the scarps, of about 2 m (see Chapter 2). As in Chapter 3, a surface roughness map was calculated, this time using a 5×5 m moving window as this window size was found to more clearly highlight the roughness contrast between different geomorphological surfaces (*Frankel and Dolan*, 2007; *Grohmann et al.*, 2011). We also calculated the 5th, 25th, 50th, 75th and 95th percentiles of the surface roughness raster for each of the mapped geomorphological units, except for T4 for which there was insufficient data (see Figures 4.1 (c) and 4.1 (d)). The median roughness values show an initial decrease with age, followed by a slight increase for the oldest terrace. This agrees with the results of *Frankel and Dolan* (2007): the initial bar and swale topography on the fan surface is smoothed over time by erosion, but eventually the surface is made rougher again by channel incision. We then used the DEM in combination with the surface roughness data and the original imagery to map the fault scarps and geomorphology in detail, tying our remote sensing observations to our field investigations.

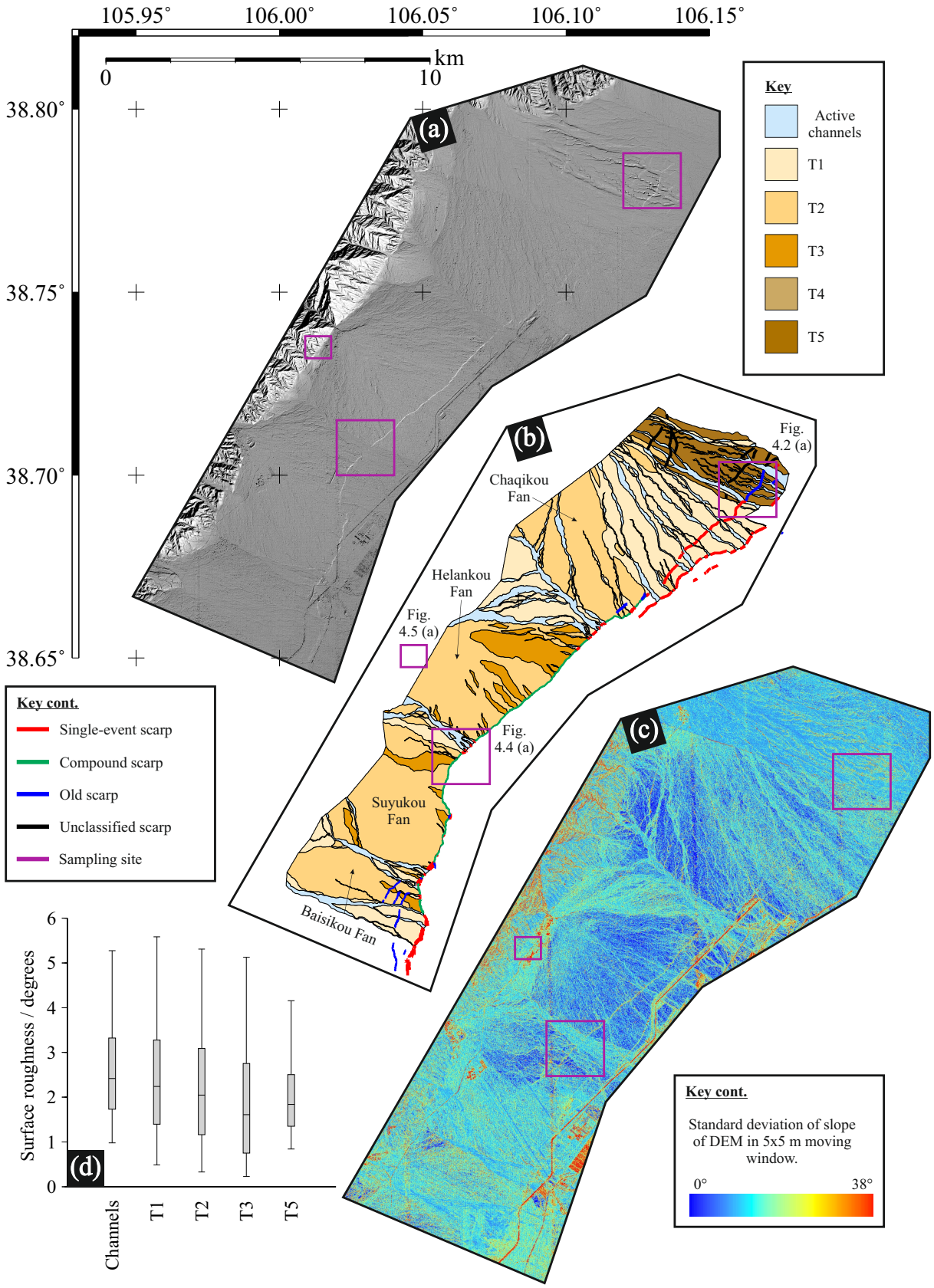


Figure 4.1: (a) Pleiades DEM for the Suyukou scarps at the southern end of the East Helanshan Fault. (b) Interpreted tectonic geomorphology for the Suyukou scarps at the southern end of the East Helanshan Fault. Purple squares indicate the locations of ^{10}Be sampling sites. (c) Surface roughness map derived from the Pleiades DEM by taking the standard deviation of the slope of the DEM in a 5×5 m moving window (*Frankel and Dolan*, 2007). (d) Box-and-whisker plot of the surface roughness for each alluvial unit. The horizontal bar inside each box is the median roughness; the ends of the boxes are the 25th and 75th percentiles; and the whiskers indicate the 5th and 95th percentiles.

4.3.2 Offset measurements

We measured vertical offsets across fault traces using the same methodology as in Chapters 2 and 3 (see Section 2.4.3 for a full description). Again, the quoted errors on our vertical offset measurements refer to the root mean square (RMS) residuals from our line fitting process.

4.3.3 ^{10}Be dating of offset features

On the East Helanshan Fault the alluvial fans comprise poorly consolidated, sub-angular gravels, pebbles, cobbles and boulders, with very little vegetation. The coarse grain size and lack of preserved organic material preclude dating by either radiocarbon or IRSL methods (with the exception of a few very recent deposits, which are well-exposed in modern river channels—see Chapter 2 and Section 4.3.4). We therefore used ^{10}Be exposure dating of boulder tops and suites of quartz pebbles to provide age constraints on fan surfaces deformed by the East Helanshan Fault. Background to the ^{10}Be dating procedure and details of the sample preparation and analysis are given below and the final results are shown in Table 4.1.

Background to ^{10}Be dating

Cosmic rays produce in situ cosmogenic radionuclides, such as ^{10}Be, when they interact with the Earth's surface. The concentration of ^{10}Be in an object can therefore be used to determine the length of time that an object has been at the surface (*Lal*, 1991; *Gosse and Phillips*, 2001; *Hetzel*, 2013; *Benedetti and van der Woerd*, 2014). The production rate (P_0) of ^{10}Be decays exponentially with depth over an e-folding length of about 50-70 cm, so only the top few centimetres can be used for dating. Since ^{10}Be is also radioactive its concentration at any one time in a surface object is a balance between the rate of production, the rate of decay and the erosion rate; at secular equilibrium, the rate of production is equal to the rate of decay and the concentration of ^{10}Be equilibrates to the erosion rate (*Gosse and Phillips*, 2001; *Granger and Schaller*, 2014). For ^{10}Be in quartz, secular equilibrium is reached after around 4 Ma (*Burbank and Anderson*, 2012).

Table 4.1: ^{10}Be dating results

Location	Name	Type[a]	Lat °	Long °	Elevation m	Thickness cm	Density g cm^{-3}	Shielding factor	[^{10}Be][b] 10^3 atoms g^{-1}	Exposure age[c] / ka
Range-front terrace	9	A	38.7359	106.0117	1461	2	2.65	0.9628	1498.0±22.7	120.6±1.9
Range-front terrace	1	B	38.7363	106.0111	1486	3	2.70	0.9674	1409.0±24.7	111.5±2.0
Range-front fan	3	B	38.7354	106.0143	1414	3	2.65	0.9832	206.2±7.0	16.5±0.6
Range-front fan	4	B	38.7353	106.0138	1413	3	2.73	0.9832	163.5±11.4	13.1±0.9
Range-front fan	5	B	38.7354	106.0138	1411	3	2.75	0.9832	101.9±13.3	8.2±1.1
Range-front fan	6	B	38.7354	106.0138	1419	3	2.73	0.9832	138.7±6.5	11.1±0.5
Range-front fan	7	B	38.7349	106.0149	1400	3	2.73	0.9795	219.0±6.7	17.8±0.6
Range-front fan	8	B	38.7344	106.0150	1399	3	2.74	0.9795	469.0±16.4	38.3±1.4
T5	10	A	38.7839	106.1343	1193	2	2.67	0.9996	2288.0±38.3	221.5±3.9
T5	11A	C	38.7828	106.1398	1162	4	2.65	0.9996	1560.6±32.5	154.4±3.3
T5	11B	C	38.7828	106.1398	1162	4	2.65	0.9996	2161.5±29.8	217.0±3.2
T5	11C	C	38.7828	106.1398	1162	4	2.65	0.9996	2094.9±23.4	209.6±2.5
T5	11D	C	38.7828	106.1398	1162	4	2.65	0.9996	1084.5±17.0	105.6±1.7
T5	11E	C	38.7828	106.1398	1162	4	2.65	0.9996	1820.7±43.3	181.3±4.5
T5	11F	C	38.7828	106.1398	1162	4	2.65	0.9996	2215.7±23.4	223.4±2.5
T5	11G	C	38.7828	106.1398	1162	4	2.65	0.9996	2134.5±36.8	213.9±3.9
T5	11H	C	38.7828	106.1398	1162	4	2.65	0.9996	2054.8±46.8	205.4±4.9
T5 (inheritance)	12	A	38.7766	106.1285	1194	2	2.67	0.9996	299.0±7.5	27.5±0.7
T5 (inheritance)	13A	C	38.7766	106.1285	1194	4	2.68	0.9996	679.6±12.2	64.3±1.2
T5 (inheritance)	13B	C	38.7766	106.1285	1194	4	2.68	0.9996	85.4±3.8	8.0±0.4
T2	14	A	38.7047	106.0248	1254	2	2.66	0.9993	209.9±5.5	18.5±0.5
T2	14A	C	38.7047	106.0248	1254	4	2.66	0.9993	96.9±3.6	8.7±0.3
T2	14B	C	38.7047	106.0248	1254	4	2.66	0.9993	859.5±16.2	78.0±1.5
T2	14C	C	38.7047	106.0248	1254	4	2.66	0.9993	110.4±7.7	9.8±0.7
T3	15	A	38.7063	106.0270	1251	2	2.67	0.9993	475.7±11.5	42.3±1.0
T2 & T3 (inheritance)	16	A	38.7080	106.0330	1264	2	2.69	0.9993	165.0±8.0	14.4±0.7
T2 & T3 (inheritance)	16A	C	38.7080	106.0330	1264	5	2.69	0.9993	108.3±3.3	9.7±0.3
T2 & T3 (inheritance)	16B	C	38.7080	106.0330	1264	5	2.69	0.9993	226.1±5.4	20.3±0.5
T2 & T3 (inheritance)	16C	C	38.7080	106.0330	1264	5	2.69	0.9993	107.4±3.7	9.6±0.3
T2 & T3 (inheritance)	16D	C	38.7080	106.0330	1264	5	2.69	0.9993	373.8±8.3	33.6±0.8

[a] A = amalgamation of pebbles; B = boulder top; C = clast

[b] Background corrected values. Errors are analytical AMS uncertainties for samples and blanks propagated in quadrature. The NIST_27900 standard, with a ratio of 2.79×10^{-11}, was used for all samples.

[c] Exposure ages were calculated with the CRONUS-Earth online calculator (version 2.2), using a constant production rate model and a sea-level high-latitude reference production rate of 4.49±0.39 atoms g^{-1} a^{-1} (*Lal*, 1991; *Stone*, 2000; *Balco et al.*, 2008).

A number of other factors must also be accounted for when using ^{10}Be concentrations for age determination of exposed surface objects. The local production rate varies from mineral to mineral. Typically quartz is used for analysis, since ^{10}Be is produced from ^{18}O, and ^{18}O is abundant in quartz; the production rate is typically 4.49±0.39 atoms of ^{10}Be per gram of quartz per year of exposure (at sea level in high latitudes) (*Lal*, 1991; *Stone*, 2000). Since cosmic rays are steered by the Earth's magnetic field and absorbed by the Earth's atmosphere, both latitude and altitude must also be taken into account. Furthermore, nearby topography can shield a sample from cosmic rays, so a shielding factor must be calculated and corrected for (*Balco et al.*, 2008; *Hetzel*, 2013).

When dating depositional surfaces the primary concern is inheritance (*Benedetti and van der Woerd*, 2014). During exhumation, transport within a hillslope system, transport within a fluvial system, and final deposition a rock sample will have been exposed to cosmic rays and will start to accumulate ^{10}Be (*Anderson et al.*, 1996). This inherited component can be estimated by measuring the concentration of ^{10}Be in pebbles from modern river channels. However, this assumes that rates of erosion and sediment transport do not vary over time, for example over glacial-interglacial cycles (*Schmidt et al.*, 2011). Finally, post-depositional erosion (or soil inflation) can cause a sample to appear younger (or older) than it actually is; assuming no erosion gives a minimum exposure age. By picking samples from boulders with a dark desert varnish the effects of erosion can be minimised (*Schmidt et al.*, 2011).

Methodology for ^{10}Be dating

The measured concentration of ^{10}Be in the sample is typically very small, so quartz grains must be separated from the sample rock and the sample analysed in an accelerator mass spectrometer (AMS).

Initial sample preparation was carried out in the Department of Earth Sciences at the University of Oxford. Samples were broken into fist-sized chunks with a rock splitter, their density was estimated using a Walker steelyard beam balance (see Appendix A.1), and they were then crushed with a steel jaw crusher. For samples comprising an amalgamation of quartz pebbles the pebbles were sieved, and where necessary split into smaller pieces,

so that only pebbles in the size range 8 to 16 mm were included. Further grinding was done in a TEMA swing mill with a tungsten carbide bowl. The crushate was then sieved to obtain the 250 to 500 μm fraction and passed through a Frantz magnetic separator to remove magnetic minerals.

Quartz purification and ^{10}Be extraction were then completed at the Scottish Universities Environmental Research Centre (SUERC) in East Kilbride according to the methodology set out by *Corbett et al.* (2016). Boulder top samples that did not consist of pure quartz underwent froth flotation to remove unwanted feldspars and micas (other samples consisted of nearly pure quartz pebbles). Be carrier was added to each sample before being dissolved in HF. The solution was evaporated and re-dissolved in HCl a number of times to eliminate residual fluorides. Be was then separated using ion exchange chromatography. Fe species were removed by anion exchange in HCl and Ti species were removed by cation exchange with dilute H_2SO_4. Be was then precipitated as beryllium hydroxide and ignited to beryllium oxide, mixed with Nb powder, and pressed into copper cathodes.

^{10}Be-^{9}Be ratios were measured by AMS at SUERC (*Maden et al.*, 2007; *Xu et al.*, 2010). All measurements were normalised to the standard NIST_27900, with an assumed ^{10}Be-^{9}Be ratio of 2.79×10^{-11}. Final exposure ages were calculated with the CRONUS-Earth online calculator (version 2.2) (*Balco et al.*, 2008), using a Be half-life of 1.36 Ma (*Nishiizumi et al.*, 2007) and the constant production rate model of *Lal* (1991) and *Stone* (2000). Topographic shielding values were also calculated using the CRONUS-Earth calculator based on between 7 and 13 measurements of azimuth and angular elevation to the horizon at each sampling site in the field (*Balco et al.*, 2008). We assumed zero erosion.

Quoted errors refer to "internal uncertainties": 1σ analytical uncertainties on measured nuclide concentrations. We do not include errors in the production rate as we are only interested in comparing our exposure ages within the local study area (*Balco et al.*, 2008). We propagate errors in quadrature unless otherwise stated. A number of our ^{10}Be ages are from amalgamated samples and in these cases we do not have any constraints on the spread of ages within the population of sampled clasts. It should be emphasised, therefore, that the errors on the amalgamated samples still refer to analytical uncertain-

ties and not the standard deviations within the populations. We also note that these formal errors are significantly smaller than the likely geomorphological uncertainties at each sampling site, and hence we propose that the errors on our final slip rates should be treated with caution.

4.3.4 IRSL dating of offset features

At one site at the northern end of the East Helanshan Fault, sand and silt horizons were sufficiently abundant for us to use IRSL dating. Full details of the IRSL dating methodology are given in Section 3.3.3 and the final results from this site are shown in Table 4.2. The quoted errors refer to 1σ analytical uncertainties unless otherwise stated. In order to calculate errors on our slip rate estimates we propagated fractional uncertainties from our offset measurements and age results in quadrature.

Table 4.2: IRSL dating results for the East Helanshan Fault

Location	Name	Lat °	Long °	Elevation m	Depth m	Equivalent Dose[a] Gy	Dose Rate[a] mGy a^{-1}	Age[a] ka
East Helanshan Fault	4	106.6575	39.2360	1374	0.54	5.25±0.50	4.13±0.19	1.27±0.14
East Helanshan Fault	5	106.6575	39.2360	1374	1.27	16.0±0.6	4.99±0.25	3.21±0.21

[a] Including 1σ analytical uncertainties.

4.4 The East Helanshan Fault

4.4.1 T5 at the northern end of the Suyukou scarps

Overview and offset measurement

Our first throw-rate site is on T5, at the northern end of the Suyukou scarps (see Figure 4.2 and Figure 4.1 for location). Multiple fault scarps cut T5, all of which must have formed since the abandonment of this surface. Topographic profiles from the Pleiades DEM show a combined offset across all of these scarps of 19.4±1.1 m (see Figure 4.2 and Section 2.4.3 for methodology).

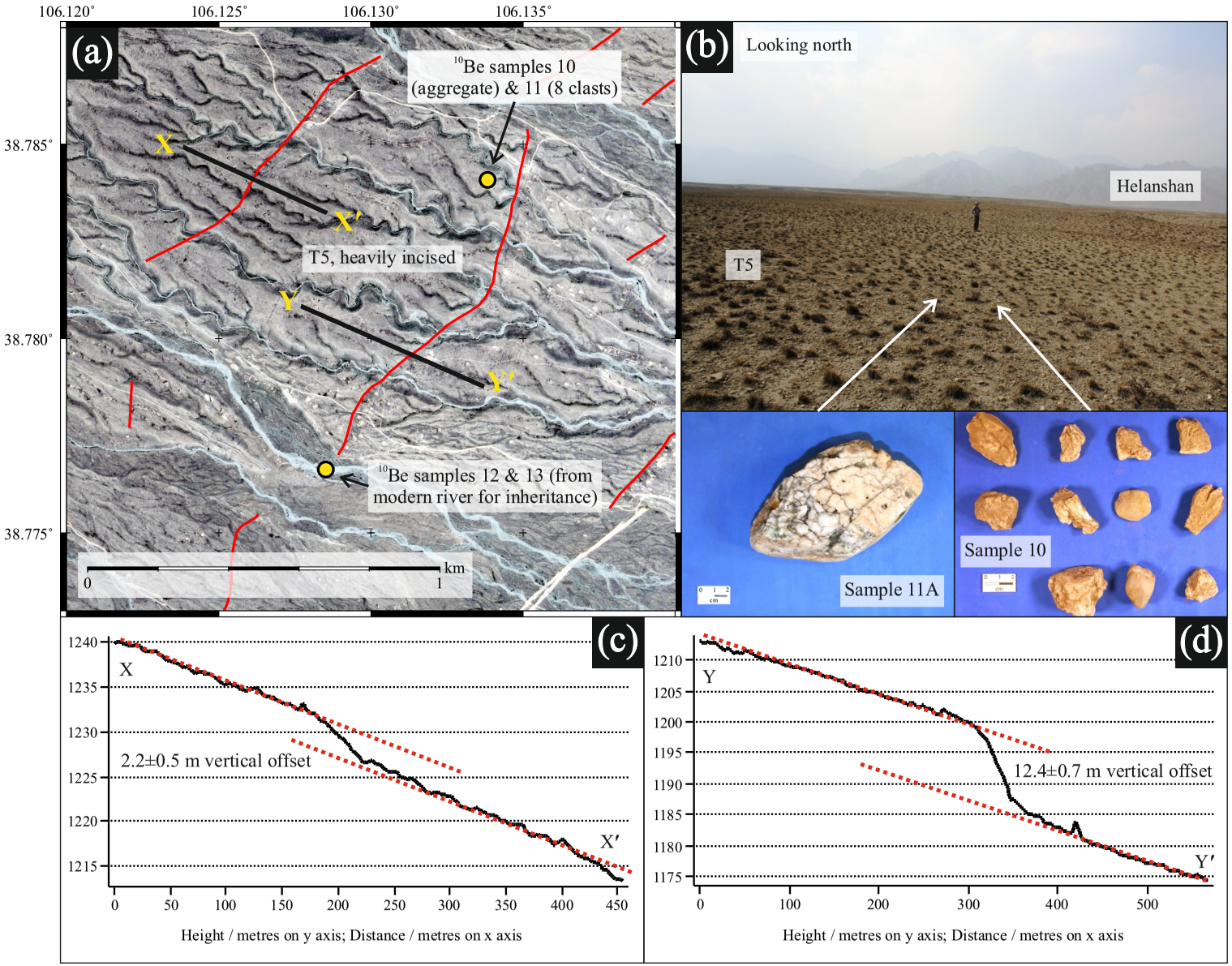


Figure 4.2: (a) Pleiades imagery showing the heavily incised T5 alluvial surface at the northern end of the Suyukou scarps. Fault traces are marked in red and ^{10}Be sample locations are shown by yellow circles. (b) Field photograph (taken at 38.784 °N, 106.134 °E) of the T5 surface. Inset photographs show representative quartz pebbles collected from this surface for ^{10}Be dating. (c) Topographic profile along the line X-X′ in (a), showing the vertical offset on one fault strand. (d) Topographic profile along the line Y-Y′ in (a), showing the vertical offset on another fault strand. Note that two other minor fault strands also offset T5 further to the northwest, giving a combined offset of 19.4±1.1 m.

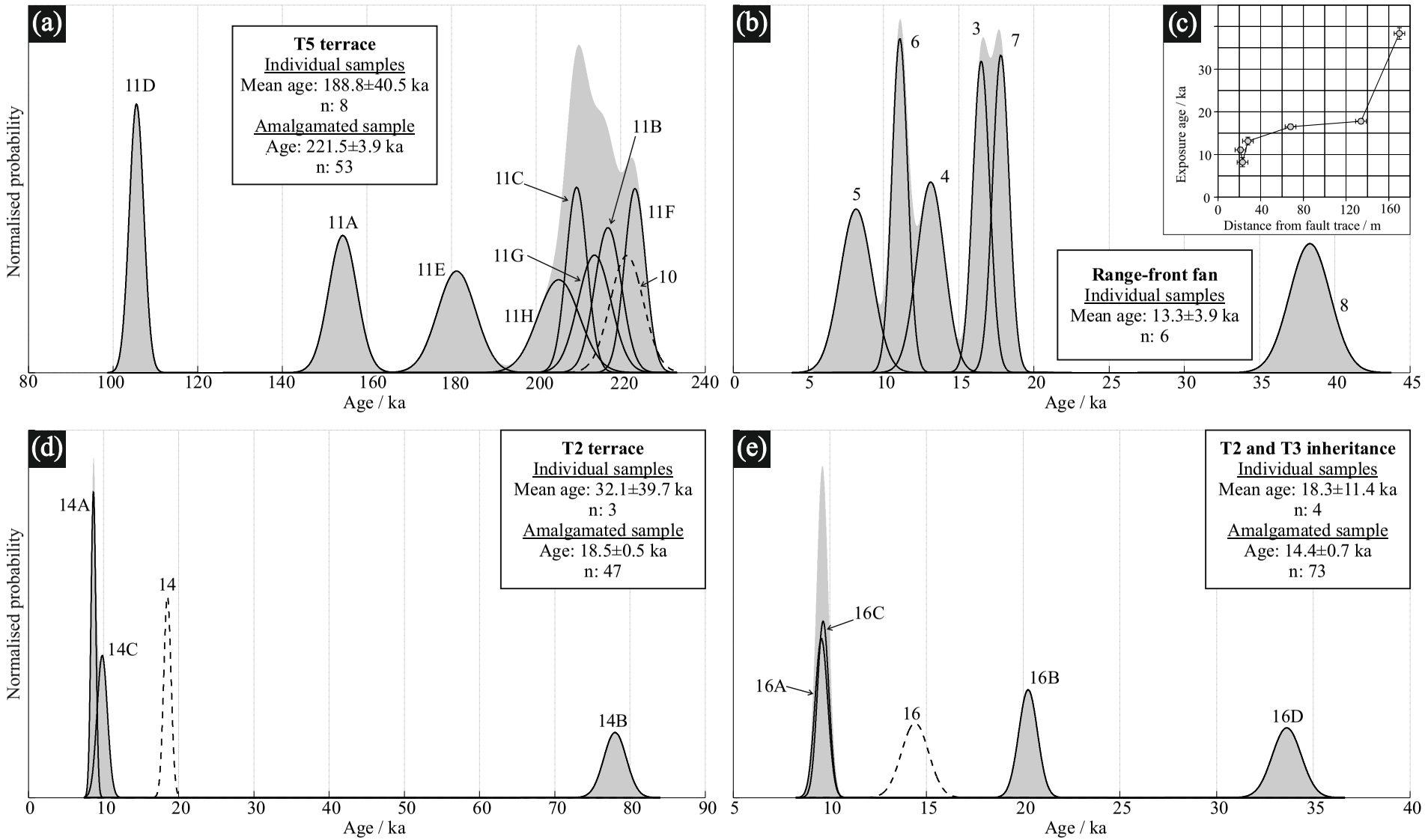


Figure 4.3: ^{10}Be age results for (a) T5, (b) the range-front fan, (d) T2, and (e) the T2 and T3 inheritance. Black curves are normally distributed probability density functions (PDFs) for individual samples, defined by the age and the 1σ analytical error. Grey curves are normal kernel density estimates (or camel plots), obtained by summing the individual PDFs. Dashed black curves are normally distributed PDFs for amalgamated samples. (c) Plot of ^{10}Be exposure age for boulder top samples from the range-front fan against their distance from the fault trace. Error bars show 1σ analytical error on age measurements and an assumed error of ± 5 m on the distance measurements.

Age constraints and throw rate

We use ^{10}Be dating to obtain ages for a suite of eight quartz cobbles (samples 11A to 11H, from 38.783 °N, 106.140 °E) and an amalgamated sample of 53 smaller pebbles (sample 10, from 38.784 °N, 106.134 °E) from the surface of T5 (see Figure 4.2). The results are shown in Figure 4.3 (a) and Table 4.1. Five of the eight cobbles are in relatively close agreement with the amalgamated sample age of 221.5±3.9 ka. We therefore interpret the three younger cobbles (samples 11A, 11D and 11E) as outliers. We also use an amalgamated sample of 42 pebbles (sample 12) and two individual cobbles (samples 13A and 13B) from the modern river (at 38.777 °N, 106.129 °E, see Figure 4.2 for location) to estimate the inheritance in this particular system. We obtain ^{10}Be ages of 27.5±0.7 ka for the amalgamated sample, and 64.3±1.2 ka and 8.0±0.4 ka respectively for the two individual clasts. Although the small number of samples indicate a large range in the inherited component, the inheritance is nonetheless much less than the ages from the T5 surface itself. A zero inheritance model gives a T5 age of 221.5±3.9 ka, whilst the largest measured inheritance (sample 13A) gives a T5 age of 157.2±4.1 ka. When combined with the total throw of 19.4±1.1 m, these ages correspond to vertical throw rates of 0.09±0.01 mm/a and 0.12±0.01 mm/a respectively (see Table 4.3). The large uncertainty in the inheritance therefore has little effect on the calculated throw rate.

4.4.2 Central Suyukou scarps

Overview and offset measurement

Our second sampling site is at a location where a major river from the Helanshan crosses the Suyukou scarps (see Figures 4.1, 4.4 (a) and 4.4 (b)). Here, the staircase pattern of aggradational footwall terraces proposed by *Deng and Liao* (1996) (see Figure 4.4 (e)) can be seen to the southwest of the current channel. These terraces are also partially evident in the surface roughness map (see Figure 4.4 (c)). Topographic profiles extracted from the Pleiades DEM confirm the stepped pattern, with heights for T1, T2 and T3 relative to the hanging wall level of 3.5±0.8 m, 5.2±0.5 m and 11.2±1.5 m respectively (see Figure 4.4 (d) and Section 2.4.3 for the full methodology).

Table 4.3: Calculated throw rates and slip rates on the East Helanshan Fault

Location	Sample No.	Latitude °	Longitude °	Age ka	Error ka	Vertical offset m	Error m	Throw rate mm/a	Error mm/a
Southern end of East Helanshan Fault									
Suyukou scarps, T5	10[a]	38.7839	106.1343	221.5	3.9	19.4	1.1	0.09	0.01
Suyukou scarps, T5	10[b]	38.7839	106.1343	157.2	4.1	19.4	1.1	0.12	0.01
Central Suyukou scarps	15[c]	38.7063	106.0270	27.9	1.2	11.2	1.5	0.40	0.06
Central Suyukou scarps	15[d]	38.7063	106.0270	32.7	1.1	11.2	1.5	0.34	0.05
Helanshan range front	9[a]	38.7359	106.0117	120.6	1.9	24.0	4.0	0.20	0.03
Helanshan range front	9[e]	38.7359	106.0117	56.3	2.2	24.0	4.0	0.43	0.07
Total throw rate[f]								**< 0.8**	**0.1**
Extension rate[g]								**< 1.0**	**0.1**
Location	Sample No.	Latitude °	Longitude °	Age ka	Error ka	Horizontal offset m	Error m	Slip rate mm/a	Error mm/a
Northern end of East Helanshan Fault									
Northern end of fault	IRSL 4	39.2360	106.6575	1.27	0.14	16.0	5.0	12.6	4.2
Northern end of fault	IRSL 5	39.2360	106.6575	3.21	0.21	16.0	5.0	5.0	1.6

[a] Assuming a zero inheritance model.
[b] Corrected for inheritance by subtracting age of sample 13A.
[c] Corrected for inheritance by subtracting age of sample 16.
[d] Corrected for inheritance by subtracting age of sample 16C.
[e] Corrected for inheritance by subtracting age of sample 13A.
[f] Found by summing 0.40 and 0.43 mm/a for parallel Suyukou and range-front strands to give a likely maximum throw rate.
[g] Assuming fault dip of 39 ° from *Fang et al.* (2009).

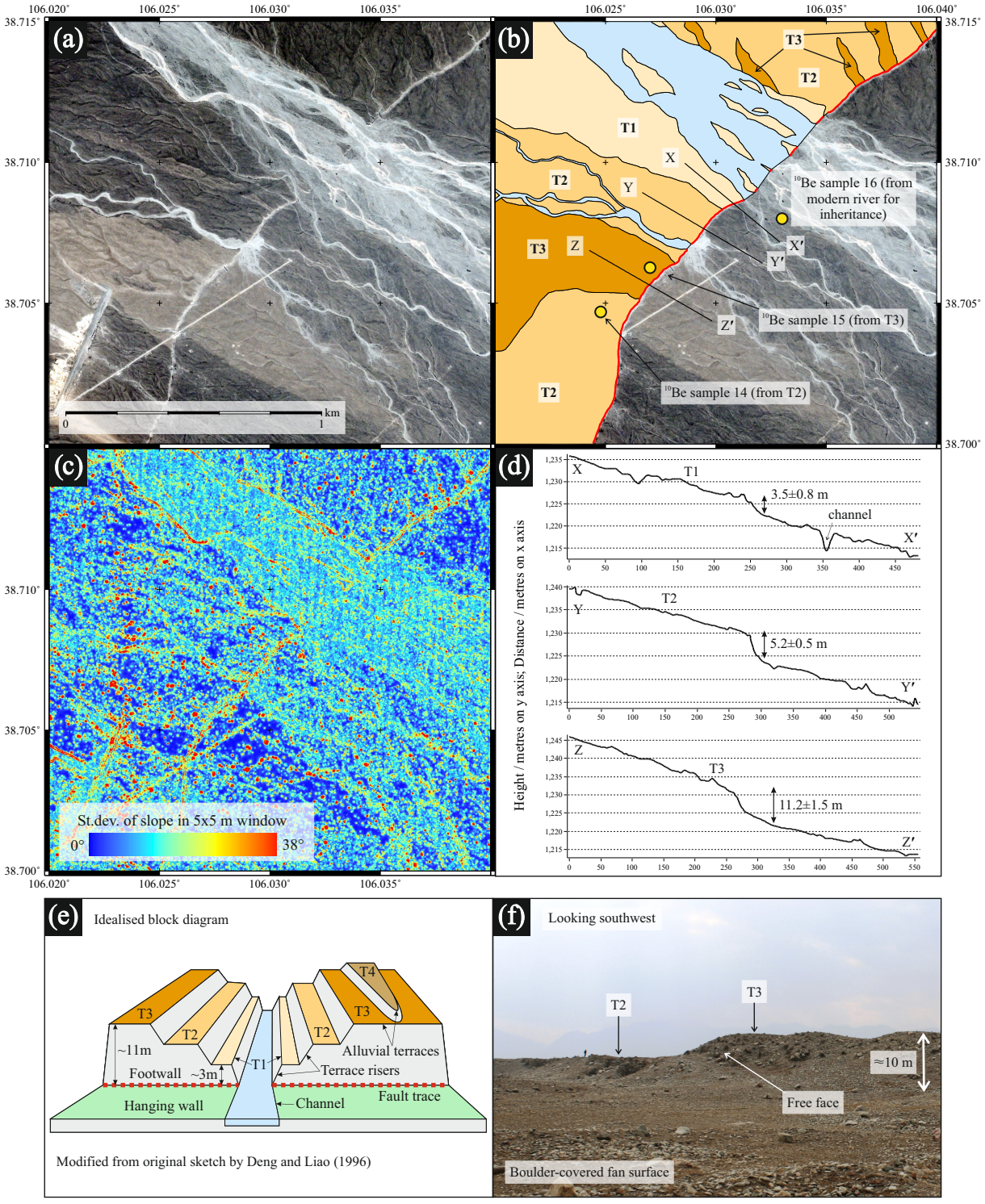


Figure 4.4: (a) Pleiades imagery showing an anastomosing river channel crossing the Suyukou scarps. (b) Annotated version of (a) showing mapped alluvial terrace surfaces, fault trace (in red), and ^{10}Be sample locations (yellow circles). The locations of profiles X-X′, Y-Y′, and Z-Z′ are also indicated. (c) Surface roughness map derived from the Pleiades DEM by taking the standard deviation of the slope of the DEM in a 5×5 m moving window (*Frankel and Dolan*, 2007). A number of the terraces mapped in (b) are visible in this image. (d) Three topographic profiles along the lines X-X′, Y-Y′, and Z-Z′ at the locations shown in (b). The three profiles show typical scarp heights for representative T1, T2, and T3 alluvial terrace surfaces. (e) Idealised block diagram showing the expected preservation of aggradational alluvial terraces in the footwall of a normal fault over multiple earthquake cycles. Modified from *Deng and Liao* (1996). (f) Field photograph (taken at 38.706 °N, 106.028 °E) of the Suyukou scarps showing T2 and T3.

Age constraints

^{10}Be samples 14, 15 and 16 (consisting of amalgamations of 47, 49 and 73 quartz pebbles respectively) are from T2, T3 and the modern river (see Figure 4.4 (b) and Table 4.1 for locations). They yield ages of: 18.5±0.5 ka for T2, 42.3±1.0 ka for T3 and 14.4±0.7 ka for the modern river. Correcting for inheritance by subtracting the amalgamated sample age from the modern river gives a T2 age of 4.1±0.9 ka and a T3 age of 27.9±1.2 ka. However, individual clasts from T2 (samples 14A to 14C) vary in age between 8.7±0.3 and 78.0±1.5 ka (see Figure 4.3 (d)). Similarly, individual clasts from the modern river (samples 16A to 16D) give ages between 9.6±0.3 and 33.6±0.8 ka (see Figure 4.3 (e)).

These results suggest that there is significant variation in the magnitude of the inherited component and that the ages are not sufficiently reliable to determine the precise abandonment times of T2 and T3. Nonetheless, the inheritance-corrected, amalgamated T3 sample age of 27.9±1.2 ka and the vertical offset of 11.2±1.5 m suggest a throw rate of 0.40±0.06 mm/a (see Table 4.3). The discrepancy between this and the 1.3 mm/a from the data of *Deng and Liao* (1996) is likely to be because there is not a one-to-one correlation between the colluvial wedges in the trenches and the terraces preserved at the surface.

Alternatively, the amalgamated T3 sample age of 42.3±1.0 ka and the youngest clast from the modern river of 9.6±0.3 ka (i.e. our lowest measure of what the inheritance might be) give a T3 age of 32.7±1.1 ka that we can consider to be an upper bound. Combined with the vertical offset of 11.2±1.5 m, this suggests a minimum throw rate of 0.34±0.05 mm/a over the last 30 ka (see Table 4.3). This is notably larger than the 0.09 to 0.12 mm/a obtained for T5 over the last 200 ka (see Section 4.4.1), which is just along strike to the north. Assuming that any earthquakes uplifting T3 also uplifted T5, this may imply an increase in the throw rate over time.

4.4.3 Helanshan range front

Overview and offset measurement

Our third throw-rate site is at the Helanshan range front, at the location indicated in Figure 4.1. Here, a boulder conglomerate fan straddles the range-front fault and a terrace is preserved on either side of the channel on the footwall side of the fault (see Figure 4.5). Topographic profiles extracted from the Pleiades DEM indicate that the terrace records an offset on the range-front fault of 24.0±4.0 m (see Figure 4.5 (e) and Section 2.4.3 for methodology).

Age constraints and throw rate

We collected an amalgamated sample of 83 quartz pebbles (sample 9, from 38.736 °N, 106.012 °E) and a single boulder top (sample 1, from 38.736 °N, 106.011 °E) from the terrace surface southwest of the channel (see Figure 4.5 (b) for locations). We were not able to collect more boulder top samples because there were very few large boulders with well-preserved desert varnish on top of the terrace. The samples yield ^{10}Be ages of 120.6±1.9 ka (sample 9) and 111.5±2.0 ka (sample 1). Despite the small number of samples, the relatively close agreement between the two gives us confidence that the amalgamated sample age is reliable.

We use the amalgamated sample age of 120.6±1.9 ka to calculate a throw rate of 0.20±0.03 mm/a (see Table 4.3), which is a minimum rate because it does not account for inherited ^{10}Be. If we allow for a large inheritance (of 64.3±1.2 ka, as measured for sample 13A in a different catchment) we obtain a minimum terrace age of 56.3±2.2 ka and hence a maximum vertical throw rate of 0.43±0.07 mm/a (see Table 4.3). In other words, even though the uncertainty on the inheritance is large, the maximum throw rate is still small (less than 0.5 mm/a).

In addition, we collected six boulder tops (samples 3 to 8) from the boulder fan that straddles the range-front fault (see Figure 4.5 (b) and Table 4.1 for locations). Since no scarps are preserved in the boulder fan itself, it must post-date the most recent surface-rupturing event at this location. The boulder tops range in age from 8.2±1.1 ka to

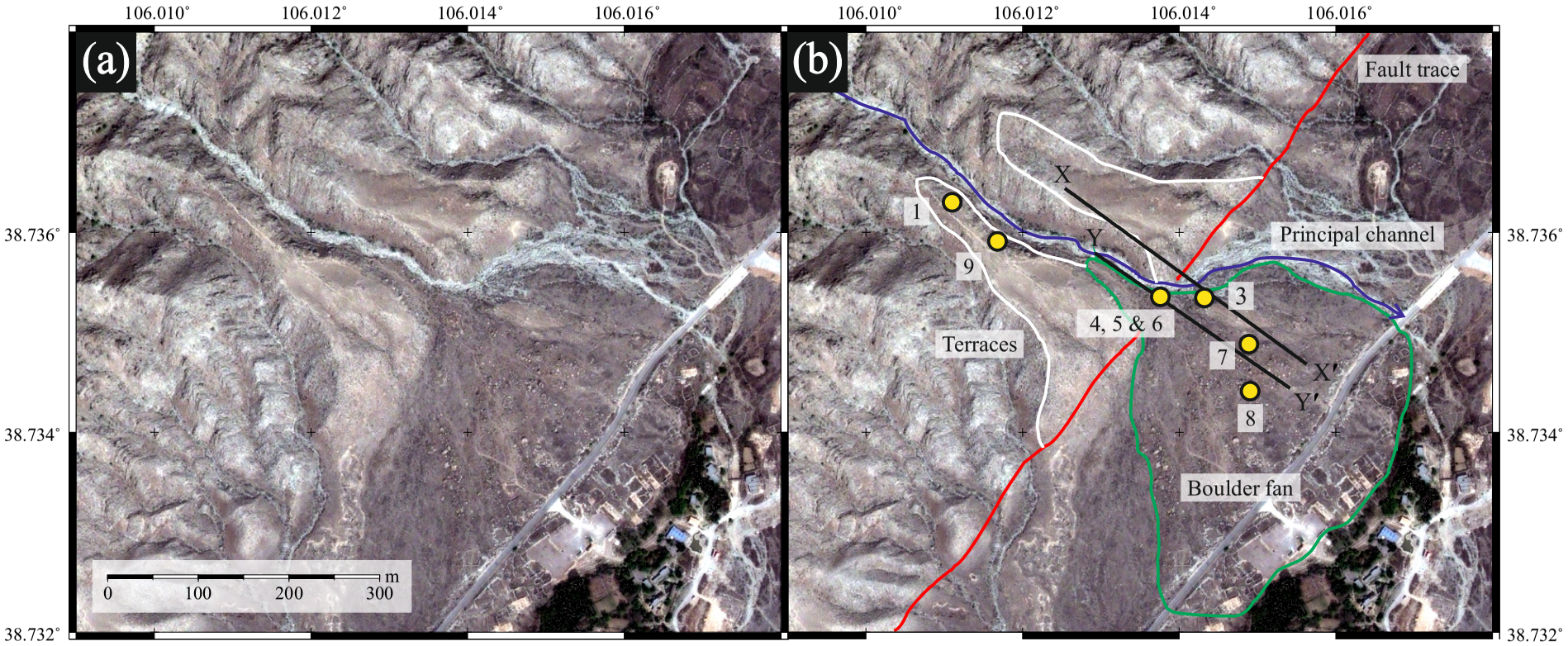


Figure 4.5: (a) Pleiades imagery of the range-front fault on the eastern flank of the Helanshan. (b) Annotated version of (a) showing fault trace (in red), two uplifted footwall terraces (in white), and an alluvial fan that has been deposited on top of the fault (in green). Yellow circles mark locations where boulder tops were collected for ^{10}Be exposure dating.

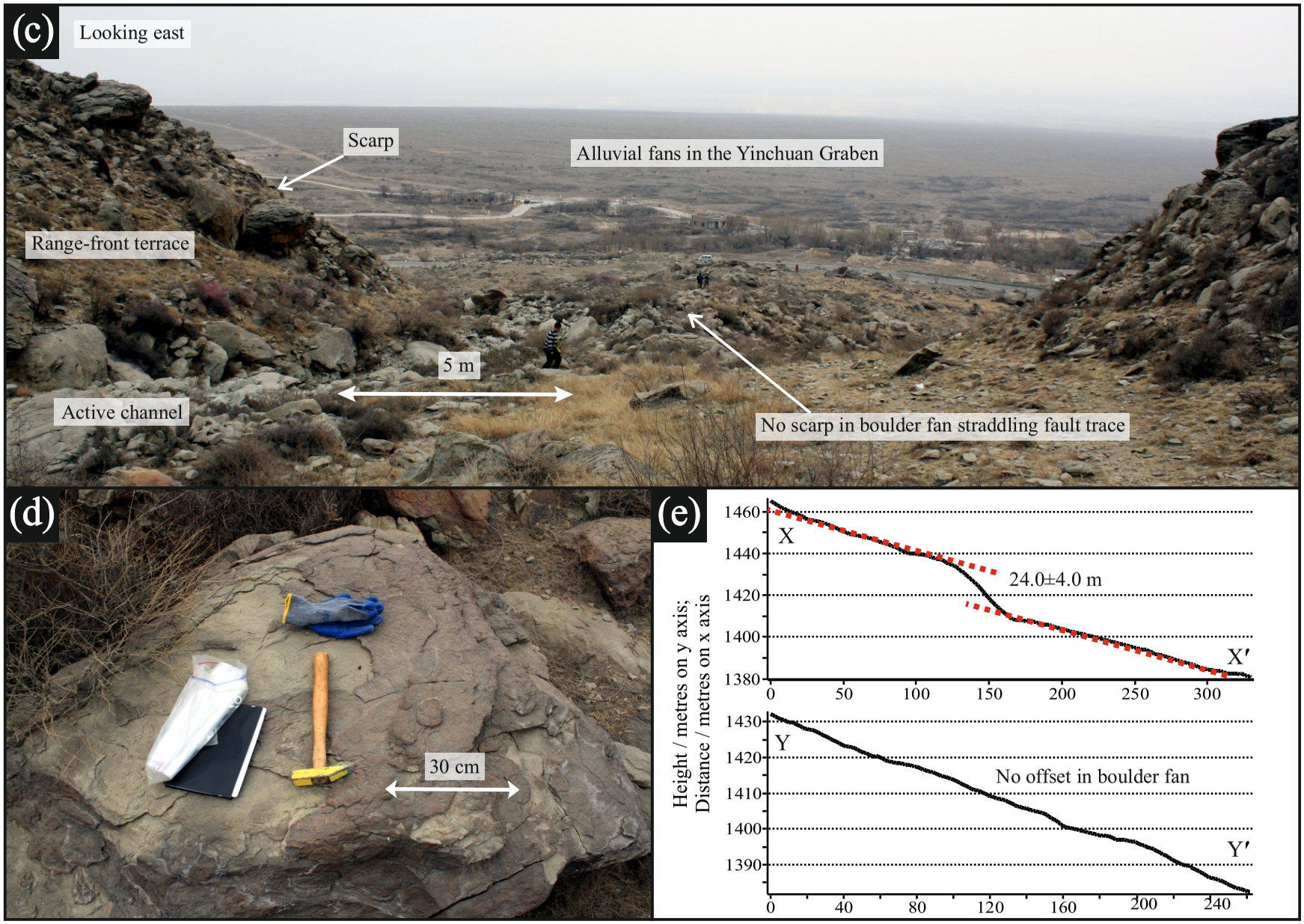


Figure 4.5: (continued) (c) Annotated field photograph (taken at 38.735 °N, 106.014 °E) looking from the footwall, across the range-front fault trace, towards the boulder fan in the hanging wall. (d) Field photograph (taken at 38.735 °N, 106.014 °E) showing desert varnish on the top of the boulder where sample 4 was collected. (e) Topographic profiles from the Pleiades DEM along the lines marked X-X′ and Y-Y′ in (b).

38.3±1.4 ka (see Figure 4.3 (b)). A plot of ^{10}Be exposure age against distance down slope from the fault trace shows that more distal samples have older exposure ages (see Figure 4.3 (c)). This suggests that the boulder fan has been generated in more than one event, with the most recent episode of deposition being restricted to near the apex of the fan. Samples 4, 5 and 6, all from near the apex of the fan, have ages of 13.1±0.9, 8.2±1.1 and 11.1±0.5 ka respectively, and we propose that these three ages represent the probable abandonment age of the boulder fan.

4.4.4 Northern end of the East Helanshan Fault

Overview and offset measurement

At the northern end of the East Helanshan Fault we found evidence for right-lateral motion (see Figure 3.2 for location). Here, three boulder ridges on top of an alluvial fan surface and an incised gully are right-laterally offset (see Figure 4.6). The scarp is fresh, with a free face, and this site is at the northernmost end of the rupture trace from the 1739 Yinchuan earthquake (see Chapter 2). The incised channel is offset by 4 m (see Figures 4.6 (b) and 4.6 (c)), probably representing displacement in the 1739 event. The boulder ridges form indistinct linear markers, but they are not completely aligned by a restoration of 4 m; our best visual restoration is at 16 m, though with visually estimated uncertainties of at least ±5 m (see Figure 4.6 (d)).

Age constraints and slip rate

IRSL samples 4 and 5 are from an exposure in the wall of the main river channel, which cuts across the displaced boulder ridges (39.236 °N, 106.658 °E), at depths of 54 cm and 127 cm respectively. IRSL sample 4 is from a 10 cm thick lens of medium brown silt, covered by a 50 cm thick layer of poorly sorted cobbles up to 30 cm in size (see Figure 4.6 (e)); IRSL sample 5 is from a stratigraphically lower, 20 cm thick layer of orange sand surrounded by coarse gravels and cobbles (see Figure 4.6 (f)). Sample 4 provides an age of 1.27±0.14 ka and sample 5 gives an age of 3.21±0.21 ka (see Table 4.2). These results are stratigraphically consistent.

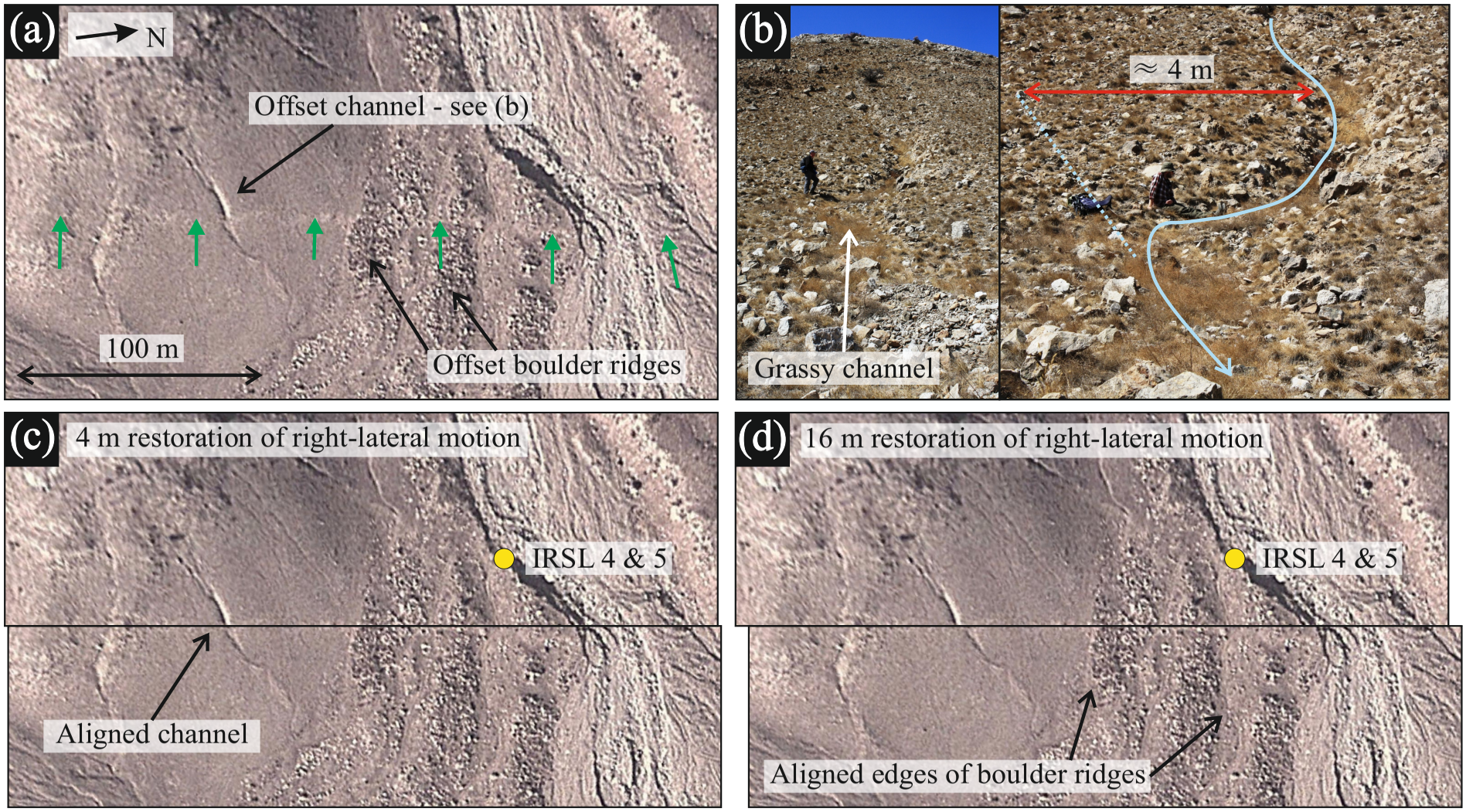


Figure 4.6: (a) Google Earth imagery from November 2011 (source: http://earth.google.com) of the northern end of the East Helanshan Fault, 10 km west of Huinong city. Fault scarp marked by green arrows and small offset visible in edges of boulder ridges. (b) Field photographs (taken at 39.235 °N, 106.658 °E, at the location marked in (a)). People for scale. The grassy channel records a right-lateral offset of approximately 4 m. (c) Same as (a) with a 4 m restoration of the right-lateral motion, which aligns the small channel shown in (b). Yellow circle indicates the location of IRSL samples 4 and 5. (d) Same as (a) with a 16 m restoration of the right-lateral motion, which aligns the edges of the boulder ridges as shown. Yellow circle indicates the location of IRSL samples 4 and 5.

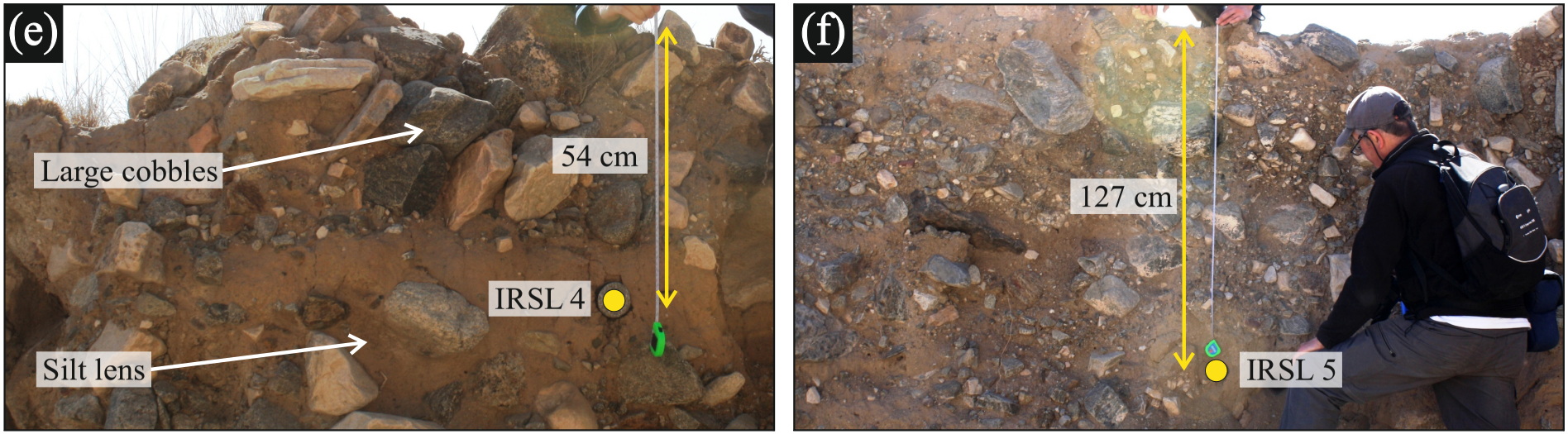


Figure 4.6: (continued) (e) Field photograph (taken at 39.236 °N, 106.658 °E) showing the sedimentary context of IRSL sample 4. (f) Field photograph (from the same location) showing the sedimentary context of IRSL sample 5.

The 1.27 ka age implies a horizontal slip rate of 12.6±4.2 mm/a, which appears unrealistically large; whilst the 3.21 ka age implies a horizontal slip rate of 5.0±1.6 mm/a (see Table 4.3). However, we note that both samples are taken from the fill of a channel that lies between two of the boulder ridges. It is possible that this fill might post-date the deposition of the boulder ridges and hence that both IRSL ages underestimate the time at which the boulder ridges were displaced. If this is the case, then our rate of 5.0±1.6 mm/a provides a maximum possible slip rate estimate.

4.5 Discussion

4.5.1 Rates of faulting along the western Ordos Plateau

On the East Helanshan Fault our major result is that the overall throw rate, and hence the extension rate, is comparatively small (i.e. $\leq$ 1 mm/a). Since the Suyukou scarps run parallel to the Helanshan range front, we add our throw rate estimate from Suyukou (of 0.40±0.06 mm/a) to our maximum throw rate estimate from the range front (of 0.43±0.07 mm/a) to obtain a likely maximum Late Quaternary throw rate for the fault as a whole of 0.8±0.1 mm/a (see Table 4.3). This is consistent with the Quaternary average of 0.5 to 0.8 mm/a from *Zhang et al.* (1990). Using the fault dip found in the literature of 39° (*Fang et al.*, 2009), we find an extension rate across the East Helanshan Fault of 0.9±0.1 mm/a (see Table 4.3). If we also include the throw rates and fault dips of the other faults within the graben (Yellow River Fault: 0.25 mm/a and 72° (*Liao et al.*, 2000; *Fang et al.*, 2009); Yinchuan-Pingluo Fault: 0.14 mm/a and 71° (*Lei et al.*, 2008, 2015); Luhuatai Fault: 0.18 mm/a and 60° (*Fang et al.*, 2009; *Lei et al.*, 2011)) we obtain a likely maximum extension rate across the whole graben of 1.3±0.1 mm/a. Additionally, our suggested increase in throw rate on the Suyukou scarps (see Section 4.4.2) could indicate that motion is being transferred from the range-front fault to the Suyukou scarps in the alluvial fans—possibly in order to cut off a corner in the range front and straighten the fault.

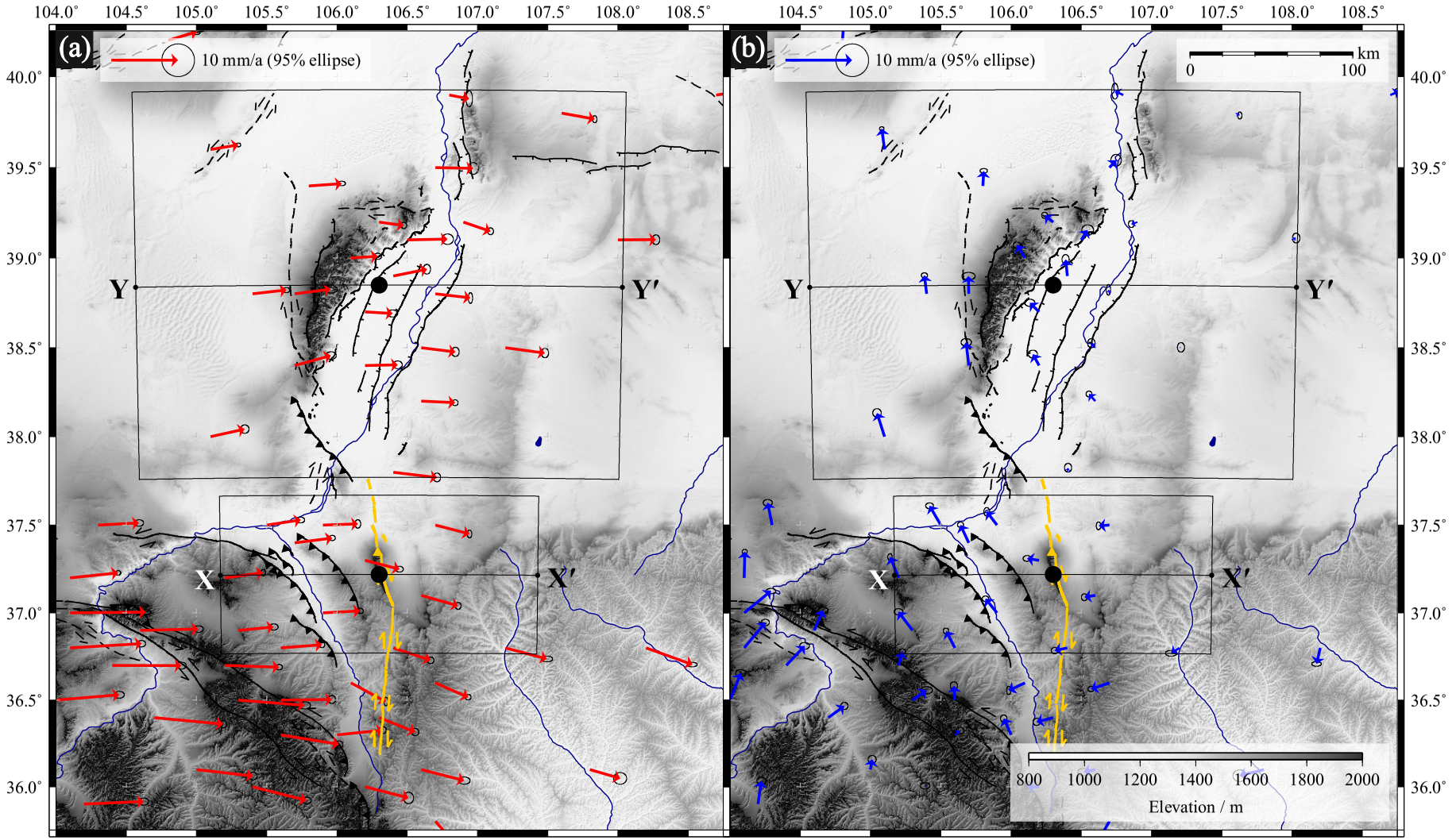


Figure 4.7: (a) SRTM topography (30 m resolution) of the western Ordos region, Ningxia Province, northern China (*Farr et al.*, 2007). The Luoshan Fault and Yunwushan Fault are marked in orange. Red vectors show campaign GPS measurements relative to stable Eurasia made over a period of 4 years (occupations in 2009, 2011 and 2013) (*Zhao et al.*, 2015). (b) Same as (a) but blue vectors show GPS measurements (*Zhao et al.*, 2015) with a best fitting rigid body rotation (about an Euler pole at 46 °N, 72 °W, estimated from the vectors within the region shown) subtracted from all of the vectors.

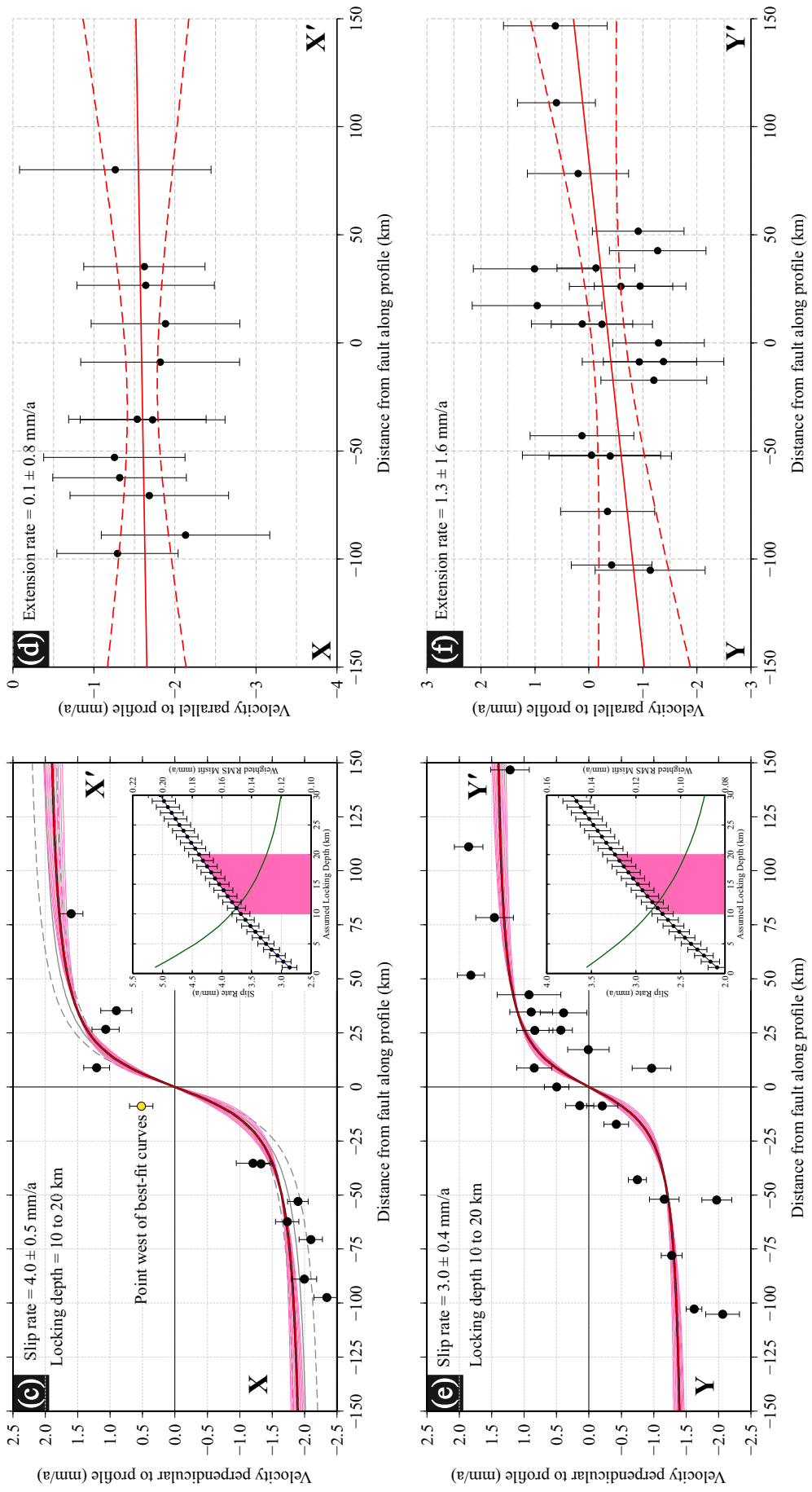


Figure 4.7: (continued) (c) Swath profile X-X′ through the GPS data in (b) showing the component of velocity perpendicular to the profile azimuth of 90°. The red line shows the best fitting arctangent function ($u = tan^{-1}\left(\frac{x}{d}\right)$, where u is the velocity, x is the distance from the fault and d is the locking depth). The dashed grey lines indicate the geologically determined slip rate on the Luoshan Fault of 4.3±0.4 mm/a, assuming a locking depth of 15 km. The pink lines represent the range of best fitting solutions for assumed locking depths of between 10 and 20 km. The inset figure shows the trade-off between slip rate and locking depth. For this range of locking depths, we estimate a right-lateral slip rate of 4.0±0.5 mm/a. (d) Swath profile X-X′ showing the component of velocity parallel to the profile. The red lines show the best fit least squares regression to the data and the 95% confidence envelopes on this best fit line. No shortening or extension is resolvable within error along this profile. (e) Swath profile Y-Y′ through the GPS data in the Yinchuan Graben showing the component of velocity perpendicular to the profile. Annotations as in (c). We estimate a right-lateral slip rate of 3.0±0.4 mm/a. (f) Swath profile Y-Y′ showing the component of velocity parallel to the profile. Annotations as in (d). We estimate an average extension rate across the whole profile of 1.3±1.6 mm/a.

Meanwhile, in Chapter 3 we found that the mean right-lateral Holocene slip rate on the Luoshan Fault is 4.3±0.4 mm/a—notably larger than the extension rate across the Yinchuan Graben. Campaign GPS measurements (*Zhao et al.*, 2015) also indicate that right-lateral shearing is the major motion occurring in the western Ordos region (see Figure 4.7). Figure 4.7 (b) shows the data from *Zhao et al.* (2015) with a best fitting rigid body rotation (about an Euler pole at 46 °N, 72 °W, estimated from the vectors within the region shown) subtracted from all of the vectors. This ensures that rotations associated with this rigid-body-like motion do not distort our slip rate estimates. We model the fault-parallel interseismic motion across the Luoshan Fault as a buried screw dislocation in an elastic half-space using the formulation from *Savage and Burford* (1973), where the velocity u at a perpendicular distance x from the fault is given by $u = \frac{s}{\pi} tan^{-1}\left(\frac{x}{d}\right)$, where s is the slip rate and d is the locking depth. The density of data is not sufficient to provide an independent constraint on the locking depth, so we assume locking depths in the range of 10 to 20 km (*Wright et al.*, 2013) in order to calculate the distribution of possible slip rate estimates. In Figure 4.7 (c), the range of possible arctangent functions fitted to the data indicates a right-lateral slip rate on the Luoshan and northern Yunwushan Faults of 4.0±0.5 mm/a. Our geological slip rate of 4.3±0.4 mm/a agrees well with this geodetic rate (see Chapter 3). We also note that one GPS point lies noticeably to the west of our best fitting curves (see yellow dot in Figure 4.7 (c)). This may indicate that the centre of the shear zone at depth is displaced to the west of the surface trace of the Luoshan Fault, but there is not enough data to test this. Figure 4.7 (d) shows that, although the errors on the data are large, there is no resolvable fault-perpendicular motion along profile X-X′; significant crustal shortening only occurs further to the south of our profile. The data in Figure 4.7 (e), for profile Y-Y′ across the Yinchuan Graben, are more scattered than in Figure 4.7 (c). If we assume that all of the right-lateral motion is localised onto a single structure, we obtain a right-lateral slip rate of 3.0±0.4 mm/a (allowing for the same 10 to 20 km range of locking depths). However, the scatter in the data suggests that it is more likely that right-lateral motion is distributed across a number of the buried faults within the Yinchuan Graben. In Figure 4.7 (f), the scatter in the data is again very large—and extension is barely resolvable—but we obtain a best fitting extension rate of

1.3±1.6 mm/a across the Yinchuan Graben. This is consistent with our Late Quaternary extension rate of < 1.3±0.1 mm/a and also supports our suggestion that right-lateral motion is dominant over the extension in the Yinchuan Graben.

4.5.2 A geometric model for the western Ordos Plateau

Based on our results from Chapters 3 and 4, we propose a geometric model in which the faults of the western Ordos Plateau accommodate principally north-south right-lateral shearing. This occurs on the Luoshan Fault in the south and is split between the Alxa Desert and East Helanshan Faults in the north (see Figure 4.8). Satellite imagery shows evidence of right-lateral displacements on the Alxa Desert Fault, but its slip rate is unknown (see Figure 4.8 (c)). Meanwhile, our observations of offset boulder ridges at the northern end of the East Helanshan Fault (see Section 4.4.4) provide evidence for the continuation of right-lateral motion up the western side of the Ordos Plateau north of the Yinchuan Graben. Some right lateral motion is also taken up on the intervening Niushoushan Fault (*Lei et al.*, 2016). A Kostrov summation for the two largest earthquakes in northern Ningxia in the last 700 years also indicates that north-south right-lateral motion is one of the most significant strains (*Wesnousky et al.*, 1984). Furthermore, one of the few focal mechanisms from the instrumental record (for a M 5.2 event in 1988—see Figure 3.2) is also consistent with north-south right-lateral motion.

If this model is correct, then the (oblique reverse) Niushoushan Fault accommodates transpression as the strike-slip faulting steps to the left and that the normal faulting in the Yinchuan Graben accommodates transtension as the strike-slip faulting steps to the right. The estimated slip vector for the most recent earthquake on the East Helanshan Fault appears to show pure normal motion (see Chapter 2). We therefore speculate that the transtension in the Yinchuan Graben is partitioned between normal motion on the East Helanshan Fault and right-lateral strike-slip motion on one or more of the buried faults within the graben (i.e. the Luhuatai, Yinchuan-Pingluo or Yellow River Fault).

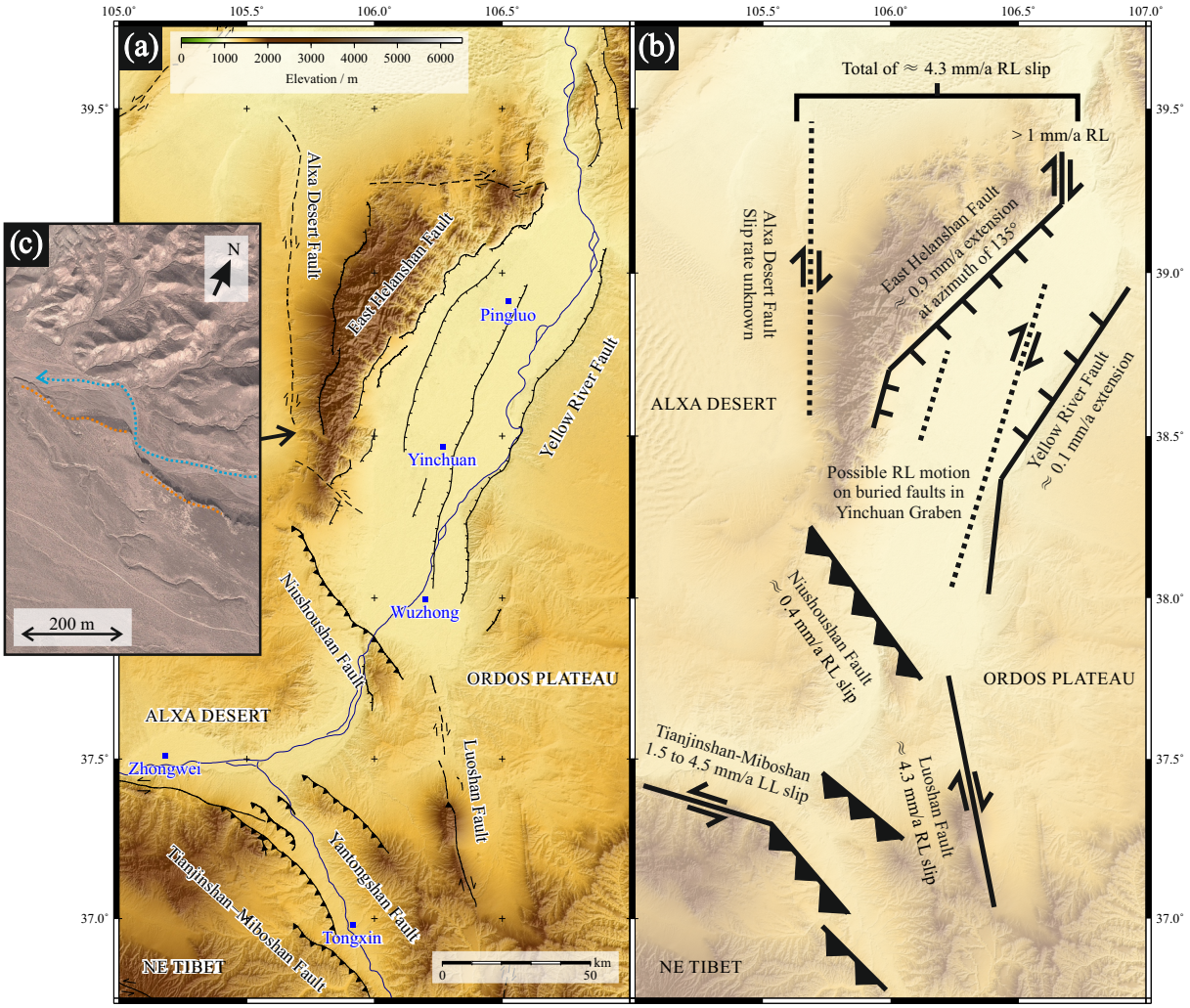


Figure 4.8: (a) SRTM topography (30 m resolution) of the western Ordos region in northern China (*Farr et al.*, 2007). Cities are marked by blue squares and faults, marked as thin black lines, have been mapped from satellite imagery (source: http://earth.google.com) based upon earlier fault maps from *Tapponnier and Molnar* (1977), *Deng et al.* (1984a), *Zhang et al.* (1990), *Darby and Ritts* (2002) and *Darby et al.* (2005). (b) Geometric model for the tectonics of the western Ordos region showing the principal faults and their slip rates, from *Zhang et al.* (1990), *Min et al.* (2003), *Deng et al.* (2007), *Lei et al.* (2016) and this study. (c) Google Earth imagery from March 2011 (source: http://earth.google.com) showing right-lateral displacement of a channel (blue) and channel riser (orange) on the Alxa Desert Fault at 38.478 °N, 105.721 °E.

4.6 Conclusions

Our key result from Chapters 3 and 4 is that the rate of right-lateral strike-slip motion on the Luoshan Fault (4.3±0.4 mm/a) is substantially larger than the throw rate on the normal East Helanshan Fault (< 0.8±0.1 mm/a). This implies that, despite the topographic prominence of the Helanshan, the thick sediments in the Yinchuan Graben and the fresh tectonic geomorphology on the East Helanshan Fault, north-south right-

lateral shearing is the principal tectonic motion in the western Ordos region. Indeed, pull-apart basins on strike-slip faults often contain large accumulations of sediment (e.g. *Rodgers*, 1980), which could explain the 6-7 km of deposits in the Yinchuan Graben; and normal faulting is less important than it first seems for the tectonics of the western Ordos. Furthermore, the existence of predominantly right-lateral motion in the western Ordos complements the right-lateral shearing in the Shanxi Grabens on the eastern side of the Ordos and provides evidence in support of anticlockwise rotation models for the kinematics of the whole Ordos block (see Sections 3.1 and 6.6.2).

Chapter 5

Extension in the northern Shanxi Grabens

5.1 Introduction

Discrepancies between geological, seismic and geodetic rates of deformation are a cause of controversy in many regions of active faulting (*Thatcher*, 2009). Yet these discrepancies are important for our understanding of how both crustal deformation and seismic hazard may vary through time. In California and western New Guinea, for example, seismic strain rates appear to match relative plate velocities, whilst in the Aegean, Iran and parts of Asia the rates of seismic deformation are substantially lower than those predicted from plate velocities (*Jackson and McKenzie*, 1988; *Ekström and England*, 1989). In the New Madrid seismic zone, present-day geodetic observations are not able to detect any significant strain, and yet major earthquakes took place in 1811 and 1812 and the palaeoseismic record indicates that large earthquakes have occurred every 500 years (*Stein et al.*, 2009; *Craig and Calais*, 2014). On the scale of individual faults, there is significant disagreement between geological and geodetic slip rate estimates on faults such as the San Andreas, Altyn Tagh, Kunlun and Haiyuan (*Searle et al.*, 2011; *Wang et al.*, 2011; *He et al.*, 2013b; *Tong et al.*, 2014). Are these differences because fault slip rates vary substantially through time? Can off-fault deformation explain the discrepancies (e.g. *Milliner et al.*, 2015)? Could large fractions of strain build-up be accommodated by

aseismic creep on major faults (e.g. *Jolivet et al.*, 2012)? Or is tectonic loading on the continents distributed across complex systems of interacting faults (e.g. *Stein et al.*, 2009; *Liu et al.*, 2011)?

The northern Shanxi Grabens lie at the northeastern corner of the Ordos Plateau. Extension in the northern Shanxi Grabens and the associated seismicity is of significant concern because the adjacent North China Plain is one of the most densely populated regions on Earth. The cities of Beijing, Datong, Shijiazhuang and Taiyuan, with a total population in excess of 35 million people, all lie in or next to the northern Shanxi Grabens. Yet previous studies have disagreed significantly about the magnitude and pattern of strain release in this region (see Section 5.2 for details).

5.2 Previous work in the northern Shanxi Grabens

Estimates of Quaternary slip rates exist for many of the major faults in the northern Shanxi Grabens (*Cheng et al.*, 1995; *Xu and Deng*, 1996; *Xu et al.*, 1997; *Cheng and Yang*, 1998; *Pavlides et al.*, 1999; *Xu et al.*, 2002; *Jiang et al.*, 2003; *Yu*, 2004; *Deng et al.*, 2007; *Ding et al.*, 2009; *Wang*, 2012). In general, the slip rates are small and the calculated rates of extension rarely exceed 0.5 mm/a for any of the faults in the region. *Zhang et al.* (1998) suggested a total Pliocene-Quaternary extension rate across the whole northern Shanxi region of between 0.2 and 0.5 mm/a based on a cross-sectional area balance. *Zhang et al.* (1998) also estimated a principal extension direction of 165±15 ° from the maximum height of triangular facets, whilst *Zhang et al.* (2003b) estimated an extension direction of 120 to 150 ° from fault striation measurements.

Earthquake records indicate that the faults in the northern Shanxi Grabens have been seismically active over the last few thousand years, although there are relatively few recorded events in the last ≈ 250 years (*Lee et al.*, 1976, 1978; *Liu et al.*, 2011). A Kostrov summation of seismic moment tensors for the four largest historical earthquakes in the Shanxi Grabens gave a north-south extension rate of 0.4 mm/a (although this is not necessarily along the direction of the maximum extension) (*Wesnousky et al.*, 1984). *Xue and Yan* (1984) inferred a mean extension direction of 153 ° from T axes of focal mech-

anisms, whilst *Li et al.* (2015a) concluded from another catalogue of focal mechanisms that the minimum compressive stress (σ_3) is at an azimuth of 139 ° (although orientations of principal stress need not coincide with orientations of principal strain). *Wang et al.* (2012a) even claimed, from their analysis of P axes of focal mechanisms, that prior to 2001 the maximum compressive stress (σ_1) was oriented northwest-southeast.

Geodetic constraints on current crustal surface motion in northeast China are provided by numerous GPS studies (*Shen et al.*, 2000; *Wang et al.*, 2001; *He et al.*, 2003, 2004; *Gan et al.*, 2007; *Wang*, 2009; *Zhang and Gan*, 2008; *Li et al.*, 2012; *Zhao et al.*, 2015). *Shen et al.* (2000) concluded that 4±2 mm/a of extension occurs across the northern Shanxi Grabens at an azimuth of 105 °. They also noted that their extension direction is ≈ 45 ° anticlockwise from geological estimates, and postulated that this is because the geological estimates did not take account of hidden faulting occurring within the grabens at a different azimuth. Meanwhile, *He et al.* (2003) and *He et al.* (2004) found no evidence of any extension across the northern Shanxi Grabens at all, which they attributed to time-dependent fault behaviour. *Wang et al.* (2011) fitted a block model to the GPS data of *Zhang and Gan* (2008) and obtained an extension rate in the Shanxi Grabens of 0.8±0.3 mm/a. Similarly, *Qu et al.* (2014) fitted a block model to the GPS data of *Wang* (2009) and obtained a strain rate of 28 nanostrain/a (roughly equivalent to an extension rate of 2.8 mm/a) at an azimuth of 95 °.

According to these studies, therefore, extension occurs in the northern Shanxi Grabens at anywhere between 0 and 6 mm/a at an azimuth of between 95 and 180 °. In this study we compile fault extension rates from ages of offset geomorphological features and estimates of fault dip; we construct a catalogue of historical earthquakes with $M_s > 5$ for the period 1315 to 2015 and apply Kostrov's relation to this dataset; and we analyse the latest campaign GPS data from *Zhao et al.* (2015). We then compare these geological, seismic and geodetic observations and seek to ascertain whether or not there are any real discrepancies between these different estimates of the magnitude and pattern of strain release in the northern Shanxi Grabens.

5.3 Tectonic setting

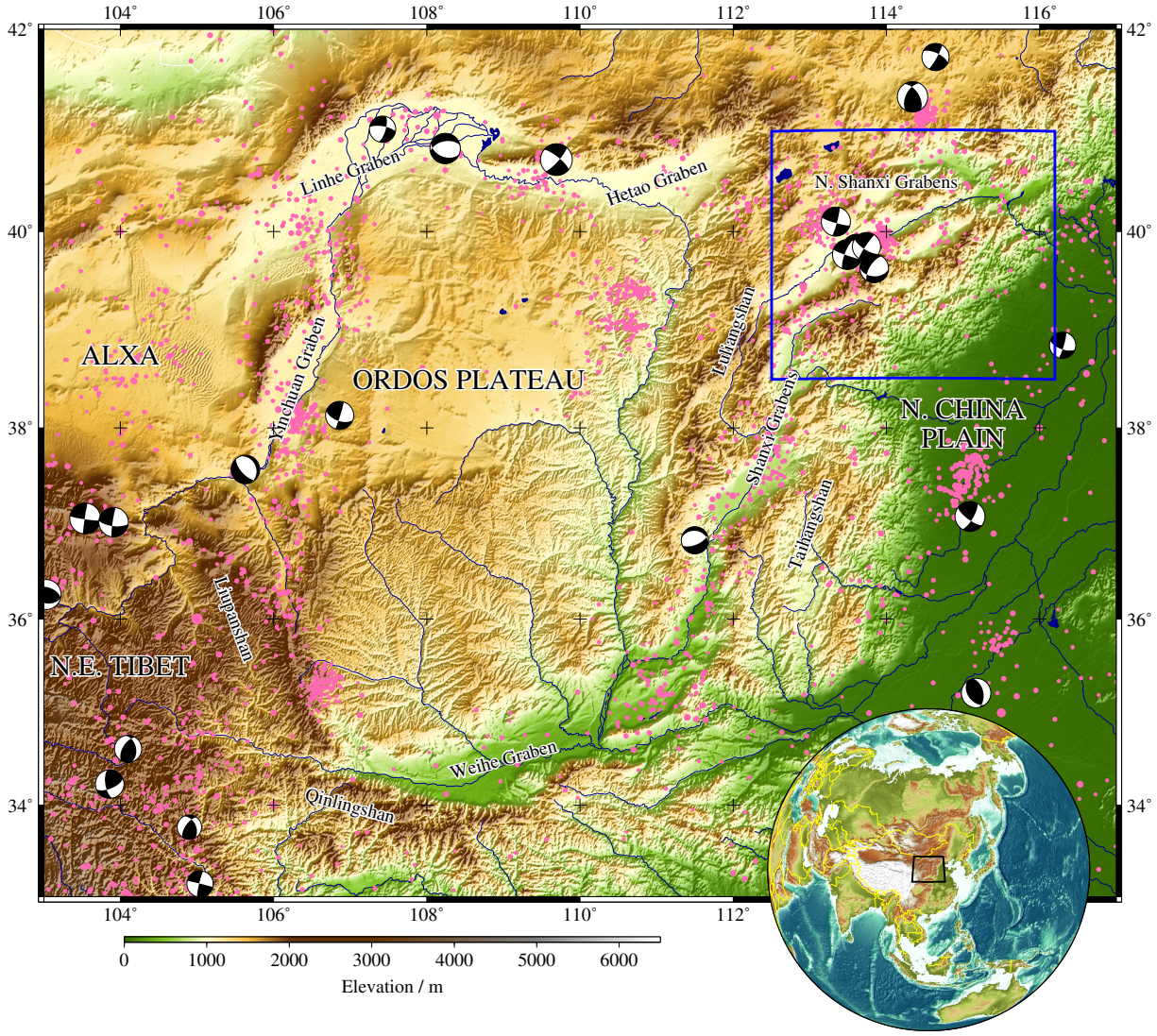


Figure 5.1: SRTM topography (*Farr et al.*, 2007) of the Ordos Plateau in northeastern China. Focal mechanisms from the Global CMT catalogue (*Ekström et al.*, 2012) are shown for earthquakes since 1976 with magnitudes greater than M_w 5.0. Pink dots indicate earthquakes of M_w 2.0-5.0 between 1920 and 2011 from the ISC catalogue (*International Seismological Centre*, 2013). Rivers are indicated in dark blue and inset globe shows the location of Figure 5.1 within Asia. The blue polygon indicates the region shown in Figure 5.2.

The Shanxi Grabens lie to the east of the Ordos Plateau in northern China, where they form an S-shaped series of en echelon basins some 1200 km long (see Figure 5.1). The grabens can be divided into three broad zones, two of which are wide, ENE trending, extensional zones (in the north and the south), separated by a third, narrow, NNE trending, right-lateral transtensional zone in the centre (*Xu and Ma*, 1992; *Xu et al.*, 1993). Although extension in the Shanxi Grabens only started in the Pliocene or the very end of

the Miocene (*Ye et al.*, 1987; *Zhang et al.*, 1998, 2003b), it is likely that the location and geometry of the grabens are in part determined by the pre-existing, northeast striking, fold-and-thrust belt structures of the Late Triassic (235 to 200 Ma old) Indosinian orogeny and the Middle Jurassic-Cretaceous (150 to 65 Ma old) Yanshanian orogeny (*Xu and Ma*, 1992; *Xu et al.*, 1993; *Zhang et al.*, 1998). Manifestations of these older orogenies are still evident today as thickened crust (40-44 km) and a corresponding gravity anomaly over the region (*Xu and Ma*, 1992). *Tapponnier and Molnar* (1977) noted that the width and length of individual grabens decrease from south to north, whilst the mean elevation of the graben floors increases (from 380 m in the south to 1010 m in the north (*Li et al.*, 2015a)), suggesting a northward propagation of the onset of rifting through time.

The northern Shanxi Grabens form a zone around 390 km long and 160 km wide (see Figure 5.2), and are characterised by ENE striking normal faults and asymmetric half-grabens with footwall blocks tilted to the SSE, creating typical basin-and-range topography. *Xu and Ma* (1992) estimated a total of 8 km of crustal extension in the southwest of the zone and 1.5 km of crustal extension in the northeast of the zone, based upon the tilting of Pliocene-Quaternary sediments within the grabens. Initial sedimentation in the northern Shanxi Grabens commenced in the Miocene, but this earliest period of extension was confined to the Huaizhuo and Yanfan Grabens in the far northeast (see Figure 5.2)—an exception to the general northward propagation of rifting. The main phase of rifting in the northern Shanxi Grabens occurred during the Pliocene and Quaternary (*Xu and Ma*, 1992). Most of the grabens are also blanketed by a thick cover of yellow, Upper Pleistocene loess (*Li et al.*, 1998; *Zhang et al.*, 2003b).

This chapter is primarily concerned with the major normal faults in the northern Shanxi Grabens that accommodate the approximately northwest-southeast extension (see Figure 5.2). The Wutaishan and Hengshan Faults dip to the northwest and border the northern sides of the Wutaishan (Wutai mountains) and Hengshan (Heng mountains) respectively. The Hengshan Fault also forms part of the southern boundary of the Datong Graben. The Kouquan-Emokou Fault dips southeast and runs along the northwestern side of the Datong Graben, near the city of Datong. Further east, the Yuguang Graben Fault runs along the southeastern side of the Yuguang Graben and dips to the northwest. The

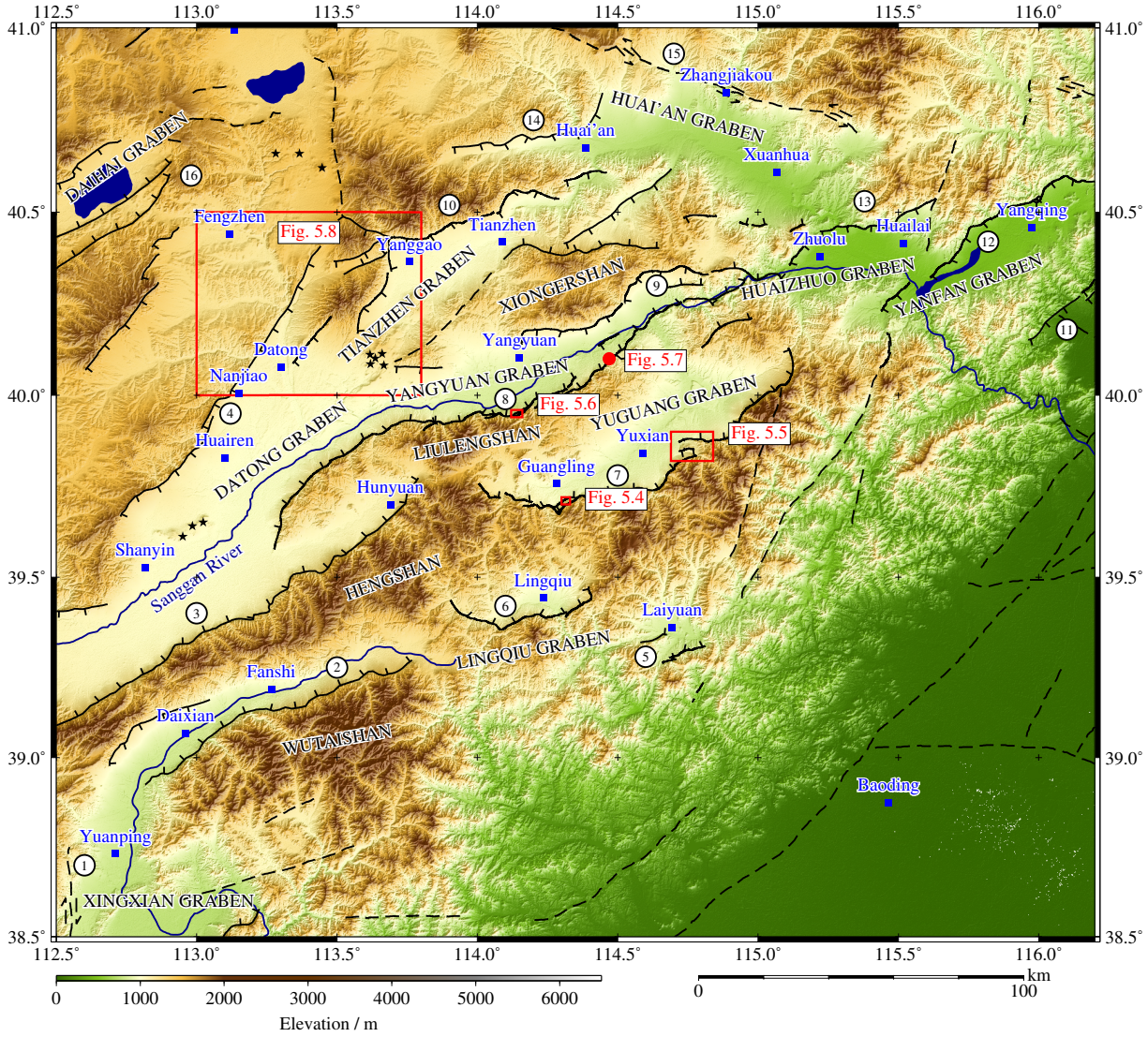


Figure 5.2: SRTM topography (30 m resolution) of the northern Shanxi Grabens (*Farr et al.*, 2007). Faults, marked as thin black lines, have been mapped from satellite imagery (source: http://earth.google.com) based upon earlier fault maps from *Tapponnier and Molnar* (1977), *Xu and Ma* (1992), *Yu* (2004) and *Deng et al.* (2007). Cities are marked by blue squares and black stars show the positions of Quaternary volcanic cones. Red outlines and circles indicate the locations of later figures. Faults are numbered as follows: 1 Yunzhongshan Fault, 2 Wutaishan Fault, 3 Hengshan Fault, 4 Kouquan-Emokou Fault, 5 Laiyuan Graben Fault, 6 Lingqiu Graben Fault, 7 Yuguang Graben Fault, 8 Liulengshan Fault, 9 Yangyuan Graben Fault, 10 Yanggao-Tianzhen Graben Fault, 11 Nankou Fault, 12 Yanqing Fault, 13 Huailai Fault, 14 Huai'an Graben Fault, 15 Zhangjiakou-Bohai-Penglai Fault, 16 Daihai Graben Faults (see also Table 5.3).

Liulengshan Fault borders the northern and western sides of the Liulengshan (Liuleng mountains), running along the eastern side of the Datong Graben and the southern side of the subsidiary Yangyuan Graben, also dipping to the northwest. In the northeast of the northern Shanxi Grabens, the Yanqing and Huailai Faults dip southeast on the

northwestern sides of the Huaizhuo and Yanfan Grabens. The northern boundary of the whole zone is the WNW striking, left-lateral Zhangjiakou-Bohai-Penglai Fault.

The Yuguang Graben has a maximum sediment thickness of 600 m on its southeastern side, adjacent to the Yuguang Graben Fault; in the Yangyuan Graben the maximum sediment thickness is less than 500 m; and in the Datong Graben sediment thicknesses reach 1500 m adjacent to the Kouquan-Emokou Fault (*Xu and Ma*, 1992; *Li et al.*, 1998). The Datong Graben also hosts tholeiitic and alkaline flood basalts and volcanic cinder cones (see Figure 5.2). These rocks are largely Early Pleistocene in age and are thought to result from local mantle decompression during the ongoing crustal extension (*Xu and Ma*, 1992; *Xu et al.*, 1993).

5.4 Methods

5.4.1 DEMs and offset measurements

We constructed a high-resolution digital elevation model (DEM) of the Guangling section of the Yuguang Graben Fault (see Section 5.5.1) using a stereo pair of 0.5 m Worldview-1 images, acquired on 25th July 2008 and 21st September 2011. The images were processed using the ENVI DEM Extraction Module. Seventeen ground control points (GCPs) were identified on Google Earth (source: http://earth.google.com) and used to refine the sensor model. An additional 91 tie points were identified in ENVI and added as constraints in the refinement. Key points (points with pre-defined features in ENVI) were identified in one image and then matched in the other image, based on a window size of 5×5 pixels and a minimum correlation coefficient of 0.7. The apparent offset of a given key point on the ground between the two images was then triangulated in order to determine the three-dimensional position of that key point. The resulting point cloud was gridded with a pixel spacing of 1 m using continuous curvature splines in tension and a tension factor of 0.75 (*Smith and Wessel*, 1990). Approximately 60% of 1 m by 1 m grid cells contain at least one point, giving an $\approx$ 1 m resolution DEM.

We measured vertical offsets across fault traces by drawing swath profiles through DEMs at the relevant sites. At Guangling we used the Worldview DEM, and elsewhere we used 30 m horizontal resolution data from either the Panchromatic Remote-sensing Instrument for Stereo Mapping (PRISM) of the Japan Aerospace Exploration Agency (JAXA) Advanced Land Observing Satellite (ALOS) (*Takaku et al.*, 2014; *Tadono et al.*, 2014) or the Shuttle Radar Topography Mission (SRTM) (*Farr et al.*, 2007). At each site, all DEM points within a 100 to 300 m wide swath were projected onto the profile, and straight lines were fitted to the data above and below the scarp. If the pre-existing topography prior to faulting has a constant gradient, it is possible to fit two straight line segments with the same gradient to the elevation data above and below the scarp. In this instance the vertical offset is constant, regardless of where on the profile it is measured. However, if the pre-existing topography does not have a constant gradient, then separate line segments have to be fitted to the data above and below the scarp and the vertical offset then depends on where along the profile it is measured. We tried to fit parallel lines to the data above and below the scarp, but this was not always possible. In the case of non-parallel lines, the vertical offset was measured halfway up the fault scarp, where the fault plane was inferred to intersect the land surface. The quoted errors on our vertical offset measurements refer to the root mean square (RMS) residuals from this line fitting process. Further details of the methodology are given in Section 2.4.3.

5.4.2 Quaternary dating of offset features

In addition to the existing radiocarbon (^{14}C), thermoluminescence (TL), optically stimulated luminescence (OSL) and K-Ar dates, we used infrared stimulated luminescence (IRSL) dating of sedimentary feldspar grains and Ar-Ar dating of basaltic feldspars to determine the ages of offset features. At each of our sites we sampled whatever material was available; unfortunately, we were unable to find further samples for ^{14}C dating during our field visit. Full details of the IRSL dating methodology are given in Section 3.3.3 and the procedure for Ar-Ar dating is described below in Section 5.4.3. The age data collected in this study are summarised in Table 5.1.

Table 5.1: IRSL and Ar-Ar dating results from the northern Shanxi Grabens

Sample	Location	Lat / °	Long / °	Elevation / m	Depth / m	Equivalent Dose / Gy	Dose Rate / mGy a^{-1}	Age / ka
IRSL 15	Qifengpocun	39.948	114.138	1080	1.85	55.1±5.8	3.38±0.15	16.3±1.9
IRSL 16	Qifengpocun	39.950	114.138	1045	2.13	54.5±2.2	3.43±0.15	15.9±1.0
Ar-Ar	Datong	40.781	113.125	1375	N/A	N/A	N/A	8290±270

5.4.3 Ar-Ar dating

Background to Ar-Ar dating

^{40}K decays with an overall half life of 1.25×10^{9} years; 11% decays to ^{40}Ar and 89% decays to ^{40}Ca. An igneous rock typically contains no initial ^{40}Ar. When the rock cools below around 350 °C (the blocking temperature), diffusion of Ar becomes negligible and ^{40}Ar, produced from the decay of ^{40}K, becomes trapped in the rock. Assuming that no radiogenic Ar escapes and that no Ar from external sources is absorbed, the amount of ^{40}Ar, measured on a mass spectrometer, can then be used to determine a crystallisation time for the igneous rock. In K-Ar dating the age of a sample is given by (*Philpotts and Ague*, 2009):

$$t = \frac{1}{\lambda_K} ln \left(\frac{\lambda_K \, {}^{40}Ar^*}{\lambda_{Ar} \, {}^{40}K} + 1 \right) \tag{5.1}$$

where λ_K is the overall decay constant for ^{40}K (combining the Ar and Ca decay constants), λ_{Ar} is the decay constant for decay to ^{40}Ar and $^{40}Ar^*$ is the radiogenic ^{40}Ar. However, with standard K-Ar dating, some ^{40}Ar may escape or be absorbed along grain boundaries and mineral cleavages and there is no way of knowing where in a given mineral grain the K and Ar are from. ^{40}Ar-^{39}Ar dating, on the other hand, allows distinction between loosely bound Ar at grain boundaries and Ar in the cores of grains (*Philpotts and Ague*, 2009).

In ^{40}Ar-^{39}Ar dating, K is converted to ^{39}Ar by placing the sample in a flux of high energy neutrons, typically in a nuclear reactor. The sample is then heated in a stepwise manner and the ^{40}Ar-^{39}Ar ratio is determined at each step (*Merrihue and Turner*, 1966). Ar from grain boundaries is released first, and Ar from the cores of mineral grains is released towards the end. If the ^{40}Ar-^{39}Ar ratio stabilises to produce a plateau, a reliable

age can be determined (*McDougall and Harrison*, 1999; *Philpotts and Ague*, 2009). The age equation for ^{40}Ar-^{39}Ar dating is given by (*McDougall and Harrison*, 1999):

$$t = \frac{1}{\lambda_K} ln \left(\frac{^{40}Ar^*}{^{39}Ar} J + 1 \right) \tag{5.2}$$

where λ_K is the overall decay constant for ^{40}K, $^{40}Ar^*$ is the radiogenic ^{40}Ar, ^{39}Ar is produced by neutron activation of K, and J is the irradiation flux parameter. J will depend on the time period of irradiation, the neutron flux density and the neutron capture cross-section (*McDougall and Harrison*, 1999). J is typically estimated from a mineral standard of known age that is irradiated with the samples:

$$J = \frac{e^{\lambda t_{std}} - 1}{^{40}Ar^*_{std}/^{39}Ar_{std}} \tag{5.3}$$

where t_{std} is the age of the standard and $^{40}Ar^*_{std}$ and $^{39}Ar_{std}$ also refer to the known standard. During irradiation other isotopes of Ar can be produced from K, Ca, Ar and Cl. These additional interference reactions also have to be corrected for. Plateau ages are then assessed by calculating the mean square weighted deviation (MSWD) to assess the scatter in the step ages.

Methodology for Ar-Ar dating

Our samples for Ar-Ar dating was prepared in the Department of Environment, Earth and Ecosystems at the Open University in Milton Keynes. The sample was crushed and dry-sieved. Plagioclase-rich bulk rock grains were then picked by hand under a binocular microscope and cleaned ultrasonically in acetone and de-ionised water. They were then irradiated at the McMaster Nuclear Reactor at McMaster University in Canada for 4 hours with cadmium shielding in position 8D. The neutron flux was monitored using a biotite mineral standard (GA1550), which has an age of 98.8±0.5 Ma (*Renne et al.*, 1998). Standards were packed for irradiation either side of the unknown sample. The calculated J value for our sample was 2.88432×10^{-4} with a typical error of 1%. The results were

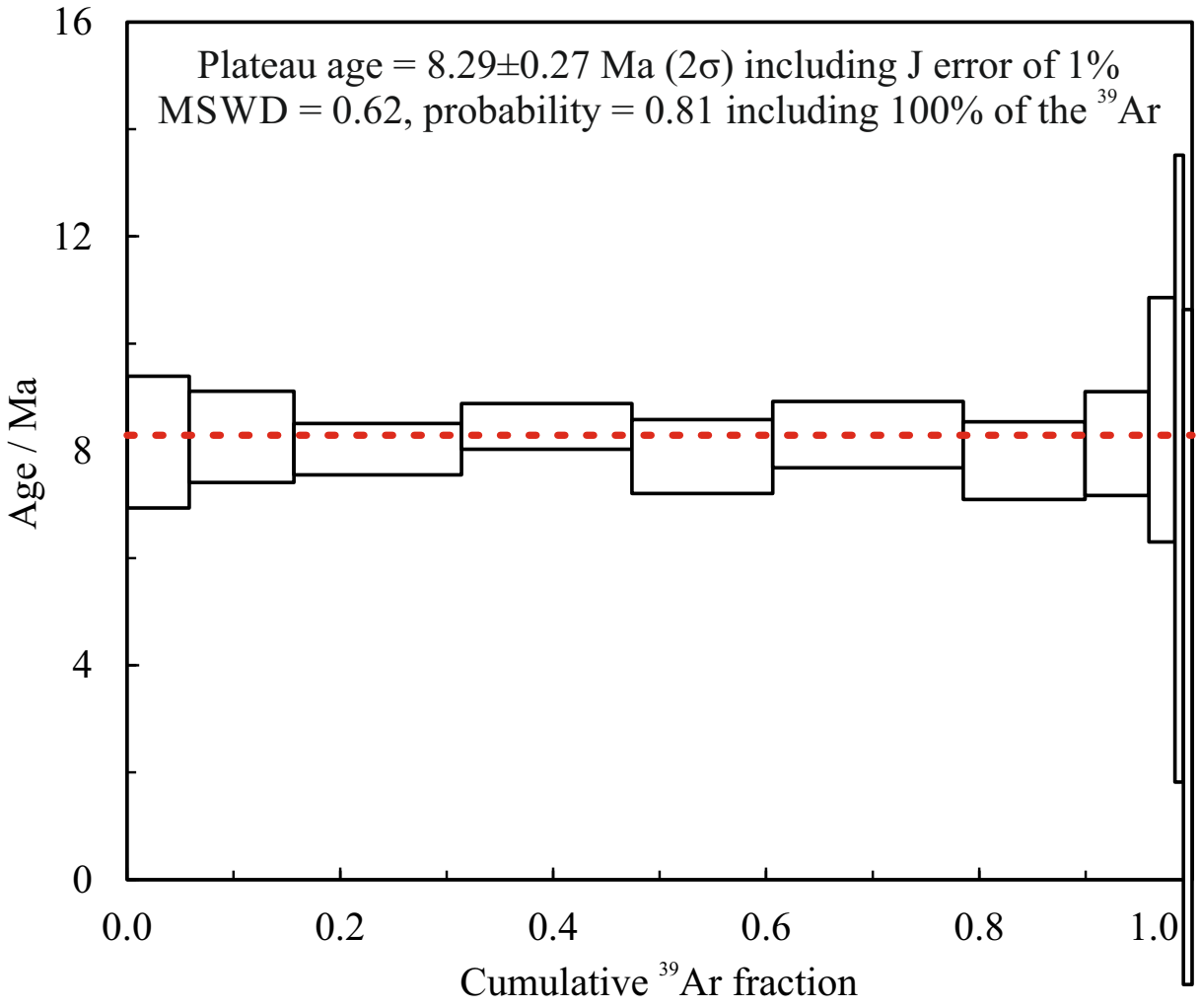


Figure 5.3: Plot of sample age against cumulative ^{39}Ar fraction for 11 incremental heating steps on the basalt sample. Box heights indicate 2σ error on each age estimate. We obtain a plateau age of 8.29±0.27 Ma (2σ).

also corrected for ^{37}Ar decay, and neutron-induced interference reactions. The following correction factors were used based on analyses of Ca and K salts:

$$\left(\frac{^{39}Ar}{^{37}Ar}\right)_{Ca} = 6.5 \pm 0.0325 \times 10^{-4} \tag{5.4}$$

$$\left(\frac{^{36}Ar}{^{37}Ar}\right)_{Ca} = 2.65 \pm 0.01325 \times 10^{-4} \tag{5.5}$$

$$\left(\frac{^{40}Ar}{^{37}Ar}\right)_{Ca} = 85 \pm 0.425 \times 10^{-4} \tag{5.6}$$

The irradiated sample was then loaded into an ultra-high vacuum system and mounted on a New Wave Research UP-213 stage. A 1059 nm CSI fibre laser was focussed onto the sample and used to step heat the sample. Extracted gases were passed through a liquid nitrogen trap and cleaned for 5 minutes using two SAES AP-10 gas purifiers running at 450 °C and room temperature. The cleaned gases were then measured on a MAP 215-50 mass spectrometer. System blanks were measured before and after every two sample analyses. The mass discrimination value for atmospheric $^{40}Ar/^{36}Ar$, which corrects for any bias in the mass spectrometer, was measured to be 283. Isotopes of ^{40}Ar, ^{39}Ar, ^{38}Ar, ^{37}Ar, and ^{36}Ar were measured fifteen times per scan, and for ten scans. The final measurements are extrapolations back to the inlet time.

Figure 5.3 shows the age estimate for each heating step, indicating that a reliable plateau age was obtained. A plateau criterion of at least 50% of the ^{39}Ar release in at least 3 consecutive steps was used.

5.4.4 Kostrov summations

Kostrov (1974) showed that the strain rate tensor for N earthquakes that have occurred in a volume V can be calculated from:

$$\dot{\epsilon}_{ij} = \frac{1}{2\mu\tau V} \sum_{n=1}^{N} M_{ij}^{n} \tag{5.7}$$

where $\dot{\epsilon}_{ij}$ is the ijth component of the strain rate tensor, μ is the rigidity modulus, τ is the time period of observation, and M_{ij}^{n} is the ijth component of the seismic moment tensor of the nth earthquake. We used Kostrov's relation to calculate strain rate tensors for the northern Shanxi Grabens for different earthquake catalogues, different time periods, and different magnitude ranges. See Appendix B.1 for further mathematical details of these calculations.

On the basis of population density maps and Gutenberg-Richter statistics, the earthquake catalogues in northern Shanxi are thought to be complete for earthquakes with $M_s \geq 6$ since 1291 (i.e. soon after the beginning of the Yuan Dynasty in 1271) and $M_s \geq 4.75$ since 1484 (*Huang et al.*, 1994). We therefore constructed a catalogue of

25 earthquakes with $M_s > 5$ for the 700 year period from 1315 to 2015 based on *Lee et al.* (1976), *Lee et al.* (1978), *Liu et al.* (2011) and the Global Centroid Moment Tensor (GCMT) catalogue (*Ekström et al.*, 2012). Our catalogue is unlikely to be complete for events with $5 < M_s < 6$ between 1315 and 1484, but we chose to include those earthquakes that are known about; in any case, their contribution to the total moment release is relatively small.

Lee et al. (1976) reported surface-wave magnitudes (M_s), calculated from the maximum historically recorded intensities of shaking (I_0) using the empirical relationship $M_s = 0.58\times I_0 + 1.5$. *Lee et al.* (1978) also reported surface-wave magnitudes. We assumed that the magnitudes given in the *Liu et al.* (2011) catalogue were surface-wave magnitudes. For $M_s \leq 8$ we approximated surface-wave magnitude (M_s) as equal to moment magnitude (M_w) (*Kanamori*, 1983) and we therefore calculated seismic moment (M_0) using:

$$M_0 = 10^{\frac{3}{2}(M_w+6.03)} \tag{5.8}$$

Liu et al. (2011) suggested an error on the magnitudes in their catalogue of ±0.3. This seems reasonable given that a number of other historical catalogues quote magnitudes to the nearest quarter of a magnitude unit. Furthermore, a moment magnitude with an error of ±0.3 equates to a seismic moment that varies by a factor of 2.8 either way. This is similar to *Wesnousky et al.* (1984), who estimated that the seismic moments in their catalogue of earthquakes around the Ordos are correct to within a factor of 3 either way. Indeed, magnitudes calculated from historical records of shaking for other large earthquakes in the vicinity are believed to be overestimates because amplification effects in graben sediments have not been accounted for (see Chapter 2 and *Zhou*, 2016).

Focal parameters for some of these earthquakes were available in the literature (*Wesnousky et al.*, 1984; *Pavlides et al.*, 1999; *Liu et al.*, 2007) or the GCMT catalogue (*Ekström et al.*, 2012). For the remaining historical earthquakes, we estimated focal parameters from nearby instrumental earthquakes or fault striation measurements on adjacent faults. In the second case, we assumed that the sense of slip during the earthquake was the same

Table 5.2: Focal parameters (FP) for historical earthquakes in the northern Shanxi Grabens

Year	Month	Day	Lat / °	Long / °	M_w [a]	M_0 [b] / Nm	Eq. ref.	Strike / °	Dip / °	Rake / °	FP ref.	Assigned fault	FP notes
1337	9	8	40.4	115.7	6.5	6.24×10^{18}	*Lee et al.* (1976)	55	75	-77	This study, *Pavlides et al.* (1999)	Yanqing Fault	Av. 5 striations
1467	6	18	39.6	112.3	5.5	1.97×10^{17}	*Liu et al.* (2011)	20	74	138	This study	Not named	Nearest instrumental eq
1484	2	7	40.5	116.1	6.8	1.76×10^{19}	*Liu et al.* (2011)	55	75	-77	This study, *Pavlides et al.* (1999)	Yanqing Fault	Av. 5 striations
1502	12	4	39.0	112.6	5.3	9.89×10^{16}	*Liu et al.* (2011)	45	62	-90	This study, *Li et al.* (2015d)	Yunzhongshan Fault	
1514	10	30	38.7	113.0	5.3	9.89×10^{16}	*Liu et al.* (2011)	129	85	18	This study	Not named	Nearest instrumental eq
1545	2	x	40.0	114.0	5.3	9.89×10^{16}	*Liu et al.* (2011)	250	65	-135	This study, *Li et al.* (2015d)	Liulengshan Fault	
1580	9	15	39.5	112.3	5.8	5.56×10^{17}	*Liu et al.* (2011)	20	74	138	This study	Not named	Nearest instrumental eq
1581	5	18	39.8	114.5	6.0	1.11×10^{18}	*Lee et al.* (1976)	250	60	-110	This study, *Liu et al.* (2007)	Yuguang Graben Fault	
1583	5	18	39.7	113.8	5.5	1.97×10^{17}	*Lee et al.* (1976)	225	65	-116	This study, *Li et al.* (2015d)	Hengshan Fault	
1618	11	16	39.8	114.5	6.0	1.11×10^{18}	*Lee et al.* (1976)	250	60	-110	This study, *Liu et al.* (2007)	Yuguang Graben Fault	
1626	6	28	39.4	114.2	7.2	8.10×10^{19} [c]	*Lee et al.* (1976)	220	60	-120	*Wesnousky et al.* (1984)	Lingqiu Graben Fault	
1628	10	7	40.6	114.2	6.5	6.24×10^{18}	*Liu et al.* (2011)	75	45	-97	This study, *Li et al.* (2015d)	Yanggao-Tianzhen Graben Fault	
1664	x	x	38.7	112.7	5.5	1.97×10^{17}	*Lee et al.* (1976)	200	62	-160	This study, *Li et al.* (2015d)	Yunzhongshan Fault	
1673	10	18	40.5	114.1	5.5	1.97×10^{17}	*Lee et al.* (1976)	75	45	-97	This study, *Li et al.* (2015d)	Yanggao-Tianzhen Graben Fault	
1683	11	22	38.7	112.7	7.4	1.42×10^{20} [c]	*Lee et al.* (1976)	200	60	-160	*Wesnousky et al.* (1984)	Yunzhongshan Fault	
1720	7	12	40.4	115.5	6.8	1.48×10^{19}	*Lee et al.* (1976)	67	69	-81	This study, *Pavlides et al.* (1999)	Huailai Fault	Av. 3 striations
1898	9	22	39.1	113.0	5.5	1.97×10^{17}	*Lee et al.* (1976)	230	60	-135	This study, *Li et al.* (2015d)	Wutaishan Fault	
1911	1	25	39.8	114.5	5.9	7.85×10^{17}	*Liu et al.* (2011)	250	60	-110	This study, *Liu et al.* (2007)	Yuguang Graben Fault	
1952	10	8	39.0	112.7	5.5	1.97×10^{17}	*Liu et al.* (2011)	45	62	-90	This study, *Li et al.* (2015d)	Yunzhongshan Fault	
1967	7	28	40.5	115.6	5.4	1.40×10^{17}	*Liu et al.* (2011)	67	69	-81	This study, *Pavlides et al.* (1999)	Huailai Fault	Av. 3 striations
1989	10	18	39.63	113.84	5.4	1.40×10^{17}	GCMT[d]	92	44	-39	GCMT	Hengshan Fault	
1989	10	18	39.77	113.49	5.6	2.79×10^{17}	GCMT[d]	200	75	-175	GCMT	Liulengshan Fault	
1989	10	18	39.83	113.61	5.4	1.40×10^{17}	GCMT[d]	204	76	-176	GCMT	Liulengshan Fault	
1991	3	25	40.10	113.34	5.4	1.40×10^{17}	GCMT[d]	106	82	7	GCMT	Datong Basin Fault	
1999	11	1	39.85	113.74	5.2	7.00×10^{16}	GCMT[d]	122	72	-7	GCMT	Liulengshan Fault	

[a] Magnitudes for historical earthquakes are estimated from intensities on the *New Chinese Intensity Scale* using $M_s = 0.58\times I_0 + 1.5$. M_s is considered equal to M_w for $M_s \leq 8$ (*Kanamori*, 1983).
[b] M_0 calculated from M_w using $M_0 = 10^{\frac{3}{2}(M_w+6.03)}$.
[c] M_0 from (*Wesnousky et al.*, 1984) rather than calculated from M_w.
[d] See *Ekström et al.* (2012).

as the Quaternary motion on the nearest adjacent fault. All 25 earthquakes and their associated parameters are listed in Table 5.2. We then performed a variety of sensitivity tests to check how uncertainties in fault strike, fault dip, rake, magnitude, seismogenic thickness and time period affect our results. We also conducted Kostrov summations with the modern instrumental catalogue of *Li et al.* (2015a), which contains 36 earthquakes in the region of interest from between 1965 and 2014, with magnitudes (M_w) in the range 3.1 to 5.8—although this catalogue only extends as far as 114.5 °E.

5.4.5 Strain rate field from GPS

The Crustal Motion Observation Network of China (CMONOC) was established in 1998 by the State Seismological Bureau of China (now the China Earthquake Administration) (*Liu et al.*, 2007). Today, the network includes 260 continuous GPS stations and a total of 2056 temporary survey stations across the whole of China, which were visited most recently during field campaigns in 2009, 2011 and 2013 (*Li et al.*, 2012; *Zhao et al.*, 2015). We calculated a continuously varying strain rate field from the latest campaign GPS measurements (*Zhao et al.*, 2015), comprising these 3 occupations, according to the method of *Shen et al.* (1996) and *Floyd et al.* (2010). The motivation for considering a continuous strain rate field was that a number of theories of continental deformation postulate that the whole lithosphere in a deforming region responds to stresses that are either applied at its edges or result from gradients in gravitational potential energy (*Bird and Piper*, 1980; *England and McKenzie*, 1982).

Of the 78 stations in the region of interest, we removed 5 with errors greater than 0.5 mm/a (see later Figure 5.13). We solved for the best-fitting rigid body rotation and subtracted this motion from all vectors to account for the general eastward translation of northeastern China. Subtracting this rigid body rotation did not influence the subsequent strain rate calculations, it simply allowed for easier visualisation of the deformation occurring within the region of interest. We then solved for the easterly and northerly components of velocity and the four horizontal velocity gradients at each GPS site using a least squares inversion, assuming uniform velocity gradients in both the northerly and

easterly directions. All GPS sites within a radius r_{max} were included in each inversion (except for the GPS site at which the calculation was being performed), but they were given a Gaussian weighting (W) according to the square of their distance (r) from the calculation site:

$$W = e^{\frac{-r^2}{\alpha^2}} \tag{5.9}$$

where α is a constant that defined the width of the Gaussian smoothing function and determined the horizontal resolution of the continuous model. Following the method of *Floyd et al.* (2010), we determined a minimum value for α (r_{min}) by requiring that 75% of GPS sites had at least 6 sites (the site itself plus its five nearest neighbours) within a distance r_{min}. For the GPS stations in northern Shanxi, we obtained r_{min} = 48 km. Most of the figures below are for α = 80 km, though we also tested the effects of different values of α on our results (see Appendix B.2). We then compared the velocities that we obtained from our inversion to the original GPS vectors and calculated a residual at each site. We removed sites with residual velocities greater than 1 mm/a (i.e. those that did not fit a smoothly varying velocity field) to leave 57 sites in the region of interest (73% of the original data). We then re-calculated the strain rate field on a regular 0.5 ° grid. In other words, we assumed locally homogeneous but regionally varying velocity gradients. See Appendix B.2 for mathematical details of these calculations.

5.5 Fault slip rates from Quaternary geology

In this section we describe field observations at sites along three of the major faults in the northern Shanxi Grabens: the Yuguang Graben Fault, the Liulengshan Fault, and the Kouquan-Emokou Fault. We chose these faults because of their topographic and geomorphological prominence and because they are relatively close to Beijing and the densely populated North China Plain, hence they potentially pose a significant seismic hazard. The Quaternary slip rates on the other faults in the northern Shanxi Grabens are summarised later in Table 5.3 and Figure 5.10.

5.5.1 Yuguang Graben Fault

The Yuguang Graben Fault is a large, arcuate, normal fault that borders the southeastern side of the Yuguang Graben, a basin which contains the cities of Yuxian and Guangling (see Figure 5.2). The fault extends ENE-WSW for approximately 120 km (from 39.759 °N, 114.005 °E to 40.130 °N, 115.108 °E), dips to the northwest, and consists of multiple fault segments. *Wang* (2012) measured fault striations with a rake of -80 to -90 °, indicating predominantly normal motion. Towards the western end of the fault the footwall lithologies include Cambrian and Precambrian limestones and dolomites, whilst the eastern end is composed of Jurassic rocks (*Wang*, 2012). The hanging wall is covered by Pleistocene and Holocene alluvial sediments.

Guangling section

The first slip rate site is 7 km south of the city of Guangling, where the most recently active fault segment cuts through the toe of an alluvial fan 1.4 km from the main range front near the village of Yixingzhuang (see Figure 5.4). We measured topographic profiles across the scarp along lines A-A′ and B-B′ from the Worldview-1 DEM (see Section 5.4.1 and Figures 5.4 (c) and 5.4 (d)). We obtain an average vertical offset at this site of 13±1 m. Figure 5.5 (a) shows a field photograph of the triangular facets along the main range front, with the most recently active fault segment in the foreground.

Wang (2012) excavated two palaeoseismic trenches at 39.710 °N, 114.310 °E, 1.5 km south of Yixingzhuang village. They identified two prehistoric earthquakes, the older of which occurred between 16.66±1.39 and 10.62±0.87 ka ago on the basis of OSL dates from the trenches. *Wang* (2012) also estimated a total throw in the two earthquakes of ≈ 7 m. Our 13±1 m offset of the alluvial fan surface suggests that more than the two earthquakes visible in the trench have occurred at this site. Combining the ages with the throw of 7 m and a fault dip of 60 ° (*Li et al.*, 2015d), we obtain a throw rate of between 0.4 and 0.7 mm/a and an extension rate of between 0.2 and 0.4 mm/a.

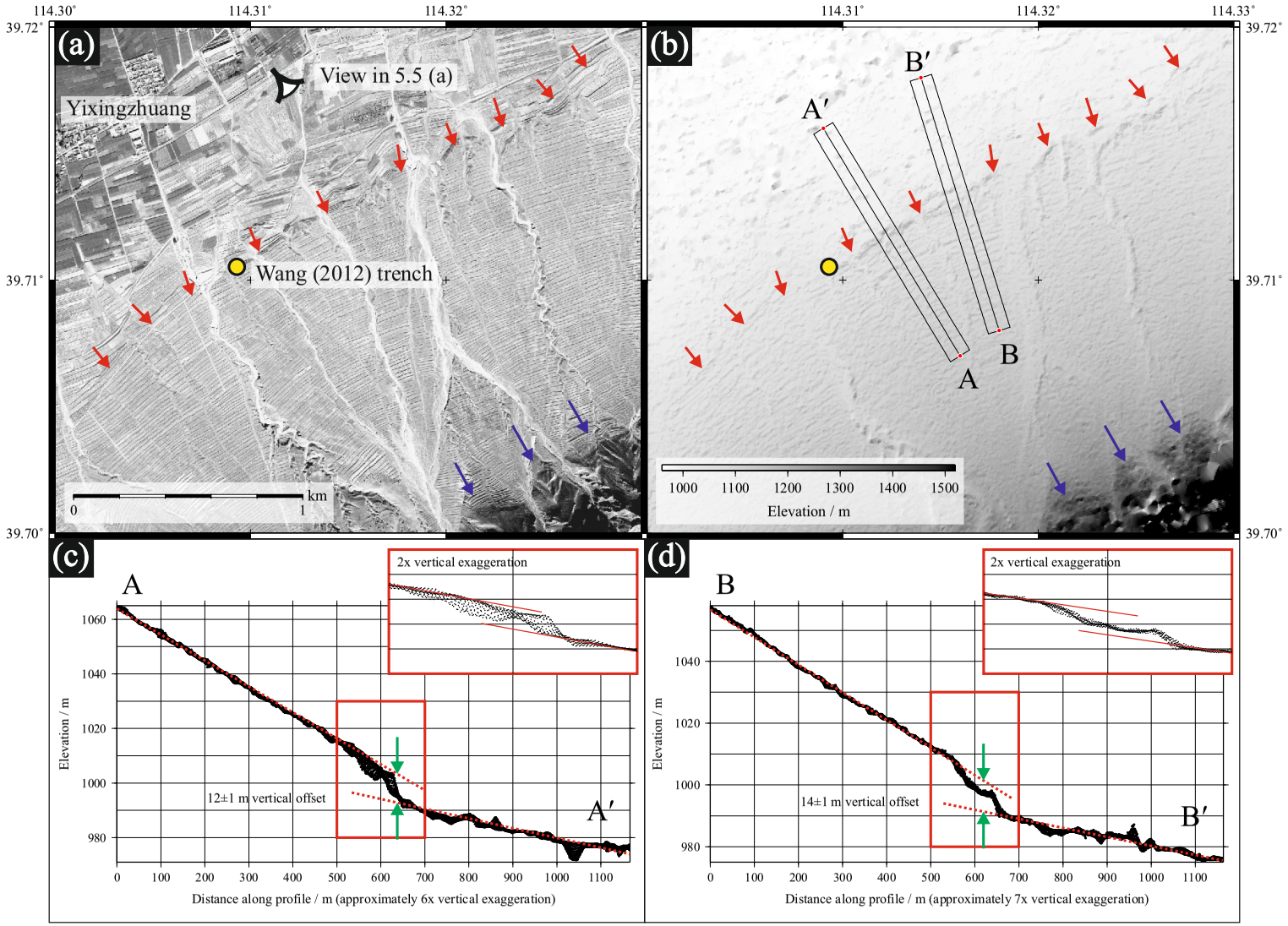


Figure 5.4: (a) Single-band (0.5 m resolution panchromatic) Worldview-1 image from 21st September 2011 of the Yuguang Graben Fault around 7 km south of the city of Guangling. Blue arrows mark position of the range-front normal fault, which dips to the northwest; red arrows mark the most recently active fault segment. Yellow circle marks the location of the trench opened by *Wang* (2012). Location of field photograph in Figure 5.5 (a) also shown. (b) 1 m resolution DEM of the same area as (a) derived from a stereo pair of Worldview-1 images from July 2008 and September 2011. (c) 100 m wide swath profile A-A′. Dots show DEM points that fall within the swath. Red lines indicate best-fitting lines for the upper and lower slopes. We measure a vertical offset of 12±1 m. Note that the vertical exaggeration exacerbates the $\approx 3^\circ$ difference in slope between the upper and lower surfaces—see the inset profile in the red box with reduced vertical exaggeration for comparison. (d) 100 m wide swath profile B-B′. Annotations the same as (c). We measure a vertical offset of 14±1 m.

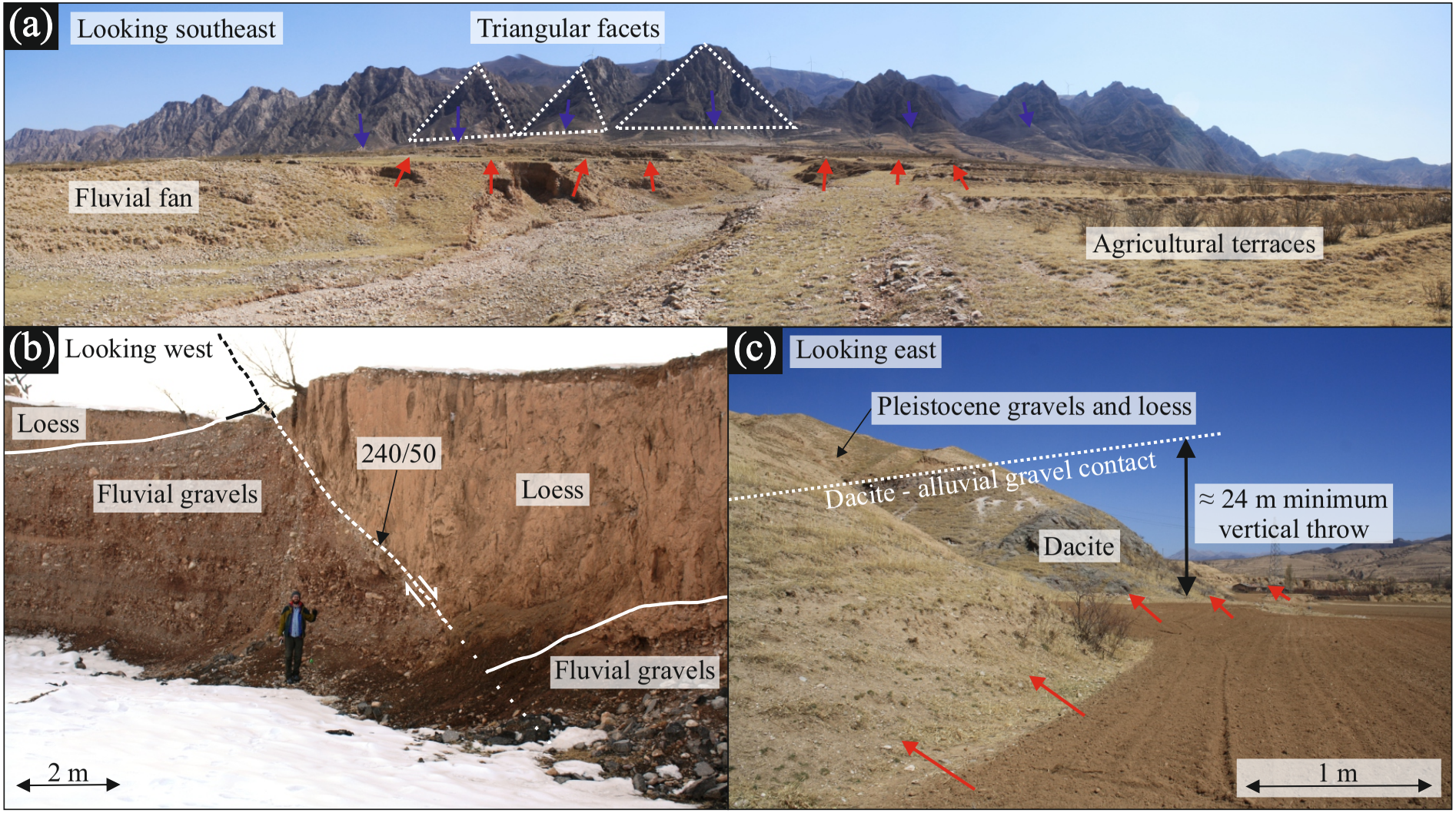


Figure 5.5: (a) Field photograph (taken at 39.718 °N, 114.312 °E) looking southeast at the Yuguang Graben Fault around 7 km south of the city of Guangling (see Figure 5.4 (a) for location). Blue arrows mark position of range-front normal fault; red arrows mark the most recently active fault segment in the foreground. (b) Field photograph from the Jiugongkou overlap zone (taken at 39.880 °N, 114.766 °E) looking west at the Yuguang Graben Fault exposed in a river cutting. (c) Field photograph, also from the Jiugongkou overlap zone, (taken at 39.852 °N, 114.769 °E) looking east along the antithetic fault and showing uplifted dacite in the footwall (see Figure 5.6 (b) for location).

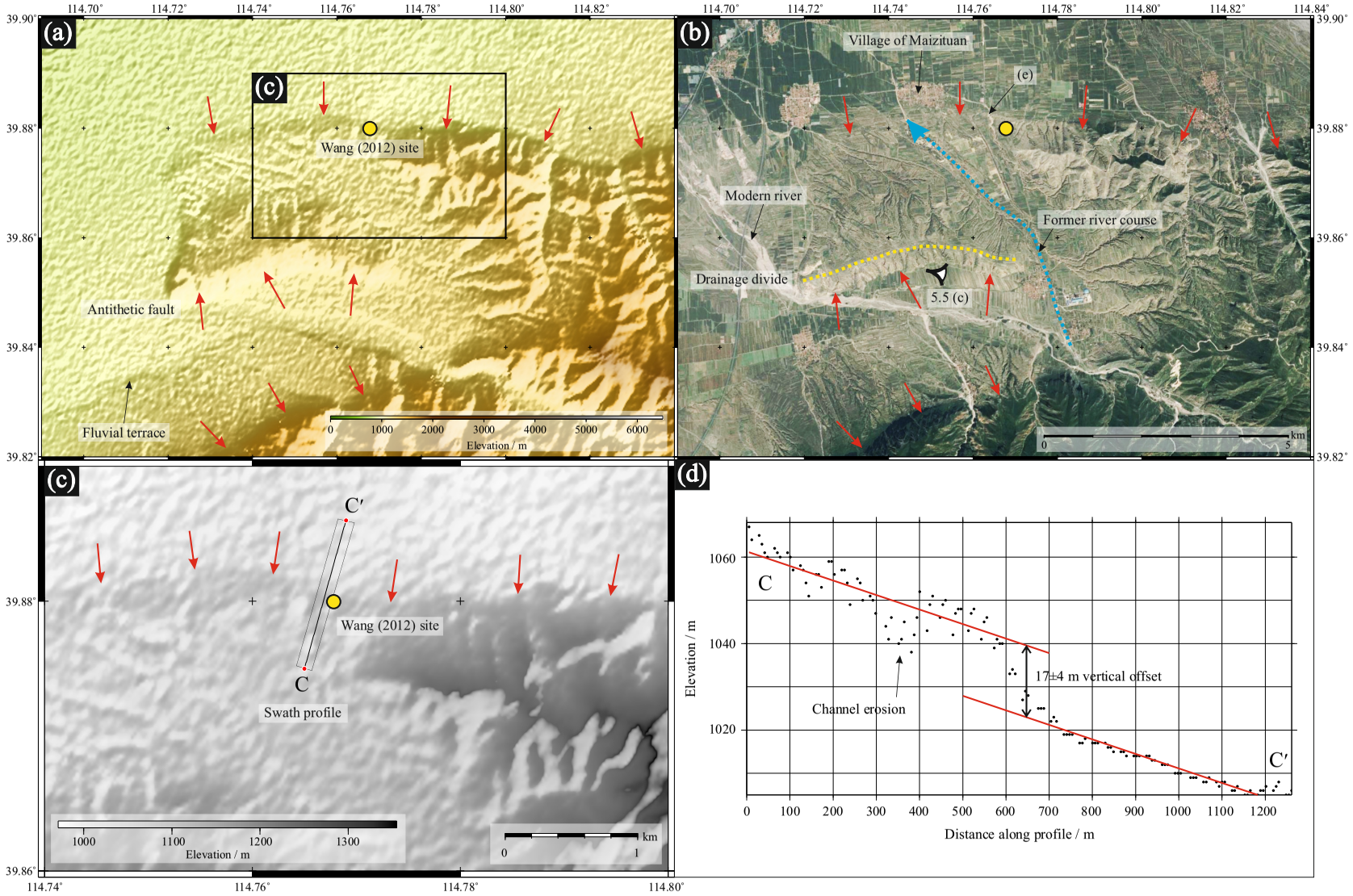


Figure 5.6: (a) SRTM topography (30 m resolution) of the Jiugongkou overlap zone on the Yuguang Graben Fault 15 km east of Yuxian city (*Farr et al.*, 2007). Red arrows indicate active faults, including a small antithetic fault within the overlap zone. Yellow circle indicates the dating site of *Wang* (2012) (at 39.880 °N, 114.766 °E). (b) Google Earth imagery from August 2015 (source: http://earth.google.com) of the same region as (a). Westward growth of the northern fault segment and movement on the antithetic fault have caused uplift of a central horst block that has deflected the major river exiting the mountains. The dotted yellow line marks the position of the drainage divide within this horst block. (c) Zoomed view of the SRTM topography on the northern fault segment, showing location of the swath profile C-C′. (d) 150 m wide swath profile C-C′. Dots show DEM points that fall within the swath. Red lines indicate best-fitting lines for the upper and lower slopes. We measure a vertical offset of 17±4 m.

Jiugongkou overlap zone

The second slip rate site on the Yuguang Graben Fault is on the 7 km long Jiugongkou fault segment overlap zone, 15 km east of Yuxian city at 39.880 °N, 144.766 °E. Within the overlap zone, a minor antithetic fault approximately 5 km long dips to the south (see Figure 5.6). On the northeasternmost fault strand, 1.3 km southeast of the village of Maizituan, we measure a throw of 17±4 m (see Figures 5.6 (c) and 5.6 (d)). Figure 5.5 (b) shows an exposure of the fault in an adjacent river cutting. *Cheng and Yang* (1998) obtained a TL age of 26.0±2.1 ka for the alluvial sediments at this site, suggesting a throw rate of 0.65±0.16 mm/a.

On the antithetic fault a dacite covered by Pleistocene sediments is uplifted in the footwall. *Cheng and Yang* (1998) measured a minimum vertical separation across the fault of ≈ 24 m and obtained a TL date for the overlying fluvial deposits of 27.4±2.2 ka, giving a minimum throw rate of 0.88±0.07 mm/a. This faster throw rate on the antithetic fault is consistent with the asymmetry of the intervening horst.

Adding the rates on these parallel strands and using fault dips of 60 ° (*Li et al.*, 2015d) yields an extension rate at this site of 0.88±0.10 mm/a.

5.5.2 Liulengshan Fault

The Liulengshan Fault runs along the northwestern side of the Liulengshan, an S-shaped mountain range in the centre of the northern Shanxi Grabens (between 39.577 °N, 113.276 °E and 40.256 °N, 114.727 °E), forming part of the eastern edge of the Datong Graben and the southern edge of the subsidiary Yangyuan Graben (see Figure 5.2). The fault comprises numerous segments (each typically ≈ 25 km long), which all dip to the northwest, and is approximately 150 km long in total. *Xu et al.* (1997) measured striations with rakes of -77 to -90 ° towards the eastern end of the Liulengshan Fault, indicating that the fault undergoes predominantly normal motion, at least on this segment. The principal footwall lithologies are Precambrian metamorphic rocks and Palaeozoic limestones, whilst the hanging wall consists primarily of alluvial and fluvial fan deposits, shed from the growing

range front (*Xu et al.*, 1997). These sediments are interbedded with, and subsequently capped by, substantial loess deposits.

Two earthquake swarms, with maximum magnitudes of M_s 6.1 and M_s 5.8, occurred on the Liulengshan Fault in October 1989 and March 1991 respectively (*Xu et al.*, 1997). The focal depths of these earthquakes are thought to be in the range of 10 to 20 km (*Xu et al.*, 1993) and there are no reports of surface ruptures associated with these events. The GCMT mechanisms for the four largest events (M_s 5.0 to M_s 6.1) suggest right-lateral strike-slip motion. With the exception of one other event in 1545, there is no other recorded seismicity on the Liulengshan Fault. Such historical inactivity is further corroborated by fluvial fans and soils which cover the fault trace, but have not been offset. *Xu et al.* (1997) found that no surface-rupturing earthquakes can have occurred on the Liulengshan Fault for at least the last 1500 years and in some locations since 23 ka ago.

Xu et al. (1997) measured throw rates at nine different sites along the Liulengshan Fault using TL dating of offset features and, in one location, K-Ar dating of basaltic feldspars. Using a fault dip of 65° (*Li et al.*, 2015d), they obtained extension rates of between 0.2 and 0.4 mm/a for different locations along strike (see Figure 5.10). Here, we seek to corroborate these results by using IRSL dating on samples from an independent site, at Qifengpocun. We also present observations from a second site, at Jiankoucun.

Qifengpocun

The first site on the Liulengshan Fault is at Qifengpocun, 17 km south of the city of Yangyuan (at 39.950 °N, 114.138 °E). Here, a recently active fault strand cuts through alluvial fans north of the range front (see Figure 5.7). Two terraces are preserved on either side of a channel exiting the Liulengshan, although their surfaces have been heavily modified for agriculture. We measure a vertical offset for the second, older terrace of 18±4 m from the ALOS PRISM data (see Figures 5.7 (c) and 5.7 (d)). The topographic data are not sufficiently high-resolution to resolve the height of the lower terrace, but our field observations suggest a height of 3 to 4 m.

We collected IRSL samples for dating from both terraces (see Figures 5.7 (f) and 5.7 (g) and Figure 5.7 (b) for locations). IRSL sample 15 is from the riser between T1 and T2

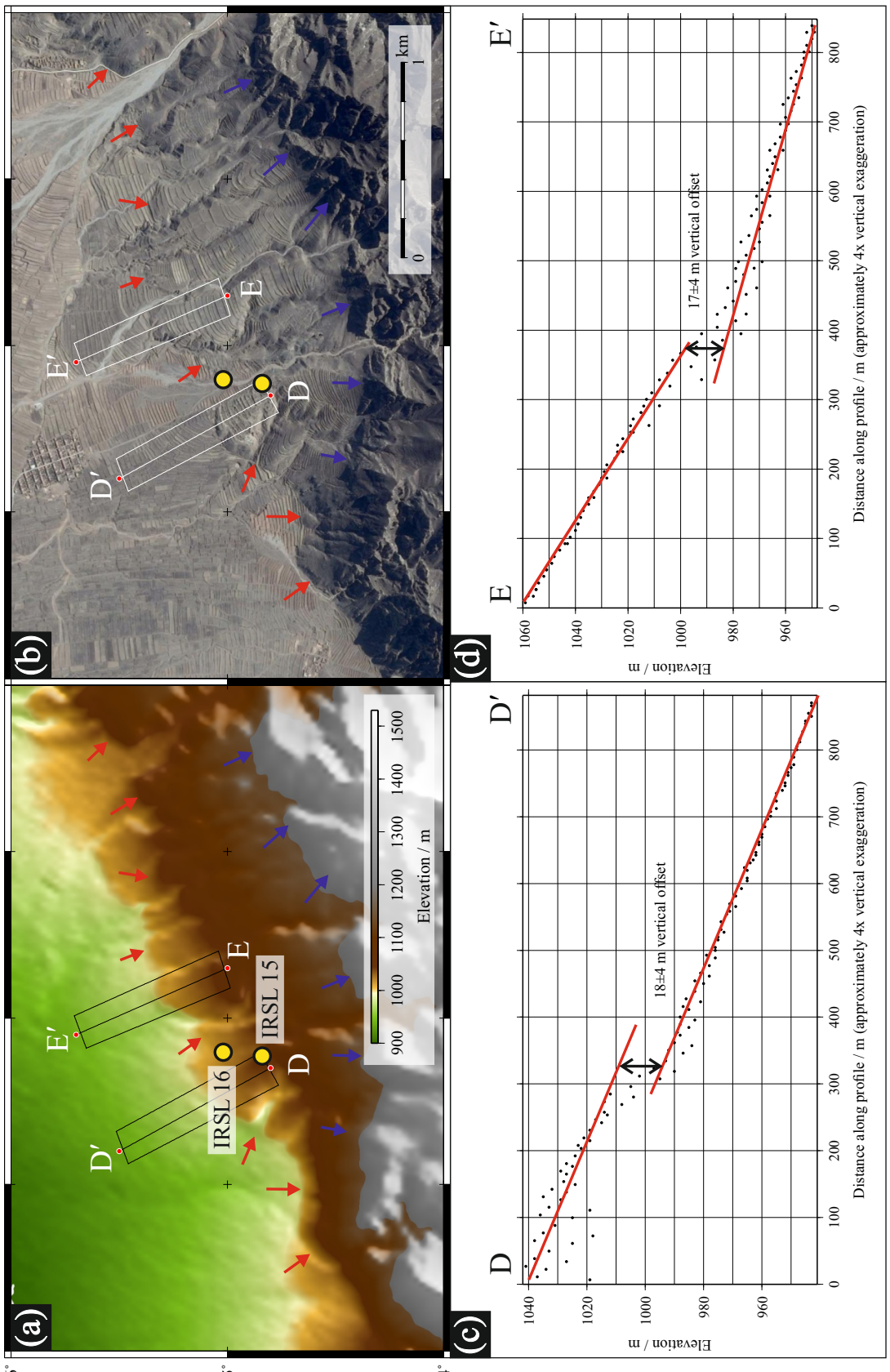


Figure 5.7: (a) 30 m resolution ALOS PRISM topography of Qifengpocun in the centre of the Liulengshan Fault (*Takaku et al.*, 2014; *Tadono et al.*, 2014). Blue arrows mark position of the range-front normal fault; red arrows mark the most recently active fault segment. Yellow circles indicate the locations of IRSL samples 15 and 16. (b) Google Earth imagery from March 2014 (source: http://earth.google.com) of the same area as (a). (c) 200 m wide swath profile D-D′. Dots show DEM points that fall within the swath. Red lines indicate best-fitting (non-parallel) lines for the upper and lower slopes. We measure a vertical offset of 18±4 m. (d) 200 m wide swath profile E-E′. Annotations the same as (c). We measure a vertical offset of 17±4 m.

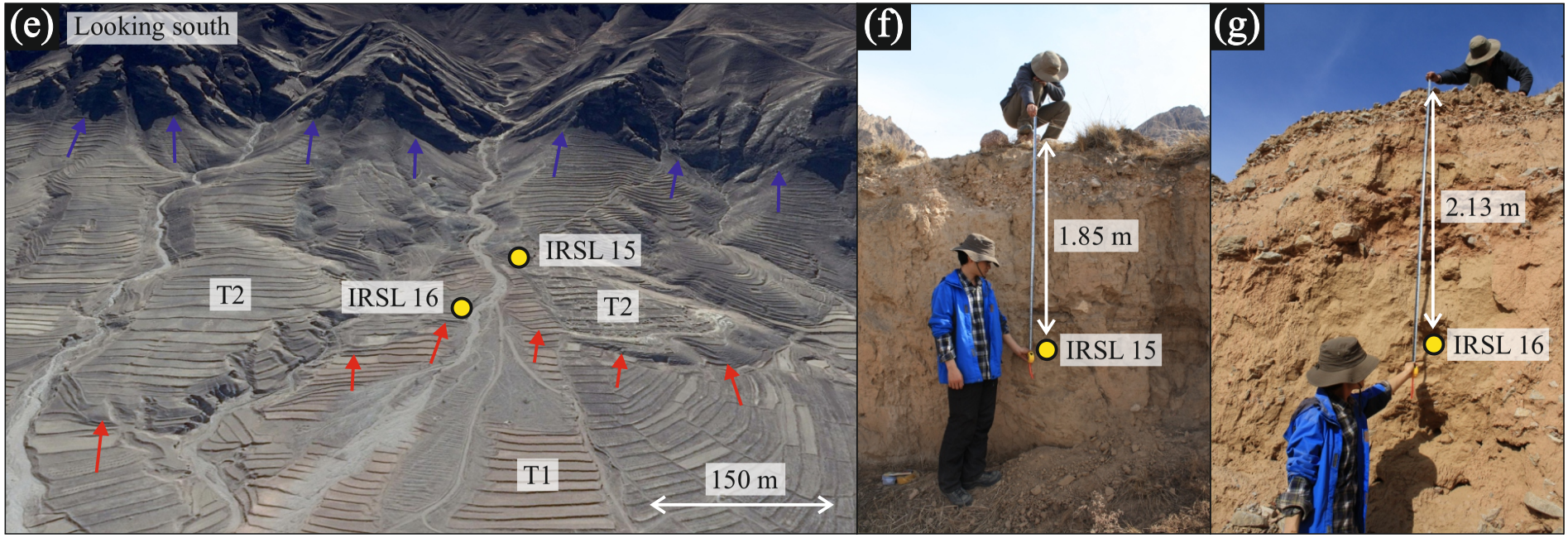


Figure 5.7: (continued) (e) Perspective view of the Google Earth imagery looking south at the Liulengshan Fault. Two terrace levels (T1 and T2) are visible. Blue arrows mark position of range-front normal fault; red arrows mark the most recently active fault segment. (f) and (g) Field photographs (taken at 39.948 °N, 114.138 °E and 39.950 °N, 114.138 °E) showing IRSL samples 15 and 16, taken from the sides of the T2 and T1 terraces respectively.

(at 39.948 °N, 114.138 °E). The sample is from a homogeneous layer of yellow-brown loess 185 cm below the ground surface and 80 cm below a layer of sub-rounded fluvial gravels with clasts up to 10 cm in diameter. IRSL 15 yields an age of 16.3±1.9 ka. IRSL sample 16 is from the side of a gully incised into T1 (at 39.950 °N, 114.138 °E). The sample is from a yellow loess layer 213 cm below the ground surface and 50 cm below a series of layers of coarse, angular gravels. IRSL 16 yields an age of 15.9±1.0 ka.

The age of IRSL 15 and the offset of 18±4 m gives a throw rate of 1.10±0.28 mm/a and an extension rate of 0.51±0.13 mm/a; the age of IRSL 16 and the offset of 4±1 m gives a throw rate of 0.25±0.02 mm/a and an extension rate of 0.12±0.03 mm/a (both for a 65 ° dipping fault (*Li et al.*, 2015d)). These extension rates are similar to the previous rates of 0.2 to 0.4 mm/a obtained by *Xu et al.* (1997). However, we also note that the similarity in the two IRSL ages suggest that they might both come from the same deposit. This could be because IRSL 16 actually sampled an incised wall of T2 and the T1 deposits at this site are thinner than 213 cm. The multiple gravel layers above IRSL 16 (see Figure 5.7 (g)) may also indicate that the sample is from an older deposit than T1. If this is the case, then we prefer 0.51±0.13 mm/a as the more reliable extension rate.

Jiankoucun section

Towards the eastern end of the Liulengshan Fault, the footwall relief decreases from ≈ 325 m to ≈ 50 m, indicating that this portion of the fault has experienced considerably less slip. The ≈ 50 m high escarpment continues eastwards, cutting across where the main drainage leaves the Yuguang Graben, and joins an older fault that strikes northeast immediately adjacent to the Sanggan River as it flows east out of the Yangyuan Graben (see Figure 5.2). It appears, therefore, that this fault segment, with uplifted former basin sediments in its footwall, is linking two older fault segments that have larger total displacements (see Figure 5.2). Furthermore, the uplifted basin sediments include some of the earliest evidence for the presence of humans in northeast Asia (1.36 Ma ago) at the Xiaochangliang palaeolithic site (40.221 °N, 114.662 °E) (*Zhu et al.*, 2001). Fault linkage has occurred since this time, implying a throw rate of > 0.04 mm/a.

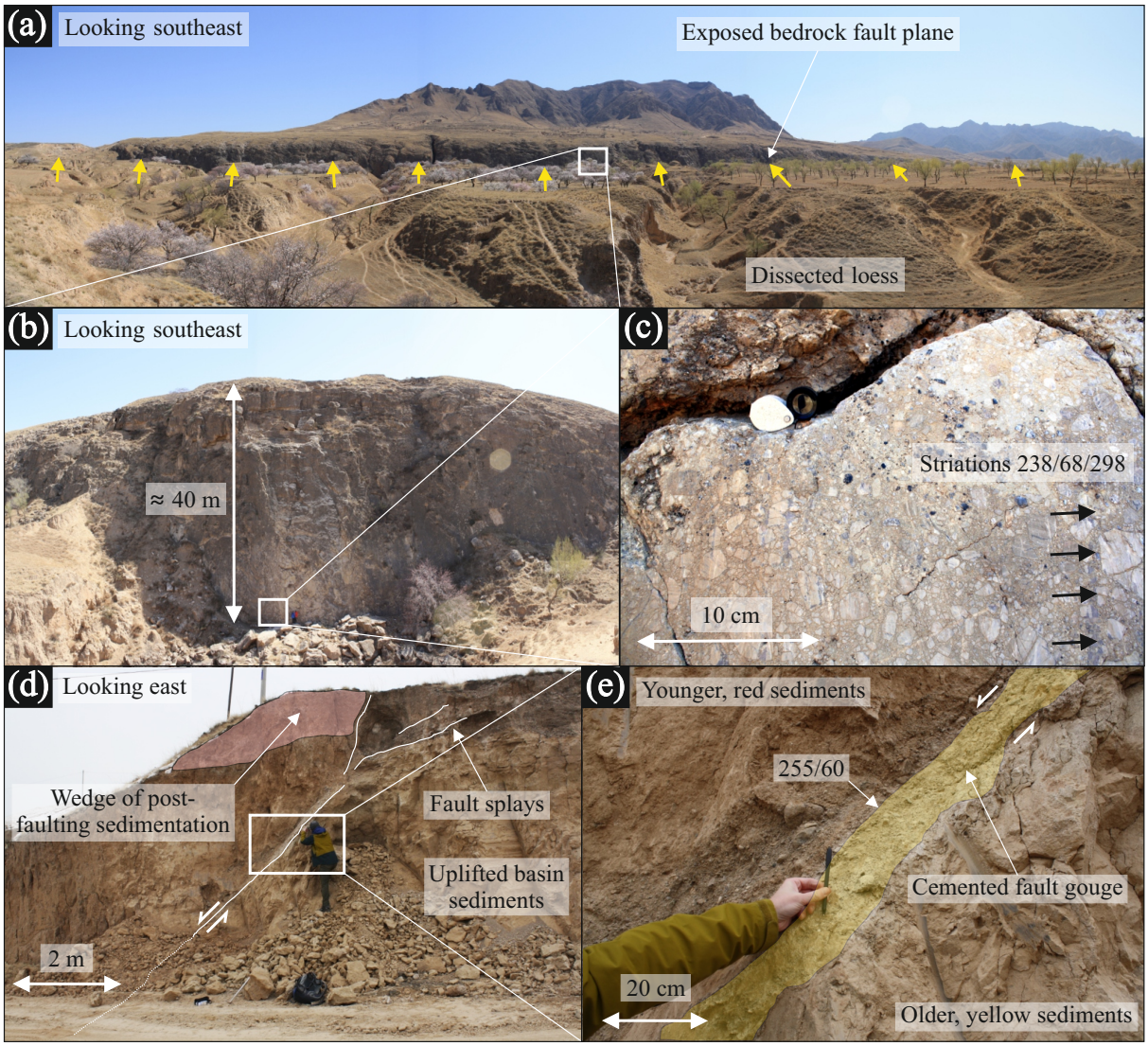


Figure 5.8: (a) Field photograph looking southeast at an exposed bedrock fault plane on the Liulengshan Fault. Yellow arrows indicate the position of the fault. (b) Field photograph (taken at 40.097 °N, 114.468 °E) showing a closer view of the ≈ 40 m high bedrock fault plane. (c) Zoomed in photograph at the same location showing the polished fault plane surface. Black arrows highlight the orientation of striations (238/68/298). (d) Field photograph (taken at 40.115 °N, 114.499 °E) looking east at a road-cut exposure of the Liulengshan Fault in the uplifted basin sediments towards the eastern end of the fault. (e) Zoomed in photograph at the same location showing the orientation of the fault plane (255/60) and the calcite-cemented fault gouge.

At the eastern end of the Liulengshan topography (at 40.097 °N, 114.468 °E) a 1.8 km long section of bedrock fault plane is exposed (see Figure 5.8 (a)). The exposure is ≈ 40 m high and we find an average fault striation measurement (strike/dip/rake) of 238/68/298 (see Figures 5.8 (b) and 5.8 (c)). (This and other fault striation measurements are discussed in more detail in Section 5.8.3.) Further east, within the uplifted basin

sediments, fault exposures are also visible (at 40.115 °N, 114.499 °E—see Figures 5.8 (d) and 5.8 (e)).

5.5.3 Kouquan-Emokou Fault

The 100 km long Kouquan-Emokou Fault borders the northwestern edge of the Datong Graben, running from 39.668 °N, 112.728 °E in the southwest to 40.408 °N, 113.442 °E in the northeast. The fault dips to the southeast causing uplift on the northwestern side of the fault trace. A major segment boundary occurs 10 km southwest of the city of Nanjiao at 39.944 °N, 113.059 °E (see Figure 5.2). *Yu* (2004) described the Kouquan-Emokou Fault as having both vertical and right-lateral components of motion, at suggested rates of 0.5 to 0.6 mm/a (*Yu*, 2004) and 3.6 mm/a (*Deng et al.*, 2007) respectively.

A M_s 5 earthquake in 1582 has an approximate epicentral location that is adjacent to the Kouquan-Emokou fault, just to the west of Datong (*Liu et al.*, 2011). Two further earthquakes, both of M_s 6.5, occurred in 1022 and 1305 further south within the Datong Graben (*Liu et al.*, 2011). Although both epicentres apparently lie within the city of Huairen, and a number of smaller faults are thought to cross the centre of the Datong Graben, it seems probable that these two earthquakes also occurred on the Kouquan-Emokou Fault and were simply recorded by the inhabitants of Huairen. A further earthquake with M_s 5.4 was recorded on 25th March 1991 within the urban area of Datong itself. The epicentral location for this event indicates that it probably took place on a separate, smaller fault 12 km southeast of the main fault (see Figure 5.9 (a)); the earthquake had a right-lateral strike-slip mechanism.

Tuotuoying, Datong section

At its northern end, the Kouquan-Emokou fault passes through the western side of Datong city and offsets a Cenozoic basaltic lava flow as shown in Figure 5.9 (a). The flow infills older topography and varies substantially in thickness. We measure a scarp height adjacent to the village of Tuotuoying of 119±5 m (see Figures 5.9 (b) and 5.9 (c)). However, we were not able to find exposures of the basalt on the hanging wall side, so this

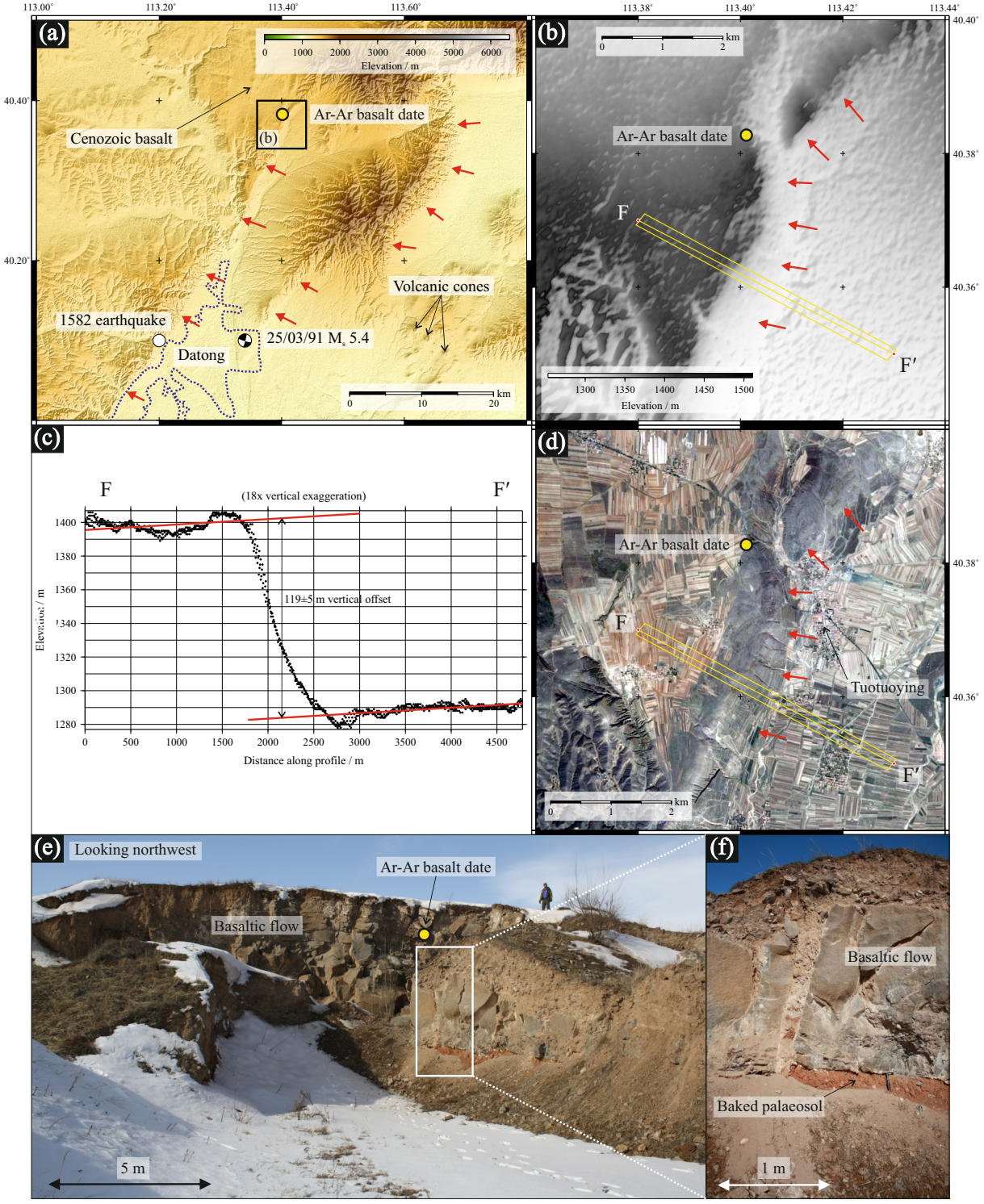


Figure 5.9: (a) SRTM topography (30 m resolution) of the northern end of the Datong Graben (*Farr et al.*, 2007). Red arrows mark the positions of active faults, including the Kouquan-Emokou Fault, which bounds the northwestern edge of the graben. The yellow circle marks the location of the Ar-Ar dating sample. (b) Zoomed view of the SRTM topography at the northern end of the Kouquan-Emokou Fault, where an escarpment is preserved in a Cenozoic basalt flow. (c) 300 m wide swath profile F-F′. Dots show DEM points that fall within the swath. Red lines indicate best-fitting lines for the upper and lower slopes. We measure a vertical offset of 119±5 m. (d) Google Earth imagery from November 2015 (source: http://earth.google.com) of the same area as (b). (e) Field photograph (taken at 40.383 °N, 113.401 °E) of a quarry in the footwall of the Kouquan-Emokou Fault. The yellow circle indicates the position of a basalt sample taken for Ar-Ar dating. (f) Zoomed in photograph at the same location shows the basaltic lava flow overlying a baked palaeosol; the flow is particularly thin at this location.

height gives us a minimum fault throw. A sample of the basalt was taken from a quarry in the footwall of the fault 2 km northwest of Tuotuoying (see Figures 5.9 (d), 5.9 (e) and 5.9 (f)). We obtain an Ar-Ar age for the basalt of 8.29±0.27 Ma (see Section 5.4.3). This gives us a minimum throw rate of 0.014±0.001 mm/a and, for a 70° dipping fault (*Li et al.*, 2015d), a minimum extension rate of 0.005 mm/a. Given that the fault extends for 16.72 km into the basalt flow, we are also able to determine a minimum horizontal propagation rate of 2.02 mm/a. It should be emphasised that these are minimum constraints on the extension rate and propagation rate; the basaltic lava dates to the Late Miocene and hence is older than much of the graben formation in northern Shanxi. The lava likely remained undisturbed for an extended period of time before the onset of fault displacement. In addition, the low extension rate could also be because motion at the northern end of the Kouquan-Emokou Fault is transferred onto short, normal faults further east (see Figure 5.9 (a)).

5.5.4 Summary of fault slip rates from Quaternary geology

Table 5.3 summarises all of the Quaternary rates from this study and the literature. Our re-assessment of some of these sites, along with our re-measurement of some of the offsets and our additional dating on the Liulengshan and Kouquan-Emokou Faults is in good agreement with the previous measurements.

All of the rates originally determined are vertical throw rates across normal faults. We therefore use fault dips from *Li et al.* (2015d) to convert throw rates to extension rates. Where dips were not given by *Li et al.* (2015d), we use the mean dip from the dip ranges quoted by *Yu* (2004). All of the extension rates are plotted in Figure 5.10. Blue circles show locations from this study; red circles show locations from other studies; and black labels are rates from *Yu* (2004) and *Deng et al.* (2007), where the location of the actual measurement site is unknown. The calculated errors for individual throw rate measurements (from propagating offset and age errors in quadrature) are typically around ±0.1 mm/a—see sites described above. However, these errors are not quoted in

Table 5.3: Summary of Quaternary rates for major faults in the northern Shanxi Grabens

ID	Fault name			Strike[a] °	Dip[a] °	Rake[a] °	Throw rate mm/a	Extension rate mm/a	Dating method	References
	Location	*Lat / °*	*Long / °*							
1	Yunzhongshan Fault			10	62	-135	0.4	0.2		*Yu* (2004)
2	Wutaishan Fault			230	60	-135				
	Nanyukou	39.214	113.587				0.76	0.4	OSL	*Zhang et al.* (2007)
	Nanyukou	39.214	113.587				1.57[d]	0.9	^{14}C	*Ding et al.* (2009)
3	Hengshan Fault			225	65	-115				
	Hezhuang Trench	39.158	112.657				0.68	0.3	^{14}C	*Jiang et al.* (2003)
	Niucaoyu Trench	39.510	113.351				1.09	0.5	^{14}C	*Jiang et al.* (2003)
4	Kouquan-Emokou Fault			35	70	-158	0.6	0.2		*Yu* (2004)
	Tuotuoying	40.383	113.401				0.01	0.01	Ar-Ar	This study
5	Laiyuan Graben Fault			252[b]	60[c]					
6	Lingqiu Graben Fault			255	45	-101	0.3	0.3		*Xu et al.* (2002); *Deng et al.* (2007)
7	Yuguang Graben Fault			235	60	-174				
	Western end	39.696	114.245				0.62	0.4	OSL	*Wang* (2012)
	Guangling Trench	39.710	114.307				0.54[e]	0.3	OSL	*Wang* (2012)
	Jiugongkou	39.880	144.766				1.53[f]	0.9	TL	This study; *Cheng and Yang* (1998)
8	Liulengshan Fault			250	65	-135				
	Donghouzikou	39.897	113.659		65		0.43	0.2	TL	*Xu et al.* (1997)
	Xiaowang	39.923	113.715		65		0.95	0.4	TL	*Xu et al.* (1997)
	Qiulin	39.933	113.939		65		0.36	0.2	K-Ar	*Xu et al.* (1997)
	Qifengpocun	39.950	114.138		65		1.10	0.5	IRSL	This study
	Dusanpu	39.985	114.235		65		0.43	0.2	TL	*Xu et al.* (1997)
	Dashuikou	40.006	114.280		65		0.75	0.3	TL	*Xu et al.* (1997)
	Jijiayao	40.016	114.314		65		0.53	0.2	TL	*Xu et al.* (1997)
	Xiejiayao	40.043	114.341		65		0.43	0.2	TL	*Xu et al.* (1997)
	Longmazhuang	40.023	114.373		65		0.53	0.2	TL	*Xu et al.* (1997)
	Gongjiawan	40.080	114.450		65		0.55	0.3	TL	*Xu et al.* (1997)
9	Yangyuan Graben Fault			69[b]	68[c]		0.1	0.04		*Deng et al.* (2007)
10	Yanggao-Tianzhen Graben Fault			75	45	-97	0.3	0.3		*Xu and Deng* (1996); *Deng et al.* (2007)
11	Nankou Fault			47[b]	65[c]					
12	Yanqing Fault			61[b]	65[c]		0.3	0.2		
	Canfanying	40.400	115.743				0.33	0.2	TL	*Cheng et al.* (1995); *Pavlides et al.* (1999)
	Yaojiaying	40.453	115.808				0.17	0.1	TL	*Cheng et al.* (1995); *Pavlides et al.* (1999)
	Yuhuangmiao	40.512	115.897				0.34	0.2	TL	*Cheng et al.* (1995); *Pavlides et al.* (1999)
	Baicaowa	40.569	116.034				0.33	0.2	TL	*Cheng et al.* (1995); *Pavlides et al.* (1999)
	Heiyukou	40.594	116.114				0.47	0.2	TL	*Cheng et al.* (1995); *Pavlides et al.* (1999)
13	Huailai Fault			65[b]	63[c]		0.4	0.2		*Yu* (2004); *Deng et al.* (2007)
14	Huai'an Graben Fault			45	45	-33	0.2	0.2		*Deng et al.* (2007)
15	Zhangjiakou-Bohai-Penglai Fault			108[b]	65[c]					
16	Daihai Graben Faults			55[b]	45[b]		0.3	0.3		*Shen et al.* (2000)

[a] All fault strikes, dips and rakes from *Li et al.* (2015d) unless otherwise indicated.
[b] Estimated from fault mapping in this study.
[c] Mean dip from range given by *Yu* (2004).
[d] Updated throw rate with ^{14}C dating preferred.
[e] Average of range.
[f] Summed throw rate, adding northeastern strand and antithetic fault.

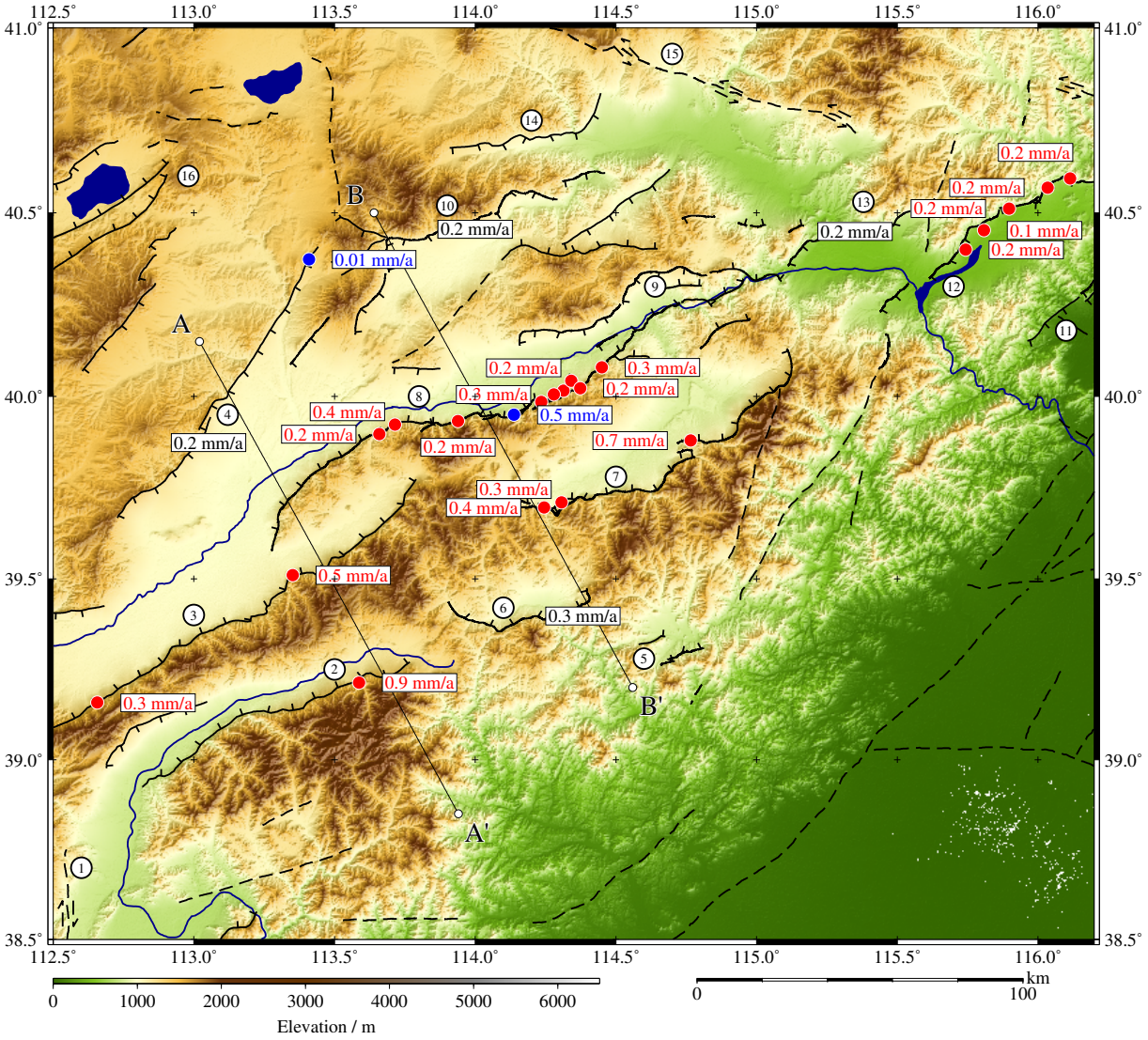


Figure 5.10: SRTM topography (30 m resolution) of the northern Shanxi Grabens (*Farr et al.*, 2007). Faults as shown in Figure 5.2. Blue circles (and numbers) indicate rates of horizontal extension measured in this study. Red circles (and numbers) indicate rates of horizontal extension measured by *Cheng et al.* (1995); *Xu et al.* (1997); *Cheng and Yang* (1998); *Jiang et al.* (2003); *Ding et al.* (2009); *Wang* (2012)—some labels have been omitted where they are similar to adjacent sites. Black labels are extension rates from *Yu* (2004) and *Deng et al.* (2007), where the location of the actual measurement site is unknown. Faults are numbered as follows: 1 Yunzhongshan Fault, 2 Wutaishan Fault, 3 Hengshan Fault, 4 Kouquan-Emokou Fault, 5 Laiyuan Graben Fault, 6 Lingqiu Graben Fault, 7 Yuguang Graben Fault, 8 Liulengshan Fault, 9 Yangyuan Graben Fault, 10 Yanggao-Tianzhen Graben Fault, 11 Nankou Fault, 12 Yanqing Fault, 13 Huailai Fault, 14 Huai'an Graben Fault, 15 Zhangjiakou-Bohai-Penglai Fault, 16 Daihai Graben Faults (see also Table 5.3).

Table 5.3 or Figure 5.10 because they are notably smaller than the errors introduced by uncertainties in fault dips—see below.

The total extension across the northern Shanxi Grabens can be found by summing extension rates across parallel faults. For example, along profile A-A′ in Figure 5.10

the total extension rate is ≈ 1.8 mm/a; along profile B-B′ the total extension rate is ≈ 1.1 mm/a. In general, there is a small decrease in extension rate on moving northeast through the region. For a 165 km wide zone (see Section 5.6.2), these extension rates correspond to strain rates of ≈ 11 nanostrain/a and ≈ 6.7 nanostrain/a respectively.

However, uncertainties in fault dips have a large effect on the magnitudes of these extension rates. Allowing for dip uncertainties of ±15° (approximately equivalent to the ranges quoted by *Yu* (2004)), we obtain extension rates of 0.7 to 3.3 mm/a along profile A-A′ and 0.6 to 2.0 mm/a along profile B-B′. In other words, the dip uncertainties can lead to a potential halving or doubling of the summed extension rates.

5.6 Strain rates from seismicity

5.6.1 Rate of moment release in the northern Shanxi Grabens

Figure 5.11 (a) shows the magnitudes of all 25 historical earthquakes with $M_w > 5$ in the northern Shanxi Grabens over the last 700 years (see also Table 5.2). No events with $M_w > 6$ have occurred since 1750. Figure 5.11 (b) shows 100, 200 and 300 year moving averages of the logarithm of the rate of moment release through time. There is a noticeable decrease in the rate of moment release (of around a hundred-fold, from 6.3×10^{17} Nm/a to 7.9×10^{15} Nm/a) in the northern Shanxi Grabens, starting at around 1750. More than 99% of the total moment release over the last 700 years occurred prior to 1750. This decrease is larger than the variations that can be accounted for with the errors of ±0.3 on the M_w values. The implications of this observation are discussed further in Section 5.8.

5.6.2 Kostrov summations

Figure 5.12 shows all of the earthquakes used for conducting Kostrov summations according to the methodology outlined in Section 5.4.4 and Appendix B.1. The full results are recorded in Table 5.4. The area of the region highlighted in Figure 5.12 is 64,076 km^2. We use a shear modulus (μ) of 3.3 GPa and a seismogenic thickness (T_s) of 20 km for all calculations unless otherwise stated. We choose $T_s = 20$ km as this was the value used by

Table 5.4: Summary of principal strain rate results from Kostrov summations in the northern Shanxi Grabens

Earthquakes used	Time years	No. eqs	Σ M_0 Nm	M_0 rate Nm/a	$\dot{\epsilon}_1$ a^{-1}	% change[a]	$\dot{\epsilon}_2^b$ a^{-1}	% change[a]	$\dot{\epsilon}_1$ az. °	% change[a]	$\dot{\epsilon}_1/\dot{\epsilon}_2$	% change[a]
All historical	700	25	2.7×10^{20}	3.9×10^{17}	4.1×10^{-9}	0	-1.9×10^{-9}	0	151	0	2.19	0
Strikes +15 °	700	25	2.7×10^{20}	3.9×10^{17}	4.1×10^{-9}	0	-1.9×10^{-9}	0	166	10	2.19	0
Strikes -15 °	700	25	2.7×10^{20}	3.9×10^{17}	4.1×10^{-9}	0	-1.9×10^{-9}	0	136	10	2.19	0
Dips +15 °	700	25	2.7×10^{20}	3.9×10^{17}	3.5×10^{-9}	-14	-2.4×10^{-9}	25	154	2	1.50	-32
Dips -15 °	700	25	2.7×10^{20}	3.9×10^{17}	4.1×10^{-9}	0	-1.4×10^{-9}	-25	148	-2	2.94	34
Rakes +15 °	700	25	2.7×10^{20}	3.9×10^{17}	4.2×10^{-9}	0	-1.3×10^{-9}	-30	143	-5	3.13	43
Rakes -15 °	700	25	2.7×10^{20}	3.9×10^{17}	4.0×10^{-9}	-3	-2.5×10^{-9}	31	157	4	1.62	-26
M_w +0.3	700	25	7.3×10^{20}	1.1×10^{18}	1.1×10^{-8}	168	-5.1×10^{-9}	172	150	-1	2.16	-1
M_w -0.3	700	25	9.2×10^{19}	1.3×10^{17}	1.4×10^{-9}	-66	-6.5×10^{-10}	-66	150	-1	2.15	-2
T_s = 10 km[c]	700	25	2.7×10^{20}	3.9×10^{17}	8.3×10^{-9}	100	-3.8×10^{-9}	99	151	0	2.20	0
T_s = 15 km[c]	700	25	2.7×10^{20}	3.9×10^{17}	5.5×10^{-9}	33	-2.5×10^{-9}	33	151	0	2.19	0
T_s = 22 km[c]	700	25	2.7×10^{20}	3.9×10^{17}	3.8×10^{-9}	-9	-1.7×10^{-9}	-9	151	0	2.19	0
Pre 1750	435	16	2.7×10^{20}	6.3×10^{17}	6.6×10^{-9}	60	-3.0×10^{-9}	60	151	0	2.19	0
Post 1750	265	9	2.1×10^{18}	7.9×10^{15}	7.9×10^{-11}	98	-2.9×10^{-11}	98	162	7	2.70	23
All historical	700	25	2.7×10^{20}	3.9×10^{17}	4.1×10^{-9}	0	-1.9×10^{-9}	0	151	0	2.19	0
(*Wesnousky et al.*, 1984)	700	2	2.2×10^{20}	3.2×10^{17}	3.6×10^{-9}	-12	-1.9×10^{-9}	0	151	0	1.92	-12
Historical minus Wesnousky	700	23	5.1×10^{19}	7.3×10^{16}	5.2×10^{-10}	-87	-2.1×10^{-12}	-100	145	-4	245.07	11088
(*Li et al.*, 2015a)	50	36	1.5×10^{18}	3.0×10^{16}	3.4×10^{-10}	-92	-3.1×10^{-10}	-84	155	3	1.09	-50
(*Li et al.*, 2015a) M > 5	50	6	1.4×10^{18}	2.9×10^{16}	3.3×10^{-10}	-92	-3.0×10^{-10}	-84	155	3	1.07	-51
GPS	6	N/A	N/A	7.3×10^{17}	7.9×10^{-9}	N/A	-2.3×10^{-9}	N/A	144	N/A	3.46	N/A

[a] Compared to all historical earthquakes (first line of table).
[b] Negative principal strain rate indicates shortening.
[c] T_s is seismogenic thickness i.e. thickness of Kostrov volume.

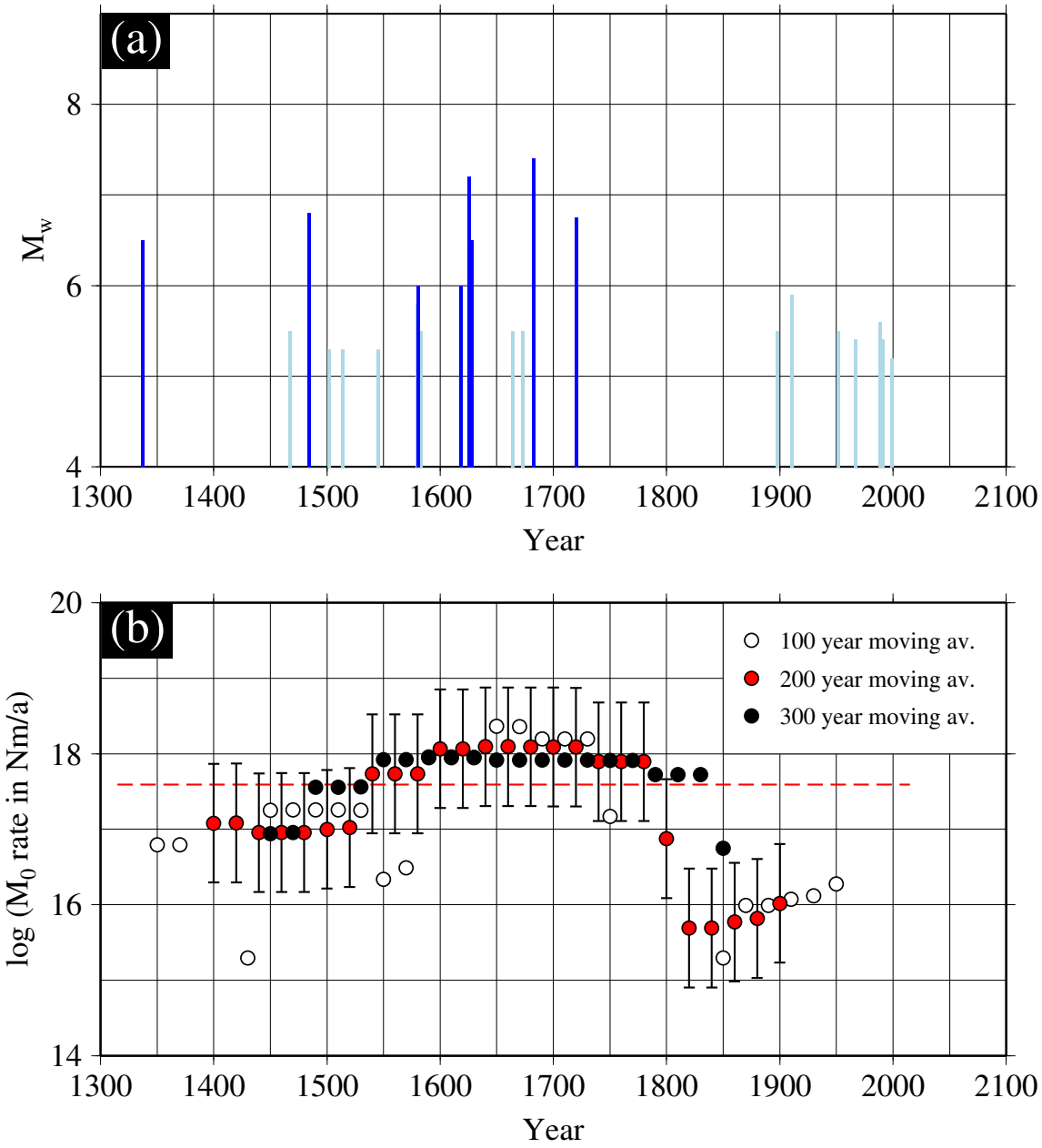


Figure 5.11: (a) Plot of magnitude (M_w) against time for historical earthquakes with $M_w > 5$ in the northern Shanxi Grabens over the last 700 years. Earthquakes with $M_w \geq 6.0$ are shown in darker blue. (b) Moving averages of the log of the seismic moment rate (in Nm/a) for the last 700 years, calculated every 20 years. White dots show 100 year moving average; red dots show 200 year moving average; black dots show 300 year moving average. Error bars, based on the assumption that values of M_w are known to the nearest ± 0.3 magnitude units, are shown for the 200 year moving average. Dashed red line shows the log of the average M_0 rate (log $(3.9 \times 10^{17}) = 17.6$) for the whole 700 year period, from 1315 to 2015.

Wesnousky et al. (1984) and because the epicentres of recent earthquakes do not exceed a depth of 22 km (*Li et al.*, 2015b).

The result of the Kostrov summation for our catalogue of 25 historical earthquakes is a maximum principal extensional strain rate ($\dot{\epsilon}_1$) of 4.1 nanostrain/a at an azimuth

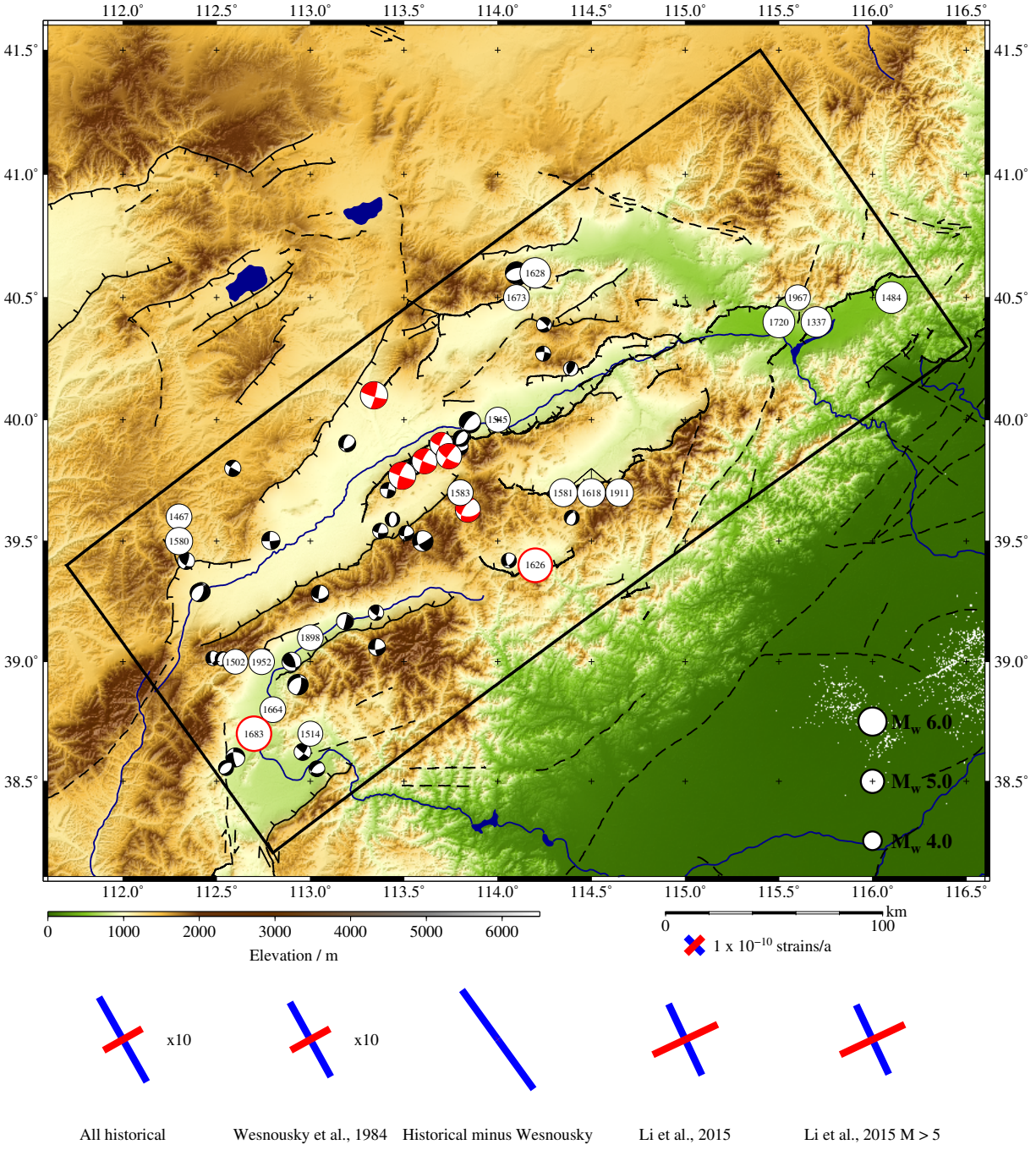


Figure 5.12: SRTM topography (30 m resolution) of the northern Shanxi Grabens (*Farr et al.*, 2007). Faults as shown in Figure 5.2. The black rectangle indicates the approximately 164 km by 390 km region included in the Kostrov volume. Historical earthquakes occurring in the volume are shown as white circles scaled according to their magnitude and including the year in which they occurred (*Lee et al.*, 1976; *Liu et al.*, 2011)—see Table 5.2 for details. The two earthquakes ringed in red are the ones used by *Wesnousky et al.* (1984) in their Kostrov summation. Focal mechanisms are from *Li et al.* (2015a); mechanisms for earthquakes with M > 5 are shown in red. Strain rate crosses below the map show the results of Kostrov summations for (from left to right): all of the historical earthquakes with known focal parameters; the two earthquakes used by *Wesnousky et al.* (1984); all of the historical earthquakes with known focal parameters except the two used by *Wesnousky et al.* (1984); all of the mechanisms from *Li et al.* (2015a); and all of the mechanisms with M > 5 from *Li et al.* (2015a). Note that the first two strain rate crosses are displayed at one tenth of their real size. See Table 5.4 for further details.

of 151° and a minimum principal strain rate ($\dot{\epsilon}_2$) of -1.9 nanostrain/a perpendicular to the maximum principal strain rate (see left-hand strain rate cross in Figure 5.12). The width of the Kostrov volume at an azimuth of 151° is ≈ 165 km, giving a historical seismic extension rate across the northern Shanxi Grabens of 0.7 mm/a. The negative value of the minimum principal strain rate indicates shortening, suggesting that as well as the extension there must be a component of right-lateral motion on approximately northeast-southwest striking faults or a component of left-lateral motion on approximately northwest-southeast striking faults. Given the observed strike of faults within the zone (approximately northeast-southwest) and previously recorded right-lateral displacements (*Deng et al.*, 2007), we suggest that right-lateral motion is most likely.

We now investigate how sensitive the Kostrov summation is to variations in the input parameters (see Table 5.4 for full details). *Wesnousky et al.* (1984) suggested typical uncertainties in their focal parameters of ±15°. Varying the fault strikes by ±15° does not alter the magnitudes of the principal strain rates, but changes their azimuth by 10%. Varying the fault dips by ±15° changes the magnitudes of the principal strain rates by up to 25%, but only changes their azimuth by about 2%. Similarly, varying the rakes by ±15° changes the magnitudes of the principal strain rates by up to 31%, but only changes their azimuth by up to 5%.

Altering the values of M_w has a more significant effect. Varying M_w by ±0.3 magnitude units changes the magnitudes of the principal strain rates by up to 172%. For example, if all earthquakes were 0.3 magnitude units larger, then the maximum principal extensional strain rate ($\dot{\epsilon}_1$) would be 11.1 nanostrain/a, corresponding to a seismic extension rate of 1.8 mm/a; if all earthquakes were 0.3 magnitude units smaller the maximum principal extensional strain rate ($\dot{\epsilon}_1$) would be 1.4 nanostrain/a, corresponding to a seismic extension rate of 0.2 mm/a. However, varying M_w by ±0.3 magnitude units only changes the azimuth of the maximum principal extensional strain rate by 1%.

Seismogenic thickness is inversely proportional (in a linear sense) to the magnitudes of the principal strain rates and has no influence on their azimuths. However, T_s is not likely to be wrong by more than ±10 km, so it is a less important influence on the magnitudes of the principal strain rates than M_w. In general, the uncertainties in M_w are

the major potential source of error in our estimated strain rates, although the azimuth of maximum principal extensional strain rate is largely insensitive to variations in all of the input parameters.

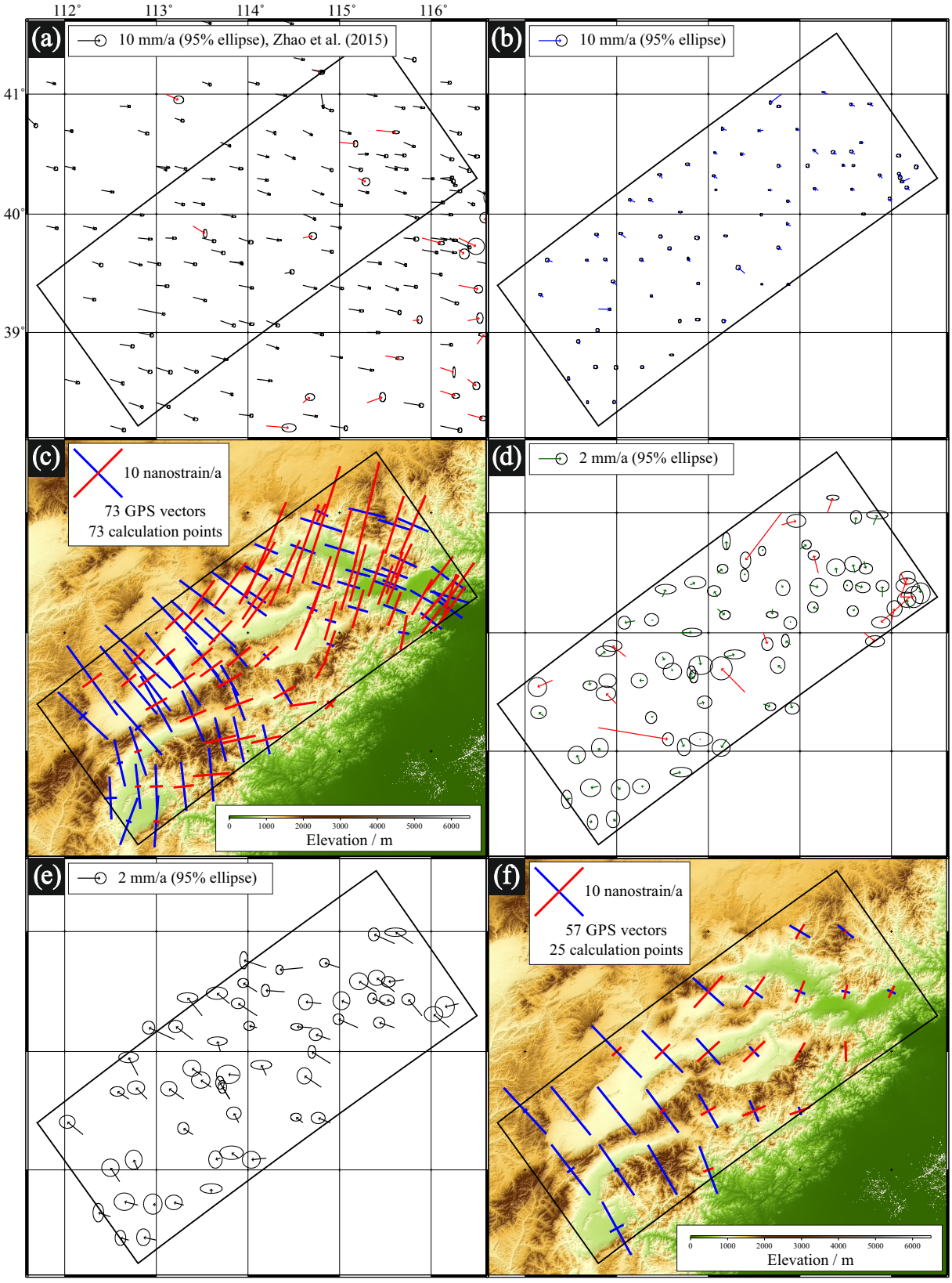
Finally, given the observation in Section 5.6.1 that the moment rate likely dropped significantly after 1750, we calculate pre-1750 and post-1750 summations. Prior to 1750 the maximum principal extensional strain rate ($\dot{\epsilon}_1$) is 6.6 nanostrain/a, corresponding to a seismic extension rate of 1.1 mm/a; after 1750 the maximum principal extensional strain rate ($\dot{\epsilon}_1$) is 0.08 nanostrain/a, corresponding to a seismic extension rate of 0.01 mm/a. (Allowing for the $\pm$0.3 errors in M_w, the pre-1750 extension rate could vary between 0.4 and 3.1 mm/a.)

The majority of the strain rate we measure is contributed by the 1626 and 1683 earthquakes, as shown by *Wesnousky et al.* (1984); together these two events account for 81% of the total moment release during the 700 years of observation (see second strain rate cross in Figure 5.12). When these two events are removed from the summation (see third strain rate cross in Figure 5.12), both principal strain rates are an order of magnitude smaller but $\dot{\epsilon}_2$ drops most significantly leaving effectively pure extension at an azimuth of 145 °.

The events in the *Li et al.* (2015d) catalogue represent 0.5% of the moment release of the historical catalogue (and the majority of this is accounted for by the 6 events that have M> 5) and hence yield significantly smaller magnitudes for the principal strain rates. The resulting strain rate crosses (see fourth and fifth strain rate crosses in Figure 5.12) also indicate a greater component of strike-slip motion; $\dot{\epsilon}_1/\dot{\epsilon}_2$ changes from 2.2 to nearly 1. However, the azimuth of the maximum principal extensional strain rate (155 °) is remarkably consistent with that from the historical catalogue (151 °).

5.7 Strain rate field from GPS

Figure 5.13 illustrates the different stages in the derivation of a continuous strain rate field from the campaign GPS data of *Zhao et al.* (2015). A number of observations can be made about the final strain rate field (see Figure 5.13 (f)). The mean principal strain


112°
113°
114°
115°
116°
41°
40°
39°
(a)
10 mm/a (95% ellipse), Zhao et al. (2015)
(b)
10 mm/a (95% ellipse)
(c)
10 nanostrain/a
73 GPS vectors
73 calculation points
0 1000 2000 3000 4000 5000 6000
Elevation / m
(d)
2 mm/a (95% ellipse)
(e)
2 mm/a (95% ellipse)
(f)
10 nanostrain/a
57 GPS vectors
25 calculation points
0 1000 2000 3000 4000 5000 6000
Elevation / m

rates ($\dot{\epsilon}_1$ and $\dot{\epsilon}_2$) are 7.9 nanostrain/a and -2.3 nanostrain/a. The maximum principal extensional strain rate is at a mean azimuth of 144 ° and corresponds to a geodetic extension rate of ≈ 1.3 mm/a. These results are similar to the strain rate tensors derived from Kostrov summations—particularly the pre-1750 calculation. However, the GPS-derived strain rate field also highlights variations within the Kostrov volume. In the southwest, the strain is almost entirely extensional: the mean of the maximum principal extensional strain rate ($\dot{\epsilon}_1$) is 8.6 nanostrain/a, corresponding to a geodetic extension rate of 1.4 mm/a. The mean azimuth of the maximum principal extensional strain rate is still 144 °. In the northeast, however, the motion becomes almost entirely strike-slip and the mean of the maximum principal extensional strain rate ($\dot{\epsilon}_1$) reduces to 2.5 nanostrain/a at an azimuth of 126 ° (corresponding to a geodetic extension rate of ≈ 0.4 mm/a). The strike-slip motion in the northeast could be accommodated by right-lateral slip on approximately north-south faults (perhaps via oblique right-lateral slip on the northeast trending normal faults) or left-lateral slip on approximately east-west faults (perhaps on the Zhangjiakou-Bohai-Penglai fault system). Furthermore, the second invariant of the strain rate tensor decreases by about an order of magnitude from the southwest to the northeast (see Figure 5.14 (a)). These variations within the Kostrov volume are in good agreement with geological estimates of total extension, which are greater in the southwest (≈ 8 km) than the northeast (≈ 1.5 km) (*Xu and Ma*, 1992).

Figure 5.13 ***(preceding page)*:** (a) GPS data from *Zhao et al.* (2015) relative to stable Eurasia. Red vectors indicate stations where northerly or easterly error is ≥ 0.5 mm/a and are not used in subsequent calculations. Black box indicates region of interest (same as Kostrov volume). 78 stations lie within this region, of which 73 have errors < 0.5 mm/a. (b) GPS data with best-fitting rigid body rotation subtracted. Best-fitting rotation is about a pole at 30 °N, 53 °W. (c) Strain rate field calculated from GPS at each GPS station, using $\alpha = 80$ km and $r_{max} = 200$ km. Crosses indicate orientation and magnitude of maximum and minimum horizontal strain rate; blue indicates extension and red indicates contraction. (d) Residual vectors obtained when velocities from inversion in (c) are subtracted from the original data in (b). Red vectors indicate stations with residuals ≥ 1 mm/a. 57 stations have residuals < 1 mm/a. Note different scale to panels (a) and (b). (e) Remaining 57 vectors from (b), with the best-fitting rigid body rotation removed, that are used in the final strain rate calculation. Again, note different scale to panels (a) and (b). (f) Strain rate field calculated on a regular grid including 25 nodes within the region of interest. Again, $\alpha = 80$ km and $r_{max} = 200$ km. Blue and red bars as above.

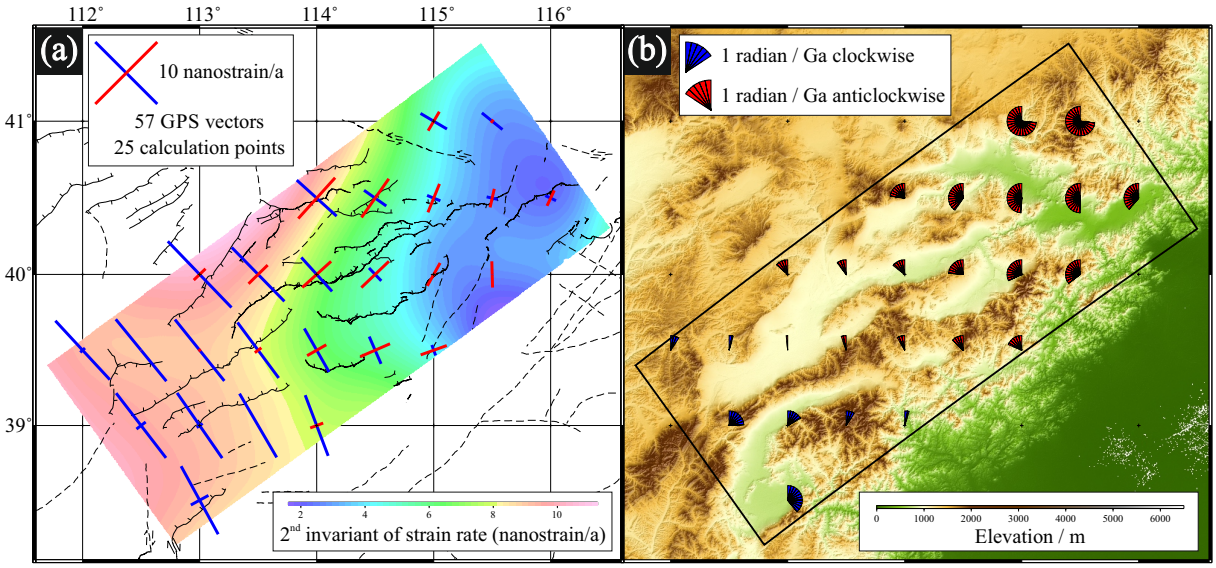


Figure 5.14: (a) Second invariant $\left(\dot{E} = (\dot{\epsilon}_{ij}\dot{\epsilon}_{ij})^{\frac{1}{2}}\right)$ of the derived strain rate field within the polygon of interest. Crosses indicate orientation and magnitude of maximum and minimum horizontal strain rate; blue indicates extension and red indicates contraction. (b) Rotation rates $\left(\dot{\omega}_{xy} = \frac{1}{2}\left(\frac{\partial V_x}{\partial y} - \frac{\partial V_y}{\partial x}\right)\right)$ of the velocity gradient field derived from the GPS data of *Zhao et al.* (2015), where wedges represent the rotation rate multiplied by 1 Ga (1 radian / Ga = 0.57 ° / 10 Ma). Blue wedges show clockwise rotation rates; red wedges show anticlockwise rotation rates.

The rotation rates within the northern Shanxi Grabens predicted by the strain rate field are very small (see Figure 5.14 (b)—rotations are shown for a period of 1 Ga so that they are large enough to be seen). Since the earliest extension in the northern Shanxi Grabens occurred in the Miocene (at most 23 Ma ago), if we assume constant rates through time, then the total expected rotation within the region of interest is typically about 1 ° and at most 6 ° (in an anticlockwise sense). Such small rotations are unlikely to be resolvable in palaeomagnetic studies. Although some data from the northern Shanxi Grabens exist (*Xu et al.*, 1994), they are not of a sufficiently high accuracy to test these predicted rotations.

Figure 5.15 shows swath profiles through the GPS data in the southwestern portion of the northern Shanxi Grabens. Vectors with northerly or easterly errors of more than 0.5 mm/a are not included in the profiles. Profile X-X′ at an azimuth of 150 ° (parallel to the maximum principal extensional strain rate direction and perpendicular to the main active normal faults) yields an extension rate of 1.1±1.1 mm/a, which is consistent with the rate obtained from the smoothly varying strain rate field. However, profile Y-

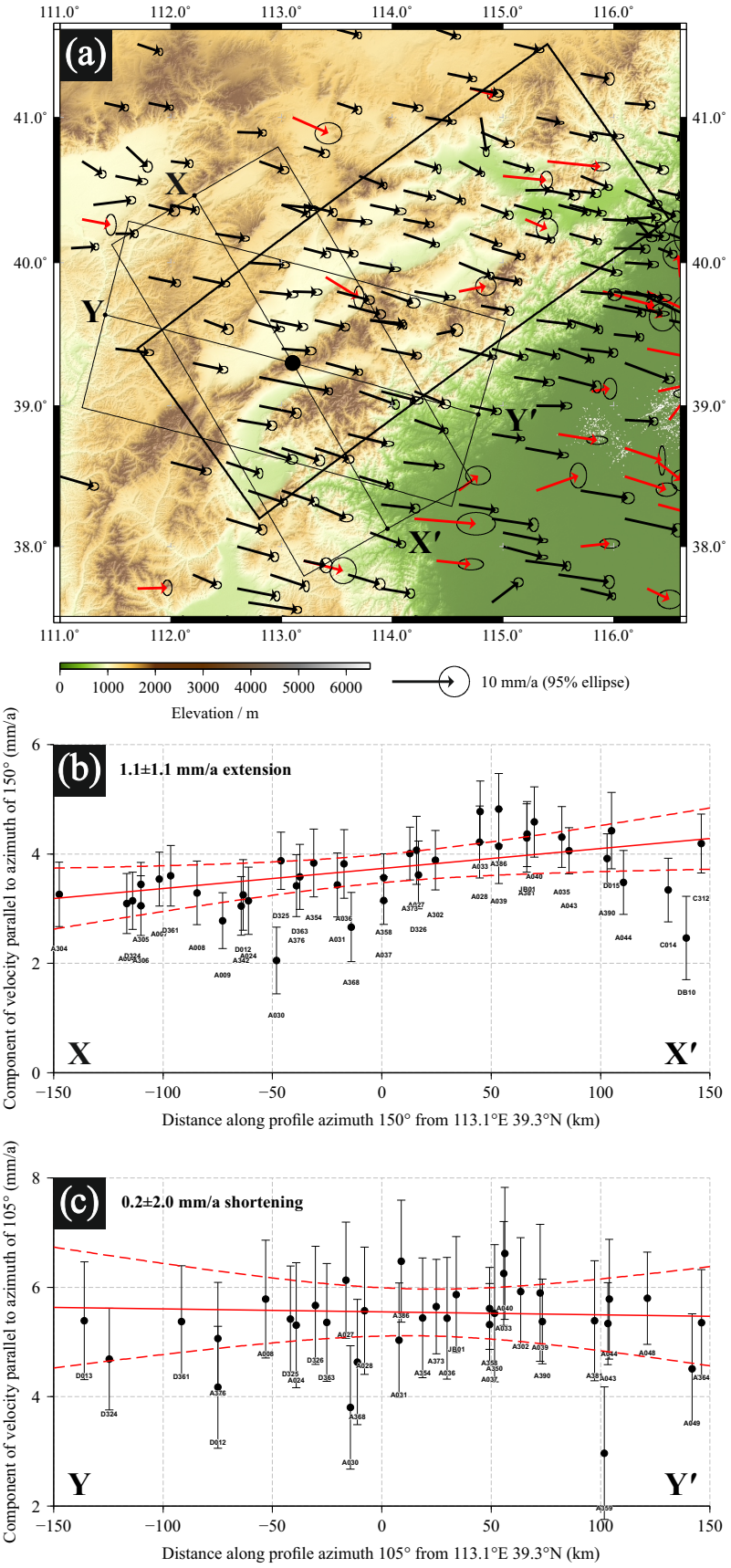


Figure 5.15: (a) GPS data from *Zhao et al.* (2015) relative to stable Eurasia (no rigid body rotation removed). Red vectors indicate stations where northerly or easterly error is ≥ 0.5 mm/a. Black box indicates Kostrov volume. (b) 150 km wide swath profile X-X′ through the GPS data in the southwestern part of the Kostrov volume at an azimuth of 150 °. Profile shows 1.1±1.1 mm/a extension. (c) 150 km wide swath profile Y-Y′ through the GPS data at an azimuth of 105 °. When the profile is drawn at this azimuth, no extension is observed (*He et al.*, 2003, 2004).

Y′ at an azimuth of 105° (the azimuth used by *He et al.* (2003) and *He et al.* (2004), and roughly parallel to the observed velocity vectors) shows significant scatter and no observable extension. We therefore infer that *He et al.* (2003) and *He et al.* (2004) were not able to observe extension in the northern Shanxi Grabens because their profiles were drawn parallel to the observed velocity vectors rather than parallel to the azimuth of the maximum principal extensional strain rate. Furthermore, their profiles were not drawn perpendicular to the main active normal faults.

5.8 Discussion

5.8.1 Earthquake recurrence times from geodetic strain rates

The geodetic moment rate ($\dot{M}_0$) for a strain rate of $|\dot{\epsilon}_{ij}|$ is given by (see Appendix B.3):

$$\dot{M}_0 = \frac{M_{tot}}{\tau} = 2\mu V|\dot{\epsilon}_{ij}| \tag{5.10}$$

where M_{tot} is the total seismic moment released in the time period τ, μ is the shear modulus, and V is the volume of crust under consideration.

We assume that the strain in the southwestern part of the northern Shanxi Grabens can be treated as biaxial (i.e. extension is matched purely by vertical thinning). The mean maximum principal extensional strain rate from GPS is 8.6 nanostrain/a at an azimuth of 144°. We therefore obtain a geodetic moment rate of 7.3×10^{17} Nm/a. For comparison, the Kostrov summation over the last 700 years gives a seismic moment rate of 3.9×10^{17} Nm/a. However, the Kostrov summation for the 435 years prior to 1750 gives a seismic moment rate of 6.3×10^{17} Nm/a. In other words, the seismic moment rate prior to 1750 agrees well with the present-day geodetic moment rate—see Section 5.8.2.

The recurrence interval (T) for earthquakes of scalar seismic moment $\geq M$ is then given by (see Appendix B.3):

$$T(M) = \frac{\beta M_{max}^{1-\beta} M^{\beta}}{\dot{M}_0 (1-\beta)} \tag{5.11}$$

where M_{max} is the scalar seismic moment of the largest earthquake expected in the region and β is the constant in the Gutenberg-Richter moment-frequency relationship. Using the usual β value of $\frac{2}{3}$ and the maximum observed scalar seismic moment of 1.42×10^{20} Nm (M_w 7.4) for the 1683 earthquake (see Table 5.2), we find a recurrence interval for earthquakes $\geq M$ 7.0 of 154 years, and a recurrence interval for earthquakes $\geq M$ 6.0 of 15 years. However, these recurrence intervals depend heavily on the value of M_{max}. For example, with $M_{max} = 1 \times 10^{21}$ Nm ($\approx M_w$ 8), we obtain recurrence intervals of 296 years and 30 years respectively.

5.8.2 Comparing magnitudes of strain

Our best estimates for the extension rate across the northern Shanxi Grabens from all three methods—geology, seismicity and geodesy—are in good agreement. From Quaternary geology, we obtain rates of $\approx$ 1.8 mm/a and $\approx$ 1.1 mm/a for two possible profiles across the region—although the uncertainties in fault dips could either halve or double these summed rates. From Kostrov's relation and our catalogue of historical earthquakes we obtain a seismic extension rate of $\approx$ 0.7 mm/a. The major contribution to the uncertainty in this case is the earthquake magnitude errors of $\pm$0.3, leading to a seismic extension rate of between 0.2 and 1.8 mm/a. We also note that the 0.7 mm/a extension can be sub-divided into a pre-1750 rate of $\approx$ 1.1 mm/a and a post-1750 rate of $\approx$ 0.01 mm/a. Finally, from the GPS-derived continuous strain rate field, we obtain an extension rate of 1.4 mm/a, diminishing to 0.4 mm/a in the northeastern part of the region.

All three methods of strain measurement agree to within error—although the errors are large. Nonetheless, there is reasonable consensus that the extension rate is of the order of 1 to 2 mm/a. Given the different timescales of these measurements (tens of thousands of years, hundreds of years, and years respectively) we therefore propose that there have not been any resolvable changes in the extension rate across the northern Shanxi Grabens over the Late Quaternary. The notable exception is that the post-1750 Kostrov summation obtains an extension rate that is two orders of magnitude smaller

than the suggested Late Quaternary rate of 1 to 2 mm/a—well beyond even the large error bounds. We therefore conclude that the current rate of seismic strain release does not match either the geological or geodetic strain rates.

There are three possible explanations for this present-day seismic strain rate deficit. One possibility, suggested by *Stein et al.* (2009) and *Liu et al.* (2011), is that the tectonic loading in northern China is shared by a complex system of interacting faults spread over hundreds of kilometres; clusters of earthquakes may therefore oscillate between the Shanxi Grabens, the Weihe Graben and the North China Plain. However, if this is the case it is unclear why, beyond coincidence, the pre-1750 Kostrov summation should agree so well with the geological and geodetic rates. A second possibility is that strain in the northern Shanxi Grabens is currently being accommodated aseismically—although no field observations of fault creep are reported in the literature. Finally, the discrepancy could suggest that the post-1750 Kostrov summation does not span a long enough time interval (i.e. it is shorter than the typical recurrence interval for large earthquakes) and hence we expect large earthquakes to occur in the relatively near future.

The deficit in the post-1750 Kostrov summation (compared to the estimated rate of moment release from the GPS) is 1.9×10^{20} Nm over the last 265 years (between 1750 and 2015), which is equivalent to a single M_w 7.5 earthquake. The calculations in Section 5.8.1 suggest that the recurrence interval for earthquakes $\geq M$ 6.0 should be of the order of a few decades, whilst the recurrence interval for earthquakes $\geq M$ 7.0 could be centuries. There have been no earthquakes $\geq M$ 6.0 since 1750. Hence it is conceivable that the deficit may be accommodated by a single $\approx M_w$ 7.5 earthquake (or a cluster of slightly smaller events) in the future. Such an earthquake would require a fault length on the order of 150 km, but suitable faults do exist in the northern Shanxi Grabens—such as the Hengshan, Kouquan-Emokou and Liulengshan Faults—and $> M_w$ 7.5 earthquakes have occurred at other margins of the Ordos Plateau—such as the 1556 Huaxian event and the 1739 Yinchuan event (see Chapter 2 and *Zhou* (2016)).

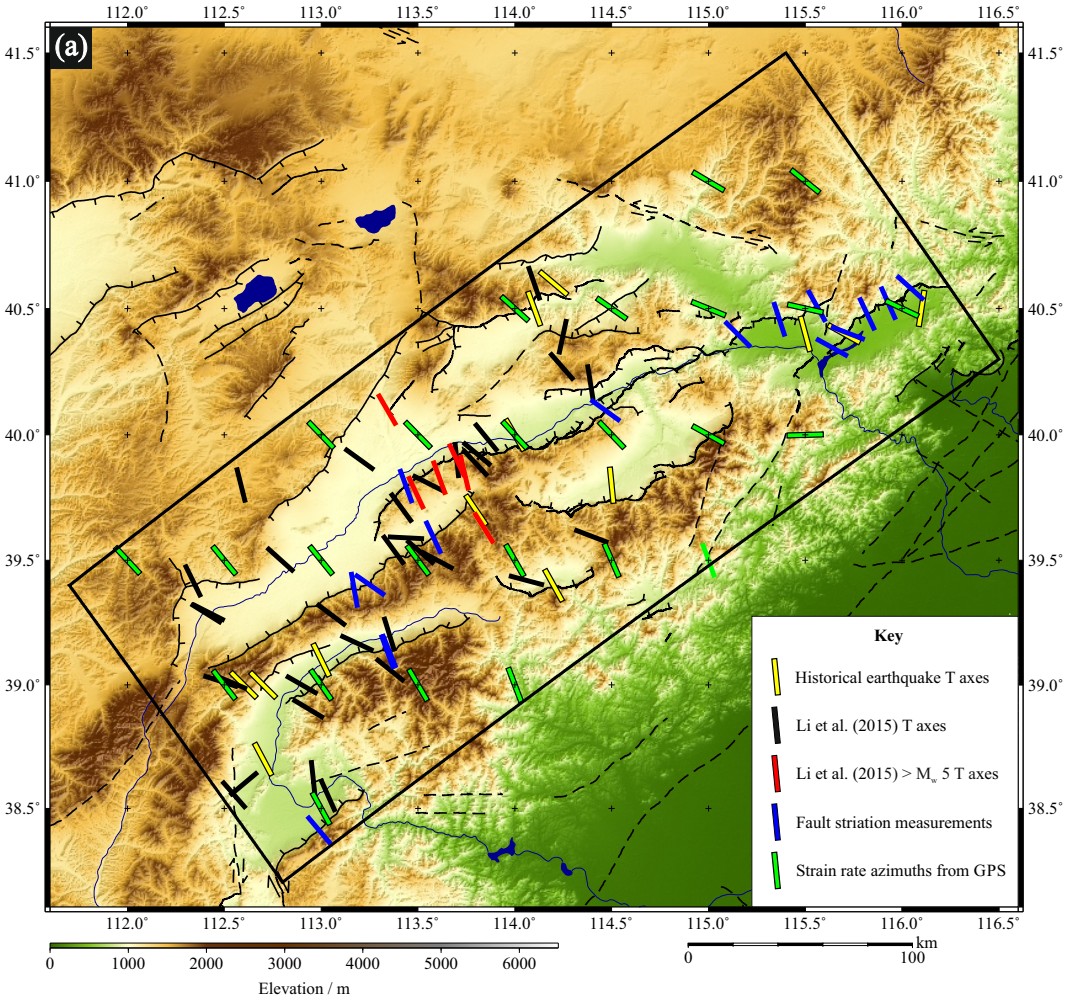
Finally, we note that both the geological and geodetic observations indicate a southwestward increase in the extension rate. It also appears that the extension is accommodated on fewer, larger structures in the southwest of the region. This implies that the

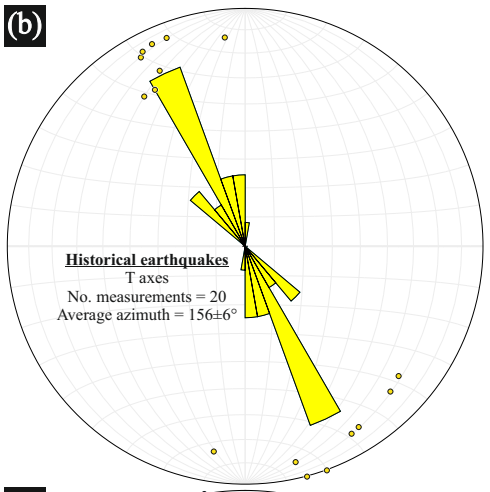
Wutaishan and Hengshan Faults are potentially the fastest slipping faults in the northern Shanxi Grabens; further Quaternary dating and palaeoseismological work on these two faults would therefore be valuable.

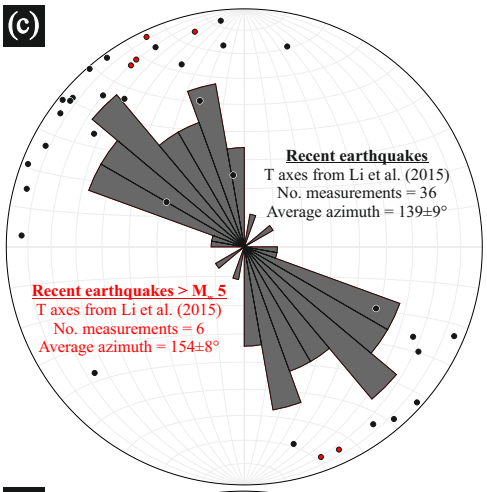
5.8.3 Comparing patterns of strain

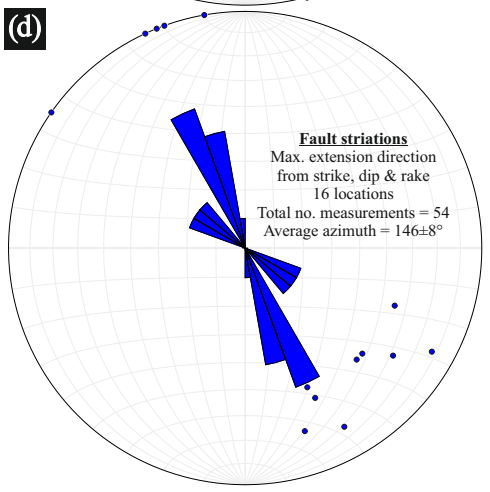
The pattern of strain revealed by the geological, seismic and geodetic observations is consistent. Figure 5.16 shows principal extension directions from fault striation measurements, T axes of historical and recent earthquakes, and maximum principal extensional strain rate azimuths from the GPS. (We calculate the equivalent of a T axis from the measured strikes, dips and rakes of fault striations on fault plane surfaces, as this is more directly comparable to the other data than the striation azimuth, which could be up to 45 ° away from the T axis direction in the case of highly oblique slip. A summary of the striation data is also given in Table 5.5.) The average azimuth of maximum extension from these different types of measurement varies between 135±6 ° and 156±6 °. Furthermore, the maximum principal extensional strain rate azimuth from GPS is biased by grid nodes to the northeast of the region, which are given equal weighting even though rates of deformation are known to be significantly slower in this part of northern Shanxi; the average maximum principal extensional strain rate azimuth in the southwestern part of the region is 144 °. Note too that the average T axis azimuth for the historical earthquakes (156 °) is different to the azimuth of maximum principal extensional strain rate from the Kostrov summation for historical earthquakes (151 °) because in the Kostrov summation the contribution of each earthquake is weighted by its magnitude.

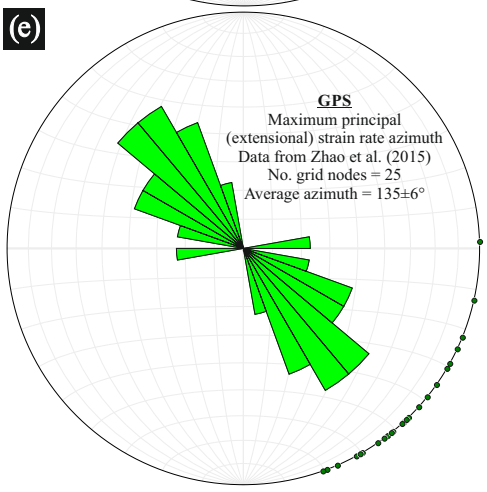
In addition, there is good agreement in the pattern of strain amongst the different Kostrov summations (see Table 5.4). Varying the input parameters within their suggested error bounds does not change the maximum principal extensional strain rate azimuth by more than ±15 °. Furthermore, the use of different earthquake catalogues does not change the maximum principal extensional strain rate azimuth by more than 4 °. Despite the fact that the events in the *Li et al.* (2015d) catalogue represent 0.5% of the moment release of the historical catalogue and that they cover only 50 years as opposed to 700 years


(a)
112.0° 112.5° 113.0° 113.5° 114.0° 114.5° 115.0° 115.5° 116.0° 116.5°
41.5° 41.0° 40.5° 40.0° 39.5° 39.0° 38.5°
Key
Historical earthquake T axes
Li et al. (2015) T axes
Li et al. (2015) > M$_w$ 5 T axes
Fault striation measurements
Strain rate azimuths from GPS
0 1000 2000 3000 4000 5000 6000
Elevation / m
0 100 km


(b)
Historical earthquakes
T axes
No. measurements = 20
Average azimuth = 156±6°


(c)
Recent earthquakes
T axes from Li et al. (2015)
No. measurements = 36
Average azimuth = 139±9°
Recent earthquakes > M$_w$ 5
T axes from Li et al. (2015)
No. measurements = 6
Average azimuth = 154±8°


(d)
Fault striations
Max. extension direction
from strike, dip & rake
16 locations
Total no. measurements = 54
Average azimuth = 146±8°


(e)
GPS
Maximum principal
(extensional) strain rate azimuth
Data from Zhao et al. (2015)
No. grid nodes = 25
Average azimuth = 135±6°

of activity, the predicted style of deformation is almost identical. This corroborates the suggestion by *Ekström and England* (1989) that patterns of strain from seismic observations can be reliably extrapolated from small earthquake catalogues covering relatively short time periods—perhaps even as little as a decade, and certainly much less than the average recurrence interval for the largest earthquakes in the region (which we estimate in Section 5.8.1 to be more than a century).

The average fault strike in the northern Shanxi region is $\approx 239^\circ$ (the mean of the values given in Table 5.3). Normal faults at this azimuth are therefore optimally oriented to accommodate extension at an azimuth of 149°. This is in good agreement with all of the above methods for estimating the extension azimuth. Hence it may be possible, if the type of faulting is known, to accurately predict the orientation of the faults in a deforming continental region from geodetic measurements alone. We note, though, that these normal faults are also accommodating smaller amounts of right-lateral motion.

Figure 5.16 ***(preceding page)*:** (a) SRTM topography (30 m resolution) of the northern Shanxi Grabens (*Farr et al.*, 2007). Faults, marked as thin black lines, have been mapped from satellite imagery (source: http://earth.google.com) based upon earlier fault maps from *Tapponnier and Molnar* (1977), *Xu and Ma* (1992), *Yu* (2004) and *Deng et al.* (2007). The black rectangle indicates the region included in the Kostrov volume. T axes from historical earthquakes and *Li et al.* (2015a) are shown in yellow, black and red. Extension azimuths calculated from fault striation measurements are shown in blue—see Table 5.5. Maximum principal (extensional) strain rate azimuths from GPS are shown in green. (b) Rose diagram and lower hemisphere stereoplot of T axes from historical earthquakes. (c) Rose diagram and lower hemisphere stereoplot of T axes from *Li et al.* (2015a). (d) Rose diagram and lower hemisphere stereoplot of extension azimuths from field-based fault striation measurements. (e) Rose diagram of maximum principal (extensional) strain rate azimuths from GPS data of *Zhao et al.* (2015). (Errors on average azimuths refer to 95% confidence limits for a best fitting Fisher mean vector.)

Table 5.5: Azimuths of maximum extension estimated from fault striations in the northern Shanxi Grabens

Latitude °	Longitude °	No. measurements	Extension azimuth[a] °	Plunge °	Fault name	Reference
39.382	113.171	6	350	0[b]	Hengshan Fault	(*Zhang et al.*, 2003b)
39.402	113.251	7	305	0[b]	Hengshan Fault	(*Zhang et al.*, 2003b)
39.134	113.342	6	340	0[b]	Wutaishan Fault	(*Zhang et al.*, 2003b)
39.135	113.347	5	340	0[b]	Wutaishan Fault	(*Zhang et al.*, 2003b)
39.136	113.351	3	338	0[b]	Wutaishan Fault	(*Zhang et al.*, 2003b)
39.797	113.438	7	340	0[b]	Liulengshan Fault	(*Zhang et al.*, 2003b)
39.592	113.579	6	335	0[b]	Hengshan Fault	(*Zhang et al.*, 2003b)
40.097	114.468	6	126	24	Liulengshan Fault	This study
40.398	115.152	1	135	34	Huailai Fault	(*Pavlides et al.*, 1999)
40.458	115.366	1	162	20	Huailai Fault	(*Pavlides et al.*, 1999)
40.510	115.559	1	151	15	Huailai Fault	(*Pavlides et al.*, 1999)
40.346	115.638	1	119	11	Yanqing Fault	(*Pavlides et al.*, 1999)
40.403	115.720	1	111	33	Yanqing Fault	(*Pavlides et al.*, 1999)
40.479	115.819	1	155	31	Yanqing Fault	(*Pavlides et al.*, 1999)
40.521	115.929	1	156	36	Yanqing Fault	(*Pavlides et al.*, 1999)
40.581	116.043	1	132	34	Yanqing Fault	(*Pavlides et al.*, 1999)

[a] Extension azimuth determined by finding the orientation of the T axis for a given set of strike, dip and rake measurements.
[b] *Zhang et al.* (2003b) do not give plunge of T axis in their paper.

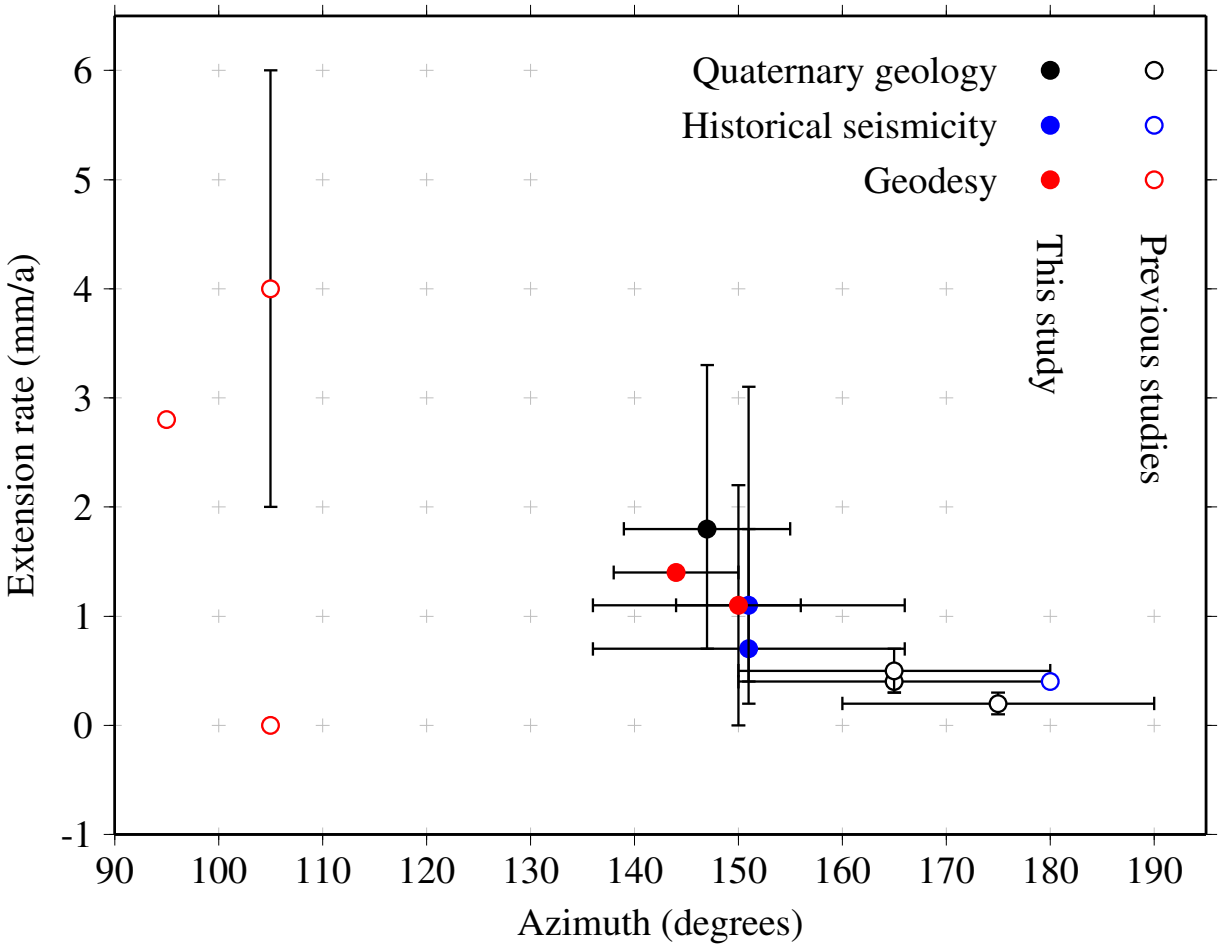


Figure 5.17: Scatter plot of summed extension rate across the northern Shanxi Grabens against azimuth of extension for different timescales of observation. Black circles are measurements from Quaternary geology; blue circles are measurements from seismicity; red circles are measurements from GPS. Error bars are plotted where uncertainties are quantified. Open circles are from previous studies (*Wesnousky et al.*, 1984; *Zhang et al.*, 1998; *Shen et al.*, 2000; *He et al.*, 2003; *Qu et al.*, 2014); filled circles are from analyses in this study.

5.9 Conclusions

On the basis of our three approaches we conclude that the northern Shanxi Grabens are extending. We find good agreement between Quaternary, seismic and geodetic rates of strain, and we find that the northern Shanxi Grabens are extending at around 1 to 2 mm/a at an azimuth of $\approx 151\,^{\circ}$. Figure 5.17 illustrates how the previously discrepant strain measurements have largely been reconciled in this study. The azimuth of extension is particularly well constrained and can be reliably inferred from catalogues of small earthquakes. We do not find evidence for any substantial variations in extension rate through time. However, there is a notable seismic strain rate deficit since 1750 that is

equivalent in size to a single $\approx$ M_w 7.5 earthquake. This could indicate complex fault interactions across large regions, aseismic accommodation of deformation, or that larger earthquakes are likely in the relatively near future.

Chapter 6

Kinematics of the Ordos Plateau

In this chapter we summarise the active tectonics of the Ordos Plateau, incorporating our results from the foregoing chapters into an overall view. We survey the kinematics of the plateau using Quaternary fault slip rates, a new set of Kostrov summations, and the latest campaign GPS measurements. We describe previous kinematic models for the Ordos region and then develop our own anticlockwise rotation model. Simple calculations are used to predict how we would expect this model to behave. Finally, we discuss how various observations support our proposed model for the kinematics.

6.1 Introduction: geological history and setting

The Ordos Plateau lies immediately northeast of Tibet in northern China. It largely consists of Archaean basement and undeformed Triassic rocks, overlain by a cover of Quaternary aeolian loess up to a few hundred metres thick (*Zhang and Gan*, 2008). To the west lies the Alxa Desert and to the east the North China plain (see Figure 6.1). Together these regions form part of the Archaean North China Craton (NCC), an old and stable piece of continental lithosphere (*Liu et al.*, 2007). The NCC collided with Mongolia to the north in the Permo-Triassic (*Dong et al.*, 2014). Then, in the Triassic, the South China Craton (SCC) collided with the NCC during the Qinling orogeny, producing the Qinlingshan at the southern edge of the Ordos Plateau. The Indosinian (235 to 200 Ma ago) and Yanshanian (150 to 65 Ma ago) orogenies created northeast striking fold-and-

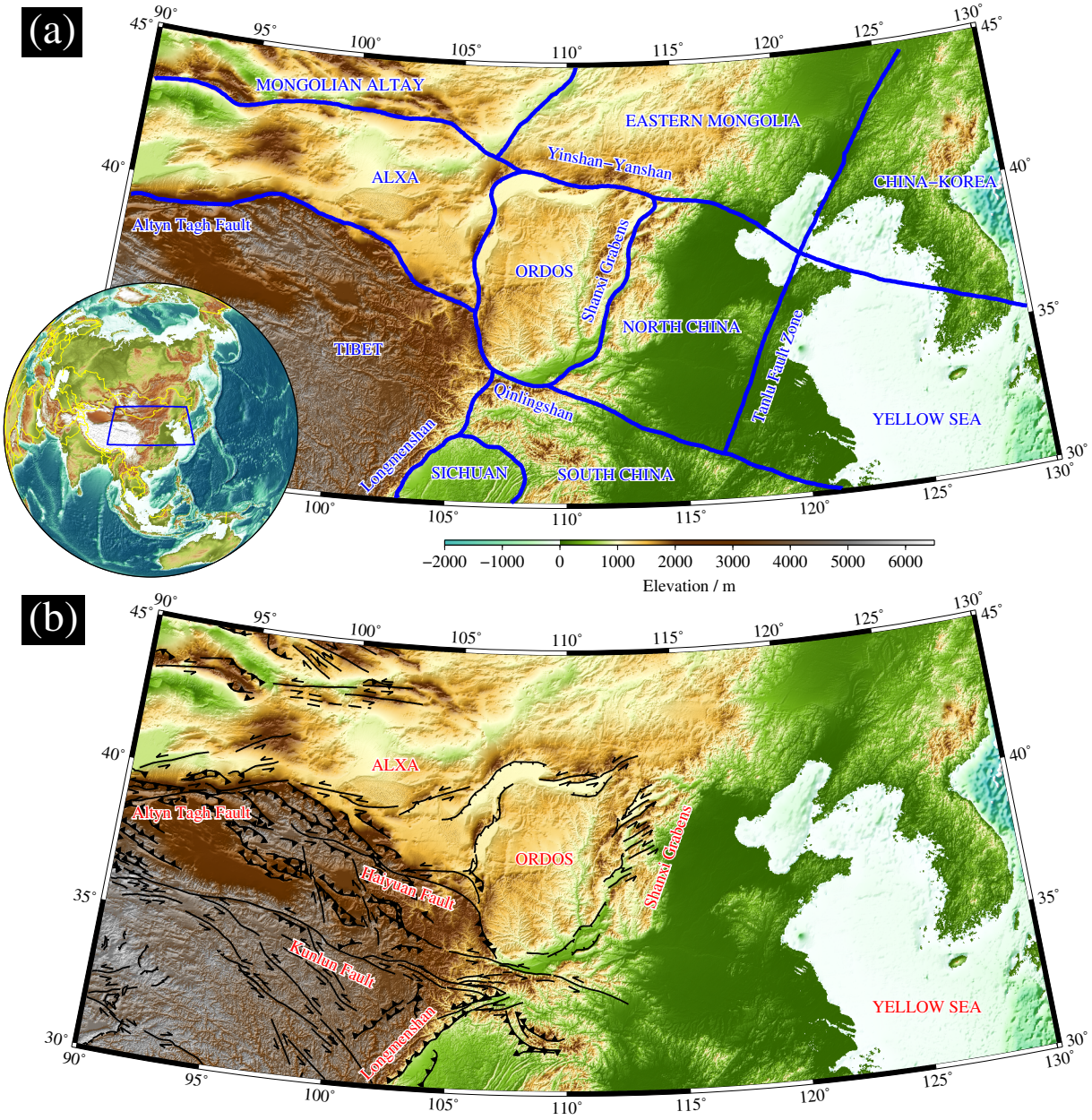


Figure 6.1: (a) Albers equal-area projection of the SRTM topography in northern China (*Farr et al.*, 2007). Inset globe shows the location of Figure 6.1 (a) within Asia. Major tectonic divisions after *Zhang et al.* (2003a); *Li et al.* (2003); *Zhang and Gan* (2008). (b) Major faults in northern China. Fault map from *Taylor and Yin* (2009).

thrust belt structures on both the eastern and western sides of the Ordos Plateau, in the Shanxi highlands and the Helanshan (*Zhang et al.*, 1998). In the Late Mesozoic the lithosphere of the eastern NCC was dramatically thinned, undergoing extension, high heat flow, and voluminous magmatism (*Ren et al.*, 2002; *Liu et al.*, 2007; *Chen et al.*, 2009). Subduction of the palaeo-Pacific plate began in the Cretaceous; and the India-Eurasia collision started around 55 Ma ago. In the Early Tertiary graben formation occurred in

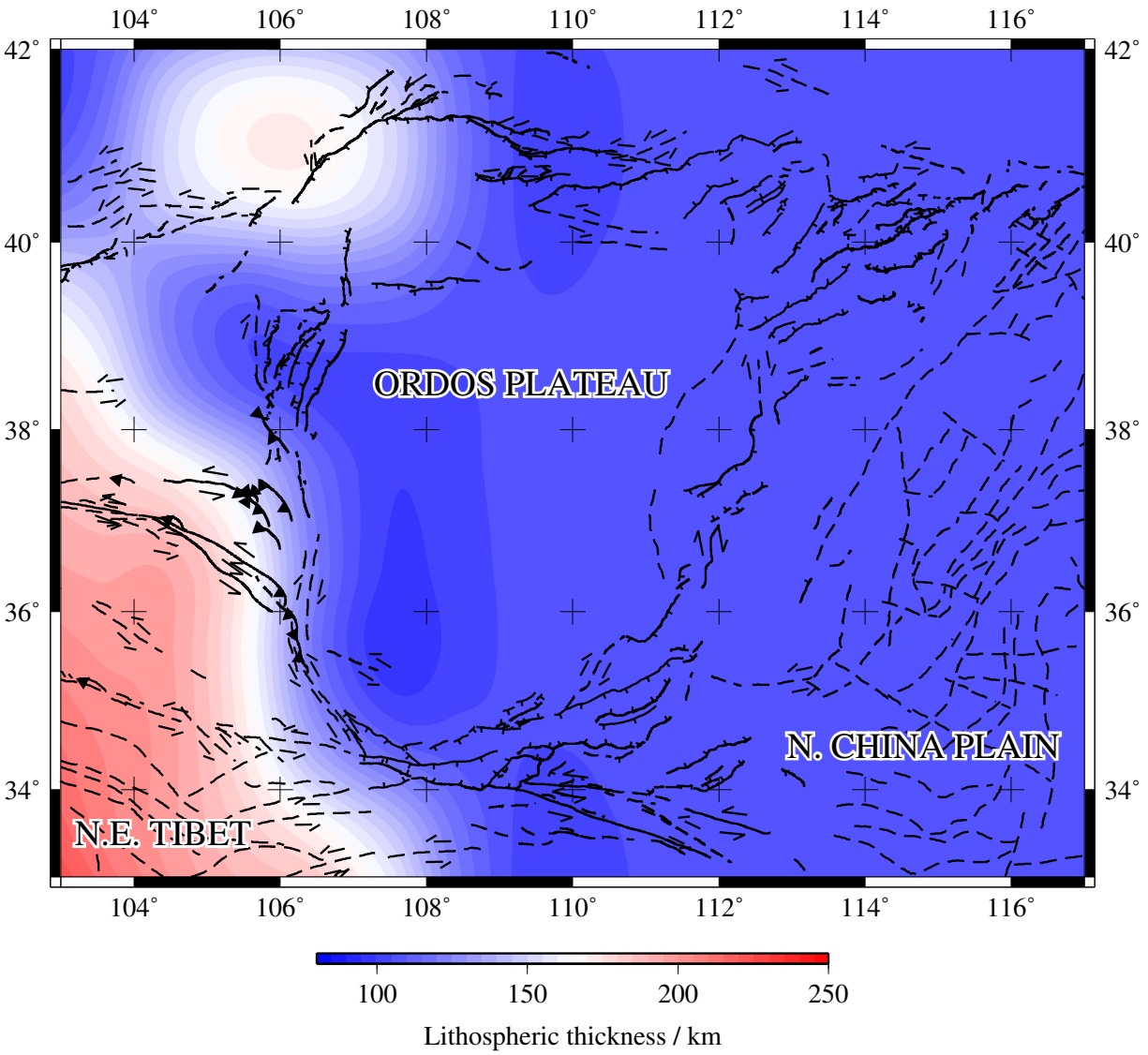


Figure 6.2: Lithospheric thickness map for the Ordos Plateau from *Priestley and McKenzie* (2006). Faults from Figure 6.4 are also shown.

the Linhe, Hetao, Yinchuan and Weihe Grabens and across the North China Plain (see Figure 1.4 for locations); however, the most rapid period of extension around the Ordos Plateau (including the formation of the Shanxi Grabens) took place in the Pliocene and Quaternary (*Ye et al.*, 1987; *Ma and Wu*, 1987; *Zhang et al.*, 1998). Many of these Cenozoic grabens reactivated inherited structures from the Indosinian and Yanshanian orogenies (*Zhang et al.*, 1998; *Liu and Yang*, 2000; *Darby and Ritts*, 2002).

Wang et al. (2014) found an average crustal thickness for the Ordos region of 42 km. However, the lithosphere under the Ordos Plateau remains abnormally thin at about 80 to 100 km, compared to nearly 250 km under the adjacent Tibetan Plateau (*Priestley*

and McKenzie, 2006; Figure 6.2). This step in lithospheric thickness may be important for explaining the seismicity in the region because it has been suggested that stresses concentrate at the boundary between thick and thin lithosphere due to the rheological contrast (*Li et al.*, 2007). Nonetheless, the crustal and lithospheric thicknesses for the Ordos Plateau are not particularly different to those for the adjacent North China Plain; what makes the Ordos distinctive, though, is its composition (it is underlain by stable, Archaean basement) and its subsequent geological history.

6.2 Quaternary fault slip rates at the margins of the Ordos Plateau

Figure 6.3 (a) shows all of the active faults around the Ordos Plateau from the *Map of Active Tectonics in China* (*Deng et al.*, 2007); Figure 6.3 (b) shows the fault map from *Taylor and Yin* (2009). Figure 6.4 shows the final fault map from the mapping conducted in this thesis. On Figure 6.4, buried faults in the North China Plain, inferred from seismic reflection profiles, are digitised from *Deng et al.* (2007). No faults are mapped in the interior of the Ordos block, with the exception of the Hangjinqi Fault zone in the northwest of the plateau (*Yang et al.*, 2013). However, we are not able to find evidence of any recent activity on the Hangjinqi Fault zone from satellite imagery.

Detailed fault maps for specific regions at the margins of the Ordos Plateau are given in the subsequent sections and Quaternary slip rates for the major faults around the Ordos Plateau are summarised in Table 6.1. We start by describing the major strike-slip motions adjacent to the Ordos—on the Haiyuan and Zhangjiakou-Bohai-Penglai Faults (see Figure 6.4 for locations)—and then focus on the faulting at the margins of the plateau itself, beginning with the northern margin and then moving to the southern, western and, finally, eastern sides.

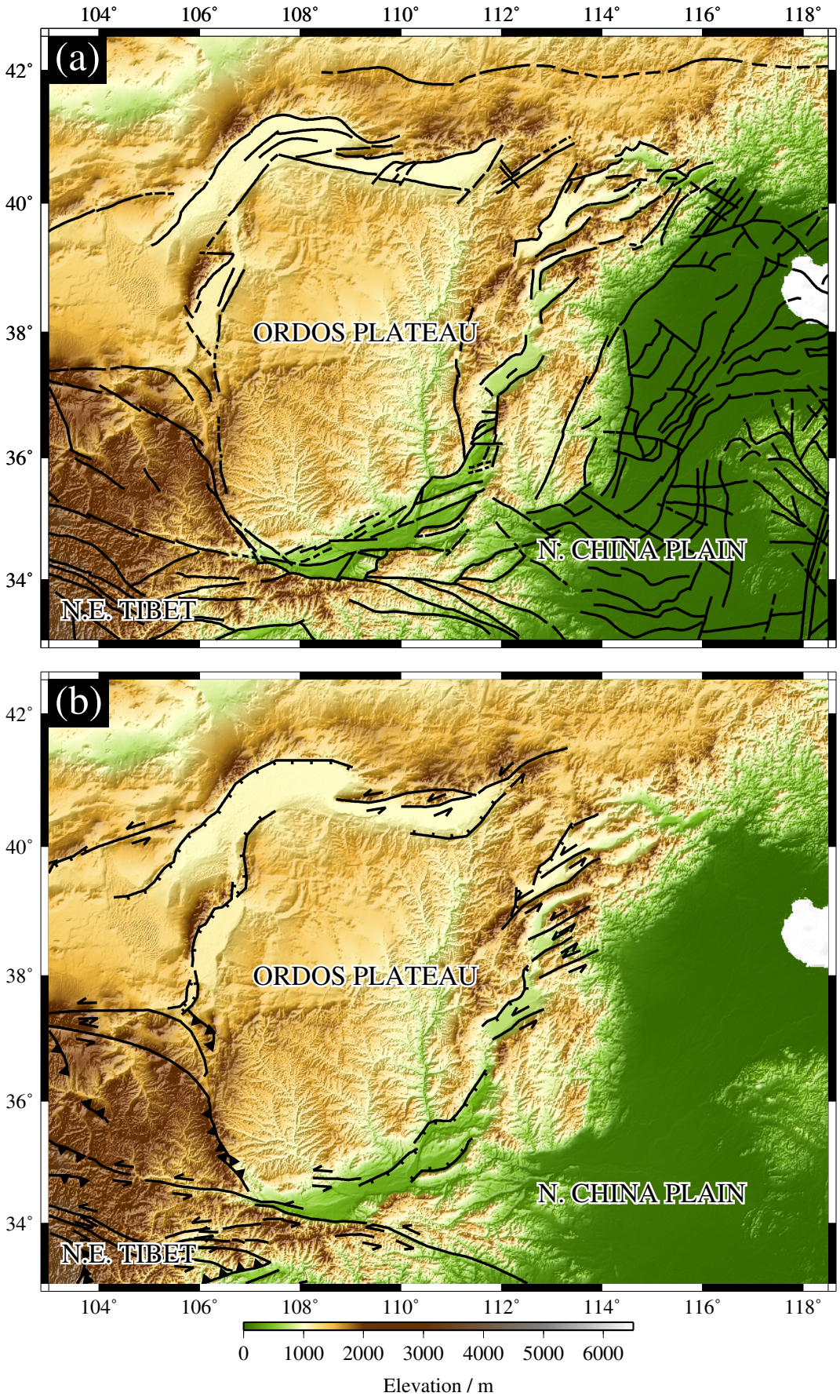


Figure 6.3: (a) SRTM topography (90 m resolution) of the Ordos Plateau (*Farr et al.*, 2007). Faults, marked as thin black lines, are from the *Map of Active Tectonics in China* (*Deng et al.*, 2007). (b) Fault map from *Taylor and Yin* (2009).

Table 6.1: Summary of Quaternary rates for major faults around the Ordos Plateau

ID	Fault name	Location	Lat °	Long °	Offset m	Error m	Age ka	Error ka	Dating method	Slip rate[a] mm/a	Error[b] mm/a	Reference
The northern Ordos: the Linhe and Hetao Grabens—see Figure 6.8												
1	Langshan Fault									3.6		*Deng et al.* (2007)
2	Seertengshan Fault	Qingdamu Gully	41.289	107.828	12.90	0.10	14.45	0.00	TL	0.9	0.0	*Yang et al.* (2003)
		Qingdamu Gully	41.289	107.828	4.00	0.00	7.24	0.59	TL	0.6	0.0	*Yang et al.* (2003)
		Benghongkou Gully	41.287	107.895	9.25	0.25	24.50	2.50	TL	0.4	0.0	*Yang et al.* (2003)
		Heikouzi	41.286	107.879	6.20	0.00	8.83	0.71	TL	0.7	0.1	*Yang et al.* (2003)
		Fendou	41.286	107.979	5.80	0.00	5.57	0.45	TL	1.0	0.1	*Yang et al.* (2003)
		Dashetai	41.023	109.152	4.30	2.20	29.64	2.33	TL	0.1	0.1	*Chen et al.* (2003)
		Wulanhudong	40.958	109.274	3.40	2.60	29.46	2.33	TL	0.1	0.1	*Chen et al.* (2003)
3	South Wulashan Fault									2.6		*Deng et al.* (2007)
4	Daqingshan Fault									1.0		*Deng et al.* (2007)
		Kuisu	40.942	111.891	7.00	2.00	19.99	3.95	^{14}C	0.4	0.1	*Ran et al.* (2003b)
5	Horinger Fault									Unknown		
The southern Ordos: the Weihe Graben—see Figure 6.10												
1	West Qinling Fault									2.5 LL		*Yuan et al.* (2007)
2	Qishan-Mazhao Fault				1850		1300			1.5 LL		*Lin et al.* (2015b)
3	Taibai Fault									Unknown		
4	Qianxian-Fuping Fault									Unknown		
5	Weihe Fault									Unknown		
6	North Qinlingshan Fault									0.3		*Deng et al.* (2007)
										0.6		*Deng et al.* (2007)
										0.5		*Deng et al.* (2007)
7	Luonan Fault				750	100	100	20	Climate	7.5 LL	1.8	*Zhang et al.* (1995)
8	Danfeng Fault				600	100	650	50	Climate	0.9 LL	0.2	*Zhang et al.* (1995)
9	Huashan Fault	Shiduyu	34.463[c]	109.748[c]	6.00		21.27	1.59	TL	0.3	0.0	*Hou et al.* (1998)
		Huangpuyu	34.527[c]	110.098[c]	12.00		20.12	1.33	TL	0.6	0.0	*Hou et al.* (1998)
										0.4		*Deng et al.* (2007)
10	Sanmenxia-Lingbao Fault									0.1		*Deng et al.* (2007)
										0.5		*Deng et al.* (2007)
11	North Zhongtiaoshan Fault									0.4		*Deng et al.* (2007)
12	Zhaoyi Fault									0.2		*Li et al.* (2015d)
13	Luoyunshan Fault									0.3		*Deng et al.* (2007)
										1.5		*Deng et al.* (2007)

[a] All rates are throw rates unless otherwise indicated. LL = left-lateral strike-slip; RL = right-lateral strike-slip.
[b] Error refers to formal uncertainties on offset and age, propagated in quadrature. The quoted error does not reflect the geomorphological uncertainty associated with the throw rate estimate. Errors of 0.0 are only zero when quoted to one decimal place.
[c] Approximate location of field site. Exact location not known.

Table 6.1: (continued) Summary of Quaternary rates for major faults around the Ordos Plateau

ID	Fault name	Location	Lat °	Long °	Offset m	Error m	Age ka	Error ka	Dating method	Slip rate[a] mm/a	Error[b] mm/a	Reference
The western Ordos: the Yinchuan Graben, the Luoshan and the Liupanshan—see Figure 6.12												
1	Alxa Desert Fault									Unknown		
2	Zhengyiguan Fault									Inactive		
3	East Helanshan Fault								^{10}Be	< 0.8	0.1	This study
4	Luhuatai Fault	Qianjin Farm	38.856	106.271	9.92	0.00	55.00	2.70	TL	0.2	0.0	*Lei et al.* (2011)
5	Yinchuan-Pingluo Fault	Xingqushao	38.528	106.342	2.25	0.00	16.39	0.24	^{14}C	0.1	0.0	*Lei et al.* (2008, 2015)
6	Yellow River Fault	Miaogou	38.225	106.36	2.33	0.00	9.20	0.07	TL	0.3	0.0	*Liao et al.* (2000)
7	Niushoushan Fault									0.4 RL		*Lei et al.* (2016)
8	Baima Fault									Unknown		
9	Luoshan Fault								IRSL	4.3 RL	0.4	This study
10	Tianjinshan-Miboshan Fault									3.6 LL		*Min et al.* (2001)
11	Yantongshan Fault									Unknown		
12	Haiyuan Fault									4.5 LL	1.0	*Li et al.* (2009a)
13	Liupanshan Fault									Unknown		
14	Yunwushan Fault									Unknown		
The eastern Ordos: the Shanxi Grabens—see Figure 6.13												
1	Yunzhongshan Fault									1.2 4.2		*Ma and Wu* (1987)
2	Xizhoushan Fault	Gucheng	38.202[c]	112.757[c]	50.60		8.90	0.28	^{14}C	5.7 RL	0.2	*Xu et al.* (1986)
3	Jiaocheng Fault									1.4		*Deng et al.* (2007)
4	Taigu Fault									1.0		*Deng et al.* (2007)
5	Huoshan Fault	North of Shawo	36.470[c]	111.821[c]	20.10		4.05	0.11	^{14}C	5.0 RL	0.2	*Xu and Deng* (1990); *Xu et al.* (1993)
		Xingwangyu	36.364	111.824	41.50		8.33	0.13	^{14}C	5.0 RL	0.1	*Xu and Deng* (1990); *Xu et al.* (1993)
		South of Shawo	36.440[c]	111.819[c]	107.20		16.72	0.55	^{14}C	6.4 RL	0.2	*Xu and Deng* (1990); *Xu et al.* (1993)
6	Luoyunshan Fault									2 4		*Ma and Wu* (1987)

[a] All rates are throw rates unless otherwise indicated. LL = left-lateral strike-slip; RL = right-lateral strike-slip.

[b] Error refers to formal uncertainties on offset and age, propagated in quadrature. The quoted error does not reflect the geomorphological uncertainty associated with the throw rate estimate. Errors of 0.0 are only zero when quoted to one decimal place.

[c] Approximate location of field site. Exact location not known.

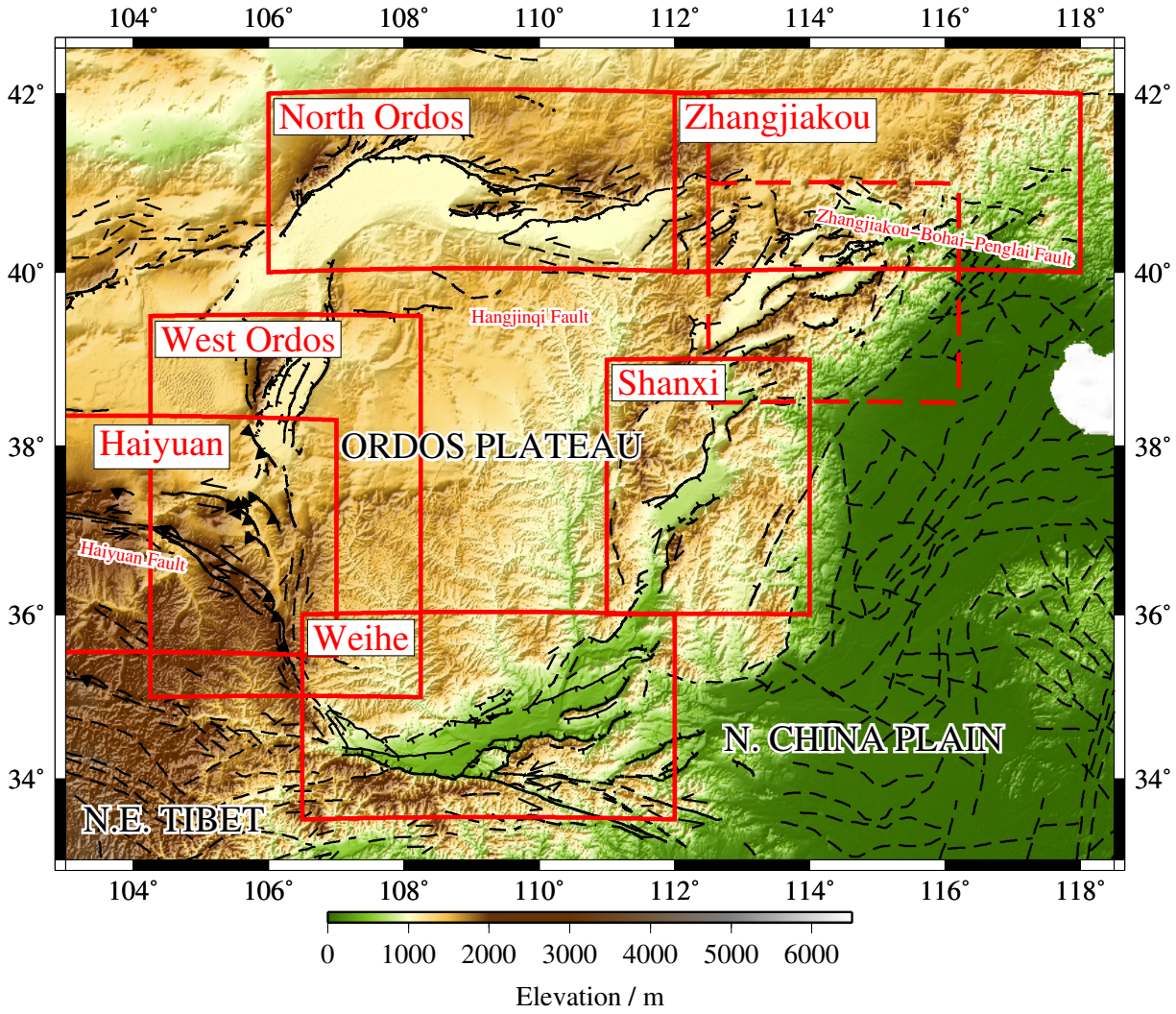


Figure 6.4: SRTM topography (90 m resolution) of the Ordos Plateau (*Farr et al.*, 2007) with our own improved faults, mapped from satellite imagery (source: http://earth.google.com) and based upon earlier fault maps from *Tapponnier and Molnar* (1977), *Deng et al.* (1984a), *Zhang et al.* (1986), *The Research Group on Active Fault System around Ordos Massif* (1988), *Zhang et al.* (1990), *Xu and Ma* (1992), *Deng and Liao* (1996), *Darby and Ritts* (2002), *Yu* (2004) and *Darby et al.* (2005). Faults that are inferred or show no evidence of Quaternary activity are marked by dashed lines. Buried faults in the North China Plain are digitised from the *Map of Active Tectonics in China* (*Deng et al.*, 2007). Red polygons indicate regions covered in more detail in Figures 6.5, 6.6, 6.8, 6.10, 6.12 and 6.13. Dashed red polygon indicates the northern Shanxi Grabens—see Figure 5.2 for fault map of this region.

6.2.1 The Haiyuan Fault

The Haiyuan Fault is around 1000 km long (extending from approximately 38 °N, 100 °E in the west to 36 °N, 106 °E in the east) and is one of the major left-lateral strike-slip faults of the northeastern Tibetan Plateau (*Deng et al.*, 1984a; *Lasserre et al.*, 2002; *Liu-Zeng et al.*, 2007). The fault comprises three principal sections (*Lasserre et al.*, 1999): the Leng Long Ling section in the west, the central Maomaoshan and Laohushan section (also known as the Tianzhu seismic gap), and the eastern section that borders the northern edge of the Xihuashan and Nanhuashan (see Figure 6.5).

Lasserre et al. (2002) obtained a Late Pleistocene slip rate of 19±5 mm/a on the (western) Leng Long Ling section from ^{10}Be and ^{26}Al dating of an offset glacial moraine. On the (central) Maomaoshan section, *Lasserre et al.* (1999) found a post-glacial slip rate of 12±4 mm/a from ^{14}C dating of offset terraces, although other studies have obtained rates of less than 5 mm/a (*Yuan et al.*, 1997; *Liu-Zeng et al.*, 2007). For comparison, *Cavalié et al.* (2008) obtained a geodetic rate of between 4.2 and 8 mm/a from two interseismic InSAR tracks covering the same fault section.

For our study of the Ordos kinematics we are most concerned with the eastern section of the Haiyuan Fault, which directly abuts the Ordos Plateau. On this section, the total offset of geological markers since the end of the Pliocene is estimated to be between 10.5 and 15.5 km, yielding a slip rate of between 5 and 10 mm/a (*Burchfiel et al.*, 1991). Meanwhile, *Zhang et al.* (1988) estimated a Holocene slip rate of 8±2 mm/a from ^{14}C dating of six offset stream valleys on the Xihuashan and Nanhuashan. Most recently, *Li et al.* (2009a) re-visited a number of sites on the eastern section and obtained an average Late Quaternary slip rate of 4.5±1.0 mm/a. They also found a geodetic rate of 4.3±1.5 mm/a from the GPS data of *Zhang et al.* (2004).

These Quaternary rates appear to suggest an eastward decrease in the rate of left-lateral slip on the Haiyuan Fault, although a number of these estimates are contested. Nevertheless, the rate of motion on the Haiyuan Fault is notably higher than the rates of motion for the majority of faults around the Ordos Plateau.

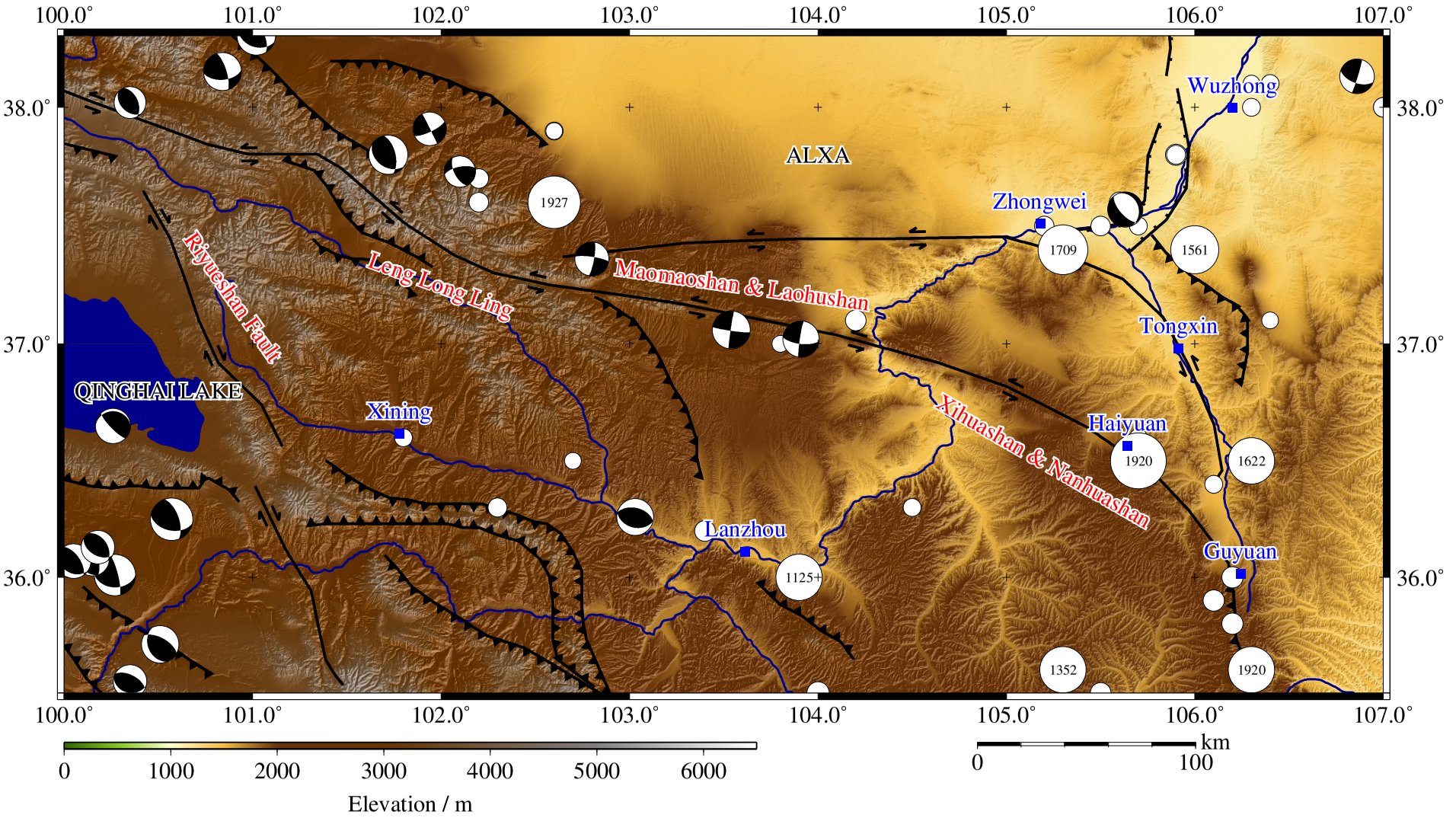


Figure 6.5: SRTM topography (30 m resolution) of the Haiyuan Fault and surrounding region (*Farr et al.*, 2007). Fault map from *Taylor and Yin* (2009). Focal mechanisms from the Global CMT catalogue (*Ekström et al.*, 2012) are shown for earthquakes since 1976 with magnitudes greater than M_w 5.0. Historical earthquakes with $M_w \geq 7$ are shown by white circles, including the year in which they occurred. Historical earthquakes with $5 \leq M_w < 7$ are shown as white dots. Data comes from *Lee et al.* (1976), *Lee et al.* (1978) and *Liu et al.* (2011). Rivers are indicated in dark blue and cities are marked by blue squares. Sections of the Haiyuan Fault are labelled in red.

6.2.2 The Zhangjiakou-Bohai-Penglai Fault zone

The Zhangjiakou-Bohai-Penglai Fault zone is approximately 700 km long and is one of the major WNW trending structural features in north China (*Zheng et al.*, 1981; *Fu et al.*, 2004; *Guo et al.*, 2015). It extends from Zhangjiakou in the northwest (41 °N, 115 °E) to Penglai in the southeast (38 °N, 121 °E) and comprises around 20 segments, each 40 to 60 km long (*Guo et al.*, 2015). The western part of the fault zone is shown in Figure 6.6.

A number of studies have described the Zhangjiakou-Bohai-Penglai Fault zone as an important part of the kinematics of northern China (*Zhang et al.*, 1985; *Xu and Ma*, 1992; *Xu et al.*, 1993; *Shen et al.*, 2000; *Liu*, 2000; *Deng et al.*, 2003; *Zhang et al.*, 2003a; *Wang et al.*, 2003; *Yu*, 2004; *Fu et al.*, 2004; *Liu et al.*, 2007; *Wang et al.*, 2011; *Li et al.*, 2012; *Guo et al.*, 2015; *Li et al.*, 2015a), but comparatively little is reported about its Quaternary activity. Scattered seismicity attests to its recent motion and focal mechanisms indicate predominantly left-lateral strike-slip movement (*Guo et al.*, 2015). Some geodetic slip rates of around 1 to 2 mm/a have been reported (see Section 6.4.2), but there are no Quaternary slip rate constraints.

Figure 6.7 shows a newly identified fault segment to the northwest of Zhangjiakou (see Figure 6.6 for location). Along this segment we see evidence for left-lateral (see Figure 6.7 (e)) and vertical (see Figure 6.7 (b)) components of motion expressed in Late Quaternary sediments. This westward continuation of the fault zone is consistent with the idea that it forms the northern boundary of the whole NCC.

6.2.3 The northern Ordos: the Linhe and Hetao Grabens

The northern margin of the Ordos Plateau is bordered by the Linhe and Hetao Grabens, each of which is up to 60 km wide (see Figure 6.8). These grabens are principally controlled by large, south-dipping, normal faults on their northern sides. The Langshan and Seertengshan Faults lie to the north of the Linhe Graben, whilst the South Wulashan and Daqingshan Faults lie to the north of the Hetao Graben, which contains the cities of Baotou and Hohhot (*Ran et al.*, 2003a).

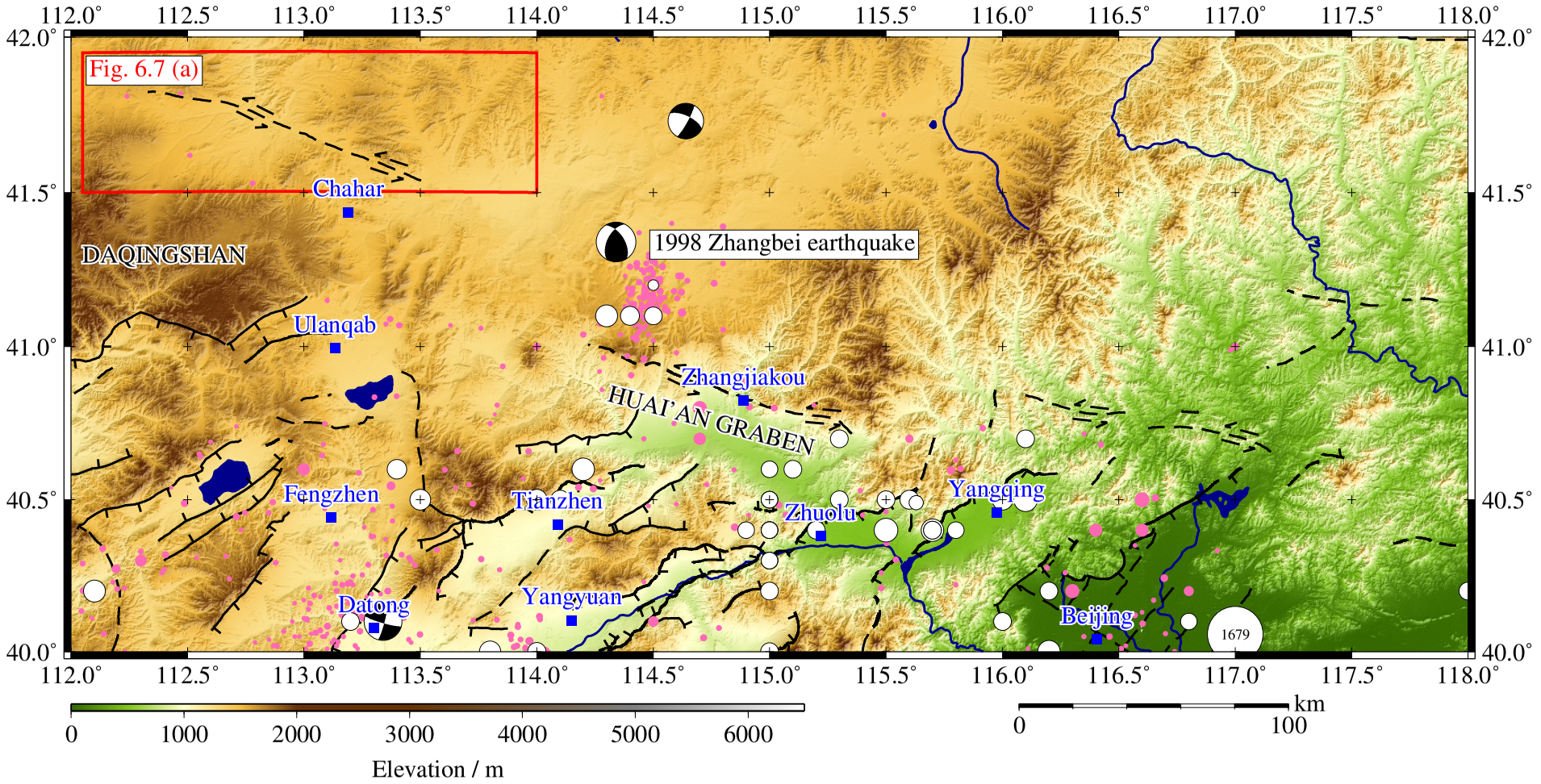


Figure 6.6: SRTM topography (30 m resolution) of the central and northwestern sections of the Zhangjiakou-Bohai-Penglai Fault zone (*Farr et al.*, 2007). Faults, marked as thin black lines, have been mapped from satellite imagery (source: http://earth.google.com) based upon the earlier fault map by *Tapponnier and Molnar* (1977). Faults that are inferred or show no evidence of Quaternary activity are marked by dashed lines. Historical earthquakes with $M_w \geq 7$ are shown by white circles, including the year in which they occurred. Historical earthquakes with $5 \leq M_w < 7$ are shown as white dots. Data comes from *Lee et al.* (1976), *Lee et al.* (1978) and *Liu et al.* (2011). Focal mechanisms from the Global CMT catalogue (*Ekström et al.*, 2012) are shown for earthquakes since 1976 with magnitudes greater than M_w 5.0. Pink dots indicate earthquakes of M_w 2.0-5.0 between 1920 and 2011 from the ISC catalogue (*International Seismological Centre*, 2013), scaled according to their magnitude. The concentration of earthquakes around 114.5 °E are aftershocks of the M_w 5.7 1998 Zhangbei earthquake (*Li et al.*, 2008). Rivers are indicated in dark blue and cities are marked by blue squares. Red polygon indicates region shown in Figure 6.7 (a).

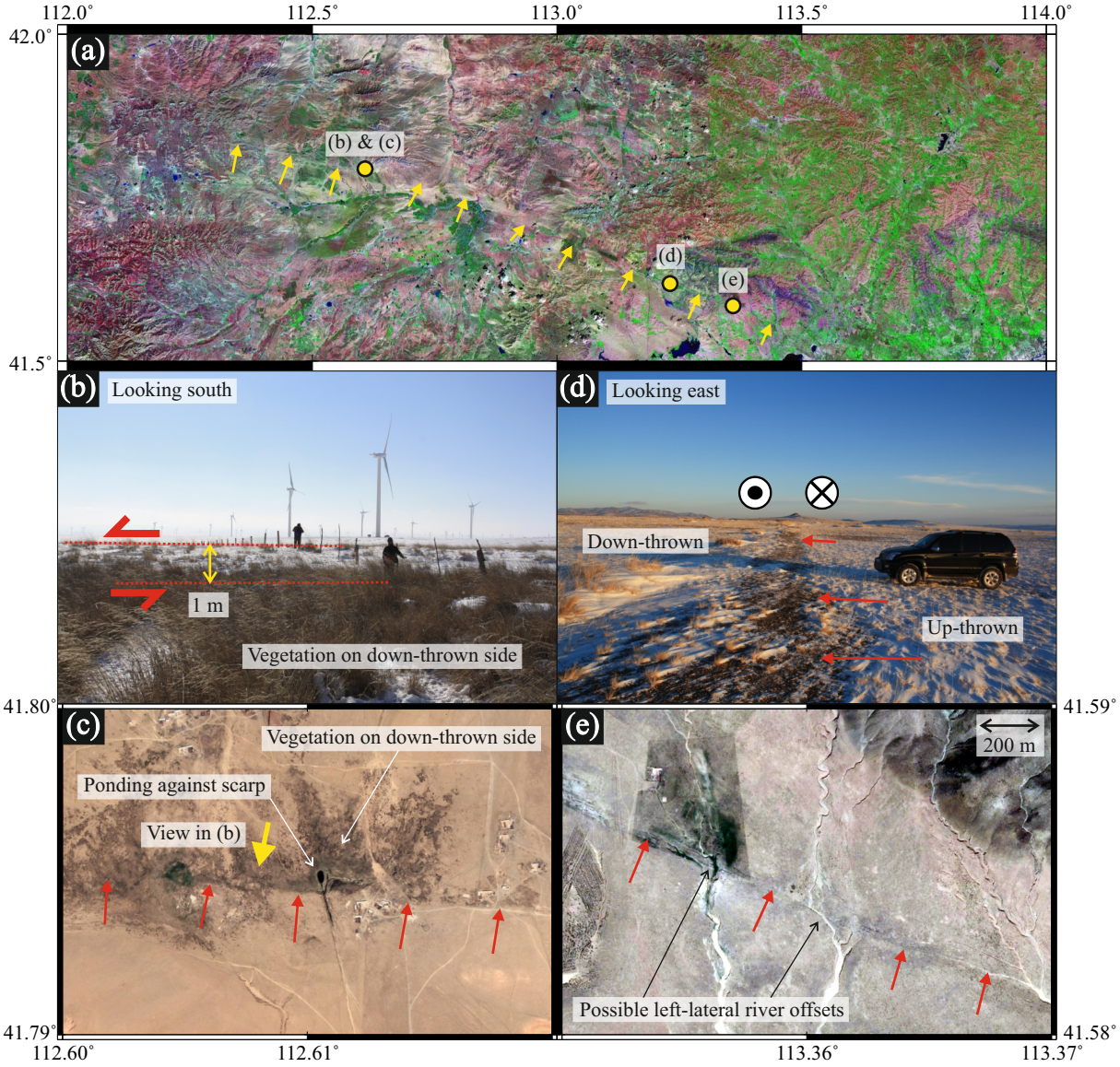


Figure 6.7: (a) Landsat imagery (742 band combination) showing a westward continuation of the Zhangjiakou-Bohai-Penglai Fault zone. Location of fault marked by yellow arrows (see Figure 6.6 for location). (b) Field photograph from November 2012 (taken at 41.794 °N, 112.610 °E) showing a view of the ≈ 1 m high scarp. The fault is primarily left-lateral, but the northern side has also been down-thrown. (c) Google Earth imagery from June 2006 (source: http://earth.google.com) of the same location as (b). Ponding and vegetation can be seen on the northern side of the fault scarp. (d) Field photograph from November 2012 (taken at 41.619 °N, 113.230 °E) of the fault trace in an agricultural field. The northern side is again down-thrown, preserving a small scarp. (e) Google Earth imagery from February 2015 (source: http://earth.google.com) of another site further east, where possible left-lateral river offsets of ≈ 120 m and ≈ 160 m can be seen in young alluvium.

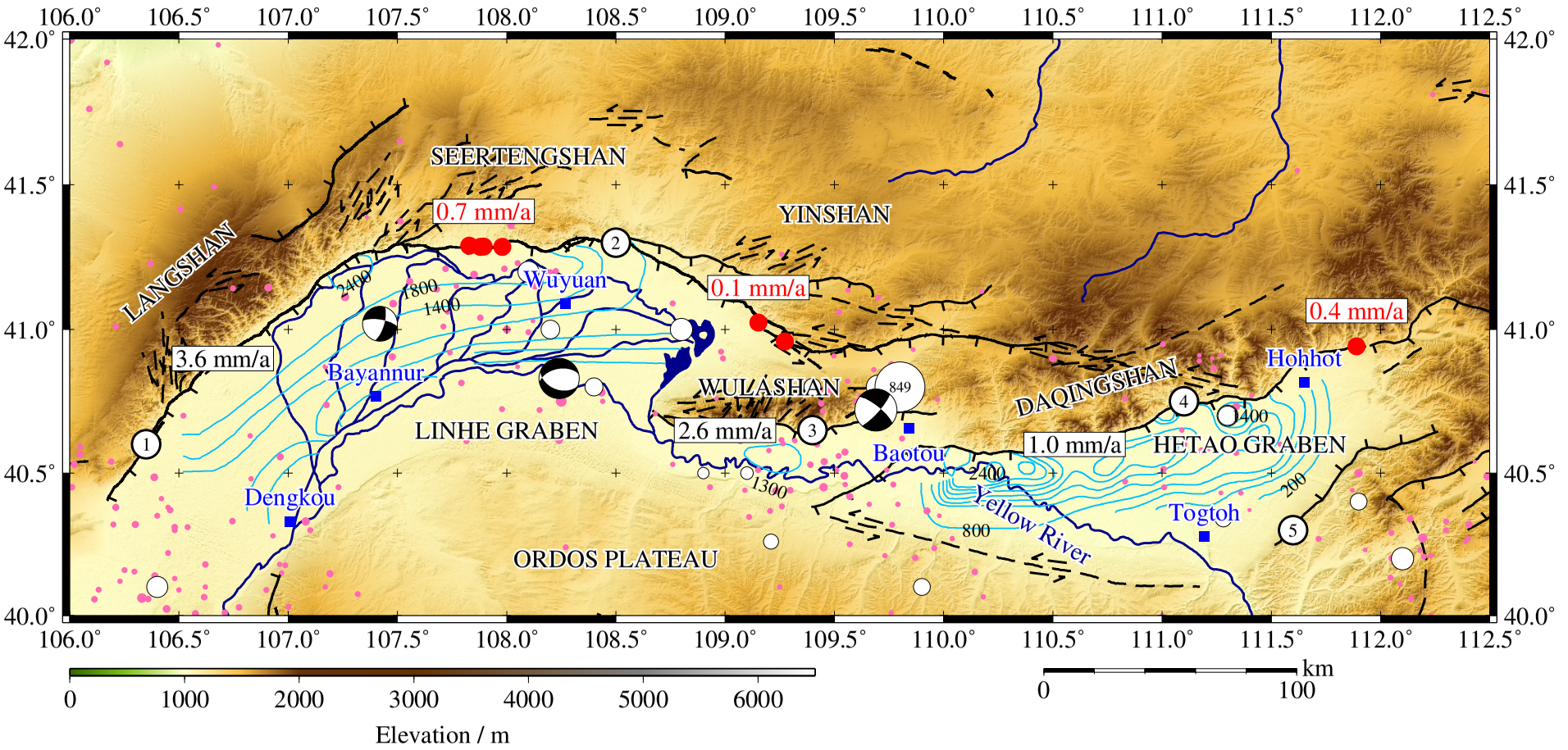


Figure 6.8: New fault map for the Linhe and Hetao Grabens based upon the earlier fault map by *Tapponnier and Molnar* (1977). Annotations as in Figure 6.6. Light blue lines are Quaternary isopachs from *Ran et al.* (2003a) and *Ran et al.* (2003b). Red circles (and numbers) indicate throw rates measured by *Yang et al.* (2003), *Chen et al.* (2003) or *Ran et al.* (2003b)—some labels have been omitted where they are similar to adjacent sites. Black labels are throw rates from *Deng et al.* (2007), where the location of the actual measurement site is unknown. Faults are numbered as follows: 1 Langshan Fault; 2 Seertengshan Fault; 3 South Wulashan Fault; 4 Daqingshan Fault; 5 Horinger Fault.

Geological mapping of the Langshan and Seertengshan Faults was first completed in the 1990s (*Yang et al.*, 2003). *Deng et al.* (2007) reported a throw rate on the Langshan Fault of 3.6 mm/a. *Yang et al.* (2003) studied the western 70 km of the Seertengshan Fault and obtained a typical throw rate of around 0.7 mm/a in the Late Pleistocene and Holocene from TL dates of offset geomorphological features (see Table 6.1 for details). *Chen et al.* (2003) summarised a number of palaeoseismological studies on the Seertengshan Fault. They estimated typical throw rates towards the eastern end of the fault of 0.1 mm/a, again on the basis of TL dates (see Table 6.1 for details).

The Daqingshan Fault is around 220 km long and formed in the Eocene (*Ran et al.*, 2003b). *Deng et al.* (2007) reported throw rates on the South Wulashan and western Daqingshan Faults of 2.6 and 1.0 mm/a respectively. *Li et al.* (1994) obtained relatively fast Late Pleistocene throw rates on the Daqingshan Fault, of up to 4.8 to 6.4 mm/a on the central portions. However, recent palaeoseismological work suggests slower rates (*Ran et al.*, 2002, 2003b). At Kuisu, 16 km northeast of Hohhot, a 7±2 m offset and a ^{14}C age of 19.99±3.95 ka give a throw rate of 0.4±0.1 mm/a (see Table 6.1) (*Ran et al.*, 2003b). It is also possible that the southern margin of the Hetao Graben is bordered by a left-lateral strike-slip fault (*Zhang et al.*, 1985), but there is scant geomorphological evidence for any recent activity (see Figure 6.8). Overall, the slip rates in the northern Ordos are largely consistent with the total Quaternary extension rates of 3.1±1.0 mm/a in the Linhe Graben and 2.3±0.8 mm/a in the Hetao Graben, which were obtained from cross-sectional area balances by *Zhang et al.* (1998).

It is also thought that the M 7.5 849 earthquake (see Figure 6.8), involving 3 to 7 m of slip, occurred on the Daqingshan Fault (*Ran et al.*, 2003a,b; *He and Ma*, 2015), although relatively fresh-looking scarps are also found west of Baotou on the South Wulashan Fault. A M 6.8 earthquake also occurred nearby in 1934, but it is not known which fault this occurred on (*Ran et al.*, 2003a). The M 6.4 1996 Baotou earthquake had an epicentre immediately northwest of the city of Baotou (see Figure 6.8) and appears to have occurred on a left-lateral strike-slip fault that dissects the Wulashan (*Guo et al.*, 2002), possibly on a structure that continues the Seertengshan Fault. *Jiang et al.* (2000) also found evidence for left-lateral offsets at the western end of the Daqingshan Fault, and even proposed a

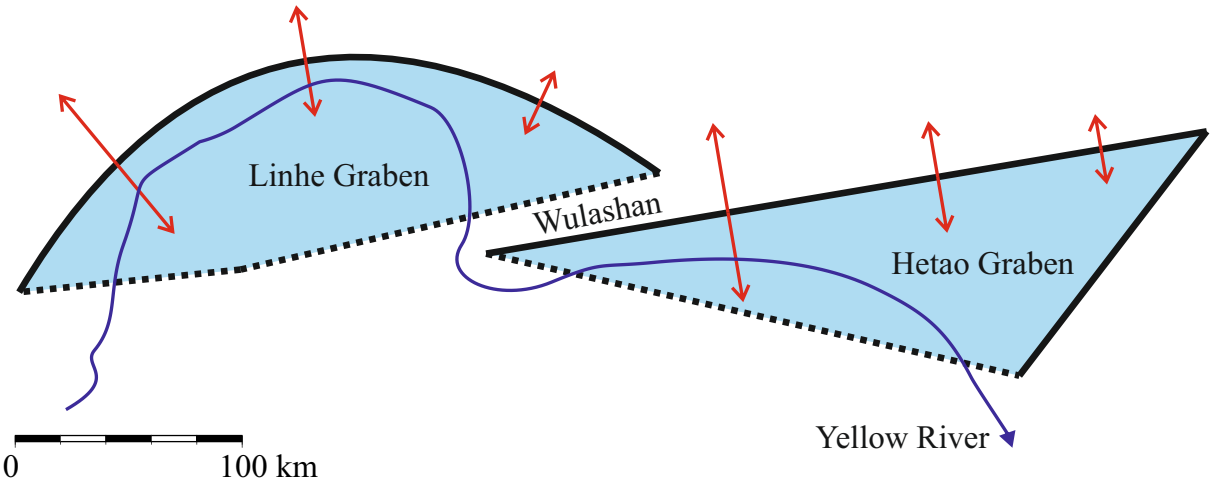


Figure 6.9: Simple sketch to illustrate the pattern of extension in the Linhe and Hetao Grabens, to the north of the Ordos Plateau. Black lines indicate major graben-bounding faults, dashed black lines mark edges of basins, blue areas show regions of sedimentation, and red arrows indicate (schematically) the magnitude of the throw rate at different points along strike. In each graben, the throw rate (and hence the extension rate, given a fairly constant fault dip) on the major basin-bounding normal faults increases to the west. The thickness of Quaternary sediments is also greatest in the northwest of each graben (see Figure 6.8).

Holocene left-lateral slip rate of 5 mm/a, although it is not clear where this rate comes from.

Figure 6.9 shows a simple sketch to illustrate the pattern of deformation in the northern Ordos region. The right-stepping en echelon arrangement of the Linhe and Hetao Grabens implies that east-west left-lateral motion is potentially important (*Zhang et al.*, 1998). In each graben, the throw rate (and hence the extension rate, given a fairly constant fault dip) on the major basin-bounding normal faults increases to the west (see Figure 6.8). Furthermore, the thickness of Quaternary sediments is also greatest in the northwest of each graben (again, see Figure 6.8), suggesting that the spatial variations in extension rate may have persisted throughout the Pleistocene and Holocene.

We propose possible explanations for this pattern of deformation. The arcuate shape of the Langshan and Seertengshan Faults results in a change in strike of around 90 °. This could explain why the eastern end of the Linhe Graben has a lower rate of vertical motion (as it will have more strike-slip motion instead). Secondly, the two grabens overlap, to the north and south of the Wulashan. The lower throw rate at the eastern end of the Linhe Graben to the north, could be compensated for by a higher throw rate at the western end

of the Hetao Graben to the south. Finally, it is possible that the extension rate increases regionally from east to west across the northern Ordos region.

6.2.4 The southern Ordos: the Weihe Graben

The Weihe Graben lies to the south of the Ordos Plateau and is up to 70 km wide at its widest point (see Figure 6.10). The western Weihe Graben is bounded by the steep range front of the Qinlingshan on its southern side, whilst the Qianxian-Fuping and Weihe Faults lie further north and dip to the south (see Figure 6.10, faults 4, 5 and 6). East of the city of Xi'an (around 109 °E) the pattern of faulting changes. Two, large, left-lateral faults—the Luonan and Danfeng Faults (see Figure 6.10, faults 7 and 8)—extend from the eastern end of the Qinlingshan striking ESE; meanwhile large normal faults continue to the northeast along the Huashan range front (see Figure 6.11), the Weinan Tableland, the Zhongtiaoshan range front, and the Emei Tableland (see Figure 6.10, faults 9, 10 and 11). A number of other buried normal faults exist within the graben itself (*Wang*, 1987; *Bellier et al.*, 1988). The Wei River (Wei He) runs from west to east through the graben and meets the Yellow River (Huang He) in front of the Huashan range front.

There is much debate about the rate of left-lateral motion on the southern margin of the Ordos Plateau because lateral extrusion models for the India-Eurasia collision tend to require large amounts of shear to be accommodated in this region (see Section 1.2). West of the Weihe Graben, the slip rate on the Kunlun Fault (see Figure 6.1 (b)) appears to die out eastwards from $>$ 10 mm/a to $<$ 3 mm/a by 102 °E (*Harkins et al.*, 2010). Some authors have suggested that this left-lateral motion is transferred to the southern margin of the Ordos via the West Qinling and Taibai Faults (see Figure 6.10, faults 1 and 3) (*Tapponnier and Molnar*, 1977; *Zhang et al.*, 1995). However, the slip rate on the West Qinling Fault is thought to be only 2 to 3 mm/a (*Deng et al.*, 2007; *Yuan et al.*, 2007; *Harkins et al.*, 2010) and the slip rate on the Taibai Fault is not known. *Lin et al.* (2015b) suggested a left-lateral slip rate of 1.5 mm/a on the Qishan-Mazhao Fault (see Figure 6.10, fault 2), immediately northwest of the Weihe Graben, but their offsets and ages are poorly constrained. Therefore, the principal structure to the west of the Ordos

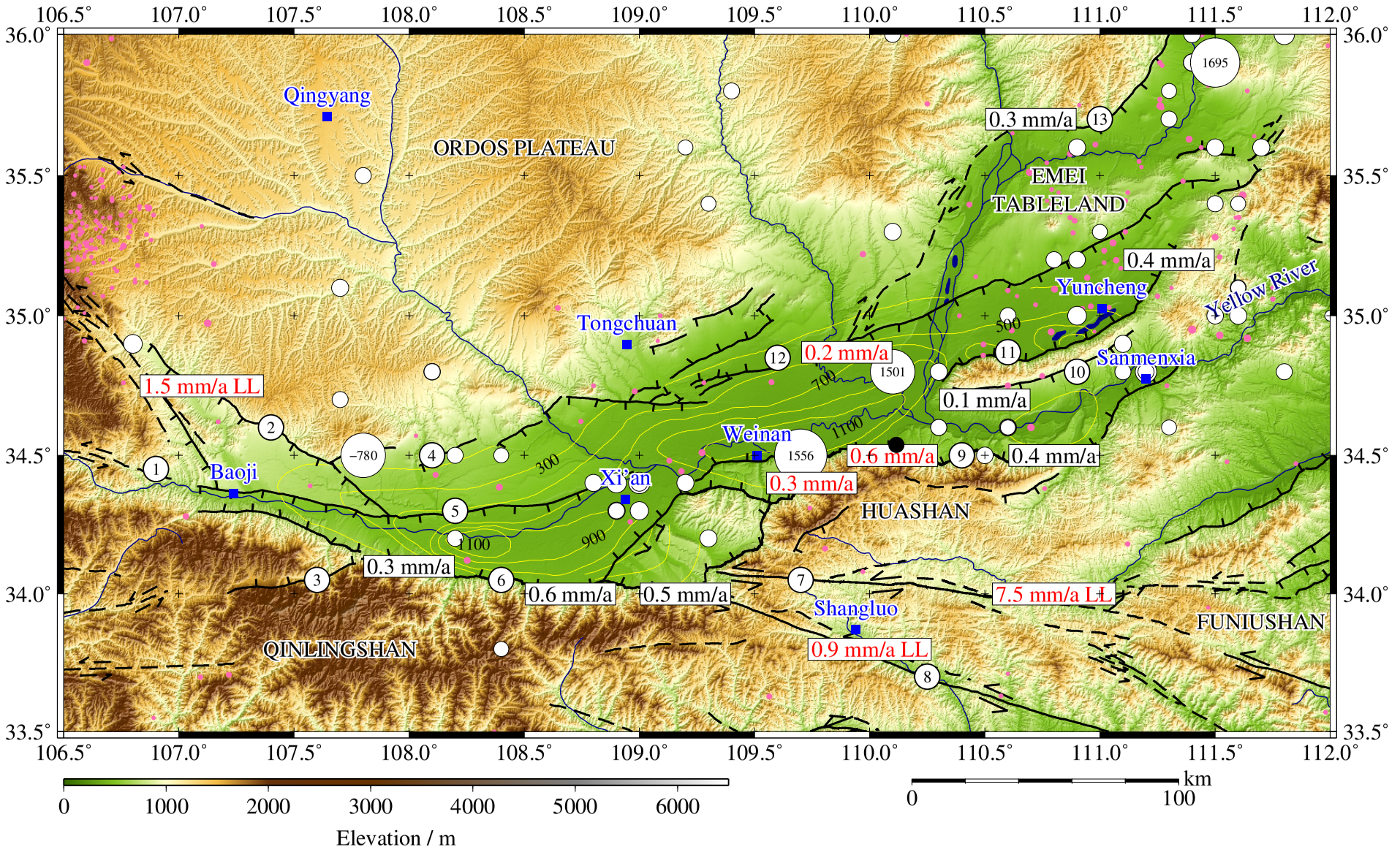


Figure 6.10: New fault map for the Weihe Graben, based upon earlier fault maps from *Tapponnier and Molnar* (1977), *Zhang et al.* (1998) and *Yuan and Feng* (2010). Annotations as in Figure 6.6. Yellow lines are Quaternary isopachs from *Zhang et al.* (1998). Red numbers indicate rates measured by *Zhang et al.* (1995), *Hou et al.* (1998), *Li et al.* (2015d) or *Lin et al.* (2015b). Throw rates given in black are from *Deng et al.* (2007). Black dot indicates the location of Figure 6.11. Faults are numbered as follows: 1 West Qinling Fault; 2 Qishan-Mazhao Fault; 3 Taibai Fault; 4 Qianxian-Fuping Fault; 5 Weihe Fault; 6 North Qinlingshan Fault; 7 Luonan Fault; 8 Danfeng Fault; 9 Huashan Fault (Weinan Tableland Fault in the west); 10 Sanmenxia-Lingbao Fault; 11 North Zhongtiaoshan Fault; 12 Zhaoyi Fault; 13 Luoyunshan Fault.

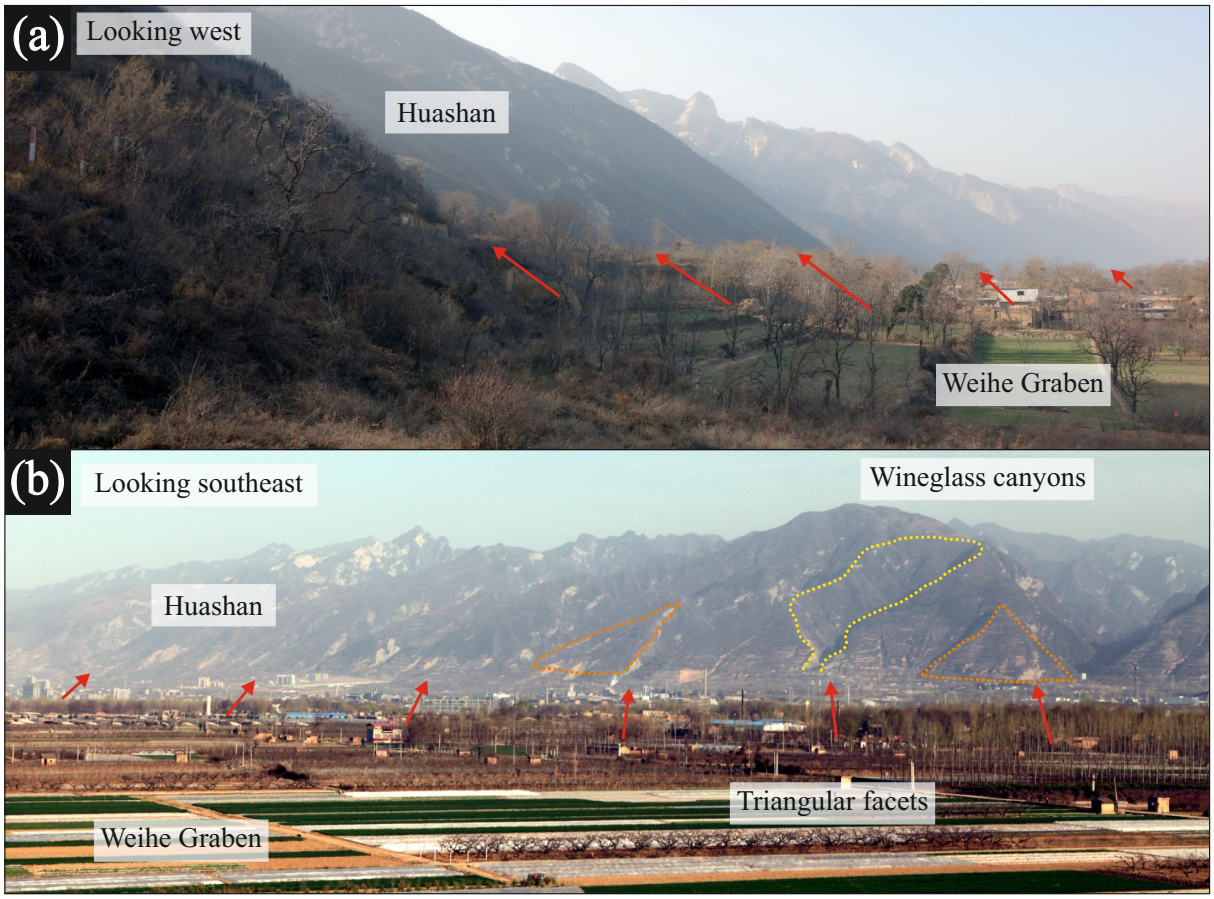


Figure 6.11: Field photograph taken by Ji Ma (from 34.537 °N, 110.116 °E, around 110 km east of Xi'an—see Figure 6.10 for location) showing a view looking west along the range front at the southern margin of the Weihe Graben. Red arrows mark approximate trace of active normal fault. This part of the Huashan Fault is believed to have ruptured in the 1556 earthquake (*Yuan and Feng*, 2010). (b) Field photograph also taken by Ji Ma (from the same location) looking southeast at the Huashan Fault. Clear triangular facets and wineglass canyons attest to recent fault activity.

Plateau that accommodates left-lateral motion is the Haiyuan Fault—at around 4.5 mm/a (see Section 6.2.1). Indeed, left-lateral motion may be transferred from the Kunlun to the Haiyuan Fault via the Elashan and Riyueshan Faults—see Figure 6.5 (*Nockles*, 2015).

Bellier et al. (1988) obtained a left-lateral slip rate on the North Qinlingshan Fault of 5.5±2.5 mm/a (see Figure 6.10, fault 6). Similarly, *Wang* (1987) estimated 7.2 mm/a of left-lateral strike-slip motion on the North Qinlingshan Fault since the Pleistocene from offset river channels. However, it is not clear how *Wang* (1987) dated the offset features, and different channels appear to give very different slip rates. Furthermore, more recent work has not found any evidence for left-lateral motion (*Deng et al.*, 2007), and interseismic InSAR shows no resolvable motion on the North Qinlingshan Fault (approximately

0±2 mm/a in the line of sight direction)—although coherence in the Qinlingshan is poor due to the dense vegetation cover (*Zhou*, 2016).

Zhang et al. (1995) obtained large, left-lateral rates on the strike-slip faults to the southeast of the Weihe Graben: 7.5 mm/a on the Luonan Fault and 0.9 mm/a on the Danfeng Fault. If these rates are reliable, then it is not clear how the left-lateral motion is transferred through the Weihe Graben. One possibility is that this motion is taken up by buried faults within the graben or unmapped faults south of the Qinlingshan range front. However, the uncertainties on the rates estimated by *Zhang et al.* (1995) are likely to be large since their only age control comes from correlating fluvial terraces with climatic changes during the Quaternary. Using their "longer chronology"—where the terraces are correlated with a different interglacial period—on the Luonan Fault, for example, they obtained a much lower slip rate of 2.7±0.4 mm/a.

The other faults in the region whose rates of motion are known all have comparatively low Quaternary throw rates of less than 1 mm/a (see Figure 6.10 and Table 6.1) (*Deng et al.*, 2007). For example, *Hou et al.* (1998) estimated throw rates on the Huashan Fault of around 0.3 to 0.6 mm/a from TL ages of fluvial terraces. Although some authors suggest higher throw rates (*Yang et al.*, 2012; *Rao et al.*, 2014), recent work by *Li et al.* (2015e) has confirmed throw rates of ≈ 0.6 mm/a since the mid-Pleistocene on the Huashan Fault and ≈ 0.4 mm/a since the Early Pleistocene on the Weinan Tableland Fault. These rates are smaller than, but not dissimilar to, the total extension rate since 2.4 Ma ago of 1.6±0.5 mm/a obtained from a cross-sectional area balance by *Zhang et al.* (1998). Overall, it appears that there is a small increase in the total throw rate (summed across all faults in the Weihe Graben) on moving from west to east (see Figure 6.10).

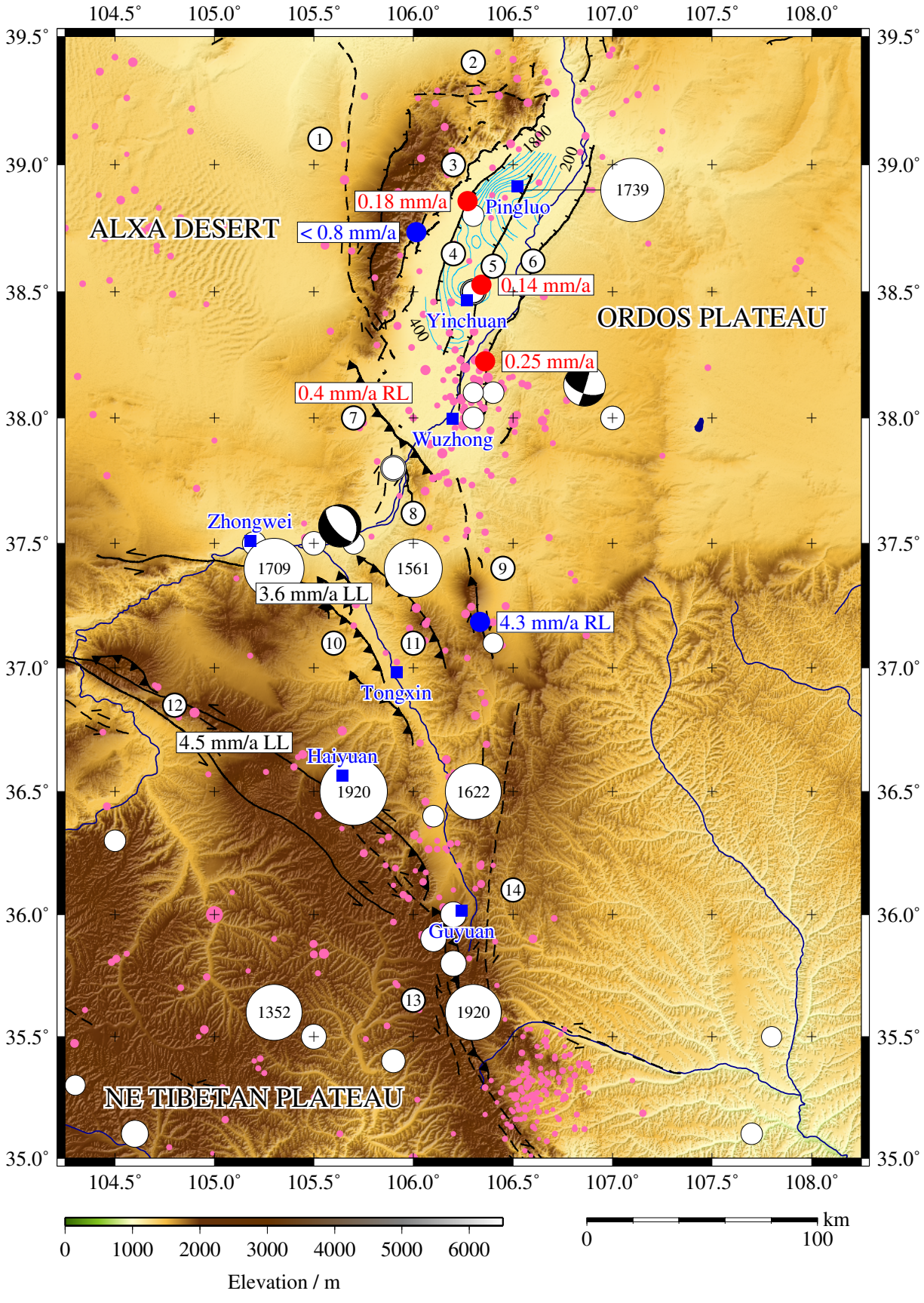
The 1556 Huaxian earthquake occurred in the Weihe Graben and is the deadliest earthquake on record, resulting in the deaths of an estimated 830,000 people (*Hou et al.*, 1998; *Yuan and Feng*, 2010; *Feng et al.*, 2016; *Zhou*, 2016). It is thought to have ruptured the Huashan and Weinan Tableland Faults with a total rupture length of ≈ 90 km and a maximum slip of 10 m (*Feng et al.*, 2016)—though some authors question whether or not the Weinan Tableland Fault ruptured in 1556 (*Li et al.*, 2015e). Isoseismal maps indicate a magnitude of 8.2 to 8.5 (*Yuan and Feng*, 2010), but simple scaling relationships

suggest a preferred magnitude in the range 7.3 to 7.9 (*Feng et al.*, 2016; *Zhou*, 2016). In a similar manner to the 1739 Yinchuan earthquake (see Chapter 2), it is thought that the historical records of shaking may overestimate the earthquake magnitude because they do not take account of amplification effects within the basin sediments. *Zhou* (2016) also estimated a likely recurrence interval of 6 to 8 ka. Combined with the vertical throw of 7.5 m in the 1556 earthquake, this suggests a long-term throw rate of $\approx$ 1 mm/a, which is not dissimilar to the rates obtained by *Hou et al.* (1998). The other major historical earthquake, the M 7 1501 Zhaoyi earthquake, is thought to have occurred on the Zhaoyi Fault (see Figure 6.10), and may have resulted in a Coulomb stress increase that triggered the 1556 earthquake (*Li et al.*, 2015d).

6.2.5 The western Ordos: the Yinchuan Graben, the Luoshan and the Liupanshan

In Chapters 3 and 4, we have already described the tectonics of the western Ordos—particularly the roles played by the Luoshan and East Helanshan Faults—in detail. Here, we present a short summary of what is known about the other faults in the region (see Figure 6.12 and Table 6.1).

The Haiyuan Fault—with a Late Quaternary slip rate of 4.5±1.0 mm/a (see Section 6.2.1) (*Li et al.*, 2009a)—enters the southern part of the western Ordos region striking northwest-southeast and terminates in a series of reverse faults. These reverse faults form a south trending fold-and-thrust zone that reaches as far as the Liupanshan at the southernmost extent of the region, uplifting Lower Cretaceous sedimentary rocks which were deposited in a former rift basin (*Deng et al.*, 1984a; *Li et al.*, 2013). The M 7.8 1920 earthquake occurred on the easternmost part of this fault (*Zhang et al.*, 1987). The Liupanshan Fault strikes north-south and forms a décollement-like thrust that dips shallowly to the west. The current slip rate on the Liupanshan Fault is not known, but the region is thought to have accommodated a total of 12.9 to 17.4 km of shortening (*Zhang et al.*, 1991).


104.5°
105.0°
105.5°
106.0°
106.5°
107.0°
107.5°
108.0°
39.5°
39.0°
38.5°
38.0°
37.5°
37.0°
36.5°
36.0°
35.5°
35.0°
ALXA DESERT
ORDOS PLATEAU
NE TIBETAN PLATEAU
0.18 mm/a
< 0.8 mm/a
0.14 mm/a
0.25 mm/a
0.4 mm/a RL
3.6 mm/a LL
4.3 mm/a RL
4.5 mm/a LL
Pingluo
Yinchuan
Wuzhong
Zhongwei
Tongxin
Haiyuan
Guyuan
1739
1709
1561
1920
1622
1352
1920
1800
200
400
1
2
3
4
5
6
7
8
9
10
11
12
13
14
0
1000
2000
3000
4000
5000
6000
Elevation / m
km
0
100

To the north of the Haiyuan Fault are two more oblique left-lateral faults: the Tianjinshan-Miboshan Fault (also called the Zhongwei-Tongxin Fault) and the Yantongshan Fault (see Figure 6.12, faults 10 and 11). The existence and orientation of these ranges implies ENE crustal shortening and it is thought that they were initially formed as a far-field effect of the India-Eurasia collision (*Li et al.*, 2013). Modern GPS studies also indicate northeast-southwest shortening across this region (*Gan et al.*, 2007).

The Tianjinshan-Miboshan Fault is around 130 km long, stretching from south of Zhongwei to west of Tongxin, dips to the southwest at 63 to 70 ° and is estimated to have an average left-lateral Quaternary slip rate of between 1.5 and 4.5 mm/a (*Zhang et al.*, 1990; *Min et al.*, 2000, 2001; *Deng et al.*, 2007; *Li et al.*, 2013). The M 7.5 1709 earthquake is also thought to have occurred on this fault. *Min et al.* (2001) excavated seven trenches across the Tianjinshan-Miboshan Fault and found evidence for six earthquakes in the last 14 ka. *Ding* (1993) also claimed that the 3 km wide meander where the Yellow River crosses the Tianjinshan-Miboshan Fault (at approximately 37.4 °N, 105.0 °E) records left-lateral motion over the last 1.4 Ma. The Yantongshan Fault is 110 km long and dips to the southwest, but little else is known about its recent activity (*Zhang et al.*, 1990; *Li et al.*, 2013). The Luoshan Fault lies to the east of the Yantongshan Fault (see Chapter 3) and the Niushoushan Fault to the north (see Figure 6.12, faults 7 and 9). The Niushoushan Fault dips to the southwest at between 62 and 85 ° (*Li et al.*, 2013), and recent work suggests a Late Quaternary right-lateral slip rate of ≈ 0.4 mm/a (*Lei et al.*, 2016). Immediately west of the Niushoushan, adjacent to the Yellow River, is the 50 km long Baima Fault, which dips to the west at 75 ° and appears to display normal motion

Figure 6.12 ***(preceding page)*:** New fault map for the western Ordos Plateau, based upon earlier fault maps from *Tapponnier and Molnar* (1977), *Deng et al.* (1984a), *Zhang et al.* (1990), *Darby and Ritts* (2002) and *Darby et al.* (2005). Annotations as in Figure 6.6. Light blue lines are Quaternary isopachs from *Lei et al.* (2008) and *Lei et al.* (2011). Red circles (and numbers) indicate rates measured by *Liao et al.* (2000), *Min et al.* (2001), *Lei et al.* (2008), *Lei et al.* (2011), *Lei et al.* (2015) and *Lei et al.* (2016); blue circles and numbers are rates measured in this study. Throw rates given in black are from *Deng et al.* (2007), where the location of the actual measurement site is unknown. Faults are numbered as follows: 1 Alxa Desert Fault; 2 Zhengyiguan Fault; 3 East Helanshan Fault; 4 Luhuatai Fault; 5 Yinchuan-Pingluo Fault; 6 Yellow River (Huang He) Fault; 7 Niushoushan Fault; 8 Baima Fault; 9 Luoshan Fault; 10 Tianjinshan-Miboshan (Zhongwei-Tongxin) Fault; 11 Yantongshan Fault; 12 Haiyuan Fault; 13 Liupanshan Fault; 14 Yunwushan Fault.

(*Chen et al.*, 2015). ^{14}C dating of snail fossils within loess deposits cut by the Baima Fault indicate that it has been active since ≈ 40 ka ago (*Chen et al.*, 2015). A number of authors have proposed that the Niushoushan Fault is linked to the Luoshan Fault (e.g. *Li et al.*, 2013; *Wang et al.*, 2013; *Chen et al.*, 2015), forming a continuous fault zone some 300 km long.

6.2.6 The eastern Ordos: the Shanxi Grabens

The Shanxi Grabens lie to the east of the Ordos Plateau, where they form an S-shaped series of en echelon basins some 1200 km long. The grabens can be divided into three broad zones: two, wide, ENE trending extensional zones in the north and the south, separated by a narrow, NNE trending right-lateral transtensional zone in the centre (*Xu and Ma*, 1992; *Xu et al.*, 1993). Although extension in the Shanxi Grabens only started in the Miocene, it is likely that the location and geometry of the grabens are in part determined by the pre-existing, northeast striking, fold-and-thrust belt structures of the Late Triassic (235 to 200 Ma old) Indosinian orogeny and the Middle Jurassic-Cretaceous (150 to 65 Ma old) Yanshanian orogeny (*Xu and Ma*, 1992; *Xu et al.*, 1993; *Zhang et al.*, 1998). Manifestations of these older orogenies are still evident today as thickened crust (40-44 km) and a corresponding gravity anomaly over the region (*Xu and Ma*, 1992). *Tapponnier and Molnar* (1977) note that the width and length of individual grabens decrease from south to north, whilst the mean elevation of the graben floors increases from 380 m in the south to 1010 m in the north (*Li et al.*, 2015a), suggesting a northward propagation of the onset of rifting through time.

The active faults in the northern Shanxi Grabens are described in detail in Chapter 5; here we focus on the central and southern sections of the Shanxi Grabens (see Figure 6.13 and Table 6.1).

The main feature in the central Shanxi Grabens is the ≈ 200 km long and ≈ 60 km wide Taiyuan (or Jinzhong) Graben (*Shi et al.*, 2015). It is bounded to the northwest by the Jiaocheng Fault and the Luliangshan (Luliang mountains) and to the southeast by the Taigu Fault and the Taihangshan (Taihang mountains) (*Xu and Ma*, 1992; *Xu*

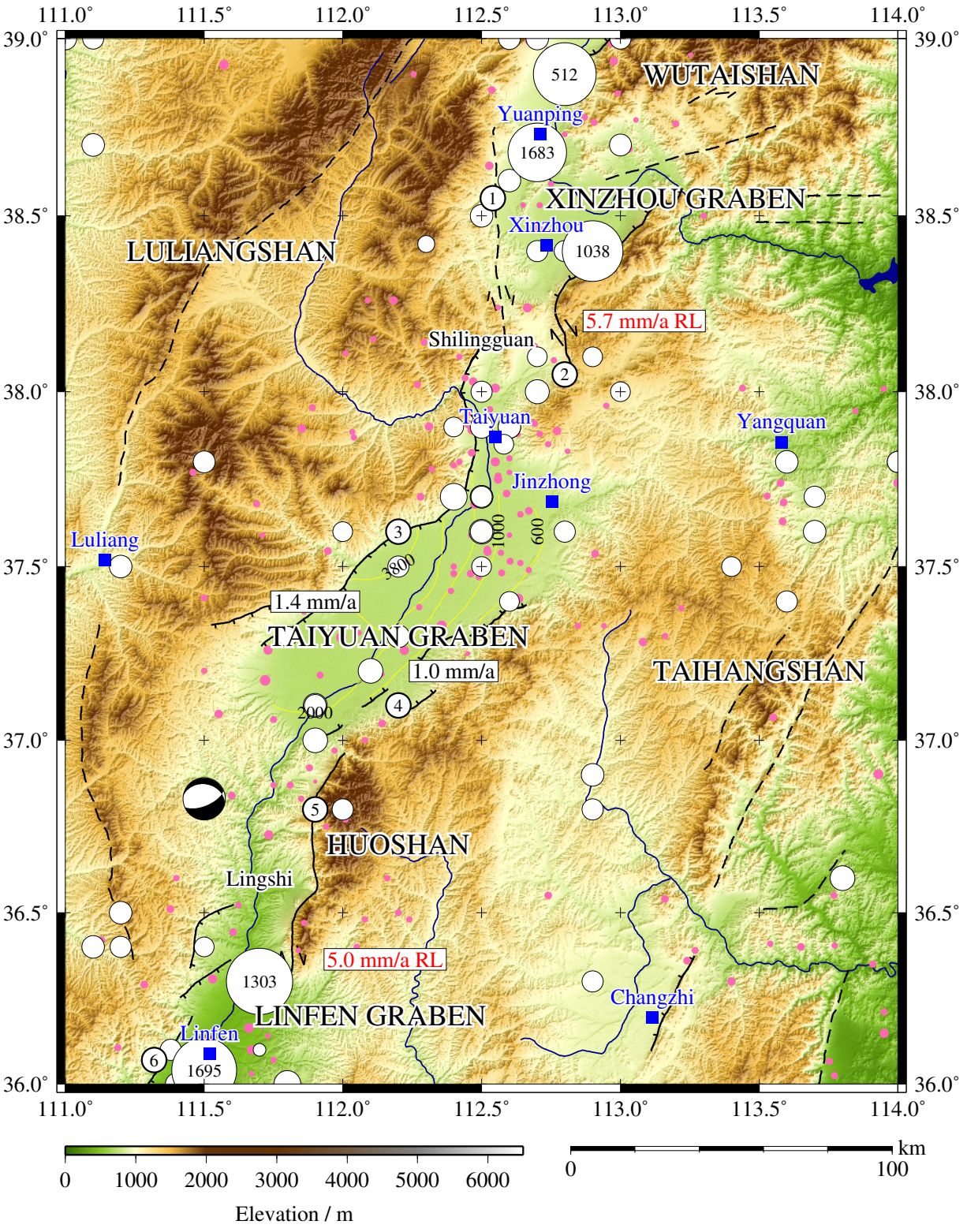


Figure 6.13: New fault map for the central Shanxi Grabens, based upon earlier fault maps from *Tapponnier and Molnar* (1977) and *Xu and Ma* (1992). Annotations as in Figure 6.6. Yellow lines are Quaternary and Pliocene isopachs from *Xu and Ma* (1992). Red numbers indicate slip rates measured by *Xu et al.* (1986), *Xu and Deng* (1990) and *Xu et al.* (1993). Throw rates given in black are from *Deng et al.* (2007). Faults are numbered as follows: 1 Yunzhongshan Fault; 2 Xizhoushan Fault; 3 Jiaocheng Fault; 4 Taigu Fault; 5 Huoshan Fault; 6 Luoyunshan Fault.

et al., 1993). Both the Jiaocheng and Taigu Faults are high-angle normal faults, dipping southeast and northwest respectively (*Li et al.*, 2015c). Palaeoseismic trenching on the Jiaocheng Fault suggests that at least three $M_s \geq 7$ earthquakes have occurred on this fault in the last 10,000 years (*Zhao et al.*, 2005; *Xie et al.*, 2008). Quaternary and Pliocene sediment accumulation in the Taiyuan Graben is thickest immediately adjacent to the Jiaocheng Fault (see Figure 6.13) (*Xu and Ma*, 1992), which is consistent with the Quaternary throw rate on the Jiaocheng Fault (1.4 mm/a) being higher than on the Taigu Fault (1.0 mm/a) (*Deng et al.*, 2007). Other studies have suggested that the throw rate on the Taigu Fault is even as low as 0.1 mm/a (*Xie et al.*, 2008). Assuming 45 ° dipping faults, these figures suggest an extension rate across the Taiyuan Graben of between 1.1 and 1.7 mm/a, which is slightly larger than the the total Quaternary extension rate of 0.5±0.1 mm/a obtained from a cross-sectional area balance by *Zhang et al.* (1998). *Li et al.* (2015c) inferred from a recent compilation of focal mechanisms that the principal motion in the Taiyuan Graben is NNW-SSE extension, occurring as normal faulting with a subsidiary strike-slip component.

The Taiyuan Graben is separated from the Xinzhou Graben to the north by the Shilingguan "push-up" (*Shi et al.*, 2015). The Xizhoushan Fault is a north-south oblique right-lateral strike-slip fault that runs between the Shilingguan "push-up" to the west and the Xizhoushan (Xizhou mountains) to the east, before bending to the northeast and forming the southeastern margin of the Xinzhou Graben (see Figure 6.13). The Yunzhongshan Fault runs along the western side of the Xinzhou Graben, abutting the eastern Luliangshan, and connects the Taiyuan Graben to the Xingxian Graben further north (see Chapter 5). The Xizhoushan Fault has a strike of 185 to 195 ° and dips west at ≈ 65 ° (*Xu et al.*, 1993). It is exposed at the surface for around 10 km in a zone 10 m wide (*Xu et al.*, 1993). *Xu et al.* (1986) estimated a right lateral slip rate on the Xizhoushan Fault of 5.7 mm/a from a single ^{14}C sample (age 8.90±0.28 ka) taken from a gully offset by 50.6 m.

Immediately south of the Taiyuan Graben is the Lingshi "push-up" and the Huoshan (Huo mountains) (*Shi et al.*, 2015). The oblique right-lateral Huoshan Fault runs between the Lingshi "push-up" and the Huoshan, forming the northeastern boundary of the Linfen

Graben at its southern end. The Huoshan Fault strikes at 190 to 195 ° and dips west at ≈ 70 ° (*Xu et al.*, 1993). Lateral offsets can be seen in 56 different gullies along a 35 km long segment of the fault. *Xu and Deng* (1990) obtained ^{14}C ages from three different gullies of 4.05±0.11 ka, 8.33±0.13 ka and 16.72±0.55 ka. They measured corresponding offsets of 30.3, 61.2 and 107.2 m. However, *Xu et al.* (1993) revised these offsets to 20.1, 41.5 and 107.2 m, giving slip rates of 5.0, 5.0 and 6.4 mm/a (see Table 6.1).

The M 8 1303 Hongdong earthquake, which killed an estimated 200,000 people, is thought to have ruptured the Huoshan Fault, the Taigu Fault, and the intervening Mianshan Fault (at the northern end of the Huoshan) forming a surface rupture zone 160 km long (*Jiang et al.*, 2004; *Xie et al.*, 2004; *Li et al.*, 2015b). Along the central and northern Huoshan Fault, 26 offset measurements indicate a coseismic right-lateral displacement of 7 to 9 m, with an additional vertical displacement of 3 to 5 m in a normal sense (*Jiang et al.*, 2004). Ages for numerous offset features on the Huoshan Fault confirm that these scarps are from the 1303 event (*Jiang et al.*, 2004). On the Taigu Fault, evidence for recent rupturing can be seen along 70 km of the 100 km long fault, with right-lateral offsets of 7 to 13 m and scarps 2 to 3 m high (*Jiang et al.*, 2004; *Xie et al.*, 2004). ^{14}C and TL ages from a number of trenches along the Taigu Fault indicate that the scarps here are younger than 3 to 4 ka old (*Xie et al.*, 2004). Furthermore the Cixiangsi temple, adjacent to the Taigu Fault, is believed to have been built in 1195 and destroyed before 1600—probably by the 1303 earthquake (*Meng et al.*, 1982). Nonetheless, other authors suggest that only the Huoshan Fault ruptured in the 1303 earthquake and that it involved smaller right-lateral offsets of around 5 to 8 m (*Xu and Deng*, 1990; *Xu and Ma*, 1992; *Xu et al.*, 1993; *Zhang et al.*, 1998). In addition, palaeoseismological work on the Huoshan Fault indicates two further earthquakes since the mid-Holocene, implying a recurrence interval of 1500 to 2000 years (*Xu and Ma*, 1992). Other major historical earthquakes include the M 7.3 1038 event adjacent to the Xizhoushan and the M 7.8 1695 Linfen earthquake in the Linfen Graben, although its seismogenic fault remains undetermined (*Xu and Ma*, 1992; *Xu et al.*, 1993; *Wang et al.*, 2012a; *Li et al.*, 2015a,d). The single focal mechanism in Figure 6.13 (for an almost pure normal-faulting event) is from the M_s 5.5 1979 Jiexiu earthquake, which presumably occurred on the Taigu Fault (*Li et al.*, 2015c).

6.3 Kostrov summations at the margins of the Ordos Plateau

We use Kostrov's relation to calculate strain rate tensors for each of the deforming margins of the Ordos Plateau in a similar manner to that adopted in Chapter 5. We aim to assess and update the previous calculations from *Wesnousky et al.* (1984), who used a total catalogue of 19 earthquakes with magnitudes greater than 6.5. However, the earthquake catalogues in the Ordos region are thought to be complete for earthquakes with $M_s \geq 6$ since 1291 (*Huang et al.*, 1994). We therefore construct a catalogue of 54 earthquakes with $M_s > 6$ for the 700 year period from 1315 to 2015 based on *Lee et al.* (1976), *Lee et al.* (1978), *Liu et al.* (2011), the China Seismological Bureau (CSB) catalogue (*Qin et al.*, 2002), and the Global Centroid Moment Tensor (GCMT) catalogue (*Ekström et al.*, 2012). We also include an additional 34 earthquakes with $5 < M_s \leq 6$, based on the same sources, for which focal mechanisms have already been inferred—but we note that the catalogue is not necessarily complete over this magnitude range. In total, our catalogue includes 88 earthquakes. As in Chapter 5, we approximate surface-wave magnitude (M_s) as equal to moment magnitude (M_w) for $M_s \leq 8$ (*Kanamori*, 1983).

Focal parameters for some of these 88 earthquakes are available in the literature (*Wesnousky et al.*, 1984; *Pavlides et al.*, 1999; *Xu et al.*, 2000; *Liu et al.*, 2007; *Li et al.*, 2015d) or the GCMT catalogue (*Ekström et al.*, 2012). For the remaining historical events, we estimate focal parameters from nearby instrumental earthquakes or adjacent faults. In the second case, we assume that the sense of slip during the earthquake was the same as the Quaternary motion on the nearest adjacent fault. All 88 earthquakes and their associated parameters are listed in Table 6.2.

Figure 6.14 (a) shows the results of the Kostrov summations for the *Wesnousky et al.* (1984) catalogue; Figure 6.14 (b) shows the results of the Kostrov summations for the earthquake catalogue compiled in this study. Following the divisions used by *Wesnousky et al.* (1984) we split our calculation into five regions, which we call (clockwise from top left): North Ningxia, Hetao, Shanxi, Weihe and South Ningxia. We use a shear modulus (μ) of 3.3 GPa and a seismogenic thickness (T_s) of 20 km for all calculations. We choose

Table 6.2: Focal parameters for historical earthquakes around the Ordos Plateau

Year	Month	Day	Lat / °	Long / °	M_w [a]	M_0 [b] / Nm	Eq. ref.	Strike / °	Dip / °	Rake / °	FP ref.	Assigned fault	FP notes
1337	9	8	40.4	115.7	6.5	6.24×10^{18}	*Lee et al.* (1976)	55	75	-77	This study, *Pavlides et al.* (1999)	Yanqing Fault	Av. 5 striations
1352	4	18	35.6	105.3	6.8	1.90×10^{19}	*Lee et al.* (1976)	130	45	90	*Wesnousky et al.* (1984)		
1363	7	8	37.6	112.5	6.0	1.11×10^{18}	*Lee et al.* (1976)	50	60	-90	This study	Jiaocheng Fault	Nearest fault
1467	6	18	39.6	112.3	5.5	1.97×10^{17}	*Liu et al.* (2011)	20	74	138	This study		Nearest instrumental eq
1477	5	13	38.5	106.3	6.5	6.70×10^{18}	*Lee et al.* (1976)	30	75	-150	*Wesnousky et al.* (1984)		
1484	2	7	40.5	116.1	6.8	1.76×10^{19}	*Liu et al.* (2011)	55	75	-77	This study, *Pavlides et al.* (1999)	Yanqing Fault	Av. 5 striations
1487	8	19	34.4	108.9	6.3	3.13×10^{18}	*Liu et al.* (2011)	270	60	-90	This study, *Rao et al.* (2015)	Lishan Piedmont Fault	Nearest fault
1495	4	10	37.6	105.6	6.3	2.63×10^{18}	*Lee et al.* (1976)	120	45	45	This study, *Liu-Zeng et al.* (2015)	Zhongwei-Tongxin Fault	Nearest fault
1501	1	29	34.8	110.1	7.0	3.30×10^{19}	*Liu et al.* (2011)	230	60	-30	*Wesnousky et al.* (1984)		
1502	12	4	39.0	112.6	5.3	9.89×10^{16}	*Liu et al.* (2011)	45	62	-90	This study, *Li et al.* (2015d)	Yunzhongshan Fault	
1514	10	30	38.7	113.0	5.3	9.89×10^{16}	*Liu et al.* (2011)	129	85	18	This study		Nearest instrumental eq
1545	2	x	40.0	114.0	5.3	9.89×10^{16}	*Liu et al.* (2011)	250	65	-135	This study, *Li et al.* (2015d)	Liulengshan Fault	
1556	1	23	34.5	109.7	7.9	8.32×10^{20} [c]	*Liu et al.* (2011)	270	60	-30	*Wesnousky et al.* (1984)	Huashan/Weinan Tableland Fault	
1561	7	25	37.4	106.0	7.2	6.90×10^{19}	*Lee et al.* (1976)	145	30	90	*Wesnousky et al.* (1984)		
1568	5	15	34.4	109.0	6.8	1.80×10^{19}	*Liu et al.* (2011)	270	60	-30	*Wesnousky et al.* (1984)		
1573	1	10	34.4	104.0	6.8	1.48×10^{19}	*Lee et al.* (1976)	196	57	151	This study, *Zheng et al.* (2007)	Lintan-Dangchang Fault	Nearest instrumental eq
1580	9	15	39.5	112.3	5.8	5.56×10^{17}	*Liu et al.* (2011)	20	74	138	This study		Nearest instrumental eq
1581	5	18	39.8	114.5	6.0	1.11×10^{18}	*Lee et al.* (1976)	250	60	-110	This study, *Liu et al.* (2007)	Yuguang Graben Fault	
1583	5	18	39.7	113.8	5.5	1.97×10^{17}	*Lee et al.* (1976)	225	65	-116	This study, *Li et al.* (2015d)	Hengshan Fault	
1604	10	25	34.2	105.0	6.0	1.11×10^{18}	*Lee et al.* (1976)	334	46	38	This study		Nearest instrumental eq
1614	10	23	37.2	112.1	6.0	1.11×10^{18}	*Liu et al.* (2011)	230	60	-65	*Li et al.* (2015d)	Jiexiu-Taigu	
1618	5	20	37.0	111.9	6.0	1.11×10^{18}	*Liu et al.* (2011)	15	90	180	This study	Huoshan Fault	Nearest fault
1618	11	16	39.8	114.5	6.0	1.11×10^{18}	*Lee et al.* (1976)	250	60	-110	This study, *Liu et al.* (2007)	Yuguang Graben Fault	
1622	10	25	36.5	106.3	7.7	3.42×10^{20}	*Lee et al.* (1976)	180	45	90	*Wesnousky et al.* (1984)		
1624	7	4	35.4	105.9	6.0	1.11×10^{18}	*Lee et al.* (1976)	160	45	45	This study	Liupanshan Fault	Nearest fault
1626	6	28	39.4	114.2	7.2	8.10×10^{19}	*Lee et al.* (1976)	220	60	-120	*Wesnousky et al.* (1984)	Lingqiu Graben Fault	
1627	2	16	37.5	105.5	6.0	1.11×10^{18}	*Lee et al.* (1976)	120	45	45	This study	Zhongwei-Tongxin Fault	Nearest fault
1628	10	7	40.6	114.2	6.5	6.24×10^{18}	*Liu et al.* (2011)	75	45	-97	This study, *Li et al.* (2015d)	Yanggao-Tianzhen Graben Fault	
1634	1	x	34.0	105.2	6.0	1.11×10^{18}	*Lee et al.* (1976)	334	46	38	This study		Nearest instrumental eq
1642	6	30	35.0	110.9	6.5	7.30×10^{18}	*Liu et al.* (2011)	230	60	-30	*Wesnousky et al.* (1984)		
1654	7	21	34.3	105.5	7.7	4.27×10^{20}	*Lee et al.* (1976)	105	90	0	*Wesnousky et al.* (1984)		
1658	2	3	39.4	115.7	6.0	1.11×10^{18}	*Liu et al.* (2011)	45	90	180	This study		
1664	x	x	38.7	112.7	5.5	1.97×10^{17}	*Lee et al.* (1976)	200	62	-160	This study, *Li et al.* (2015d)	Yunzhongshan Fault	
1665	4	16	39.9	116.6	6.5	6.24×10^{18}	*Liu et al.* (2011)	205	50	160	This study, *Liu et al.* (2007)		
1673	10	18	40.5	113.5	6.0	1.11×10^{18}	*Liu et al.* (2011)	235	45	-93	*Li et al.* (2015d)	Yanggao-Tianzhen Graben Fault	
1673	10	18	40.5	114.1	5.5	1.97×10^{17}	*Lee et al.* (1976)	75	45	-97	This study, *Li et al.* (2015d)	Yanggao-Tianzhen Graben Fault	
1683	11	22	38.7	112.7	7.4	1.42×10^{20}	*Lee et al.* (1976)	200	60	-160	*Wesnousky et al.* (1984)	Yunzhongshan Fault	
1695	5	18	36.0	111.5	7.2	8.10×10^{19}	*Liu et al.* (2011)	90	60	30	*Wesnousky et al.* (1984)		
1704	9	28	34.9	106.8	6.0	1.11×10^{18}	*Lee et al.* (1976)	140	45	-90	This study		Nearest fault
1709	10	14	37.4	105.3	7.5	1.78×10^{20}	*Lee et al.* (1976)	295	30	30	*Wesnousky et al.* (1984)		
1718	6	19	35.0	105.2	7.3	8.90×10^{19}	*Lee et al.* (1976)	105	90	0	*Wesnousky et al.* (1984)		
1720	7	12	40.4	115.5	6.8	1.48×10^{19}	*Lee et al.* (1976)	67	69	-81	This study, *Pavlides et al.* (1999)	Huailai Fault	Av. 3 striations
1730	9	30	40.0	116.2	6.5	6.24×10^{18}	*Liu et al.* (2011)	30	45	-90	This study		Nearest fault
1739	1	3	38.9	106.5	7.6	2.72×10^{20} [d]	*Lee et al.* (1976)	40[d]	40[d]	-90[d]	This study	East Helanshan Fault	

[a] Magnitudes for historical earthquakes are estimated from intensities on the *New Chinese Intensity Scale* using $M_s = 0.58\times I_0 + 1.5$. M_s is considered equal to M_w for $M_s \leq 8$ (*Kanamori*, 1983).

[b] M_0 calculated from M_w using $M_0 = 10^{\frac{3}{2}(M_w+6.03)}$.

[c] Seismic moment and focal parameters for 1556 earthquake re-estimated from *Feng et al.* (2016).

[d] Seismic moment and focal parameters for 1739 earthquake re-estimated from Chapter 2.

Table 6.2: (continued) Focal parameters for historical earthquakes around the Ordos Plateau

Year	Month	Day	Lat / °	Long / °	M_w [a]	M_0 [b] / Nm	Eq. ref.	Strike / °	Dip / °	Rake / °	FP ref.	Assigned fault	FP notes
1765	9	2	34.8	105.0	7.0	4.00×10^{19}	*Lee et al.* (1976)	105	90	0	*Wesnousky et al.* (1984)		
1815	10	23	34.8	111.2	7.1	4.20×10^{19}	*Liu et al.* (2011)	230	60	-30	*Wesnousky et al.* (1984)		
1852	5	26	37.5	105.2	6.0	1.11×10^{18}	*Lee et al.* (1976)	290	30	90	This study		Nearest fault
1881	7	20	33.6	104.6	6.5	6.24×10^{18}	*Lee et al.* (1976)	120	90	0	This study		Nearest fault
1885	1	14	34.5	105.7	6.0	1.11×10^{18}	*Lee et al.* (1976)	90	90	0	This study		Nearest fault
1888	11	2	37.1	104.2	6.3	2.63×10^{18}	*Lee et al.* (1976)	285	30	90	This study		Nearest fault
1898	9	22	39.1	113.0	5.5	1.97×10^{17}	*Lee et al.* (1976)	230	60	-135	This study, *Li et al.* (2015d)	Wutaishan Fault	
1911	1	25	39.8	114.5	5.9	7.85×10^{17}	*Liu et al.* (2011)	250	60	-110	This study, *Liu et al.* (2007)	Yuguang Graben Fault	
1920	12	16	36.5	105.7	8.0	1.20×10^{21}	*Lee et al.* (1978)	115	90	0	*Wesnousky et al.* (1984)		
1920	12	25	35.6	106.3	7.0	3.51×10^{19}	*Lee et al.* (1978)	160	45	45	This study	Liupanshan Fault	Nearest fault
1920	12	28	35.5	105.5	6.3	2.63×10^{18}	*Lee et al.* (1978)	160	45	45	This study	Liupanshan Fault	Nearest fault
1921	4	12	35.8	106.2	6.5	6.24×10^{18}	*Lee et al.* (1978)	160	45	45	This study	Liupanshan Fault	Nearest fault
1929	1	14	40.7	111.3	6.0	1.11×10^{18}	*Liu et al.* (2011)	70	60	-90	This study	Daqingshan Fault	Nearest fault
1934	1	21	41.0	108.8	6.3	3.13×10^{18}	*Liu et al.* (2011)	120	60	-90	This study	Seertengshan Fault	Nearest fault
1936	8	1	34.2	105.7	6.0	1.11×10^{18}	*Lee et al.* (1978)	334	46	38	This study		Nearest instrumental eq
1952	10	8	39.0	112.7	5.5	1.97×10^{17}	*Liu et al.* (2011)	45	62	-90	This study, *Li et al.* (2015d)	Yunzhongshan Fault	
1962	12	7	38.1	106.3	5.5	1.97×10^{17}	*Qin et al.* (2002)	108	36	144	CSB		
1965	1	13	35.0	111.6	5.5	1.97×10^{17}	*Qin et al.* (2002)	201	65	-158	CSB		
1967	7	28	40.5	115.6	5.4	1.40×10^{17}	*Liu et al.* (2011)	67	69	-81	This study, *Pavlides et al.* (1999)	Huailai Fault	Av. 3 striations
1967	12	18	36.5	111.2	5.4	1.40×10^{17}	*Qin et al.* (2002)	355	80	-161	CSB		
1970	12	3	35.9	105.6	5.1	4.95×10^{16}	*Qin et al.* (2002)	9	74	132	CSB		
1971	6	28	37.9	106.3	5.1	4.95×10^{16}	*Qin et al.* (2002)	213	63	46	CSB		
1976	4	6	40.2	112.1	6.2	2.21×10^{18}	*Liu et al.* (2011)	209	75	164	CSB		
1976	9	23	39.9	106.4	6.2	2.21×10^{18}	*Qin et al.* (2002)	79	68	28	CSB		
1979	6	19	36.83	111.50	5.0	3.51×10^{16}	GCMT	278	30	-63	GCMT		
1979	8	24	40.83	108.24	5.7	3.94×10^{17}	GCMT	111	44	-65	GCMT		
1981	8	13	40.50	113.40	5.5	1.97×10^{17}	*Qin et al.* (2002)	183	80	-178	CSB		
1987	1	7	34.23	103.86	5.4	1.40×10^{17}	GCMT	170	65	28	GCMT		
1987	8	10	37.57	105.63	5.3	9.89×10^{16}	GCMT	336	25	-75	GCMT		
1988	1	3	38.13	106.86	5.2	7.00×10^{16}	GCMT	110	57	5	GCMT		
1989	10	18	39.63	113.84	5.4	1.40×10^{17}	GCMT	92	44	-39	GCMT	Hengshan Fault	
1989	10	18	39.77	113.49	5.6	2.79×10^{17}	GCMT	200	75	-175	GCMT	Liulengshan Fault	
1989	10	18	39.83	113.61	5.4	1.40×10^{17}	GCMT	204	76	-176	GCMT	Liulengshan Fault	
1989	10	19	39.94	113.84	6.1	1.57×10^{18}	*Li et al.* (2015d)	200	44	136	*Li et al.* (2015d)	Dawang-Tuanbao Fault	
1989	10	19	39.92	113.91	5.9	7.85×10^{17}	*Xu et al.* (2000)	210	76	-167	*Xu et al.* (2000)		
1991	3	25	40.10	113.34	5.4	1.40×10^{17}	GCMT	106	82	7	GCMT	Datong Basin Fault	
1996	5	3	40.72	109.69	6.0	1.11×10^{18}	GCMT	308	75	-12	GCMT		
1998	1	10	41.34	114.34	5.7	3.94×10^{17}	GCMT	207	54	135	GCMT		
1999	11	1	39.85	113.74	5.2	7.00×10^{16}	GCMT	122	72	-7	GCMT	Liulengshan Fault	
2000	6	6	37.02	103.91	5.5	1.97×10^{17}	GCMT	96	68	-6	GCMT		
2003	11	13	34.61	104.10	5.1	4.95×10^{16}	GCMT	347	42	53	GCMT		
2013	7	21	34.60	104.31	6.0	1.11×10^{18}	GCMT	196	57	151	GCMT		
2013	7	22	34.65	104.35	5.4	1.40×10^{17}	GCMT	153	37	103	GCMT		
2015	4	15	39.74	106.39	5.5	1.97×10^{17}	GCMT	356	81	-177	GCMT		

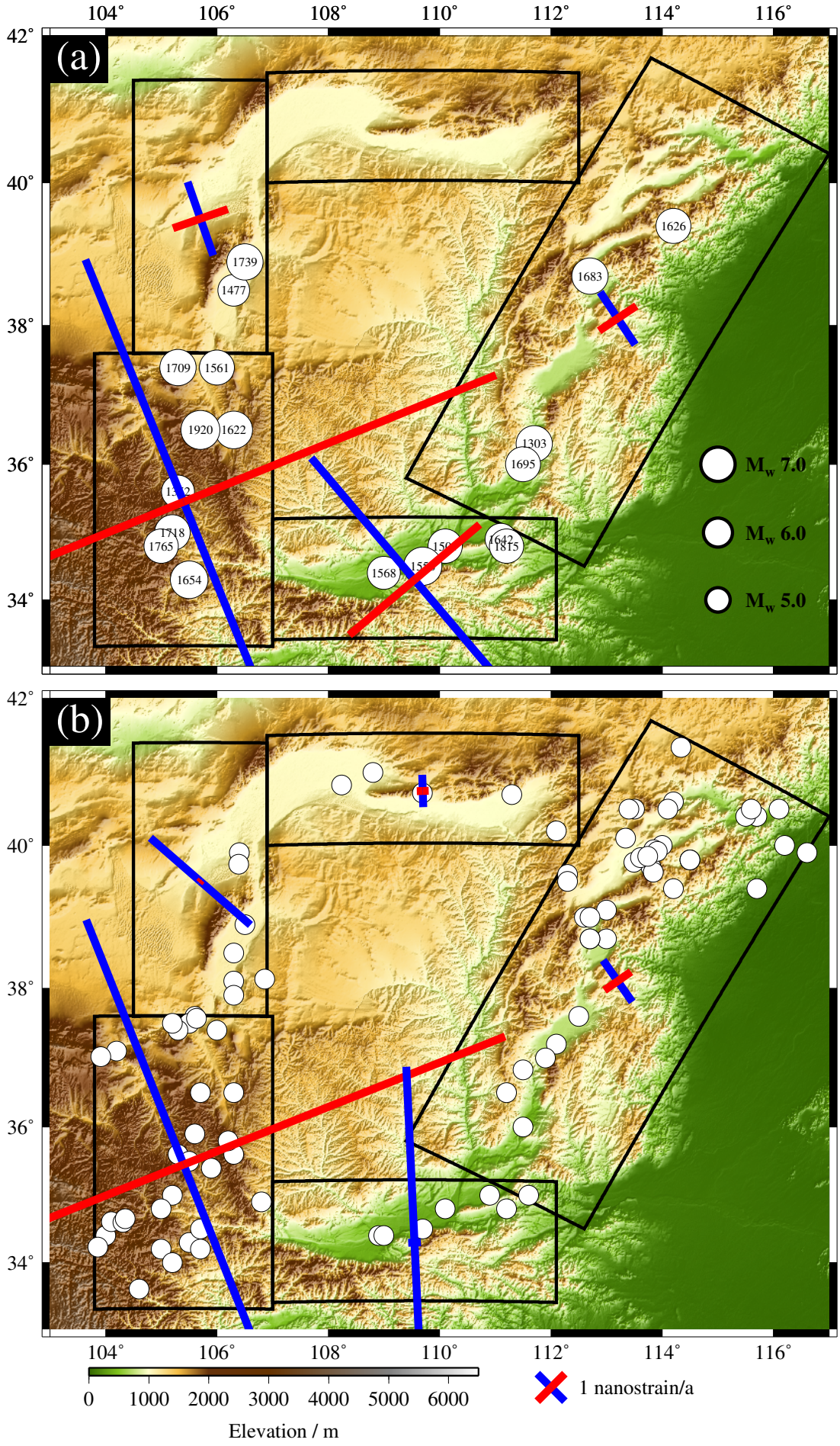
[a] Magnitudes for historical earthquakes are estimated from intensities on the *New Chinese Intensity Scale* using $M_s = 0.58\times I_0 + 1.5$. M_s is considered equal to M_w for $M_s \leq 8$ (*Kanamori*, 1983).

[b] M_0 calculated from M_w using $M_0 = 10^{\frac{3}{2}(M_w+6.03)}$.

T_s = 20 km as this was the value used by *Wesnousky et al.* (1984) and because the epicentres of recent earthquakes are found to have not exceeded a depth of ≈ 20 km (*Molnar et al.*, 1984; *Li et al.*, 2015b). The full results of the Kostrov summations are recorded in Table 6.3.

The Kostrov summations based on the earthquake catalogue compiled in this study do not differ significantly from the results of *Wesnousky et al.* (1984). This is to be expected given that the total seismic moment released by the earthquakes in the *Wesnousky et al.* (1984) catalogue ($M_s \geq 6.5$) constitutes between 58 and 97% (depending on the region) of the seismic moment released by the earthquakes in our catalogue (see Table 6.3). The magnitudes of the maximum and minimum principal strain rates depend heavily on the parameters assigned to the largest earthquake in each region—particularly the 1739 Yinchuan, the 1920 Haiyuan, the 1556 Huaxian, and the 1303 Hongdong events (which is not included in our catalogue, but was used by *Wesnousky et al.* (1984)). Furthermore, in Chapter 5 we showed that the largest uncertainty in the Kostrov summations stems from errors on the magnitude estimates for the historical earthquakes. A moment magnitude with a typical error of ±0.3 (*Liu et al.*, 2011) equates to a seismic moment that varies by a factor of 2.8 either way. In other words, the total moment release (ΣM_0), the moment release rate (M_0 rate), the maximum principal strain rate ($\dot{\epsilon}_1$) and the minimum principal strain rate ($\dot{\epsilon}_2$) in Table 6.3 are all uncertain by up to a factor of ≈ 3 either way. In contrast, the azimuths of the maximum and minimum principal strain rate are thought to be correct to within ±15 ° (see Chapter 5).

The general pattern of strain release is as follows (see Appendix C.1 for the theory associated with interpreting the strain rate results). In northern Ningxia, the deformation appears to be dominated by extension at a strain rate of 3.4 nanostrain/a and an azimuth of 131 °. This extension could readily be accommodated on the NNE-SSW normal faults in the Yinchuan Graben, particularly on the East Helanshan Fault. However, 96% of the total moment release is due to the 1739 Yinchuan earthquake, so the result depends very heavily on the parameters used for this event: indeed, *Wesnousky et al.* (1984) used different parameters and obtained a much larger component of north-south right-lateral


(a)
(b)
104°
106°
108°
110°
112°
114°
116°
42°
40°
38°
36°
34°
1739
1477
1626
1683
1709
1561
1920
1622
1303
1695
1718
1765
1654
1568
1642
1815
M_w 7.0
M_w 6.0
M_w 5.0
0
1000
2000
3000
4000
5000
6000
Elevation / m
1 nanostrain/a

strike-slip motion (see Figure 6.14 (a)). We really need a longer catalogue with more large-magnitude events to provide a more accurate summation.

In southern Ningxia, the maximum and minimum principal strain rates are roughly equal in magnitude and opposite in sign, indicating predominantly strike-slip faulting with a small component of contraction. The strain could therefore be taken up on WNW-ESE left-lateral strike-slip faults or NNE-SSW right-lateral strike-slip faults. From the pattern of active faulting, it appears that both types of fault are present: the Haiyuan, Yantongshan and Tianjinshan-Miboshan Faults are all predominantly left-lateral whilst the Luoshan and Niushoushan Faults, which lie approximately at right-angles, are right-lateral. In addition, northeast-southwest contraction at a strain rate of 18 nanostrain/a and an azimuth of 68 ° (which corresponds to ≈ 5 mm/a of shortening) is taken up on NNW-SSE striking reverse faults, such as the Liupanshan Fault.

North of the Ordos, in the Linhe and Hetao Grabens, the dominant motion is north-south extension at a strain rate of 0.083 nanostrain/a and an azimuth of 178 °. This motion could be taken up on the Seertengshan, South Wulashan and Daqingshan Faults. In addition, there is a small amount of strike-slip motion to be accommodated. This could be achieved by northwest-southeast left-lateral strike-slip faulting on, for example, an extension of the Seertengshan Fault—as occurred in the 1996 Baotou earthquake. However, the strain rate in the northern Ordos is two orders of magnitude smaller than at other margins of the plateau. This difference is much larger than the factor of ≈ 3 that could arise from errors on the magnitude estimates. Either the strain rate really is much lower in the northern Ordos, or we are missing rare, large-magnitude events from our 700 year catalogue. For example, including the M 7.5 849 earthquake in the summation

Figure 6.14 *(preceding page)*: (a) SRTM topography (90 m resolution) of the Ordos Plateau (*Farr et al.*, 2007). Black rectangles indicate Kostrov regions at the margins of the plateau. Historical earthquakes from *Wesnousky et al.* (1984) are shown as white circles, scaled according to their magnitude and including the year in which they occurred. Crosses indicate orientation and magnitude of maximum and minimum horizontal strain rate from a Kostrov summation in each region using the *Wesnousky et al.* (1984) earthquake catalogue; blue indicates extension and red indicates contraction. (b) Same as (a), but white dots show earthquakes from the catalogue compiled in this study—see Table 6.2. Strain rate crosses as in (a), but calculated for our earthquake catalogue. See Table 6.3 for further details. Note that the scale is exaggerated 10× for the Kostrov strain rate cross in the Linhe and Hetao Grabens.

adds an additional 2.0×10^{20} Nm to the total moment release, increasing it by more than a factor of 10 (see Section 6.2.3 and Table 6.3). Assuming a pure normal mechanism for this event, the updated Kostrov summation indicates a strain rate of 2.4 nanostrain/a at an azimuth of 161°. Furthermore, palaeoseismological work on the Daqingshan Fault indicates typical recurrence intervals for large earthquakes of more than 2000 years, so it is plausible that our 700 year time window is too short to capture the most important events (*Ran et al.*, 2002, 2003b,c).

In the Weihe Graben, extension occurs at a strain rate of 9 nanostrain/a (equivalent to ≈ 1.8 mm/a) and an azimuth of 177°, which is consistent with normal-faulting on the Qianxian-Fuping, Weihe, North Qinlingshan, Huashan, Weinan Tableland, Sanmenxia-Lingbao, North Zhongtiaoshan and Zhaoyi Faults. This extension appears to be almost completely biaxial (i.e. matched by vertical thinning rather than any east-west strain). Again, though, 89% of the total moment release is due to the 1556 Huaxian earthquake, so the result depends very heavily on the parameters used for this event. We used recent observations from *Zhou* (2016) to constrain the focal mechanism for this earthquake, but *Wesnousky et al.* (1984) used different parameters and obtained a much larger component of strike-slip motion (see Table 6.3).

Finally, in the Shanxi Grabens, the predominant motion is strike-slip: either right-lateral strike-slip on faults striking NNE-SSW or left-lateral strike-slip on faults striking WNW-ESE. Given the orientation of faults in the Shanxi Grabens, right-lateral motion is more likely. The Xizhoushan and Huoshan Faults are major right-lateral structures in the Shanxi Grabens, but motion can also be accommodated by oblique slip on the intervening en echelon normal faults. The pattern of strain release in the northern Shanxi Grabens is discussed in much more detail in Chapter 5.

Table 6.3: Summary of results from Kostrov summations and GPS around the Ordos Plateau

Earthquakes used	Time years	No. eqs	Area km^2	Σ M_0 Nm	M_0 rate Nm/a	$\dot{\epsilon}_1$ a^{-1}	$\dot{\epsilon}_2^a$ a^{-1}	$\dot{\epsilon}_1$ az. $^\circ$	$\dot{\epsilon}_1/\dot{\epsilon}_2$	ϕ^b radians	Faulting[c]
Earthquake catalogue from Wesnousky et al. (1984)											
North Ningxia	700	2	86,992	1.66×10^{20}	2.37×10^{17}	2.00×10^{-9}	-1.49×10^{-9}	161	-1.34	2.50	SS + normal
South Ningxia	700	8	138,561	2.36×10^{21}	3.38×10^{18}	1.34×10^{-8}	-1.73×10^{-8}	158	-0.77	2.23	SS + reverse
Hetao	700	0	78,661	N/A	N/A	N/A	N/A	N/A	N/A	N/A	N/A
Weihe	700	5	93,765	7.61×10^{20}	1.09×10^{18}	8.19×10^{-9}	-4.39×10^{-9}	140	-1.87	2.65	SS + normal
Shanxi	700	4	239,349	4.22×10^{20}	6.03×10^{17}	1.62×10^{-9}	-1.16×10^{-9}	146	-1.40	2.52	SS + normal
Earthquake catalogue from this study											
North Ningxia	700	8	86,992	2.84×10^{20}	4.06×10^{17}	3.40×10^{-9}	-8.12×10^{-11}	131	-41.87	3.12	Normal + SS
South Ningxia	700	30	138,561	2.44×10^{21}	3.49×10^{18}	1.35×10^{-8}	-1.78×10^{-8}	158	-0.76	2.22	SS + reverse
Hetao	700	5	78,661	7.95×10^{18}	1.14×10^{16}	8.30×10^{-11}	-3.02×10^{-11}	178	-2.75	2.79	Normal + SS
Weihe	700	7	93765	9.36×10^{20}	1.34×10^{18}	9.03×10^{-9}	3.20×10^{-10}	177	28.22	3.18	Normal + normal
Shanxi	700	40	239,349	3.76×10^{20}	5.37×10^{17}	1.30×10^{-9}	-8.32×10^{-10}	145	-1.56	2.57	SS + normal
GPS derived strain rates in Kostrov regions—see Section 6.4.1											
North Ningxia	4	10[d]	86,992	N/A	N/A[e]	5.00×10^{-9}	-5.40×10^{-9}	146	-0.93	2.32	SS + reverse
South Ningxia	4	14[d]	138,561	N/A	N/A[e]	3.30×10^{-9}	-1.20×10^{-8}	163	-0.28	1.84	Reverse + SS
Hetao	4	19[d]	78,661	N/A	N/A[e]	2.61×10^{-9}	-2.41×10^{-9}	133	-1.08	2.40	SS + normal
Weihe	4	18[d]	93,765	N/A	N/A[e]	-3.10×10^{-9}	-4.30×10^{-9}	156	0.72	0.95	Reverse + reverse
Shanxi	4	130[d]	239,349	N/A	N/A[e]	2.40×10^{-9}	-9.40×10^{-10}	131	-2.55	2.77	Normal + SS

[a] Negative principal strain rate indicates shortening.
[b] $tan\,(\phi) = \frac{\dot{\epsilon}_2}{\dot{\epsilon}_1}$
[c] Expected pattern of faulting depends on exact value of ϕ—see Appendix C.1.
[d] Indicates number of GPS stations in Kostrov region used to solve for best-fitting velocity gradients.
[e] Moment rate can only be calculated from strain rate under conditions of biaxial strain.

6.4 Present-day motions from GPS observations

Numerous GPS studies conducted in the last two decades have provided us with knowledge of the crustal motion in northeast China (*Shen et al.*, 2000; *Wang et al.*, 2001; *He et al.*, 2003; *Zhang et al.*, 2004; *Gan et al.*, 2007; *Li et al.*, 2012; *Zhao et al.*, 2015).

6.4.1 A GPS-derived continuously varying strain rate field

We calculate a continuously varying strain rate field from the latest campaign GPS measurements (*Zhao et al.*, 2015) according to the method outlined in Chapter 5 and Appendix B.2 (*Shen et al.*, 1996; *Floyd et al.*, 2010). Again, the motivation for considering a continuous strain rate field is that a number of theories of continental deformation postulate that the whole lithosphere in a deforming region responds to stresses that are either applied at its edges or result from gradients in gravitational potential energy (*Bird and Piper*, 1980; *England and McKenzie*, 1982).

Of the 790 stations in the region of interest (31 to 44 °N, and 102 to 120 °E), we remove 130 with errors greater than 0.5 mm/a (see Figure 6.15 (a)). The majority of these 130 stations are located in the North China Plain—possibly because there are fewer reliably stable monuments in this low-lying, sedimentary terrain. We solve for the easterly and northerly components of velocity and the four horizontal velocity gradients at each GPS site using a least squares inversion, assuming uniform velocity gradients in both the northerly and easterly directions (see Figure 6.15 (b)). All GPS sites within a radius r_{max} are included in each inversion (except for the GPS site at which the calculation is being performed), but they are given a Gaussian weighting (W) according to the square of their distance (r) from the calculation site:

$$W = e^{\frac{-r^2}{\alpha^2}} \tag{6.1}$$

where α is a constant that defines the width of the Gaussian smoothing function and determines the horizontal resolution of the continuous model. Following the method of *Floyd et al.* (2010), we determine a minimum value for α (r_{min}) by requiring that 75% of

GPS sites have at least 6 GPS sites (the site itself plus its five nearest neighbours) within a radial distance r_{min}. We obtain $r_{min} = 78$ km. We investigate the effects of different values of α and r_{max} below. We then compare the velocities that we obtain from our inversion to the original GPS vectors and calculate a residual at each site (see Figure 6.15 (c)). We remove sites with residual velocities greater than 1 mm/a (i.e. sites that do not fit a locally smooth field) to leave 348 sites in the region of interest (44% of the original data). In other words, we assume locally homogeneous but regionally varying velocity gradients. For comparison, 500 sites have residuals less than 2 mm/a (63% of the original data). We then re-calculate the strain rate field on a regular 0.5 ° grid. If any calculation point does not include at least 6 GPS stations within a radius of r_{max}, then no calculation is performed at this site.

Figure 6.16 (a) shows the results of the strain rate calculation for $\alpha = 80$ km and $r_{max} = 200$ km. The results appear to show relatively high strain rates in the interior of the Ordos Plateau. However, these results are due to "leakage" from the deforming margins of the plateau. Figures 6.16 (b), 6.16 (c) and 6.16 (d) show that when r_{max} is reduced, the calculation points in the interior of the plateau do not have enough GPS stations nearby to allow calculation of the velocity gradients and the strain rate.

Figure 6.17 shows a zoomed in view of the results of the strain rate calculation for $\alpha = 80$ km and $r_{max} = 200$ km. Figure 6.18 shows an interpolated map of the second invariant of the strain rate tensor at each calculation node for the same parameters. Finally, in order to compare the GPS results with our Kostrov summations, we solve for a single set of velocity gradients (and hence a single strain rate tensor) in each Kostrov box. For each of these calculations we select GPS sites that fall within the relevant Kostrov box from the 348 GPS vectors that fit a smoothly varying field (see Figure 6.15 (d)). These calculations are not weighted by the Gaussian smoothing parameter α, so each GPS site contributes equally to the inversion. The results are given in Table 6.3 and Figure 6.19.

We interpret our GPS-derived strain rate results with the help of the theory outlined in Appendix C.1. For comparison, Figure 6.20 shows the focal mechanisms for our catalogue of historical earthquakes at the margins of the Ordos Plateau. We ignore the interior of

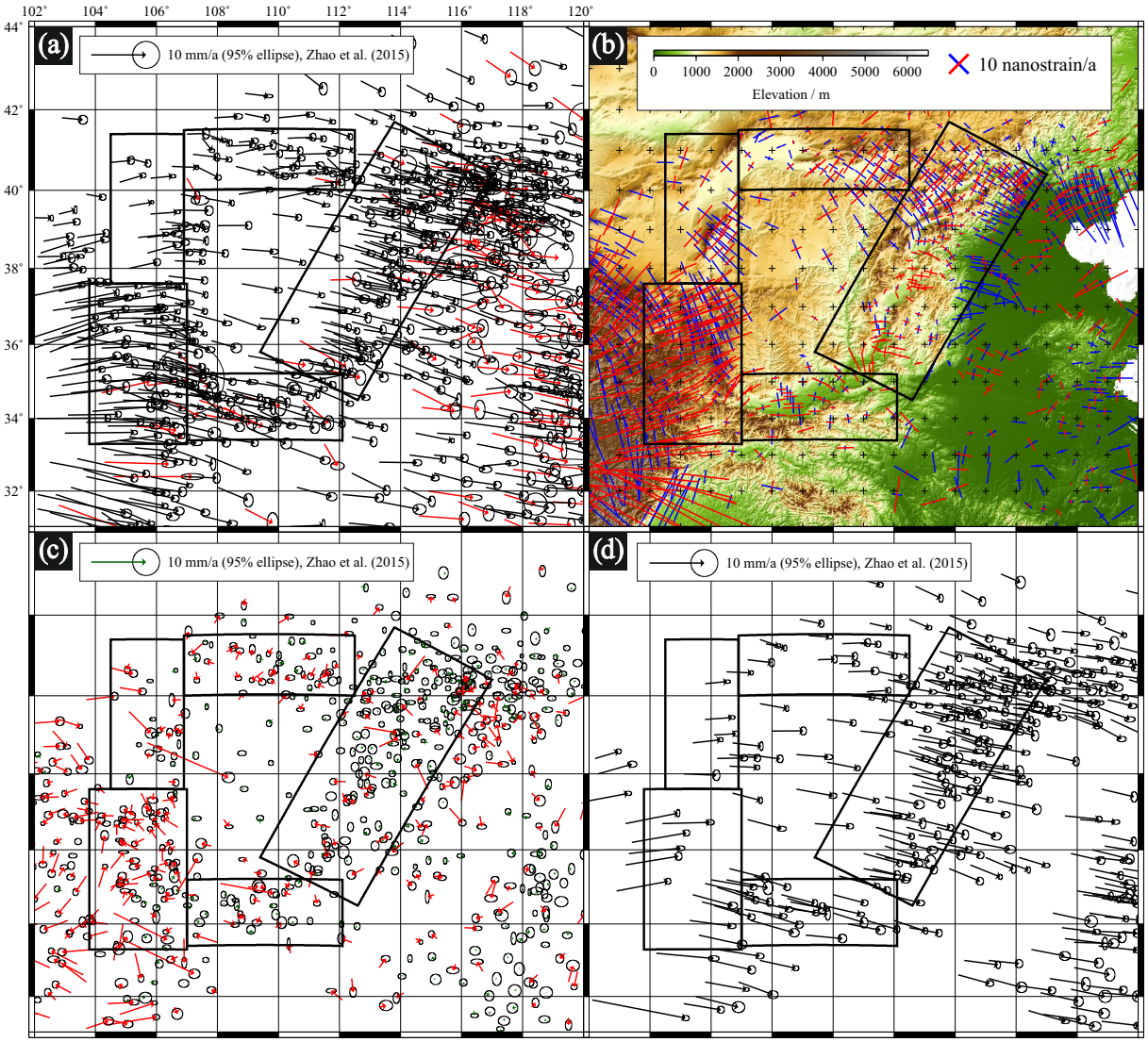


Figure 6.15: (a) GPS data from *Zhao et al.* (2015) relative to stable Eurasia. Red vectors indicate stations where northerly or easterly error is ≥ 0.5 mm/a. Black boxes indicate regions in which Kostrov summations were performed. 790 stations lie within the region shown, of which 660 have errors < 0.5 mm/a. (b) Strain rate field calculated from GPS at each GPS station, using $\alpha = 80$ km and $r_{max} = 200$ km. Crosses indicate orientation and magnitude of maximum and minimum horizontal strain rate; blue indicates extension and red indicates contraction. (c) Residual vectors obtained when velocities from inversion in (b) are subtracted from the original data in (a). Red vectors indicate stations with residuals ≥ 1 mm/a. 348 stations have residuals < 1 mm/a. (d) Remaining 348 vectors from (a) that are used in final strain rate calculation.

the plateau, due to the lack of GPS stations, and instead focus on the pattern of strain release at the margins of the plateau.

In the northern Ningxia region, on the western side of the Ordos Plateau, the predominant strain is consistent with either north-south, right-lateral motion or east-west left-lateral motion (see Figure 6.17). Given that most faults in northern Ningxia are oriented north-south, we assume that the predominant strain is north-south right-lateral

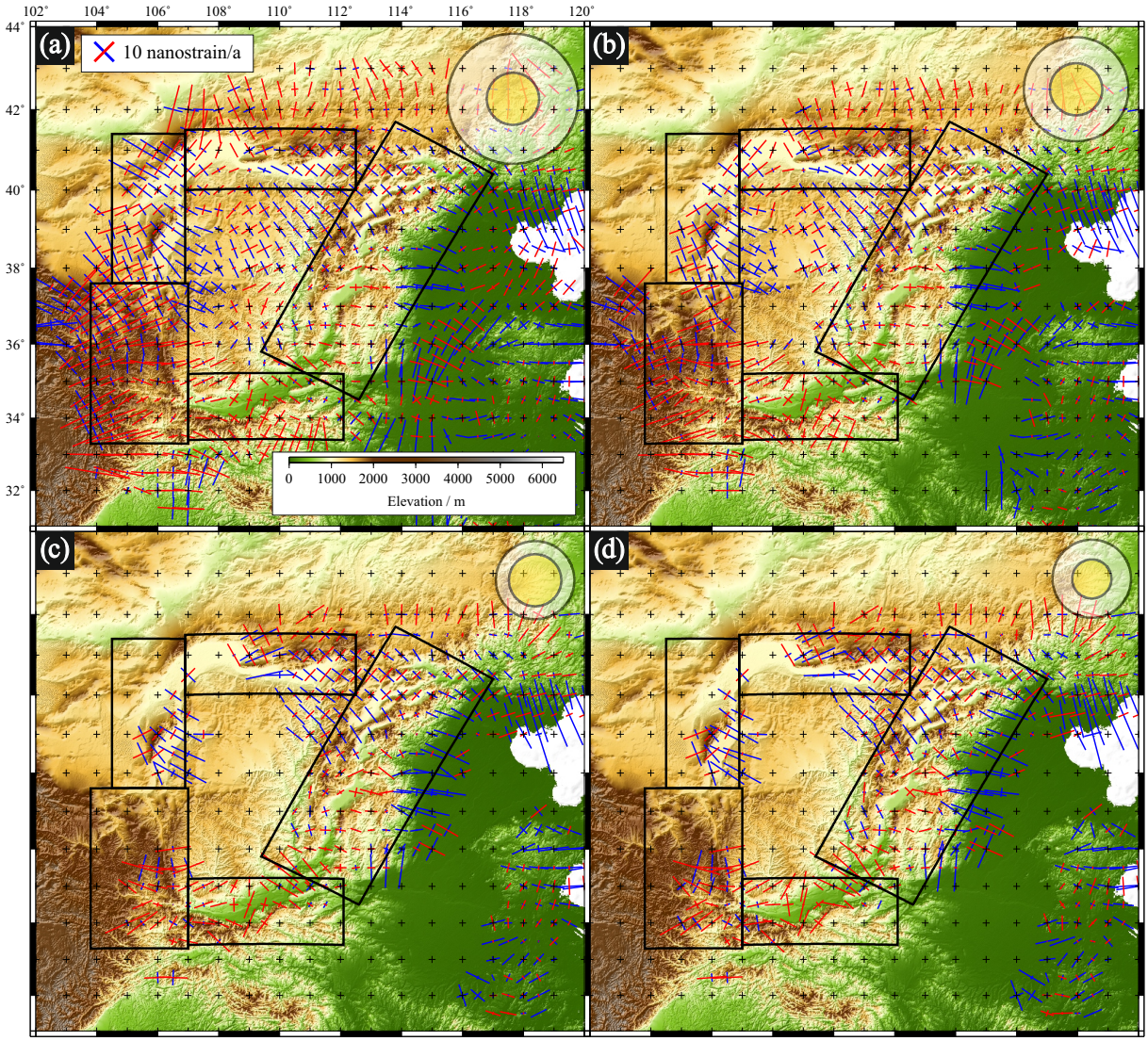


Figure 6.16: (a) Strain rate field calculated on a regular 0.5 ° grid from the 348 stations with residuals < 1 mm/a (see Figure 6.15 (d)). Black boxes indicate Kostrov regions. Crosses indicate orientation and magnitude of maximum and minimum horizontal strain rate; blue indicates extension and red indicates contraction. Yellow circle indicates value of α (radius of circle is 80 km) and white circle indicates value of r_{max} (radius of circle is 200 km). (b) Same as (a) with $\alpha = 80$ km and $r_{max} = 160$ km. (c) $\alpha = 80$ km and $r_{max} = 120$ km. (d) $\alpha = 60$ km and $r_{max} = 120$ km.

motion. The extensional strain rate is also slightly larger than the contractional strain rate indicating a small component of normal motion. The azimuth of the maximum principal (extensional) strain rate rotates from $\approx 120\,^\circ$ to $\approx 160\,^\circ$ on moving from the north of the region to the south, but otherwise the pattern of strain is relatively uniform. The difference in the geodetic and seismic strain rates in Figure 6.19 can be attributed to either the focal parameters used for the 1739 earthquake (*Wesnousky et al.* (1984) used

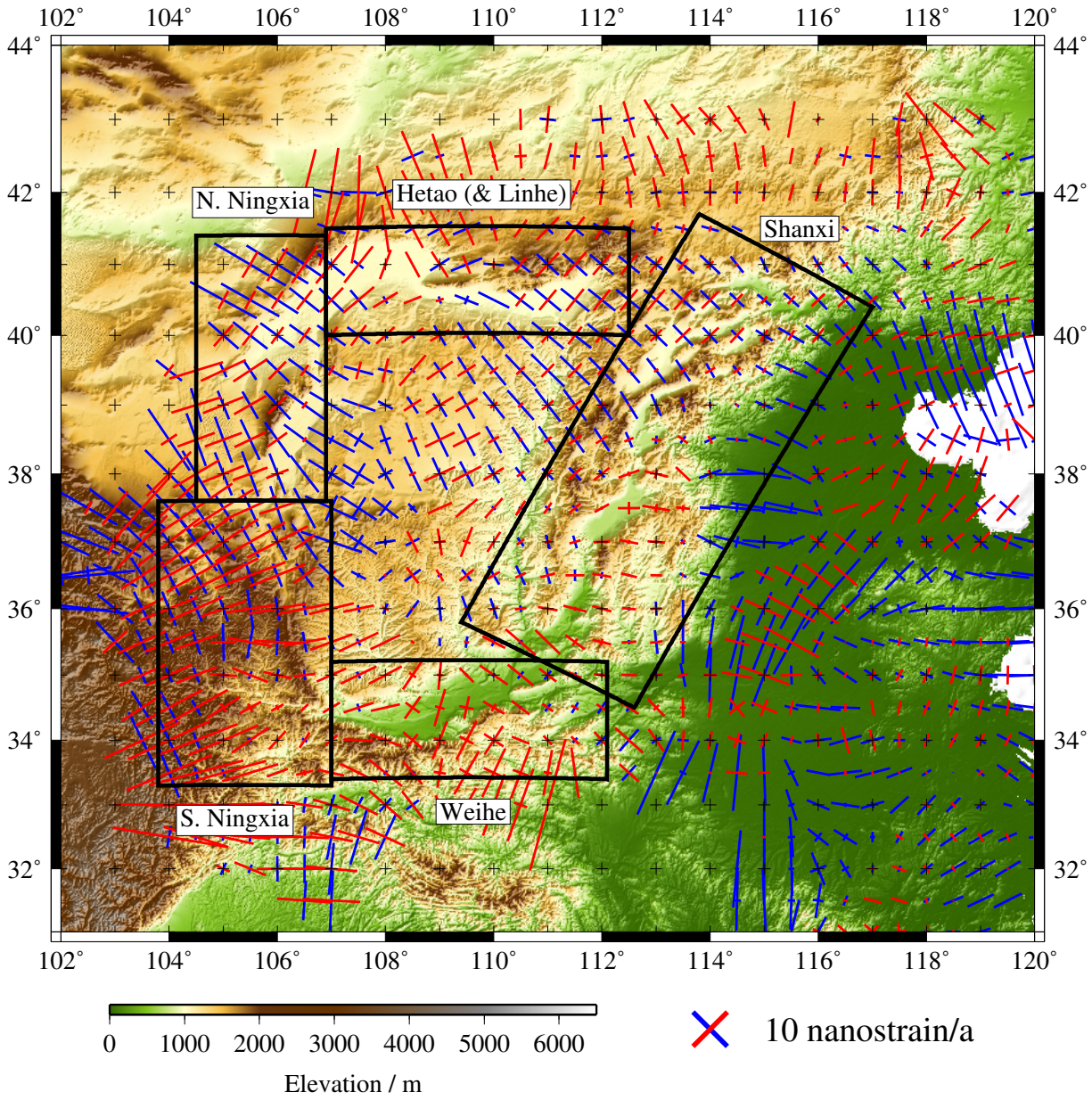


Figure 6.17: Strain rate field calculated on a regular 0.5 ° grid with $\alpha = 80$ km and $r_{max} = 200$ km. Black boxes indicate Kostrov regions. Crosses indicate orientation and magnitude of maximum and minimum horizontal strain rate; blue indicates extension and red indicates contraction.

different focal parameters and obtained strain rates similar to our geodetic result—see Table 6.3) or a lack of strike-slip events in our earthquake catalogue.

In the southern Ningxia region the predominant strain is approximately east-west contraction, accompanied by approximately north-south extension (see Figure 6.17). The azimuth of the contraction rotates through the region so as to remain roughly perpendicular to the edge of the Tibetan Plateau. The magnitude and azimuth of these results

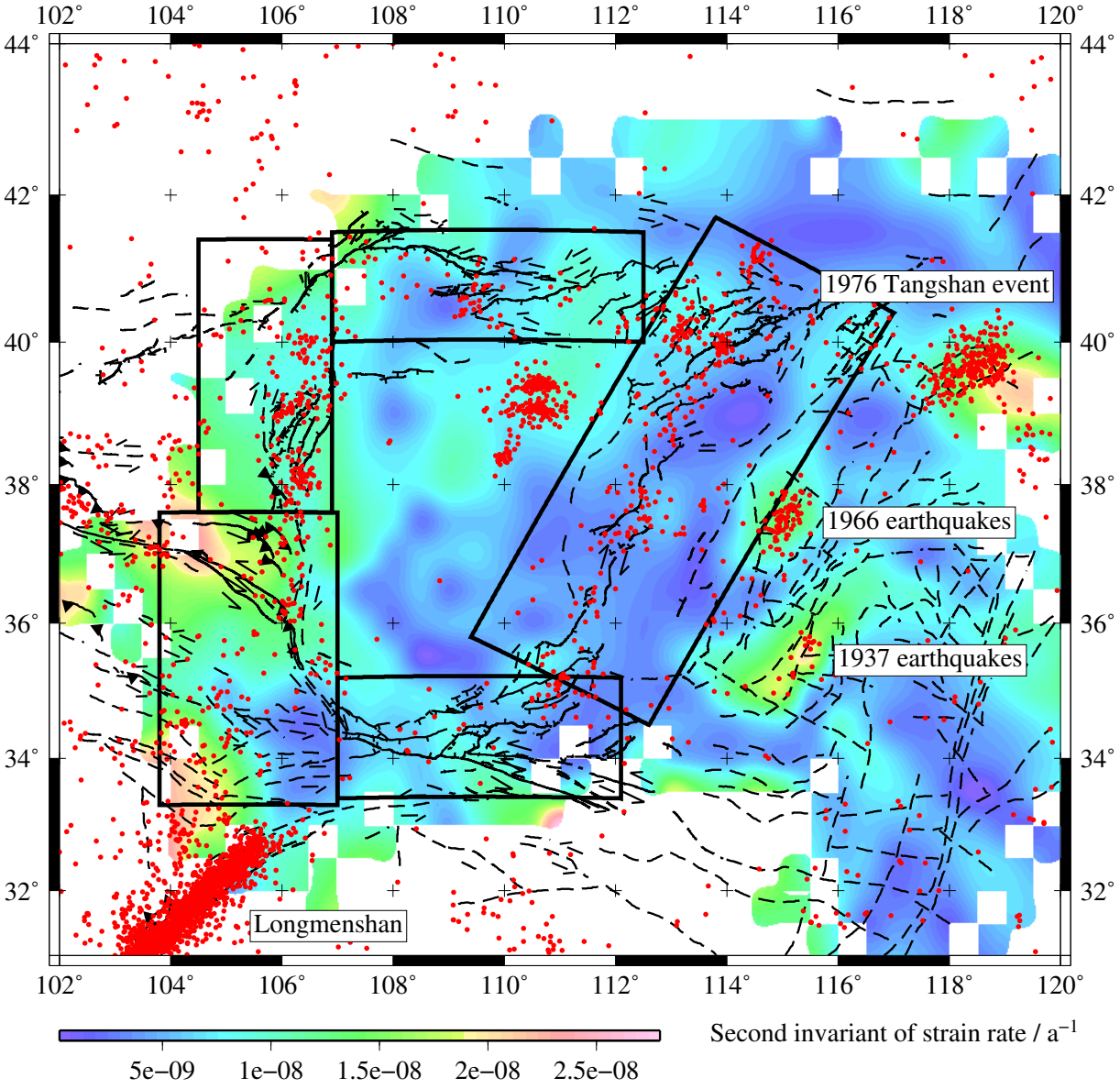


Figure 6.18: Second invariant $\left(\dot{E} = (\dot{\epsilon}_{ij}\dot{\epsilon}_{ij})^{\frac{1}{2}}\right)$ of the strain rate field calculated on a regular 0.5 ° grid with $\alpha = 80$ km and $r_{max} = 200$ km. Black boxes indicate Kostrov regions. Earthquakes of $M_w > 2.0$ between 1920 and 2011 from the ISC catalogue (*International Seismological Centre*, 2013) are shown as red dots. Faults from Figure 6.4 are also shown.

appear to be reasonably consistent with our Kostrov summation (see Figure 6.19). That said, the geodetic result indicates that reverse faulting dominates over strike-slip faulting, whereas the seismic result indicates that strike-slip faulting dominates over reverse.

To the north of the Ordos there is a lack of GPS sites in the Linhe Graben (on the western side of the Kostrov volume) and so the strain rate cannot be reliably resolved (see for example Figure 6.15 (c)). In the eastern part of the volume, in the Hetao Graben, the predominant GPS-derived strain is east-west left-lateral motion and the typical azimuth

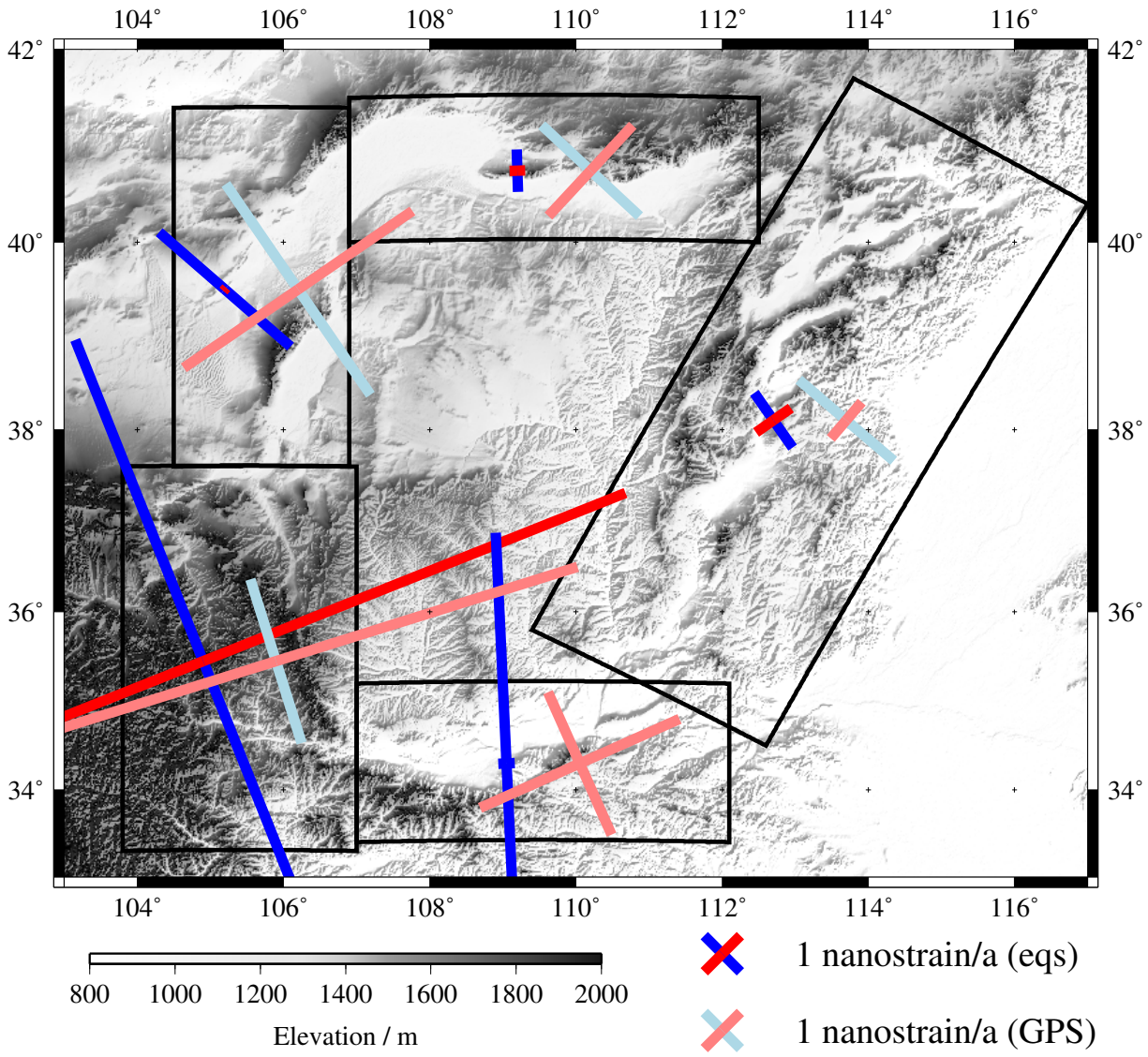


Figure 6.19: Comparison between Kostrov summations and GPS-derived strain rates. Black boxes indicate Kostrov regions. Brighter coloured crosses indicate orientation and magnitude of maximum and minimum horizontal strain rate from Kostrov summations; blue indicates extension and red indicates contraction. Paler coloured crosses indicate orientation and magnitude of maximum and minimum horizontal strain rate, calculated from the GPS data within each Kostrov region; again, blue indicates extension and red indicates contraction. Note that the scale is exaggerated 10× for the Kostrov strain rate cross in the Hetao Graben.

of the maximum principal (extensional) strain rate is 135 ° (see Figure 6.17). There is a discrepancy here with the strain rate tensor from the Kostrov summation, which is two orders of magnitude smaller and rotated by ≈ 45 ° (see Figure 6.19). As discussed previously (see Section 6.3), this could indicate that our earthquake catalogue is missing infrequent but large-magnitude events on this boundary of the plateau.

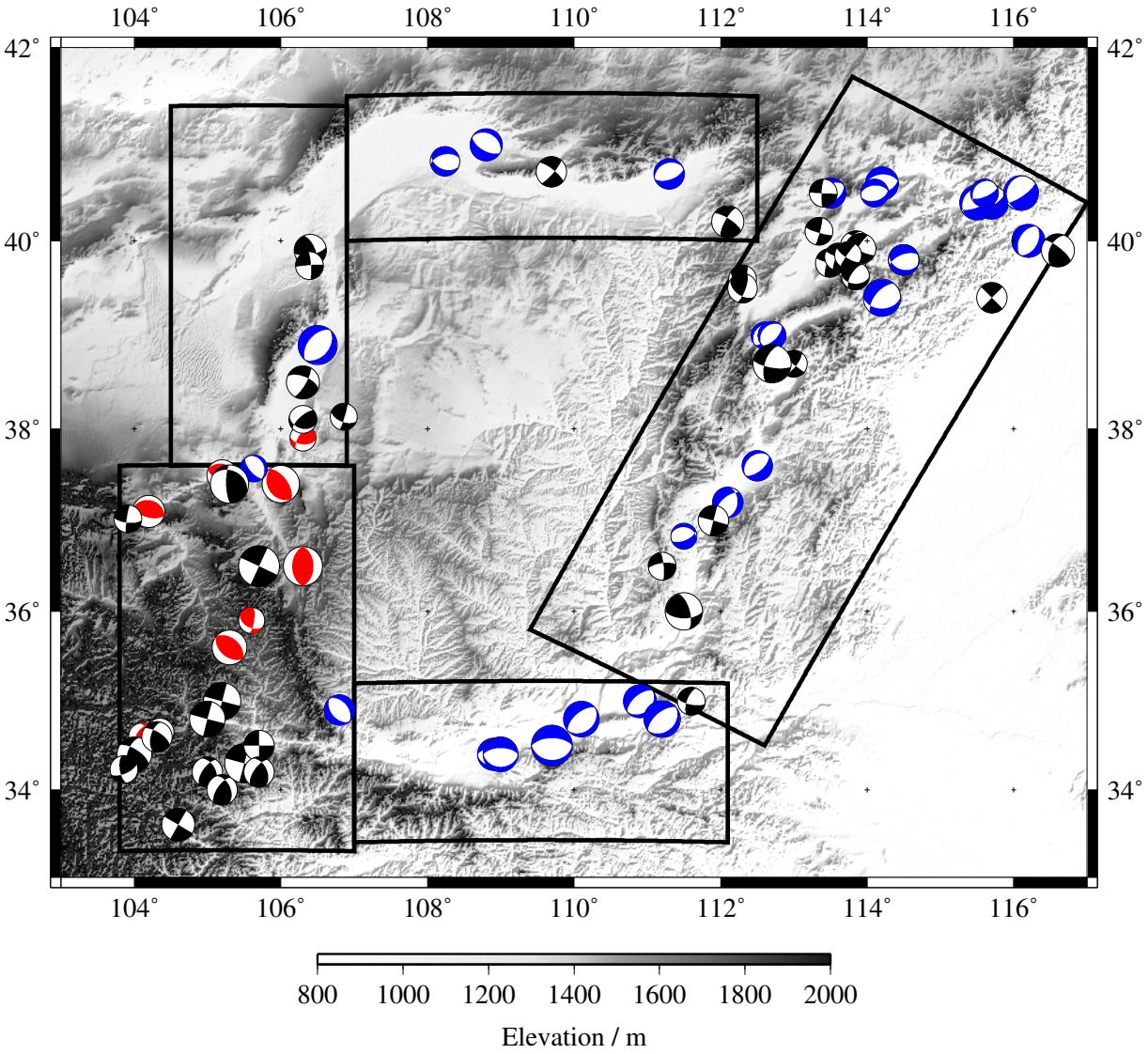


Figure 6.20: Inferred focal mechanisms for our catalogue of historical earthquakes around the margins of the Ordos Plateau (see Table 6.2). Reverse faulting mechanisms are shown in red, normal faulting mechanisms are shown in blue, and strike-slip mechanisms are shown in black. Black boxes indicate Kostrov regions. The observed mechanisms are consistent with the pattern of faulting expected from the geodetic strain rates in South Ningxia, Hetao and Shanxi, but not in North Ningxia or Weihe (see Table 6.3).

In the Weihe Graben, the GPS-derived strain rate field appears to indicate predominantly contraction in a variety of orientations (see Figure 6.17). This is surprising given the mapped normal faults in the region. In addition, these results are inconsistent with the strain rate field calculated at the GPS sites (see Figure 6.15 (b)) and the Kostrov summation (see Figure 6.19), which both show north-south extension. Furthermore, the lack of a consistent orientation for the direction of maximum shortening in the strain

rate field shown in Figure 6.17 suggests that this result is incorrect—presumably due to "leakage" from other areas or unreliable GPS monuments in the Weihe Graben.

The Shanxi Grabens on the eastern side of the Ordos display different patterns of strain in the north and the south (see Figure 6.17). As described in Chapter 5, the northern Shanxi Grabens change from almost pure northwest-southeast extension in the southwest to more oblique motion in the northeast. In the central and southern Shanxi Grabens the rates of strain are notably smaller (see Figure 6.18). The Kostrov summation for the Shanxi Grabens averages across the whole region and is therefore largely consistent with the GPS-derived strain rate field (see Figure 6.19). There is a small seismic moment deficit in comparison to the geodetic result, but this deficit would be reduced if we included the M 8 1303 Hongdong earthquake in our Kostrov summation.

In the North China Plain, there are three distinct patches of higher strain rate (see Figure 6.18). These appear to correspond to specific seismic events: a pair of earthquakes in 1937 (M 7.6 and 6.8), the 1966 Xingtai series of earthquakes (including events up to M 7.2) and the M_w 7.8 1976 Tangshan earthquake. It is therefore possible that these high strain rates could be due to continuing aftershock sequences or ongoing postseismic motion. For example, *Stein et al.* (2009) indicated that aftershock sequences on the continents, particularly on slowly moving faults, can last for decades or sometimes even centuries after the mainshock. However, the high strain rates around the 1937 earthquakes are poorly constrained given the GPS coverage (see Figure 6.16).

We now examine the GPS data in a few selected regions in order to estimate slip rates on specific faults.

6.4.2 Slip rate on the Zhangjiakou-Bohai-Penglai Fault zone

Shen et al. (2000) obtained a left-lateral geodetic slip rate of 2 mm/a across the Zhangjiakou-Bohai-Penglai Fault zone. *Wang et al.* (2011) estimated a left-lateral slip rate of 1.9±0.4 mm/a from a block model fitted to the GPS data, and *Li et al.* (2012) proposed a geodetic slip rate of 1 to 3 mm/a.

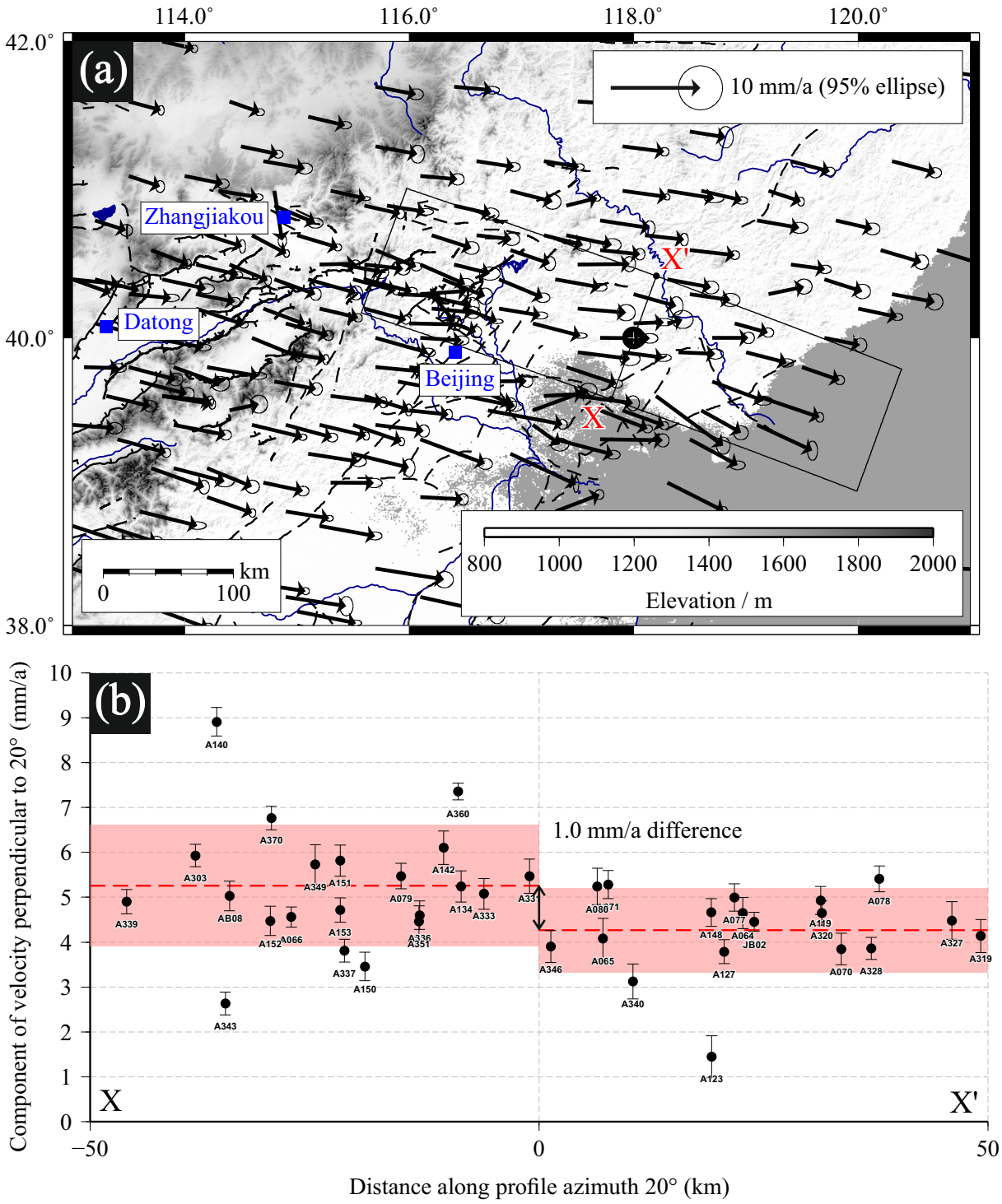


Figure 6.21: (a) SRTM topography (30 m resolution) of the Zhangjiakou-Bohai-Penglai Fault zone to the northeast of the Ordos Plateau (*Farr et al.*, 2007). Black vectors show campaign GPS measurements relative to Eurasia from occupations in 2009, 2011 and 2013 (*Zhao et al.*, 2015); vectors are not shown if the northerly or easterly error is greater than 0.5 mm/a. Cities are marked by blue squares. (b) Swath profile X-X′ through the GPS data showing the component of velocity perpendicular to the profile azimuth of 20 °. The dashed red lines and red boxes show the average and standard deviation of the velocities either side of the approximate location of the fault trace (at 0 km). The data are consistent with approximately 1 mm/a of left-lateral motion occurring on the Zhangjiakou-Bohai-Penglai fault system.

A profile through the latest campaign measurements from *Zhao et al.* (2015) yields a left-lateral slip rate of approximately 1.0 mm/a (see Figure 6.21). However, there is significant scatter in the data and this rate is poorly constrained.

6.4.3 Slip rates on the Xizhoushan and Huoshan Faults

No previous geodetic estimates exist for the slip rates on the right-lateral Xizhoushan and Huoshan Faults in the Shanxi Grabens, though they are estimated to have Quaternary rates of 5.7 and 5.0 mm/a respectively (see Section 6.2.6). However, the latest GPS measurements (*Zhao et al.*, 2015) show no resolvable shear within the scatter of the data (see Figure 6.22). (Other shorter profiles centred on the individual faults also show no resolvable strike-slip motion.)

There are three potential explanations for this discrepancy. Firstly, the Quaternary rates on the Xizhoushan and Huoshan Faults could be wrong. These rates are estimated from very few sites on each fault and they should be checked by further Quaternary dating and site interpretation. Figure 6.23 shows that a number of gullies preserve clear right-lateral offsets on both faults, but the geomorphology is likely to have been complicated by human modifications. Secondly, the GPS data could be wrong. However, given that there was good agreement between the GPS and the Quaternary rates in the western Ordos (see Chapter 4) and the northern Shanxi Grabens (see Chapter 5), it is not clear why the GPS would be any less reliable here. The third option is that both measurements are correct. In other words, right-lateral motion occurred on these faults during the Quaternary, but no right-lateral motion is currently being accommodated. If this is the case, this could be linked to time-dependent earthquake behaviour in north China (see Section 6.7) (*Liu et al.*, 2011).

6.4.4 Slip rate on the Luonan and Danfeng Faults

Zhang et al. (1995) estimated a combined Quaternary left-lateral slip rate on the Luonan and Danfeng Faults of between 3.6 and 8.4 mm/a, depending on whether they used their "shorter" or "longer" chronology (i.e. which terraces they correlated with which

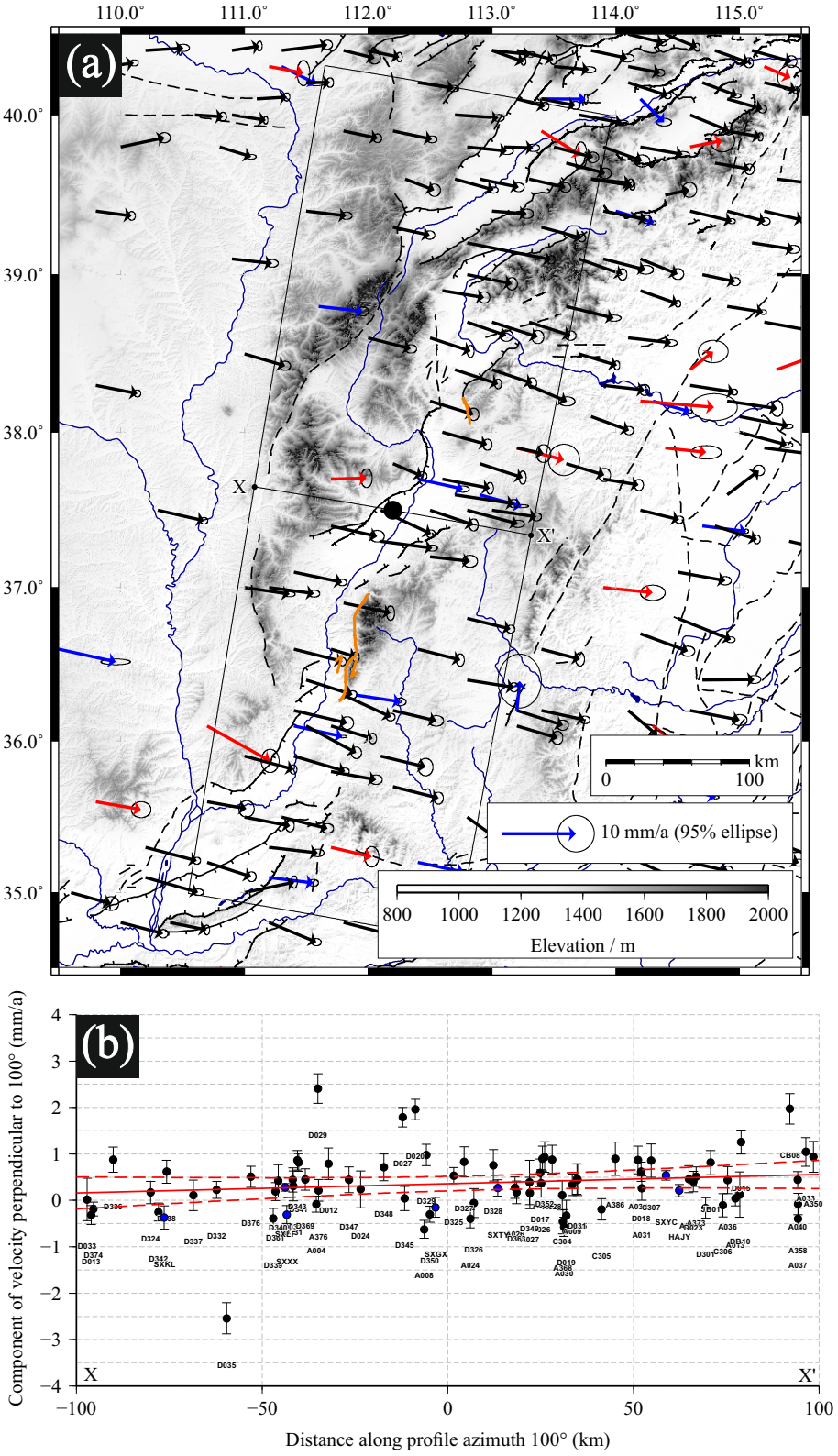


Figure 6.22: (a) SRTM topography (30 m resolution) of the Shanxi Grabens on the eastern side of the Ordos Plateau (*Farr et al.*, 2007). The right-lateral Xizhoushan and Huoshan Faults are marked in orange. Black vectors show campaign GPS measurements relative to Eurasia from occupations in 2009, 2011 and 2013 (*Zhao et al.*, 2015); vectors are coloured red if the northerly or easterly error is greater than 0.5 mm/a. Blue vectors show continuous GPS measurements relative to Eurasia from the period 1999 to 2014 (*Zhao et al.*, 2015). (b) Swath profile X-X′ through the GPS data showing the component of velocity perpendicular to the profile azimuth of 100 °. The red lines show the best fit least squares regression to the data and the 95% confidence envelopes on this best fit line. No strike-slip motion is resolvable within the scatter of the data.

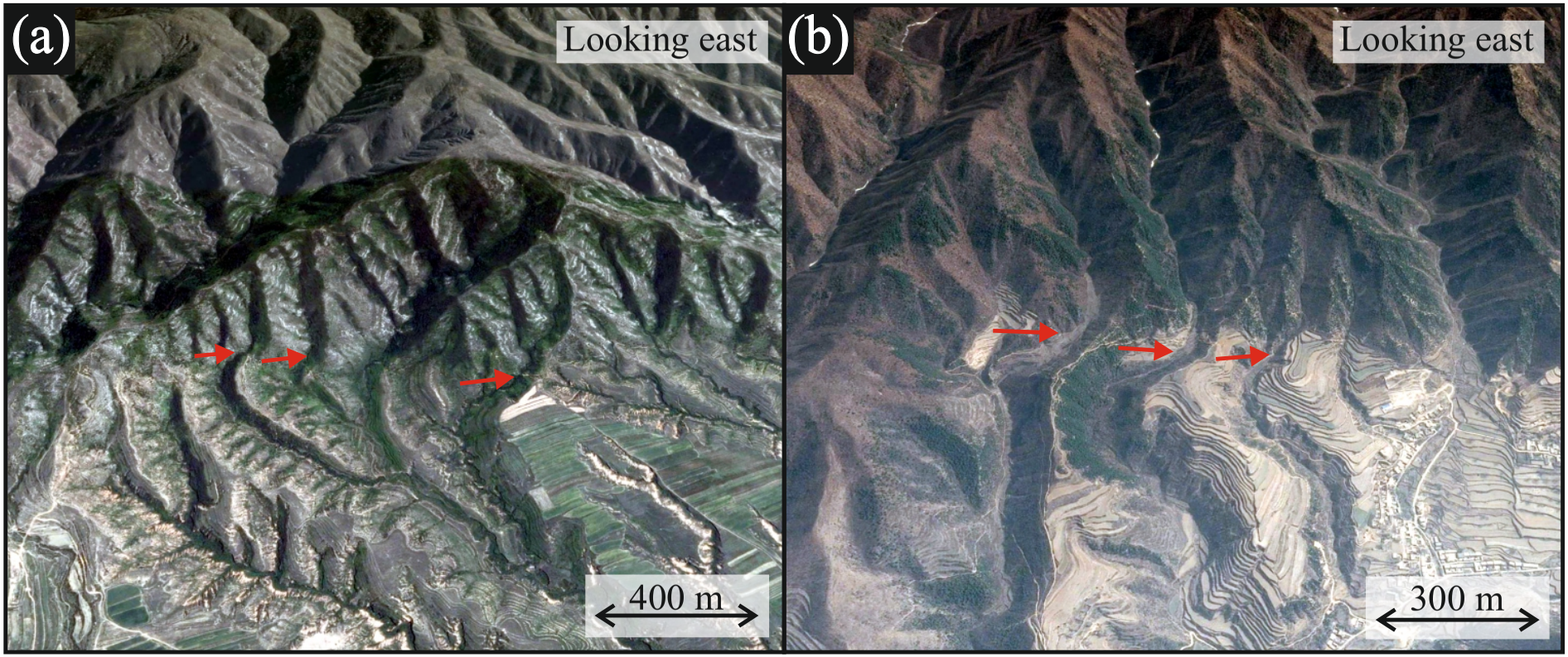


Figure 6.23: (a) Oblique view of Google Earth imagery on the Xizhoushan Fault (source: http://earth.google.com) from May 2016 around 38.126 °N, 122.803 °E. Offset gullies indicated with red arrows. (b) Oblique view of Google Earth imagery on the Huoshan Fault from April 2014 around 36.440 °N, 111.819 °E. Region shown corresponds to the site south of Shawo studied by *Xu and Deng* (1990) and *Xu et al.* (1993) (see Table 6.1). Again, offset gullies indicated with red arrows.

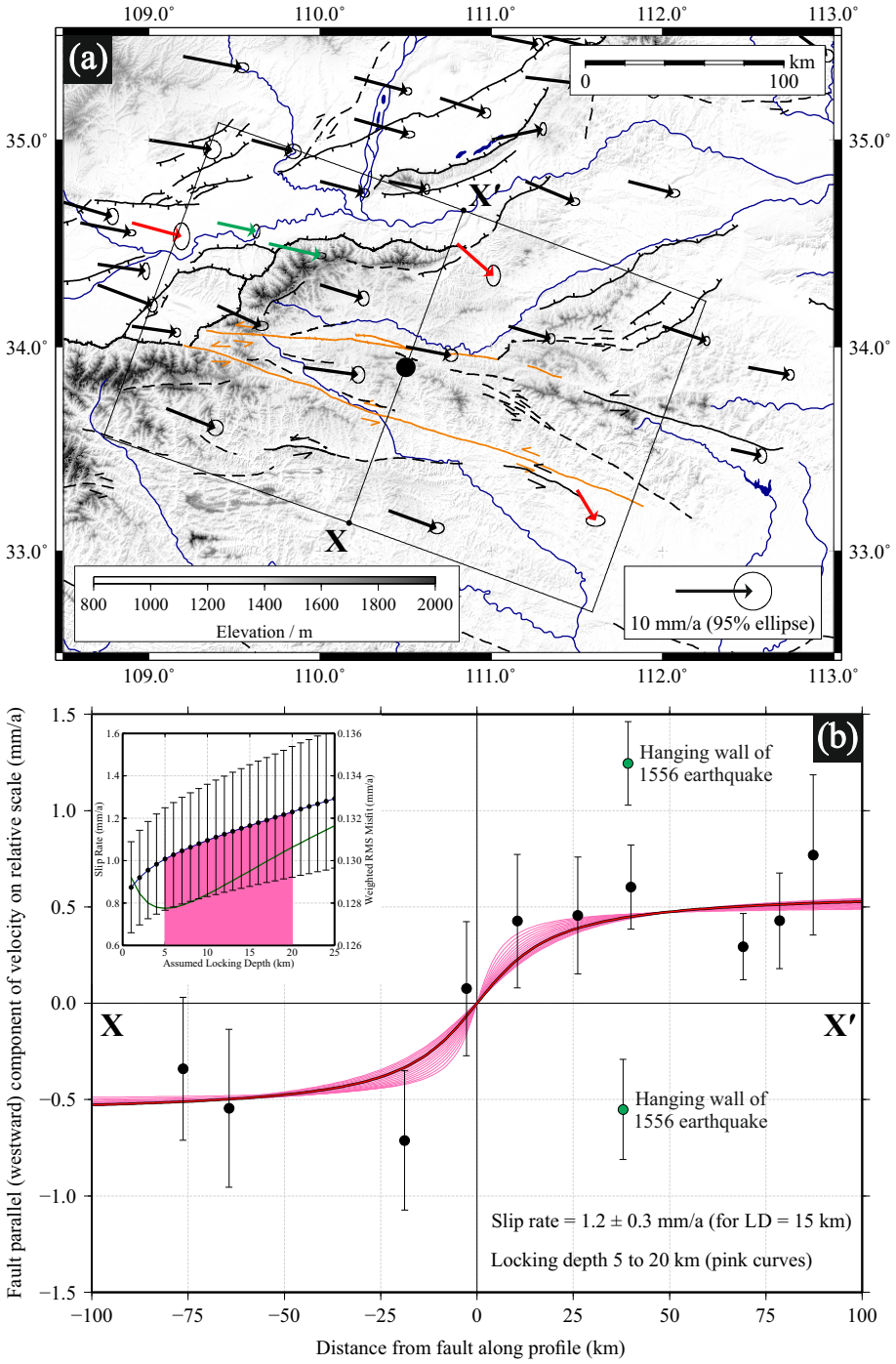


Figure 6.24: (a) SRTM topography (30 m resolution) of the region immediately southeast of the Ordos Plateau (*Farr et al.*, 2007). The Luonan and Danfeng Faults are marked in orange. Black vectors show campaign GPS measurements relative to Eurasia from occupations in 2009, 2011 and 2013 (*Zhao et al.*, 2015); vectors are coloured red if the northerly or easterly error is greater than 0.5 mm/a. (b) Swath profile X-X′ through the GPS data showing the component of velocity perpendicular to the profile azimuth of 20 °. The red line shows the best fitting arctangent function ($u = tan^{-1}\left(\frac{x}{d}\right)$, where u is the velocity, x is the distance from the fault and d is the locking depth) for a fixed locking depth of 15 km. The pink lines represent the range of best fitting solutions for assumed locking depths of between 5 and 20 km. The inset figure shows the trade-off between slip rate and locking depth. For a locking depth of 15 km, we estimate a left-lateral slip rate of 1.2±0.3 mm/a. Two stations that are not well fit by the arctangent function (shown in green) are from the immediate hanging wall of the 1556 Huaxian earthquake.

interglacial period). Figure 6.24 shows a swath profile through the GPS data from *Zhao et al.* (2015). As in Chapter 5, we model the fault parallel interseismic motion across both the Luonan and Danfeng Faults as a buried screw dislocation in an elastic half-space (*Savage and Burford*, 1973). The density of data is not sufficient to provide an independent constraint on the locking depth, so we assume locking depths in the range of 5 to 20 km (*Wright et al.*, 2013) in order to calculate the distribution of possible slip rate estimates. In Figure 6.24 (b), the RMS misfit curve indicates a preferred locking depth of $\approx$ 5 km. However, the range of RMS values does not change significantly and 5 km is shallow compared to the seismogenic thickness indicated by earthquake depths (*Molnar et al.*, 1984). We therefore prefer a locking depth of 15 km, for which we obtain a combined left-lateral slip rate of 1.2$\pm$0.3 mm/a.

The difference between the geodetic and Quaternary rates could be because the GPS data are unreliable or the fault motion is time-dependent. However, it seems more likely that the terrace ages inferred by *Zhang et al.* (1995) via the climatic correlation method are incorrect.

6.4.5 Slip rates in the North China Plain

Seismic reflection profiles indicate a large number of faults in the North China Plain, most of which strike NNE-SSW (*Deng et al.*, 2007). The most prominent of these is the Tanlu Fault zone, around 600 km east of the Ordos Plateau. Fault striations indicate that the Tanlu Fault zone has moved in a right-lateral sense since the Pliocene (*Zhang et al.*, 1999b). It is estimated to have a slip rate of 2 to 3 mm/a (*Deng et al.*, 2007) and is thought to be the seismogenic source for the M 8.5 1668 Tancheng earthquake in Shandong Province (*Zhang et al.*, 1985, 2003b; *Liu et al.*, 2007)

Figure 6.25 shows profiles through the GPS data from *Zhao et al.* (2015) in the vicinity of the 1937 earthquakes (see Figure 6.18) and on the Tanlu Fault zone. In both cases the data are scattered, and neither profile indicates any resolvable strike-slip motion. In the vicinity of the 1937 earthquakes the GPS station coverage is comparatively poor, so this is perhaps to be expected, but the station coverage near the Tanlu Fault zone is quite good

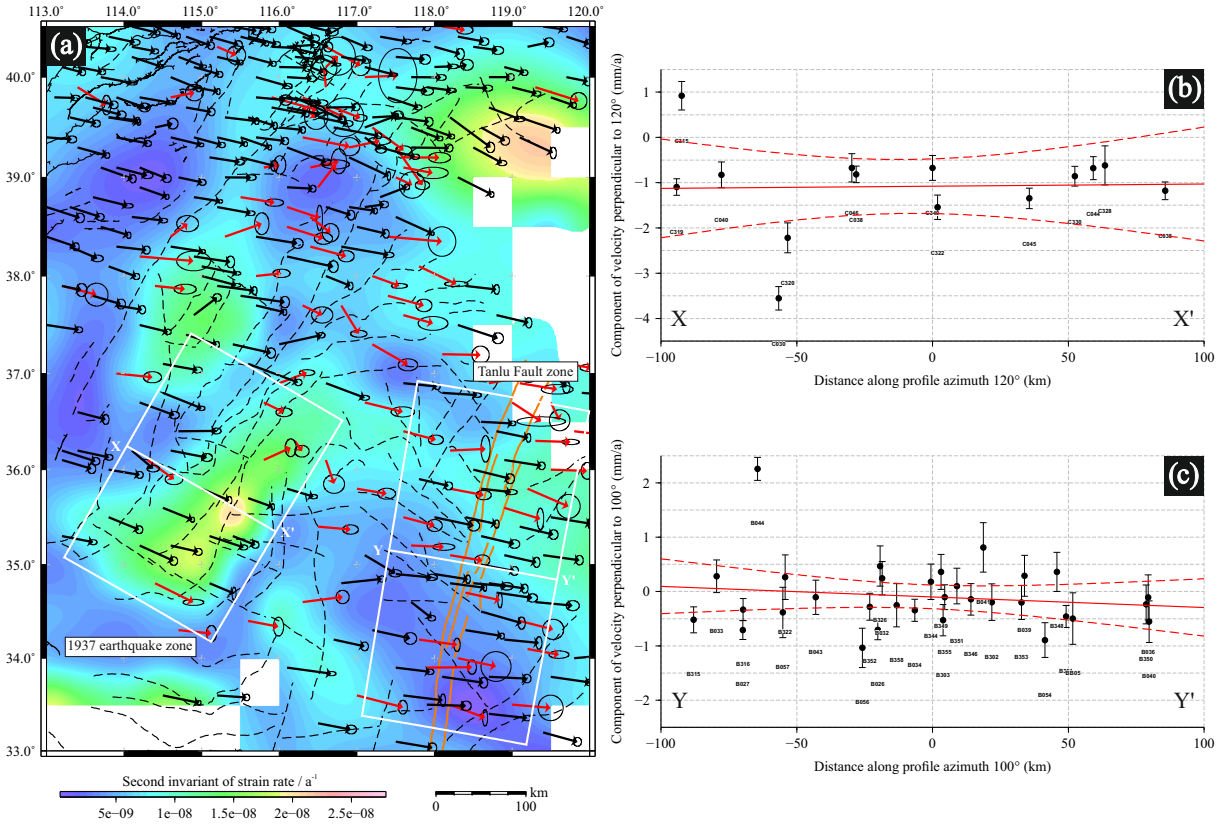


Figure 6.25: (a) Second invariant $\left(\dot{E} = (\dot{\epsilon}_{ij}\dot{\epsilon}_{ij})^{\frac{1}{2}}\right)$ of the strain rate field calculated on a regular 0.5 ° grid with $\alpha = 80$ km and $r_{max} = 200$ km for the North China Plain region. Black vectors show campaign GPS measurements relative to Eurasia from occupations in 2009, 2011 and 2013 (*Zhao et al.*, 2015); vectors are coloured red if the northerly or easterly error is greater than 0.5 mm/a. Inferred faults, marked as black dashed lines, are from the *Map of Active Tectonics in China* (*Deng et al.*, 2007). The Tanlu Fault zone is marked in orange. (b) Swath profile X-X′ through the GPS data in the 1937 earthquake zone showing the component of velocity perpendicular to the profile azimuth of 120 °. Vectors with a northerly or easterly error greater than 0.5 mm/a are excluded. The red lines show the best fit least squares regression to the data and the 95% confidence envelopes on this best fit line. No strike-slip motion is resolvable within the scatter of the data. (c) Swath profile Y-Y′ through the GPS data on the Tanlu Fault zone showing the component of velocity perpendicular to the profile azimuth of 100 °. Again, no strike-slip motion is resolvable within the scatter of the data.

(see Figure 6.15 (d)). Furthermore, Figure 6.17 does not show the strain rate pattern expected for a right-lateral fault around the Tanlu Fault zone. Again, this discrepancy on the Tanlu Fault zone could indicate that the Quaternary rate is wrong, that the GPS data are unreliable or that the fault motion is time-dependent.

6.5 Existing kinematic models for the Ordos Plateau

6.5.1 Grabens as conjugate shear fractures

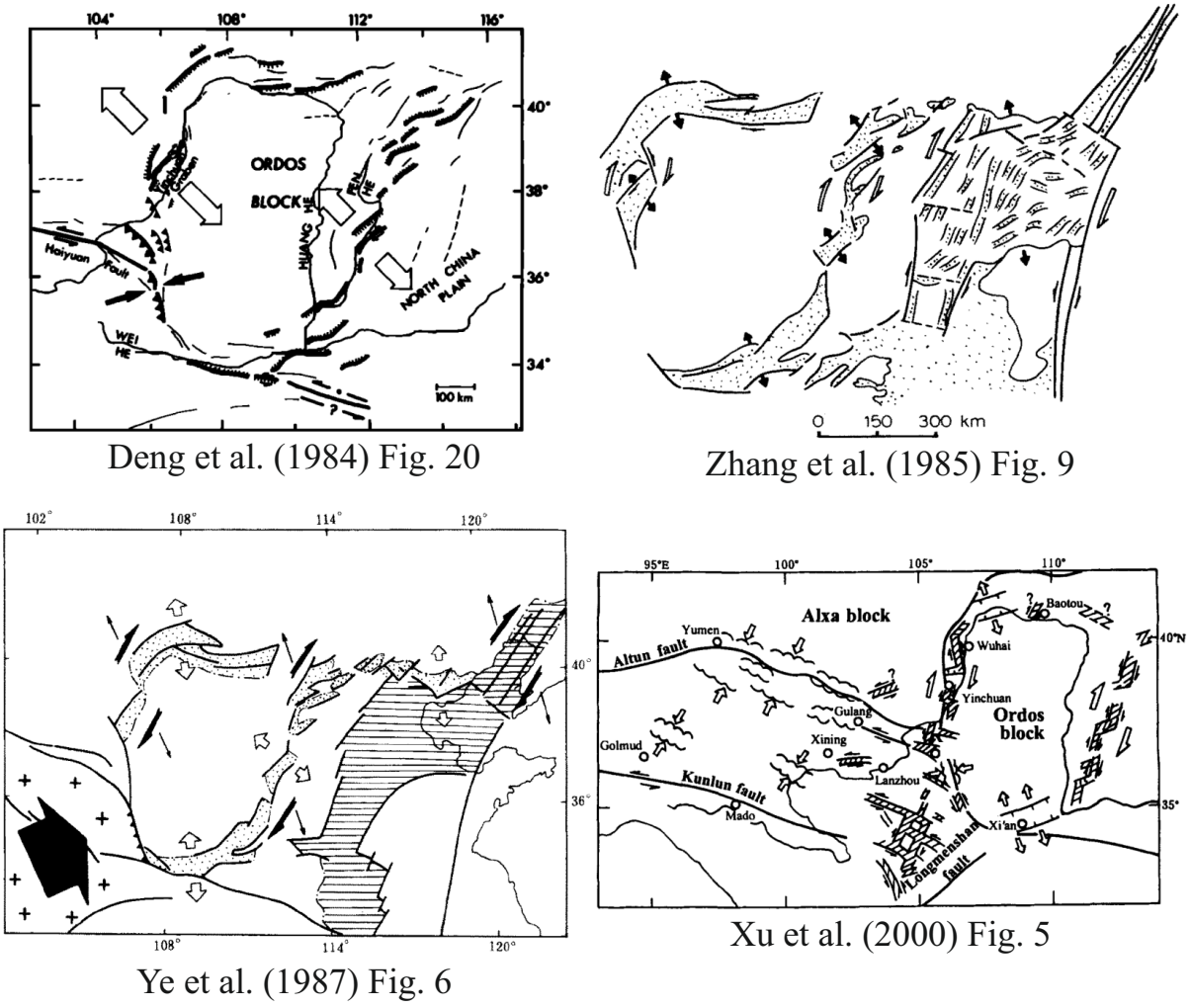


Figure 6.26: Previous "conjugate shear fracture" models for the kinematics of the Ordos Plateau from *Deng et al.* (1984a), *Zhang et al.* (1985), *Ye et al.* (1987) and *Xu et al.* (2000).

One set of kinematic models proposes that the Ordos region undergoes principally northwest-southeast extension (see Figure 6.26) (*Deng and Fan*, 1980; *Deng et al.*, 1984a; *Wesnousky et al.*, 1984; *Zhang et al.*, 1985; *Ye et al.*, 1987; *Xu et al.*, 2000). In these models, the graben systems around the four sides of the Ordos Plateau are thought to represent conjugate shear fractures that enable the overall extension (see Figure 6.27). The Kostrov summation from *Wesnousky et al.* (1984) yielded a total strain rate tensor for the whole Ordos Plateau that consists of a maximum principal extensional strain rate of 3.0 nanostrain/a at an azimuth of 160 ° and a minimum principal strain rate

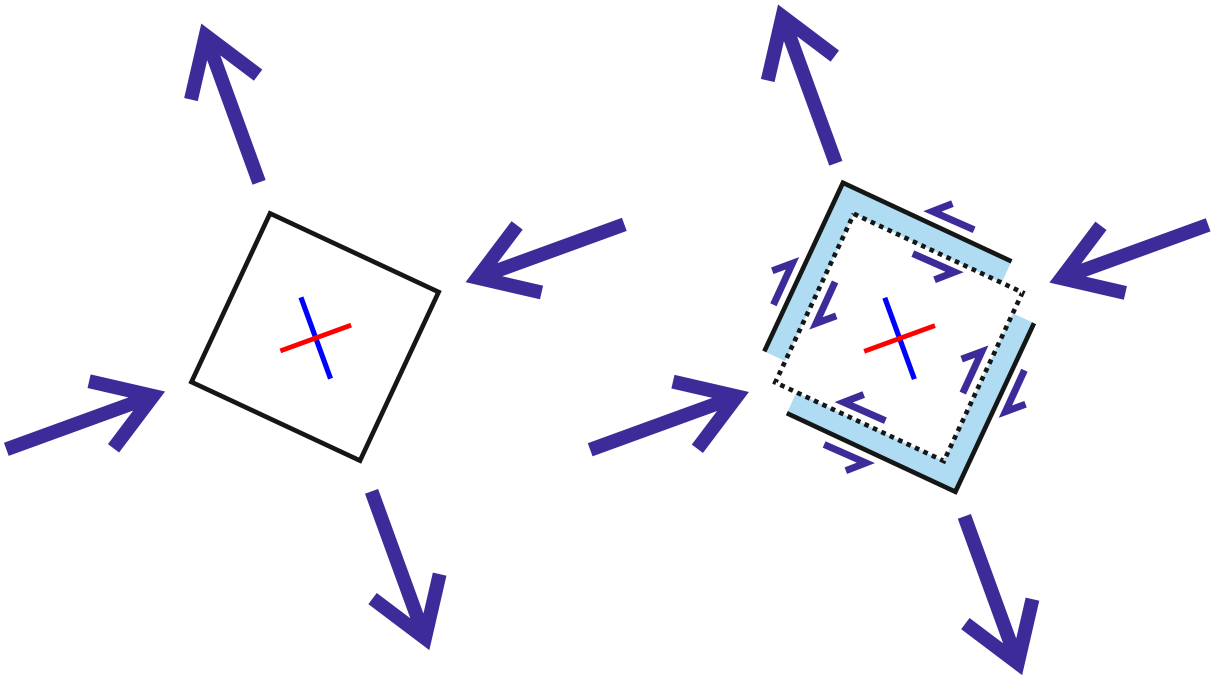
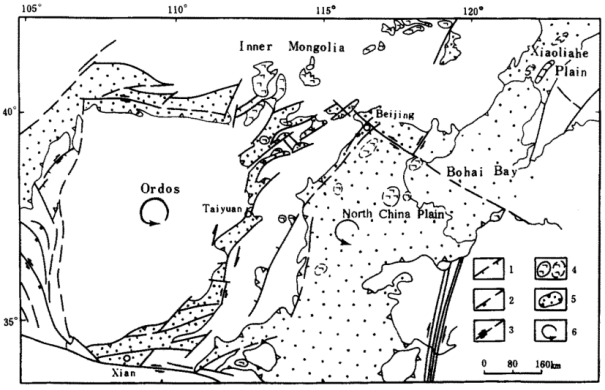


Figure 6.27: The "conjugate shear fracture" model for the kinematics of the Ordos Plateau. Blue bar indicates orientation and magnitude of maximum principal (extensional) strain rate, and red bar indicates orientation and magnitude of minimum principal (contractional) strain rate, according to a Kostrov summation for the whole Ordos Plateau by *Wesnousky et al.* (1984). Light blue shading indicates the location of the transtensional graben systems that could develop in this strain field.

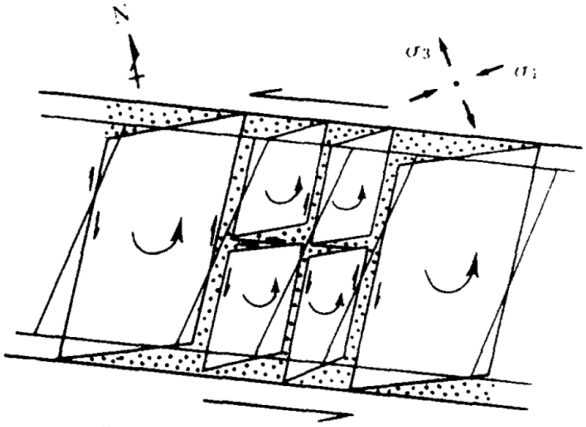
of -2.6 nanostrain/a (i.e. 2.6 nanostrain/a of contraction) at right angles to this (see Figure 6.27). The sense of strike-slip motion on each boundary of the Ordos Plateau (left-lateral to the north and south and right-lateral to the east and west) is consistent with the conjugate shear fracture model. However, *Zhang et al.* (1985) noted that the strike-slip components of motion at the boundaries of the Ordos Plateau are often larger than the dip-slip components. They therefore proposed that the northwest-southeast extension is also accompanied by NNE-SSW right-lateral shearing (see Figure 6.26). *Ye et al.* (1987) highlighted that, as the extension is likely to be related to the India-Eurasia collision, it should also involve northeast-southwest shortening, at least in the southwestern corner of the Ordos Plateau.

6.5.2 Anticlockwise rotation

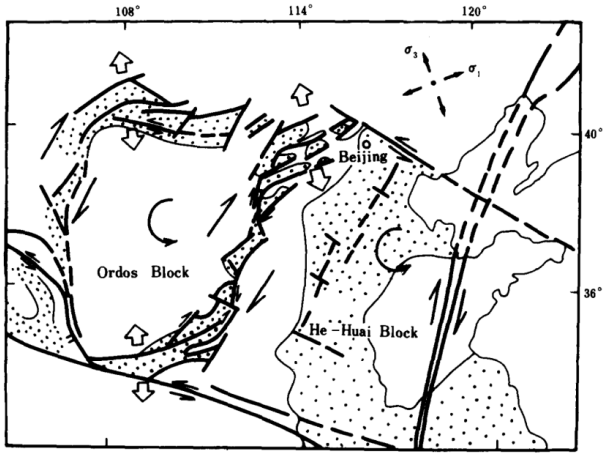
A second set of kinematic models proposes that the Ordos Plateau is undergoing anti-clockwise rotation (see Figure 6.28) (*Lu and Ding*, 1985; *Xu and Ma*, 1992; *Xu et al.*, 1993;



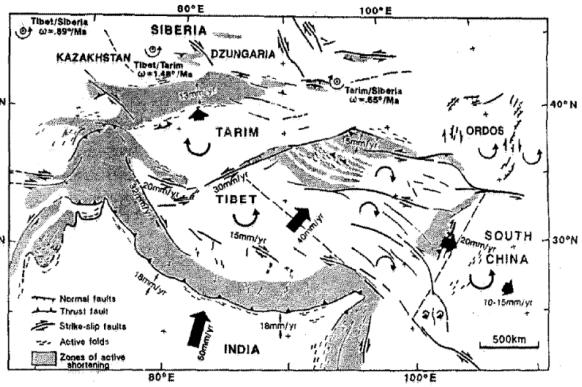
Xu & Ma (1992) Fig. 3



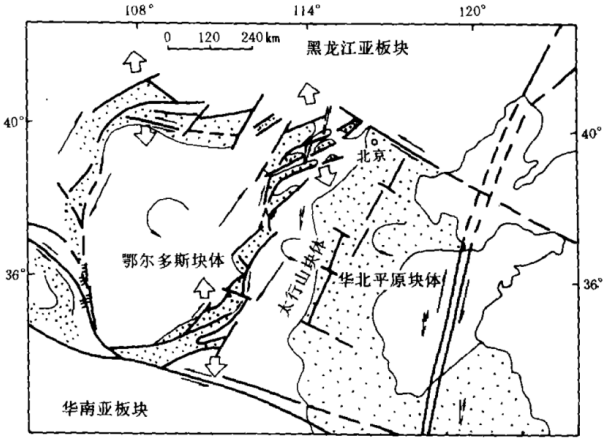
Xu & Ma (1992) Fig. 12



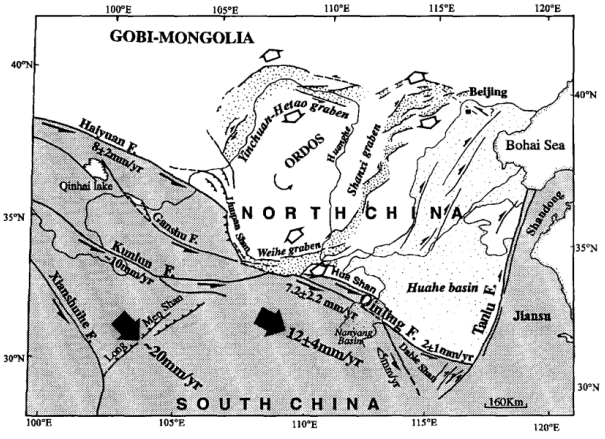
Xu et al. (1993) Fig. 15



Avouac & Tapponnier (1993) Fig. 3

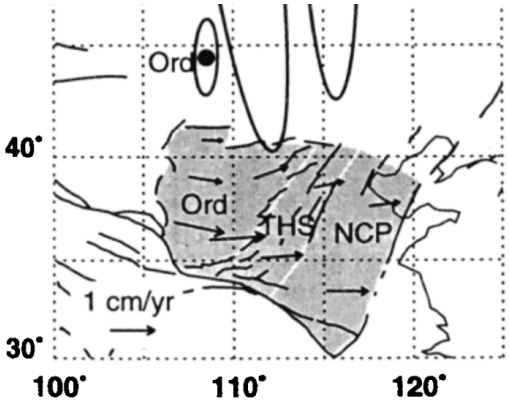


Xu et al. (1994) Fig. 1

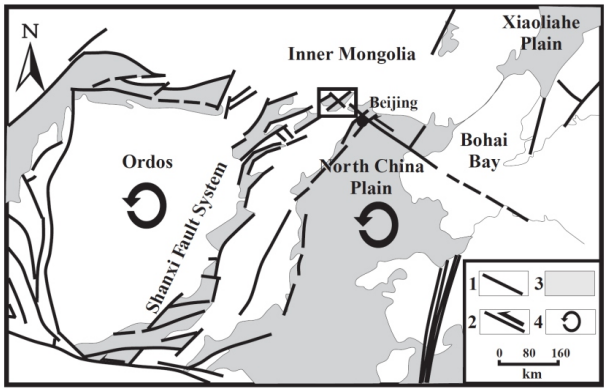


Zhang et al. (1995) Fig. 15

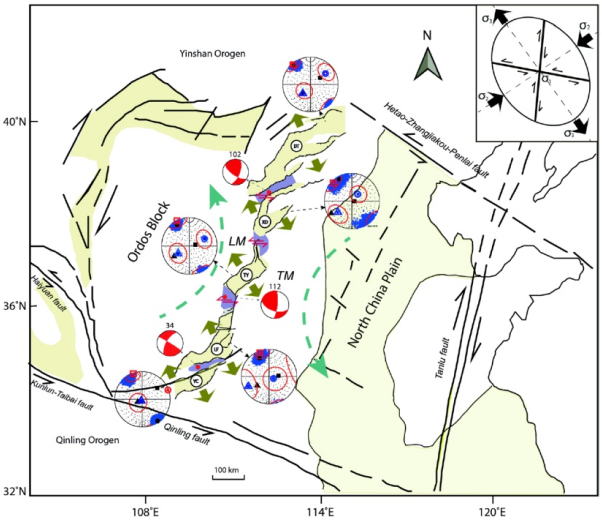
Figure 6.28: Previous anticlockwise rotation models for the kinematics of the Ordos Plateau (shown in chronological order) from *Xu and Ma* (1992), *Xu et al.* (1993), *Avouac and Tapponnier* (1993), *Xu et al.* (1994) and *Zhang et al.* (1995).



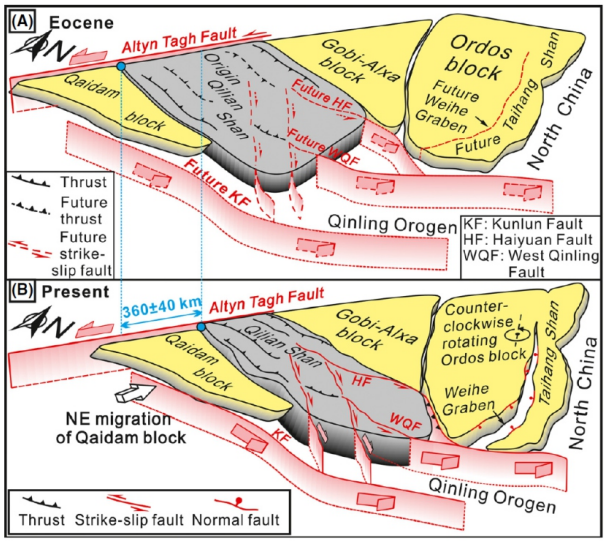
Peltzer & Saucier (1996) Fig. 6



Pavlides et al. (1999) Fig. 1



Li et al. (2015) Fig. 12



Cheng et al. (2015) Fig. 5

Figure 6.28: (continued) Previous anticlockwise rotation models (continued) for the kinematics of the Ordos Plateau (shown in chronological order) from *Peltzer and Saucier* (1996), *Pavlides et al.* (1999), *Li et al.* (2015a) and *Cheng et al.* (2015).

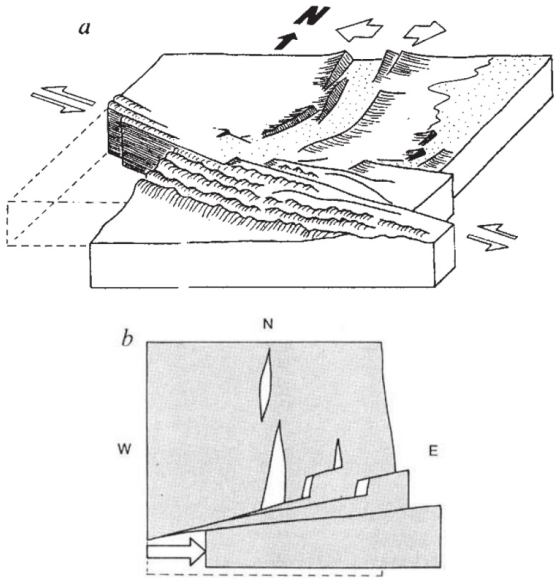
Avouac and Tapponnier, 1993; *Xu et al.*, 1994; *Peltzer and Saucier*, 1996; *Zhang et al.*, 1998). The idea was first proposed by *Lu and Ding* (1985) and has since been adjusted by other authors. For example, *Xu and Ma* (1992), *Xu et al.* (1993), *Xu et al.* (1994) and *Pavlides et al.* (1999) all proposed that both the Ordos Plateau and the North China Plain are undergoing anticlockwise rotation as a result of left-lateral motion on WNW-ESE trending faults and subsidiary right-lateral shear on NNE-SSW trending faults. *Xu and Ma* (1992) and *Xu et al.* (1994) also noted that an overall north-south widening of the zone is required in order to permit the anticlockwise rotations. Some authors have questioned the rotation model, claiming that anticlockwise rotation should be accompanied by right-lateral motion on all four boundaries of the Ordos Plateau and that this does not

match observations of the active faulting (*Xu et al.*, 2000; *Fan and Ma*, 2003). But if the Ordos Plateau is pinned at locations on its northern and southern boundaries, then it is possible for left-lateral motion to the north and south of the block to be accompanied by right-lateral motion to the east and west (see Section 6.6).

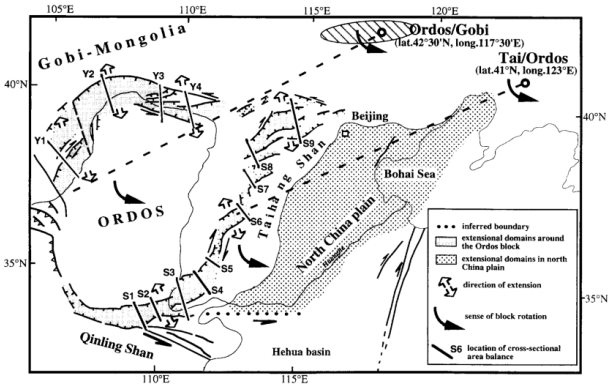
Avouac and Tapponnier (1993) and *Peltzer and Saucier* (1996) developed the same concept by incorporating anticlockwise rotation of the Ordos Plateau into larger kinematic models of the India-Eurasia collision zone that also involve clockwise rotations of parts of eastern Tibet and anticlockwise rotation of the South China block (see Figure 6.28). Meanwhile, *Zhang et al.* (1995) included the rotation of the Ordos block as a partial mechanism for the large-scale eastward extrusion of the Tibetan Plateau. They estimated an eastward motion of South China relative to Mongolia at a rate of 12±4 mm/a, of which the anticlockwise rotation of the Ordos block contributes 5±2 mm/a (see Figure 6.28). *Li et al.* (2015a) proposed that anticlockwise rotation of both the Ordos Plateau and the adjacent Taihangshan can explain the pattern of recent focal mechanisms that they observe in the Shanxi Grabens (see Figure 6.28). Finally, *Cheng et al.* (2015) emphasised that the northward motion of the Qaidam Basin (by ≈ 360 km) has resulted in significant shortening and eastward extrusion in the comparatively deformable Qilianshan. It is this extrusion, accomplished by the various left-lateral faults in the region, that drives the anticlockwise rotation of the Ordos (see Figure 6.28). A number of these studies have also estimated the rate of rotation and the location of the Euler pole about which the Ordos Plateau rotates (see Section 6.5.5, Table 6.4 and Figure 6.31).

6.5.3 Left-lateral slip and rotation

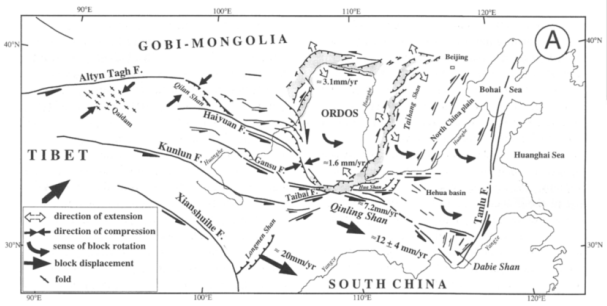
The "left-lateral slip and rotation" models proposed by *Zhang et al.* (1998) and *Zhang et al.* (2003b) are slightly different to the other anticlockwise rotation models (see Figure 6.29). Following ideas from *Peltzer et al.* (1985), they suggested that the rotations of the Ordos Plateau and the North China Plain are linked to the termination of major left-lateral strike-slip faults (see Figure 6.30). In this set-up, the Haiyuan Fault terminates against the Ordos block: some of the motion is absorbed as thrusting in the Liupan-



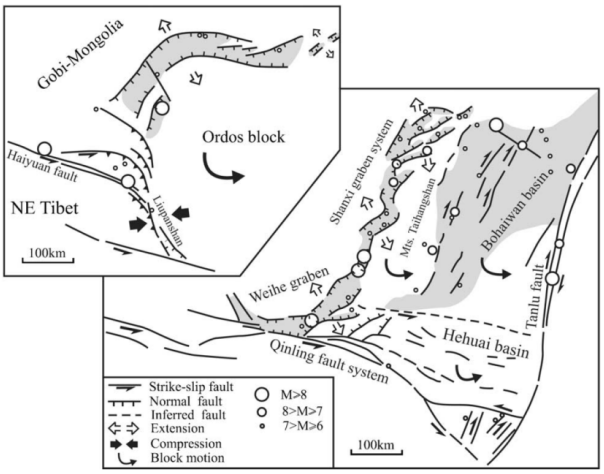
Peltzer et al. (1985) Fig. 6



Zhang et al. (1998) Fig. 16



Zhang et al. (1998) Fig. 18a



Zhang et al. (2003) Fig. 10

Figure 6.29: Previous "left-lateral slip and rotation" models for the kinematics of the Ordos Plateau. *Peltzer et al.* (1985) illustrate how left-lateral faults can terminate in a series of extensional grabens. *Zhang et al.* (1998) and *Zhang et al.* (2003b) show how this concept could be combined with anticlockwise rotation to describe the kinematics of the Ordos Plateau.

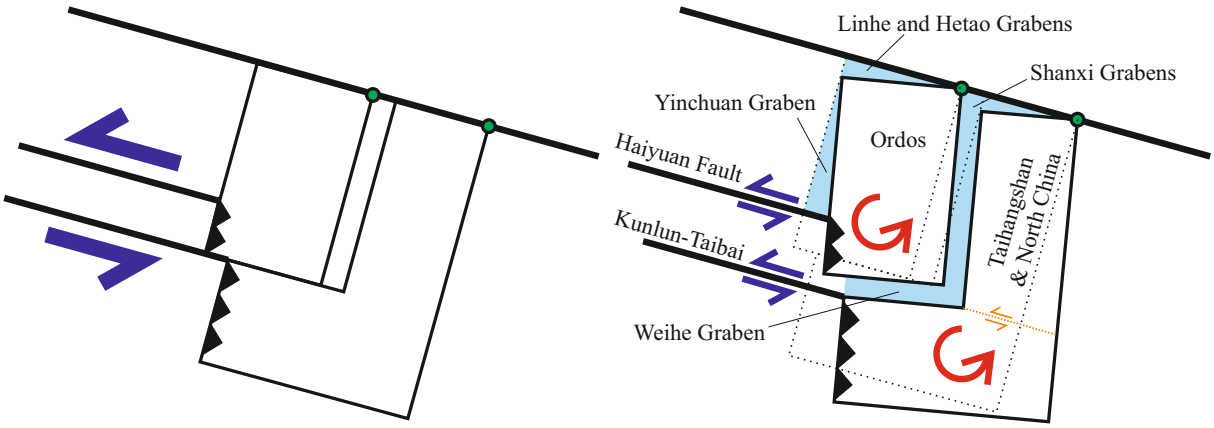


Figure 6.30: The "left-lateral slip and rotation" model for the kinematics of the Ordos Plateau (*Zhang et al.*, 1998, 2003b). Black triangles indicate regions of reverse faulting in the Liupanshan and Longmenshan. Light blue shading indicates the location of the graben systems that develop. Dotted orange line indicates approximate location of the Luonan and Danfeng Faults.

shan and the remaining motion pushes the Ordos block anticlockwise, opening up the Yinchuan, Linhe and Hetao Grabens in the process. Meanwhile, the Kunlun-Taibai Fault system terminates at the southwestern corner of the Ordos block: similarly, some motion is absorbed as thrusting in the Longmenshan to the south and the remaining motion forces anticlockwise rotation of an L-shaped North China Plain block (including the Taihangshan), opening up the Shanxi Grabens in the process (see Figure 6.30). This would be consistent with the observation that the opening of the Shanxi Grabens propagated from south to north (*Tapponnier and Molnar*, 1977; *Zhang et al.*, 2003b).

However, there are a number of problems with this subset of rotation models. Firstly, the existence of the Luonan and Danfeng Faults to the southeast of the Ordos Plateau (see the dotted orange line in Figure 6.30) means that there cannot be a rigid connection between the Sichuan Basin and the Taihangshan (see Section 6.2.4). Furthermore, even if the slip rates on the Luonan and Danfeng Faults are relatively slow (we obtain a geodetic shearing rate of 1.2±0.3 mm/a—see Section 6.4.4) they are still of a similar magnitude to the rates seen on the Taibai and eastern Kunlun Faults (*Deng et al.*, 2007; *Yuan et al.*, 2007; *Harkins et al.*, 2010), implying that there is insufficient left-lateral motion remaining to cause rotation of the Taihangshan. Indeed, it is not even clear that any significant left-lateral motion is transferred from the Kunlun Fault as far east as the Ordos (*Nockles*, 2015).

Secondly, the left-lateral slip and rotation model does not predict large right-lateral slip rates on the eastern and western sides of the Ordos. Right-lateral motion in the Shanxi Grabens can be no faster than the extension rate in the Weihe Graben (see Figure 6.30). This is inconsistent with our findings in Chapters 3 and 4, and Sections 6.2.5 and 6.2.6. We find that right-lateral motion is dominant over extension in both the Yinchuan Graben and the Shanxi Grabens. In addition, the left-lateral slip and rotation model does not predict wedge-shaped opening of the Weihe Graben.

6.5.4 Crustal strength contrasts

A fourth, and final, model for the kinematics of the Ordos Plateau is based on crustal strength contrasts. This model re-asserts that the Ordos region is undergoing simple northwest-southeast extension, but explains the location and geometry of the rifting on the basis of pre-existing crustal weak zones.

For example, *He et al.* (2003) and *He et al.* (2004) argued that the Ordos Plateau cannot be undergoing anticlockwise rotation because the GPS data they analysed appeared to show the entire north China region moving coherently to the ESE. *He et al.* (2004) then used a viscoelastic model to show that extension in the Shanxi Grabens could be caused by lateral changes in crustal rheology and the loading effect of the Taihangshan. Similarly, *He et al.* (2005) claimed that the apparently asymmetric flank uplift in the Yinchuan Graben can be explained by a crustal strength contrast between the Ordos Plateau and the Alxa block. However, we have shown in Chapter 5 that the apparent lack of extension in the Shanxi Grabens obtained by *He et al.* (2003) and *He et al.* (2004) results from the azimuth of their profile through the GPS data. Furthermore, *He et al.* (2005) assumed for their model that the entire topography of the Helanshan on the western side of the Yinchuan Graben results from uplift in the footwall of the current normal fault, but a number of studies have proposed that much of the topography may be a remnant of a Jurassic fold-and-thrust belt (*Liu and Yang*, 2000; *Darby and Ritts*, 2002).

It is quite possible that the location and geometry of the rifting has been determined by the presence of crustal weak zones, but this need not preclude a kinematic model that involves anticlockwise block rotations.

6.5.5 Existing Euler poles for the rotation of the Ordos Plateau

Lu and Ding (1985) proposed an Euler pole at 42 °N, 94 °E for the rotation of the Ordos Plateau by finding the locus of intersection of lines drawn perpendicular to the T axes of a series of focal mechanisms, but they were not able to calculate a rotation rate. *Peltzer and Saucier* (1996) used geological slip rates on major faults in Asia to build a finite element model of the deformation and produce a velocity field. They then determined Euler poles

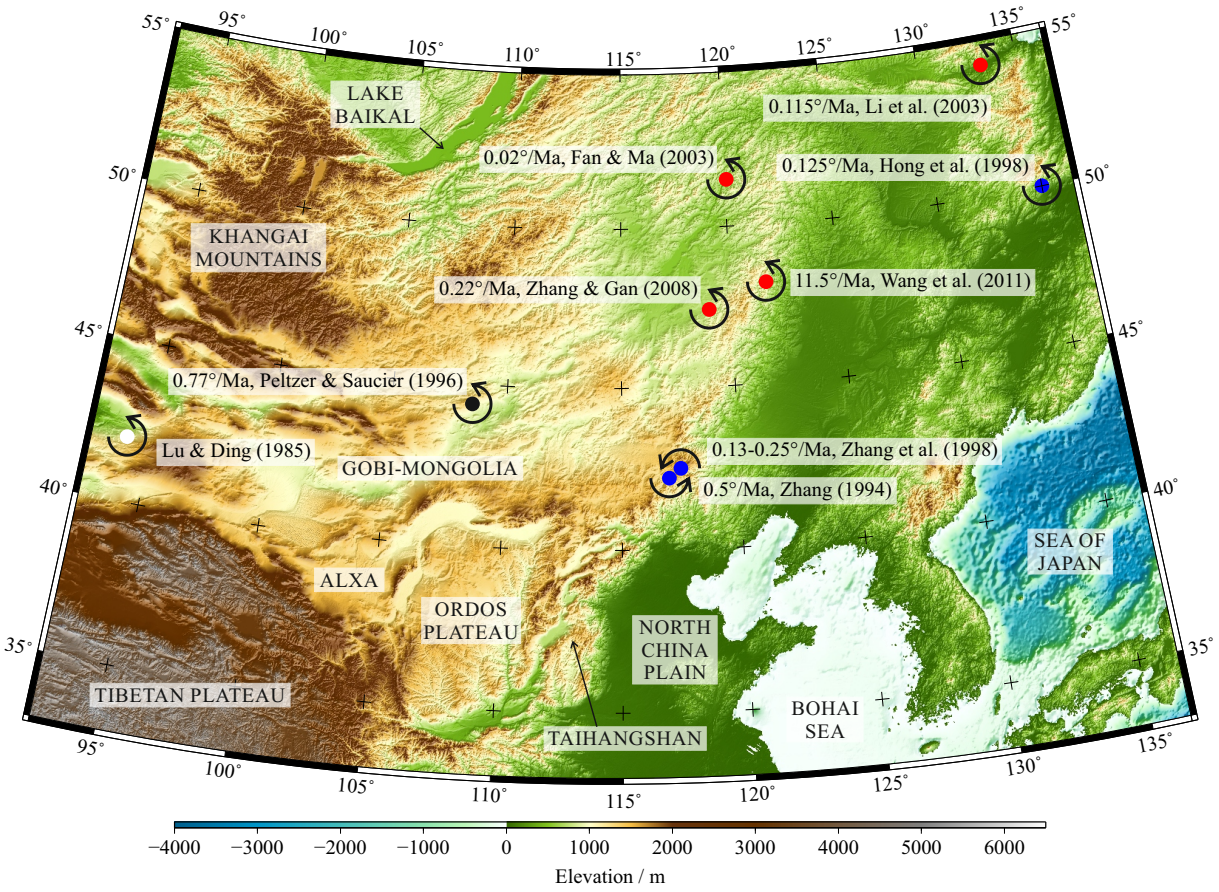


Figure 6.31: Albers equal-area projection of the SRTM topography in northeast Asia (*Farr et al.*, 2007). Dots show proposed locations of the Euler pole describing the anticlockwise rotation of the Ordos Plateau with respect to stable Eurasia (*Lu and Ding*, 1985; *Zhang*, 1994; *Peltzer and Saucier*, 1996; *Zhang et al.*, 1998; *Hong et al.*, 1998; *Fan and Ma*, 2003; *Li et al.*, 2003; *Zhang and Gan*, 2008; *Wang et al.*, 2011). White dot from earthquake T axes; black dot from finite element model based on fault slip rates; blue dots from fault kinematics; red dots from GPS-based studies. (Note: we believe there is an error in the 11.5 °/Ma from *Wang et al.* (2011).)

describing the motion of their major blocks relative to stable Eurasia. They found a pole at 44.4 °N, 108.5 °E and a rotation rate of 0.77 °/Ma for the Ordos Plateau. Similarly, they obtained a pole at 53.1 °N, 110.0 °E and a rate of 0.27 °/Ma for the Taihangshan; and a pole at 51.5 °N, 115.3 °E and a rate of 0.27 °/Ma for the North China Plain.

Zhang (1994) and *Zhang et al.* (1998) used fault kinematic data to obtain Euler poles. The strike of normal faults between any two stable blocks should form great circles through the Euler pole, whilst both the tension axes of focal mechanisms and extension directions from fault plane striations should lie on small circles about the Euler pole. *Zhang* (1994) used measurements in the Yinchuan and Hetao Grabens to estimate an Euler pole at 42.2 °N, 117 °E and a rotation rate of 0.5 °/Ma for the Ordos Plateau with respect to the

Table 6.4: Euler poles and rotation rates for previous kinematic models

Data	Rotation relative to	Lat / °	Long / °	Angular velocity[a] / °Ma^{-1}	Reference
Perpendiculars to T axes	Unknown	42	94	Unknown	*Lu and Ding* (1985)
Fault kinematics	Alxa desert[b]	42.2	117	0.5	*Zhang* (1994); *Replumaz and Tapponnier* (2003)
Finite element model	Eurasia	44.4	108.5	0.77	*Peltzer and Saucier* (1996)
Fault kinematics	Gobi-Mongolia[b]	42.5	117.5	0.13-0.25	*Zhang et al.* (1998)
Fault kinematics	Unknown	50	135	0.125	*Hong et al.* (1998); *Fan and Ma* (2003)
GPS block model	Eurasia	51.5	120.1	0.02	*Fan and Ma* (2003); *Wang et al.* (2001)
GPS block model	Unknown	54.2	133.2	0.115	*Li et al.* (2003)
GPS block model	Eurasia	47.4	119.0	0.22	*Zhang and Gan* (2008)
GPS block model	Eurasia	48.2	121.7	11.5[c]	*Wang et al.* (2011)
GPS block model	Eurasia	77.9	-0.18	0.42	*Ding et al.* (2014); *Zhao et al.* (2015)

[a] Positive angular velocity indicates anticlockwise rotation.
[b] Assumed to be fixed to a stable Eurasia.
[c] We think that *Wang et al.* (2011) have made a mistake in their paper, and confused radians with degrees. If this is the case, then their result is actually 0.20 °/Ma, which is in much closer agreement with *Zhang and Gan* (2008).

Alxa desert and Gobi-Mongolia (which they assumed to be fixed to stable Eurasia)—see also *Replumaz and Tapponnier* (2003). Similarly, *Zhang et al.* (1998) found a pole at 42.5 °N, 117.5 °E and a rate of 0.13 to 0.25 °/Ma. Meanwhile, measurements in the Weihe and Shanxi Grabens give a pole at 41 °N, 123 °E and a rate of 0.02 to 0.08 °/Ma for the motion of the Taihangshan with respect to the Ordos Plateau (*Zhang et al.*, 1998). *Hong et al.* (1998) also used kinematic data, but got a very different Euler pole, at 50 °N, 135 °E (see Figure 6.31).

Fan and Ma (2003) used the fairly sparse GPS data from *Wang et al.* (2001) (including only 6 sites on the Ordos Plateau) to estimate a pole at 51.5 °N, 120.1 °E and a rate of 0.02 °/Ma for the anticlockwise rotation of the Ordos Plateau with respect to a stable Eurasia. Similarly, they found a pole at 49.8 °N, 122.5 °E and a rate of 0.03 °/Ma for the Taihangshan (using 7 sites) and a pole at 52.5 °N, 111.3 °E and a rate of 0.01 °/Ma for the Alxa block (using 3 sites)—both with respect to a stable Eurasia. *Li et al.* (2003) used a similar method (with 41 sites on the Ordos Plateau) to obtain an Euler pole at 54.2 °N, 133.2 °E and a rotation rate of 0.115 °/Ma. *Zhang and Gan* (2008) used 25 sites on the Ordos Plateau and obtained an Euler pole at 47.4 °N, 119.0 °E and a rotation rate of 0.221 °/Ma. *Wang et al.* (2011) fitted an elastic block model for the whole of China to

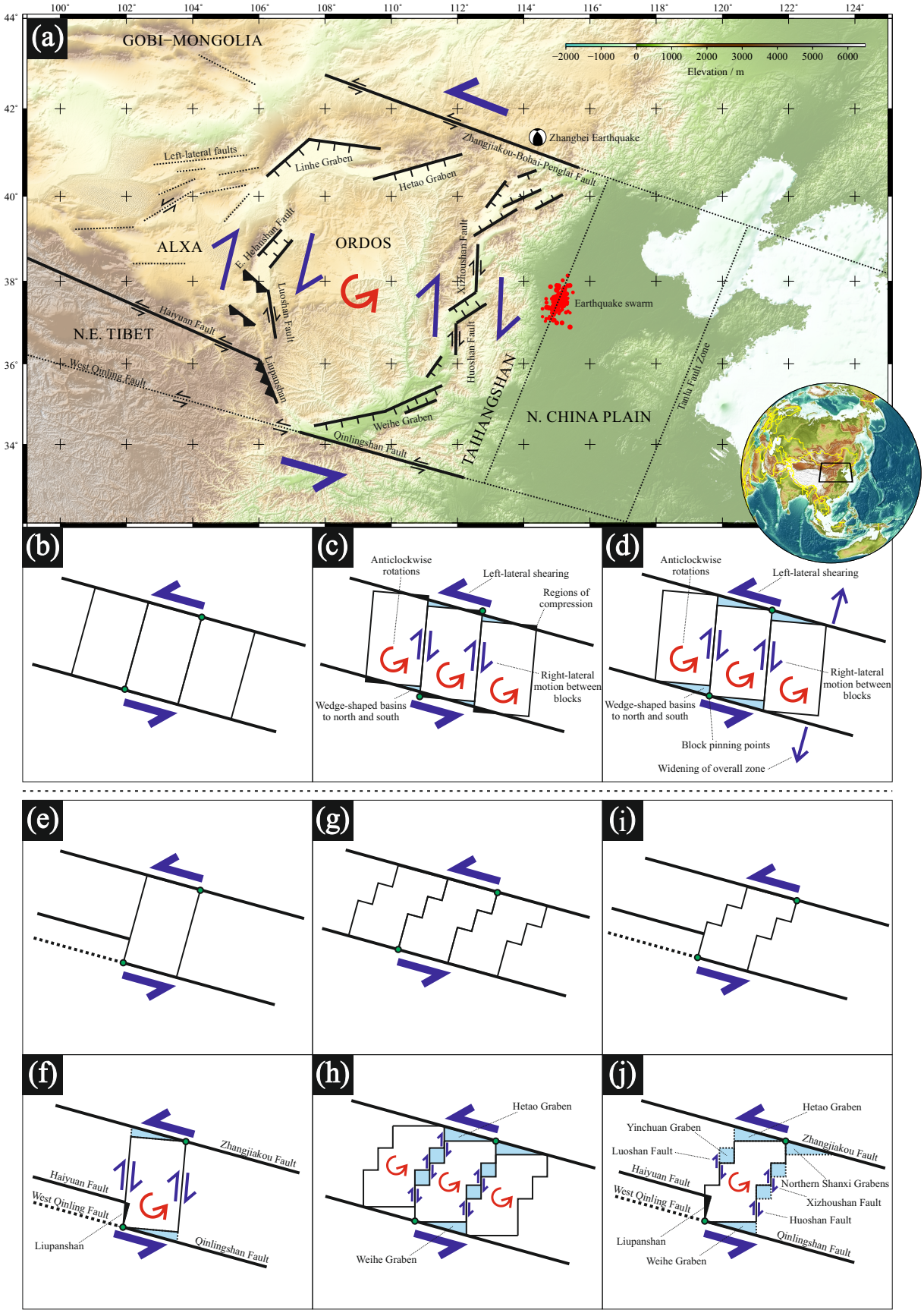
the same data as *Zhang and Gan* (2008). They found an Euler pole at 48.2 °N, 121.7 °E and a rotation rate of 11.5 °/Ma.[1]

One of the main problems with approaches based on fault kinematics in the Yinchuan and Hetao Grabens is that neither the Alxa block nor Gobi-Mongolia are necessarily stable with respect to Eurasia. In fact, geodetic and geological evidence suggests that potentially significant left-lateral shearing is occurring on WNW-ESE faults just north of the Ordos Plateau and in Gobi-Mongolia (e.g. see Sections 6.2.2 and 6.4.2). Euler poles based on fault data from Yinchuan and Hetao do not therefore describe the motion of the Ordos Plateau with respect to stable Eurasia. On the other hand, Euler poles from GPS vectors with respect to stable Eurasia largely describe the general eastward translation of the whole of northeast China and do not reveal anything about rotation of the Ordos Plateau with respect to its immediate surroundings.

6.6 The kinematic model proposed in this study

We investigate a similar kinematic model to those outlined in Section 6.5.2, involving anticlockwise rotation of the Ordos Plateau within a large-scale zone of WNW-ESE left-lateral shearing. Our model is closely comparable to those of *Xu and Ma* (1992) and *Xu et al.* (1993), but we also seek to extend the previous work by explaining the widespread normal faulting at the margins of the plateau (see Figure 6.32). In addition, many of the previous anticlockwise rotation models proposed independent Taihangshan and North China Plain "blocks" to the east of the Ordos, as shown by the dotted lines in Figure 6.32 (a) (*Xu and Ma*, 1992; *Xu et al.*, 1993, 1994; *Pavlides et al.*, 1999). However, given the extensive network of mapped active faults in the North China Plain (see Figure 6.4 and *Deng et al.*, 2007), it seems unlikely that the Taihangshan and North China Plain regions behave as contiguous rigid blocks. Meanwhile, little is known about the faulting to the west of the Ordos Plateau, but a series of mapped east-west trending left-lateral faults in the Alxa Desert could be accommodating distributed shearing. Again, there is no good

[1] We think that *Wang et al.* (2011) have made a mistake in their paper, and confused radians with degrees. If this is the case, then their result is actually 0.20 °/Ma, which is in much closer agreement with *Zhang and Gan* (2008).


(a)
GOBI–MONGOLIA
ALXA
ORDOS
N.E. TIBET
N. CHINA PLAIN
TAIHANGSHAN
Left-lateral faults
Linhe Graben
Hetao Graben
Zhangjiakou-Bohai-Penglai Fault
Zhangbei Earthquake
E. Helanshan Fault
Luoshan Fault
Haiyuan Fault
West Qinling Fault
Liupanshan
Weihe Graben
Qinlingshan Fault
Xizhoushan Fault
Huoshan Fault
Earthquake swarm
Tanlu Fault Zone
Elevation / m
(b)
(c)
Anticlockwise rotations
Left-lateral shearing
Regions of compression
Right-lateral motion between blocks
Wedge-shaped basins to north and south
(d)
Block pinning points
Widening of overall zone
(e)
(g)
(i)
(f)
Zhangjiakou Fault
(h)
(j)
Yinchuan Graben
Northern Shanxi Grabens

evidence for a rigid Alxa "block". Therefore, the cartoons in Figures 6.32 and 6.33 show multiple blocks for illustrative purposes only (specifically to show the right-lateral motion on the eastern and western sides of the main block), not because there is any strong evidence for the existence of any additional blocks.

Figures 6.32 (b), 6.32 (c) and 6.32 (d) show schematic representations of the kinematics in which three (illustrative) blocks, pinned at their northeast and southwest corners, are rotating anticlockwise within a WNW-ESE left-lateral shear zone. For the rotations to be accommodated, either compression must occur at the northeastern and southwestern corners of each block, or the overall zone has to widen. Figures 6.32 (e) and 6.32 (f) show how the geometry of the system can be modified to account for the fact that the slip rate on the Haiyuan Fault is notably larger than that on the West Qinling Fault, thereby providing a possible explanation for the development of the Liupanshan. Figures 6.32 (g) and 6.32 (h) show how initially irregular block boundaries (as perhaps determined by the location of pre-existing structures) can lead to the development of en echelon grabens and intervening right-lateral faults on the eastern and western margins of the block. (Faults in both the Yinchuan Graben and the Shanxi Grabens are known to have reactivated pre-existing structures (*Xu and Ma*, 1992; *Xu et al.*, 1993; *Liu*, 2000; *Darby and Ritts*, 2002).) Figures 6.32 (i) and 6.32 (j) combine the above modifications into a single schematic representation of the kinematics. Appendix D.1 includes a link to a video of a cardboard model that illustrates our kinematic scheme.

Figure 6.32 ***(preceding page)*:** (a) SRTM topography of the Ordos Plateau in northeastern China (*Farr et al.*, 2007). Inset globe shows the location of Figure 6.32 (a) within Asia. Black lines indicate major faults or fault zones and their sense of movement. Dotted lines show possible additional blocks—the Taihangshan and North China Plain blocks—to the east of the Ordos Plateau. General kinematic scheme after *Xu and Ma* (1992), *Xu et al.* (1993) and *Xu et al.* (1994). (b), (c) and (d) Before and (two possible) after views showing a schematic kinematic representation of the anticlockwise rotation of three crustal blocks in a WNW-ESE left-lateral shear zone. (c) and (d) indicate that for the rotation to be accommodated, either compression must occur at the northeastern and southwestern corners of each block, or the overall zone has to widen. (e) and (f) Before and after views showing a more realistic geometry for the Haiyuan Fault and the resulting development of the Liupanshan. (g) and (h) Before and after views showing how irregular block boundaries can lead to the development of en echelon grabens with intervening right-lateral faults (e.g. the Luoshan, Huoshan and Xizhoushan Faults). (i) and (j) Before and after views combining the above modifications into a single schematic kinematic representation.

6.6.1 Details of the kinematic model

We now derive some of the expected properties of our kinematic model. We consider a simplified case consisting of a set of equidimensional crustal blocks with sides of length a, pinned at their northeast and southwest corners (see Figure 6.33).

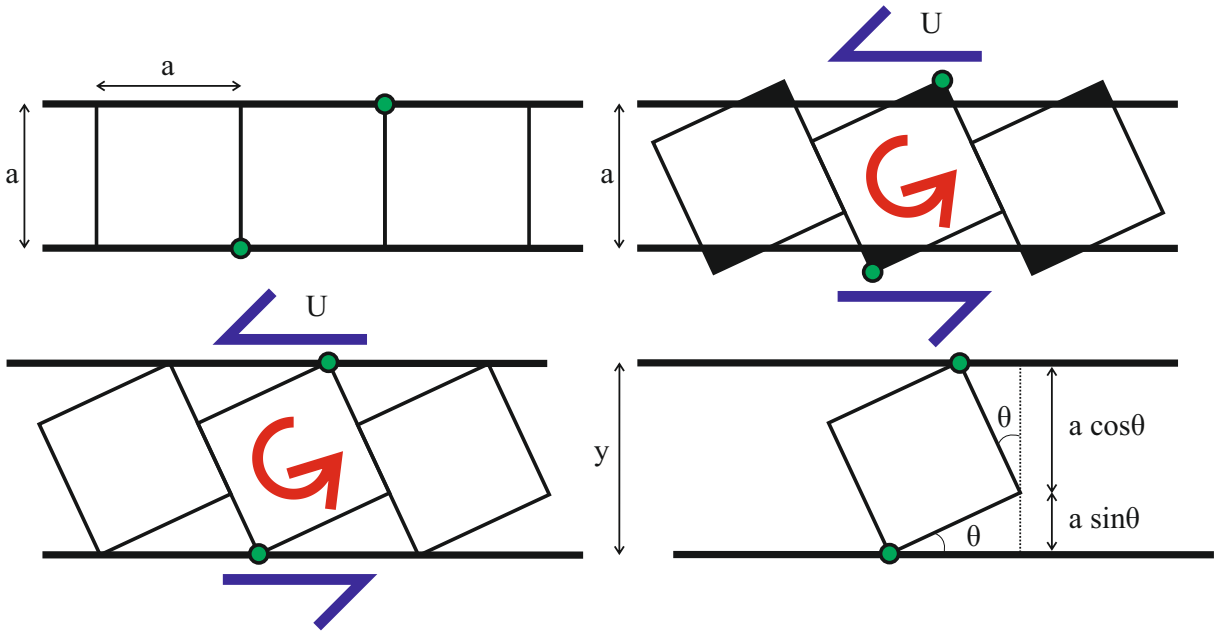


Figure 6.33: Block rotation cartoons, showing the set-up of our simplified kinematic model. The cartoons also show that for the rotation to be accommodated, compression must occur at the corners of the blocks, or the overall zone has to widen.

If the rate of (left-lateral) shearing across the blocks is U, then the rotation rate (W) is initially equal to $\frac{U}{a}$. In general, the rate of rotation of a pinned block depends on the current width of the zone (y), which varies during the rotation:

$$\frac{d\theta}{dt} = W = \frac{U}{y} \tag{6.2}$$

After a finite rotation of θ, y is given by:

$$y = a\sin\theta + a\cos\theta \tag{6.3}$$

Therefore:

$$\frac{dy}{d\theta} = a\cos\theta - a\sin\theta \tag{6.4}$$

And:

$$\frac{d\theta}{dt} = \frac{U}{a\sin\theta + a\cos\theta} \tag{6.5}$$

And so:

$$\frac{dy}{dt} = \frac{dy}{d\theta}\frac{d\theta}{dt} = (a\cos\theta - a\sin\theta)\left(\frac{U}{a\sin\theta + a\cos\theta}\right) = U\left(\frac{\cos\theta - \sin\theta}{\cos\theta + \sin\theta}\right) \tag{6.6}$$

For an equidimensional block, the rate of widening of the zone ($\frac{dy}{dt}$) is therefore independent of the starting dimension of the block (a). However, the rate of widening does depend on the total finite rotation so far (θ). For the Ordos block, the rate of left lateral shearing across the block is $\approx$ 5 mm/a (see Section 6.6.2). In the Weihe Graben, the angle between the southern margin of the Ordos block and the Qinlingshan is $\approx 25\,°$. Therefore, at the present day, we would expect the rate of widening of the zone ($\frac{dy}{dt}$) to be $\approx$ 1.8 mm/a.

Similarly, the current width of the zone (y) is approximately 800 km. Therefore, we expect the rotation rate at the present day ($\frac{d\theta}{dt}$) to be $\approx 6.25\times10^{-9}$ radians/a, or $0.36\,°$/Ma.

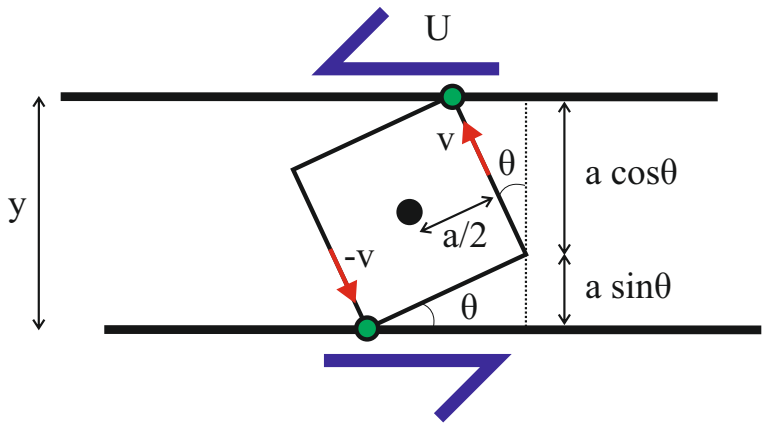


Figure 6.34: Second block rotation cartoon, showing the parameters used to calculate v_{diff}, the east-west velocity difference across a block.

We can also calculate the expected rate of strike-slip motion (v) on the eastern and western boundaries of the block (see Figure 6.34):

$$v = Wr = \frac{d\theta}{dt} \times \frac{a}{2} \tag{6.7}$$

Therefore:

$$v = \frac{U}{a\sin\theta + a\cos\theta} \times \frac{a}{2} = \frac{U}{2\left(\sin\theta + \cos\theta\right)} \tag{6.8}$$

The velocity difference (v_{diff}) across the block in the east-west direction is:

$$v_{diff} = 2v = \frac{U}{\sin\theta + \cos\theta} \tag{6.9}$$

For $U = 5$ mm/a and $\theta = 25\,^{\circ}$, $v_{diff} = 3.8$ mm/a. If we imagine a second, identical block adjacent to the first, the rate of strike-slip motion between the two blocks is the same as the velocity difference across one of the blocks in the east-west direction (v_{diff}).

6.6.2 Tests of the kinematic model

Palaeomagnetic data

One way to test the anticlockwise rotation model for the kinematics of the Ordos block would be to use palaeomagnetic samples from the interior of the plateau. Various studies have investigated the palaeogeographic position of the Ordos Plateau (and the whole North China Craton) using apparent polar wander paths (*Lin et al.*, 1985; *Zhao and Coe*, 1987; *Enkin et al.*, 1992; *Ma et al.*, 1993; *Cheng and Yang*, 1998), but very little palaeomagnetic data about the rotation of the whole Ordos Plateau have been published. *Xu et al.* (1994) estimated a total anticlockwise rotation of 1.3 to 3.7 ° with respect to the Xinjiang region of northwest China since the Late Tertiary (approximately 2.58 Ma ago), corresponding to a rotation rate of 0.5 to 1.4 °/Ma. This is not dissimilar to the rotation rate of 0.36 °/Ma predicted by our kinematic model. However, their samples are from the deforming eastern margin of the Ordos Plateau (see Figure 6.35), and so are likely to be affected by local rotations within this deforming belt. Furthermore, typical

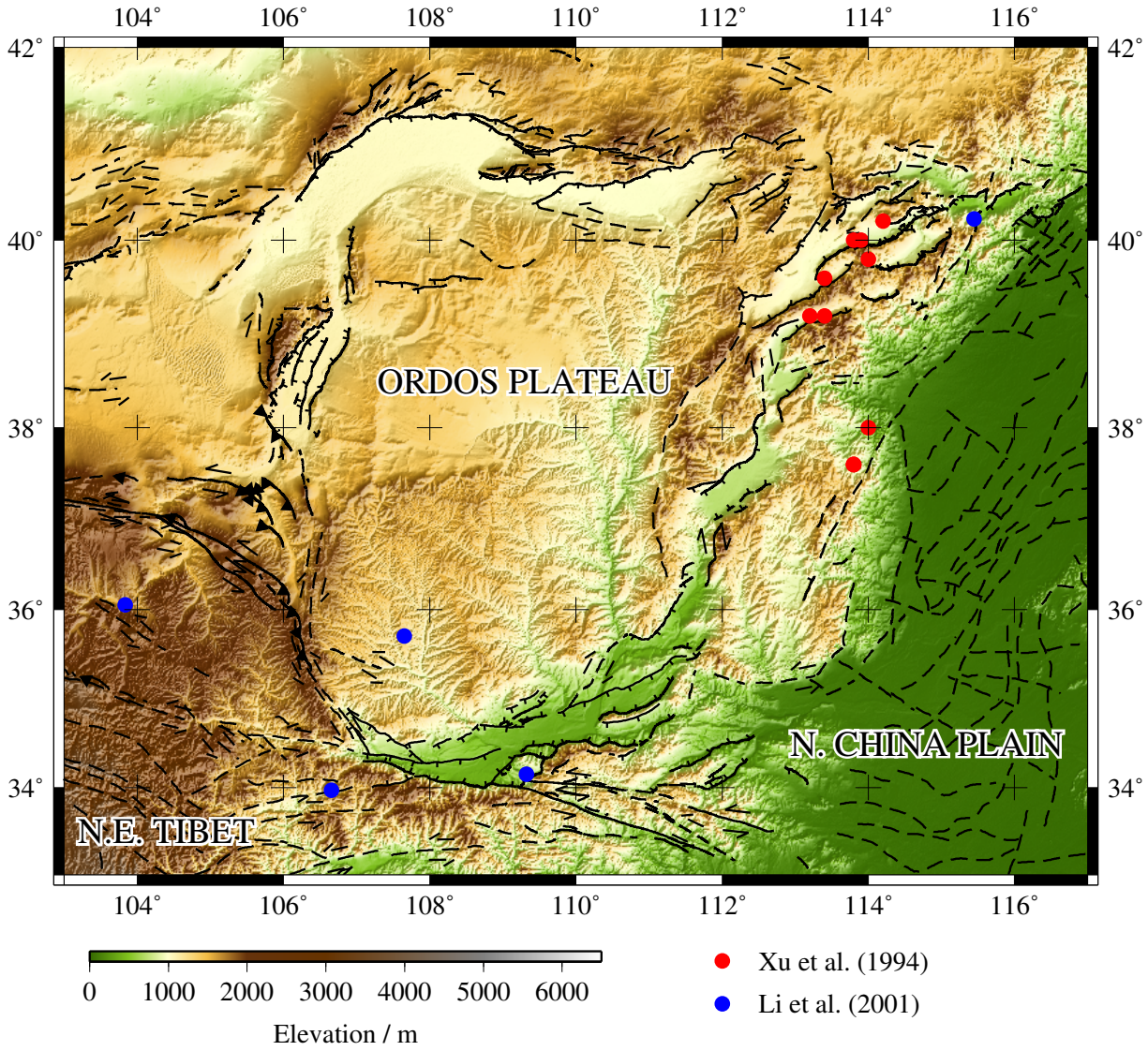


Figure 6.35: SRTM topography (90 m resolution) of the Ordos Plateau (*Farr et al.*, 2007). Faults from Figure 6.4 are also shown. Red dots show locations of palaeomagnetic samples used by *Xu et al.* (1994); blue dots show locations of palaeomagnetic samples used by *Li et al.* (2001).

errors for palaeomagnetic determinations of tectonic rotations are of the order of 10 or 15° (*Demarest*, 1983), so it is likely that these results involve large uncertainties (i.e. around ±5°/Ma). Indeed, *Li et al.* (2001) reported much higher anticlockwise rotation rates of tens of degrees per million years, also on the basis of palaeomagnetic data—although their samples were also primarily from the deforming margins of the Ordos Plateau (see Figure 6.35). Very little data exists from the stable interior of the plateau, presumably because of the thick cover of aeolian loess. Therefore, no sufficiently reliable palaeomagnetic data exists to provide constraints on the anticlockwise rotation of the Ordos block.

Left-lateral shearing

As indicated in Sections 6.5.2 and 6.6, the principal requirement for our anticlockwise rotation model is the existence of a large, left-lateral shear zone. Many previous authors have found evidence for this left-lateral motion. Around the southern margins of the plateau, this shearing is manifested as slip on the Haiyuan Fault at ≈ 4.5 mm/a (*Yuan et al.*, 1997; *Liu-Zeng et al.*, 2007; *Li et al.*, 2009a), the West Qinling Fault at 2-3 mm/a (*Deng et al.*, 2007; *Harkins et al.*, 2010), and the Luonan and Danfeng Faults at up to 8.4 mm/a (*Zhang et al.*, 1995; *Deng et al.*, 2007); to the north there is geological and geodetic evidence for around 2 mm/a of left-lateral motion on the Zhangjiakou-Bohai-Penglai Fault system (*Zheng et al.*, 1981; *Xu et al.*, 1993; *Shen et al.*, 2000).

The latest campaign GPS measurements also attest to the left-lateral motion (*Zhao et al.*, 2015). Figure 6.36 shows two profiles across the whole Ordos Plateau. Profile P-P′, to the west of the plateau, shows left-lateral shear of 8.1±1.5 mm/a averaged over the extent of the profile—with approximately 5 mm/a being taken up on the Haiyuan Fault. This is consistent with the Quaternary rate on the eastern Haiyuan Fault of 4.5±1.0 mm/a (*Li et al.*, 2009a). Profile Q-Q′, through the centre of the plateau, shows left-lateral shear of 4.6±1.1 mm/a averaged over the extent of the profile—though it does not appear to be localised on any one individual structure. The difference between the two profiles is potentially due to absorption of some of the eastward motion in the Liupanshan thrust belt. According to this data we would expect this shortening to be occurring at around 3.5 mm/a, which is not dissimilar to our Kostrov estimation of ≈ 5 mm/a of shortening (see Section 6.3). Profile Q-Q′ clearly indicates that ≈ 5 mm/a of left-lateral motion must be taken up across the Ordos block.

Wedge-shaped grabens

As illustrated in Figure 6.32, another prediction of our anticlockwise rotation model is the opening of wedge-shaped grabens to the north and south of the Ordos block. Our summary of Quaternary slip rates appears to show that extension in the Linhe and Hetao Grabens is slightly faster in the west than the east, whilst extension in the Weihe Graben

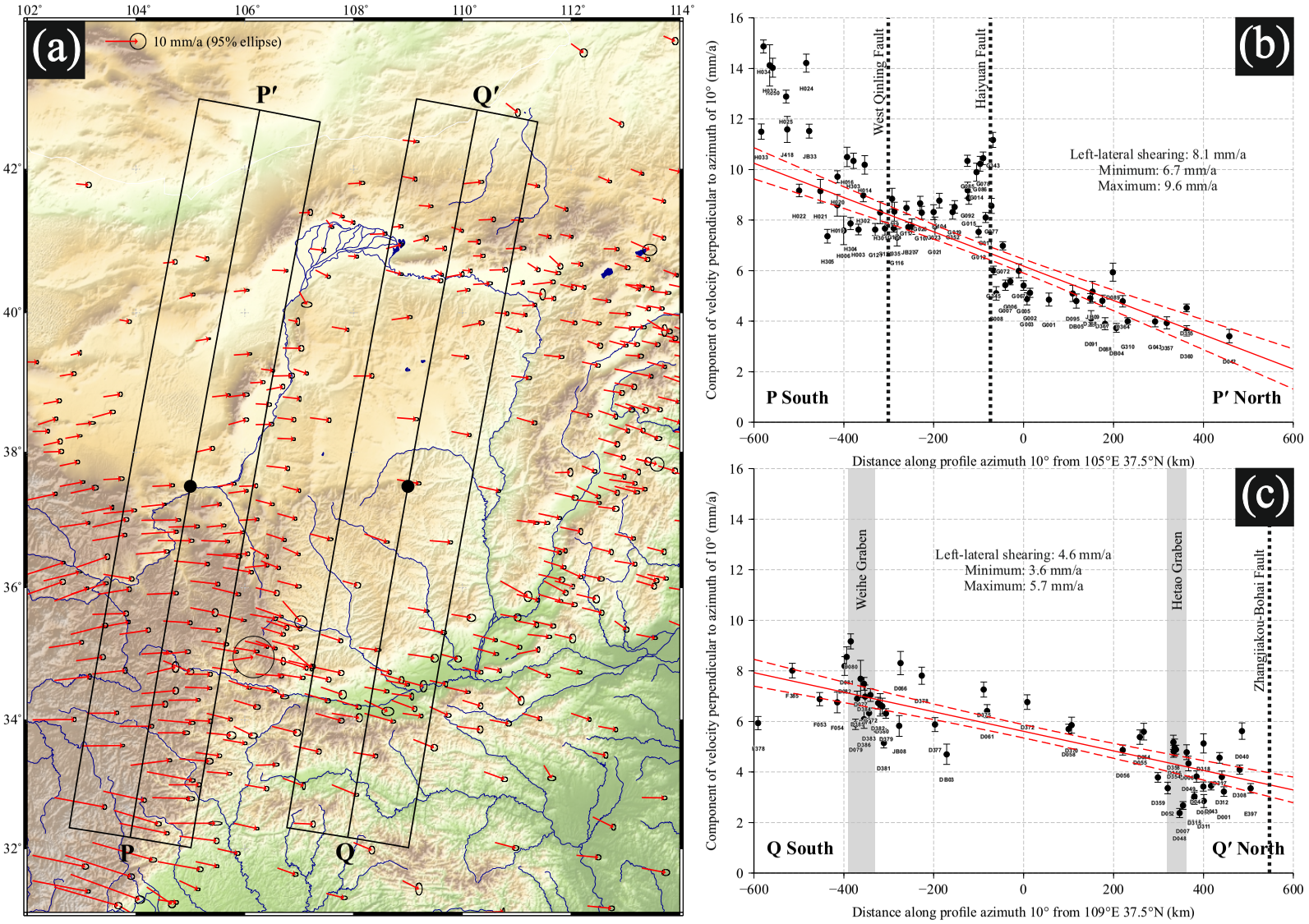


Figure 6.36: (a) SRTM topography of the Ordos Plateau in northeastern China (*Farr et al.*, 2007). Red arrows show the campaign GPS measurements made over a period of 4 years (occupations in 2009, 2011 and 2013) from *Zhao et al.* (2015) relative to stable Eurasia. (b) Swath profile P-P′ through the GPS data west of the Ordos Plateau showing the velocity component perpendicular to the profile. The red line is the best fit least squares regression to the data and the dashed red lines are the 95% confidence envelopes on this best fit line. (c) Same as (b), but for swath profile Q-Q′ through the centre of the Ordos Plateau.

is slightly faster in the east than the west (see Sections 6.2.3 and 6.2.4 and Figures 6.8, 6.9 and 6.10). These variations in extension rate would allow for the development of wedge-shaped grabens. Furthermore, graben widths and sediment thicknesses are greatest at the western ends of the Linhe and Hetao Grabens and at the eastern end of the Weihe Graben (see Sections 6.2.3 and 6.2.4). This implies that these spatial variations in extension rate may have persisted throughout the Pleistocene and Holocene, forming the wedge-shaped grabens that we observe today.

Fault slip rates in the eastern and western Ordos

For an equidimensional crustal block that is rotating within a large-scale shear zone, the secondary strike-slip motion on either side of the block is expected to be of a similar magnitude and opposite sense to the overall shear across the block (see Section 6.6.1).

In the case of the Ordos Plateau, *Fan and Ma* (2003) expressed concern that the left-lateral slip rates on the northern and southern margins are two to three times larger than the right-lateral slip rates on the eastern and western margins. In this study we found otherwise. The GPS data in Figure 6.36 (c) indicate an overall left-lateral shear across the block of ≈ 5 mm/a. Meanwhile, we have shown in Chapters 3 and 4 that the dominant motion on the western side of the Ordos block is right-lateral, at a Quaternary rate of ≈ 4 mm/a. Right-lateral shearing also occurs on the eastern side of the block by oblique normal slip on the en echelon Shanxi Grabens and right-lateral slip on the Xizhoushan and Huoshan Faults (see Section 6.2.6)—again, at Quaternary rates of ≈ 5 mm/a (although this is not seen in the GPS). In other words, the Ordos Plateau behaves as expected, with the secondary strike-slip motion on either side of the block occurring at a similar rate but in the opposite sense to the motion of the overall shear zone.

Widening of the overall zone

Finally, as shown in Figure 6.32, our kinematic model requires either compression at the corners of the Ordos block or widening of the overall zone. From the calculations in Section 6.6.1, we predict a current rate of widening of ≈ 1.8 mm/a.

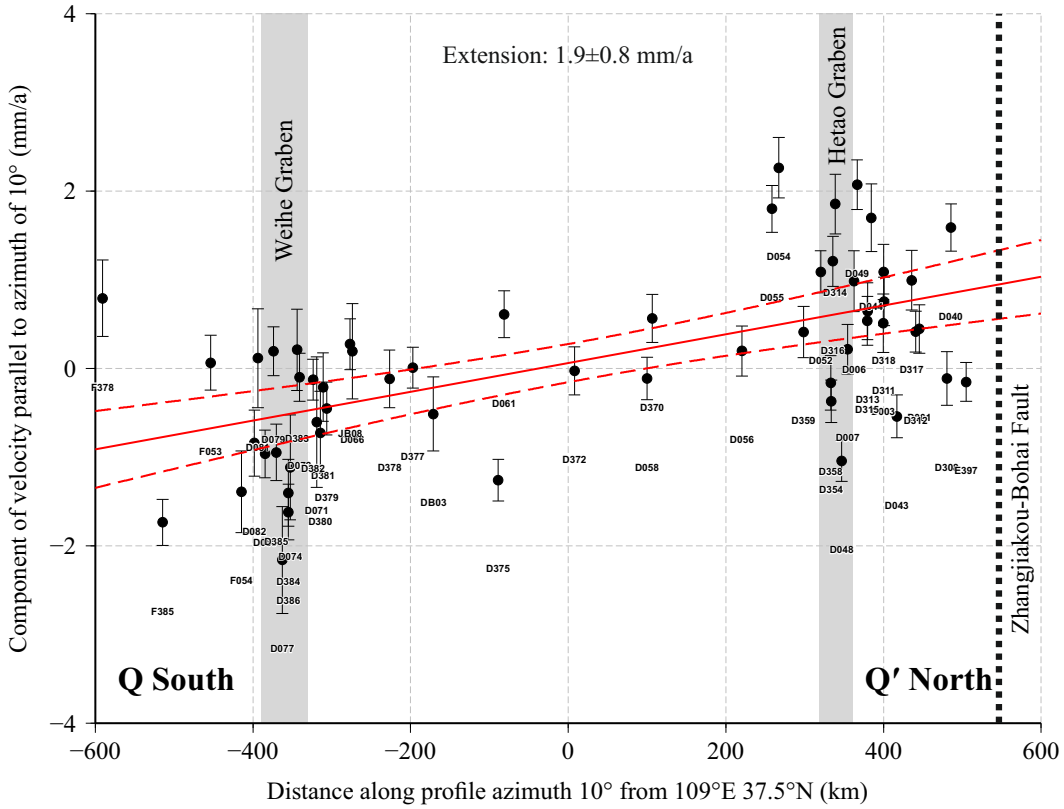


Figure 6.37: Swath profile Q-Q′ through the GPS data from *Zhao et al.* (2015) showing the velocity component parallel to the profile azimuth of 10 °. See Figure 6.36 (a) for location. The red line is the best fit least squares regression to the data and the dashed red lines are the 95% confidence envelopes on this best fit line. The profile shows north-south extension of 1.9±0.8 mm/a averaged over the extent of the profile.

The 1998 M_w 5.7 Zhangbei earthquake had a reverse-faulting mechanism and occurred near the northeastern corner of the Ordos Plateau (*Li et al.*, 2008) (see Figure 6.32 (a)). This event could therefore represent part of the compression necessary for anticlockwise rotation of the Ordos Plateau. However, the GPS data in Figure 6.37 indicate NNE-SSW extension across the whole zone of 1.9±0.8 mm/a. This is in close agreement with the prediction of our kinematic model and therefore suggests that widening of the zone is the dominant mechanism allowing anticlockwise rotation, without shortening at the corners of the block.

6.7 Discussion

Section 6.6.2 shows how the majority of the observations around the Ordos Plateau are consistent with our anticlockwise rotation model of the kinematics. However, a number

of questions still remain. Why are the most recent GPS measurements unable to resolve any right-lateral motion in the Shanxi Grabens when ^{14}C dates of offset gullies indicate slip rates of at least 5 mm/a? Similarly, why are there very few recent earthquakes in the Hetao Graben when geodetic measurements appear to indicate significant strain accumulation north of the Ordos?

One possible explanation for these apparent discrepancies is an earthquake switching model (*Friedrich et al.*, 2003; *Dolan et al.*, 2007; *Stein et al.*, 2009; *Li et al.*, 2009b; *Liu et al.*, 2011; *Liu and Wang*, 2012). At plate boundary zones, constant loading results in quasi-periodic strain release on one or two major faults with relatively uniform slip (see Figures 6.38 (a) and (b)), and seismic hazard assessment is comparatively simple (*Friedrich et al.*, 2003; *Liu et al.*, 2011). However, in intracontinental regions, slow tectonic loading is accommodated by a complex system of interacting faults spread over a large region (*Liu et al.*, 2011). Different faults are active at different times, and so earthquakes on any one individual fault (or seismic zone) are clustered in time (see Figures 6.38 (c) and (d)). Overall, the total rate of moment release across the whole system of faults should remain constant (*Dolan et al.*, 2007), but measurements of strain accumulation and release on an individual fault may be strongly timescale dependent (*Friedrich et al.*, 2003). As such, earthquake hazard assessments based on limited historical earthquake catalogues are likely to overestimate the hazard in regions of recent large earthquakes and underestimate the hazard elsewhere (*Li et al.*, 2009b). This complex earthquake switching behaviour on the continents has been observed before in the eastern USA (*Newman et al.*, 1999), Australia (*Crone et al.*, 2003), and northwest Europe (*Camelbeeck et al.*, 2007). Perhaps the most famous example, though, is from the western USA, where four bursts of seismic moment release in the Los Angeles area since 12 ka ago oscillate with bursts of moment release in the East California Shear Zone (*Dolan et al.*, 2007).

In China, temporal clustering of earthquakes was proposed by *Xu and Deng* (1996), who observed that many palaeoseismological studies appear to show widely varying recurrence intervals. Meanwhile, *Li et al.* (2009b), *Liu et al.* (2011) and *Liu and Wang* (2012) argued that an earthquake switching model could explain the observations in the Shanxi Grabens, Weihe Graben and North China Plain. For example, *Liu et al.* (2011) showed

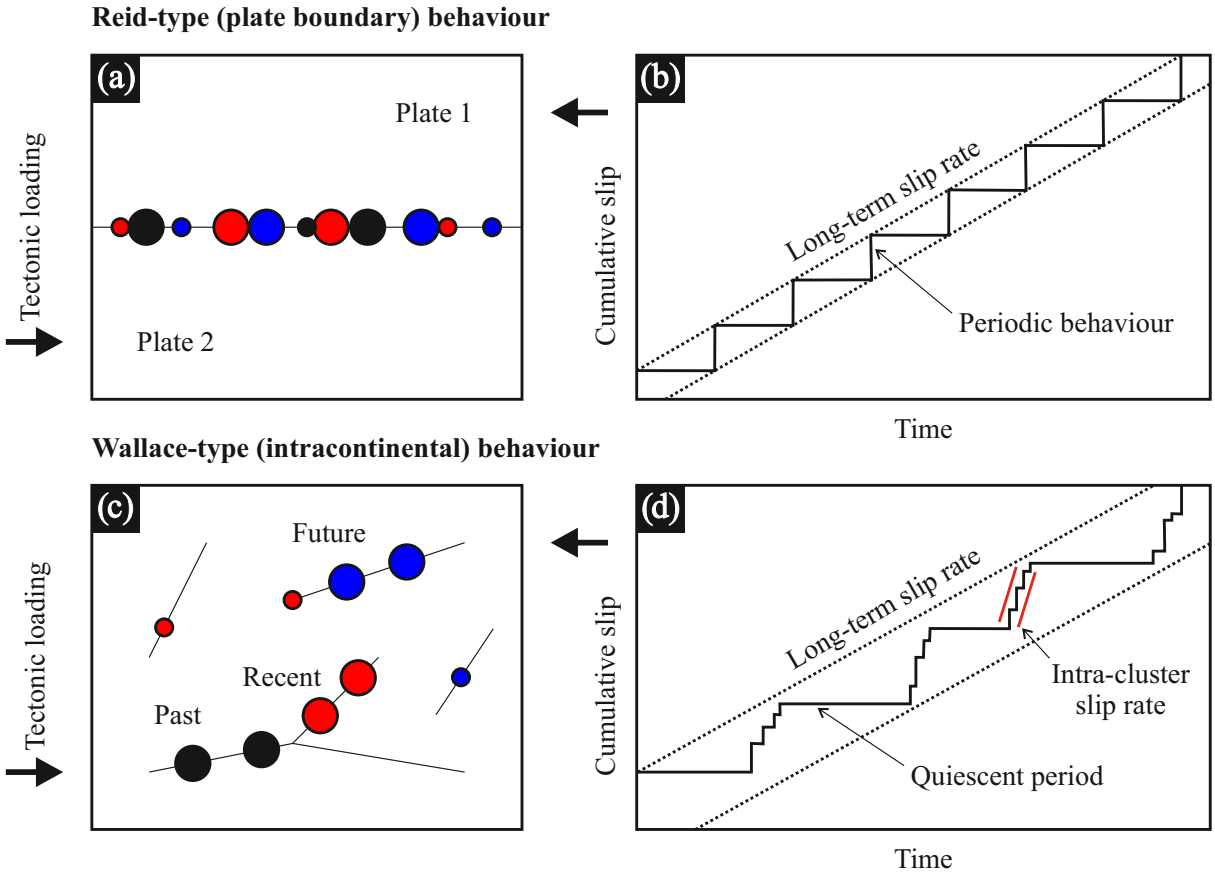


Figure 6.38: (a) Cartoon from *Liu et al.* (2011) showing typical occurrence of earthquakes at a plate boundary zone fault (Reid-type behaviour). Different colours indicate earthquakes occurring at different times. The plate boundary fault is loaded at a constant rate resulting in near-periodic earthquake occurrence. (b) Cumulative slip on the plate boundary fault versus time after *Reid* (1911); *Scholz* (1990); *Friedrich et al.* (2003). Sketch shows perfectly periodic behaviour, though time-predictable and slip-predictable models are also possible. (c) Cartoon from *Liu et al.* (2011) showing typical occurrence of earthquakes in an intracontinental region (Wallace-type behaviour). The region is subject to the same loading as before, but different faults are active at different times. (d) Cumulative slip versus time plot for one of the faults in (c) after *Wallace* (1987); *Friedrich et al.* (2003). Quiescent periods are interspersed with periods of higher slip rate.

that moment release in the Weihe and Shanxi Grabens appears to oscillate in antiphase with moment release in the North China Plain, switching every few centuries. However, it is not entirely clear what physical mechanism could cause such long-range earthquake switching behaviour.

One suggestion for the physical cause of the migration of seismicity between different faults is Coulomb stress transfers: an individual earthquake will alter the shear stress and normal stress on adjacent faults bringing them closer to or further from failure (*Stein*, 1999). Indeed, *Liu et al.* (2007) found that $\approx 80\%$ of the 49 earthquakes with $M \geq 6.5$

since 1303 in northern China have occurred in areas where the Coulomb stress was increased by previous large earthquakes, though their analysis assumes quite precise knowledge of the locations and focal mechanisms of these historical events. Similarly, *Li et al.* (2015d) found that 82% of small to medium magnitude instrumental earthquakes after the 1989 Datong earthquake also occurred in areas of increased Coulomb stress. However, Coulomb stress transfer alone cannot account for the long-distance migration of seismicity over hundreds of kilometres (*Liu et al.*, 2011); earthquake-induced stress transfers typically only affect faults immediately adjacent to the ruptured segment (*Stein*, 1999). Indeed, in northern China, earthquakes on the Tanlu Fault system are some 600 km from those in the Shanxi Grabens.

Other physical mechanisms involve temporal variations of physical fault properties. Earthquake clustering could therefore reflect: evolution of pore-fluid pressures (*Crone et al.*, 2003), faults that weaken during earthquakes and heal during the interseismic period (*Li et al.*, 2009b), or viscous relaxation of the lower crust that causes a sequence of ruptures with short recurrence intervals (*Kenner and Segall*, 2000).

Although the physical mechanism is poorly understood, an earthquake switching model could account for some of our observations, specifically the lack of any geodetically-observed deformation across the Shanxi Grabens and the shortage of earthquakes in the Hetao Graben (though we also note that the recent lack of earthquakes north of the Ordos Plateau could just be due to their very long recurrence intervals). Furthermore, the suggestion by *Liu et al.* (2011) that intracontinental earthquakes should be treated as a complex system is probably preferable to the assumption of quasi-periodic behaviour as a framework for considering seismic hazard.

6.8 Conclusions from the whole thesis

In this thesis, we have explored the active tectonics of the Ordos Plateau in northeastern China, using approaches that span a range of temporal and spatial scales.

In Chapter 2 we investigated the 1739 Yinchuan earthquake rupture on the western side of the Ordos Plateau using a combination of field observations, a Pleiades DEM

and ^{14}C dates. Our results strongly suggested that the earthquake occurred on the East Helanshan Fault and, based on our measurements, we calculated a moment magnitude for the earthquake in the range M_w 7.1 to M_w 7.6. Previous earthquake magnitudes from isoseismal maps likely overestimated the size of the event because they did not take account of amplification effects within the graben sediments. It is therefore possible that the size of other large-magnitude earthquakes in the historical catalogues have been similarly overestimated (see Section 6.9).

In Chapter 3, we used IRSL dating and a Pleiades DEM to determine a right-lateral strike-slip rate on the Luoshan Fault of 4.3±0.4 mm/a; meanwhile, in Chapter 4, we used ^{10}Be dating to determine a throw rate on the normal East Helanshan Fault of $< 0.8\pm0.1$ mm/a. We also found that these rates were consistent with the latest campaign GPS measurements. We therefore concluded that north-south right-lateral shearing is the principal tectonic motion in the western Ordos region, and proposed a simple geometric model to explain the pattern of faulting.

In Chapter 5, we compared Quaternary, seismic and geodetic rates of strain in the northern Shanxi Grabens. Contrary to previous studies, we found that the grabens are actively extending, and we obtained good agreement between our three different methods. We concluded that the northern Shanxi Grabens are extending at around 1 to 2 mm/a at an azimuth of $\approx 151\,^{\circ}$. We also found a notable seismic strain rate deficit since 1750, which could indicate: complex fault interactions across large regions, aseismic accommodation of deformation, or that we are quite late in the earthquake cycle with the potential for larger earthquakes in the relatively near future.

Lastly, in Chapter 6, we have summarised the active tectonics of the whole plateau on the basis of published Quaternary slip rates, updated Kostrov summations and the latest campaign GPS measurements. We concluded that the majority of observations were consistent with a kinematic model in which the Ordos Plateau rotates anticlockwise within a large-scale zone of WNW-ESE left-lateral shearing. Left-lateral shear of ≈ 8 mm/a is observed to the west of the plateau, of which ≈ 4.5 mm/a is taken up on the Haiyuan Fault. Around 3 mm/a is probably absorbed as shortening in the Liupanshan, leaving ≈ 5 mm/a of shear to be taken up by anticlockwise rotation of the whole Ordos

Plateau. This is achieved via right-lateral motion on the eastern and western sides of the block at Quaternary rates of ≈ 4 mm/a. The rotation of the Ordos Plateau therefore contributes to the lateral extrusion of eastern Asia as part of the India-Eurasia collision zone. Nonetheless, there remain some discrepant observations. Recent GPS measurements in the central Shanxi Grabens do not detect the right-lateral motion suggested by the Quaternary studies, whilst the difference between the seismic and geodetic rates of strain in the Hetao Graben may indicate a lack of recent large-magnitude events. An earthquake switching model may help to explain the long-range spatiotemporal migration of seismicity in northeastern China.

Finally, our conclusions have implications for the seismic hazard in the region. Our reduced magnitude estimate for the 1739 earthquake in Chapter 2 implies an increased frequency of such events in order to accommodate a given strain rate. In addition, although the isoseismal map for the event gives a good indication of the actual shaking, the likely amplification effects mean that the damage was caused by a smaller event than previously thought: if a magnitude 8.0 event did occur in future, it would cause even more damage than in 1739. In Chapter 5, the seismic strain rate deficit since 1750 (compared to Quaternary and geodetic measurements of strain) could indicate that the northern Shanxi Grabens are an area of increased seismic hazard. The deficit is equivalent to a single ≈ M_w 7.5 earthquake—and a number of faults are long enough to host such an event—but a series of smaller earthquakes is also conceivable. Similarly, in Chapter 6, we found a notable discrepancy between the seismic and geodetic strain rates in the Linhe and Hetao Grabens, to the north of the Ordos Plateau, indicating that this is also likely to be an area of high seismic hazard. Again, a single ≈ M_w 7.5 earthquake (like the 849 event on the Daqingshan Fault) could account for the difference.

6.9 Suggestions for future work

There are three important lines of further work that should be pursued. Firstly, following our work on the 1739 Yinchuan earthquake in Chapter 2, the magnitudes of other large earthquakes in northern China should be checked against what remains of the geological

evidence, especially since these magnitudes affect the assessment of seismic hazard. As noted above, *Feng et al.* (2016) and *Zhou* (2016) found that although isoseismal maps indicate a magnitude of 8.2 to 8.5 for the 1556 Huaxian earthquake (*Yuan and Feng*, 2010), measurements of the rupture and simple scaling relationships suggest a preferred magnitude in the range 7.3 to 7.9. If possible, the recorded sizes of the 849 Daqingshan earthquake (M 7.5), the 1038 Xizhoushan earthquake (M 7.3), the 1303 Hongdong earthquake (M 8), the 1501 Zhaoyi earthquake (M 7), the 1695 Linfen earthquake (M 7.8), the 1709 Zhongwei earthquake (M 7.5), and the 1920 Haiyuan earthquake (M 7.8) should all be checked against the geomorphological evidence preserved along their rupture zones. Indeed, it is often not clear how the quoted magnitudes of these earthquakes were estimated. Many of them are derived from the empirical relationship between maximum recorded intensity on the *New Chinese Intensity Scale* and surface wave magnitude ($M_s = 0.58\times I_0 + 1.5$), but this relationship does not consider the areal distribution of shaking or the influence of local site effects (e.g. amplification of shaking in surficial sediments) and hence it may be overly simplistic as a conversion tool. Yet once these magnitudes have been published, they are often cited by others without caveats or further scrutiny. Magnitude estimates in northern China could therefore be improved upon by re-evaluating the isoseismal data (using features other than just the maximum intensity, for example the radii of the isoseismals) (*Ambraseys and Douglas*, 2004), and calibrating the scale against both instrumental events and historical magnitudes based on the geological evidence.

Secondly, the Quaternary slip rates on the Huoshan and Xizhoushan Faults in the Shanxi Grabens should be verified. Although the original rates are based on a total of four ^{14}C ages, the lack of any resolvable geodetic motion means that it is important that they are re-visited. Furthermore, significant right-lateral motion in the Shanxi Grabens is a key part of our kinematic model. If right-lateral strike-slip faults and en echelon normal faults do not, together, account for $\approx$ 4 mm/a of shearing, then our kinematic model would need to be reconsidered. Verifying the rates on the Huoshan and Xizhoushan Faults is likely to be challenging since the geomorphology has been extensively modified by agriculture and is heavily vegetated in places (see Figure 6.23); it is likely that new

high-resolution DEMs (such as the Pleiades DEMs used in this thesis) would be needed in order to identify any subtle morphologies that have been preserved.

Finally, further work is needed on the apparent earthquake switching behaviour in northern China—particularly in the central Shanxi Grabens. The ongoing Crustal Motion Observation Network of China GPS campaigns will continue to improve the accuracy of geodetic strain measurements around the Ordos Plateau. Improved GPS data may yet reveal small geodetic strains across the central Shanxi Grabens and the Tanlu Fault zone. In addition to updating the Quaternary slip rate measurements on the Huoshan and Xizhoushan Faults, detailed palaeoseismological investigations on these two faults would also be beneficial, as they could potentially reveal temporal clustering of earthquakes in the recent geological past. If such studies continue to show a discrepancy between the geodetic and Quaternary rates of deformation for the central Shanxi Grabens, then further work is needed on the possible physical mechanisms controlling this time-varying fault behaviour. More realistic computer simulations of intracontinental fault interactions could help to highlight which faults are expected to be active at any given time (*Li et al.*, 2009b; *Liu et al.*, 2011). If *Stein et al.* (2009), *Liu et al.* (2011) and *Liu and Wang* (2012) are correct that intracontinental earthquakes behave as a complex system, then these sorts of models are urgently needed to assist with the assessment of seismic hazard: the central Shanxi Grabens have been effectively dormant for 300 years, but when might they switch back on again?

Bibliography

Ambraseys, N. N., and J. Douglas (2004), Magnitude calibration of north Indian earthquakes, *Geophysical Journal International*, *159*(1), 165–206, doi:10.1111/j.1365-246X.2004.02323.x. 6.9

Anderson, R. S., J. L. Repka, and G. S. Dick (1996), Explicit treatment of inheritance in dating depositional surfaces using in situ 10Be and 26Al, *Geology*, *24*, 47–51, doi:10.1130/0091-7613(1996)024<0047. 4.3.3

Avouac, J.-P., and P. Tapponnier (1993), Kinematic model of active deformation in Central Asia, *Geophysical Research Letters*, *20*(10), 895, doi:10.1029/93GL00128. 1.2, 1.2, 3.1, 6.28, 6.5.2

Bai, M., and D. Jiao (2005), The historical analysis for M=8 earthquake in 1739 at Yinchuan-Pingluo area, *Northwestern Seismological Journal*, *27*(2), 135–140 (in Chinese). 2.1, 2.3, 2.4.4

Bai, Y., and S. Wang (2014), Silk-road economic belt: the strategic corridor of China going global, *Journal of Northwest University: Philosophy and Social Sciences Edition*, *44*(4), 32–38 (in Chinese). 1.4.2

Balco, G., J. O. Stone, N. A. Lifton, and T. J. Dunai (2008), A complete and easily accessible means of calculating surface exposure ages or erosion rates from 10Be and 26Al measurements, *Quaternary Geochronology*, *3*(3), 174–195, doi:10.1016/j.quageo.2007.12.001. 4.1, 4.3.3, 4.3.3

Bellier, O., J.-L. Mercier, P. Vergèly, C. Long, and C. Ning (1988), Evolution sedimentaire et tectonique du graben cenozoique de la Wei He (province du Shaanxi, Chine du Nord), *Bull Soc Geol France*, *8*, 979–994 (in French). 6.2.4, 6.2.4

Benedetti, L. C., and J. van der Woerd (2014), Cosmogenic Nuclide Dating of Earthquakes, Faults, and Toppled Blocks, *Elements*, *10*, 357–362, doi:10.2113/gselements.10.5.357. 1.14, 4.3.3

Bilham, R. (2004), Urban Earthquake Fatalities: A Safer World, or Worse to Come?, *Seismological Research Letters*, *75*(6), 706–712, doi:10.1785/gssrl.75.6.706. 1.4.1, 1.4.2

Bilham, R. (2009), The seismic future of cities, *Bulletin of Earthquake Engineering*, *7*(4), 839–887, doi:10.1007/s10518-009-9147-0. 1.4.1, 1.4.2

Bilham, R., and P. England (2001), Plateau 'pop-up' in the great 1897 Assam earthquake, *Nature*, *410*(6830), 806–809, doi:10.1038/35071057. 2.1

Bird, P., and K. Piper (1980), Plane-stress finite-element models of tectonic flow in southern California, *Physics of the Earth and Planetary Interiors*, *21*, 158–175. 1.1, 5.4.5, 6.4.1

Bourne, S., P. England, and B. Parsons (1998), The motion of crustal blocks driven by flow of the lower lithosphere and implications for slip rates of continental strike-slip faults, *Nature*, *391*, 655–659, doi:10.1038/35556. 1.1

Brock, F., T. Higham, P. Ditchfield, and C. Bronk (2010), Current pretreatment methods for AMS radiocarbon dating at the Oxford Radiocarbon Accelerator Unit (ORAU), *Radiocarbon*, *52*(1), 103–112. 2.4.1, 2.2

Bronk Ramsey, C., and S. Lee (2013), Recent and Planned Developments of the Program OxCal, *Radiocarbon*, *55*(2-3), 720–730, doi:10.2458/azu_js_rc.55.16215. 2.4.1

Bronk Ramsey, C., T. Higham, and P. Leach (2004), Towards high-precision AMS: progress and limitations, *Radiocarbon*, *46*(1), 17–24. 2.4.1, 2.2

Burbank, D. W., and R. S. Anderson (2012), *Tectonic Geomorphology*, 2nd ed., 472 pp., Wiley-Blackwell, Chichester. 1.14, 3.3.3, 4.3.3

Burchfiel, B., P. Zhang, Y. Wang, W. Zhang, F. Song, Q. Deng, P. Molnar, and L. Royden (1991), Geology of the Haiyuan fault zone, Ningxia-Hui autonomous region, China, and its relation to the evolution of the northeastern margin of the Tibetan plateau, *Tectonics*, *10*(6), 1091–1110, doi:10.1029/90TC02685. 3.2, 6.2.1

Buylaert, J. P., A. Murray, K. J. Thomsen, and M. Jain (2009), Testing the potential of an elevated temperature IRSL signal from K-feldspar, *Radiation Measurements*, *44*(5-6), 560–565, doi:10.1016/j.radmeas.2009.02.007. 3.3.3

Camelbeeck, T., K. Vanneste, P. Alexandre, K. Verbeeck, T. Petermans, P. Rosset, M. Everaerts, R. Warnant, and M. Van Camp (2007), Relevance of active faulting and seismicity studies to assessments of long-term earthquake activity and maximum magnitude in intraplate northwest Europe, between the Lower Rhine Embayment and the North Sea, in *Continental Intraplate Earthquakes: Science, Hazard, and Policy Issues*, vol. 425, edited by S. Stein and S. Mazzotti, pp. 193–224, Geological Society of America, doi:10.1130/2007.2425(14). 6.7

Caskey, S. J., S. G. Wesnousky, P. Zhang, and D. B. Slemmons (1996), Surface Faulting of the 1954 Fairview Peak (Ms 7.2) and Dixie Valley (Ms 6.8) Earthquakes, Central Nevada, *Bulletin of the Seismological Society of America*, *86*(3), 761–787. 2.5.2

Cavalié, O., C. Lasserre, M.-P. Doin, G. Peltzer, J. Sun, X. Xu, and Z.-K. Shen (2008), Measurement of interseismic strain across the Haiyuan fault (Gansu, China), by InSAR, *Earth and Planetary Science Letters*, *275*, 246–257, doi:10.1016/j.epsl.2008.07.057. 6.2.1

Chai, C., G. Meng, P. Du, Y. Wang, B. Liu, W. Shen, Q. Lei, Y. Liao, C. Zhao, S. Feng, X. Zhang, and X. Xie (2006), Comprehensive multi-level exploration of buried active fault: an example of Yinchuan buried active fault, *Seismology and Geology*, *28*(4), 536–546 (in Chinese). 2.1, 2.3

Chen, H., J. Hu, W. Gong, R. Kang, and L. Li (2015), Characteristics and transition mechanism of late Cenozoic structural deformation within the Niushoushan-Luoshan fault zone at the northeastern margin of the Tibetan Plateau, *Journal of Asian Earth Sciences*, *114*(1), 73–88, doi:10.1016/j.jseaes.2015.06.034. 3.2, 6.2.5

Chen, L., Y. Ran, and X. Yang (2003), Late Quaternary activity and segmentation model of the Sertengshan piedmont fault, *Earthquake Research in China*, *19*(3), 255–265 (in Chinese). 6.1, 6.8, 6.2.3

Chen, L., C. Cheng, and Z. Wei (2009), Seismic evidence for significant lateral variations in lithospheric thickness beneath the central and western North China Craton, *Earth and Planetary Science Letters*, *286*(1-2), 171–183, doi:10.1016/j.epsl.2009.06.022. 6.1

Cheng, B., S. Cheng, G. Zhang, and D. Zhao (2014), Seismic structure of the Helan-Liupan-Ordos western margin tectonic belt in North-Central China and its geodynamic implications, *Journal of Asian Earth Sciences*, *87*, 141–156, doi:10.1016/j.jseaes.2014.01.006. 2.6.2

Cheng, F., M. Jolivet, G. Dupont-Nivet, L. Wang, X. Yu, and Z. Guo (2015), Lateral extrusion along the Altyn Tagh Fault, Qilian Shan (NE Tibet): insight from a 3D crustal budget, *Terra Nova*, *27*(6), 416–425, doi:10.1111/ter.12173. 6.28, 6.5.2

Cheng, S., and G. Yang (1998), Fault growth, displacement transfer, and evolution of the Jiugongkou fault overlap zone in Weixian, Hebei, *Seismology and Geology*, *20*(1), 1–8 (in Chinese). 5.2, 5.5.1, 5.3, 5.10, 6.6.2

Cheng, S., Z. Fang, G. Yang, and Z. Yang (1995), On segmentation of the fault zone along the northern margin of the Yanqing Basin and earthquake prediction, *Seismology and Geology*, *17*(3), 231–240 (in Chinese). 5.2, 5.3, 5.10

Columbia University, Center for International Earth Science Information Network (2015), Gridded Population of the World, Version 4 (GPWv4): Population Density Adjusted to Match 2015 Revision of UN WPP Country Totals. 1.9, 1.10

Copley, A., J.-P. Avouac, J. Hollingsworth, and S. Leprince (2011), The 2001 Mw 7.6 Bhuj earthquake, low fault friction, and the crustal support of plate driving forces in India, *Journal of Geophysical Research*, *116*(B8), 1–11, doi:10.1029/2010JB008137. 2.1

Copley, A., J. Hollingsworth, and E. Bergman (2012), Constraints on fault and lithosphere rheology from the coseismic slip and postseismic afterslip of the 2006 Mw 7.0 Mozambique earthquake, *Journal of Geophysical Research*, *117*(B3), 1–16, doi:10.1029/2011JB008580. 2.1

Corbett, L. B., P. R. Bierman, and D. H. Rood (2016), An approach for optimizing in situ cosmogenic 10Be sample preparation, *Quaternary Geochronology*, *33*, 24–34, doi:10.1016/j.quageo.2016.02.001. 4.3.3

Cowgill, E. (2007), Impact of riser reconstructions on estimation of secular variation in rates of strike slip faulting: Revisiting the Cherchen River site along the Altyn Tagh Fault, NW China, *Earth and Planetary Science Letters*, *254*, 239–255, doi:10.1016/j.epsl.2006.09.015. 1.2, 3.3.2, 3.4.2

Craig, T. J., and E. Calais (2014), Strain accumulation in the New Madrid and Wabash Valley seismic zones from 14 years of continuous GPS observation, *Journal of Geophysical Research: Solid Earth*, *119*(12), 9110–9129, doi:10.1002/2014JB011498. 5.1

Crone, A. J., P. M. D. Martini, M. N. Machette, K. Okumura, and J. R. Prescott (2003), Paleoseismicity of Two Historically Quiescent Faults in Australia: Implications for Fault Behavior in Stable Continental Regions, *Bulletin of the Seismological Society of America*, *93*(5), 1913–1934. 6.7, 6.7

Darby, B., B. Ritts, Y. Yue, and Q. Meng (2005), Did the Altyn Tagh fault extend beyond the Tibetan Plateau?, *Earth and Planetary Science Letters*, *240*(2), 425–435, doi:10.1016/j.epsl.2005.09.011. 3.2, 4.8, 6.4, 6.12

Darby, B. J., and B. D. Ritts (2002), Mesozoic contractional deformation in the middle of the Asian tectonic collage: the intraplate Western Ordos fold-thrust belt, China, *Earth and Planetary Science Letters*, *205*(1-2), 13–24, doi:10.1016/S0012-821X(02)01026-9. 2.2.2, 3.2, 4.8, 6.1, 6.4, 6.12, 6.5.4, 6.6

Demarest, H. H. (1983), Error analysis for the determination of tectonic rotation from paleomagnetic data, *Journal of Geophysical Research*, *88*, 4321–4328. 6.6.2

DeMets, C., R. G. Gordon, D. F. Argus, and S. Stein (1990), Current plate motions, *Geophysical Journal International*, *101*(2), 425–478, doi:10.1111/j.1365-246X.1990.tb06579.x. 1.1

DeMets, C., R. G. Gordon, D. F. Argus, and S. Stein (1994), Effect of recent revisions to the geomagnetic reversal time scale on estimates of current plate motions, *Geophysical Research Letters*, *21*(20), 2191–2194, doi:10.1029/94GL02118. 1.1

Deng, Q., and F. Fan (1980), Cenozoic and recent geotectonic characteristics of North China fault block region, in *Formation and Development of North China Fault Block Region*, pp. 192–205 (in Chinese), Science Press, Beijing. 6.5.1

Deng, Q., and Y. Liao (1996), Paleoseismology along the range-front fault of Helan Mountains, north central China, *Journal of Geophysical Research*, *101*, 5873–5893. 2.1, 2.2, 2.3, 2.3, 2.4.3, 2.1, 2.1, 2.5, 2.4.4, 2.5.1, 2.5.1, 2.5.2, 2.5.2, 2.14, 2.6.1, 2.16, 2.6.2, 2.6.2, 2.17, 4.2, 4.4.2, 4.4, 4.4.2, 6.4

Deng, Q., F. Sung, S. Zhu, M. Li, T. Wang, W. Zhang, B. C. Burchfiel, P. Molnar, and P. Zhang (1984a), Active faulting and tectonics of the Ningxia-Hui autonomous region, China, *Journal of Geophysical Research*, *89*, 4427–4445. 3.1, 3.2, 4.8, 6.4, 6.2.1, 6.2.5, 6.12, 6.26, 6.5.1

Deng, Q., Y. Wang, Y. Liao, W. Zhang, and M. Li (1984b), Colluvial wedges and Holocene activity along the range-front fault of Helan Shan, *Chinese Science Bulletin*, *29*, 557–560 (in Chinese). 2.3, 2.4.4

Deng, Q., P. Zhang, Y. Ran, X. Yang, W. Min, and Q. Chu (2003), Basic characteristics of active tectonics of China, *Science in China (Series D)*, *46*(4), 356–372. 1.1, 6.2.2

Deng, Q., Y. Ran, X. Yang, W. Min, and Q. Chu (2007), Map of Active Tectonics in China (in Chinese). 1.3.1, 3.2, 4.8, 5.2, 5.2, 5.5.3, 5.5.4, 5.3, 5.10, 5.6.2, 5.16, 6.2, 6.3, 6.1, 6.1, 6.4, 6.8, 6.2.3, 6.2.4, 6.10, 6.2.5, 6.12, 6.13, 6.2.6, 6.4.5, 6.25, 6.5.3, 6.6, 6.6.2

Ding, G. (1993), Offset of Yellow River, Shapotou, Zhongwei County, Ningxia, *Quaternary Sciences*, pp. 370–377 (in Chinese). 6.2.5

Ding, K., Z. Li, R. Zou, and Q. Wang (2014), Model analysis of crust motion in the Chinese mainland by CMONOC, *Geodesy and Geodynamics*, *5*(4), 1–8, doi:10.3724/SP.J.1246.2014.04001. 6.4

Ding, M. (1981), Some paleoseismic evidence in the north China region, *Seismology and Geology*, *3*(1), 67–74 (in Chinese). 2.3

Ding, R., J. Ren, and S. Zhang (2009), Late Quaternary activity and paleoearthquakes along the Nanyukou segment of the northern piedmont fault of the Wutai Mountain, *Earthquake Research in China*, *25*(1), 41–53 (in Chinese). 5.2, 5.3, 5.10

Dolan, J. F., D. D. Bowman, and C. G. Sammis (2007), Long-range and long-term fault interactions in Southern California, *Geology*, *35*(9), 855–858, doi:10.1130/G23789A.1. 6.7

Dong, H., W. Wei, G. Ye, S. Jin, A. G. Jones, J. Jing, L. Zhang, C. Xie, F. Zhang, and H. Wang (2014), Three-dimensional electrical structure of the crust and upper mantle in Ordos Block and adjacent area: Evidence of regional lithospheric modification, *Geochemistry, Geophysics, Geosystems*, *15*(6), 2414–2425, doi:10.1002/2014GC005270. 6.1

Doxsey-Whitfield, E., K. Macmanus, S. B. Adamo, L. Pistolesi, J. Squires, O. Borkovska, and S. R. Baptista (2015), Taking Advantage of the Improved Availability of Census Data: A First Look at the Gridded Population of the World, Version 4, *Papers in Applied Geography*, *1*(3), 226–234, doi:10.1080/23754931.2015.1014272. 1.9, 1.10

Ekström, G., and P. England (1989), Seismic strain rates in regions of distributed continental deformation, *Journal of Geophysical Research*, *94*, 10,231–10,257. 5.1, 5.8.3

Ekström, G., M. Nettles, and A. Dziewonski (2012), The global CMT project 2004–2010: Centroid-moment tensors for 13,017 earthquakes, *Physics of the Earth and Planetary Interiors*, *200-201*, 1–9, doi:10.1016/j.pepi.2012.04.002. 1.3, 1.4, 2.1, 3.1, 3.2, 5.1, 5.4.4, 5.4.4, 5.2, 6.5, 6.6, 6.3, 6.3

Elliott, A. J., M. E. Oskin, J. Liu, and Y. Shao (2015), Rupture termination at restraining bends: The last great earthquake on the Altyn Tagh fault, *Geophysical Research Letters*, *42*(7), 2164–2170, doi:10.1002/2015GL063107. 3.3.2

Elliott, J. R. (2009), Strain accumulation & release on the Tibetan Plateau measured using InSAR, D.Phil. thesis, University of Oxford. 1.5

England, P., and R. Bilham (2015), The Shillong Plateau and the great 1897 Assam earthquake, *Tectonics*, *34*(9), 1792–1812, doi:10.1002/2015TC003902. B.3

England, P., and G. Houseman (1985), Role of lithospheric strength heterogeneities in the tectonics of Tibet and neighbouring regions, *Nature*, *315*(May), 297–301. 1.2, 1.2

England, P., and G. Houseman (1986), Finite strain calculations of continental deformation 2. Comparison with the India-Asia collision zone, *Journal of Geophysical Research*, *91*, 3664–3676, doi:10.1029/JB091iB03p03664. 1.2

England, P., and J. Jackson (2011), Uncharted seismic risk, *Nature Geoscience*, *4*(6), 348–349, doi:10.1038/ngeo1168. 1.6, 1.4.1

England, P., and D. McKenzie (1982), A thin viscous sheet model for continental deformation, *Geophysical Journal International*, *70*(2), 295–321, doi:10.1111/j.1365-246X.1982.tb04969.x. 1.1, 1.2, 5.4.5, 6.4.1

England, P., and P. Molnar (1997), The field of crustal velocity in Asia calculated from Quaternary rates of slip on faults, *Geophysical Journal International*, *130*, 551–582. 1.1

England, P., and P. Molnar (2005), Late Quaternary to decadal velocity fields in Asia, *Journal of Geophysical Research*, *110*, 1–27, doi:10.1029/2004JB003541. 1.1

England, P., G. Houseman, and L. Sonder (1985), Length scales for continental deformation in convergent, divergent, and strike-slip environments: analytical and approximate solutions for a Thin Viscous Sheet model, *Journal of Geophysical Research*, *90*(7), 3551–3557. 1.2

Enkin, R. J., Z. Yang, Y. Chen, and V. Courtillot (1992), Paleomagnetic constraints on the geodynamic history of the major blocks of China from the Permian to the present, *Journal of Geophysical Research*, *97*, 13,953–13,989. 6.6.2

Fan, J., and J. Ma (2003), Movement of Ordos block and alternation of activity along its boundaries, *Science in China (Series D)*, *46*(October), 168–180, doi:10.1360/03dz0013. 1.1, 6.5.2, 6.31, 6.4, 6.5.5, 6.6.2

Fang, S., C. Zhao, C. Chai, B. Liu, S. Feng, M. Liu, Q. Lei, and H. Liu (2009), Seismological Evidences of the Crustal Structures and Tectonics in the Yinchuan Downfaulted Basin, *Chinese Journal of Geophysics*, *52*(5), 1101–1110, doi:10.1002/cjg2.1435. 2.1, 2.2, 2.2.1, 2.2.2, 2.5.1, 2.6.1, 2.3, 2.6.2, 4.3, 4.5.1

Farr, T. G., P. A. Rosen, E. Caro, R. Crippen, R. Duren, S. Hensley, M. Kobrick, M. Paller, E. Rodriguez, L. Roth, D. Seal, S. Shaffer, J. Shimada, J. Umland, M. Werner, M. Oskin, D. Burbank, and D. Alsdorf (2007), The Shuttle Radar Topography Mission, *Reviews of Geophysics*, *45*(2), 1–33, doi:10.1029/2005RG000183. 1.3, 1.4, 1.5, 1.7, 1.8, 1.13, 2.1, 3.1, 3.2, 4.7, 4.8, 5.1, 5.2, 5.4.1, 5.6, 5.9, 5.10, 5.12, 5.16, 6.1, 6.3, 6.4, 6.5, 6.6, 6.14, 6.21, 6.22, 6.24, 6.31, 6.32, 6.35, 6.36

Faure Walker, J. P., G. P. Roberts, P. A. Cowie, I. D. Papanikolaou, P. R. Sammonds, A. M. Michetti, and R. J. Phillips (2009), Horizontal strain-rates and throw-rates across breached relay zones, central Italy: Implications for the preservation of throw deficits at points of normal fault linkage, *Journal of Structural Geology*, *31*(10), 1145–1160, doi:10.1016/j.jsg.2009.06.011. 2.6.2, 3.5

Feng, X., J. Ma, Y. Zhou, R. T. Walker, B. Parsons, P. England, and M. A. Rizza (2016), Repeated high stress-drop ruptures on the 1556 Huaxian earthquake normal fault (in prep.), *Earth and Planetary Science Letters*. 1.4.2, 6.2.4, 6.2, 6.9

Flesch, L. M., A. J. Haines, and W. E. Holt (2001), Dynamics of the India-Eurasia collision zone, *Journal of Geophysical Research*, *106*, 16,435–16,460, doi:10.1029/2001JB000208. 1.1

Floyd, M. A., H. Billiris, D. Paradissis, G. Veis, A. Avallone, P. Briole, S. McClusky, J.-M. Nocquet, K. Palamartchouk, B. Parsons, and P. C. England (2010), A new velocity field for Greece: Implications for the kinematics and dynamics of the Aegean, *Journal of Geophysical Research*, *115*(B10), 1–25, doi:10.1029/2009JB007040. 5.4.5, 5.4.5, 6.4.1, 6.4.1, B.2.2

Frankel, K. L., and J. F. Dolan (2007), Characterizing arid region alluvial fan surface roughness with airborne laser swath mapping digital topographic data, *Journal of Geophysical Research: Earth Surface*, *112*(2), 1–14, doi:10.1029/2006JF000644. 3.3.1, 3.4.3, 3.8, 4.3.1, 4.1, 4.4

Friedrich, A. M., B. P. Wernicke, N. A. Niemi, R. A. Bennett, and J. L. Davis (2003), Comparison of geodetic and geologic data from the Wasatch region, Utah, and implications for the spectral character of Earth deformation at periods of 10 to 10 million years, *Journal of Geophysical Research*, *108*, 1–23, doi:10.1029/2001JB000682. 6.7, 6.38

Fu, Z., J. Liu, and G. Liu (2004), On the long-term seismic hazard analysis in the Zhangjiakou-Penglai seismotectonic zone, China, *Tectonophysics*, *390*, 75–83, doi:10.1016/j.tecto.2004.03.021. 6.2.2

Gan, W., P. Zhang, Z.-K. Shen, Z. Niu, M. Wang, Y. Wan, D. Zhou, and J. Cheng (2007), Present-day crustal motion within the Tibetan Plateau inferred from GPS measurements, *Journal of Geophysical Research*, *112*(B8), 1–14, doi:10.1029/2005JB004120. 3.2, 5.2, 6.2.5, 6.4

Ganev, P. N., J. F. Dolan, S. F. McGill, and K. L. Frankel (2012), Constancy of geologic slip rate along the central Garlock fault: implications for strain accumulation and release in southern California, *Geophysical Journal International*, *190*(2), 745–760, doi:10.1111/j.1365-246X.2012.05494.x. 3.5

Gilder, S. A., G. R. Keller, M. Luo, and P. C. Goode (1991), Eastern Asia and the Westem Pacific Timing and spatial distribution of rifting in China, *Tectonophysics*, *197*, 225–243. 1.3.1

Gordon, R. G., and G. A. Houseman (2015), Deformation of Indian Ocean lithosphere: Evidence for a highly nonlinear rheological law, *Journal of Geophysical Research: Solid Earth*, *120*(6), 4434–4449, doi:10.1002/2015JB011993. C.1

Gosse, J. C., and F. M. Phillips (2001), Terrestrial in situ cosmogenic nuclides: theory and application, *Quaternary Science Reviews*, *20*(14), 1475–1560, doi:10.1016/S0277-3791(00)00171-2. 4.3.3

Granger, D. E., and M. Schaller (2014), Cosmogenic Nuclides and Erosion at the Watershed Scale, *Elements*, *10*, 369–374, doi:10.2113/gselements.10.5.369. 4.3.3

Green, O. R., M. P. Searle, R. I. Corfield, and R. M. Corfield (2008), Cretaceous-Tertiary Carbonate Platform Evolution and the Age of the India-Asia Collision along the Ladakh Himalaya (Northwest India), *The Journal of Geology*, *116*(4), 331–353, doi:10.1086/588831. 1.2

Grohmann, C. H., M. J. Smith, and C. Riccomini (2011), Multiscale Analysis of Topographic Surface Roughness in the Midland Valley, Scotland, *IEEE Transactions on Geoscience and Remote Sensing*, *49*(4), 1200–1213. 3.3.1, 4.3.1

Guo, L., W. Bo, X. Hu, and M. Wang (2002), Characteristics of crustal strain associated with M=6.4 Baotou earthquake in 1996, *Acta Seismologica Sinica*, *15*(4), 363–373. 6.2.3

Guo, L., S. Li, Y. Suo, Y. Ji, L. Dai, S. Yu, X. Liu, and I. D. Somerville (2015), Experimental study and active tectonics on the Zhangjiakou-Penglai fault zone across North China, *Journal of Asian Earth Sciences*, *114*, 18–27, doi:10.1016/j.jseaes.2015.03.045. 6.2.2

Hammond, W. C., G. Blewitt, and C. Kreemer (2011), Block modeling of crustal deformation of the northern Walker Lane and Basin and Range from GPS velocities, *Journal of Geophysical Research*, *116*(B15), 1–28, doi:10.1029/2010JB007817. 1.1

Hanks, T. C. T., and H. Kanamori (1979), A moment magnitude scale, *Journal of Geophysical Research*, *84*(B5), 2348–2350, doi:10.1029/JB084iB05p02348. 2.1

Harkins, N., E. Kirby, X. Shi, E. Wang, D. Burbank, and F. Chun (2010), Millennial slip rates along the eastern Kunlun fault: Implications for the dynamics of intracontinental deformation in Asia, *Lithosphere*, *2*(4), 247–266, doi:10.1130/L85.1. 6.2.4, 6.5.3, 6.6.2

He, J., M. Liu, and Y. Li (2003), Is the Shanxi rift of northern China extending?, *Geophysical Research Letters*, *30*(23), 1–4, doi:10.1029/2003GL018764. 5.2, 5.15, 5.7, 5.17, 6.4, 6.5.4

He, J., D. Cai, Y. Li, and Z. Gong (2004), Active extension of the Shanxi rift, north China: does it result from anticlockwise block rotations?, *Terra Nova*, *16*(1), 38–42, doi:10.1046/j.1365-3121.2003.00523.x. 5.2, 5.15, 5.7, 6.5.4

He, J., Y. Li, and C. Teng (2005), Asymmetric flank uplift of the Yinchuan graben, north central China: Implications for lateral variation of crustal rheology from the Alashan to the Ordos, *Geophysical Research Letters*, *32*(23), 1–4, doi:10.1029/2005GL023661. 2.2.2, 2.6.2, 6.5.4

He, J., S. Lu, and W. Wang (2013a), Three-dimensional mechanical modeling of the GPS velocity field around the northeastern Tibetan plateau and surrounding regions, *Tectonophysics*, *584*, 257–266, doi:10.1016/j.tecto.2012.03.025. 1.2

He, J., P. Vernant, J. Chéry, W. Wang, S. Lu, W. Ku, W. Xia, and R. Bilham (2013b), Nailing down the slip rate of the Altyn Tagh fault, *Geophysical Research Letters*, *40*(October), 5382–5386, doi:10.1002/2013GL057497. 5.1

He, Z., and B. Ma (2015), Holocene paleoearthquakes of the Daqingshan fault detected from knickpoint identification and alluvial soil profile, *Journal of Asian Earth Sciences*, *98*, 261–271, doi:10.1016/j.jseaes.2014.11.025. 6.2.3

Hetzel, R. (2013), Active faulting, mountain growth, and erosion at the margins of the Tibetan Plateau constrained by in situ-produced cosmogenic nuclides, *Tectonophysics*, *582*, 1–24, doi:10.1016/j.tecto.2012.10.027. 3.5, 4.3.3

Hijmans, R. (2009), Global Administrative Areas, http://gadm.org/. 1.8

Hong, H., Y. Wang, and J. Shen (1998), Mean velocity field and its dynamic implication of continental crust—block's motion in China, in *Research on Active Fault 6*, Seismological Press, Beijing. 6.31, 6.4, 6.5.5

Hou, J., M. Han, B. Chai, and H. Han (1998), Geomorphological observations of active faults in the epicentral region of the Huaxian large earthquake in 1556 in Shaanxi Province, China, *Journal of Structural Geology*, *20*(5), 549–557, doi:10.1016/S0191-8141(97)00112-0. 1.4.2, 6.1, 6.10, 6.2.4

Houseman, G., and P. England (1986), Finite strain calculations of continental deformation 1. Method and general results for convergent zones, *Journal of Geophysical Research*, *91*(4), 3651–3663. 1.1, C.1

Hu, S., L. He, and J. Wang (2000), Heat flow in the continental area of China: a new data set, *Earth and Planetary Science Letters*, *179*(2), 407–419, doi:10.1016/S0012-821X(00)00126-6. 1.3.1

Huang, W., W. Li, and X. Cao (1994), Research on the completeness of earthquake data in the Chinese mainland (I) - North China, *Acta Seismologica Sinica*, *7*(3), 351–359. 1.4.2, 5.4.4, 6.3

Huntley, D. J., D. I. Godfrey-Smith, and M. L. W. Thewalt (1985), Optical dating of sediments, *Nature*, *313*, 105–107. 3.3.3

Hütt, G., I. Jaek, and J. Tchonka (1988), Optical dating: K-feldspars optical response stimulation spectra, *Quaternary Science Reviews*, *7*, 381–385, doi:10.1016/0277-3791(88)90033-9. 3.3.3

International Seismological Centre (2013), On-Line Bulletin. 1.4, 2.1, 3.1, 5.1, 6.6, 6.18

Jackson, J. (2008), Surviving natural disasters, in *Survival*, chap. 6, pp. 123–145, Cambridge University Press, Cambridge. 1.4.1

Jackson, J., and M. Leeder (1994), Drainage systems and the development of normal faults: an example from Pleasant Valley, Nevada, *Journal of Structural Geology*, *16*(8), 1041–1059. 2.1

Jackson, J., and D. McKenzie (1988), The relationship between plate motions and seismic moment tensors, and the rates of active deformation in the Mediterranean and Middle East, *Geophysical Journal International*, *93*(1), 45–73, doi:10.1111/j.1365-246X.1988.tb01387.x. 1.1, 1.2, 5.1

Jackson, J. A., and N. J. White (1989), Normal faulting in the upper continental crust: observations from regions of active extension, *Journal of Structural Geology*, *11*(1/2), 15–36. 2.1, 2.6.2

Jiang, W., Z. Xiao, and H. Wang (2000), Sinistral strike-slip along western end of the piedmont active fault of Daqingshan mountain, Inner Mongolia, China, *Earthquake Research in China*, *16*(3), 203–212 (in Chinese). 6.2.3

Jiang, W., X. Xie, H. Wang, and X. Feng (2003), Holocene palaeoseismic activities along the northern piedmont fault of Hengshan Mountain, Datong Basin, Shanxi Province, *Earthquake Research in China*, *19*(1), 8–19 (in Chinese). 5.2, 5.3, 5.10

Jiang, W., Q. Deng, X. Xu, and X. Xie (2004), Surface rupture zone of the 1303 Hongtong M=8 earthquake, Shanxi Province, *Acta Seismologica Sinica*, *17*(4), 389–397. 6.2.6

Jolivet, R., C. Lasserre, M.-P. Doin, S. Guillaso, G. Peltzer, R. Dailu, J. Sun, Z.-K. Shen, and X. Xu (2012), Shallow creep on the Haiyuan fault (Gansu, China) revealed by SAR interferometry, *Journal of Geophysical Research: Solid Earth*, *117*(6), 1–18, doi:10.1029/2011JB008732. 5.1

Jordan, T. H., Y. Chen, P. Gasparini, R. Madariaga, I. Main, W. Marzocchi, G. Papadopoulos, G. Sobolev, K. Yamaoka, and J. Zschau (2011), Operational Earthquake Forecasting: State of Knowledge and Guidelines for Utilization, *Annals of Geophysics*, *54*(May), 315–391, doi:10.4401/ag-5350. 1.4.2, 1.4.2

Kanamori, H. (1983), Magnitude scale and quantification of earthquakes, *Tectonophysics*, *93*, 185–199. 5.4.4, 5.2, 6.3, 6.2, 6.2

Kenner, S. J., and P. Segall (2000), A Mechanical Model for Intraplate Earthquakes: Application to the New Madrid Seismic Zone, *Science*, *289*(5488), 2329–2332, doi:10.1126/science.289.5488.2329. 6.7

Kim, Y. S., and D. J. Sanderson (2005), The relationship between displacement and length of faults: A review, *Earth-Science Reviews*, *68*(3-4), 317–334, doi:10.1016/j.earscirev.2004.06.003. 2.6.2, 2.6.2

Kostrov, V. (1974), Seismic moment and energy of earthquakes, and seismic flow of rock, *Izv. Acad. Sci. USSR Phys. Solid Earth*, *1*, 23–40. 5.4.4, B.1, B.3

Kreemer, C., W. Holt, and A. Haines (2003), An integrated global model of present-day plate motions and plate boundary deformation, *Geophysical Journal International*, *154*, 8–34, doi:10.1046/j.1365-246X.2003.01917.x. 1.9, 1.12

Lal, D. (1991), Cosmic ray labeling of erosion surfaces: in situ nuclide production rates and erosion models, *Earth and Planetary Science Letters*, *104*, 424–439. 4.3.3, 4.1, 4.3.3

Lamothe, M., S. Balescu, and M. Auclair (1994), Natural IRSL intensities and apparent luminescence ages of single feldspar grains extracted from partially bleached sediments, *Radiation Measurements*, *23*(2-3), 555–561, doi:10.1016/1350-4487(94)90099-X. 3.3.3

Lasserre, C., P. Morel, Y. Gaudemer, P. Tapponnier, F. J. Ryerson, G. C. P. King, F. Metivier, M. Kasser, M. Kashgarian, B. Liu, T. Lu, and D. Yuan (1999), Postglacial left slip rate and past occurrence of M $>$ 8 earthquakes on the western Haiyuan fault, Gansu, China, *Journal of Geophysical Research*, *104*, 17,633–17,651. 6.2.1

Lasserre, C., Y. Gaudemer, P. Tapponnier, A.-S. Mériaux, J. Van der Woerd, Y. Daoyang, F. Ryerson, R. Finkel, and M. Caffee (2002), Fast late Pleistocene slip rate on the Leng Long Ling segment of the Haiyuan fault, Qinghai, China, *Journal of Geophysical Research*, *107*, doi:10.1029/2000JB000060. 3.2, 6.2.1

Lawson, M. J., B. J. Roder, D. M. Stang, and E. J. Rhodes (2012), OSL and IRSL characteristics of quartz and feldspar from southern California, USA, *Radiation Measurements*, *47*(9), 830–836, doi:10.1016/j.radmeas.2012.03.025. 3.3.3

Lee, W. H. K., F. T. Wu, and C. Jacobsen (1976), A catalog of historical earthquakes in China compiled from recent Chinese publications, *Bulletin of the Seismological Society of America*, *66*(6), 2003–2016. 1.7, 1.4.2, 2.2, 2.2.1, 5.2, 5.4.4, 5.2, 5.12, 6.5, 6.6, 6.3, 6.2, 6.2

Lee, W. H. K., F. T. Wu, and S. C. Wang (1978), A catalog of instrumentally determined earthquakes in China (magnitude greater than 6) compiled from various sources, *Bulletin of the Seismological Society of America*, *68*(2), 383–398. 1.7, 1.4.2, 2.2, 2.2.1, 5.2, 5.4.4, 6.5, 6.6, 6.3, 6.2

Lei, Q., C. Chai, G. Meng, P. Du, Y. Wang, X. Xie, and X. Zhang (2008), Composite drilling section exploration of Yinchuan Buried Fault, *Seismology and Geology*, *30*(1), 250–263 (in Chinese). 2.6.1, 4.2, 4.5.1, 6.1, 6.12

Lei, Q., C. Chai, P. Du, Y. Wang, and G. Meng (2011), Activity characteristics of Luhuatai Buried Fault since Late Quaternary revealed by drilling, *Seismology and Geology*, *33*(3), 602–614 (in Chinese). 4.2, 4.5.1, 6.1, 6.12

Lei, Q., C. Chai, W. Zheng, P. Du, X. Xie, Y. Wang, J. Cui, and G. Meng (2014), Activity and slip rate of the northern section of Yellow River Fault revealed by drilling, *Seismology and Geology*, *36*(2), 464–477 (in Chinese). 2.2, 2.2.2, 2.14, 2.6.1

Lei, Q., C. Chai, P. Du, J. Yu, X. Xie, and Y. Wang (2015), Re-discussion of the seismogenic structure of the M8.0 Pingluo earthquake in 1739, *Seismology and Geology*, *37*(2), (in Chinese). 2.1, 2.2, 2.2.2, 2.3, 2.3, 2.6.1, 2.14, 2.6.1, 4.2, 4.5.1, 6.1, 6.12

Lei, Q., P. Zhang, W. Zheng, C. Chai, W. Wang, P. Du, and J. Yu (2016), Dextral strike-slip of Sanguankou-Niushoushan fault zone and extension of arc tectonic belt in the northeastern margin of the Tibet Plateau, *Science China Earth Sciences*, *59*(5), 1025–1040, doi:10.1007/s11430-016-5272-1. 3.2, 4.5.2, 4.8, 6.1, 6.2.5, 6.12

Li, B., K. Atakan, M. B. Sørensen, and J. Havskov (2015a), Stress pattern of the Shanxi rift system, North China, inferred from the inversion of new focal mechanisms, *Geophysical Journal International*, *201*(2), 505–527, doi:10.1093/gji/ggv025. 5.2, 5.3, 5.4.4, 5.4, 5.12, 5.16, 6.2.2, 6.2.6, 6.2.6, 6.28, 6.5.2

Li, B., J. Havskov, L. Ottemöller, and M. B. Sørensen (2015b), New magnitude scales ML and spectrum-based Mw for the area around Shanxi Rift System, North China, *Journal of Seismology*, *19*(1), 141–158, doi:10.1007/s10950-014-9455-y. 5.6.2, 6.2.6, 6.3

Li, B., Z. Li, M. B. Sørensen, R. Løvlie, L. Liu, and K. Atakan (2015c), Regional stress field around the Taigu fault zone in Shanxi Province, China, *Earthquake Science*, *28*(5-6), 333–345, doi:10.1007/s11589-015-0135-y. 6.2.6

Li, B., M. B. Sørensen, and K. Atakan (2015d), Coulomb stress evolution in the Shanxi rift system, North China, since 1303 associated with coseismic, post-seismic and interseismic deformation, *Geophysical Journal International*, *203*(3), 1642–1664, doi:10.1093/gji/ggv384. 5.2, 5.5.1, 5.5.1, 5.5.2, 5.5.2, 5.5.3, 5.5.4, 5.3, 5.6.2, 5.8.3, 6.1, 6.10, 6.2.4, 6.2.6, 6.3, 6.2, 6.2, 6.7

Li, C., P. Zhang, J. Yin, and W. Min (2009a), Late Quaternary left-lateral slip rate of the Haiyuan fault, northeastern margin of the Tibetan Plateau, *Tectonics*, *28*, 1–26, doi:10.1029/2008TC002302. 3.2, 6.1, 6.2.1, 6.2.5, 6.6.2

Li, D., J. Du, Y. Ma, and A. Xiao (2015e), Active faults and dip slip rates along the northern margins of the Huashan Mountain and Weinan loess tableland in the southeastern Weihe Graben, central China, *Journal of Asian Earth Sciences*, *114*, 266–278, doi:10.1016/j.jseaes.2015.08.013. 6.2.4

Li, K., W. Wu, F. Yang, Z. Nie, W. Guo, and B. Ma (1994), A study on segmentation of Daqingshan piedmont active fault, in *Research on Active Faults in China*, pp. 102–113 (in Chinese), Seismological Press, Beijing. 6.2.3

Li, M., and Z. Wan (1984), Characteristics of the earthquake-generating structures for magnitude 8.0 Pingluo earthquake of 1739 and the process of its preparation, *Seismology and Geology*, *6*(3), 23–28 (in Chinese). 2.3

Li, Q., M. Liu, Q. Zhang, and E. Sandvol (2007), Stress evolution and seismicity in the central-eastern United States: Insights from geodynamic modeling, in *Continental Intraplate Earthquakes: Science, Hazard, and Policy Issues*, vol. 425, pp. 149–166, The Geological Society of America, doi:10.1130/2007.2425(11). 6.1

Li, Q., M. Liu, and S. Stein (2009b), Spatiotemporal Complexity of Continental Intraplate Seismicity: Insights from Geodynamic Modeling and Implications for Seismic Hazard Estimation, *Bulletin of the Seismological Society of America*, *99*(1), 52–60, doi:10.1785/0120080005. 6.7, 6.7, 6.9

Li, Q., X. You, S. Yang, R. Du, X. Qiao, R. Zou, and Q. Wang (2012), A precise velocity field of tectonic deformation in China as inferred from intensive GPS observations, *Science China Earth Sciences*, *55*(5), 695–698, doi:10.1007/s11430-012-4412-5. 5.2, 5.4.5, 6.2.2, 6.4, 6.4.2

Li, W., Y. Lu, and G. Ding (2001), Paleomagnetic evidence from loess for the relative motion between the Ordos and its adjacent blocks, *Quaternary Sciences*, *21*(6), 551–559 (in Chinese). 6.35, 6.6.2

Li, W., Y. Dong, A. Guo, X. Liu, and D. Zhou (2013), Chronology and tectonic significance of Cenozoic faults in the Liupanshan Arcuate Tectonic Belt at the northeastern margin of the Qinghai-Tibet Plateau, *Journal of Asian Earth Sciences*, *73*, 103–113, doi:10.1016/j.jseaes.2013.04.026. 3.2, 6.2.5

Li, Y., J. Yang, Z. Xia, and D. Mo (1998), Tectonic geomorphology in the Shanxi Graben System, northern China, *Geomorphology*, *23*, 77–89. 5.3

Li, Y., G. Yang, Z. Li, L. Guo, C. Huang, W. Zhu, Y. Fu, Q. Wang, Z. Jiang, and M. Wang (2003), Movement and strain conditions of active blocks in the Chinese mainland, *Science in China (Series D)*, *46*(October), 82–117, doi:10.1360/Dz0008. 1.1, 6.1, 6.31, 6.4, 6.5.5

Li, Z., W. Feng, Z. Xu, P. Cross, and J. Zhang (2008), The 1998 Mw 5.7 Zhangbei-Shangyi (China) earthquake revisited: A buried thrust fault revealed with interferometric synthetic aperture radar, *Geochemistry Geophysics Geosystems*, *9*(4), 1–11, doi:10.1029/2007GC001910. 6.6, 6.6.2

Liao, Y., and Z. Pan (1982), Dislocation of the great wall in the Hongguozigou, Ningxia autonomous region, *Seismology and Geology*, *4*(2), 77–80 (in Chinese). 2.3, 2.5.2, 2.6.2, 2.6.2, 4.2

Liao, Y., C. Chai, W. Zhang, and W. Xu (2000), The active features and slip rate of Lingwu faults in late Quaternary, *Earthquake Research in China*, *16*(2), 158–165. 4.2, 4.5.1, 6.1, 6.12

Lin, A., G. Rao, J. Hu, and W. Gong (2013), Reevaluation of the offset of the Great Wall associated with the ca. M 8.0 Pingluo earthquake of 1739, Yinchuan graben, China, *Journal of Seismology*, *17*(4), 1281–1294, doi:10.1007/s10950-013-9391-2. 2.1, 2.3, 2.3, 2.5.2

Lin, A., J. Hu, and W. Gong (2015a), Active normal faulting and the seismogenic fault of the 1739 M 8.0 Pingluo earthquake in the intracontinental Yinchuan Graben, China, *Journal of Asian Earth Sciences*, *114*, 155–173, doi:10.1016/j.jseaes.2015.04.036. 2.1, 2.2.1, 2.3, 2.3, 2.6.1, 2.14, 2.15

Lin, A., G. Rao, and B. Yan (2015b), Flexural fold structures and active faults in the northernwestern Weihe Graben, central China, *Journal of Asian Earth Sciences*, *114*, 226–241, doi:10.1016/j.jseaes.2015.04.012. 6.1, 6.2.4, 6.10

Lin, J., M. Fuller, and W. Zhang (1985), Preliminary Phanerozoic polar wander paths for the North and South China blocks, *Nature*, *313*, 444–449. 6.6.2

Liu, B., C. Chai, S. Feng, C. Zhao, and H. Yuan (2008), Seismic exploration method for buried fault and its up-breakpoint in Quaternary sediment area—An example of Yinchuan buried active fault, *Chinese Journal of Geophysics*, *51*(5), 1039–1047. 2.2, 2.2.1, 2.2.2, 2.6.2

Liu, G. (2000), The Cenozoic rift system of the North China Plain and the deep internal process, *Tectonophysics*, *133*(1987), 277–285. 2.2.2, 6.2.2, 6.6

Liu, J., P. Zhang, D. Zheng, J. Wan, W. Wang, P. Du, and Q. Lei (2010), Pattern and timing of late Cenozoic rapid exhumation and uplift of the Helan Mountain, China, *Science in China (Series D)*, *53*(3), 345–355, doi:10.1007/s11430-010-0016-0. 2.2.2, 3.2

Liu, M., and H. Wang (2012), Roaming earthquakes in China highlight midcontinental hazards, *Eos*, *93*(45), 453–454, doi:10.1029/2012EO450001. 6.7, 6.7, 6.9

Liu, M., Y. Yang, Z. Shen, S. Wang, M. Wang, and Y. Wan (2007), Active tectonics and intracontinental earthquakes in China: The kinematics and geodynamics, in *Continental Intraplate Earthquakes: Science, Hazard, and Policy Issues*, vol. 425, pp. 299–318, Geological Society of America, doi:10.1130/2007.2425(19). 1.3.2, 5.4.4, 5.2, 5.4.5, 6.1, 6.2.2, 6.3, 6.2, 6.2, 6.4.5, 6.7

Liu, M., S. Stein, and H. Wang (2011), 2000 years of migrating earthquakes in North China: How earthquakes in midcontinents differ from those at plate boundaries, *Lithosphere*, *3*(2), 128–132, doi:10.1130/L129.1. 1.7, 1.4.2, 2.2.1, 3.2, 5.1, 5.2, 5.4.4, 5.4.4, 5.2, 5.5.3, 5.12, 5.8.2, 6.5, 6.6, 6.3, 6.2, 6.2, 6.3, 6.4.3, 6.7, 6.7, 6.38, 6.9

Liu, S., and S. Yang (2000), Upper Triassic-Jurassic sequence stratigraphy and its structural controls in the western Ordos Basin, China, *Basin Research*, *12*, 1–18. 1.3.1, 6.1, 6.5.4

Liu-Zeng, J., Y. Klinger, X. Xu, C. Lasserre, G. Chen, W. Chen, P. Tapponnier, and B. Zhang (2007), Millennial recurrence of large earthquakes on the Haiyuan fault near Songshan, Gansu Province, China, *Bulletin of the Seismological Society of America*, *97*(1B), 14–34, doi:10.1785/0120050118. 3.2, 6.2.1, 6.6.2

Liu-Zeng, J., Y. Shao, Y. Klinger, K. Xie, D. Yuan, and Z. Lei (2015), Variability in magnitude of paleoearthquakes revealed by trenching and historical records, along the Haiyuan Fault, China, *Journal of Geophysical Research: Solid Earth*, *120*(12), 8304–8333, doi:10.1002/2015JB012163. 6.2

Lu, Y., and G. Ding (1985), Rotation model and dynamics of blocks in North China and its adjacent areas, *Quaternaria Sinica*, *6*(2), 124–131 (in Chinese). 6.5.2, 6.5.5, 6.31, 6.4

Ma, X., and D. Wu (1987), Cenozoic extensional tectonics in China, *Tectonophysics*, *133*(3-4), 243–255, doi:10.1016/0040-1951(87)90268-X. 1.3.2, 6.1, 6.1

Ma, X., L. Xing, Z. Yang, S. Xu, and J. Zhang (1993), Paleomagnetic study since Late Paleozoic in the Ordos Basin, *Acta Geophysica Sinica*, *36*(1), 68–79 (in Chinese). 6.6.2

Maden, C., P. a. F. Anastasi, a. Dougans, S. P. H. T. Freeman, R. Kitchen, G. Klody, C. Schnabel, M. Sundquist, K. Vanner, and S. Xu (2007), SUERC AMS ion detection, *Nuclear Instruments and Methods in Physics Research, Section B: Beam Interactions with Materials and Atoms*, *259*(1), 131–139, doi:10.1016/j.nimb.2007.01.151. 4.3.3

McDougall, I., and T. M. Harrison (1999), *Geochronology and Thermochronology by the 40Ar/39Ar Method*, 2nd ed., 269 pp., Oxford University Press, New York. 5.4.3, 5.4.3

McKenzie, D., and J. Jackson (1983), The relationship between strain rates, crustal thickening, palaeomagnetism, finite strain and fault movements within a deforming zone, *Earth and Planetary Science Letters*, *65*(1), 182–202, doi:10.1016/0012-821X(83)90198-X. 1.1, 1.2

McKenzie, D., and R. Parker (1967), The North Pacific: an Example of Tectonics on a Sphere, *Nature*, *216*, 1276–1280, doi:10.1038/2161276a0. 1.1

Meade, B., and B. Hager (2005), Block models of crustal motion in southern California constrained by GPS measurements, *Journal of Geophysical Research*, *110*, 1–19, doi:10.1029/2004JB003209. 1.1

Meng, F., G. Liu, and Z. Xiao (1982), The geological and archaeological study of the recent tectonic movement of active faults at Pingyao, Shanxi Province [A], in *The Active Faults in China*, edited by Committee on Seismogeology the Seismological Society of China, pp. 127–132 (in Chinese), Seismological Press, Beijing. 6.2.6

Merrihue, C., and G. Turner (1966), Potassium-argon dating by activation with fast neutrons, *Journal of Geophysical Research*, *71*(11), 2852–2857. 5.4.3

Milliner, C. W. D., J. F. Dolan, J. Hollingsworth, S. Leprince, F. Ayoub, and C. G. Sammis (2015), Quantifying near-field and off-fault deformation patterns of the 1992 Mw 7.3 Landers earthquake, *Geochemistry, Geophysics, Geosystems*, *16*(5), 1577–1598, doi:10.1002/2014GC005693. 5.1

Min, W., Z. Chai, P. Wang, P. Yang, C. Chai, P. Wang, and P. Yang (1992), Preliminary study on the Holocene active fault features at the eastern piedmont of the Luoshan mountain, *Earthquake Research in China*, *8*(4), 49–54 (in Chinese). 3.1, 3.2

Min, W., Z. Chai, P. Wang, and P. Yang (1993), The study on the paleoearthqukes on the eastern piedmont fault of the Luoshan mountains in Holocene, *Earthquake Research in China*, *5*(4), 97–102 (in Chinese). 3.1, 3.2

Min, W., P. Zhang, and Q. Deng (2000), Primary study on regional paleoearthquake recurrence behavior, *Acta Seismologica Sinica*, *13*(2), 180–188, doi:10.1007/s11589-000-0008-9. 6.2.5

Min, W., P. Zhang, and Q. Deng (2001), The study of Holocene paleoearthquakes on Zhongwei-Tongxin fault zone, *Seismology and Geology*, *23*(3), 357–366 (in Chinese). 3.2, 6.1, 6.2.5, 6.12

Min, W., D. Jiao, C. Chai, P. Zhang, and F. Mao (2003), Characteristics of the active Luoshan Fault since Late Pleistocene, North Central China, *Annals of Geophysics*, *46*(5), 997–1013. 3.1, 3.2, 3.1, 3.4, 3.3, 3.3, 3.4.3, 3.4.3, 3.8, 3.4.3, 3.4.4, 3.4.4, 4.8

Molnar, P. (1979), Earthquake recurrence intervals and plate tectonics, *Bulletin of the Seismological Society of America*, *69*(1), 115–133. B.3

Molnar, P., and K. E. Dayem (2010), Major intracontinental strike-slip faults and contrasts in lithospheric strength, *Geosphere*, *6*(4), 444–467, doi:10.1130/GES00519.1. 1.2

Molnar, P., and J. Stock (2009), Slowing of India's convergence with Eurasia since 20 Ma and its implications for Tibetan mantle dynamics, *Tectonics*, *28*, 1–11, doi:10.1029/2008TC002271. 1.2, 3.2

Molnar, P., and P. Tapponnier (1975), Cenozoic Tectonics of Asia: Effects of a Continental Collision, *Science*, *189*(4201), 419–426. 1.1

Molnar, P., D. Qidong, and Q. Deng (1984), Faulting associated with large earthquakes and the average rate of deformation in central and eastern Asia, *Journal of Geophysical Research*, *89*, 6203–6228, doi:10.1029/JB089iB07p06203. 2.1, 2.6.2, 6.3, 6.4.4

Molnar, P., P. England, and J. Martinod (1993), Mantle dynamics, uplift of the Tibetan Plateau, and the Indian monsoon, *Reviews of Geophysics*, *31*, 357–396, doi:10.1029/93RG02030. 1.2

Murray, A. S., and A. G. Wintle (2000), Luminescence dating of quartz using an improved single-aliquot regenerative-dose protocol, *Radiation Measurements*, *32*, 57–73. 3.3.3

Neudorf, C. M., R. G. Roberts, and Z. Jacobs (2012), Sources of overdispersion in a K-rich feldspar sample from north-central India: Insights from De, K content and IRSL age distributions for individual grains, *Radiation Measurements*, *47*(9), 696–702, doi:10.1016/j.radmeas.2012.04.005. 3.3.3

Newman, A., S. Stein, J. Weber, J. Engeln, A. Mao, and T. Dixon (1999), Slow Deformation and Lower Seismic Hazard at the New Madrid Seismic Zone, *Science*, *284*(April), 619–621. 6.7

Nie, Z., and W. Lin (1993), Middle segment of Zhongwei-Tongxin fault zone: seismic deformation band of 1709 earthquake with M 7.5 along Xiangshan-Tianjingshan fault zone, *Earthquake*, *2*(1), 41–44 (in Chinese). 3.2

Nishiizumi, K., M. Imamura, M. W. Caffee, J. R. Southon, R. C. Finkel, and J. McAninch (2007), Absolute calibration of 10Be AMS standards, *Nuclear Instruments and Methods in Physics Research, Section B: Beam Interactions with Materials and Atoms*, *258*(2), 403–413, doi:10.1016/j.nimb.2007.01.297. 4.3.3

Nissen, E., R. T. Walker, A. Bayasgalan, A. Carter, M. Fattahi, E. Molor, C. Schnabel, A. J. West, and S. Xu (2009), The late Quaternary slip-rate of the Har-Us-Nuur fault (Mongolian Altai) from cosmogenic 10Be and luminescence dating, *Earth and Planetary Science Letters*, *286*(3-4), 467–478, doi:10.1016/j.epsl.2009.06.048. 3.5

Nockles, V. A. (2015), Investigating Continental Deformation using PS InSAR, D.Phil. thesis, University of Oxford. 6.2.4, 6.5.3

Northrup, C. J., L. H. Royden, and B. C. Burchfiel (1995), Motion of the Pacific plate relative to Eurasia and its potential relation to Cenozoic extension along the eastern margin of Eurasia, *Geology*, *23*, 719–722, doi:10.1130/0091-7613(1995)023<0719. 1.3.2

Parsons, B., Y. Zhou, J. Elliott, I. Barisin, and R. Walker (2014), Assessing the Ability of Pleiades Stereo Imagery to Determine Height Changes in Earthquakes: A Case Study for the El Mayor-Cucapah Epicentral Area, *AGU Fall Meeting Abstracts*. 2.4.2

Pavlides, S. B., N. C. Zouros, Z. Fang, S. Cheng, M. D. Tranos, and A. A. Chatzipetros (1999), Geometry, kinematics and morphotectonics of the Yanqing-Huailai active faults (northern China), *Tectonophysics*, *308*, 99–118. 5.2, 5.4.4, 5.2, 5.3, 5.5, 6.3, 6.2, 6.2, 6.28, 6.5.2, 6.6

Peacock, D. (2002), Propagation, interaction and linkage in normal fault systems, *Earth-Science Reviews*, *58*(1-2), 121–142, doi:10.1016/S0012-8252(01)00085-X. 2.6.2, 2.6.2

Peltzer, G., and F. Saucier (1996), Present-day kinematics of Asia derived from geologic fault rates, *Journal of Geophysical Research*, *101*, 27,943–27,956, doi:10.1029/96JB02698. 1.1, 3.1, 6.28, 6.5.2, 6.5.5, 6.31, 6.4

Peltzer, G., and P. Tapponnier (1988), Formation and evolution of strike-slip faults, rifts, and basins during the India-Asia collision - An experimental approach, *Journal of Geophysical Research*, *93*(B12), 15,085–15,117, doi:10.1029/JB093iB12p15085. 1.2, 1.2

Peltzer, G., P. Tapponnier, Z. Zhang, and Z. Q. Xu (1985), Neogene and Quaternary faulting in and along the Qinling Shan, *Nature*, *317*, 500–505. 6.5.3, 6.29

Peltzer, G., P. Tapponnier, and R. Armijo (1989), Magnitude of Late Quaternary left-lateral displacements along the north edge of Tibet., *Science*, *246*(4935), 1285–1289, doi:10.1126/science.246.4935.1285. 1.2

Philpotts, A., and J. J. Ague (2009), *Principles of Igneous and Metamorphic Petrology*, 2nd ed., 667 pp., Cambridge University Press, Cambridge. 5.4.3, 5.4.3

Priestley, K., and D. McKenzie (2006), The thermal structure of the lithosphere from shear wave velocities, *Earth and Planetary Science Letters*, *244*, 285–301, doi:10.1016/j.epsl.2006.01.008. 6.2, 6.1

Qin, C., C. Papazachos, and E. Papadimitriou (2002), Velocity field for crustal deformation in China derived from seismic moment tensor summation of earthquakes, *Tectonophysics*, *359*(1-2), 29–46, doi:10.1016/S0040-1951(02)00401-8. 6.3, 6.2

Qu, W., Z. Lu, Q. Zhang, Z. Li, J. Peng, Q. Wang, J. Drummond, and M. Zhang (2014), Kinematic model of crustal deformation of Fenwei basin, China based on GPS observations, *Journal of Geodynamics*, *75*, 1–8, doi:10.1016/j.jog.2014.01.001. 5.2, 5.17

Ran, Y., P. Zhang, B. Hu, and W. Guo (2002), Paleoseismic activity on the Hohhot segment of Daqingshan piedmont fault in the Late Quaternary history, *Earthquake Research in China*, *18*(1), 15–27 (in Chinese). 6.2.3, 6.3

Ran, Y., L. Chen, X. Yang, and Z. Han (2003a), Recurrence characteristics of late-quaternary strong earthquakes on the major active faults along the northern border of Ordos block, *Science in China (Series D)*, *46*(October), 189–200, doi:10.1360/03dz0015. 6.2.3, 6.8, 6.2.3

Ran, Y., P. Zhang, and L. Chen (2003b), Late Quaternary history of paleoseismic activity along the Hohhot Segment of the Daqingshan piedmont fault in Hetao depression zone, North China, *Annals of Geophysics*, *46*(October), 1053–1069. 6.1, 6.8, 6.2.3, 6.3

Ran, Y., P. Zhang, and L. Chen (2003c), Research on the completeness of paleoseismic activity history since Late Quaternary along the Daqingshan piedmont fault in Hetao depression zone, north China, *Earth Science Frontiers*, *10*, 207–216 (in Chinese). 6.3

Rao, G., A. Lin, B. Yan, D. Jia, and X. Wu (2014), Tectonic activity and structural features of active intracontinental normal faults in the Weihe Graben, central China, *Tectonophysics*, *636*, 270–285, doi:10.1016/j.tecto.2014.08.019. 6.2.4

Rao, G., A. Lin, and B. Yan (2015), Paleoseismic study on active normal faults in the southeastern Weihe Graben, central China, *Journal of Asian Earth Sciences*, *114*, 212–225, doi:10.1016/j.jseaes.2015.04.031. 6.2

Reid, H. F. (1911), The California earthquake of April 18, 1906, The mechanics of the earthquake, Report 2, *State Earthquake Invest. Comm., Carnegie Institute, Washington DC*. 6.38

Reimann, T., K. J. Thomsen, M. Jain, A. S. Murray, and M. Frechen (2012), Single-grain dating of young sediments using the pIRIR signal from feldspar, *Quaternary Geochronology*, *11*, 28–41, doi:10.1016/j.quageo.2012.04.016. 3.3.3

Reimer, P. J., E. Bard, A. Bayliss, J. W. Beck, P. G. Blackwell, C. Bronk Ramsey, C. E. Buck, H. Cheng, R. L. Edwards, and M. Friedrich (2013), IntCal13 and Marine13 Radiocarbon Age Calibration Curves 0–50,000 Years cal BP, *Radiocarbon*, *55*(4), 1869–1887, doi:10.2458/azu_js_rc.55.16947. 2.4.1

Ren, J., K. Tamaki, S. Li, and Z. Junxia (2002), Late Mesozoic and Cenozoic rifting and its dynamic setting in Eastern China and adjacent areas, *Tectonophysics*, *344*(3-4), 175–205, doi:10.1016/S0040-1951(01)00271-2. 6.1

Ren, Z., Z. Zhang, T. Chen, S. Yan, J. Yin, P. Zhang, W. Zheng, H. Zhang, and C. Li (2015), Clustering of offsets on the Haiyuan fault and their relationship to paleoearthquakes, *Geological Society of America Bulletin*, *128*(June), 4–18, doi:10.1130/B31155.1. 1.4.2, 3.2

Renne, P. R., C. C. Swisher, A. L. Deino, D. B. Karner, T. L. Owens, and D. J. Depaolo (1998), Intercalibration of standards, absolute ages and uncertainties in 40Ar/39Ar dating, *Chemical Geology*, *145*, 117–152. 5.4.3

Replumaz, A., and P. Tapponnier (2003), Reconstruction of the deformed collision zone Between India and Asia by backward motion of lithospheric blocks, *Journal of Geophysical Research*, *108*, doi:10.1029/2001JB000661. 1.2, 6.4, 6.5.5

Rhodes, E. J. (2011), Optically Stimulated Luminescence Dating of Sediments over the Past 200,000 Years, *Annual Review of Earth and Planetary Sciences*, *39*(1), 461–488, doi:10.1146/annurev-earth-040610-133425. 3.3.3, 3.3.3

Rhodes, E. J. (2015), Dating sediments using potassium feldspar single-grain IRSL: Initial methodological considerations, *Quaternary International*, *362*, 14–22, doi:10.1016/j.quaint.2014.12.012. 3.3.3, 3.3.3

Rodgers, D. A. (1980), Analysis of pull-apart basin development produced by en echelon strike-slip faults, *Sedimentation in Oblique-Slip Mobile Zones*, *4*, 27–41. 4.6

Savage, J. C., and R. O. Burford (1973), Geodetic Determination of Relative Plate Motion in Central California, *Journal of Geophysical Research*, *78*(5), 832–845, doi:10.1029/JB078i005p00832. 4.5.1, 6.4.4

Scharer, K. M., J. B. Salisbury, J. R. Arrowsmith, and T. K. Rockwell (2014), Southern San Andreas Fault Evaluation Field Activity: Approaches to Measuring Small Geomorphic Offsets—Challenges and Recommendations for Active Fault Studies, *Seismological Research Letters*, *85*(1), 68–76, doi:10.1785/0220130108. 3.3.2

Schmidt, S., R. Hetzel, F. Mingorance, and V. A. Ramos (2011), Coseismic displacements and Holocene slip rates for two active thrust faults at the mountain front of the Andean Precordillera (33S), *Tectonics*, *30*, 1–15, doi:10.1029/2011TC002932. 4.3.3

Scholz, C. H. (1982), Scaling laws for large earthquakes: Consequences for physical models, *Bulletin of the Seismological Society of America*, *72*(1), 1–14. 2.1, 2.6.2

Scholz, C. H. (1990), *The Mechanics of Earthquakes and Faulting*, 461 pp., Cambridge University Press, New York. 6.38

Scholz, C. H. (2002), *The Mechanics of Earthquakes and Faulting*, 2nd ed., 504 pp., Cambridge University Press, Cambridge. 2.1, 2.6.2

Searle, M. (1996), Geological evidence against large-scale pre-Holocene offsets along the Karakoram Fault: Implications for the limited extrusion of the Tibetan plateau, *Tectonics*, *15*, 171–186, doi:10.1029/95TC01693. 1.2

Searle, M. P., B. F. Windley, M. P. Coward, D. J. W. Cooper, A. J. Rec, D. Rex, L. I. Tingdong, X. Xuchang, M. Q. Jan, V. C. Thakur, and S. Kumar (1987), The closing of Tethys and the tectonics of the Himalaya, *Geological Society of America Bulletin*, *98*(6), 678–701, doi:10.1130/0016-7606(1987)98<678:TCOTAT>2.0.CO;2. 1.3.2

Searle, M. P., J. R. Elliott, R. J. Phillips, and S.-L. Chung (2011), Crustal-lithospheric structure and continental extrusion of Tibet, *Journal of the Geological Society, London*, *168*, 633–672, doi:10.1144/0016-76492010-139. 5.1

Shen, Z., C. Zhao, A. Yin, Y. Li, D. D. Jackson, P. Fang, and D. Dong (2000), Contemporary crustal deformation in east Asia constrained by Global Positioning System measurements, *Journal of Geophysical Research*, *105*, 5721–5734. 5.2, 5.3, 5.17, 6.2.2, 6.4, 6.4.2, 6.6.2

Shen, Z.-K., D. D. Jackson, and B. X. Ge (1996), Crustal deformation across and beyond the Los Angeles basin from geodetic measurements, *Journal of Geophysical Research*, *101*(B12), 27,927–27,957, doi:10.1029/96JB02544. 5.4.5, 6.4.1, B.2.2, B.2.2

Shen, Z.-K., M. Wang, Y. Li, D. D. Jackson, A. Yin, D. Dong, and P. Fang (2001), Crustal deformation along the Altyn Tagh fault system, western China, from GPS, *Journal of Geophysical Research*, *106*(12), 30,607–30,621, doi:10.1029/2001JB000349. 1.2

Shi, W., M. Cen, L. Chen, Y. Wang, X. Chen, J. Li, and P. Chen (2015), Evolution of the late Cenozoic tectonic stress regime in the Shanxi Rift, central North China Plate inferred from new fault kinematic analysis, *Journal of Asian Earth Sciences*, *114*, 54–72, doi:10.1016/j.jseaes.2015.04.044. 6.2.6

Smedley, R. K., G. A. T. Duller, N. J. G. Pearce, and H. M. Roberts (2012), Determining the K-content of single-grains of feldspar for luminescence dating, *Radiation Measurements*, *47*(9), 790–796, doi:10.1016/j.radmeas.2012.01.014. 3.3.3

Smedley, R. K., G. A. T. Duller, and H. M. Roberts (2015), Bleaching of the post-IR IRSL signal from individual grains of K-feldspar: Implications for single-grain dating, *Radiation Measurements*, *79*, 33–42, doi:10.1016/j.radmeas.2015.06.003. 3.3.3

Smith, W. H. F., and P. Wessel (1990), Gridding with continuous curvature splines in tension, *Geophysics*, *55*(3), 293–305, doi:10.1190/1.1442837. 2.4.2, 5.4.1

State Seismological Bureau, Institute of Geophysics, and Institute of Chinese Historical Geography Fudan University (1990), *Atlas of the historical earthquakes in China (the Qing Dynasty period)*, 244 pp., China Cartographic Publishing House (in Chinese), Beijing. 2.1, 2.1, 2.2, 2.3, 2.6.2

Stein, R. (1999), The role of stress transfer in earthquake occurrence, *Nature*, *402*, 605–609, doi:10.1038/45144. 6.7

Stein, S., and A. M. Friedrich (2014), How much can we clear the crystal ball?, *Astronomy & Geophysics*, *55*(2), 11–17, doi:10.1093/astrogeo/atu076. 1.4.2

Stein, S., M. Liu, E. Calais, and Q. Li (2009), Mid-continent earthquakes as a complex system, *Seismological Research Letters*, *80*(4), 551–553, doi:10.1785/gssrl.80.4.551. 5.1, 5.8.2, 6.4.1, 6.7, 6.9

Stein, S., R. J. Geller, and M. Liu (2012), Why earthquake hazard maps often fail and what to do about it, *Tectonophysics*, *562-563*, 1–25, doi:10.1016/j.tecto.2012.06.047. 1.4.2

Stone, J. O. (2000), Air pressure and cosmogenic isotope production, *Journal of Geophysical Research*, *105*(B10), 23,753–23,759. 4.1, 4.3.3, 4.3.3

Tadono, T., H. Ishida, F. Oda, S. Naito, K. Minakawa, and H. Iwamoto (2014), Precise Global DEM Generation by ALOS PRISM, *ISPRS Annals of Photogrammetry, Remote Sensing and Spatial Information Sciences*, *II-4*(May), 71–76, doi:10.5194/isprsannals-II-4-71-2014. 5.4.1, 5.7

Takaku, J., T. Tadono, and K. Tsutsui (2014), Generation of high resolution global DSM from ALOS PRISM, *International Archives of the Photogrammetry, Remote Sensing and Spatial Information Sciences - ISPRS Archives*, *40*(4), 243–248, doi:10.5194/isprsarchives-XL-4-243-2014. 5.4.1, 5.7

Tapponnier, P., and P. Molnar (1976), Slip-line field theory and large-scale continental tectonics, *Nature*, *264*(November), 319–324. 1.2

Tapponnier, P., and P. Molnar (1977), Active faulting and tectonics in China, *Journal of Geophysical Research*, *82*(20), 2905–2930, doi:10.1029/JB082i020p02905. 1.2, 1.3.1, 2.2, 3.2, 4.8, 5.3, 5.2, 5.16, 6.4, 6.6, 6.8, 6.2.4, 6.10, 6.12, 6.2.6, 6.13, 6.5.3

Tapponnier, P., G. Peltzer, A. Y. Le Dain, R. Armijo, and P. Cobbold (1982), Propagating extrusion tectonics in Asia: New insights from simple experiments with plasticine, *Geology*, *10*, 611–616, doi:10.1130/0091-7613(1982)10<611. 1.2

Tapponnier, P., Z. Xu, F. Roger, B. Meyer, N. Arnaud, G. Wittlinger, and J. Yang (2001), Oblique stepwise rise and growth of the Tibet plateau., *Science*, *294*(5547), 1671–1677, doi:10.1126/science.105978. 1.1

Taylor, M., and A. Yin (2009), Active structures of the Himalayan-Tibetan orogen and their relationships to earthquake distribution, contemporary strain field, and Cenozoic volcanism, *Geosphere*, *5*(3), 199–214, doi:10.1130/GES00217.1. 6.1, 6.2, 6.3, 6.5

Thatcher, W. (2009), How the Continents Deform: The Evidence From Tectonic Geodesy, *Annual Review of Earth and Planetary Sciences*, *37*, 237–262, doi:10.1146/annurev.earth.031208.100035. 1.1, 1.1, 5.1

The Research Group on Active Fault System around Ordos Massif (1988), *Active Fault System around Ordos Massif*, 335 (in Chinese) pp., State Seismological Bureau, Seismological Press, Beijing. 3.2, 6.4

Toda, S., J. Lin, M. Meghraoui, and R. S. Stein (2008), 12 May 2008 M=7.9 Wenchuan, China, earthquake calculated to increase failure stress and seismicity rate on three major fault systems, *Geophysical Research Letters*, *35*(May), 1–6, doi:10.1029/2008GL034903. 1.4.2

Tong, X., B. Smith-Konter, and D. T. Sandwell (2014), Is there a discrepancy between geological and geodetic slip rates along the San Andreas Fault System?, *Journal of Geophysical Research: Solid Earth*, *119*(3), 2518–2538, doi:10.1002/2013JB010765. 5.1

Trauerstein, M., S. Lowick, F. Preusser, D. Rufer, and F. Schlunegger (2012), Exploring fading in single grain feldspar IRSL measurements, *Quaternary Geochronology*, *10*, 327–333, doi:10.1016/j.quageo.2012.02.004. 3.3.3

Trauerstein, M., S. E. Lowick, F. Preusser, and F. Schlunegger (2014), Small aliquot and single grain IRSL and post-IR IRSL dating of fluvial and alluvial sediments from the Pativilca valley, Peru, *Quaternary Geochronology*, *22*, 163–174, doi:10.1016/j.quageo.2013.12.004. 3.3.3

Tucker, B. E. (2004), Trends in Global Urban Earthquake Risk: A Call to the International Earth Science and Earthquake Engineering Communities, *Seismological Research Letters*, *75*(6), 695–700. 1.4.1

Tucker, B. E. (2013), Reducing earthquake risk, *Science*, *341*(6150), 1070–1072, doi:10.1126/science.1239236. 1.4.1

USGS (2016), Earthquakes with 1,000 or More Deaths 1900-2014, http://earthquake.usgs.gov/earthquakes/world/world_deaths.php. 1.4.1, 1.5, 1.1, 1.4.2

Wallace, R. E. (1987), Grouping and migration of surface faulting and variations in slip rates on faults in the Great Basin province, *Bulletin of the Seismological Society of America*, *77*(June), 868–876. 6.38

Wang, C.-Y., E. Sandvol, L. Zhu, H. Lou, Z. Yao, and X. Luo (2014), Lateral variation of crustal structure in the Ordos block and surrounding regions, North China, and its tectonic implications, *Earth and Planetary Science Letters*, *387*, 198–211, doi:10.1016/j.epsl.2013.11.033. 6.1

Wang, H., C. Deng, R. Zhu, Q. Wei, Y. Hou, and E. Boëda (2005), Magnetostratigraphic dating of the Donggutuo and Maliang Paleolithic sites in the Nihewan Basin, North China, *Quaternary Research*, *64*(1), 1–11, doi:10.1016/j.yqres.2005.04.001. 1.2

Wang, H., M. Liu, X. Shen, and J. Liu (2010), Balance of seismic moment in the Songpan-Ganze region, eastern Tibet: Implications for the 2008 Great Wenchuan earthquake, *Tectonophysics*, *491*(1), 154–164. 1.4.2

Wang, J. (1987), The Fenwei rift and its recent periodic activity, *Tectonophysics*, *133*, 257–275, doi:10.1016/0040-1951(87)90269-1. 6.2.4, 6.2.4

Wang, J. (2004), Historical earthquake investigation and research in China, *Annals of Geophysics*, *47*(June), 831–838. 1.4.2

Wang, K. (2006), Predicting the 1975 Haicheng Earthquake, *Bulletin of the Seismological Society of America*, *96*(3), 757–795, doi:10.1785/0120050191. 1.4.2

Wang, K., J. Ma, and G. Diao (2012a), Present day stress state of the Shanxi tectonic belt, *Geodynamics and Tectonophysics*, *3*(3), 195–202, doi:10.5800/GT. 5.2, 6.2.6

Wang, L. (2012), Research of basin marginal active normal faults through multi-scale tectonic geomorphology - a case study on the Yuguang Basin south margin fault, PhD thesis, China Earthquake Administration, Beijing (in Chinese). 5.2, 5.5.1, 5.5.1, 5.4, 5.6, 5.3, 5.10

Wang, L., Q. Tian, D. Li, and X. Zhang (2011), The growth of the south margin fault of the Yuxian-Guangling basin in northwest Beijing area, *Seismology and Geology*, *33*(4), 828–838 (in Chinese). 5.1, 5.2, 6.2.2, 6.4.2, 6.31, 6.4, 6.5.5, 1

Wang, M. (2009), Analysis of GPS data with high precision and study on present-day crustal deformation in China, PhD thesis, China Earthquake Administration, Beijing (in Chinese). 5.2

Wang, M., Z. Shen, Z. Niu, Z. Zhang, H. Sun, W. Gan, Q. Wang, and Q. Ren (2003), Contemporary crustal deformation of the Chinese continent and tectonic block model, *Science in China (Series D)*, *46*(October), 25–40, doi:10.1360/03dz0003. 6.2.2

Wang, Q., P. Zhang, J. T. Freymueller, R. Bilham, K. M. Larson, X. Lai, X. You, Z. Niu, J. Wu, Y. Li, J. Liu, Z. Yang, and Q. Chen (2001), Present-day crustal deformation in China constrained by global positioning system measurements, *Science*, *294*, 574–7, doi:10.1126/science.1063647. 1.1, 5.2, 6.4, 6.4, 6.5.5

Wang, T., J. Zhuang, T. Kato, and M. Bebbington (2013), Assessing the potential improvement in short-term earthquake forecasts from incorporation of GPS data, *Geophysical Research Letters*, *40*(February), 2631–2635, doi:10.1002/grl.50554. 3.2, 6.2.5

Wang, X., C. Chai, P. Du, Q. Lei, G. Yin, and Y. Lu (2012b), Luminescence age constraints on palaeo-earthquake events along the Lingwu fault in the Yinchuan Basin, China, *Geochronometria*, *39*(1), 57–61, doi:10.2478/s13386-011-0051-4. 2.14, 2.6.1

Wang, Y., P. Du, and Q. Lei (2007), Summary on Recent Progress of Active Fault exploration project in Yinchuan City, *Technology for Earthquake Disaster Prevention*, *2*(2), 166–175 (in Chinese). 2.6.1, 2.14

Wells, D. L., and K. J. Coppersmith (1994), New empirical relationships among magnitude, rupture length, rupture width, rupture area, and surface displacement, *Bulletin of the Seismological Society of America*, *84*(4), 974–1002. 2.6.1, 2.3, 2.6.2

Wesnousky, S. G., L. M. Jones, C. H. Scholz, and Q. Deng (1984), Historical seismicity and rates of crustal deformation along the margins of the Ordos block, North China, *Bulletin of the Seismological Society of America*, *74*(5), 1767–1783. 2.6.2, 4.5.2, 5.2, 5.4.4, 5.4.4, 5.2, 5.4, 5.6.2, 5.12, 5.17, 6.3, 6.3, 6.2, 6.2, 6.3, 6.14, 6.3, 6.4.1, 6.5.1, 6.27

Wesnousky, S. G., J. M. Bormann, C. Kreemer, W. C. Hammond, and J. N. Brune (2012), Neotectonics, geodesy, and seismic hazard in the Northern Walker Lane of Western North America: Thirty kilometers of crustal shear and no strike-slip?, *Earth and Planetary Science Letters*, *329-330*, 133–140, doi:10.1016/j.epsl.2012.02.018. 3.1

Whittaker, A. C., and S. J. Boulton (2012), Tectonic and climatic controls on knickpoint retreat rates and landscape response times, *Journal of Geophysical Research*, *117*, 1–19, doi:10.1029/2011JF002157. 2.5.2

Wright, T. J., J. R. Elliott, H. Wang, and I. Ryder (2013), Earthquake cycle deformation and the Moho: Implications for the rheology of continental lithosphere, *Tectonophysics*, *609*, 504–523, doi:10.1016/j.tecto.2013.07.029. 4.5.1, 6.4.4

Xie, X., W. Jiang, H. Wang, and X. Feng (2004), Holocene activities of the Taigu fault zone, Shanxi province, in relation to the 1303 Hongdong M=8 earthquake, *Acta Seismologica Sinica*, *26*(3), 281–293 (in Chinese). 6.2.6

Xie, X., W. Jiang, C. Sun, C. Yan, and X. Feng (2008), Comparison study on Holocene paleoseismic activities among multi-trenches along the Jiaocheng fault zone, Shanxi, *Seismology and Geology*, *30*(2), 412–430 (in Chinese). 6.2.6

Xu, S., A. B. Dougans, S. P. Freeman, C. Schnabel, and K. M. Wilcken (2010), Improved 10Be and 26Al-AMS with a 5MV spectrometer, *Nuclear Instruments and Methods in Physics Research Section B: Beam Interactions with Materials and Atoms*, *268*(7-8), 736–738, doi:10.1016/j.nimb.2009.10.018. 4.3.3

Xu, X., and Q. Deng (1990), The features of late Quaternary activity of the piedmont fault of Mt. Huoshan, Shanxi province and 1303 Hongdong earthquake (Ms=8), *Seismology and Geology*, *12*(1), 21–32 (in Chinese). 3.1, 6.1, 6.13, 6.2.6, 6.23

Xu, X., and Q. Deng (1996), Nonlinear characteristics of paleoseismicity in China, *Journal of Geophysical Research*, *101*(B3), 6209–6231. 5.2, 5.3, 6.7

Xu, X., and X. Ma (1992), Geodynamics of the Shanxi Rift system, China, *Tectonophysics*, *208*(1-3), 325–340, doi:10.1016/0040-1951(92)90353-8. 1.3.2, 3.1, 5.3, 5.3, 5.2, 5.7, 5.16, 6.4, 6.2.2, 6.2.6, 6.2.6, 6.13, 6.5.2, 6.28, 6.6, 6.32

Xu, X., Q. Deng, and H. You (1986), Evidence on dextral dislocation of fault at the western foothills of Mt. Xizhoushan, Shanxi province and its slip rate during the Holocene, *Seismology and Geology*, *8*(3), 44–46 (in Chinese). 3.1, 6.1, 6.13, 6.2.6

Xu, X., X. Ma, and Q. Deng (1993), Neotectonic activity along the Shanxi rift system, China, *Tectonophysics*, *219*(4), 305–325, doi:10.1016/0040-1951(93)90180-R. 1.3.2, 3.1, 3.1, 5.3, 5.3, 5.5.2, 6.1, 6.2.2, 6.2.6, 6.2.6, 6.13, 6.23, 6.5.2, 6.28, 6.6, 6.32, 6.6.2

Xu, X., G. Cheng, X. Ma, Y. Sun, and Z. Han (1994), Rotation model and dynamics of blocks in north China and its adjacent areas, *Earth Science - Journal of China University of Geosciences*, *19*(2), 129–138 (in Chinese). 3.1, 5.7, 6.28, 6.5.2, 6.6, 6.32, 6.6.2, 6.35

Xu, X., Q. Deng, Y. Wang, Y. Nobuyuki, and Y. Suzuki (1997), Geomorphic evidence for irregular faulting along the north piedmont of Liulengshan range, Shanxi rift system, China, in *Proceedings of the 30th International Geological Congress Volume 5 - Contemporary Lithospheric Motion Seismic Geology*, edited by H. Ye, pp. 87–99, VSP BV, The Netherlands. 5.2, 5.5.2, 5.5.2, 5.3, 5.10

Xu, X., W. Wu, and X. Zhang (2002), Latest crust movement and earthquakes in and around capital region, pp. 43–104 (in Chinese), Science Press, Beijing. 5.2, 5.3

Xu, Z., S. Wang, and A. Gao (2000), Present-day tectonic movement in the northeastern margin of the Qinghai-Xizang (Tibetan) plateau as revealed by earthquake activity, *Acta Seismologica Sinica*, *13*(5), 507–515, doi:10.1007/s11589-000-0050-7. 6.3, 6.2, 6.26, 6.5.1, 6.5.2

Xue, H., and J. Yan (1984), The contemporary crustal stress field around the Ordos block, *Acta Geophysica Sinica*, *27*(2), 144–152 (in Chinese). 5.2

Yang, M., L. Li, J. Zhou, X. Qu, and D. Zhou (2013), Segmentation and inversion of the Hangjinqi fault zone, the northern Ordos basin (North China), *Journal of Asian Earth Sciences*, *70-71*, 64–78, doi:10.1016/j.jseaes.2013.03.004. 6.2

Yang, X., Y. Ran, B. Hu, and W. Guo (2003), Paleoseismic activity on Wujiahe segment of Serteng piedmont fault, Inner Mongolia, *Acta Seismologica Sinica*, *16*(1), 67–78. 6.1, 6.8, 6.2.3

Yang, Y., Z. Gao, and W. Xu (2012), Geomorphic expression and response of the activity along the middle section of Huashan front fault in the Late Quaternary period, *Technol. Earthq. Disater Prevent.*, *7*(4), 335–347 (in Chinese). 6.2.4

Ye, H., B. Zhang, and F. Mao (1987), The Cenozoic tectonic evolution of the Great North China: two types of rifting and crustal necking in the Great North China and their tectonic implications, *Tectonophysics*, *133*(3-4), 217–227, doi:10.1016/0040-1951(87)90265-4. 1.3.1, 1.3.2, 5.3, 6.1, 6.26, 6.5.1

Yu, S. (2004), A study on characteristics of tectonic block motion and tectonic setting of strong earthquakes in northern part of the Shanxi fault depression zone, *Acta Seismologica Sinica*, *17*(4), 417–425, doi:10.1007/s11589-004-0021-5. 5.2, 5.2, 5.5.3, 5.5.4, 5.3, 5.10, 5.16, 6.4, 6.2.2

Yuan, D., B. Liu, T. Lu, W. He, and X. Liu (1997), Slip rates of the Maomaoshan Fault zone in Gansu province obtained by using ages of loess-palaeosoil sequence, *Seismology and Geology*, *19*(1), 1–8 (in Chinese). 6.2.1, 6.6.2

Yuan, D., Z. Lei, W. Ge, X. Liu, B. Liu, and J. Zhang (2007), A new opinion about the west of Gangu M 7.0 earthquake in 143 AD in Gansu Province, *Northwestern Seismological Journal*, *29*(1), 58–63 (in Chinese). 6.1, 6.2.4, 6.5.3

Yuan, D., W. Ge, Z. Chen, C. Li, Z. Wang, H. Zhang, P. Zhang, D. Zheng, W. Zheng, W. H. Craddock, K. E. Dayem, A. R. Duvall, B. G. Hough, R. O. Lease, J.-D. Champagnac, D. W. Burbank, M. K. Clark, K. A. Farley, C. N. Garzione, E. Kirby, P. Molnar, and G. H. Roe (2013), The growth of northeastern Tibet and its relevance to large-scale continental geodynamics: A review of recent studies, *Tectonics*, *32*(5), 1358–1370, doi:10.1002/tect.20081. 3.2

Yuan, T., and X. Feng (2010), *The great 1556 Huaxian earthquake*, Seismological Press, Beijing (in Chinese). 1.4.2, 6.10, 6.11, 6.2.4, 6.9

Zhang, B., S. Jia, T. Wang, and B. Zheng (1985), Intraplate seismotectonic features of North China, *Tectonophysics*, *117*, 177–191. 1.3.2, 6.2.2, 6.2.3, 6.4.5, 6.26, 6.5.1

Zhang, B., Y. Liao, S. Guo, R. E. Wallace, R. C. Bucknam, and T. C. Hanks (1986), Fault scarps related to the 1739 earthquake and seismicity of the Yinchuan Graben, Ningxia Huizu Zizhiqu, China, *Bulletin of the Seismological Society of America*, *76*(5), 1253–1287. 2.1, 2.2, 2.2.1, 2.2.2, 2.3, 2.3, 2.4.4, 2.5.2, 2.5.2, 2.6.2, 2.6.2, 2.6.2, 6.4

Zhang, P. (2013), A review on active tectonics and deep crustal processes of the Western Sichuan region, eastern margin of the Tibetan Plateau, *Tectonophysics*, *584*, 7–22, doi:10.1016/j.tecto.2012.02.021. 1.2, 1.4.1

Zhang, P., and W. Gan (2008), Combined model of rigid-block motion with continuous deformation: Patterns of present-day deformation in continental China, in *Investigations into the Tectonics of the Tibetan Plateau: Geological Society of America Special Paper 444*, edited by B. Burchfiel and E. Wang, pp. 59–71, doi:10.1130/2008.2444(04). 1.1, 1.2, 1.3.1, 5.2, 6.1, 6.1, 6.31, 6.4, 6.5.5, 1

Zhang, P., P. Molnar, B. C. Burchfiel, and L. Royden (1988), Bounds on the Holocene slip rate of the Haiyuan Fault, north-central China, *Quaternary Research*, *30*, 151–164. 3.2, 6.2.1

Zhang, P., B. C. Burchfiel, P. Molnar, W. Zhang, D. Jiao, Q. Deng, Y. Wang, L. Royden, and F. Song (1990), Late Cenozoic tectonic evolution of the Ningxia-Hui Autonomous Region, China, *Geological Society of America Bulletin*, *102*(11), 1484–1498,

doi:10.1130/0016-7606(1990)102<1484. 2.2.1, 2.2.2, 2.3, 2.6.1, 3.2, 4.1, 4.2, 4.5.1, 4.8, 6.4, 6.2.5, 6.12

Zhang, P., D. B. Slemmons, and F. Mao (1991), Geometric pattern, rupture termination and fault segmentation of the Dixie Valley-Pleasant Valley active normal fault system, Nevada, U.S.A., *Journal of Structural Geology*, *13*(2), 165–176. 6.2.5

Zhang, P., Z. Yang, H. K. Gupta, S. C. Bhatia, and K. M. Shedlock (1999a), Global Seismic Hazard Assessment Program (GSHAP) in continental Asia, *Annali di Geophysica*, *42*(December), 1167–1190. 1.4.2, 1.9, 1.11

Zhang, P., Q. Deng, G. Zhang, J. Ma, W. Gan, W. Min, F. Mao, and Q. Wang (2003a), Active tectonic blocks and strong earthquakes in the continent of China, *Science in China (Series D)*, *46*(October), 13–24, doi:10.1360/03dz0002. 1.1, 1.3.1, 1.4.2, 1.4.2, 6.1, 6.2.2

Zhang, P., Z. Shen, M. Wang, W. Gan, R. Bürgmann, P. Molnar, Q. Wang, Z. Niu, J. Sun, J. Wu, S. Hanrong, and Y. Xinzhao (2004), Continuous deformation of the Tibetan Plateau from global positioning system data, *Geology*, *32*(9), 809–812, doi:10.1130/G20554.1. 6.2.1, 6.4

Zhang, S., J. Ren, and G. Nie (2007), Paragenesia of Quaternary pediments and river terraces on the north piedmont of Wutai Mountains, *Chinese Science Bulletin*, *52*(4), 521–530, doi:10.1007/s11434-007-0081-8. 5.3

Zhang, W., Y. Liao, and Z. Pan (1982), On the piedmont scarp in diluvial fan of Mt. Helanshan, *Seismology and Geology*, *4*(2), 32–34 (in Chinese). 2.3, 2.4.4

Zhang, W., D. Jiao, P. Zhang, P. Molnar, B. C. Burchfiel, Q. Deng, Y. Wang, and F. Song (1987), Displacement along the Haiyuan Fault associated with the great 1920 Haiyuan, China, earthquake, *Bulletin of the Seismological Society of America*, *77*(1), 117–131. 1.4.2, 3.2, 6.2.5

Zhang, Y. (1994), Tectonique cenozoïque en Chine du nord: extension autour de l'ordos et décrochements sur le système de failles des Qinling et de Tanlu, PhD thesis, Université de Paris (in French). 6.31, 6.5.5, 6.4

Zhang, Y., P. Vergèly, and J. Mercier (1995), Active faulting in and along the Qinling Range (China) inferred from SPOT imagery analysis and extrusion tectonics of south China, *Tectonophysics*, *243*, 69–95. 1.2, 3.1, 6.1, 6.2.4, 6.10, 6.4.4, 6.28, 6.5.2, 6.6.2

Zhang, Y., J. L. Mercier, and P. Vergèly (1998), Extension in the graben systems around the Ordos (China), and its contribution to the extrusion tectonics of south China with respect to Gobi-Mongolia, *Tectonophysics*, *285*, 41–75. 1.3.1, 1.3.2, 2.2.1, 3.1, 3.1, 4.2, 5.2, 5.3, 5.17, 6.1, 6.2.3, 6.2.3, 6.10, 6.2.4, 6.2.6, 6.2.6, 6.5.2, 6.5.3, 6.29, 6.30, 6.31, 6.5.5, 6.4

Zhang, Y., P. Vergèly, J.-L. Mercier, Y. Wang, Y. Zhang, and D. Huang (1999b), Kinematic history and changes in the tectonic stress regime during the Cenozoic along the Qinling and southern Tanlu fault zones, *Acta Geologica Sinica (English Edition)*, *73*(3), 264–274. 6.4.5

Zhang, Y., Y. Ma, N. Yang, W. Shi, and S. Dong (2003b), Cenozoic extensional stress evolution in North China, *Journal of Geodynamics*, *36*(5), 591–613, doi:10.1016/j.jog.2003.08.001. 1.3.2, 5.2, 5.3, 5.3, 5.5, 6.4.5, 6.5.3, 6.29, 6.30

Zhao, B., X. Xie, C. Chai, H. Ma, X. Xu, D. Peng, W. Yin, and J. Tao (2007a), Imaging the graben structure in the deep basin with a microtremor profile crossing the Yinchuan City, *Journal of Geophysics and Engineering*, *4*(3), 293–300, doi:10.1088/1742-2132/4/3/S08. 2.2.2

Zhao, B., Y. Huang, C. Zhang, W. Wang, K. Tan, and R. Du (2015), Crustal deformation on the Chinese mainland during 1998-2014 based on GPS data, *Geodesy and Geodynamics*, *6*(1), 7–15, doi:10.1016/j.geog.2014.12.006. 3.1, 4.7, 4.5.1, 5.2, 5.4.5, 5.7, 5.13, 5.14, 5.15, 5.16, 6.4, 6.4.1, 6.15, 6.21, 6.4.2, 6.4.3, 6.22, 6.24, 6.4.4, 6.4.5, 6.25, 6.4, 6.6.2, 6.36, 6.37, B.3

Zhao, H., C. Liu, F. Wang, J. Wang, Q. Li, and Y. Yao (2007b), Uplift and evolution of Helan Mountain, *Science in China (Series D)*, *50*(S2), 217–226, doi:10.1007/s11430-007-6010-5. 2.2.1

Zhao, J., S. Gao, J. Bo, and D. Zhang (2005), A seismic fault which could cause earthquake larger than M 7.0 is found at an exploratory channel in Xizhang of Taiyuan, Shanxi, *Earthquake Research In Shanxi*, *3*, 1–3 (in Chinese). 6.2.6

Zhao, X., and R. S. Coe (1987), Palaeomagnetic constraints on the collision and rotation of North and South China, *Nature*, *327*, 141–144. 6.6.2

Zheng, B., S. Guo, and H. Xu (1981), Preliminary study of principal features of the NW and NWW trending fault structures in the Yanshan region, *Seismology and Geology*, *3*(2), 31–40 (in Chinese). 6.2.2, 6.6.2

Zheng, D., P. Zhang, J. Wan, D. Yuan, C. Li, G. Yin, G. Zhang, Z. Wang, W. Min, and J. Chen (2006), Rapid exhumation at $\sim$ 8 Ma on the Liupan Shan thrust fault from apatite fission-track thermochronology: Implications for growth of the northeastern Tibetan Plateau margin, *Earth and Planetary Science Letters*, *248*(1-2), 183–193, doi:10.1016/j.epsl.2006.05.023. 3.2

Zheng, W., Z. Lei, D. Yuan, W. He, W. Ge, and X. Liu (2007), Textual reasearch on the historical data of the 1573 AD Minxian earthquake in Gansu Province and disscussion on its seismogenic structure, *Earthquake Research in China*, *23*(1), 75–83 (in Chinese). 6.2

Zhou, M., T. Lü, Y. Zhang, and A. Ruan (2000), The geological structure background and the crustal structure in the northeastern margin of the Qinghai-Tibetan plateau, *Acta Seismologica Sinica*, *13*(6), 687–697, doi:10.1007/s11589-000-0071-2. 3.2

Zhou, Y. (2016), Investigating past and present continental earthquakes with high-resolution optical imagery, D.Phil. thesis, University of Oxford. 1.4.2, 5.4.4, 5.8.2, 6.2.4, 6.3, 6.9

Zhou, Y., B. Parsons, J. R. Elliott, I. Barisin, and R. T. Walker (2015), Assessing the ability of Pleiades stereo imagery to determine height changes in earthquakes: A case study for the El Mayor-Cucapah epicentral area, *Journal of Geophysical Research: Solid Earth*, *120*(12), 8793–8808, doi:10.1002/2015JB012358. 2.4.2

Zhu, R., K. Hoffman, R. Potts, C. Deng, Y. Pan, B. Guo, C. Shi, Z. Guo, B. Yuan, Y. Hou, and W. Huang (2001), Earliest presence of humans in northeast Asia., *Nature*, *413*(6854), 413–7, doi:10.1038/35096551. 5.5.2

Zhu, X., and X. Zou (2006), Idea of New Silk Road Economy Development Zone between China and Central-Asia, in *Northeast Asia Forum*, vol. 5 (in Chinese). 1.4.2

Appendix A

Walker steelyard beam balance

A.1 Density determinations for ^{10}Be samples

The densities of ^{10}Be samples were determined using a Walker steelyard beam balance (see Figure A.1). A sample is balanced against a counterweight such that the lever arm points at a given index mark on the right-hand pillar. The distance (a) from the pivot at the top of the left-hand pillar to the position of the load is recorded. The experiment is then repeated with the sample immersed in water, making sure that the lever arm points to the same index mark. The new distance (b) from the pivot at the top of the left-hand pillar to the position of the load is recorded.

According to the law of levers:

$$Mgd = \rho_r V g a = (\rho_r - \rho_w) V g b \tag{A.1}$$

where ρ_r is the density of the rock sample, ρ_w is the density of water, V is the volume of the rock sample, and g is the acceleration due to gravity. $\rho_w = 1$ g/cm^3 and therefore:

$$\rho_r a = (\rho_r - 1) b = \rho_r b - b \tag{A.2}$$

$$\therefore \rho_r = \frac{b}{b - a} \tag{A.3}$$

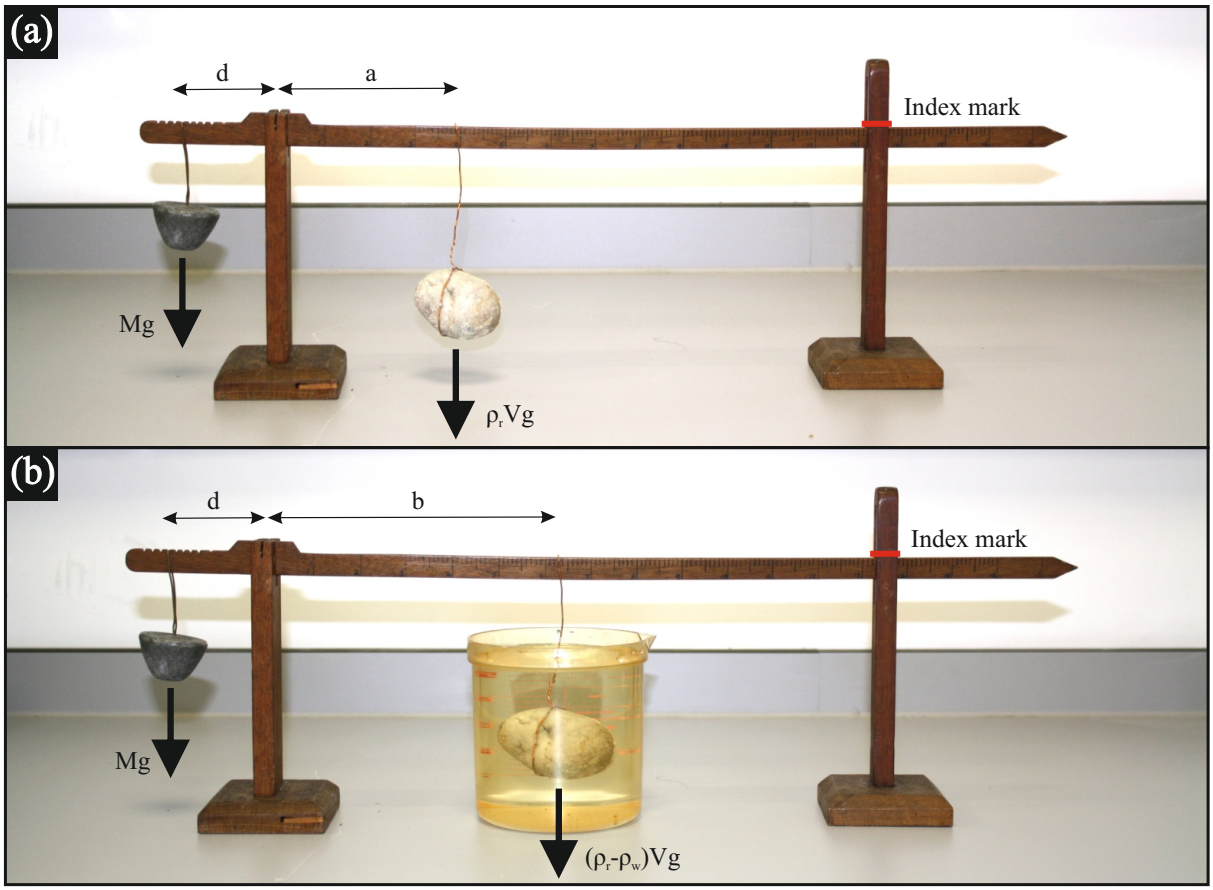


Figure A.1: (a) Photograph of the Walker steelyard beam balance apparatus. Sample (in air) balancing a counterweight. (b) Photograph showing the sample (in water) balancing the same counterweight.

If the typical measurement error on each of a and b was ± 0.2 mm, then the error on the estimates of ρ_r are expected to be around ± 0.03 g/cm^3.

Appendix B

Mathematical details

B.1 Kostrov summations and principal strain rates

The seismic moment tensor encapsulates information about the orientation and magnitude of the faulting in an earthquake. It is given by:

$$M_{ij} = M_0 \left(u_i n_j + u_j n_i \right) \tag{B.1}$$

where $\mathrm{M}_0 = \mu A \bar{u}$ is the scalar seismic moment (equal to the rigidity modulus times the fault plane area times the average slip) and $\hat{\mathbf{u}}$ and $\hat{\mathbf{n}}$ are unit vectors in the direction of slip and the direction of the normal to the fault plane respectively. Kostrov's relation allows the strain rate tensor to be calculated from a series of seismic moment tensors for N earthquakes that have occurred in a volume V (*Kostrov*, 1974):

$$\dot{\epsilon}_{ij} = \frac{1}{2\mu\tau V} \sum_{n=1}^{N} M_{ij}^{n} \tag{B.2}$$

where $\dot{\epsilon}_{ij}$ is the ijth component of the strain rate tensor, μ is the rigidity modulus, and τ is the time period of observation. The antisymmetric part of the velocity gradient tensor, the vorticity tensor, is seismically unobservable and hence seismic moment tensors provide

no information about rotations. Having obtained the strain rate tensor, we calculate the principal strain rates by solving the following eigenvalue equation:

$$\dot{\epsilon}\mathbf{v} = \lambda\mathbf{v} \tag{B.3}$$

Considering the two-dimensional case, we solved this as follows (n.b. $\dot{\epsilon}_{21} = \dot{\epsilon}_{12}$ due to the symmetry of the strain rate tensor):

$$\begin{vmatrix} \dot{\epsilon}_{11} - \lambda & \dot{\epsilon}_{12} \\ \dot{\epsilon}_{12} & \dot{\epsilon}_{22} - \lambda \end{vmatrix} = 0 \tag{B.4}$$

$$\left(\dot{\epsilon}_{11} - \lambda\right)\left(\dot{\epsilon}_{22} - \lambda\right) - \dot{\epsilon}_{12}^2 = 0 \tag{B.5}$$

$$\lambda^2 - \left(\dot{\epsilon}_{11} + \dot{\epsilon}_{22}\right)\lambda + \dot{\epsilon}_{11}\dot{\epsilon}_{22} - \dot{\epsilon}_{12}^2 = 0 \tag{B.6}$$

$$\lambda = \frac{\left(\dot{\epsilon}_{11} + \dot{\epsilon}_{22}\right) \pm \sqrt{\left(\dot{\epsilon}_{11} + \dot{\epsilon}_{22}\right)^2 - 4\left(\dot{\epsilon}_{11}\dot{\epsilon}_{22} - \dot{\epsilon}_{12}^2\right)}}{2} \tag{B.7}$$

$$\lambda = \frac{\left(\dot{\epsilon}_{11} + \dot{\epsilon}_{22}\right) \pm \sqrt{\left(\dot{\epsilon}_{11} - \dot{\epsilon}_{22}\right)^2 + 4\dot{\epsilon}_{12}^2}}{2} \tag{B.8}$$

The (anticlockwise) angle (θ_1) between the principal strain rate axis $\dot{\epsilon}_1$ and the 1-axis is found from the corresponding eigenvector (v_1, v_2). When $\lambda = \dot{\epsilon}_1$:

$$\begin{pmatrix} \dot{\epsilon}_{11} - \dot{\epsilon}_1 & \dot{\epsilon}_{12} \\ \dot{\epsilon}_{12} & \dot{\epsilon}_{22} - \dot{\epsilon}_1 \end{pmatrix} \begin{pmatrix} v_1 \\ v_2 \end{pmatrix} = 0 \tag{B.9}$$

$$\dot{\epsilon}_{11}v_1 - \dot{\epsilon}_1 v_1 + \dot{\epsilon}_{12}v_2 = 0 \tag{B.10}$$

$$v_2 = \frac{\dot{\epsilon}_1 - \dot{\epsilon}_{11}}{\dot{\epsilon}_{12}} v_1 \tag{B.11}$$

$$\tan\theta_1 = \frac{v_2}{v_1} = \frac{\dot{\epsilon}_1 - \dot{\epsilon}_{11}}{\dot{\epsilon}_{12}} \tag{B.12}$$

The azimuth of the principal strain rate axis $\dot{\epsilon}_1$ is $90\,^\circ - \theta_1$.

B.2 Strain rate field from GPS

B.2.1 Solving for the best-fitting rigid body rotation

We used the following method to solve for the best fitting rigid body rotation.

For any given point on the Earth's surface, the radial ($\hat{\mathbf{r}}$), northerly ($\hat{\mathbf{n}}$) and easterly ($\hat{\mathbf{e}}$) unit vectors are as follows:

$$\hat{\mathbf{r}} = \begin{pmatrix} r_x \\ r_y \\ r_z \end{pmatrix} = \begin{pmatrix} \sin\theta\cos\phi \\ \sin\theta\sin\phi \\ \cos\theta \end{pmatrix} \tag{B.13}$$

$$\hat{\mathbf{n}} = \begin{pmatrix} n_x \\ n_y \\ n_z \end{pmatrix} = \begin{pmatrix} -\cos\theta\cos\phi \\ -\cos\theta\sin\phi \\ \sin\theta \end{pmatrix} \tag{B.14}$$

$$\hat{\mathbf{e}} = \begin{pmatrix} e_x \\ e_y \\ e_z \end{pmatrix} = \begin{pmatrix} -\sin\phi \\ \cos\phi \\ 0 \end{pmatrix} \tag{B.15}$$

where θ is the inclination (or colatitude) and ϕ is the azimuth at each point on the Earth's surface. For every point (k) within the rigid body, the following equation describes the relationship between the velocity ($\mathbf{v}$) at that point, the rate of angular rotation (ω) of the rigid body, and the radial vector ($\mathbf{r}$) at that point (see Figure B.1):

$$\mathbf{v^k} = \omega \times \mathbf{r^k} \tag{B.16}$$

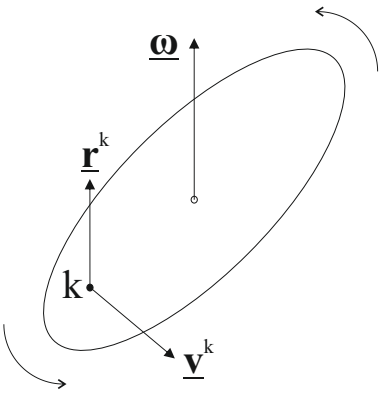


Figure B.1: Diagram illustrating the velocity vector at each point, k, the angular velocity vector for the rigid body, and the radial vector at each point.

$\mathbf{v_n^k}$ and $\mathbf{v_e^k}$ (the northerly and easterly components of $\mathbf{v^k}$) are found by taking the dot product of $\mathbf{v^k}$ with the unit vectors in the northerly and easterly directions respectively:

$$\mathbf{v_n^k} = \mathbf{v^k} \cdot \hat{\mathbf{n}} = \left(\omega \times \mathbf{r^k}\right) \cdot \hat{\mathbf{n}} \tag{B.17}$$

$$\therefore \mathbf{v_n^k} = \left(r_y n_z - r_z n_y\right) \omega_x + \left(-r_z n_x - r_x n_z\right) \omega_y + \left(r_y n_x + r_x n_y\right) \omega_z \tag{B.18}$$

$$\mathbf{v_e^k} = \mathbf{v^k} \cdot \hat{\mathbf{e}} = \left(\omega \times \mathbf{r^k}\right) \cdot \hat{\mathbf{e}} \tag{B.19}$$

$$\therefore \mathbf{v_e^k} = \left(-r_z e_y\right) \omega_x + \left(-r_z e_x\right) \omega_y + \left(r_y e_x + r_x e_y\right) \omega_z \tag{B.20}$$

which can be written in matrix form as:

$$\begin{pmatrix} \left(r_y n_z - r_z n_y\right) & \left(-r_z n_x - r_x n_z\right) & \left(r_y n_x + r_x n_y\right) \\ \left(-r_z e_y\right) & \left(-r_z e_x\right) & \left(r_y e_x + r_x e_y\right) \end{pmatrix} \begin{pmatrix} \omega_x \\ \omega_y \\ \omega_z \end{pmatrix} = \begin{pmatrix} \mathbf{v_n^k} \\ \mathbf{v_e^k} \end{pmatrix} \tag{B.21}$$

If there are a total of K nodes within the rigid body, then we have a set of $2K$ simultaneous equations and three unknowns, corresponding to a matrix of the form $\mathbf{A}\omega =$

$\mathbf{v}$. We used the Moore-Penrose inverse to find the best least squares solution to this problem:

$$\omega^{\mathbf{est}} = \left[\mathbf{A^T A}\right]^{-1} \mathbf{A^T v} \tag{B.22}$$

B.2.2 Calculating the strain rate field from GPS

We calculated a smoothly varying strain rate field from GPS data according to the method of *Shen et al.* (1996) and *Floyd et al.* (2010). We assumed uniform gradients in the components of horizontal velocity. The method below describes how to calculate the strain rate tensor at an individual point within the region of interest. The same method can be applied whether the calculation points used are the GPS sites themselves or the nodes of a regular grid.

Considering each calculation point in turn, the velocity at a given GPS measurement site is equal to the velocity at the calculation point (which has components U_x and U_y) plus the change in velocity on moving from the calculation point to the GPS site (see Figure B.2).

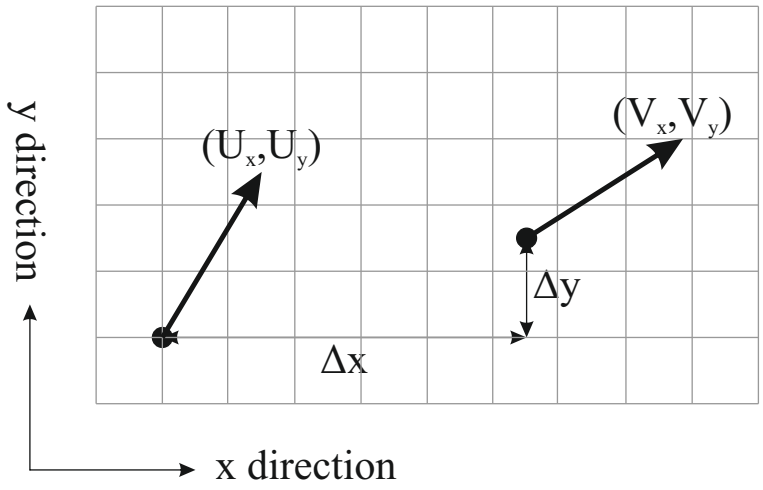


Figure B.2: U_x and U_y are the x (easterly) and y (northerly) components of velocity at the calculation point under consideration. V_x and V_y are the x and y components of velocity at the GPS measurement site. Δx and Δy are the x and y distances from the calculation point to the GPS measurement site, assuming a spherical Earth.

This can be written as:

$$V_x = U_x + \frac{\partial V_x}{\partial x}\Delta x + \frac{\partial V_x}{\partial y}\Delta y \tag{B.23}$$

$$V_y = U_y + \frac{\partial V_y}{\partial x}\Delta x + \frac{\partial V_y}{\partial y}\Delta y \tag{B.24}$$

We also know that:

$$\dot{\epsilon}_{xx} = \frac{1}{2}\left(\frac{\partial V_x}{\partial x} + \frac{\partial V_x}{\partial x}\right) = \frac{\partial V_x}{\partial x} \tag{B.25}$$

$$\dot{\epsilon}_{yy} = \frac{1}{2}\left(\frac{\partial V_y}{\partial y} + \frac{\partial V_y}{\partial y}\right) = \frac{\partial V_y}{\partial y} \tag{B.26}$$

$$\dot{\epsilon}_{xy} = \dot{\epsilon}_{yx} = \frac{1}{2}\left(\frac{\partial V_x}{\partial y} + \frac{\partial V_y}{\partial x}\right) \tag{B.27}$$

$$\dot{\omega}_{xy} = \frac{1}{2}\left(\frac{\partial V_x}{\partial y} - \frac{\partial V_y}{\partial x}\right) \tag{B.28}$$

where $\dot{\omega}_{xy}$ is the rate of rotation about a vertical axis and $\dot{\epsilon}_{xx}$, $\dot{\epsilon}_{xy}$ and $\dot{\epsilon}_{yy}$ are the horizontal components of the strain rate tensor:

$$\dot{\epsilon} = \begin{pmatrix} \dot{\epsilon}_{xx} & \dot{\epsilon}_{xy} \\ \dot{\epsilon}_{yx} & \dot{\epsilon}_{yy} \end{pmatrix} \tag{B.29}$$

And therefore:

$$\frac{\partial V_x}{\partial y} = \dot{\epsilon}_{xy} + \dot{\omega}_{xy} \tag{B.30}$$

$$\frac{\partial V_y}{\partial x} = \dot{\epsilon}_{xy} - \dot{\omega}_{xy} \tag{B.31}$$

Substituting Equations B.25, B.26, B.30 and B.31 into Equations B.23 and B.24 we obtain:

$$V_x = U_x + \dot{\epsilon}_{xx}\Delta x + \dot{\epsilon}_{xy}\Delta y + \dot{\omega}_{xy}\Delta y \tag{B.32}$$

$$V_y = U_y + \dot{\epsilon}_{xy}\Delta x + \dot{\epsilon}_{yy}\Delta y - \dot{\omega}_{xy}\Delta x \tag{B.33}$$

Which can be re-written in matrix form as:

$$\begin{pmatrix} V_x \\ V_y \end{pmatrix} = \begin{pmatrix} 1 & 0 & \Delta x & \Delta y & 0 & \Delta y \\ 0 & 1 & 0 & \Delta x & \Delta y & -\Delta x \end{pmatrix} \begin{pmatrix} U_x \\ U_y \\ \dot{\epsilon}_{xx} \\ \dot{\epsilon}_{xy} \\ \dot{\epsilon}_{yy} \\ \dot{\omega}_{xy} \end{pmatrix} \tag{B.34}$$

This is the same as that obtained by *Shen et al.* (1996). A similar equation can be written for each GPS site, and so the overall equation is given by:

$$\mathbf{v} = \mathbf{X}\mathbf{s} \tag{B.35}$$

where $\mathbf{v}$ is a column vector with $2N$ elements containing the x and y components of velocity at each of the N GPS measurement sites (from 1 to N):

$$\mathbf{v} = \begin{pmatrix} V_x^1 \\ V_y^1 \\ \vdots \\ V_x^N \\ V_y^N \end{pmatrix} \tag{B.36}$$

$\mathbf{X}$ is a $2N\times6$ matrix and Δx_N and Δy_N are the x and y distances to the Nth GPS measurement site from this calculation point:

$$\mathbf{X} = \begin{pmatrix} 1 & 0 & \Delta x_1 & \Delta y_1 & 0 & \Delta y_1 \\ 0 & 1 & 0 & \Delta x_1 & \Delta y_1 & -\Delta x_1 \\ \vdots & \vdots & \vdots & \vdots & \vdots & \vdots \\ 1 & 0 & \Delta x_N & \Delta y_N & 0 & \Delta y_N \\ 0 & 1 & 0 & \Delta x_N & \Delta y_N & -\Delta x_N \end{pmatrix} \tag{B.37}$$

and $\mathbf{s}$ is a column vector containing the various parameters listed for the calculation point being considered:

$$\mathbf{s} = \begin{pmatrix} U_x \\ U_y \\ \dot{\epsilon}_{xx} \\ \dot{\epsilon}_{xy} \\ \dot{\epsilon}_{yy} \\ \dot{\omega}_{xy} \end{pmatrix} \tag{B.38}$$

We solve Equation B.35 by a weighted least squares inversion at each calculation point:

$$\mathbf{s} = \left(\mathbf{X}^T\mathbf{W}\mathbf{X}\right)^{-1}\mathbf{X}^T\mathbf{W}\mathbf{v} \tag{B.39}$$

where $\mathbf{W}$ is a Gaussian weighting matrix which ensures that GPS sites closer to the calculation point are given greater weighting. The weighting varies with the square of the distance between the calculation point and the GPS site, r, and depends on a scale length α:

$$W_1 = e^{\frac{-r_1^2}{\alpha^2}} \tag{B.40}$$

Higher values of α lead to an increasingly smooth strain rate field, whilst lower values are more sensitive to regional variations. The full weighting matrix consists of only diagonal terms:

$$\mathbf{W} = \begin{pmatrix} W_1 & & & & \\ & W_1 & & & \\ & & \ddots & & \\ & & & W_N & \\ & & & & W_N \end{pmatrix} \tag{B.41}$$

B.2.3 The effect of selecting different α values

Figure B.3 shows histograms of the maximum principal strain rate azimuths, for different values of the Gaussian smoothing parameter α, for the strain rate calculations in the northern Shanxi Grabens (see Chapter 5). The larger the value of α, the smaller the spread of maximum principal strain rate azimuths.

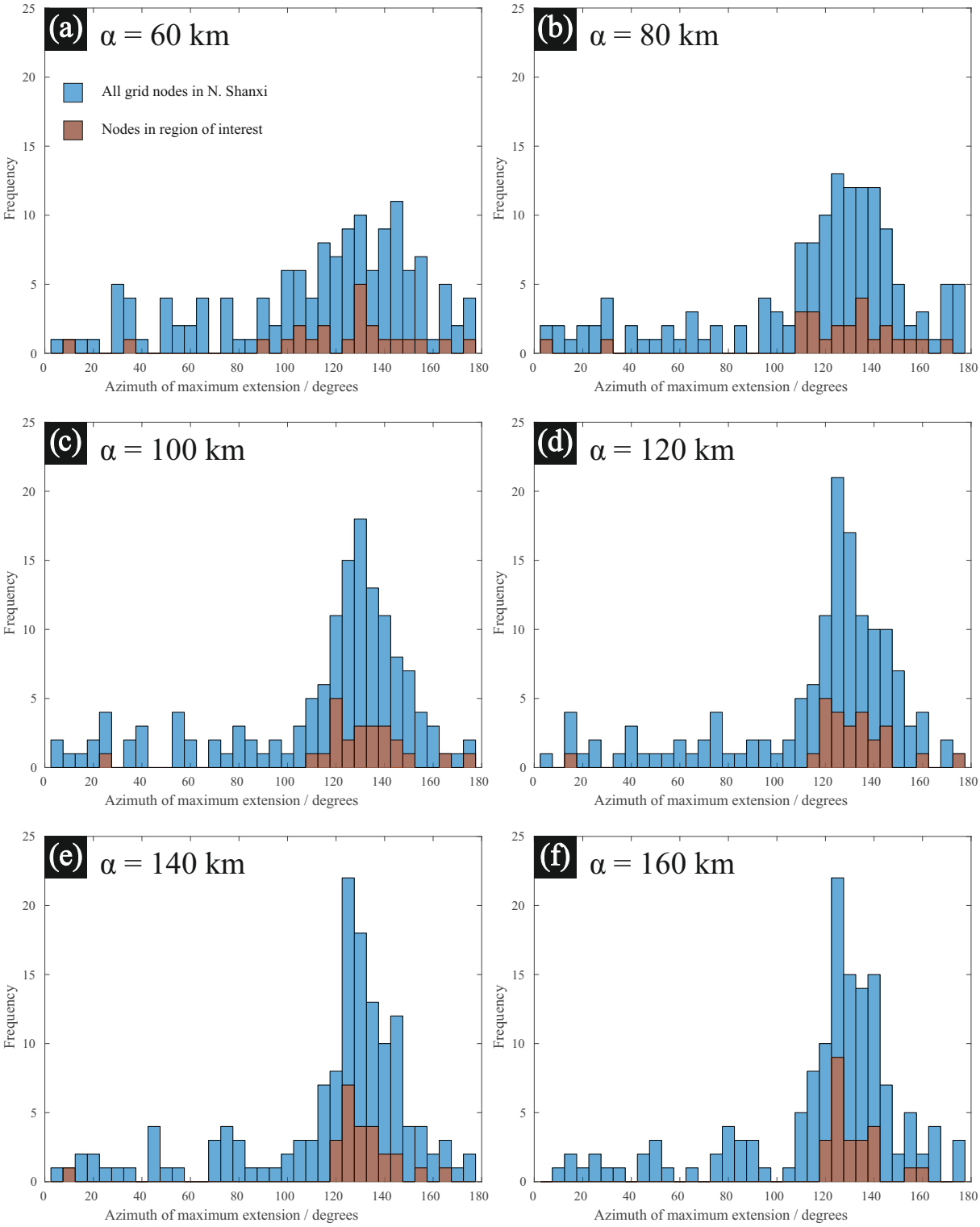


Figure B.3: Histogram of maximum principal (extensional) strain rate azimuths determined from GPS data of *Zhao et al.* (2015) for (a) $\alpha = 60$ km, (b) $\alpha = 80$ km, (c) $\alpha = 100$ km, (d) $\alpha = 120$ km, (e) $\alpha = 140$ km and (f) $\alpha = 160$ km ($r_{max} = 200$ km for all calculations). Blue bars show all grid nodes in the region 38.5 to 41.0 °N, 112.5 to 116.2 °E; brown bars show grid nodes within the Kostrov volume.

B.3 Calculating earthquake recurrence times

This derivation follows the work of *Molnar* (1979) including the correction suggested by *England and Bilham* (2015). Re-arranging Kostrov's relation (*Kostrov*, 1974), we can write:

$$\sum_{n=1}^{N} M_{ij}^{n} = M_{tot} = 2\mu\tau V\dot{\epsilon}_{ij} \tag{B.42}$$

Hence the moment rate ($\dot{M}_0$) is given by:

$$\dot{M}_0 = \frac{M_{tot}}{\tau} = 2\mu V|\dot{\epsilon}_{ij}| \tag{B.43}$$

The Gutenberg-Richter relationship between frequency and magnitude suggests that the number of earthquakes (N) that we expect to have a scalar seismic moment $\geq M$ is given by:

$$N(M) = \alpha M^{-\beta} \tag{B.44}$$

The moment density (n, the number of events per unit moment) is therefore given by:

$$n(M) = -\frac{dN(M)}{dM} = \beta\alpha M^{-\beta-1} \tag{B.45}$$

The total moment release (M_{tot}) is found by integrating the moment density times the value of the moment at each increment between the maximum scalar seismic moment (M_{max}) and zero:

$$M_{tot} = \int_0^{M_{max}} Mn(M)dM = \int_0^{M_{max}} \beta\alpha M^{-\beta}dM = \left[\frac{\beta\alpha M^{1-\beta}}{1-\beta}\right]_0^{M_{max}} = \frac{\beta\alpha M_{max}^{1-\beta}}{1-\beta} \tag{B.46}$$

Re-arranging, we find:

$$\alpha = \frac{M_{tot}\,(1-\beta)}{\beta M_{max}^{1-\beta}} \tag{B.47}$$

Substituting back into Equation B.44:

$$N(M) = \frac{M_{tot}\,(1-\beta)}{\beta M_{max}^{1-\beta}} M^{-\beta} \tag{B.48}$$

To convert from the number of events (N) to the rate of events ($\frac{N}{\tau}$) we switch M_{tot} for $\dot{M}_0$ and hence the recurrence interval (T, which is equal to the reciprocal of the rate of events) for earthquakes of scalar seismic moment $\geq M$ is given by:

$$T(M) = \frac{\beta M_{max}^{1-\beta} M^{\beta}}{\dot{M}_0\,(1-\beta)} \tag{B.49}$$

Appendix C

Interpreting strain rates

C.1 Expected pattern of faulting from strain rates

In Chapters 5 and 6 we derive strain rates around the Ordos Plateau from Kostrov summations and campaign GPS measurements. Figure C.1 illustrates qualitatively how to interpret our strain rate fields.

For a more quantitative analysis we follow a similar approach to *Houseman and England* (1986) and *Gordon and Houseman* (2015). Considering the horizontal components of the diagonalised strain rate tensor ($\dot{\epsilon}_1$ and $\dot{\epsilon}_2$), we assume that $\dot{\epsilon}_1$ is the greater (more positive) principal strain rate. We then define the angle ϕ according to:

$$tan\,(\phi) = \frac{\dot{\epsilon}_2}{\dot{\epsilon}_1} \tag{C.1}$$

We consider ϕ in the range $\frac{\pi}{4}$ to $\frac{5\pi}{4}$ (see Figures C.2 and C.3). If $\dot{\epsilon}_1$ and $\dot{\epsilon}_2$ are of the same sign, then the strain is taken up on two sets of dip-slip faults. When $\frac{\pi}{4} < \phi < \frac{\pi}{2}$ we know that $\frac{\dot{\epsilon}_2}{\dot{\epsilon}_1} > 1$, which can only be true if both $\dot{\epsilon}_1$ and $\dot{\epsilon}_2$ are negative. We therefore have contraction occurring in two orthogonal horizontal directions and we expect reverse faults in two orientations. When $\pi < \phi < \frac{5\pi}{4}$ we know that $0 < \frac{\dot{\epsilon}_2}{\dot{\epsilon}_1} < 1$, which can only be true if both $\dot{\epsilon}_1$ and $\dot{\epsilon}_2$ are positive. We therefore have extension occurring in two orthogonal horizontal directions and we expect normal faults in two orientations.

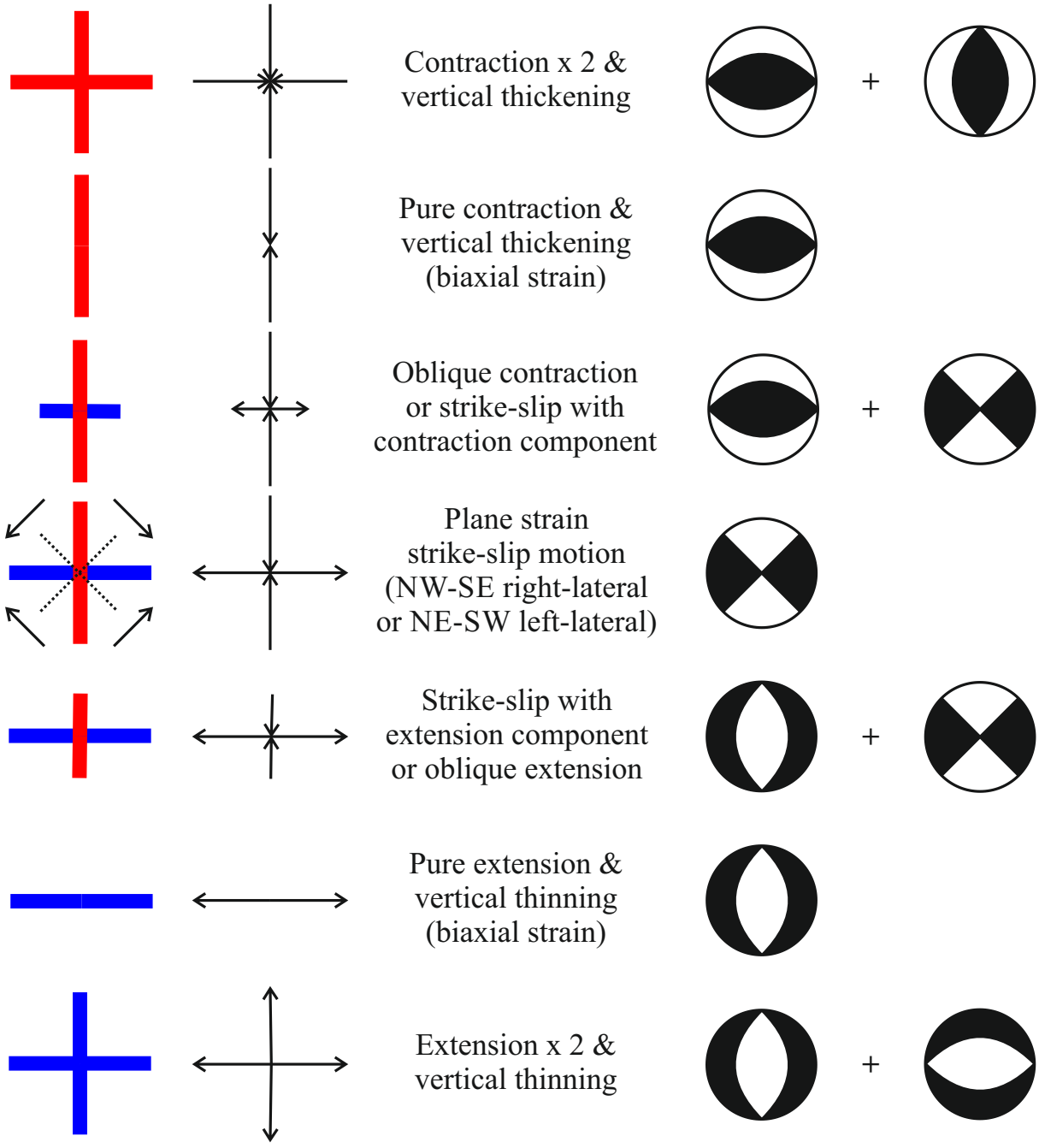


Figure C.1: Examples of strain rate crosses to show how they illustrate different patterns of strain. Red bars indicate contractional principal strain rates; blue bars indicate extensional principal strain rates (only horizontal components are shown). Focal mechanisms indicate patterns of faulting that could accommodate the given strain rates. Note that for the strike-slip mechanisms there is an ambiguity between right-lateral motion on northwest-southeast fault planes and left-lateral motion on northeast-southwest fault planes; for the dip-slip mechanisms either nodal plane could be the fault plane.

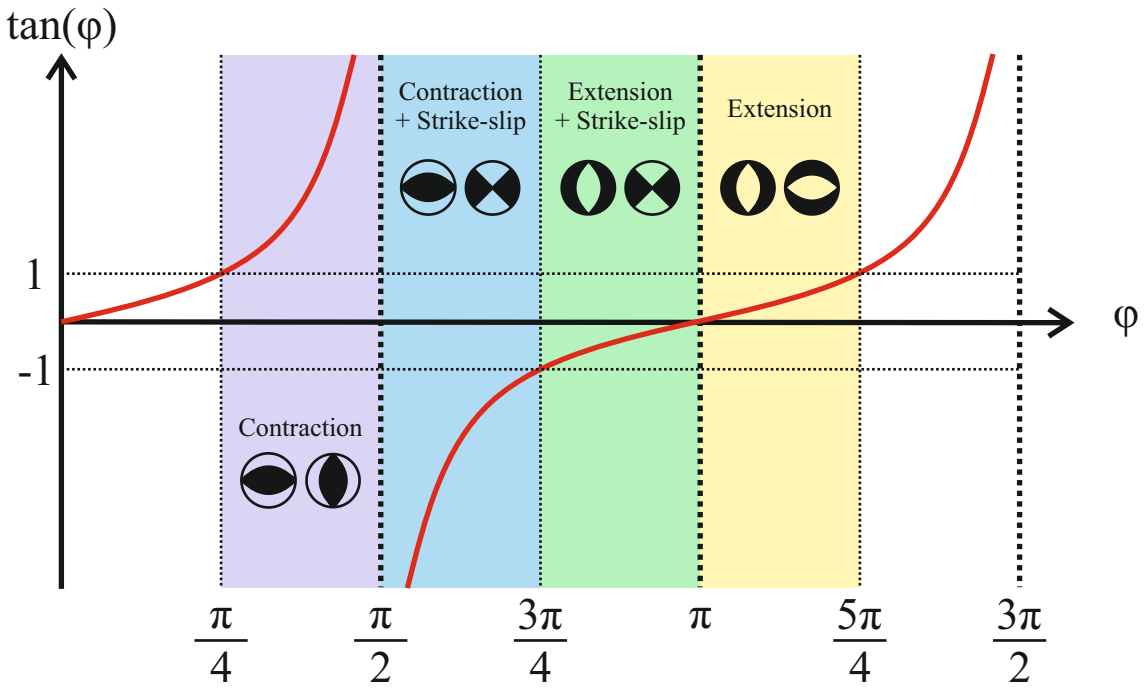


Figure C.2: Plot of $tan\,(\phi)$ against ϕ, where $tan\,(\phi) = \frac{\dot{\epsilon}_2}{\dot{\epsilon}_1}$ (red curve). Coloured zones and focal mechanisms indicate the expected styles of faulting in each ϕ range.

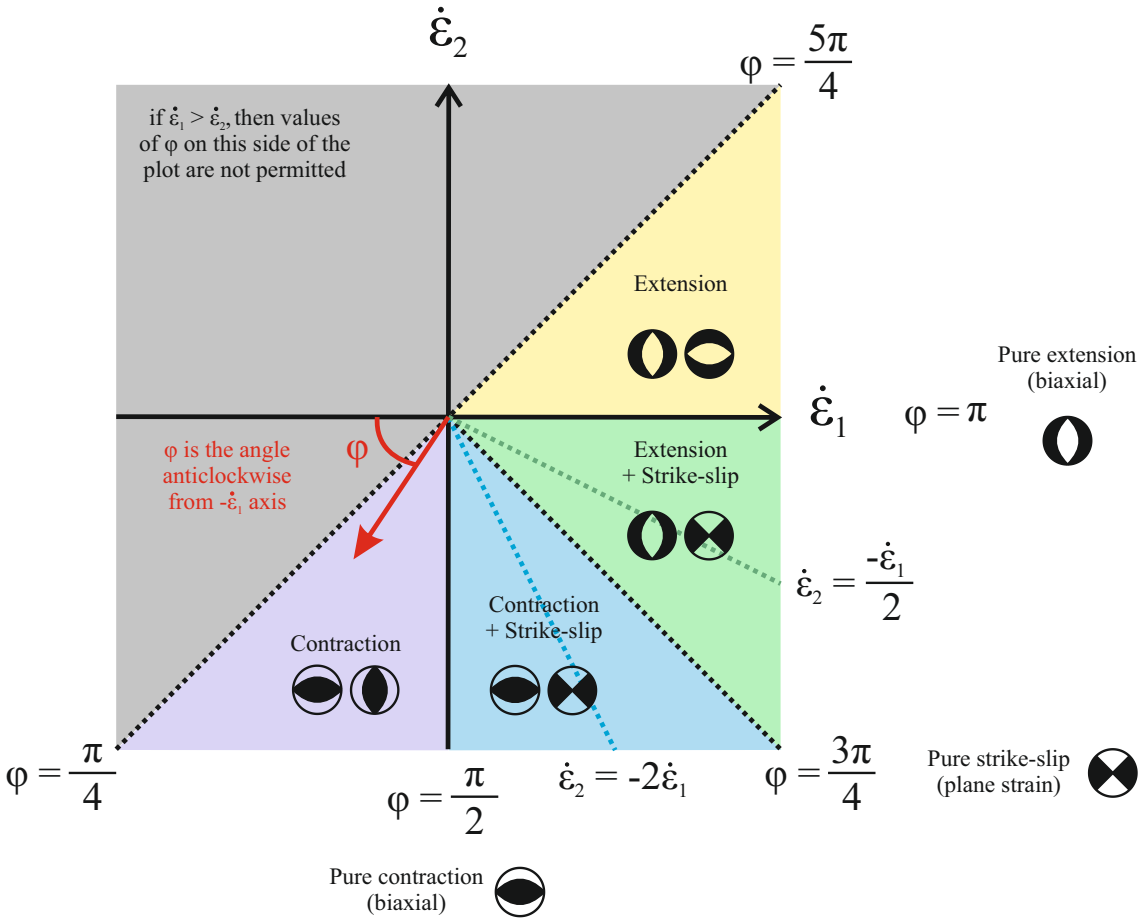


Figure C.3: Phasor diagram in $\dot{\epsilon}_2$ against $\dot{\epsilon}_1$ space. Again, coloured zones and focal mechanisms indicate the expected styles of faulting in each ϕ range.

If $\dot{\epsilon}_1$ and $\dot{\epsilon}_2$ are of opposite signs, then the strain is taken up by a combination of dip-slip and strike-slip faulting. When $\frac{\pi}{2} < \phi < \frac{3\pi}{4}$ we know that $\frac{\dot{\epsilon}_2}{\dot{\epsilon}_1} < -1$, which can only be true if $\dot{\epsilon}_1$ is positive and $\dot{\epsilon}_2$ is negative. Furthermore, $|\dot{\epsilon}_2| > |\dot{\epsilon}_1|$. We therefore expect a combination of contraction and strike-slip faulting. The relative importance of dip-slip versus strike-slip faulting can be determined from the exact value of ϕ. Reverse faulting dominates when $\dot{\epsilon}_2 < -2\dot{\epsilon}_1$ i.e. $\phi < (\pi - tan^{-1}(2))$; and strike-slip faulting dominates when $\dot{\epsilon}_2 > -2\dot{\epsilon}_1$ i.e. $\phi > (\pi - tan^{-1}(2)))$. When $\dot{\epsilon}_2 = -2\dot{\epsilon}_1$ i.e. $\phi = (\pi - tan^{-1}(2))$, the strain is accommodated by 50% reverse faulting and 50% strike-slip faulting.

Similarly, when $\frac{3\pi}{4} < \phi < \pi$ we know that $-1 < \frac{\dot{\epsilon}_2}{\dot{\epsilon}_1} < 0$, which can only be true if $\dot{\epsilon}_1$ is positive and $\dot{\epsilon}_2$ is negative. Furthermore, $|\dot{\epsilon}_1| > |\dot{\epsilon}_2|$. We therefore expect a combination of extension and strike-slip faulting. Normal faulting dominates when $\dot{\epsilon}_2 > \frac{-\dot{\epsilon}_1}{2}$ i.e. $\phi > \left(\pi - tan^{-1}\left(\frac{1}{2}\right)\right)$; and strike-slip faulting dominates when $\dot{\epsilon}_2 < \frac{-\dot{\epsilon}_1}{2}$ i.e. $\phi < \left(\pi - tan^{-1}\left(\frac{1}{2}\right)\right)$. When $\dot{\epsilon}_2 = \frac{-\dot{\epsilon}_1}{2}$ i.e. $\phi = \left(\pi - tan^{-1}\left(\frac{1}{2}\right)\right)$, the strain is accommodated by 50% normal faulting and 50% strike-slip faulting.

Appendix D

Cardboard model of Ordos Plateau kinematics

D.1 Video of the cardboard model

A video of our cardboard model illustrating the Ordos Plateau kinematics can be found at the following YouTube link.